IMPERIAL COLLEGE LONDON
Department of Civil and Environmental Engineering

Modern analysis of axisymmetric shells

Achilleas Filippidis

Submitted in fulfilment of the requirements for the degree of Doctor of Philosophy and the Diploma of Imperial College London

June 2025

Shell structures may be called
the prima donnas of structures.

Chapelle & Bathe (1998)

A sweet bit of engineering.

Bob Page (2052)

Acknowledgements

With submission of the present document, one of the more challenging chapters so far in my transition through life is nearly concluded. As with any of my previous endeavours, this effort was supported by a number of people that have not only made this possible but also an insightful experience that has allowed me to grow as both an engineer and a person, making it a meaningful journey. My utmost gratitude is due towards my supervisor, Dr. Adam J. Sadowski for his constant support and understanding throughout all years of my doctoral studies. His knowledge of the field that I have found to be increasingly more intricate as my comprehension of it grew has led to scholarly discussions generously filled with suggestions and advice.

Several people have contributed in their own way during this time, allowing me a mental break from the complexities of shell mechanics. I am very thankful for the support of all my friends, both those I have come to know through earlier years in my home town and undergraduate studies, but also the people that I have shared my experiences during these last 4 years. I wholeheartedly wish Lijithan a bright future and lasting happiness, presently sitting across me in the 412 office of the Skempton building and soon to also complete his PhD studies, extending understanding of shell structures. As always, my deepest gratitude goes to my family for supporting my efforts in every way possible, making sure that my educational journey remains unhindered.

This research was made possible through a Skempton Scholarship kindly awarded by the Department of Civil and Environmental Engineering at Imperial College London, a contribution that has been greatly appreciated.

Abstract

The load-carrying capacity of thin axisymmetric shell structures is often governed by their buckling resistance, characterised by a harmonic distribution of the modal displacement field along the shell's circumference. Despite the widespread use of commercial finite element software, the mathematical framework required for this classical stability problem is largely absent. To address this, a computational tool has been developed that tackles the inherently two-dimensional shell buckling problem on its mathematical basis, promoting the need for specialised formulations within general finite element environments and providing an open-source alternative to black-box commercial solvers. The software aligns with the EN 1993-1-6 taxonomy for shell structure design, enabling characterisation of reference systems through the capacity curve framework.

Using this tool, justification is provided for a recent amendment in the second generation of EN 1993-1-6, which concerns the assumption that the capacity curve for cylinders under meridional compression is the most conservative among reference axisymmetric shell systems. Comparative studies of cylinders under meridional compression and global bending reveal that the current provisions of the European Standard may overestimate characteristic resistance, potentially leading to unsafe designs. A detailed documentation of the sensitivity demonstrated by otherwise well-established general purpose computational software to initial modelling conditions relating to discretisation and incrementation parameters is provided as a by-product of this numerical investigation.

An analytical study of shear-flexible cylinders is also presented to establish reference solutions for the stability of thick cylinders under meridional compression and external pressure. These closed-form solutions serve as benchmarks for developing a finite-thickness two-node element for non-symmetric bifurcation buckling analysis. Finally, geometric nonlinearities are examined in meridionally compressed cylinders to identify sources of geometric hardening behaviour and the challenges in consistently modelling nonlinear axisymmetric shell response across varying slendernesses.

Declaration of Originality

I hereby declare that this thesis is the result of my own work, with any work produced by other parties appropriately acknowledged in the text. The present work has not been submitted towards a degree at any other university or institution.

Achilleas Filippidis
June 2025

Copyright Declaration

The copyright of this thesis rests with the author. Unless otherwise indicated, its contents are licensed under a Creative Commons Attribution 4.0 International Licence (CC BY).

Under this licence, you may copy and redistribute the material in any medium or format for both commercial and non-commercial purposes. You may also create and distribute modified versions of the work. This is on the condition that you credit the author.

When reusing or sharing this work, ensure you make the licence terms clear to others by naming the licence and linking to the licence text. Where a work has been adapted, you should indicate that the work has been changed and describe those changes.

Please seek permission from the copyright holder for uses of this work that are not included in this licence or permitted under UK Copyright Law.

Achilleas Filippidis
June 2025

Publications

The following journal publications are based on the present doctoral work:

- Filippidis A. & Sadowski A.J. (2023) Modern analysis of axisymmetric shells with AQUINAS: A MATLAB finite element toolbox, *SoftwareX*, 23, 101434.

- Sadowski A.J. & Filippidis A. (2025) The capacity curve framework of EN 1993-1-6 (2025): Cylindrical shells under uniform meridional compression vs uniform bending, *Journal of Constructional Steel Research*, 225, 109167.

- Filippidis A. & Sadowski A.J. (2025) Selected closed-form algebraic solutions for linear stress and buckling analyses of elastic shear-flexible axisymmetric cylindrical shells, *Structures*, 78, 109146.

A conference communication of research output was also made:

- Filippidis A. & Sadowski A.J. (2023) A MATLAB finite element toolbox for the efficient nonlinear analysis of axisymmetric shells, *ce/papers*, 6, 1735-1740.

Nomenclature

Unless explicitly stated otherwise for the purposes of a specific section, the following nomenclature holds true for the entirety of this document. Parameters and symbols that are only relevant to a specific problem statement (such as those presented in the AQUINAS Examples library of Appendix A) are omitted from this list.

A Cross-sectional area of the shell

E Young's modulus of elasticity

E_t Tangent modulus (slope of uniaxial stress–strain curve in plastic range)

G Shear modulus of material

H' Plastic hardening modulus parameter in J2 plasticity (combining E and E_t)

L Meridional length of a shell segment. Also half-length of an axisymmetric shell element (see Fig. 3.1)

M_{cl} Classical elastic critical buckling moment. Different expressions are provided for thin and thick shells

M_{el} Elastic (first-yield) bending moment. Different expressions are provided for thin and thick shells

M_{pl} Fully plastic bending moment capacity of shell. Different expressions are provided for thin and thick shells

M_ϕ Meridional bending stress resultant

M_θ Circumferential bending stress resultant

$M_{\phi\theta} - M_{\theta\phi}$ Twisting moment stress resultants

N_{pl} Fully plastic meridional load capacity of axisymmetric shell (squash load)

N_{cl} Classical elastic critical meridional load

N_{el} Elastic (first-yield) meridional load

N_ϕ Meridional membrane stress resultant

N_θ Circumferential membrane stress resultant

$N_{\phi\theta} - N_{\theta\phi}$ In-plane shear stress resultants

Q_ϕ Meridional transverse shear stress resultant

Q_θ Circumferential transverse shear stress resultant

R_{pl} Plastic reference resistance of the shell, in the context of the capacity curve framework of EN 1993-1-6 (2025)

R_{cr} Elastic critical reference resistance of the shell, in the context of the capacity curve framework of EN 1993-1-6 (2025)

R_k Characteristic buckling resistance of the shell, in the context of the capacity curve framework of EN 1993-1-6 (2025)

a Radius of a spherical segment (sphere or spherical cap). Also major (horizontal) radius of an ellipsoidal shell segment

b Minor (vertical) radius of an ellipsoidal shell segment

f_{yk} Characteristic yield stress of material

l_{gx} Imperfection reference gauge length according to EN 1993-1-6 (2025)

m Meridional half-wave number (number of half-waves along the meridian for a bifurcation buckling mode)

n Circumferential full-wave number (number of full waves around the circumference for a bifurcation buckling mode)

p_n External pressure normal to the shell reference surface

p_s Uniform distributed in-plane load (meridional traction) along the shell surface

r Radial coordinate (distance from axis of revolution to shell midsurface)

r_ϕ Meridional radius of curvature of the shell midsurface

r_θ Circumferential (hoop) radius of curvature of the shell midsurface

s Curvilinear arc-length coordinate along the shell's meridian

t Shell wall thickness

u Global radial displacement along the r axis

$\bar{u}$ Meridional displacement of the along the curvilinear s direction

v Global circumferential displacement of the shell along the θ axis

$\bar{v}$ Circumferential displacement of the shell along the θ axis. Coincides with the global circumferential displacement v for axisymmetric shells

w Global axial displacement along the z axis

$\bar{w}$ Normal to the shell wall displacement along the ζ direction

z Axial coordinate (distance along the axis of revolution)

Λ Linear elastic bending half-wavelength of cylindrical shell

Ω Dimensionless length group, see 3.95

α_G Parameter accounting for geometric nonlinear pre-buckling effects within the capacity curve framework of EN 1993-1-6 (2025) (see Table 2.2)

α_I Parameter accounting for imperfection sensitivity of shells within the capacity curve framework of EN 1993-1-6 (2025) (see Table 2.2)

β Capacity curve parameter identifying the plastic range, with $1 - \beta$ being the fraction of the full plastic load at which first yield occurs (see Table 2.2)

β_i Pseudo-rotation parameters ($i = 1, \ldots, 12$) in the nonlinear strain-displacement relations (components of vector $\{\Theta\}$ of Eq. 3.16)

$\gamma_{\phi\theta} - \gamma_{\theta\phi}$ Engineering in-plane shear strains

$\gamma_{\phi\zeta}$ Engineering meridional transverse shear strain

$\gamma_{\theta\zeta}$ Engineering circumferential transverse shear strain

δ_0 EN 1993-1-6 (2025) compliant imperfection amplitude referenced to gauge length l_{gx}

δ_m Mathematical imperfection amplitude used in the model (controls the shape function for an imperfection, approximately equal to δ_0 for the midspan weld depression imperfection)

ϵ_ϕ Meridional membrane strain

ϵ_θ Circumferential membrane strain

ζ Through the shell wall thickness coordinate, normal to the meridian

η Isoparametric meridional coordinate of a shell element

$\eta_0 - \eta_p$ Plastic range factors describing the curvature of a 'traditional' capacity curve near λ_0 and λ_p correspondingly, according to EN 1993-1-6 (2025) (see Table 2.2)

θ Circumferential angle coordinate of the shell, counter-clockwise about the axis of revolution

κ Imperfection sensitivity parameter on reference plastic collapse resista R_{pl}, according to EN 1993-1-6 (2025) (see Table 2.2)

κ_ϕ Meridional curvature (bending curvature along the meridian)

κ_θ Circumferential curvature (bending curvature in the hoop direction)

$\kappa_{\phi\theta} - \kappa_{\theta\phi}$ Twisting curvatures

λ Dimensionless slenderness parameter of a shell according to EN 1993-1-6 (2025)

λ_0 Dimensionless slenderness parameter at which the full plastic strength is attained of a shell, according to EN 1993-1-6 (2025)

λ_p Dimensionless slenderness parameter at which plasticity effects influence the load carrying capacity of a shell, according to EN 1993-1-6 (2025)

ν Poisson's ratio of material

σ_ϕ Meridional membrane stress

σ_θ Circumferential membrane stress

$\tau_{\phi\zeta}$ Meridional transverse shear stress

$\tau_{\theta\zeta}$ Circumferential transverse shear stress

ϕ Meridional angle, measuring clockwise from the axis of revolution

ϕ_0 Angular span of a spherical cap segment

χ Dimensionless buckling strength reduction factor (ratio of buckling load to plastic collapse load on a capacity curve)

ψ Dimensionless resistance of the shell, as defined in Eq. 2.29 in the context of the capacity curve framework of EN 1993-1-6 (2025)

ω Dimensionless length group, see Eq. 4.1. Also circumferential angle used in spherical harmonic functions, corresponding to Fourier mode shapes

List of abbreviations

2D 2 Dimensional
3D 3 Dimensional
DOF Degree Of Freedom
FDM Finite Difference Method (see Section 2.2.1)
FE/FEA/FEM Finite Element / Finite Element Analysis / Finite Element Method (see Section 2.2.2)
FTQC Fabrication Tolerance Quality Class
FSDT First order Shear Deformation Theory
HSDT Higher order Shear Deformation Theory
LS Limit State
LPF Load Proportionality Factor
LA Linear Analysis (see Section 1.2.2)
LBA Linear Bifurcation Analysis (see Section 1.2.2)
MNA Materially Nonlinear Analysis (see Section 1.2.2)
GNA Geometrically Nonlinear Analysis (see Section 1.2.2)
GNIA Geometrically Nonlinear Analysis with explicitly defined Imperfections (see Section 1.2.2)
GMNA Geometrically and Materially Nonlinear Analysis (see Section 1.2.2)
GMNIA Geometrically and Materially Nonlinear Analysis with explicitly defined Imperfections (see Section 1.2.2)
MITC Mixed Interpolation of Tensorial Components
PLC Primary Load Cases
RRD Reference Resistance Design (see Section 2.4.4)
SMO Surrogate Model Optimisation
TL Total Lagrangian (see Section 2.2.2.3)
UL Updated Lagrangian (see Section 2.2.2.3)

Contents

Chapter 1 Introduction **1**
1.1 Preamble . . . 1
1.2 The European Standard EN 1993-1-6 for the design of steel shells . . . 2
1.2.1 Design limit states . . . 2
1.2.2 Analysis types and their scope in EN 1993-1-6 . . . 3
1.3 Research objectives . . . 5
1.4 Research approach . . . 6
1.5 Thesis outline . . . 7

Chapter 2 Literature review **11**
2.1 Axisymmetric shell theories . . . 11
2.1.1 General assumptions . . . 11
2.1.2 Fundamental (pre-buckling) state for shells of revolution . . . 13
2.1.3 Buckling considerations for shells of revolution . . . 20
2.2 Computational methods for shells of revolution . . . 31
2.2.1 Finite difference methods . . . 32
2.2.2 Finite element formulations . . . 33
2.2.3 Meta-elements . . . 37
2.3 Axisymmetric shell solvers . . . 38
2.4 The capacity curve framework of EN 1993-1-6 . . . 42
2.4.1 Design through GMNIA . . . 46
2.4.2 Stress design . . . 47
2.4.3 The LBA-MNA method . . . 48
2.4.4 The Reference Resistance Design method . . . 49
2.4.5 On the generation of capacity curves . . . 50

Chapter 3 The AQUINAS-FE software **52**
3.1 Motivation . . . 52
3.2 Geometric definition . . . 53
3.3 Kinematic relations . . . 56
3.3.1 Linear strain-displacement relations . . . 57
3.3.2 Nonlinear strain-displacement relations . . . 58
3.4 Constitutive relations . . . 59
3.5 Finite Element Formulation . . . 62
3.5.1 Condensation of nodal variables . . . 66
3.5.2 Recovery of nodal variables . . . 70
3.6 Software capabilities . . . 70
3.6.1 Geometric definitions . . . 71
3.6.2 Analysis types . . . 76
3.6.3 Optimisation . . . 77

3.7 Software architecture . . . 79
3.7.1 Flow of control in AQUINAS . . . 82
3.7.2 Class descriptions . . . 82
3.7.3 Procedure descriptions . . . 86
3.8 Generation of capacity curves with AQUINAS-FE . . . 91
3.8.1 Capacity curves for axially compressed cylinders with weld depression imperfections . . . 91
3.8.2 Capacity curves for axially compressed cylinders with axisymmetric eigenmode affine imperfections . . . 94
3.9 Concluding remarks . . . 95

Chapter 4 On the generation of capacity curves for meridional compression and uniform bending 98
4.1 Motivation . . . 98
4.2 Uniform meridional compression vs uniform bending: a computational justification 102
4.2.1 Natively axisymmetric finite element modelling of cylindrical shells under uniform meridional compression . . . 102
4.2.2 3D finite element modelling of cylinders under uniform bending . . . 104
4.2.3 A comparison of the α_G, α_I and β capacity parameters for cylinders under uniform meridional compression vs uniform bending . . . 106
4.3 On complications in the generation of computational capacity curves . . . 108
4.3.1 Sensitivity to initial conditions . . . 112
4.3.2 Alternative generation strategy based on varying f_{yk} . . . 114
4.3.3 Limitations of the AQUINAS thin shell element formulation for low slenderness cylindrical shells . . . 116
4.4 Conclusions . . . 119

Chapter 5 Linear stress and bifurcation buckling analyses of shear-flexible axisymmetric cylindrical shells 121
5.1 Motivation . . . 121
5.2 Introduction . . . 122
5.2.1 Developments on shear-flexible shell theories for cylindrical shells . . . 122
5.2.2 A case for closed-form elastic critical buckling predictions for shear-flexible cylinders under meridional compression . . . 125
5.3 Stress analysis of finite-thickness elastic isotropic cylindrical shells under the combined action of meridional edge load and normal pressure . . . 127
5.3.1 Kinematic relations . . . 127
5.3.2 Constitutive relations . . . 128
5.3.3 Equilibrium equations for axisymmetric cylinders . . . 129
5.3.4 System of equations . . . 130
5.3.5 Solution of the homogeneous problem for a thick cylinder . . . 131
5.3.6 Particular solution to the inhomogeneous problem for a thick cylinder . . . 134
5.3.7 Bending theory solution to cylinder under meridional edge load and normal pressure . . . 134
5.4 Linear bifurcation buckling of cylindrical shells under uniform meridional compression and uniform external pressure . . . 135
5.4.1 Adjacent equilibrium criterion . . . 136
5.5 Examples . . . 140
5.5.1 Linear elastic stress analysis examples for shear-flexible axisymmetric cylinders . . . 141

5.5.2 Linearised stability analysis for shear-flexible cylinders . . . 141
5.6 Conclusions . . . 148

Chapter 6 Challenges in the development of a shear-flexible axisymmetric shell element 149
6.1 Motivation . . . 149
6.2 Approaches and scope of development . . . 150
6.2.1 Extension of the AQUINAS element formulation . . . 150
6.2.2 Derivation and implementation aspects for a new axisymmetric shell element 153
6.3 Principles of finite element formulation . . . 155
6.3.1 Derivation of shear-flexible axisymmetric shell strains . . . 155
6.3.2 Formulation of the axisymmetric finite element . . . 161
6.4 Examination of shear-flexible computational solutions and discussion . . . 167
6.4.1 Linear elastic stress analysis results . . . 167
6.4.2 Linear elastic bifurcation buckling analysis results for axisymmetric and nonsymmetric modes . . . 171
6.4.3 Materially nonlinear stress analysis performance of linearly interpolated element . . . 174
6.4.4 Capacity curve computation and solution quality scrutiny for the shear-flexible axisymmetric shell element . . . 178
6.5 Concluding remarks . . . 183

Chapter 7 Research outcomes and prospects for further research 185
7.1 Research outcomes . . . 185
7.2 Further research prospectives . . . 188

Bibliography 190

Appendix A Axisymmetric shell problem examples library of AQUINAS 211
A.1 Introduction . . . 211
A.2 LAs . . . 213
A.2.1 Example LA01: Thin cylinder under meridional compression and internal pressure . . . 213
A.2.2 Example LA02: Thin cylinder with midsurface eccentricity under meridional compression and internal pressure . . . 213
A.2.3 Example LA03: Multi-strake cylindrical silos with step-wise varying thickness under nonlinear loading . . . 216
A.2.4 Example LA04: Conical shell under axial uniform pressure . . . 218
A.2.5 Example LA05: Spherical shell segment with an outward radial edge load 220
A.2.6 Example LA06: Spherical cap subjected to uniform vertical pressure . . . 220
A.2.7 Example LA07: LA of a thin elliptical shell cap under uniform pressure . 223
A.2.8 Example LA08: LA of a thin ogival shell under self weight pressure . . . 224
A.2.9 Example LA09: LA of a thin hyperboloid under an axial edge load . . . 227
A.2.10 Example LA10: LA of a thin multi-segment shell under normal pressure . 227
A.2.11 Example LA11: Thin circular plate with clamped edges under uniform pressure . . . 230
A.2.12 Example LA12 : LA of a thin toroid shell with uniform internal pressure 231
A.3 LBAs . . . 232
A.3.1 Example LBA01: LBA of a thin cylindrical shells of varying length under uniform meridional compression . . . 234

A.3.2 Example LBA02: LBA of a thin cylinder under meridional compression and direct comparison with the Koiter circle . . . 236
A.3.3 Example LBA03: LBA of a thin cylindrical shell under uniform lateral pressure . . . 237
A.3.4 Example LBA04: Koiter ellipse for a thin truncated cone under uniform axial compression . . . 239
A.3.5 Example LBA05: Bifurcation modes of a thin spherical shell under uniform external pressure . . . 242
A.4 MNAs . . . 245
A.4.1 Example MNA01: MNA of a thin cylinder under uniform meridional compression . . . 246
A.4.2 Example MNA02: MNA of a simply-supported circular plate under concentrated load . . . 246
A.4.3 Example MNA03: MNA of a clamped spherical caps under uniform external pressure . . . 249
A.5 GNAs . . . 250
A.5.1 Example GNA01: GNA of thin cylindrical shells under uniform meridional compression . . . 250
A.5.2 Example GNA02: GNA of the Belleville spring . . . 252
A.5.3 Example GNA03: GNA of a thin spherical cap under uniform external pressure . . . 253
A.5.4 Example GNA04: GNA of a ring-loaded thin spherical cap . . . 254
A.5.5 Example GNA05: Snap-through of a shallow spherical cap . . . 256
A.5.6 Example GNA06: Nonlinear buckling analysis of a clamped shallow spherical cap under uniform external pressure . . . 256
A.6 GNIAs . . . 257
A.6.1 Example GNIA01: GNIA of a thin unpressurised cylinder under uniform axial compression with a weld depression imperfection . . . 258
A.6.2 Example GNIA02: GNIA of a thin pressurised cylinder under uniform meridional compression with a weld depression imperfection . . . 259
A.7 GMNAs . . . 262
A.7.1 Example GMNA01: Nominal capacity curve generation for cylinders of varying slenderness under uniform meridional compression . . . 264
A.7.2 Example GMNA02: Elastic-plastic collapse load predictions for a pressurised cylinder under uniform meridional compression . . . 266
A.8 GMNIAs . . . 267
A.9 Miscellaneous . . . 268
A.9.1 Example MISC01: Parallel scaling analysis . . . 268

Appendix B Comparative assessment of the AQUINAS element performance in the context of different EN 1993-1-6 analyses 269
B.1 Element efficiency comparison against the ABAQUS SAX1 and SAX2 formulations 270
B.1.1 Performance comparison through controlling the meridional discretisation 270
B.1.2 Performance comparison through controlling the sum of integration points along the meridian . . . 272
B.2 Performance characteristics of the AQUINAS element in the scope of different analysis procedures . . . 272

Appendix C Closed-form relationships for the critical bifurcation buckling load of shear-flexible cylinder under uniform meridional compression or normal pressure **276**
C.1 Uniform meridional compression 276
C.2 External pressure 277

Appendix D Strain-displacement $[B_l]$ and pseudo rotation $[G]$ matrices for shear-flexible axisymmetric shell element **279**
D.1 Linear strain-displacement matrix $[B_l]$ 279
D.2 Pseudo rotation matrix $[G]$ 280
D.3 Stress resultants array $[N_0]$ 282

List of Figures

1.1 Shell structures meeting the needs of multidisciplinary engineering demands (images obtained from wikipedia.com, airbus.com and shellbuckling.com, all accessed on 4th February 2025). 2
1.2 Experimental results for cylinders under meridional compression with illustrations of traditional lower bound fit relationships for the design of shell structures of varying slenderness (figure according to Rotter (2010a) for data collected by Harris *et al.* (1957)). 7
1.3 Collected test vs synthetic Monte Carlo datasets for χ against λ and ψ (traditional and modified forms of a capacity curve accordingly) for test specimens with a longitudinally overlap-joined systematic fabrication imperfection and an imposed deterministic load application non-uniformity (data provided by Sadowski *et al.* (2023)). 8

2.1 Geometry of axisymmetric shell. 12
2.2 Membrane N, shear Q and bending M stress resultant equilibrium expressed on an infinitesimally small $ds \cdot rd\theta$ panel of an axisymmetric shell structure, the geometric characteristics of which are displayed in Figure 2.1. 14
2.3 Different types of load-deflection paths relevant to the pre-buckling and post-buckling states of perfect and imperfect structures. λ represents a load proportionality factor (not to be confused with the slenderness parameter later on) while δ_b represents modal displacement associated with the buckling event. 21
2.4 Differences in the critical buckling load prediction for linear or nonlinear tracing of the pre-buckling state of a generic axisymmetric shell structure, with an illustration of mode-switching along the post-buckling response. 23
2.5 Effect of increasing imperfection amplitudes on the elastic response of cylindrical shells under meridional compression through different illustrations of the meridional stress level against the deformation, as analytically studied by Donnell & Wan (1950) on the left or computationally explored by Hong & Teng (2008) on the right. 25
2.6 Koiter circle for simultaneously critical pairs of meridional half-waves m and circumferential waves n for pin-ended cylinders under meridional compression. . 28
2.7 3D surface of analytical elastic buckling predictions corresponding to different $m - n$ modal pairs. 29
2.8 Schematic demonstration of strategies in the derivation of shell finite elements. . 35
2.9 Illustration of generic wire-arc shell elements (left) against solid-continuum shell elements (right) in the 2D axisymmetric modelling space. 36
2.10 3D surface plot of computed nonlinear buckling loads and mode wave numbers as a function of length, generated by Sadowski *et al.* (2018). 39

2.11 Schematic representation of the capacity curve framework used in EN 1993-1-6 (2025), in 'traditional' χ vs λ form (left) and 'modified' (Rotter) χ vs ψ form (right), as adapted from Sadowski & Filippidis (2025). 44
2.12 Analysis hierarchy to establish RRD parameters from system variables, adjusted from Sadowski *et al.* (2017a) for general shell reference systems. 51

3.1 Meridional geometry of a curved shell finite element. 54
3.2 Element Degrees of Freedom. 55
3.3 Local and global Degrees of Freedom. 55
3.4 Uniaxial stress-strain curve and incremental plastic reversibility assumption. . . 60
3.5 Segment intersection with discontinuous meridional curvature 67
3.6 Meridional geometry definition of a plate segment. 72
3.7 Meridional geometry definition of a conical segment. 72
3.8 Meridional geometry definition of an elliptical segment. 73
3.9 Meridional geometry definition of a circular arc segment defined through three points. 75
3.10 Meridional geometry definition of an interpolated segment, defined through a series of points. 76
3.11 Initial training of surrogate model. 79
3.12 First training step in the surrogate optimisation process. 79
3.13 Second training step in the surrogate optimisation process. 80
3.14 Third training step in the surrogate optimisation process. 80
3.15 Fourth training step in the surrogate optimisation process. 80
3.16 Fifth (and final) training step in the surrogate optimisation process. 80
3.17 AQUINAS Surrogate Optimisation flowchart. 81
3.18 AQUINAS general flow of control diagram 83
3.19 AQUINAS Geometrically and/or Materially Nonlinear Analysis flowchart. 90
3.20 Exaggerated imperfect meridional geometry for a Type A weld depression imperfection. 92
3.21 Dimensionless traditional (left) and modified 'Rotter' (right) nominal capacity curves for meridionally compressed cylinders with a midspan Type A weld depression imperfection shape. 93
3.22 Exaggerated imperfect meridional geometry for an eigenmode affine imperfection shape. 94
3.23 Dimensionless traditional (left) and modified 'Rotter' (right) nominal capacity curves for meridionally compressed cylinders with an eigenmode affine imperfection shape. 96

4.1 Computational illustration of the four length domains governing geometric nonlinearity in perfect elastic cylinders under uniform bending, as generated using ABAQUS by Fajuyitan *et al.* (2015). 100
4.2 Comparison of capacity curves for cylindrical shells uniform meridional compression and uniform bending in EN 1993-1-6 (2025) in χ vs λ ('traditional' form, left) and in χ vs ψ ('modified' form, right), as presented in Sadowski & Filippidis (2025). The letters A, B and C respectively represent 'Excellent', 'High' and 'Normal' Fabrication Tolerance Quality Classes (FTQCs). Note that $\kappa = 1$ for meridional compression (red results) but $\kappa \neq 1$ for bending (blue results). 101
4.3 Natively axisymmetric finite element model of a medium-length imperfect cylinder under uniform meridional compression. The full cylinder in a) is shown with grey solid lines denoting complete represented geometry and black solid lines denoting actually modelled single meridian geometry in b) using AQUINAS. 103

4.4 Variation of the $\kappa_{thin} = N_{pl,imp}/N_{pl}$ 'plastic imperfection sensitivity' relationship with r/t (which in fact shows independence) and δ_0/t for medium-length thin cylinders with $\Omega = 0.5$ and a midspan 'Type A' weld depression imperfection. . . 104
4.5 κ_{thin} for a thin cylinder under uniform meridional compression (as $N_{pl,imp}/N_{pl}$) and for one under uniform bending (as $M_{pl,imp}/M_{pl}$) representing 'plastic imperfection sensitivity' relationships for medium-length cylinders with a 'Type A' midspan weld depression imperfection. 105
4.6 Quarter-shell finite element model of a medium-length imperfect cylinder under uniform bending. The full cylinder is shown with grey solid lines denoting complete represented geometry and black solid lines denoting actually modelled quarter-shell geometry using ABAQUS. 106
4.7 A comparison of computed capacity curves for nominally perfect ($\kappa \approx 1$) medium-length cylinders ($\delta_0/t = 0.001$, $\Omega = 0.5$) under uniform meridional compression (red, computed with AQUINAS) or uniform bending (blue, computed with ABAQUS). 107
4.8 Portion of cylinders' circumferences under compression participating in critical buckling and compression or tension participating in yielding, with associated representative λ-dependent bifurcation or incremental buckling modes. 109
4.9 Dimensionless capacity curves for cylinders under uniform meridional compression (red) and uniform bending (blue) for a constant dimensionless group $\Omega = 0.5$ and varying imperfection amplitude δ_0/t. 110
4.10 Computed 'elastic imperfection reduction' α_I and corresponding 'plastic range' $1 - \beta$ parameters for varying imperfection amplitude δ_0/t. 111
4.11 A comparison of computed capacity curves for nominally perfect cylinders under uniform bending in the 'modified' χ vs ψ format for constant *dof* counts but varying circumferential mesh gradings, compared against the reference capacity curve. 112
4.12 A comparison of computed capacity curves for nominally perfect cylinders under uniform bending in the 'modified' χ vs ψ format for an increasingly refined circumferential mesh resolution, compared against the reference capacity curve. . 113
4.13 A comparison of computed capacity curves for nominally perfect cylinders under uniform bending in the 'modified' χ vs ψ format for an increasingly refined meridional mesh resolution, compared against the reference capacity curve. . . . 114
4.14 A comparison of computed capacity curves for nominally perfect cylinders under uniform bending in the 'modified' χ vs ψ format for increasingly fine max. load increments at constant mesh resolution, compared against the reference capacity curve. 114
4.15 A comparison of computed capacity curves for nominally perfect cylinders under uniform bending in the 'modified' χ vs ψ format generated by varying f_{yk}, compared against the reference capacity curve generated by varying r/t. 116
4.16 A comparison of computed capacity curves for nominally perfect cylinders under uniform meridional compression in the traditional χ vs λ format for fully axisymmetric shell models, with FE solutions obtained through ABAQUS and AQUINAS. Only axisymmetric buckling modes were permitted during the AQUINAS GMNA runs. 118

5.1 A comparison of characteristic (left) and modified (right) computed capacity curves for nominally perfect ($\kappa \approx 1$) medium-length cylinders under uniform bending, normalised against a thin shell theory critical buckling resistance $R_{cr,thin}$ or a non-shallow finite-thickness shell theory $R_{cr,thick}$ prediction. 126

5.2 Cylindrical shell system . . . 127
5.3 Cylinder under uniform meridional compression. . . . 142
5.4 Meridional (left) and circumferential (right) axisymmetric stress patterns for a cylinder under uniform meridional compression. . . . 142
5.5 Cylinder under uniform external pressure. . . . 143
5.6 Meridional (left) and circumferential (right) axisymmetric stress patterns for a cylinder under uniform external pressure. . . . 144
5.7 Normalised critical loads for cylinders under uniform meridional compression, considering only axisymmetric modes. . . . 145
5.8 Surfaces of analytically evaluated loads with respect to the $m-n$ pairs for a cylinder under uniform meridional compression, according to thin and thick cylindrical shell theories. . . . 145
5.9 Normalised critical bifurcation pressures p_{cr} for selected r/t ratios and varying lengths for any possible combinations of $m-n$ wavenumbers. . . . 147

6.1 Shape functions for the interpolation of normal displacement $\bar{w}$ (left) and meridional rotation β_ϕ (right) fields for varying amplitudes of the ψ parameter. Solid lines are associated to interpolation fields utilising the nodal translational DOF $\bar{w}$ while dashed lines utilise the nodal rotational DOF β_ϕ, as per Eq. 6.4. Higher colour transparency corresponds to higher values for the ψ stiffness ratio, representing considerably shear-flexible elements, while more opaque colours correspond to more slender elements that match regular Hermitian cubic shape functions as $\psi \to 0$. . . . 152
6.2 Axisymmetric shell system, illustrating the different conventions for the displacements and rotations used to describe its deformed geometry. . . . 156
6.3 Meridional $\bar{u}$ and normal $\bar{w}$ axisymmetric displacement profiles for a cylinder under uniform meridional compression. . . . 168
6.4 Meridional (left) and circumferential (right) axisymmetric stress patterns for a cylinder under uniform meridional compression. . . . 169
6.5 Meridional $\bar{u}$ and normal $\bar{w}$ axisymmetric displacement profiles for a cylinder under uniform external pressure. . . . 169
6.6 Meridional (left) and circumferential (right) axisymmetric stress patterns for a cylinder under uniform external pressure. . . . 170
6.7 Axisymmetric spherical part model under a radially outwards edge load, exploiting meridionally symmetry through appropriate boundary conditions. . . . 171
6.8 Global radial u and axial w axisymmetric displacement profiles for a spherical part under a radial edge load with respect to a normalised ϕ angle distance from a midspan plane of meridional symmetry. . . . 172
6.9 Meridional (left) and circumferential (right) axisymmetric stress patterns for a spherical part under a radial edge load with respect to a normalised ϕ angle distance from a midspan plane of meridional symmetry. . . . 172
6.10 Computational and analytical predictions of critical buckling loads for cylinders under uniform meridional compression, considering only axisymmetric modes. . . . 173
6.11 Computational predictions of critical bifurcation pressures p_{cr} for selected r/t ratios and varying lengths for any possible combinations of $m-n$ wavenumbers, compared against various analytically obtained theoretical results. . . . 175
6.12 Circular plate under an axial concentrated force, applied on the axis of axisymmetry. 176
6.13 Simply-supported circular plate bending under an axial force applied at the axis of revolution. . . . 177

6.14 A comparison of computed capacity curves for nominally perfect cylinders under uniform meridional compression in the traditional χ vs λ format for fully axisymmetric shell models, with FE solutions obtained through ABAQUS and AQUINAS explicitly thin and thick element formulations. Only axisymmetric buckling modes were permitted during the AQUINAS GMNA runs. 179
6.15 Equilibrium paths for stocky meridionally compressed cylindrical shell according to different finite element formulations, considering a Poisson's ratio of $\nu = 0.3$ corresponding to structural steel on the left sub-figure (a) and an unrealistic for civil engineering shell applications Poisson's ratio $\nu = 0.0$ on the right sub-figure (b). 181
6.16 A comparison of computed capacity curves for nominally perfect cylinders under uniform meridional compression in the traditional χ vs λ format for fully axisymmetric shell models, with FE solutions obtained through the AQUINAS thick formulation examining the effects of incompressible cross-sectional behaviour. Only axisymmetric buckling modes were permitted during the AQUINAS GMNA runs. 183

A.1 LA01 - System diagram. 214
A.2 LA01 - Comparison of meridional stresses in the inner, middle and outer surface of the shell wall. 214
A.3 LA01 - Comparison of circumferential stresses in the inner, middle and outer surface of the shell wall. 215
A.4 LA02 - System diagram. 215
A.5 LA02 - Comparison of meridional stresses in the inner, middle and outer surface of the shell wall. 216
A.6 LA02 - Comparison of circumferential stresses in the inner, middle and outer surface of the shell wall. 216
A.7 LA03 - System diagram. 217
A.8 LA03 - Comparison of midsurface meridional stresses of the shell wall. 218
A.9 LA03 - Comparison of midsurface circumferential stresses of the shell wall. . . . 218
A.10 LA04 - System diagram. 219
A.11 LA04 - Comparison of inner, middle and outer surface meridional stresses of the conical shell wall. 219
A.12 LA04 - Comparison of inner, middle and outer surface circumferential stresses of the conical shell wall. 220
A.13 LA05 - System diagram. 221
A.14 LA05 - Comparison of inner, middle and outer surface meridional stresses of the spherical zone. 221
A.15 LA05 - Comparison of inner, middle and outer surface circumferential stresses of the spherical zone. 222
A.16 LA06 - System diagram. 222
A.17 LA06 - Comparison of inner, middle and outer surface meridional stresses of the spherical cap. 223
A.18 LA06 - Comparison of inner, middle and outer surface circumferential stresses of the spherical cap. 223
A.19 LA07 - System diagram. 224
A.20 LA07 - Comparison of inner, middle and outer surface meridional stresses of the spherical cap. 225
A.21 LA07 - Comparison of inner, middle and outer surface circumferential stresses of the spherical cap. 225

A.22 LA08 - System diagram. . . . 226
A.23 LA08 - Comparison of meridional stresses in the inner, middle and outer surface of the shell wall. . . . 226
A.24 LA08 - Comparison of circumferential stresses in the inner, middle and outer surface of the shell wall. . . . 227
A.25 LA09 - System diagram. . . . 228
A.26 LA09 - Comparison of meridional stresses in the inner, middle and outer surface of the shell wall. . . . 228
A.27 LA09 - Comparison of circumferential stresses in the inner, middle and outer surface of the shell wall. . . . 229
A.28 LA10 - System diagram. . . . 229
A.29 LA10 - Comparison of meridional stresses in the inner, middle and outer surface of the shell wall. . . . 230
A.30 LA10 - Comparison of circumferential stresses in the inner, middle and outer surface of the shell wall. . . . 231
A.31 LA11 - System diagram. . . . 231
A.32 LA11 - Comparison of top, middle and bottom surface radial stresses of the circular plate. . . . 232
A.33 LA11 - Comparison of top, middle and bottom surface circumferential stresses of the circular plate. . . . 232
A.34 LA12 - System diagram. . . . 233
A.35 LA12 - Comparison of circumferential stresses in the inner, middle and outer surface of the shell wall. . . . 233
A.36 LA12 - Comparison of circumferential stresses in the inner, middle and outer surface of the shell wall. . . . 234
A.37 LBA01 - System diagram. . . . 235
A.38 LBA01 - Development of critical bifurcation load with respect to the dimensionless length parameter Ω. . . . 235
A.39 LBA01 - Buckling loads for various values of the dimensionless length parameter Ω and circumferential modes n. . . . 236
A.40 LBA02 - Analytically and computationally obtained buckling loads $N_{m,n}$ for a cylinder under meridional compression. . . . 237
A.41 LBA03 - System diagram. . . . 238
A.42 LBA03 - Variation of k_p and β with the Batdorf parameter Z for a C1-C1 boundary condition case. . . . 239
A.43 LBA03 - Development of critical buckling pressure ratio p_{cr}/p_{cl} with respect to the dimensionless length parameter Ω. . . . 240
A.44 LBA03 - Buckling pressures for various values of the dimensionless length parameter Ω and circumferential modes n. . . . 240
A.45 LBA04 - System diagram. . . . 241
A.46 LBA04 - Locus of simultaneous buckling modes with $N \leq 1.02N_{cone}$ for a cone with a tapering angle $\alpha = 15°$ in the $\bar{\beta}_m$ - $\bar{\beta}_c$ dimensionless wave-number space. . . . 242
A.47 LBA05 - System diagram. . . . 243
A.48 LBA05 - Normalised critical bifurcation pressure for varying r/t ratios of full spherical shells. . . . 244
A.49 LBA05 - Critical circumferential mode for varying r/t ratios of full spherical shells under external pressure. . . . 244
A.50 LBA05 - Order m and degree n of associated Legendre polynomials for spheres of varying r/t ratios under external pressure. . . . 245
A.51 MNA01 - System diagram. . . . 246

A.52 MNA01 - Top edge deflection equilibrium path for a thin unpressurised cylinder under meridional compression. 247
A.53 MNA02 - System diagram. 247
A.54 MNA02 - Dimensionless deflection equilibrium path of circular plate's centroid w_c. 248
A.55 MNA02 - Development of meridional membrane stress resultants M_ϕ. 248
A.56 MNA02 - Development of circumferential membrane stress resultants M_θ. 249
A.57 MNA03 - System diagram. 249
A.58 GNA01 - Comparison of geometrically nonlinear critical bifurcation loads and associated circumferential modes for cylinders of varying length under axial compression. 251
A.59 GNA01 - Automated identification of the critical geometrically nonlinear GNA bifurcation buckling load for a thin cylindrical shell under uniform meridional compression as a function of the Batdorf dimensionless length parameter Z, with comparison against the 3D 'panel models' from ABAQUS. 252
A.60 GNA02 - System diagram. 253
A.61 GNA02 - Equilibrium path for the Belleville spring. 253
A.62 GNA03 - System diagram. 254
A.63 GNA03 - Equilibrium path for apex deflection of shallow spherical cap under external 254
A.64 GNA04 - System diagram. 255
A.65 GNA04 - Load-deflection curves of ring loaded spherical caps 255
A.66 GNA05 - System diagram. 256
A.67 GNA06 - System diagram. 257
A.68 GNIA01 - System diagram. 260
A.69 GNIA01 - Critical dimensionless loads for increasing amplitudes of a TYPE A weld depression imperfection. 260
A.70 GNIA01 - Critical circumferential bifurcation modes for increasing amplitudes of a TYPE A weld depression imperfection. 261
A.71 GNIA01 - Bifurcation modes for selected imperfection amplitudes of a TYPE A weld depression. 261
A.72 GNIA02 - System diagram. 262
A.73 GNIA02 - Critical dimensionless loads for increasing amplitudes of a TYPE A weld depression imperfection for cylinders under combined meridional compression and internal pressure. 263
A.74 GNIA02 - Bifurcation modes for selected dimensionless pressure ratios $\bar{p}$ of cylinders with a TYPE A weld imperfection shape, with an amplitude ratio of $\delta_0/t = 1.5$, under combined meridional compression and internal pressure. 263
A.75 GMNA01 - System diagram. 264
A.76 GMNA01 - Traditional (left) and modified (right) capacity curves for cylinder under meridional compression for a dimensionless length $\Omega = 1$. 266
A.77 GMNA02 - System diagram. 267
A.78 GMNA02 - Collapse load predictions for pressurised cylinders under meridional compression for $r/t = 250, 500, 1000, 2000$ ratios. 267
A.79 MISC01 - Parallel scaling analysis of AQUINAS on a simple LA problem, where the source of concurrency is the matrix assembler. 268

B.1 Development of average execution times and associated standard deviations in a direct comparison of total solver times between ABAQUS and AQUINAS for meridional mesh resolutions corresponding to equal numbers of elements employed. 271

B.2 Development of average execution times and associated standard deviations in a direct comparison of total solver times between ABAQUS and AQUINAS for meridional mesh resolutions corresponding to equal total sums of integration points used. 273
B.3 Scaling of average computation times and associated 95% confidence intervals variability with progressively higher mesh resolutions for individual internal processes in AQUINAS associated with an LA, expressed as a percentage of total execution time. 274
B.4 Scaling of average computation times and associated 95% confidence intervals variability with progressively higher mesh resolutions for individual internal processes in AQUINAS associated with an LBA, expressed as a percentage of total execution time. 274
B.5 Scaling of average computation times and associated 95% confidence intervals variability with progressively higher mesh resolutions for individual internal processes in AQUINAS associated with an GNA, expressed as a percentage of total execution time. 275

List of Tables

1.1 Relevance of computational analyses to the four limit states LS1-LS4 in the context of EN 1993-1-6 (2025), as discussed in section 4.2 therein. 4

2.1 Different components and their purpose within the FELASH suite (Rotter, 1989; Jumikis, 1987). 41
2.2 Definitions and scope of parameters and resistances within the capacity curve framework of EN 1993-1-6 (2025), adopted from Sadowski & Filippidis (2025). . 45

A.1 Classification of shell clamped boundary conditions from Yamaki Yamaki (1984) 211
A.2 Classification of shell simply supported boundary conditions from Yamaki (1984) 212
A.3 Classification of shell boundary conditions from EN 1993-1-6 (2025) 212
A.4 LA03 - Length h and thickness t of cylindrical segments 217
A.5 LA10 - Meridional and circumferential membrane stress resultants at the shell junctions, obtained from Table 2.1 of Heyman (1977), with reference to Figure A.28. 230
A.6 MNA03 - Limit loads of clamped spherical caps under uniform pressure. 250
A.7 GNA05 - Snap-through loads $\frac{p_{cr}}{p_0}$ of shallow clamped spherical caps for a range of rise parameters λ. 257
A.8 GNA06 - Critical nonlinear buckling pressure ratios p_{cr}/p_0 for a range of rise parameters λ. 258
A.9 GNA06 - Critical circumferential buckling mode n_{cr} for a range of rise parameters λ. 258

Chapter 1

Introduction

1.1 Preamble

The significance of shell structures in any modern country's infrastructure has been extensively discussed in research works and review studies on the field. Their efficient and reliable design is of paramount importance to the economic advance of any 21^{st} century society, providing swift installations and sustainable solutions to a variety of structural problems. The rapid developments in the fabrication process of constructional steel have only facilitated the wider utilisation of shell structural systems across several sectors of human activities, from storage containers like silos and tanks all the way to aircraft fuselages. Their form manifests an optimised way of material usage, maximising load bearing capacity while maintaining a minimal overall structure weight. Capitalisation of a shell's key characteristic, its curvature, allows for a controlled distribution of stresses that enhances mechanical behaviour through a reduction of stress concentrations at corners or abrupt geometric transitions. Owing to their smooth curved surfaces, shell structures additionally exhibit an aesthetic quality that makes them highly attractive for a range of engineering challenges in which visual appeal is a factor.

In alignment with the United Kingdom's commitment to the net zero carbon emissions policy, to be achieved by 2050 as outlined in the Paris Agreement of the United Nations Framework Convention on Climate Change (2015), the energy sector is undergoing a shift toward renewable sources while reducing reliance on coal burning and other high-emission energy generation practices. Wind energy is at the heart of this transition, with the majority of renewable energy being a product of wind force conversion (Blanco, 2009; Crabtree *et al.*, 2015; Lu *et al.*, 2020), resulting in considerable efforts focused on the efficient design and erection of wind turbines (Gupta, 2015; Fadaei *et al.*, 2024), with closer examinations of their independent energy outputs (Mirecki *et al.*, 2007) but also as parts of wind farm systems (Feng & Shen, 2017). The support tower part of these assemblies, commonly comprising a series of circular cylindrical and conical shell segments, inescapably has attracted considerable research attention in a constant strive for construction economy and design automation. A recent Round-Robin study on the computational analysis of a wind turbine support tower (Sadowski & Seidel, 2023a) has provided a clear indication of the engineering community's interest to aid in efforts that will drive design resilience and economy of wind turbine towers forward, with participants from all corners of the globe.

A consequence of the optimised shape and material economy that a shell structure allows for is a lack of robustness, which could prevent local failures to escalate into global ones for the shell system. Localised buckling or yielding jeopardises the overall structural integrity of the shell, as



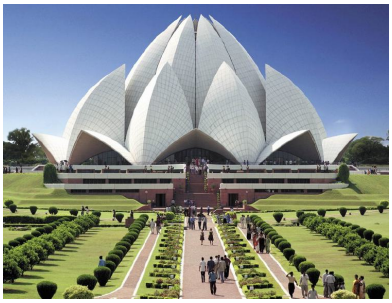


a) Cylindrical shells as storage containers, with an arrangement of silos (top) and a tank shell (bottom).



b) Corrugated cylindrical shell used as an aircraft fuselage.





c) Sydney opera house (top) and the Lotus temple in Kalkaji (bottom), exhibiting the aesthetic nature of shells.

Figure 1.1: Shell structures meeting the needs of multidisciplinary engineering demands (images obtained from wikipedia.com, airbus.com and shellbuckling.com, all accessed on 4$^{\text{th}}$ February 2025).

stress redistribution can potentially lead other parts of the shell into failure, creating a chain set of events that would render the entire structure useless. Due to this sensitive nature of shell design, standards on shell buckling are tasked with the difficult job of providing a reliable design framework that can account for these vulnerabilities, while simultaneously ensuring material efficiency and economic viability.

1.2 The European Standard EN 1993-1-6 for the design of steel shells

The European Standard EN 1993-1-6 (2007) for the strength and stability of steel metal shell structures has been one of the more advanced and pioneering parts of the Eurocode in the sense of allowing for a full design of the shell through a series of well defined computational analyses (Rotter, 2010b). The design resistance of the shell is then found using a partial factor γ_{M1} on the FE-assisted evaluated R_k. Computer-aided engineering design has now been additionally incorporated into the Eurocode 3 for the design of metal structures through the new part EN 1993-1-14 (2025) on FE-assisted design of steel structures.

1.2.1 Design limit states

As the second generation of structural Eurocodes for the strength and stability of shells has recently been released and made available to the engineering community, the new EN 1993-1-6 (2025) is mostly consistent on the definition of the limit states that will determine the design of a shell structure with its predecessor EN 1993-1-6 (2007). These limit states are formally defined as:

LS1 Plastic failure / tensile rupture
Ultimate limit state relevant to cases where the shell develops zones of yielding that in conjunction with its stress patterns hinder its ability to resist further application of the same form of loading. Tensile rupture is additionally handled through LS1, defined as the gross section failure due to membrane tension of the shell plate.

LS2 Cyclic plasticity
Ultimate limit state where repeated cycles of yielding can lead to low cycle fatigue.

LS3 Buckling
Ultimate limit state where the shell structure loses its stability due to membrane compression and/or shear, leading to excessive displacements or collapse.

LS4 Fatigue
Ultimate limit state where loading and unloading of the shell may cause cracks to develop, with further loading of the structure potentially leading to rupture.

Whilst all of the above limit states can be critical to the strength capacity of axisymmetric shell structures, it would be impossible for a single document to provide in depth insights and commentary on their assessment and significance to the structural integrity of a shell system. The scope of the present doctoral thesis is mostly focused on instability phenomena of axisymmetric shells, corresponding to LS3, with considerations of plastic failure modes relating to LS1. The effect of material nonlinearities on the buckling of shell systems will also be studied, constituting an intersection of limit states LS1 and LS3.

1.2.2 Analysis types and their scope in EN 1993-1-6

In addition to the definition of the four ultimate limit states outlined above, EN 1993-1-6 provides the formal description for a series of computational analyses to facilitate design against those ultimate limit states. These definitions have not been subject to any revisions in EN 1993-1-6 (2025), being consistent with its predecessor EN 1993-1-6 (2007) and are here provided verbatim as found in the European Standard:

LA Linear elastic shell Analysis
Analysis that predicts the behaviour of a thin-walled shell structure on the basis of the small deflection linear elastic shell bending theory, related to the perfect geometry of the middle surface of the shell.

LBA Linear elastic Bifurcation Analysis
Analysis that evaluates the linear bifurcation eigenvalue for a thin-walled shell structure on the basis of the small deflection linear elastic shell bending theory, related to the perfect geometry of the middle surface of the shell.

GNA Geometrically Nonlinear elastic Analysis
Computational analysis based on the principles of shell bending theory applied to the perfect structure, using a linear elastic material law but including nonlinear large deflection theory for the displacements that fully accounts for any change in geometry due to the actions on the shell, including a bifurcation eigenvalue check at each load level.

MNA Materially Nonlinear Analysis
Analysis based on shell bending theory applied to the perfect structure, using the assumption of small displacement theory, but adopting an ideal elastic-plastic material law and with no limitation on the plastic strain that can develop.

GMNA Geometrically and Materially Nonlinear Analysis
Computational analysis based on shell bending theory applied to the perfect structure, using the assumptions of nonlinear large deflection theory for the displacements and a fully nonlinear elastic-plastic hardening material law, where appropriate, and in which a bifurcation eigenvalue check is included at each load level.

GNIA Geometrically Nonlinear Analysis with Imperfections explicitly included
Computational analysis with imperfections explicitly included, similar to a GNA, but adopting a model for the geometry of the structure that includes one or more of the following unintended features: deviations of the middle surface from the ideal shape, residual stresses, variations of thickness, misalignment of plates and imperfections in the boundary conditions.

GMNIA Geometrically and Materially Nonlinear Analysis with Imperfections explicitly included
Computational analysis with imperfections explicitly included, based on the principles of shell bending theory applied to the imperfect structure, including nonlinear large deflection theory for the displacements that accounts fully for any change in geometry due to the actions on the shell and a fully nonlinear elastic-plastic hardening material law and including a bifurcation eigenvalue check at each load level.

It should be emphasised that the phrasing in the above definitions for the different kinds of EN 1993-1-6 (2025) analyses is by no means coincidental, as there is a careful distinction between analyses that require a strictly computational approach and those with well defined alternatives. Indeed, LA, LBA or even MNA solutions may be obtained through the use of standard formulae provided in the different Annexes of the European Standard for thoroughly studied reference axisymmetric shell systems, such as cylinders under ring loads. This permits a swift process for the design of some common shell systems to be adopted, as any kind of computational procedure would inevitably be an involved, time-consuming endeavour to some extent. It is important to mention that to the interpretation of EN 1993-1-6 (2025), a computational analysis pertains to the use of a shell analysis software for the execution of a numerical analysis of the structure on the basis of the Finite Element Method (FEM), even though alternatives of this modern computational approach exist in the shell research community and can be viable options (with a discussion on the different numerical procedures for the solution of axisymmetric shell problems provided shortly in Section 2.2).

	LS1	**LS2**	**LS3**	**LS4**
LA	✓	✓	✓	✓
LBA	✗	✗	✓	✗
GNA	✗	✓	✓	✓
MNA	✓	✓	✓	✗
GMNA	✓	✓	✓	✗
GNIA	✗	✗	✓	✓
GMNIA	✗	✗	✓	✗

Table 1.1: Relevance of computational analyses to the four limit states LS1-LS4 in the context of EN 1993-1-6 (2025), as discussed in section 4.2 therein.

The relevance of the different EN 1993-1-6 (2025) analyses to the examination of a shell structure under the four limit states described in the Standard is summarised in Table 1.1. As the scope of this document is set to a study of shell behaviour and assessment in the context of limit states

LS1 and LS3, the entirety of EN 1993-1-6 (2025) defined types of analyses are relevant and will utilised to examine different aspects of linear or nonlinear shell responses in the chapters to follow.

1.3 Research objectives

As the entirely redeveloped EN 1993-1-6 (2025) for the strength and stability of metal shell structures has been formally released as of May 2025, there is an urgent need for reliable tools that can support the examination and characterisation of reference shell systems. This task has motivated the development of a novel computational tool for the exploration of axisymmetric shell systems that are commonly found in engineering applications through the construct of the capacity curve framework, facilitating the justification of updates in the new version of EN 1993-1-6. The developed software would aim to not only be an instrument in the constant generation of capacity curve points for reference axisymmetric shell problems but also an actively maintained program with a repository of benchmarks (thoroughly documented examples) that can support development of other FE tools for the analysis of shells, as instructed by the new EN 1993-1-14 (2025). In addition to a computational tool supporting further Eurocode 3 developments, the exploration of the conservativeness and accuracy of the capacity curve framework for cylindrical shells across different ranges of slenderness will also be a focus of the present work, aiming to add to the reliability of automated curve assisted design for one of the most widely used shell structures. As such, the following objectives can be identified:

- The development of an efficient finite element toolbox for the nonlinear analysis of axisymmetric shell problems, with a special focus on the bifurcation (eigenvalue) checks at different levels of loading. A native mathematical treatment of the harmonic displacement field assumed along the circumference of the axisymmetric shell when buckling occurs shall be a key characteristic of the FE toolbox. As the purpose of the software would be to assist the European standard on the design of shells, the full EN 1993-1-6 taxonomy of computational analyses needs to be supported and made easy to implement.
- An investigation of the conservativeness and physical accuracy of the capacity curve for cylinders under meridional compression when compared to its uniform bending equivalent for models of varying slenderness, with a focus on circular cylindrical shells of intermediate slenderness, processed through a meticulously organised hierarchy of computational analyses.
- An analytical endeavour on the derivation of closed-formed relationships for the bifurcation of finite-thickness non-shallow cylindrical shells, adding to the accuracy of capacity curves through the normalisation with a more precise reference resistance R_{cr} for stocky cylinders.
- A thoroughly documented attempt on the derivation of a reliable shear-flexible finite element for the nonlinear analysis of axisymmetric shells, suitable for every range of slenderness, with the challenges in such a task to be presented and discussed.

The final tasks have been motivated by the unsuitability of the thin shell formulation employed in the initial stages of development on the AQUINAS-FE toolbox, made evident during the extensive computational investigation of meridionally compressed cylinders and associated generation of capacity curves as part of the second research-work deliverable. The accuracy of AQUINAS' formulation on low slenderness stocky cylindrical models has been found to be inappropriate for the evaluation of their squash load in the presence of pre-buckling geometric nonlinearities due to the influence these are found to have on reducing the overall stiffness of the cylinders. The solver's behaviour contradicts both established scientific knowledge and intuition

on the field of cylindrical shell responses under meridional compression, as a stocky enough model should be able to reach and exceed its plastic collapse resistance R_{pl} when supported by material hardening contributions. Robust FEA predictions of an axisymmetric shell's nonlinear resistance is of paramount importance for a tool that aims to assist and build on the integrity of the capacity curve framework of EN 1993-1-6 (2025), prompting the analytical endeavours of the last two tasks with the aim of an extension on the public repository of AQUINAS-FE.

1.4 Research approach

As is clear from the objectives of the present research work, the author hopes to contribute in the integrity of the next shell design era through the use of the European standard. While an experimental approach to the exploration of reference shell systems within a controlled lab environment may appear as the most reliable strategy for the accurate characterisation of those systems through the capacity curve construct, the logistics of such an endeavour would be reasonably discouraging. The extensive number of models that would need to be tested one-by-one at different levels of perfectly fabricated imperfection shapes and amplitudes cannot be a cost-effective approach for an exploration of this scale (with specifics on the number of models to be considered provided later in this document). And while the economics of this task would already render it impractical, the precision of a 'controlled lab environment' is often not entirely guaranteed, as the cloud of experimentally obtained data points in Figure 1.2 for cylinders under uniform meridional compression showcase. Different compilations of lab test data for the same reference shell problem can be found in Bushnell (1989); Brush & Almroth (1975); Rotter & Schmidt (2013); Castro *et al.* (2014); Wagner *et al.* (2020); Sadowski *et al.* (2023), all showcasing the extensive variability of experimental result spreads. Whilst the significance of initial imperfections on the resistance of this reference axisymmetric shell system has been extensively discussed and documented through several related works (Koiter, 1945, 1963; Yamaki, 1984; Hutchinson, 1965; Tennyson & Muggeridge, 1969), with Singer *et al.* (2002) suggesting that early experimental results would have been performed without any efforts towards estimating imperfections' magnitude and shape, standards have incorporated lab test results as empirical rules for the design of shells across their development stages. The empirical buckling rules of NASA-SP-8007 for the design of aerospace vehicles, originally available from 1965 after a short revision in 1968, have only recently been formally updated into NASA-SP-8007-2020, illustrating that provisions of relatively modern standards can potentially be unjustifiably conservative. The civil engineering discipline has already left such outdated strategies for the design of real shell structures behind with even the first drafts of the Eurocode ENV 1993-1-6 (1999) (still having the status of an ENV), adopting recommendations (Rotter, 1998) to allow for different Fabrication Tolerance Quality Classes (FTQC) that would permit engineers to establish the shell's resistance on the expected level of imperfections rather than relating it to a lower bound obtained through improperly documented lab tests. This provision additionally recognises and rewards fabricators who can construct shell structures to high quality tolerances (Rotter, 2010a).

A recent study by Sadowski *et al.* (2023) has exhibited that a similar cloud can be generated through FE simulations of axially compressed cylinders, with the details of the models obtained through Monte-Carlo sampling on appropriately distributed geometric and material parameters and computational GMNIA finite element analysis for the synthetic recreation of the cloud of Figure 1.2. The sampling parameters include the cylinder radius r, shell-wall thickness t, cylinder length L, Young's modulus E, yield stress f_y and the amplitude of the considered imperfection shape for longitudinally overlap-joined specimens, with the Empirical Cumulative Distribution Functions obtained through a statistical analysis of the available experimental dataset. Load application non-uniformity was additionally found to be an important factor

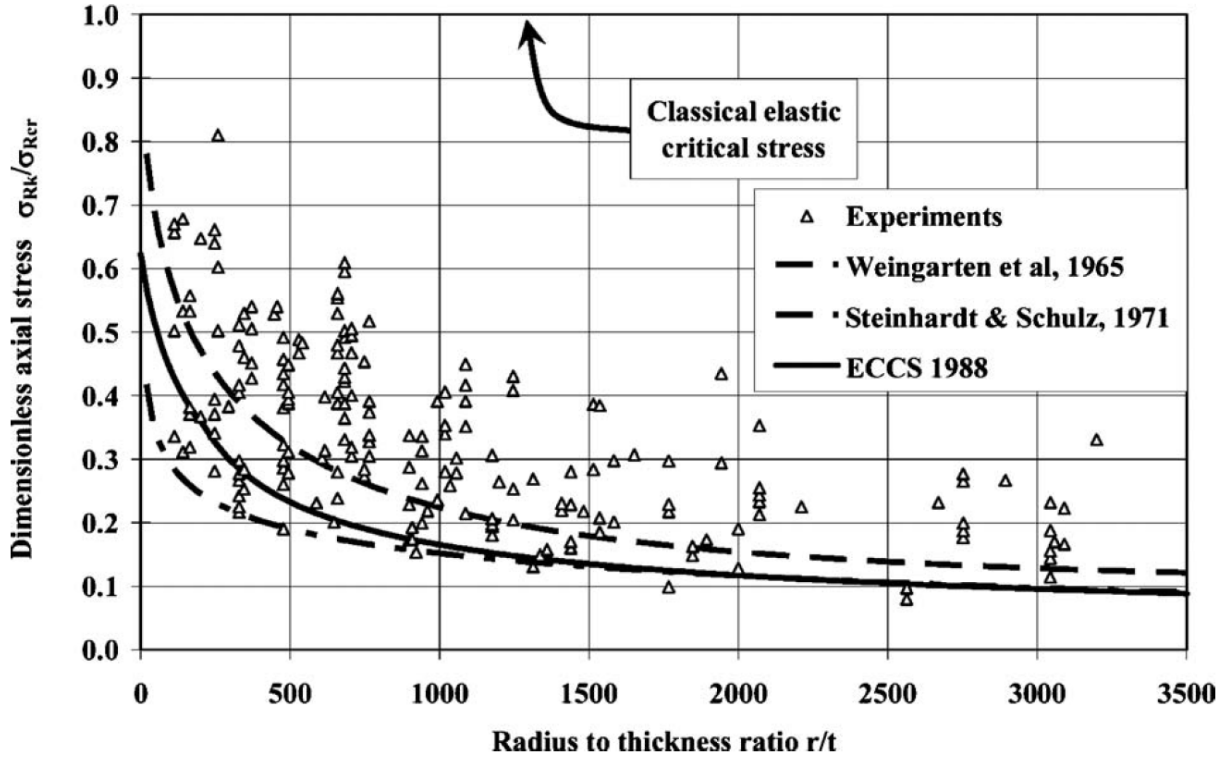


Figure 1.2: Experimental results for cylinders under meridional compression with illustrations of traditional lower bound fit relationships for the design of shell structures of varying slenderness (figure according to Rotter (2010a) for data collected by Harris *et al.* (1957)).

for the synthetically reproduced cloud to match the variability and reduced resistance of lab tests. The computational data generated and experimental results collected for Fig. 9 therein, kindly provided by the authors of that manuscript, are presented in the following Figure 1.3 in a traditional and modified capacity curve format.

Although the main objective of the computational investigation by Sadowski *et al.* (2023) was a critique on the validity of buckling design rules for shell structures derived from experimental data of uncertain quality, a secondary, yet equally important, outcome is the demonstration that laboratory tests can essentially be completely replaced by computational solutions. At least for a material as well understood as structural steel, this substitution is feasible provided that the computational models are meticulously developed to accurately replicate the structural response of the corresponding real-life shell system. In alignment with this approach, computationally evaluated resistances will be favoured over their more laborious, expensive and potentially unreliable experimental results for the extensive generation of capacity curves and subsequent characterisation of axisymmetric shell reference systems. As commercially available FE software do not provide native treatments to the problem of non-symmetric bifurcation buckling of axisymmetric shell systems (ABAQUS, 2022; ANSYS, 2022), the development of a computational toolbox that can reliably and efficiently perform this task constitutes the first deliverable of the present research work.

1.5 Thesis outline

Following this first introductory chapter, Chapter 2 presents a review of the relevant bibliography on axisymmetric shell theories, summarising the different assumptions and simplifications that

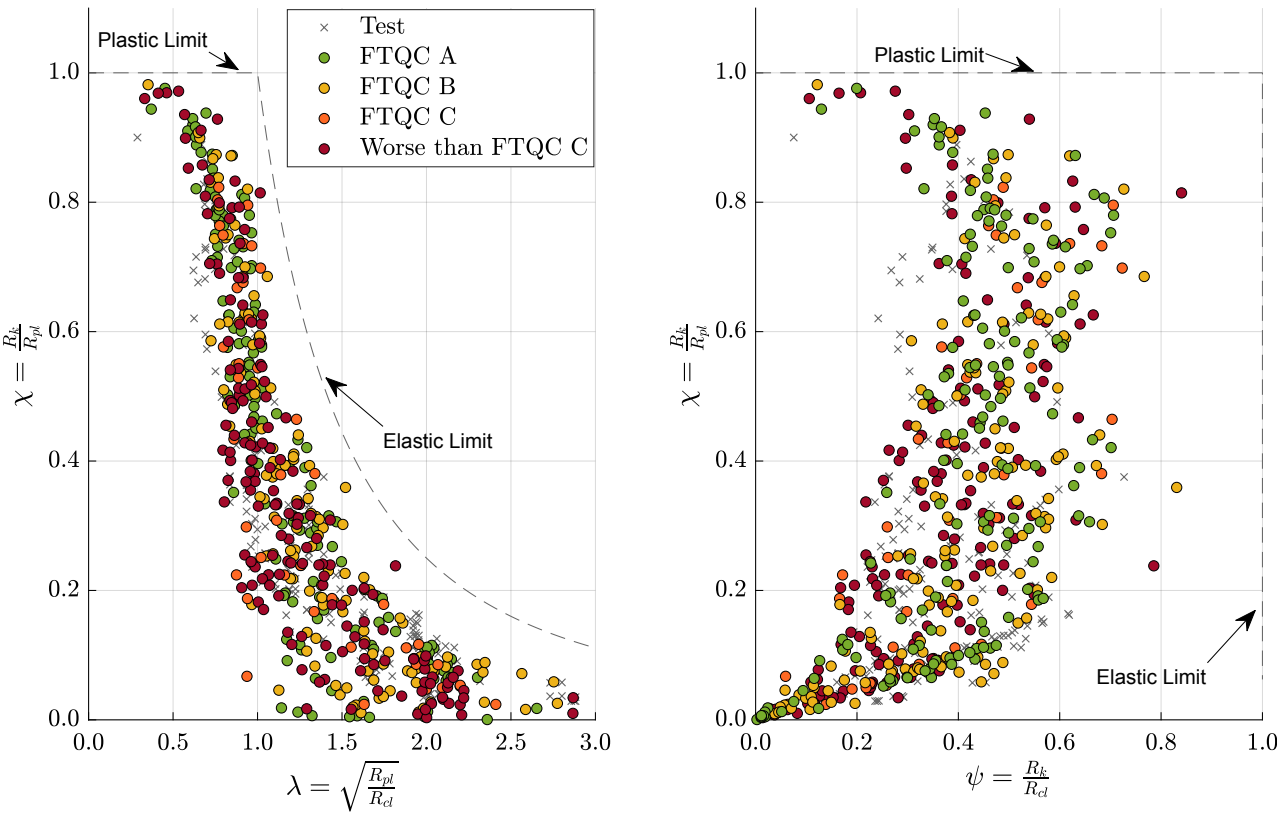


Figure 1.3: Collected test vs synthetic Monte Carlo datasets for χ against λ and ψ (traditional and modified forms of a capacity curve accordingly) for test specimens with a longitudinally overlap-joined systematic fabrication imperfection and an imposed deterministic load application non-uniformity (data provided by Sadowski *et al.* (2023)).

constitute the basis for each. Linear kinematics are thoroughly presented and discussed, with additional focus into the nonlinear kinematic relationships that govern the axisymmetric shell's behaviour. A short discussion on legacy computational solvers is subsequently provided, including finite element method packages as well as more generic numerical toolboxes. The specialised mathematical treatments that are missing from the modern era commercial FE solvers are highlighted, setting the scope for the first deliverable of the present research work. A presentation of the capacity curve construct that facilitates the design of shells according to EN 1993-1-6 concludes this chapter, with a review of all the parameters that formally define the 'traditional' and 'modified' (Rotter) forms of the curves.

Chapter 3 gives an overview of the fundamental FE formulation aspects incorporated into the AQUINAS-FE software, a scientific toolbox for the efficient and accurate nonlinear analysis of axisymmetric shell bifurcation buckling. The mixed-interpolation element kinematics, as adopted from Teng & Rotter (1989a) and Teng & Rotter (1989b), assume a harmonic distribution of the displacement field for buckling checks, a key aspect of the formulation that is crucial to the precise prediction of the buckling mode and associated critical load of an axisymmetric shell with a circumferentially uniform pre-buckling stress state. While the majority of this FE toolbox is written in the MATLAB programming environment, multi-threaded parallelisation can be employed through OpenMP and utilisation of MEX binaries, written in C++. The Surrogate Model Optimisation (SMO) algorithm, programmed from first principles within the FE toolbox, is an additional capability that aims to further reduce computational time necessary for detection of the critical mode. The work displayed in this chapter has led to the following journal article:

- Filippidis A. & Sadowski A.J. (2023) Modern analysis of axisymmetric shells with AQUINAS: A MATLAB finite element toolbox, *SoftwareX*, 23, 101434.

A conference presentation to communicate the release of AQUINAS-FE has additionally been made in Eurosteel 2023, accompanied with the following proceedings publication:

- Filippidis A. & Sadowski A.J. (2023) A MATLAB finite element toolbox for the efficient nonlinear analysis of axisymmetric shells, *ce/papers*, 6, 1735-1740.

Chapter 4 presents the contribution of the present author in a formal comparison of cylindrical shell systems under uniform meridional compression and uniform bending, within the context of the capacity curve framework of EN 1993-1-6. The fully axisymmetric problem of a cylinder under uniform meridional compression presented excellent grounds for a parametric sweep of models analysed with AQUINAS-FE. ABAQUS (2022) was the solver of choice for the case of cylinders under global bending, owing to the extended use of this commercially available FE software for the analysis of shell structures. The challenges in modelling a seemingly simple cylindrical shell problem are thoroughly discussed in this chapter, with a focus on the key discretisation and load incrementation parameters that may potentially lead to inaccurate predictions of the critical resistance. A side-by-side comparison of the effect that each of these parameters can have on the evaluation of a geometrically and materially nonlinear analysis resistance with both ABAQUS (2022) and ANSYS (2022) shows that these issues are relatively indifferent to the FE software employed and rest on the analyst to appropriately assess and possibly resubmit the analyses. Capacity curves for the two reference cylindrical shell problems are examined, with a special focus on cylinders of intermediate slenderness, as the main objective of this study was to establish the background for a recent amendment to the new version of EN 1993-1-6 (2025) where a cylindrical shell under uniform meridional compression is no further to be considered automatically as the least favourable scenario in lack of a more relevant system. This computational justification and findings, together with an outline of developments on the capacity curve construct across the years and different design standards, have been published as:

- Sadowski A.J. & Filippidis A. (2025) The capacity curve framework of EN 1993-1-6 (2025): Cylindrical shells under uniform meridional compression vs uniform bending, *Journal of Constructional Steel Research*, 225, 109167.

The comparative study of Chapter 4 has highlighted some shortcomings in the critical load evaluation of very low slenderness cylinders, owing to the geometrically nonlinear behaviour of the Teng & Rotter (1989a) element which was adopted in AQUINAS. An attempt to identify a reference result for the bifurcation of thick cylindrical shells under meridional compression that could establish a comparison point for any finite element formulations to be considered has led to the discovery that such a result does not exist in the same format as the one for a thin cylindrical shell, derived by Koiter during his PhD (Koiter, 1945).

Chapter 5 presents the analytical efforts for the derivation of a reference stability result for shear-flexible cylinders under meridional compression. Uniform external pressure buckling is additionally considered, as the steps in the process and the pre-buckling mechanics involved are consistent between the two load cases. A linear elastic stress analysis for finite-thickness cylinders under these two load cases is derived as a first step into this analytical endeavour, with the solution showcasing a very good agreement with computationally obtained results from ABAQUS while also displaying a more flexible behaviour that can be viewed as a closer approximation to the ideal continuum body. Buckling considerations of the cylindrical system under either load case introduces additional complexities into the problem, as elements of non-shallow shell theory need to be considered in the context of a low slenderness finite thickness model. Equilibrium of internal forces on the deformed state of the shell is considered on the

basis of Engesser's hypothesis, with their vector being normal to the cross sectional plane before shear strain corrections are applied. Critical buckling load predictions appear to be in good agreement with ABAQUS axisymmetric buckling results for a wide range of slendernesses, while still trending towards an analytical thin shell theory result for cylinders characterised by higher radius over wall-thickness ratios. The analytical closed-form results of this study have been published in the *Structures* journal in the following form:

- Filippidis A. & Sadowski A.J. (2025) Selected closed-form algebraic solutions for linear stress and buckling analyses of elastic shear-flexible axisymmetric cylindrical shells, *Structures*, 78, 109146.

The unjustifiably low FE results produced through AQUINAS' purely thin small strain axisymmetric shell formulation for the prediction of low slenderness meridionally compressed cylinder resistances have motivated the ongoing development of a new axisymmetric shell element. Chapter 6 discusses the challenges in constructing such an element, with an overview of the different shell theories and FE formulations considered. Different aspects and computational concepts were incorporated from a variety of FEA scientific resources on the FEM for axisymmetric shell structures, ensuring that the key characteristic of treating bifurcation into nonsymmetric modes n is handled natively by assuming a harmonic distribution of the circumferential displacement field when stiffness matrices are assembled and submitted to eigenvalue checks. A collection of critical intermediate results at different stages of the development process are presented and scrutinised against numerical solutions from ABAQUS, but also against direct analytical results produced in the shear-flexible study of cylindrical shells in the previous chapter. Alternatives that were not adopted and could possibly lead to a successful FE formulation that can be eventually coded into AQUINAS are additionally discussed.

Chapter 7 concludes the present doctoral thesis by delivering an overview of the primary research findings and contributions. Commentary and recommendations are provided for future research ventures on the topic of axisymmetric shell buckling.

Chapter 2

Literature review

A quote from Koiter's work (Koiter & Simmonds, 1973) would appropriately set the tone for introducing the theoretical aspects of axisymmetric shell theory, as well as their computational application and incorporation into design standards further on.

'Shell theory attempts the impossible: to provide a two-dimensional representation of an intrinsically three-dimensional phenomenon.'

In this spirit, a series of approximations and assumptions are made for the two-dimensional representation to be possible. These are sometimes well justified on the basis of the mechanics of structures where one dimension is considerably shorter than the other two, but other times 'are not rigorously justified but are introduced for simplicity and seem reasonable' as explicitly stated in the theory manual of the ABAQUS software (ABAQUS, 2022).

Axisymmetric shells, a sub-category of general shell structures, are characterised by the complete symmetry of a two-dimensional geometry about an axis of revolution, commonly termed as the generating meridian. It should be emphasised already from this point that an axisymmetric shell geometry, with its characteristics displayed in Figure 2.1 is a necessary but not sufficient condition for an axisymmetric shell problem. Loading or boundary conditions on an originally axisymmetric shell structure that may result in a displacement field that is not circumferentially uniform would violate the essential requirements an axisymmetric shell problem should satisfy. Axisymmetric shell bifurcation buckling with a circumferentially uniform pre-buckling stress field can often lead to non-symmetric displacement field distributions, a concept that is firmly embedded in the present research work. As post-buckling responses are beyond the scope of this study, detection of non-symmetric bifurcation modes as critical for the stability of the shell would be a terminating scenario in any analysis considered here.

2.1 Axisymmetric shell theories

2.1.1 General assumptions

Axisymmetric shells are not indifferent to general shell theory fundamental assumptions, for both their pre-buckling and bifurcation buckling states. Different levels of assumptions introduce different families of shell theories, with the more elaborate of those making none but the essential.

Assumption 1 *Stress component σ_ζ normal to the shell's midsurface is negligible in all states of deformation.*
This assumption constitutes perhaps the basis of shell theory, separating the kinematics and

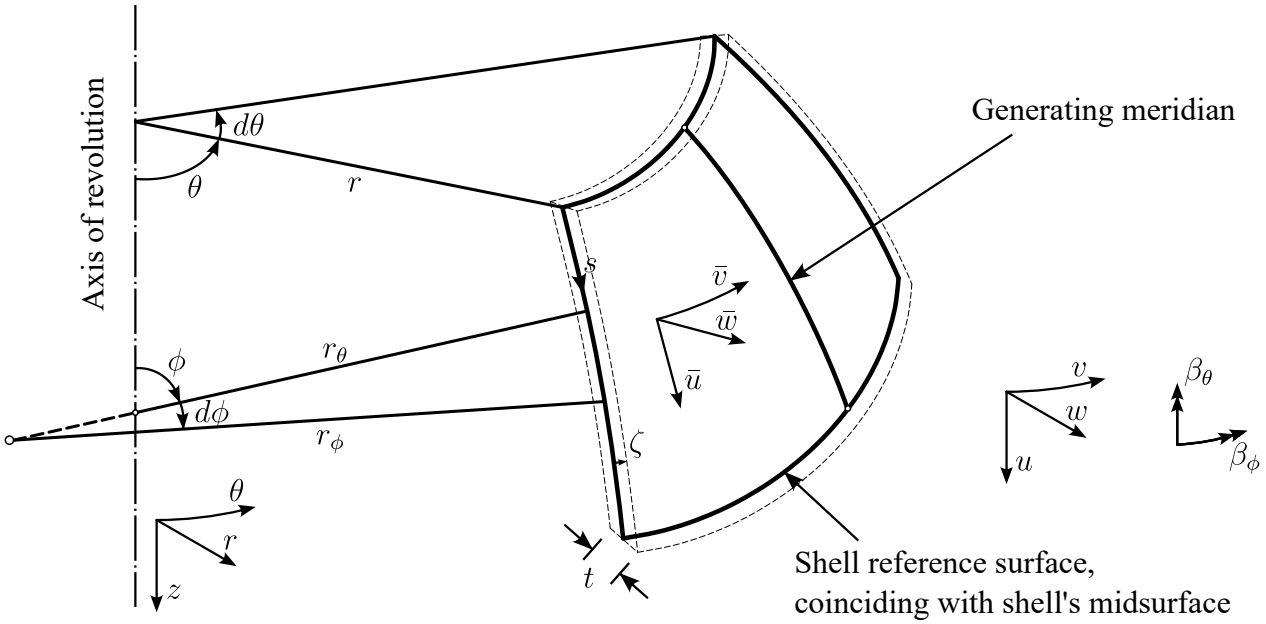


Figure 2.1: Geometry of axisymmetric shell.

constitutive laws to those of continuum solids. This introduces plane stress constitutive relations to the mechanics of shells, reducing the equations and number of terms that can be omitted compared to their solid continuum equivalents.

A negligible normal stress does not automatically imply an accompanying near-zero normal strain ϵ_ζ. On the contrary, a plane stress material law unavoidably introduces a non-zero ϵ_ζ due to Poisson effects arising from in-plane stresses. Most shell theories generally omit evaluation of the normal strains and their contribution to in-plane stresses, a simplification that while inconsistent with plane stress material laws does not necessarily introduce an error of any significance to the solution, even though complex algorithms have been proposed (De Borst, 1991) to amend this contradiction in the context of materially nonlinear analysis. While more advanced formulations (Hughes & Carnoy, 1983; ABAQUS, 2022) may not make this simplification, this is consistent with some of the additional 'thinness' assumptions that are commonly employed.

Assumption 2 *Through-thickness variations of strains and stresses are of linear order.*
The effect of changing radii at different levels through the shell-wall thickness on the strains, in particular the circumferential strain ϵ_θ (Flügge, 1990), is omitted. Terms of second order or higher with respect to the thickness direction coordinate ζ are discarded, a simplification that considerably reduces the complexity of the theory. This allows for, at most, linear through thickness variations of the strains.

Assumption 3 *The through-thickness coordinate ζ over radius r ratio is ignored during integration of stress resultants.*
Inclusion of the ζ/r terms when computing the stress resultant integrals (Brush & Almroth, 1975; Flügge, 1990) would introduce an additional layer of complexity by not allowing for the assumption of $N_{\phi\theta} \approx N_{\theta\phi}$ for the in-plane shear membrane stress resultants and $M_{\phi\theta} \approx M_{\theta\phi}$ for the twisting stress resultants. This simplification is adopted in most shell theory formulations, with the exception of Flügge's detailed thin-shell theory (Flügge, 1990).

Assumption 4 *Plane sections remain plane.*
A statement that may be also found in beam theory explorations, it ensures that the distance

from the midsurface is uniquely and unambiguously defined by the through-thickness coordinate ζ. This is not however equivalent to negligible transverse shear strains, either meridional $\gamma_{\phi\zeta}$ or circumferential $\gamma_{\theta\zeta}$, but rather rejects a higher-order shear deformation theory for cases where shear strains are indeed considered. The plane sections assumption is consistent with the 'thinness' approximations above (ABAQUS, 2022).

Assumption 5 *Transverse shear strains are assumed to be zero.*
The condition of negligible shear strains is a fundamental approximation that differentiates the Kirchhoff-Love Kirchhoff (1850) and Love & Darwin (1888) thin shell theory from the more general Reissner-Mindlin thick shell theory (Reissner, 1941), constituting an analogy to the differences between Euler-Bernoulli and Timoshenko theories for beam structures.

Assumption 6 *The contribution of meridional u and circumferential v displacements on the meridional, circumferential and twisting curvatures is neglected.*
Omission of meridional u and circumferential v displacement terms on the evaluation of curvatures refers to the shallow shell theory approximation of shell structures, first introduced in Aron (1874) with some errors (Reissner, 1941; Punera & Kant, 2019) that were later addressed by Love & Darwin (1888). This approximation is well justified in many cases of shell problems (Niordson, 1985) and has been incorporated in different linear and nonlinear shell theories.

The assumptions of Kirchhoff-Love shell theory as originally presented by Kirchhoff (1850) and later refined by Love & Darwin (1888), often termed as *Classical Shell Theory* (CST) in relevant bibliographic resources, produce a system of three midsurface strains and three curvatures for axisymmetric shells, subject to all Assumptions 1-6 presented earlier.

2.1.2 Fundamental (pre-buckling) state for shells of revolution

Stress analysis of shells is a field of mechanics that has seen considerable research activity over the past two centuries, with new scientific publications on analytical solutions for shell problems now being largely on the wane. This does not necessarily mean that it constitutes a solved problem, but rather that a subcategory of stress analysis shell problems of practical application have been either sufficiently studied and documented or abandoned as extremely laborious or unfeasible. The majority of these structural systems are thin-walled axisymmetric shell problems, allowing for all of the reductions discussed earlier. Expressing equilibrium of membrane, shear and bending stress resultants at the level of an infinitesimal shell panel, as illustrated in Figure 2.2, produces 3 equations for the equilibrium of forces along the meridional, circumferential and radial axes and another 3 for the equilibrium of moments about those same axes. This total of 6 equilibrium equations is established on the basis of the undeformed configuration of the $ds \cdot rd\theta$ panel for the pre-buckling state of the shell structure, ignoring any second order effects that midsurface displacements and rotations can introduce to these equations. Retaining the independency of in-plane shear stress resultants $N_{\phi\theta}$ and $N_{\theta\phi}$ and twisting moments $M_{\phi\theta}$ and $M_{\theta\phi}$ for the time being, the 6 equilibrium equations are given in Eqs. 2.1 below:

$$\frac{\partial r}{\partial s}N_\phi + r\frac{\partial N_\phi}{\partial s} + \frac{\partial N_{\theta\phi}}{\partial \theta} - \cos\phi N_\theta - r\frac{\partial \phi}{\partial s}Q_\phi = -rp_s \tag{2.1a}$$

$$\frac{\partial r}{\partial s}N_{\phi\theta} + r\frac{\partial N_{\phi\theta}}{\partial s} + \frac{\partial N_\theta}{\partial \theta} + \cos\phi N_{\theta\phi} - \sin\phi Q_\theta = 0 \tag{2.1b}$$

$$\sin\phi N_\theta + r\frac{\partial \phi}{\partial s}N_\phi + \frac{\partial Q_\theta}{\partial \theta} + r\frac{\partial Q_\phi}{\partial s} + \frac{\partial r}{\partial s}Q_\phi = rp_n \tag{2.1c}$$

$$r\frac{\partial M_{\phi\theta}}{\partial s} + \frac{\partial r}{\partial s}M_{\phi\theta} + \frac{\partial M_\theta}{\partial \theta} + \cos\phi M_{\theta\phi} = rQ_\theta \tag{2.1d}$$

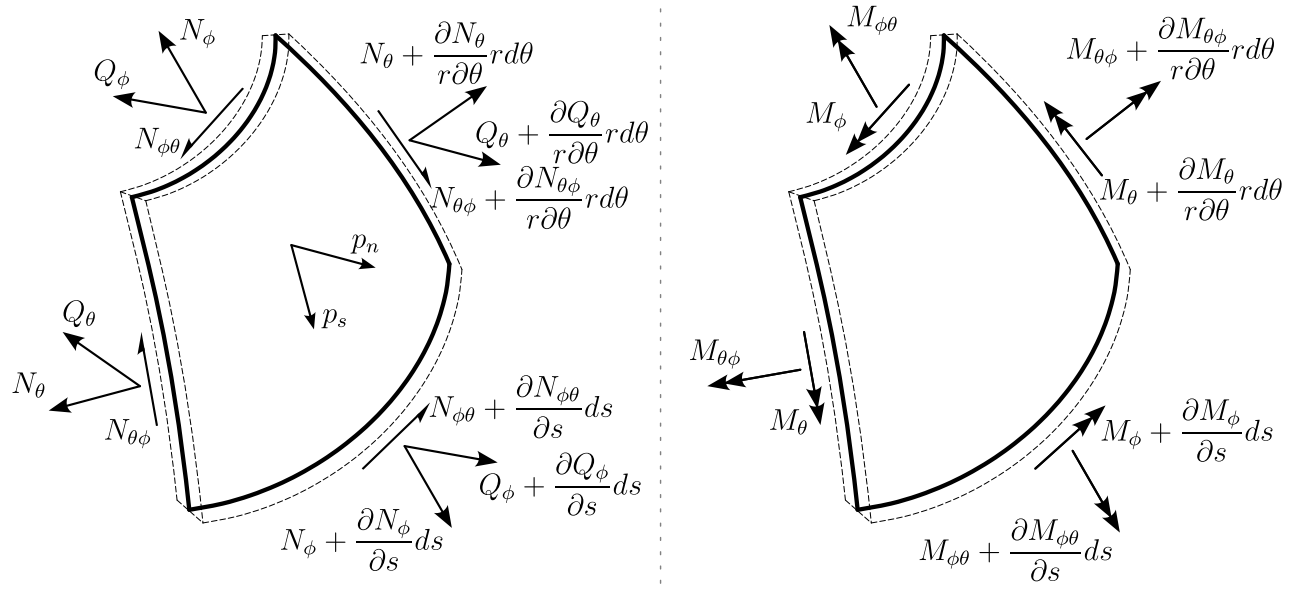


Figure 2.2: Membrane N, shear Q and bending M stress resultant equilibrium expressed on an infinitesimally small $ds \cdot rd\theta$ panel of an axisymmetric shell structure, the geometric characteristics of which are displayed in Figure 2.1.

$$r\frac{\partial M_\phi}{\partial s} + \frac{\partial r}{\partial s}M_\phi + \frac{\partial M_{\theta\phi}}{\partial \theta} - \cos\phi M_\theta = rQ_\phi \tag{2.1e}$$

$$\frac{\partial \phi}{\partial s}M_{\phi\theta} - \sin\phi\frac{M_{\theta\phi}}{r} = N_{\phi\theta} - N_{\theta\phi} \tag{2.1f}$$

where the meridional curvature is expressed as:

$$\frac{\partial \phi}{\partial s} = \frac{1}{r_\phi} \tag{2.2}$$

introducing some minor differences in the notational form for the description of generalised stress resultant equilibrium equations originally found in Flügge (1990). A review of different classical resources on the analysis of shell structures indicates that aside from minor convention and nomenclature related differences, discrepancies at the level of equilibrium equations relating to the undeformed configuration of the axisymmetric shell are uncommon (with the exception of variations relating to the midsurface radii of the shell wall with respect to the arc-length coordinate s). Any differences can be traced to the assumptions employed and mechanics considered for the kinematic relationships of the shell structure. Considerable reductions to these equations can be achieved through consideration of a pure axisymmetric stress state for the fundamental path of the shell, providing the following set of equilibrium equations:

$$\frac{\partial r}{\partial s}N_\phi + r\frac{\partial N_\phi}{\partial s} - \cos\phi N_\theta - r\frac{1}{r_\phi}Q_\phi = -rp_s \tag{2.3a}$$

$$\sin\phi N_\theta + r\frac{\partial \phi}{\partial s}N_\phi + r\frac{\partial Q_\phi}{\partial s} + \frac{\partial r}{\partial s}Q_\phi = rp_n \tag{2.3b}$$

$$r\frac{\partial M_\phi}{\partial s} + \frac{\partial r}{\partial s}M_\phi - \cos\phi M_\theta = rQ_\phi \tag{2.3c}$$

$$\tag{2.3d}$$

with equations relating to force equilibrium along the circumferential axis (Eq. 2.1b) or moment equilibrium about meridional and radial axes (Eqs. 2.1e-2.1f) reducing to identities. The system of 3 equilibrium equations for a fully axisymmetric stress state of the shell structure involves 5 stress resultant unknowns, rendering it a statically indeterminate structural system. For the purposes of solving this system it is necessary to introduce additional equations, provided in the form of strain-displacement relationships that are associated to Eqs. 2.3 through constitutive relations. Whilst such constitutive relationships are fairly simple and widely established for small strain isotropic materials, different families of such kinematic relationships may be identified, with some of the most classical formulations commonly employed in relevant investigations on shell mechanics discussed shortly.

2.1.2.1 Linear kinematics

Small-deformation linear shell theory has allowed for the analytical evaluation of stress profiles for classical shells of revolution geometries and loading. Membrane theory, the simplest form of linear stress analysis for shells provides a close approximation to the stress distributions across the shell surface for simple thin shell geometries and loading scenarios, like cylinders under uniform meridional compression or spheres under external pressure. The strain field at any point along the reference surface of an axisymmetric shell is described by the meridional and circumferential stretching components ϵ_ϕ and ϵ_θ, as well as the in plane shear strain $\gamma_{\phi\theta}$. This approximation however assumes a constant distribution of the stresses on a cross section of the shell wall, since kinematic relations are a post-solution add-on to the purely stress resultant equilibrium approach of membrane theory, ignoring bending deformations and associated stresses. As the shell geometries and loading scenarios become more intricate, or even as the thickness of the shell wall increases with respect to the other physical geometric characteristics, bending effects cannot be neglected any more if a stress profile of sufficient accuracy is desired. A bending theory solution is in most cases a considerably more challenging task to a stress analysis result obtained through simple membrane stress resultant equilibrium according to membrane theory, with the reference surface strains for a thin shell now including meridional curvatures κ_ϕ, circumferential curvatures κ_θ and twisting curvatures $\kappa_{\phi\theta} = \kappa_{\theta\phi}$. As stated earlier, equilibrium equations alone cannot provide enough sets of equations for the solution of the axisymmetric shell problem and constitutive equations and kinematic relations need to be employed, with solutions varying in level of complexity and potentially involving Bessel functions even for common problems like cones or spherical caps under axial pressure (Timoshenko & Woinowsky-Krieger, 1959a; Flügge, 1990). The intermediate of a semi-membrane theory solution (Pircher *et al.*, 2001; Blaauwendraad & Hoefakker, 2014) may be sought, as a compromise between the complexity of a full bending theory solution and the reductions of a membrane theory result, a permissible approach according to EN 1993-1-6 (2007).

Donnell - Mushtari - Vlasov theory

Linear kinematic theories for shells of revolution have been introduced for more than a century through the seminal work of Love (1892), with a series of classical textbooks establishing the fundamentals and different aspects of bending theory solutions for axisymmetric shell problems (Timoshenko & Woinowsky-Krieger, 1959a; Novozhilov, 1959; Kraus, 1967; Seide, 1975; Calladine, 1983; Flügge, 1990). The Kirchhoff-Love assumptions have been incorporated into several linear or nonlinear shell theories, notably that of Donnell-Mushtari-Vlasov (Donnell, 1935b; Mushtari, 1938a,b; Vlasov, 1944), with Donnell first incorporating them for axisymmetric shells in the broader context of cylinders under torsion, with a natively axisymmetric shell theory obtainable through strategic reductions on kinematics violating axisymmetry of deformations. Donnell-Mushtari-Vlasov (DMV) theory has been a popular choice for analytical or computational investigations on the linear behaviour of shell structures, with the significance of the shallow

shell theory approximations associated with the DMV kinematics discussed in Hoff (1955); Cantin & Clough (1968). The midsurface strains and curvatures are given as:

$$\epsilon_\phi = \frac{\partial \bar{u}}{\partial s} + \frac{\partial \phi}{\partial s}\bar{w} \tag{2.4a}$$

$$\epsilon_\theta = \frac{cos\phi}{r}\bar{u} + \frac{1}{r}\frac{\partial \bar{v}}{\partial \theta} + \frac{sin\phi}{r}\bar{w} \tag{2.4b}$$

$$\gamma_{\phi\theta} = \frac{1}{r}\frac{\partial \bar{u}}{\partial \theta} - \frac{1}{r}cos\phi\bar{v} + \frac{\partial \bar{v}}{\partial s} \tag{2.4c}$$

$$\kappa_\phi = -\frac{\partial^2 \bar{w}}{\partial s^2} \tag{2.4d}$$

$$\kappa_\theta = -\frac{cos\phi}{r}\frac{\partial \bar{w}}{\partial s} - \frac{1}{r^2}\frac{\partial^2 \bar{w}}{\partial \theta^2} \tag{2.4e}$$

$$\kappa_{\phi\theta} = \frac{2}{r^2}cos\phi\frac{\partial \bar{w}}{\partial \theta} - \frac{2}{r}\frac{\partial^2 \bar{w}}{\partial s \partial \theta} \tag{2.4f}$$

Reissner theory

Further analytical work on the linear stress analysis of shell structures by Reissner (1941) lead to the widely adopted derivations (Naghdi, 1973; Jumikis, 1987; Krauthammer & Ventsel, 2001; Zamani Nejad *et al.*, 2017) for non-shallow shear-deformable shells without the need for considering the approximations associated with Assumptions 5-6. Strains corresponding to stretching deformation modes of the shell's midsurface are consistent with the DMV theory of Eqs. 2.4, with discrepancies restricted to bending related kinematics. The inclusion of finite-thickness effects on the linear kinematics of the axisymmetric shell yields two additional transverse shear strains $\gamma_{\phi\zeta}$ and $\gamma_{\theta\zeta}$, specialised in the following Eqs. 2.5 for shells of revolution.

$$\kappa_\phi = \frac{\partial \beta_\phi}{\partial s} \tag{2.5a}$$

$$\kappa_\theta = \frac{1}{r}\frac{\partial \beta_\theta}{\partial \theta} + \frac{\cos\phi}{r}\beta_\phi \tag{2.5b}$$

$$\kappa_{\phi\theta} = \frac{\partial \beta_\theta}{\partial s} + \frac{1}{r}\frac{\partial \beta_\phi}{\partial \theta} - \beta_\theta\frac{\cos\phi}{r} \tag{2.5c}$$

$$\gamma_{\phi\zeta} = \frac{\partial \bar{w}}{\partial s} + \beta_\phi \tag{2.5d}$$

$$\gamma_{\theta\zeta} = \frac{1}{r}\frac{\partial \bar{w}}{\partial \theta} - \frac{\bar{v}}{r} + \beta_\theta \tag{2.5e}$$

The linear kinematics for shear-flexible shells presented in Eqs. 2.5 above can be reduced to thin shell theory equivalents through imposing Assumption 5, producing a simpler set of relationships to describe thin shell structures. The approximation of near zero transverse shear strains $\gamma_{\phi\zeta} \approx 0$ and $\gamma_{\theta\zeta} \approx 0$ on Eqs. 2.5d-2.5e produces relationships that relate meridional β_ϕ and circumferential β_θ rotations to the translational displacements of the midsurface, given as:

$$\beta_\phi \approx -\frac{\partial \bar{w}}{\partial s} + \bar{u}\frac{\partial \phi}{\partial s} \tag{2.6a}$$

$$\beta_\theta \approx -\frac{1}{r}\frac{\partial \bar{w}}{\partial \theta} + \bar{v}\frac{\sin\phi}{r} \tag{2.6b}$$

Substitution of Eqs. 2.6 into the linear kinematics of Eqs. 2.5 results into a non-shallow thin shell theory consistent with Reissner's derivations, compared against an established set of relationships in relevant works of shell theory kinematics (Jumikis, 1987; Teng & Rotter, 1989a).

Sanders theory Whilst the mathematical contributions of Sanders on the bending theory of shells are usually encountered in the context of nonlinear analysis (Sanders Jr, 1959, 1963; Budiansky, 1963), a set of linear strains for the analysis of thin non-shallow shells can be identified from his theory, producing a more elaborate alternative to thin shell kinematics. Shear strains are ignored, resulting in a theory consistent with Assumption 5. Once again midsurface strains are consistent with the DMV approximations, which has been the basis for the derivational work of Sanders, with any differences between theories limited to the expressions for the curvatures.

$$\kappa_\phi = -\frac{\partial^2 \bar{w}}{\partial s^2} + \frac{\partial \phi}{\partial s}\frac{\partial \bar{u}}{\partial s} + \bar{u}\frac{\partial^2 \phi}{\partial s^2} \tag{2.7a}$$

$$\kappa_\theta = \frac{1}{r}\left(\cos\phi\frac{\partial \phi}{\partial s}\bar{u} + \frac{\sin\phi}{r}\frac{\partial \bar{v}}{\partial \theta} - \cos\phi\frac{\partial \bar{w}}{\partial s} - \frac{1}{r}\frac{\partial^2 \bar{w}}{\partial \theta^2}\right) \tag{2.7b}$$

$$\kappa_{\phi\theta} = \frac{3}{2r}\frac{\partial \phi}{\partial s}\frac{\partial \bar{u}}{\partial \theta} + \left(\cos\phi\frac{\partial \phi}{\partial s} - \frac{3}{r}\sin\phi\cos\phi\right)\frac{\bar{v}}{2r} + \left(\frac{3\sin\phi}{r} - \frac{1}{2}\frac{\partial \phi}{\partial s}\right)\frac{\partial \bar{v}}{\partial s} + \frac{2}{r^2}\cos\phi\frac{\partial \bar{w}}{\partial \theta} - \frac{2}{r}\frac{\partial^2 \bar{w}}{\partial s \partial \theta} \tag{2.7c}$$

Expressions for meridional κ_ϕ and circumferential κ_θ curvatures can be found to be identical with those corresponding to Reissner's thin shell theory reduction of Eqs. 2.5 after substitution of Eqs. 2.6. The twisting curvature $\kappa_{\phi\theta}$ relationship of Eq. 2.7c however includes the additional term (Jumikis, 1987; Fajuyitan, 2018):

$$\beta_*\left(\frac{\sin\phi}{R} - \frac{d\phi}{ds}\right) \tag{2.8}$$

where the rotational term β_* is defined as:

$$\beta_* = \frac{1}{2R}\left(R\frac{d\bar{v}}{ds} + \bar{v}\cos\phi - \frac{d\bar{u}}{d\theta}\right) \tag{2.9}$$

Flügge theory
A considerably more detailed description of the linear kinematics for shells of revolution has been presented by Flügge (1990) in his seminal book *Stresses in shells*, a commonly referenced work as the most rigorous mathematical framework on shell theory. Derived from first principles, the kinematics of the shell allow not only for non-shallow effects to be considered in its deformation state, a benefit that Flügge's theory shares with those of Reissner and Sanders, but to additionally include the ζ coordinate's role in modifying the through-the-thickness radius of the shell wall and associated strain variations. As such, this is the only theory that does not explicitly rely on the approximations of Assumptions 2-3 for the bending theory solution of axisymmetric shells. The kinematics under discussion are presented in the following set of Eqs. 2.10, adapted from

their original form to comply to the nomenclature of the present document:

$$\epsilon_\phi = \frac{\partial \bar{u}}{\partial s} + \frac{\bar{w}}{r_\phi + z} \tag{2.10a}$$

$$\epsilon_\theta = \frac{1}{r}\frac{\partial \bar{v}}{\partial \theta} + \cot\phi \frac{\bar{u}}{r_\theta + \zeta} + \frac{\bar{w}}{r_\theta + \zeta} \tag{2.10b}$$

$$\gamma_{\phi\theta} = \frac{1}{\sin\phi(r_\theta + \zeta)}\frac{\partial \bar{u}}{\partial \theta} + \frac{\partial \bar{v}}{\partial \phi}\frac{1}{r_\phi + \zeta} - \frac{r_\phi \cot\phi}{r_\theta(r_\phi + \zeta)}\bar{v} \tag{2.10c}$$

$$\kappa_\phi = -\frac{\partial^2 \phi}{\partial s^2}\frac{1}{r_\phi(r_\phi + \zeta)}\bar{u} - \frac{\partial^2 \bar{w}}{\partial \phi^2}\frac{1}{r_\phi}\frac{1}{r_\phi + \zeta} + \frac{\partial^2 \phi}{\partial s^2}\frac{1}{r_\phi + \zeta}\frac{\partial \bar{w}}{\partial s} \tag{2.10d}$$

$$\kappa_\theta = \frac{\cot\phi}{r_\theta + \zeta}\frac{\bar{u}}{r_\phi} - \frac{\cot\phi}{r_\theta + \zeta}\frac{\partial \bar{w}}{\partial s} - \frac{1}{r\sin\phi(r_\theta + \zeta)}\frac{\partial^2 \bar{w}}{\partial \theta^2} \tag{2.10e}$$

$$\begin{aligned}\kappa_{\phi\theta} = {} & \frac{1}{r_\phi \sin\phi(r_\theta + \zeta)}\frac{\partial \bar{u}}{\partial \theta} - \frac{1}{r_\theta(r_\phi + \zeta)}\frac{\partial \bar{v}}{\partial \phi} - \frac{r_\phi \cot\phi}{r_\theta^2(r_\phi + \zeta)}\bar{v} \\ & + \left(\frac{\cot\phi}{r_\theta \sin\phi}\frac{\partial \bar{w}}{\partial \theta} - \frac{1}{\sin\phi}\frac{\partial^2 \bar{w}}{\partial s \partial \theta}\right)\left(\frac{1}{r_\theta + \zeta} + \frac{r_\phi}{r_\theta}\frac{1}{r_\phi + \zeta}\right)\end{aligned} \tag{2.10f}$$

A consequence of the intricacies associated with the inclusion of ζ on the midsurface definitions for the strains and curvatures is the limited application of the theory on practical analytical problems. Yamaki (1984) has presented a comparison of the critical elastic bifurcation load predictions for meridionally compressed, pressurised or torsionally loaded cylinders as analytically established on the basis of a pre-buckling stress state described by Donnell's theory or a modified Flügge theory, illustrating the complexities corresponding to the latter. Closed-form solutions for non-zero meridional curvature axisymmetric shells are considerably more scarce , owning to the need for retaining additional terms that do not vanish for $r_\phi \neq \infty$.

2.1.2.2 Nonlinear kinematics

The pre-buckling deformation of axisymmetric shells is strongly characterised by the onset and progressive development of nonlinear effects that oftentimes impede attainment of the structure's full load bearing capacity. The ongoing pursuit for more accurate predictions of a shell's resistance by the research community has lead to several nonlinear strain-displacement shell theories, providing a better description of its load-level dependent kinematics. One of the first such works has been presented by Marguerre (1950) for a shallow shell theory that considers finite-thickness effects (Debongnie, 1979), with limited however further implementations of the outlined kinematics in the context of analytical explorations or computational applications. The approximate shallow thin shell theory presented by Donnell (1935b) around the same time and extended by Mushtari (1938a) and Vlasov (1944) to eventually form the set of kinematics known as the DMV theory (with the corresponding linear strain relations presented earlier) has been shown to be appropriate for shell problems characterised by small strains and moderately large rotations. An alternative set of classical nonlinear strain-displacement relations has been independently developed by Koiter (1966) and Sanders Jr (1963), appropriate for the description of non-shallow thin shell deformation states, with the authors discussing the process of reducing their nonlinear kinematics to those of other theories through appropriate assumptions. Both of these nonlinear theories have been widely adopted for the nonlinear description of thin shell kinematics (Teng & Hong, 1998), subject to the approximations of sufficiently small strains and moderate rotations to ensure the accuracy of the underlying assumptions, with the latter being

also commonly employed in computational formulations for the solution of shells (Bushnell, 1989, 1976; Yamaki, 1984; Almroth & Brogan, 1978; ABAQUS, 2022). The nonlinear shell theories proposed by Novozhilov (1999) and Karman-Tsien (Von Karman & Tsien, 1939; Von Karman & Tsien, 1941) may also be occasionally encountered in the relevant literature for the description of path-dependent kinematics for shell structures, with the latter forming the basis for the shear deformable nonlinear shell theory of Reddy & Liu (1985).

The principal feature of all aforementioned shell theories is the omission of any curvature related terms in the description of nonlinear kinematics, an approach adopted on the presumption that they would have minimal effect in comparison to the corresponding membrane terms. As destabilising bending effects cannot be considered through a theory that ignores nonlinear curvature kinematics, there is an accompanying limitation for such shell theories in the context of stability problems which are otherwise dominated by a tensile membrane stress state. The existence of such destabilising curvature terms has been discussed in Gould & Basu (1977), with a practical example of an open toroidal shell under internal pressure examined through FEA by Jumikis (1987) to illustrate the instability phenomena that may occur on axisymmetric shells in a state of meridional and circumferential tension. An analytical exploration with the purpose of deriving first order nonlinear curvature terms was made more recently by Acharya (2000), aiming to provide a generalisation to the Koiter-Sanders theory.

Donnell - Mushtari - Vlasov theory

The nonlinear midsurface strains of the DMV theory are consistent with all the approximations employed for the derivation of their corresponding linear shell kinematics, presented in Eqs. 2.4. As a consequence of the incorporated shallow shell theory assumptions, β rotational terms reduce to expressions containing only normal displacements $\bar{w}$ and its derivatives, neglecting nonlinear effects associated with membrane straining of the shell and resulting in a theory that is only valid when the progressive deformation and potential buckling forms are dominated by normal to the shell wall displacement profiles (Jumikis, 1987). The simplicity of the DMV nonlinear relations of Eqs. 2.11 and the reality of many classical axisymmetric stability problems being characterised by predominantly normal displacements (e.g. cylindrical shells under meridional compression and spheres under external pressure) justify their extensive employment in analytical explorations on the derivation of elastic buckling loads (Koiter, 1945; Zoelly, 1915; Brush & Almroth, 1975).

$$\epsilon_{\phi,nl} = \frac{1}{2}\left(\frac{\partial \bar{w}}{\partial s}\right)^2 \tag{2.11a}$$

$$\epsilon_{\theta,nl} = \frac{1}{2}\left(\frac{\partial \bar{w}}{r\partial \theta}\right)^2 \tag{2.11b}$$

$$\gamma_{\phi\theta,nl} = \frac{\partial \bar{w}}{\partial s}\frac{\partial \bar{w}}{r\partial \theta} \tag{2.11c}$$

Koiter-Sanders theory

A nonlinear theory considered to be more accurate for shells undergoing large deflections is that of Koiter-Sanders (Yamaki, 1984), including the contribution of meridional and circumferential displacements on the rotational expressions according to non-shallow thin shell kinematics. The β_* rotational term of Eq. 2.9 is also considered in the nonlinear kinematics of the theory presented below, a key feature of the Koiter-Sanders kinematics that was considered in the linear curvatures of Eqs. 2.7a-2.7c. This is done on the basis of consistency with equilibrium equations rather than as a means of including nonlinear membrane strains (Jumikis, 1987).

Omission of β_* in the following strain-displacement expressions of Eqs. 2.12, as well as Eqs. 2.7, reduce the theory to a small rotations approach to axisymmetric shell kinematics.

$$\epsilon_{\phi,nl} = \frac{1}{2}\left(\frac{\partial\phi}{\partial s}\bar{u} - \frac{\partial\bar{w}}{\partial s}\right)^2 + \frac{1}{8r^2}\left(\cos\phi\bar{v} + r\frac{\partial\bar{v}}{\partial s} - \frac{\partial\bar{u}}{\partial\theta}\right)^2 \tag{2.12a}$$

$$\epsilon_{\theta,nl} = \frac{1}{2r^2}\left(\sin\phi\bar{v} - \frac{\partial\bar{w}}{\partial\theta}\right)^2 + \frac{1}{8r^2}\left(\cos\phi\bar{v} + r\frac{\partial\bar{v}}{\partial s} - \frac{\partial\bar{u}}{\partial\theta}\right)^2 \tag{2.12b}$$

$$\gamma_{\phi\theta,nl} = \left(\frac{\partial\phi}{\partial s}\bar{u} - \frac{\partial\bar{w}}{\partial s}\right)\left(\frac{\sin\phi\bar{v}}{r} - \frac{\partial\bar{w}}{r\partial\theta}\right) \tag{2.12c}$$

With the significant rise in computational techniques for the analysis of shell problems over the second half of the last century, precision in the strain-displacement relationships is prioritised over mathematical simplicity, as numerical solvers need to guarantee the accuracy of their results over a breadth of shell geometries. Thorough kinematic frameworks that include a variety of nonlinear effects at the cost of a small increase in computational power are hence favoured over more approximate equivalents (Hong, 2000), rationalising the transition into the Koiter-Sanders theory as a comparison reference for more recent shell element formulations (Ádány & Schafer, 2025b).

2.1.3 Buckling considerations for shells of revolution

It is well established amongst the shell research community that the load carrying capacity of thin axisymmetric shell structures is oftentimes governed by their elastic buckling resistance. This section will attempt to provide a comprehensive overview of key stability analysis aspects for shells of revolution, with a particular focus on the behaviour of essential segment geometries commonly encountered in civil engineering applications. The thoroughness of this section's review on the subject of shell buckling cannot possibly match the extensive listing of publications on the topic gathered by Bushnell (2020) on his dedicated webpage *https://shellbuckling.com*, amassing more than 15000 pages of article references related to the linear or nonlinear stability of shells. The seminal book of the same author (Bushnell, 1989) on the computational aspects of shell buckling has established the basis for modelling practice and result interpretation for analysts of the field (Hong, 2000; Teng & Rotter, 2004a; Sadowski & Rotter, 2013) and has also greatly influenced the discussion of the present section.

A review on the buckling behaviour of shells characterised by an ideally perfect initial geometry will aid in appreciating the different kinds of instability that may be encountered, but also in discerning the differences between limit points on the nonlinear pre-buckling path of the shell and actual buckling events. These two states are both critical to the axisymmetric shell's structural integrity and are quite often misinterpreted to be synonymous due to the computational similarities associated with their commencement and the swiftness of the collapse mechanism once they are triggered. The effects of initial imperfections, an inherent characteristic of any real-life structure's form, can alter the instantaneous characteristics of stability events into a more gradual phenomenon, smoothening out transition from the fundamental pre-buckling state into the post-buckling state of the shell. This behaviour will be explored in the context of cylinder under meridional compression buckling, the most classical form of axisymmetric shell stability problem.

2.1.3.1 Stability of ideal perfect shells

While perfect shell geometries are an uncommon occurrence in applications of engineering interest, as the cloud of experimental results in Figure 1.2 of the previous chapter has illustrated, they can be meaningful instruments to the study of different buckling behaviours that can possibly occur and solely depend on the ideal base shell geometry, facilitating understanding of imperfect shell structures by constituting important reference cases. The different types of buckling phenomena are classified with respect to the post-buckling path characteristics, examined on the basis of the modal displacements associated with buckling, as demonstrated in Figure 2.3.

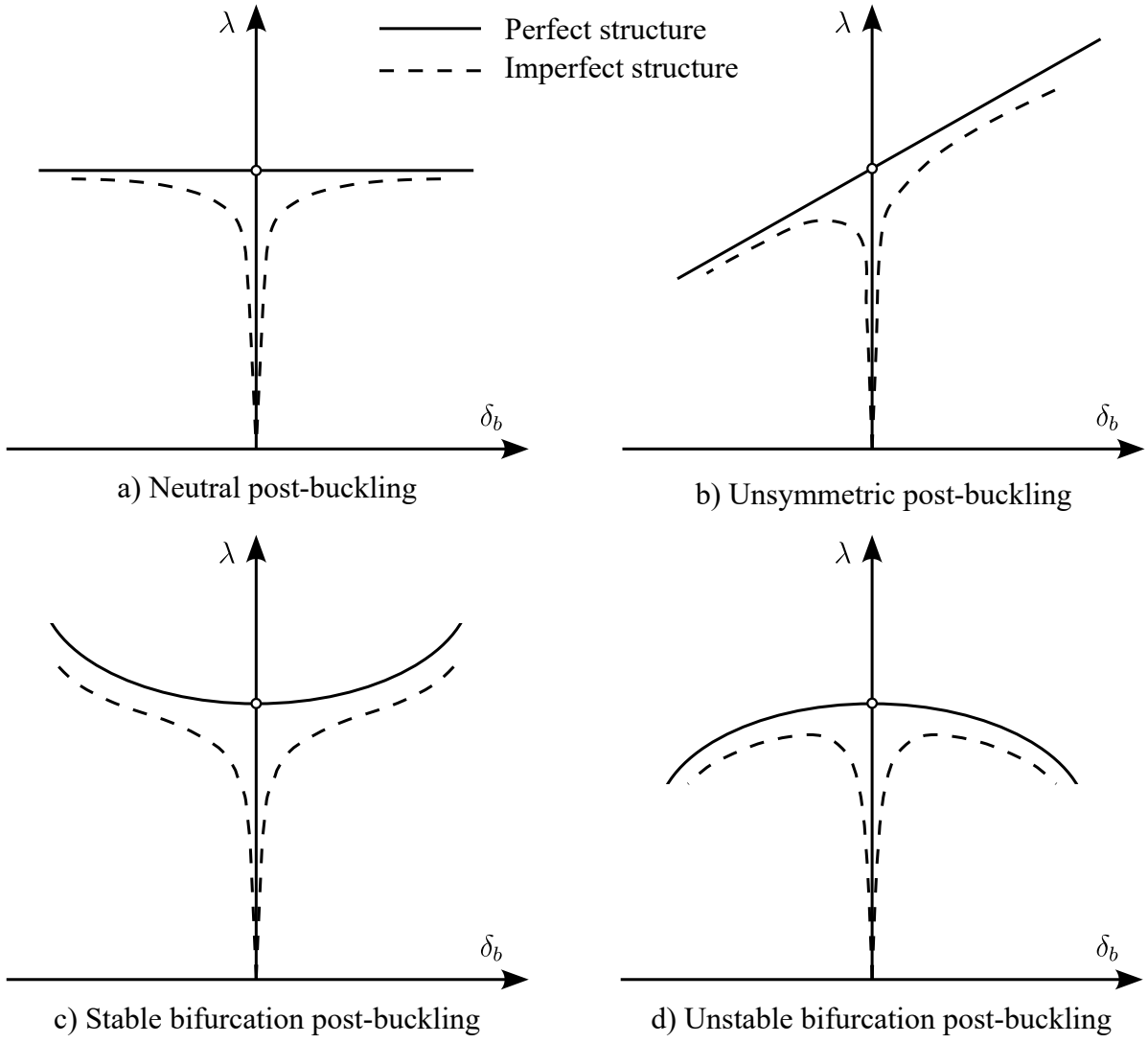


Figure 2.3: Different types of load-deflection paths relevant to the pre-buckling and post-buckling states of perfect and imperfect structures. λ represents a load proportionality factor (not to be confused with the slenderness parameter later on) while δ_b represents modal displacement associated with the buckling event.

The perfect structure load versus (modal) displacements path of Fig. 2.3(a) represents a solution to the eigenvalue problem for a linearised buckling form of the stability equations, where the magnitude of post-buckling deformations is indeterminate, implying infinitely increasing modal displacements δ_b for a constant level of externally applied loading λ. Once nonlinear post-buckling effects are accounted for, in a more comprehensive portrayal of real life structure

behaviour, the magnitude of modal deformations δ_b become a function of the load level λ, as illustrated in Figs. 2.3(b-d). The asymmetric nature of the post-buckling path in Fig. 2.3(b) suggests that a structure may continue to resist applied forces if forced to buckle one way, but can also collapse if allowed to buckle the other way. As discussed in Bushnell (1989), this behaviour is indicative of structures with parts that can move relative to each other after a buckling event has occurred, allowing them to come into contact and support one another if deformations proceed one way, but remain isolated and move away if the opposite buckling deflection profile is permitted. This type of stability response can be encountered in structures comprising a flat sheet riveted to a corrugated sheet.

Axisymmetric shell structures are commonly characterised by post-buckling responses that fall within the bifurcation categories illustrated in Figs 2.3(c,d). A stable post-buckling behaviour is illustrated in Fig. 2.3(c) where the structure is able to continue resisting applied even after buckling has initiated, while an unstable one is presented in Fig. 2.3(d) associated with the collapse of the loaded structure if permitted to buckle. The steepness of these post-buckling paths is entirely system dependent, with shell structures potentially experiencing a substantially more swift loss of their load-resisting characteristics once buckling occurs due to the lack of robustness associated with their optimised shapes. A key feature of the bifurcation eigenmodes for perfect axisymmetric shell structures is the harmonic distribution of the displacement field associated with buckling along the circumference of the shell. This inherent mathematical trait has allowed for analytical ventures into linearised predictions of critical elastic buckling load by expressing any modal displacements through sine and cosine harmonic functions relative to the circumferential coordinate θ and a positive integer number n representing circumferential waves developing during buckling. Post-buckling interaction and mode switching for different circumferential wavenumbers n has also been possible through a Fourier decomposition of the different buckling modes (Teng & Hong, 2006), a trait of post-buckling shell behaviour that was also encountered during lab testing of meridionally compressed cylinders (Yamaki *et al.*, 1975), with the circumferential harmonic n being reduced by one for each consecutive mode switch (Shen, 2017), a concept visually illustrated in Figure 2.4. Specialised computational solvers have been developed by and for the shell buckling research community, as shall be discussed in the following section 2.3.

An essential trait of bifurcation buckling, either stable or unstable, is the inability of the structure to jump into the post-buckling path in the absence of any explicitly defined perturbations that provide the necessary 'push' into either branch of the load-displacement curves in Figs. 2.3 (c,d). These perturbations are not be confused with initial imperfections applied on the perfect structure, the effect of which is often (but not always) to reduce the critical buckling resistance of the axisymmetric shell in addition to smoothening out transition into its post-buckling path. Instead, perturbations correspond to infinitesimal midsurface geometric deviations that are of a form similar to the shape assumed by the shell when following either of the two bifurcation related post-buckling paths. This concept is oftentimes exploited during computational modelling of a structure by tactically assigning deviations of insignificant importance to its base geometry, with their magnitude being such that they may not undermine the critical buckling resistance of the model, in order to explore a post-buckling response or even lead the structure into the desired load-deflection path (mostly relevant for unsymmetrical stability systems, outlined by Fig. 2.3(b)).

Geometric nonlinearities have been shown to substantially affect the pre-buckling response of thin shell structures (Stein, 1964; Teng, 1996; Edlund, 2007), with the critical elastic bifurcation buckling resistance of slender cylinders under uniform meridional compression potentially being overestimated by a factor of 10% if a large deformation analysis is not applied for the tracing of their pre-buckling state. Inclusion of large pre-buckling deformation effects in the solution

process of an axisymmetric shell system can influence not only the estimation of its critical elastic buckling resistance, leading to a reduction for most common axisymmetric shell geometries, but can theoretically result to a different harmonic n to be evaluated as the critical mode that the shell is about to bifurcate into (Teng & Song, 2001). Figure 2.4 exhibits such a possibility, where the accumulation of pre-buckling geometrically nonlinear effects can lead to a more delayed interception of an adjacent equilibrium, or even an entirely different mode n if this interception is substantially delayed due to these effects.

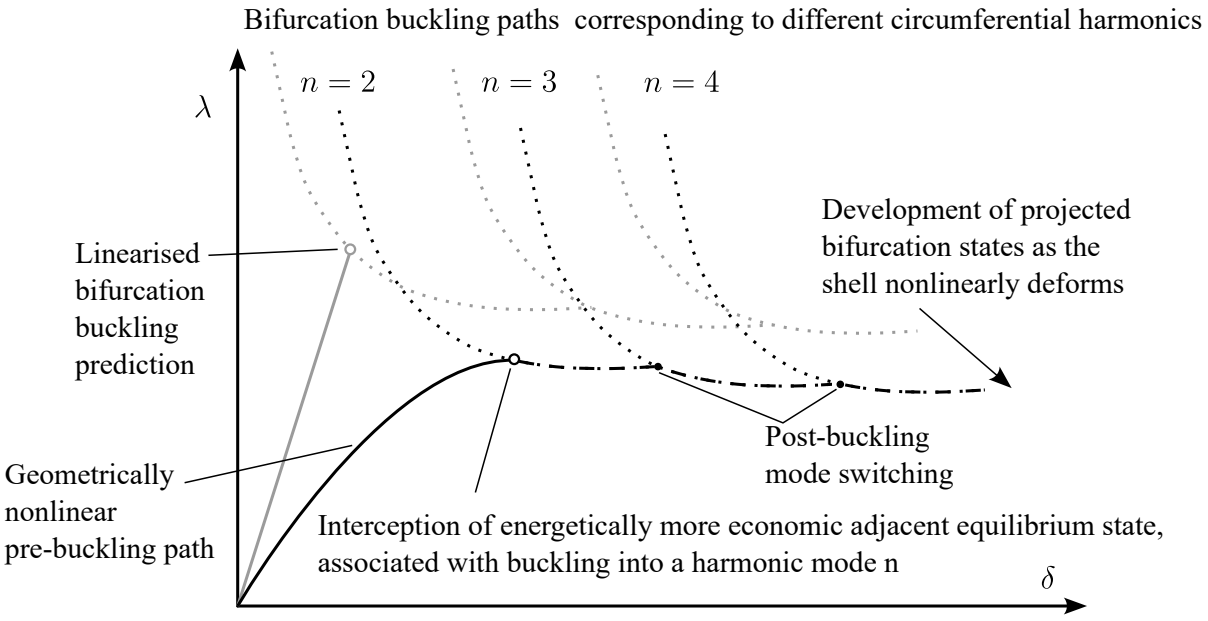


Figure 2.4: Differences in the critical buckling load prediction for linear or nonlinear tracing of the pre-buckling state of a generic axisymmetric shell structure, with an illustration of mode-switching along the post-buckling response.

Fully analytically obtained equilibrium paths are accompanied with significant levels of approximations (Yamaki, 1984), with some notable solutions being those of Donnell & Wan (1950) and Loo (1954) for cylinders under meridional compression. Consideration of nonlinearities in the response of an axisymmetric shell prior to a bifurcation buckling event produces the apparent limitation of not permitting an analytical closed-form solution for the elastic stability of axisymmetric shells to be derived, as a step-wise application of the externally applied loading is now necessary for the accurate evaluation of strains at different stages of deformation (Brush & Almroth, 1975). In cases where an analytical approach was adopted for tracing the fundamental equilibrium pre-buckling state of the shell without considerable approximation applied (Fischer, 1963; Stein, 1964), a finite difference approach was employed for the integration of nonlinear strains at different levels of externally applied loading. Nevertheless, with the onset and rapid developments of computer-aided engineering analysis, mostly applied through implementations of the finite element method, consideration of nonlinear pre-buckling effects is now the norm in scientific explorations on the stability of shell structures (Teng, 1996; Schmidt, 2000).

2.1.3.2 Effects of initial imperfections on the stability of shells

A study on the imperfection sensitivity of axisymmetric shell structures is by itself an extensive area of research, with considerable portions of annual publications investigating the effect of varying shapes and amplitudes of initial imperfections on different forms of shell segment geometries and external actions. The term 'imperfections' does not only include the effect of initial deviations from the perfect base geometry of the shell's midsurface, but additionally

envelopes the realistic cases of shell-wall thickness changes and variations, either of a progressive or abrupt nature, non-uniformly applied restraints or external action eccentricities (Edlund, 2007; Fajuyitan, 2018; Sadowski *et al.*, 2023). Material imperfections such as residual stresses or property variations are more scarcely considered (Sadowski *et al.*, 2023).

It has been shown that the imperfection sensitivity of an axisymmetric shell structure correlates to a degree to its Gaussian curvature K parameter (Eckstein *et al.*, 1979), defined as the product of the principle curvatures of the shell in Eq. 2.13 below (with reference to Fig. 2.1). Higher positive values of K are associated with greater degrees of imperfection sensitivity, while negative K values correspond to shells whose response is rather insensitive to initial imperfections. As such, spherical shells with $K > 0$ are expected to be detrimentally affected by initial imperfections of increasing magnitudes (Qiao *et al.*, 2020), while the hyperboloid shape of nuclear cooling towers with $K < 0$ ensures they remain unaffected by constructional imperfections. Cylindrical shells have a Gaussian curvature of $K = 0$ due to their straight meridian (meridional radii $r_\phi = 0$) and are consequently moderately affected by potential deviations from the perfect model characteristics. The dependence of imperfection sensitivity on the length of cylinders under global bending has been additionally examined by Fajuyitan & Sadowski (2018) and Fajuyitan (2018), while that of meridionally compressed cylindrical shells by Al Lawati (2017) (regrettably still in its embargo period, even though a similar study by the same author can be found in Al Lawati *et al.* (2023)), constituting some of the few studies where the imperfection sensitivity is examined not only on the basis of the reference model but alongside its geometric parameters.

$$K = \frac{1}{r_\phi r_\theta} \tag{2.13}$$

Initial geometric imperfections in axisymmetric shell structures are usually associated with a reduction of their critical buckling resistance (though not always (Jumikis, 1987)), smoothening transition from pre-buckling to post-buckling deformation states and obscuring any clear distinctions between these phases. Consequently, the identification and precise characterisation of buckling phenomena can become notably challenging tasks, requiring sophisticated methods to reliably capture the shell structure's response. The sharp shift into an alternative deflection path corresponding to a specific mode after occurrence of a bifurcation event is now replaced by a limit-point like behaviour when small/moderate imperfection amplitudes are considered, as illustrated in the equilibrium paths of Figure 2.5 obtained through independent research studies on cylinders under meridional compression. Further increase of the initial imperfections can render even such points completely indistinguishable from the rest of the equilibrium curve. As axisymmetric shell structures can demonstrate a late post-buckling stiffness increase through a positive load-deflection slope, after the initial surge in their resistance at the early stages of instability events, the existence of significant imperfections can make evaluation of the total load bearing capacity of the shell a very difficult endeavour. Design of highly imperfect shells can therefore be a troublesome task in the context of the GMNIA approach of the European Standard EN 1993-1-6 (2025), as the unambiguous termination criterion C1 of a maximum load factor achieved for nominally perfect shells will potentially not be the determining criterion if pre-buckling and post-buckling paths are blended together for high amplitudes of initial imperfections, leading to a C3 criterion for the termination of the GMNIA corresponding to the maximum tolerable deformation of the shell structure (with a discussion on the different EN 1993-1-6 (2025) termination criteria provided later in Section 2.4.1).

As the actual profile of midsurface deviations cannot possibly be exactly known at the design stage of an axisymmetric shell structure (or any other structure), an intimate relationship

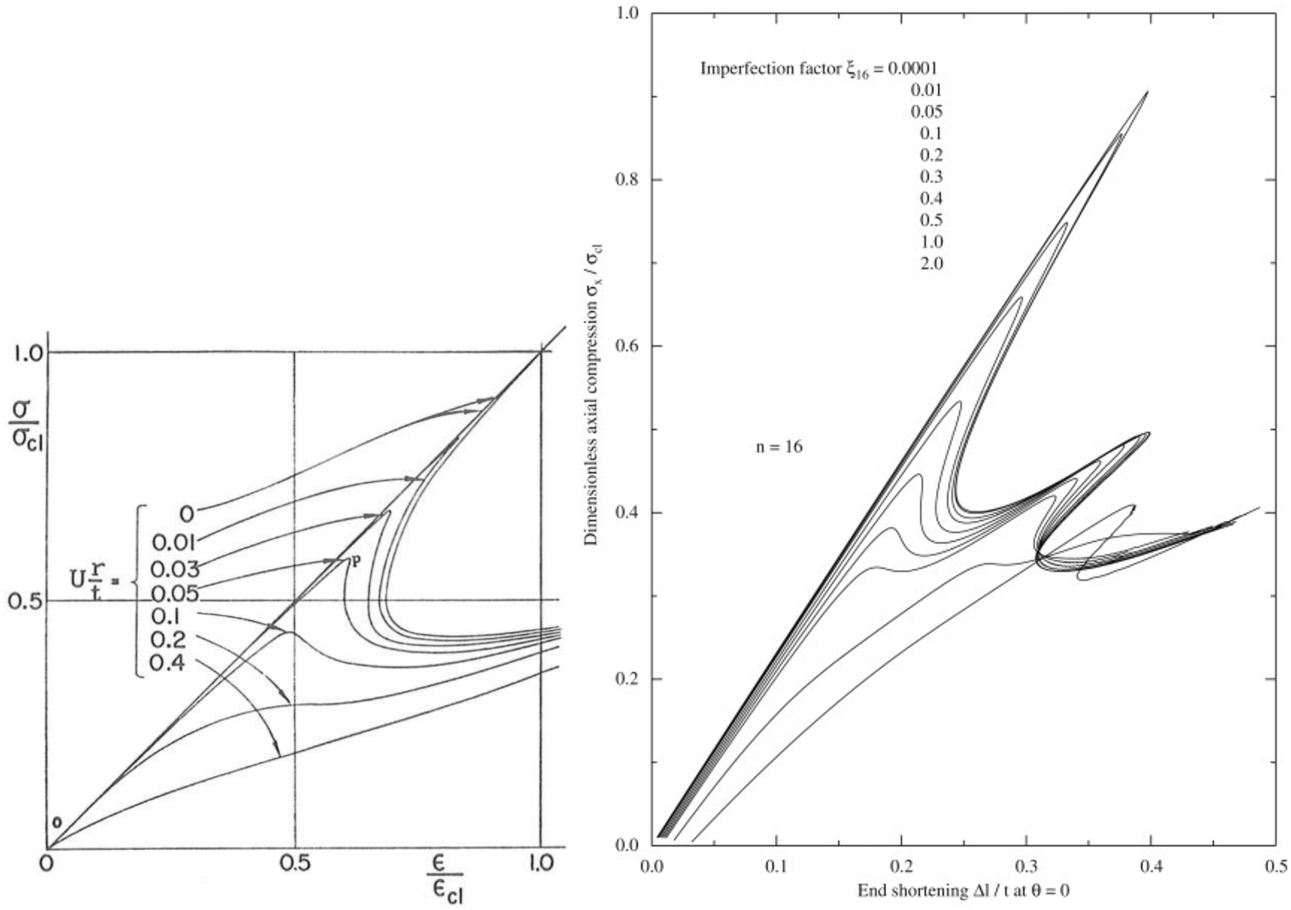


Figure 2.5: Effect of increasing imperfection amplitudes on the elastic response of cylindrical shells under meridional compression through different illustrations of the meridional stress level against the deformation, as analytically studied by Donnell & Wan (1950) on the left or computationally explored by Hong & Teng (2008) on the right.

between the a-priori assumed shape of initial imperfections and the load bearing capacity of the system is inevitable. A compromise needs to be made on the engineer's part between the conservativeness of the employed imperfection shape and the likelihood that it accurately represents the end product of the fabrication process. Chryssanthopoulos' extensive doctoral work (Chryssanthopoulos, 1989) and subsequent publications (Chryssanthopoulos *et al.*, 1991a,b) provided a probabilistic framework to the description of initial imperfections by measuring fabricated cylindrical shell models prior to their loading and performing a statistical analysis on the coefficients of a Fourier series description of their geometric imperfections. Similar processes may also be applied to quantify uncertainties in the specified boundary conditions, material properties, thickness distributions, residual stresses or other parameters that can influence to any extent the load carrying capacity of a shell, providing a reliability based design strategy (Arbocz & Starnes Jr, 2002). Hierarchical procedures would need to be executed at a preliminary level to evaluate the importance of these different mechanical variables to be included in further reliability calculations (Arbocz & Hol, 1993; Arbocz & Starnes Jr, 2002). Whilst probabilistic approaches appear to be the most sensible for incorporation of initial geometric imperfections during the design stage of a shell structural system, given a specific fabrication process, it heavily relies on the availability of substantial data sums obtained through surveys on full-scale shell structures and is thus only provided on a per system basis (Teng & Song, 2001; Arbocz & Starnes Jr, 2002). For most shell geometries such surveys have not been undertaken, limiting the applicability of this methodology.

The accuracy in the estimation of a shell's buckling resistance through numerical simulations requires alternatives for the detrimental effect of geometric imperfections to be accounted for in the absence of reliably defined fabrication related shapes. These must be provided in the form of an unfavourable shape superimposed on the base geometry after appropriate scaling, the magnitude of which is commonly linked to the quality of fabrication. Equivalent geometric imperfections that aim to reduce the computationally obtained buckling strength of the model as much as could be expected from actual full scale shell imperfection shapes have been furnished through limited studies (Rotter & Teng, 1989; Schmidt & Krysik, 1991; Speicher & Saal, 1991) and are again only available for specific systems. Even from early versions of the European Standard ENV 1993-1-6 (1999), utilisation of imperfection profiles in the form of bifurcation buckling modes is permitted with the aim to provide a general and robust approach for the shell design community to account for initial geometric imperfections during the modelling phase. This is fundamentally allowed on the rationale that eigenmode-affine imperfections would significantly accelerate the onset of buckling associated with those specific modes. Since these eigenmodes correspond to the LBA result of the ideal shell geometry, it is natural to expect that employing them yields the most conservative possible estimation of the imperfect model's buckling strength. However, even if concerns on whether such imperfection profiles can realistically occur in full-scale structures are momentarily set aside, the conservativeness of this method is not unequivocally assured. With reference to Fig. 2.4 and the preceding discussion of this section, inclusion of pre-buckling geometrically nonlinear effects during tracing of the equilibrium path can potentially alter the criticality of different harmonics n that an axisymmetric shell may be critical to bifurcate into, an essential aspect of stability considerations that an LBA cannot account for. The limitations of this methodology have been rigorously examined in Teng & Song (2001) within the context of imperfect cylindrical shells subjected to midspan radial loads.

2.1.3.3 Stability of circular cylindrical shells

Stability analysis of circular cylindrical shell structures has been an active field of research studies for more than a century, with computational methods employing FEA superseding the analytical ventures of the past (Teng, 1996; Schmidt, 2000; Teng & Rotter, 2004b; Edlund, 2007). The constant circumferential radii $r_\theta = r$ and the zero meridional base geometry curvature $\partial\phi/\partial s = 0$ for a straight meridian with $r_\phi = \infty$ have enabled considerable reductions to the equilibrium equations of Eqs. 2.3 and linear and nonlinear kinematic relations of sections 2.1.2.1 and 2.1.2.2 accordingly, permitting closed-form solutions to be derived. It should be emphasised at this point that hereafter the term cylinder will be used to refer to a circular cylindrical shell, with non-circular version of this classical shell system like elliptical or "pear-shaped" cylinders (Hutchinson, 1965; Bushnell, 1989; Soldatos, 1999; Xu *et al.*, 2017) being out of scope of the present document as non-axisymmetric systems.

Even with all the reductions that the simple geometry of a cylindrical shell allows for, analytical endeavours on their stability analysis with the aim of deriving a closed-form result for their critical elastic buckling prediction are often based on the assumption of a uniform pre-buckling membrane stress state, on top of neglecting any nonlinearities in the loading-deformation relationships for the reasons outlined in the discussion of the preceding section 2.1.3.1. Consideration of boundary layer bending effects, arising as a consequence of compatibility requirements with essential edge boundary conditions, would introduce rotations associated with the linear pre-buckling deformations that would violate the condition of meridional stress uniformity and introduce a dependency on the expression of stresses to the meridional coordinate s of Fig. 2.1. The extent of these boundary layer bending effects have been derived according to linear DMV theory kinematics of Eqs. 2.4, congruent to the Sanders linear theory for fully axisymmetric

deformation states as presented in Eqs. 2.7, and found to be equal to 2Λ at the edges of a cylindrical shell or at junctions of abrupt geometrical changes between segments. The bending half-wavelength Λ describing the spread of bending behaviour effects near boundaries may be found across classical texts on thin shell theory (Timoshenko & Woinowsky-Krieger, 1959a; Calladine, 1983) for isotropic materials as:

$$\Lambda = \frac{\pi\sqrt{rt}}{\sqrt[4]{3(1-\nu^2)}} \tag{2.14}$$

Derivation of the bending half-wavelength for orthotropic materials is also possible (Rotter & Sadowski, 2012) on the same basis employed for the isotropic result of Eq. 2.14. It should be noted that a capital Λ has been utilised here for the bending half-wavelength in contrast to the lowercase λ commonly encountered in relevant scientific resources in order to distinguish against the slenderness of the shell system in the context of the capacity curve framework of EN 1993-1-6 (2025), as described in the following section 2.4.

Whilst solution of such a linearised stability system is not impossible, as the pioneering work of Yamaki (1984) has showcased, a simpler membrane theory solution for the pre-buckling state of the cylinder ensures that the stress level at which bifurcation buckling will initiate can be expressed through a single variable, considerably reducing the mathematical complexity of the derivations. This principle has been applied by three independent analytical ventures in the early 20th century on the stability of cylindrical shells under uniform meridional compression (Lorenz, 1908; Timoshenko, 1910; Southwell, 1914), reaching the same result for the *classical elastic critical buckling stress*:

$$\sigma_{cl} = \frac{E}{\sqrt{3(1-\nu^2)}}\frac{t}{r} \tag{2.15}$$

Classical shell theory (Donnell, 1935b) has provided the kinematics foundation for the analytical work on the stability of cylinders under uniform meridional compression with pin-ended boundary conditions (Brush & Almroth, 1975), once again on the basis of a membrane pre-buckling stress state assumption. With the chequerboard patterns of the buckling modes characterised by an integer number of meridional half-waves $m \geq 1$ and circumferential full-waves $n \geq 0$, the compressive edge load associated with each mode has been derived as:

$$N_{m-n} = \frac{Et^3}{12(1-\nu^2)}\left(\frac{\bar{m}^2+n^2}{\bar{m}r}\right)^2 + \frac{Et}{r^2}\left(\frac{\bar{m}r}{\bar{m}^2+n^2}\right)^2 \tag{2.16}$$

where $\bar{m}$ is defined as:

$$\bar{m} = \frac{m\pi r}{L} \tag{2.17}$$

Later work by Koiter during his PhD (Koiter, 1945) has demonstrated that the locus of $m-n$ pairs corresponding to the critical buckling load, obtained through a minimisation approach to the $N_{m,n}$ relationship of Eq. 2.16 with respect to $\bar{m}$ and n, could be identified to be a circle:

$$\left(\bar{m} - \sqrt{\frac{r}{t}}\sqrt[4]{\frac{3}{4}\left(1-\nu^2\right)}\right)^2 + n^2 = \frac{r}{t}\sqrt{\frac{3}{4}\left(1-\nu^2\right)}\,, \tag{2.18}$$

commonly referred to in bibliography relevant to the field of shell buckling as the 'Koiter circle' (Brush & Almroth, 1975; Spagnoli, 2003; Teng & Rotter, 2004b; Sadowski *et al.*, 2018), a graphical representation of which is provided in Figure 2.6. Whilst the physical geometric parameters corresponding to this specific representation of the circle are not important for its conceptual presentation, it is worth noting that the number of competing $m-n$ combinations that are near simultaneously critical for the stability of the cylindrical shell under meridional compression can easily be in the hundreds as the r/t ratio, being the governing parameter to the model's slenderness, increases (Teng & Rotter, 2004b). The corresponding critical elastic buckling load is then given as:

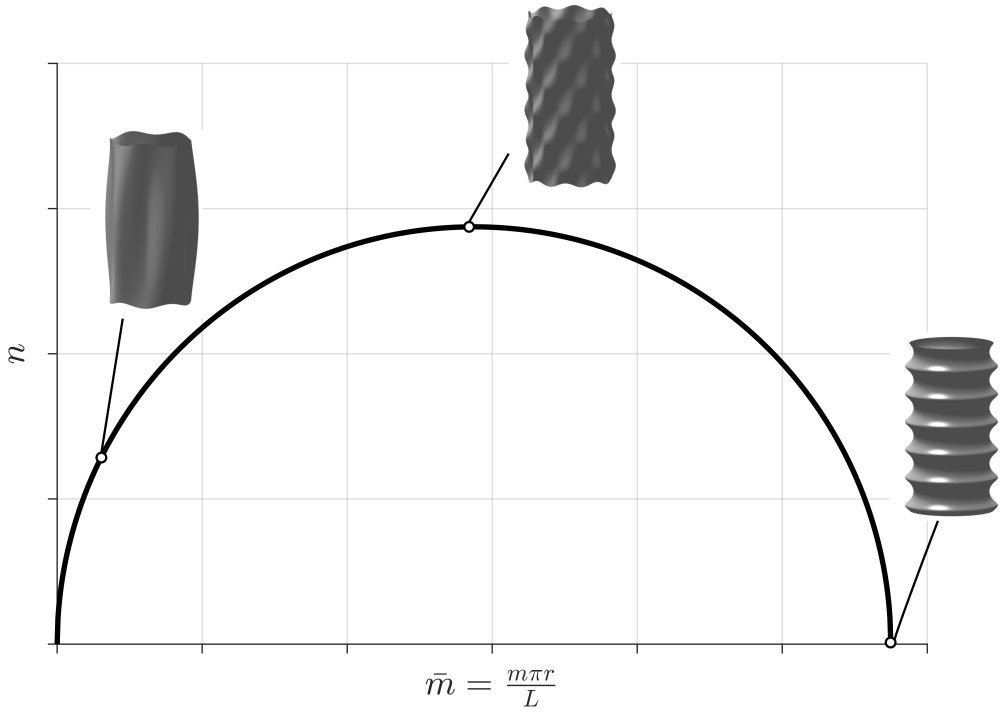


Figure 2.6: Koiter circle for simultaneously critical pairs of meridional half-waves m and circumferential waves n for pin-ended cylinders under meridional compression.

$$N_{cl} = \sigma_{cl} t = \frac{E}{\sqrt{3(1-\nu^2)}} \frac{t^2}{r} \tag{2.19}$$

It should be highlighted that this classical result for the compressive edge load of Eq. 2.19 has been evaluated on the basis of continuous real values for the $m-n$ variables, a principle that contradicts their physical interpretation as discrete integer wavenumbers associated with bifurcation buckling modes. Examination of the full 3D surface for the elastic buckling strength of cylinders provided by Eq. 2.16 and illustrated in Figure 2.7, associated with each physically possible pair of $m-n$ wavenumbers, reveals a key underlying characteristic on the criticality of different combinations of these modal parameters. As only integer values can be assumed by the $m-n$ wavenumbers in the context of actual shell bifurcation buckling, the points corresponding to most eigenmodes will inevitably fall close to Koiter circle locus but not necessarily exactly on it, as a circle like the one presented in Fig. 2.6 would only rarely cross through integer values for both the meridional half-waves m and circumferential full-waves n. Owning to the characteristics of the analytical '3D valley' of Fig. 2.7, an N_{m-n} elastic resistance is considerably more likely to fall closer to the classical result of Eq. 2.16 for $m-n$ pairs that are clustering near the right hand-side neighbourhood of the Koiter circle, as the analytical 'valley' appears to

be wider in that area and considerably steeper in the left hand-side for $\bar{m} \to 0$. This deduction is of critical importance for the modelling purposes of this axisymmetric shell problem, with specialised treatments being necessary for accurate computational results to be obtained using classical 3D-based FE approaches (Sadowski *et al.*, 2018).

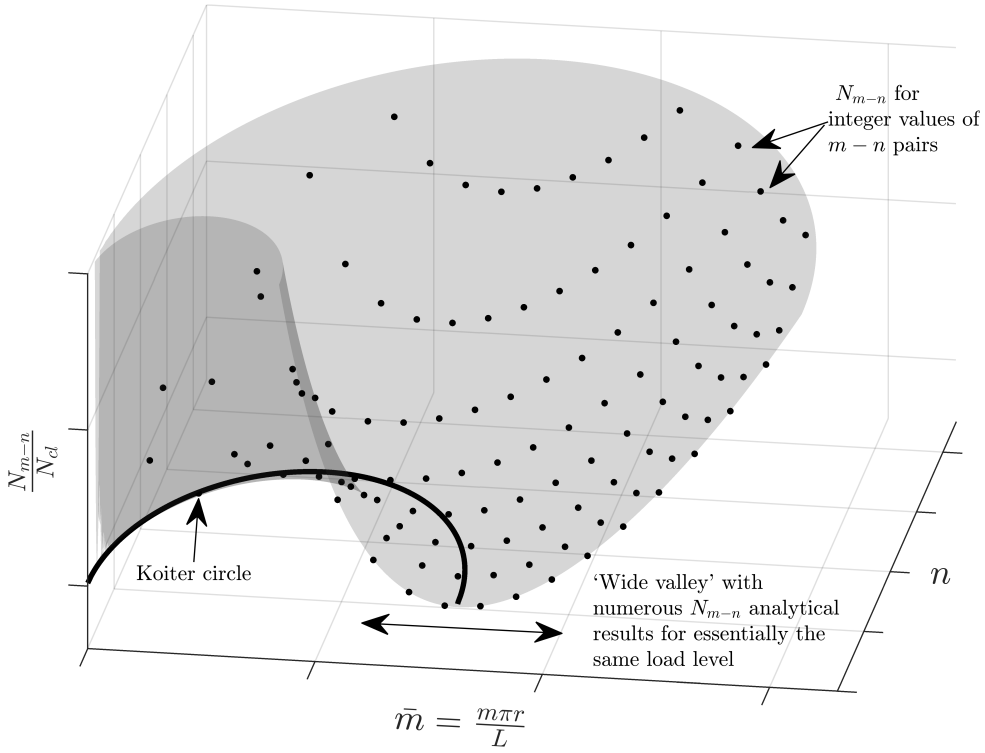


Figure 2.7: 3D surface of analytical elastic buckling predictions corresponding to different $m-n$ modal pairs.

Further processing of the Koiter circle result of Eq. 2.18 permits the calculation of the meridional length of a buckle for an axisymmetric mode by setting the number of circumferential waves equal to zero $n = 0$. This allows for the number of meridional buckles m_{axi} and their corresponding half-wavelength Λ_{axi} to be found as:

$$m_{axi} = \frac{L}{\pi}\sqrt[4]{\frac{Et}{Dr^2}} \tag{2.20}$$

and

$$\Lambda_{axi} = \frac{L}{m_{axi}} = \pi\sqrt[4]{\frac{Dr^2}{Et}} = \frac{\pi\sqrt{rt}}{\sqrt[4]{12(1-\nu^2)}} \tag{2.21}$$

While meridional compression is perhaps the most exhaustively researched loading scenario, cylinders subjected to uniform torsion and uniform external pressure have also garnered considerable attention. This is largely due to the uniformity of the pre-buckling membrane stress state in these cases, which facilitates analytical treatment, subject to the same simplifying assumptions typically adopted in analytical stability solutions of meridionally compressed cylinders. Cylindrical shells under global bending have additionally received considerable attention (Seide & Weingarten, 1961; Fajuyitan & Sadowski, 2018), with the slowly varying membrane stress state along their circumference permitting the classical elastic buckling result of Eq. 2.15 derived for the case of meridional compression to be utilised. The effect of wind loads on the

elastic stability of cylinders has also been considered (Teng, 1996; Pircher *et al.*, 2001; Pircher, 2004; Teng & Rotter, 2004b), with experimental approaches also utilised through wind-tunnel facilities (Greiner & Derler, 1995) testing to check on the validity of mathematical models. Elastic buckling resulting from combinations of these classical loads has been the focus of research studies considering more realistic conditions for cylindrical shell applications, with special emphasis on the loading ratios of two or more external actions and the potentially beneficial effect one of them may have when included in the model as an alleviating factor on the development of compressive stresses and early instability phenomena. The influence of boundary conditions on the critical elastic buckling strength of cylinders under various loading scenarios has also been examined through a series of studies (Hoff, 1966; Hong, 2000; Fajuyitan, 2018).

2.1.3.4 Stability of conical shells

An axisymmetric shell structure that may be perceived as a generalisation of cylindrical shells, but without having received the same level of attention corresponding to its buckling resistance, is that of full or truncated conical shells. For a straight meridian, with $r_\phi \to \infty$, and a meridional angle ϕ being constant a circular conical shell can be generated (with non-circular cones also being out of scope). A circular plate can be obtained as a special case for $\phi = 0$ or $\phi = \pi$, while a cylinder corresponds to $\phi = \pi/2$.

Due to the inclined nature of a conical shell's meridian, often described through an apex angle β complementary to the meridional angle ϕ, any compressive load applied along the axial z axis of the axisymmetric shell system in Fig. 2.1 will inevitably produce a complex stress state accompanied by extensive bending boundary layers that penetrate deep into the meridian of the cone. A pure membrane stress state would consequently be a simplification of questionable accuracy corresponding to the pre-buckling stress state of the shell. As a result, analytical derivations on the buckling of conical shells are limited to some very specific geometries and loading scenarios (Ifayefunmi, 2014), such as the particular case of a cone with a shell wall thickness t linearly varying with respect to the circumferential radius of curvature r_θ under external uniform axial pressure (Pflueger, 1937), considering harmonic variations for the buckling displacement field. Acknowledging the need for a higher level of approximations for closed-form critical buckling load predictions to be derived, a few more analytical studies have been carried out within the last century (Seide, 1956; Singer, 1965; Arbocz, 1968), with Tani & Yamaki (1970) considering the effect of boundary conditions on the elastic stability of this axisymmetric shell problem.

Wind turbine towers comprise assemblies of tubular and conical axisymmetric shell segments, prompting renewed interest in the stability of circular cones as a quick search through research article databases reveal, with the majority of relevant manuscripts being published within the last 20 years and capitalising on advantageous FE analyses to improve understanding of their critical buckling capacity characteristics. The computationally assisted work of Spagnoli (Spagnoli & Chryssanthopoulos, 1999; Spagnoli, 2001, 2003) has aided in the identification of a concept very similar to that of the Koiter circles in meridionally compressed cylinders. When the modal wavenumber pairs $m - n$ are plotted in a dimensionless space $\bar{\beta_m} - \bar{\beta_c}$ then FE results within 2% of the lowest eigenvalue appear to fall in the vicinity of an elliptical locus, termed by the investigating author as 'Koiter ellipses', with the characteristics of this elliptical locus depending on the geometric parameters of the conical shell. Whilst this concept relies on principles of pure membrane pre-buckling stress state, the accuracy of which degrades as the apex angle β increases, it has facilitated further numerical explorations considering conical shell segments (Sadowski & Seidel, 2023b) by providing critical wavenumber estimates for model discretisation.

2.1.3.5 Stability of spherical shells and spherical caps

From domes to storage containers and pressure vessel end heads, complete spherical shells and spherical caps have been commonly adopted in engineering applications due to their geometric simplicity, accompanied by advantageous mechanical properties. A constant meridional radius of curvature r_ϕ ensures a uniform membrane stress state for cases of normal pressure loading, aside of course from any bending effects at boundary edges or connections to different shell segments, the extent of which depends on the relative slenderness r_θ/t ratio of the shell. Assumption of a uniform pure pre-buckling membrane stress state has facilitated analytical endeavours on the evaluation of the critical elastic buckling resistance of a complete sphere under external pressure p_{cl} by Zoelly (1915), evaluated as:

$$p_{cl} = \frac{2E}{\sqrt{3(1-\nu^2)}} \left(\frac{t}{r_\theta}\right)^2 \tag{2.22}$$

A more general solution to the stability problem of complete spheres was later presented by Van der Neut (1932), considering also unsymmetrical buckling. Further analytical explorations on the stability of complete or partial spherical shells have been undertaken by Von Karman & Tsien (1939); Koiter (1969); Koga & Hoff (1969). An overview of spherical shell buckling principles may also be found in relevant to the field textbooks (Timoshenko & Woinowsky-Krieger, 1959a; Bushnell, 1989; Samuelson & Eggwertz, 1992; Teng & Rotter, 2004b) or even on more general works on the elastic stability of structures (Timoshenko & Gere, 1961), showcasing the importance of this reference shell system. The summative work of Hutchinson (2016) *'Buckling of spherical shells revisited'* provides a comprehensive overview on a century's worth of developments on the elastic buckling resistance predictions through analytical, computational and experimental investigations of this classical problem.

As previously stated, the positive Gaussian curvature of spherical shells serves as a first indicator of their sensitivity to initial imperfections (Thompson, 1961). Experimental results on their buckling suggest a reduction of their critical resistance to as low as 20% of the theoretical result of Eq. 2.22 (Hutchinson, 2016; Evkin, 2023). Whilst the effect of axisymmetric imperfections (Koga & Hoff, 1969) and eigenmode affine imperfections (Ismail *et al.*, 2023) have been considered, localised dimple imperfections are considered to be detrimental for the load bearing capacity of spheres and spherical caps (Evkin *et al.*, 2017; Wagner *et al.*, 2018), a type of initial midsurface deviation corresponding to permanent damage induced from impact in realistic engineering applications (Wagner *et al.*, 2018; Evkin *et al.*, 2017; Evkin, 2023; Zhu *et al.*, 2022). As an alternative to explicitly defined initial imperfections in the model geometry, a concentrated load is oftentimes used in conjunction with an externally applied pressure to produce a dimple-like perturbation on the surface of the sphere and consequently reduce its elastic buckling pressure prediction to a claimed theoretical lower bound (Evkin *et al.*, 2017; Zhu *et al.*, 2022).

2.2 Computational methods for shells of revolution

Where analytical methods for the solution of axisymmetric shells appear to be a formidable mathematical endeavour or a completely unfeasible task, computational methods can be employed for the exploration of a shell's linear or nonlinear response under a given loading scenario. A brief overview of the different approaches employed over the years for computational solutions to be obtained for shell geometry and loading scenarios of varying theoretical complexity will be provided in this section, outlining the fundamental characteristics of each method in the context of axisymmetric shell problems.

2.2.1 Finite difference methods

Whilst utilisation of Finite Element Methods monopolises any recent computational ventures on the solution of complex shell problems by the research and engineering design communities alike, Finite Difference Methods (FDM) have been extensively used over the past century to produce numerical results for a series of linear and nonlinear axisymmetric shell problems. Addressing the governing equations for shell bending theory through the principle of minimum potential energy in conjunction with stepwise differentiation and integration protocols permitted valuable insights into the domain of nonlinear shell responses. As outlined in (Bushnell *et al.*, 1971; Noor & Stephens, 1973), implementation of the FDM relies on a minimisation of the total energy of the system for a number of grid points along the shell reference surface, including the strain energy of shell segments or any discreet ring and the potential energy of the externally applied actions, with appropriate boundary conditions usually considered through Lagrange multipliers. Kinetic energy may additionally be incorporated in this minimisation process for the free vibration analysis of shell models. Approximation of the derivatives at discrete points facilitates resolution of the continuous system into a grid (Edmondson, 1970), with the associated equations found in relevant references (Kunz, 1957; Kalnins, 1964). The discretisation error is found to be proportional to the length between grid points and consequently can be reduced through a grid refinement (Edmondson, 1970), a concept similar to techniques applied in the FEM to achieve a higher degree of results accuracy. The pioneering work of Bushnell in the field has produced the BOSOR5 numerical tool (Bushnell, 1976) for the analysis of branched shells of revolution considering the effect of both geometric and material nonlinearities, an extensively used FORTRAN solver along with its predecessors as discussed later in the current chapter, while initial versions of the STAGS software (Almroth & Brogan, 1978) where also based on finite difference schemes for the solution of general shells.

Early applications of the FDM in the context of axisymmetric shell problems can be traced to Salvadori (1951), providing an outline of the application process for this numerical scheme to different categories of structural problems before proceeding with the solution of an infinitely long cylinder under meridional compression. As nonlinear pre-buckling deformations can severely alter the prediction of bifurcation buckling loads and associated modes, solutions that accurately traced the fundamental path of the shell before any instability phenomena occurred were in high demand by the shell buckling community. An energy-based finite difference approach has been utilised in Stein (1964) for the solution of meridionally compressed cylinders considering buckling into axisymmetric or asymmetric modes (Brush & Almroth, 1975), with Fischer (1963) performing a similar analysis while allowing for different boundary conditions for the in-plane displacements around the same time. Later work by Almroth (1966) investigated the influence of different edge conditions as an extension these FDM implementations, identifying the critical buckling load of the cylinder as the load level at which a matrix containing coefficients of the pre-buckling displacement coefficients vanishes. A combination of direct integration methods and the FDM approach was employed in Kalnins (1964) for the analysis of axisymmetric shells under symmetric or nonsymmetric loads, while Noor & Stephens (1973) examined the performance and accuracy of several finite difference schemes for the solution of first-order ODEs based on a Sanders linear theory, appropriately adapted for the inclusion of shear strains through the shell wall. A series of explorations on the mechanics of shells of revolution through FDMs (Galletly *et al.*, 1961; Penny, 1961; Radkowski *et al.*, 1962) illustrates the wide spectrum of applicability and capabilities of this computational strategy.

FDM and FEM schemes appear to have been coexistent for the later parts of the last century as the literature developments shows, with the latter eventually prevailing as the principal computational strategy for the generation of numerical solution to complex structural problems. These two methods are closely related however, adopting features of the other that appear

to be attractive in the context of different types of analysis procedures (Key & Krieg, 1973). The interpolation characteristics of finite element formulations permit not only the reduction of intricate geometries and deformation states into a series of polynomial (or any other a priori defined functional form through the mathematical definition of the element) piecewise approximations of the modelling domain, but also allow for the estimation of quantities within an element through the interpolation functions employed. As the FDM only allow for the evaluation of control parameters, commonly being the DOFs of the system at the grid points along the shell surface, any strain and stress estimated profiles are only provided for those specific nodes and are not valid for any intermediate points (Key & Krieg, 1973).

Thorough presentations and comparisons of the FDM and FEM computational strategies for the analysis of shell structures have been undertaken by several researchers Forsberg; Key & Krieg (1973); Bushnell (1973). Bushnell (1973) performed a direct comparison of these two methods, programmed within the same computational package to eliminate any sources of software related numerical discrepancies and maintain generality of the findings. Finite element and finite difference implementations where both included in the BOSOR3 package, predecessor to the popular in the shell buckling community BOSOR5 solver (Bushnell, 1976), producing results for limited cases of axisymmetric shell problems. Higher convergence rates for the same number of grid points and total DOF count are achieved by FEM for the purposes of bifurcation buckling problems or for stress analysis scenarios involving rapid meridional stress variations near restrained edges of an axisymmetric shell, while FDM was able to produce an accurate result faster for analyses governed by membrane stress fields or other scenarios characterised by smooth deformation gradients. Ease of application aspects are in favour of finite element implementations as the do not involve the introduction of fictitious nodes for the purposes of satisfying boundary constraints. It should be emphasised however that even though the bias of cross-software implementations was mitigated by using the same function definitions for any processes common to the two methods, the conclusions of Bushnell (1973) have been extracted mostly on the base of spherical cap models, producing a different type of case dependency that does not allow for a universal consensus to be drawn from this study.

2.2.2 Finite element formulations

A brief overview of the most favoured computational methodology for the analysis of shell structures (or any other kind of structural problem) will be attempted in this section, summarising key developments and concepts for the finite element solution of axisymmetric shells. As developments of finite elements for shells of revolutions and general shell elements have been historically intertwined, discussion will unavoidably include principle introduced through 3D shell element formulations. Different techniques for the derivation of such elements and updating procedures relevant to incremental nonlinear types of analyses will be reviewed, outlining the main strengths and shortcomings in the context of this powerful numerical scheme. Extensive surveys of axisymmetric shell finite elements, with discussions on early developments as well as recent formulations and implementation trends, can be found in Yang *et al.* (1990); Stolarski *et al.* (1995); Yang *et al.* (2000).

2.2.2.1 General considerations

The idea of the Finite Element Method (FEM) has been individually pursued and developed by researchers across three different disciplines of science (Key & Krieg, 1973); mathematicians physicists and structural engineers, with all three driven by the need to obtain an approximation to problems otherwise impossible to solve analytically. The limitations of the FDM approach for the solution of complex structural problems, a prime example of which is shell geometries

under arbitrary loading and boundary conditions, are circumvented through the use of piecewise interpolation functions for the description of displacement, strain and stress fields within an element. Assembly of stiffness coefficients from the individual finite elements in the model produces a multi-DOF matrix statement for the equilibrium of the problem, solution of which is carried out using ordinary linear algebra operations (reduction in triangular or echelon form, back substitution etc.) for the system, with advanced approaches capitalising on the sparsity patterns of large highly discretised models to improve computational efficiency.

Early developments on axisymmetric shell elements can be traced to the truncated cone element of Grafton & Strome (1963), being not only the first paper that presented a formulation for shells of revolution by appropriately integrating stiffness matrices around circumference of the shell's surface but also one of the very first to consider curved geometries (i.e through the circumferential component of the curvature as conical segments are singly curved shells) as prior FE applications for general shell models employed plate elements (Yang *et al.*, 1990) and provided rough computational approximations of curved surfaces through high discretisation. Doubly curved axisymmetric shell element formulations were published in the following years (Jones & Strome, 1966; Stricklin *et al.*, 1966), addressing issues associated with a piecewise linear modelling of curved meridians, such as discontinuities arising at junctions were the meeting segments are coplanar (Yang *et al.*, 1990).

2.2.2.2 Wire-arc formulations and solid-continuum formulations for axisymmetric shell problems

The kinematics of axisymmetric shell theory equally relate to both general shell theories and plane frame theories, with the same formulation potentially derived with either as a starting point. A general three-dimensional shell theory can be reduced to be made applicable to axisymmetric shells, with any transformations relating to non-meridional rotations being ignored at the level of pre-buckling deformation. Twisting and circumferential or in-plane shear forces and strains are additionally omitted during the pre-buckling state, leading to governing equations appropriately tailored for an axisymmetric shell problem. Such an approach for the derivation of an axisymmetric finite element shares similarities with strategic application of appropriate reductions on 3D solid finite elements to obtain formulations suitable for the analysis of shell structures, with these elements commonly encountered in relevant bibliographic resources as 'degenerated' shell elements (Liu *et al.*, 1986; Yang *et al.*, 1990; Bathe, 2006). The concepts associated with this methodology for the derivation of shell elements have been successfully utilised by Dvorkin & Bathe (1984); Bathe & Dvorkin (1985) for the formulation of an efficient four-node isoparametric shell element and can be equally applicable to axisymmetric shell structures (Yuan & Liang, 1989).

An alternative to the reduction techniques applied on general 3D shell elements for the derivation of purely axisymmetric formulations is the extension of planar beam elements, enriched with suitable expressions for the circumferential strains and curvatures while maintaining kinematic relationships along the longitudinal axis of the beam for the purposes of describing meridional deformations (Zienkiewicz *et al.*, 1977; Bathe, 2006). These concepts, schematically illustrated in Figure 2.8 are of critical significance in the development of FE software, with ABAQUS (2022) presenting the theoretical background of the axisymmetric shell elements SAX1 and SAX2 on the basis of the B21 and B22 beam elements. Continuum planar elements may equally be enhanced with circumferential strains (but not curvatures, as will be shortly discussed) for the analysis of axisymmetric structures (Wood & Zienkiewicz, 1977).

It is commonplace for axisymmetric shells to be modelled purely on the basis of their midsurface with Assumptions 1-6 relating to shell theory fundamentals embedded in the mathematical

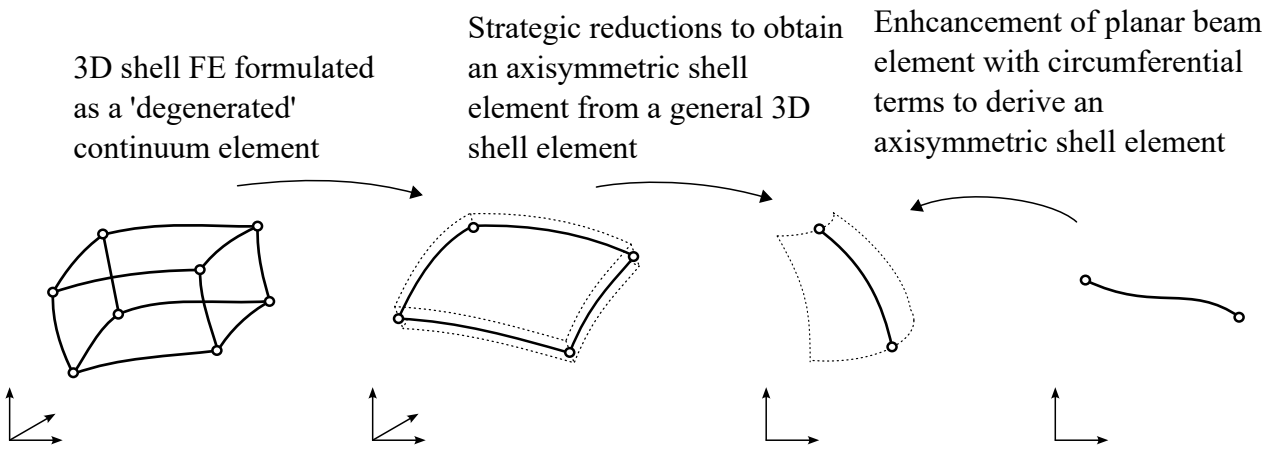


Figure 2.8: Schematic demonstration of strategies in the derivation of shell finite elements.

.

expression of the finite element to be employed. Nodal degrees of freedom commonly comprise displacements and rotations, with the exception of more advanced variational formulations like the one presented by Elias (1972) where nodal unknowns additionally include meridional bending stresses. In scenarios where the derived element is to be employed in bifurcations checks (Teng & Rotter, 1989a,b) or for the analysis of axisymmetric structures under non symmetric loads (Combescure & Garuti, 1983; Hong & Teng, 2002), appropriate extensions are made to allow periodic circumferential field distributions, either through individual trigonometric functions or Fourier series expansions for the more challenging distributions. Estimation of strains and curvatures at the midsurface of the shell precedes any evaluation of strain measures at a material point, considering a linear through-thickness field with the exception of HSDT approaches (Shen, 2017) where quadratic or higher order distributions of displacements will result in a strain field of the same order.

Inclusion of both translational and rotational DOFs as unknown nodal variables of an axisymmetric shell introduces two alternatives for the 1D interpolation field along the meridian of an element (Zienkiewicz *et al.*, 1977). Independent interpolation of displacements and rotations permits decoupling of stretching strains and curvatures, allowing for simple elements to be derived using linear shape functions for both fields along the shell's meridian. As the kinematic descriptions of section 2.1.2.1 suggests, translational and rotational deformations cannot be completely detached in the context of a complete shell theory where membrane and bending stresses both contribute in resisting externally applied loads. Their coordination is usually reinstated through transverse shear strain contributions, linking normal to the shell wall displacements $\bar{w}$ to meridional rotations β_ϕ. FSDT axisymmetric shell formulations amend the non-parabolic distribution of shear strains through the use of a shear correction factor (Cowper, 1966)

Employment of the reductive approximations relating to shell theory can be circumvented through the use of solid continuum elements for the discretisation of a shell model, explicitly rendering the thickness of the shell wall and utilising shape functions for the interpolation of nodal DOFs evaluated on the inner and outer surfaces of the shell structure. With 3D constitutive relations describing material behaviour of continuum elements, all of the simplifying Assumptions 1-6 are now redundant, including the fundamental assumption of negligible stress component σ_ζ normal to the midsurface of shell. Analogously to the formulation of axisymmetric shells through strategic reductions applied on general shell formulations, axisymmetric continuum elements can be derived through kinematic adjustments to available 3D solid elements, but also independently based on planar continuum formulations. 2D shape functions are required for the interpolation of variables within an element, in place of the 1D interpolation field associated with

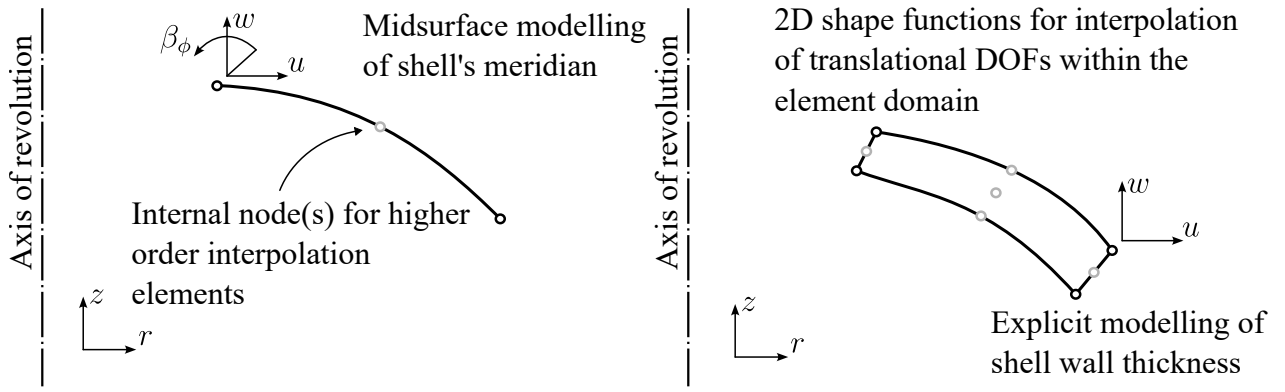


Figure 2.9: Illustration of generic wire-arc shell elements (left) against solid-continuum shell elements (right) in the 2D axisymmetric modelling space.

the 'wire' modelling of an axisymmetric shell's midsurface as illustrated in Figure 2.9. A number of solid-based elements for the analysis of axisymmetric structures have been published over the years, with some notable works those of Mitchell *et al.* (1971), Ahmad *et al.* (1970) and Surana (1982), without computational explorations leveraging these continuum formulations being as commonplace for the analysis of axisymmetric shells as the 'wire' midsurface based elements discussed earlier. The recent comparative examination of solid continuum finite elements and general shell finite elements in the context of nonlinear analysis for cylindrical shells under global bending (Sadowski & Rotter, 2013) demonstrated that for already for $r/t > 25$ utilisation of formulations that directly introduce DOFs for the description of through-thickness deformations can be increasingly uneconomical, a conclusion that explains their minimal involvement in shell-related research.

2.2.2.3 Nonlinear analysis updating schemes

Large deformation analysis of shell structures requires an accurate and effective scheme for updating the configuration of individual finite elements as the equilibrium path is incrementally traced in the presence of geometrically nonlinear effects. Three Lagrangian kinematic frameworks may be found to be commonly employed in FE formulations that aim to tackle analyses which include geometric nonlinearities: a total Lagrangian (TL) scheme, an updated Lagrangian (UL) and a corotational framework (Felippa & Haugen, 2005).

Axisymmetric shell elements are predominantly derived on the basis of a total Lagrangian formulation, relating strain quantities to the initial undeformed configuration of the shell without any updating of nodal coordinates as deformations develop. The frame invariance (i.e. the reference frame is fixed in space and does not affect the behaviour of the element) and conceptual simplicity of this approach come at the cost of strain estimations accuracy, restricted to small strains and small to moderate rotations being appropriately measured when reference to the original configuration is retained throughout the analysis. Green-Lagrange strain measures are commonly adopted in formulations built around a total Lagrangian scheme (Oliver & Onate, 1984; Teng & Rotter, 1989a,b; Jumikis, 1987; Wood & Zienkiewicz, 1977).

Updated Lagrangian schemes constantly update the reference state of an element and describe all kinematic quantities with respect to the converged configuration of the previous increment. Such an approach favours implementations where better approximations of rigid body motions are of some importance (Wood & Zienkiewicz, 1977; Murray & Wilson, 1969), allowing better approximation of the deformed configuration through small increments from a regularly updated shell midsurface. Programming of an updated Lagrangian scheme is a considerably more involved process when compared with a total Lagrangian approach, additionally associated

with higher computational costs due to the need for updating geometric reference as part of the incremental procedure. These computational costs however can be compensated through the improved convergence rates of this methodology (Bathe & Bolourchi, 1979), presenting a favourable framework for formulations dealing with plastic flow of material by alleviating pseudo strains associated with rigid body movements, potentially occurring in the context of a total Lagrangian scheme.

Whilst corotational frameworks have been introduced from the early days of developments into the finite element theory and its applications through Argyris (1964), they have only attracted attention for the analysis of shell structures after numerous formulations where published employing either of the previously described reference schemes. This popular for 3D shell formulations approach results in finite element derivations that are termed as 'geometrically exact' (Simo *et al.*, 1988; Ibrahimbegovic, 1997; Sanchez *et al.*, 2023), owning to the local coordinate frame that is attached to each individual element, following its rotations and permitting evaluation of its deformed state while eliminating any rigid body motions (Stolarski *et al.*, 1995). The preserved objectivity of strain measures obtained due to the corotated framework is highlighted in published FE formulations (Jelenić & Crisfield, 1999), allowing large rotations to be considered while ensuring accurate integration of incremental strains, especially important in the context of materially nonlinear analyses. The elaborate transformations linked with this methodology to compute local axes directions at each nonlinear step can lead to complex implementation algorithms (Crisfield, 1991; Crisfield & Moita, 1996). Development of axisymmetric shell elements on the basis of corotational frameworks can be more effectively addressed on the basis of an enhancement of corotational beam elements (Crisfield, 1991; Jelenić & Crisfield, 1999) rather than a reduction of general shell formulations (Simo *et al.*, 1988; Ibrahimbegovic, 1997), mainly due to the additional layer of transformations that a 3D modelling space requires.

2.2.3 Meta-elements

The precision of computational models utilising the principles of finite element analysis heavily relies on the relative experience of the analyst to appropriately refine the mesh resolution, a task necessary to accurately simulating the complex mechanics of a shell structure. As different regions of an axisymmetric shell's meridian require a high discretisation to sufficiently describe bending behaviour, while others only require a few elements to model constant membrane stress states, the task of a pre-modelling analysis to estimate shell element size and the meticulous finite element model generation can be quite challenging even for a skilled engineer. All of these considerations are abstracted through the use of meta-elements, appropriate for the modelling of entire axisymmetric shell segments through a single mathematically dense construct. Different functional forms are utilised to approximate response in the bending dominated regions of the meridian or the less demanding membrane stress only parts. This technique has been utilised by a few researchers as a more robust approach to the computational analysis of axisymmetric shell structures, with varying levels of success on the types of analysis the derived elements can robustly be employed at.

The conceptual basis of the eXtended FEM or General FEM methods has been employed by Boyez *et al.* (2017) for the derivation of a Cylindrical Shell Boundary Layer (CSBL) element, based on Kirchhoff-Love thin-shell theory. Membrane and bending displacement solutions are described through different interpolation fields for the linear elastic stress analysis of multi-strake cylindrical shells made of isotropic or uniformly orthotropic material. A further version of this element for the linear stress analysis of conical shell segments, termed the CoSBL, was later released by the same authors (Boyez *et al.*, 2018), showcasing good agreement with FE solutions

of considerably higher DOF counts. A robust formulation for the linear bifurcation analysis of multi-strake cylindrical or conical shell segments was unfortunately not released, as numerical precision issues did not permit reliable prediction of the critical buckling resistance of these axisymmetric shell geometries (Boyez, 2019).

A similar concept for a non-discretised cylindrical shell has been recently developed by Ádány & Schafer (2025a,b) to provide estimations for the elastic buckling of tubular members, termed as the Finite Tube Method. This numerical analysis tool that has been inspired by the Finite Strip Method (Cheung & Tham, 1997) uses two-dimensional Fourier series for the description of the displacement field within each segment, offering a meshless approach to the analysis of cylindrical shell parts under several loading scenarios. The authors are actively working towards extending this method and making it a valuable tool for the efficient analysis of wind turbine support towers.

2.3 Axisymmetric shell solvers

The load bearing capacity of thin axisymmetric shell structures with a circumferentially uniform stress state is often controlled by their buckling resistance, characterised by a harmonic distribution of the buckling displacement field along the circumference of the shell. The circumferential uniformity of the pre-buckling stress state does not allow any obvious localisation of the buckling mode, leading to awkward numerical issues for FE software attempting to solve the axisymmetric shell eigenproblem in a full 3D modelling space. Fourier series may be used for the description of the circumferentially varying displacements once buckling occurs, permitting a native mathematical treatment to the problem of nonsymmetric bifurcation of shells under a circumferentially uniform pre-buckling stress state. This particular handling of the stability problem was once commonplace in the axisymmetric shell related research of a previous era, leading to various computational packages to be distributed within the shell research community of that period but not made publicly available in the form of an executable.

Since this specialised mathematical treatment is nowhere to be found in the native 2D modelling space of commercially available FE packages, a workaround for the computation of the buckling load associated with any competing circumferential mode n has been devised by shell analysts, aiming to amend this shortcoming of general computational software. This method, termed the *'panel analysis technique'*, targets the buckling load of an unsymmetrical circumferential mode $n \geq 1$ through the analysis of a shell panel having an angular span $\theta = \pi/n$. The sympathetic to the targetted circumferential mode n panel, when coupled with a discretisation scheme that could only accurately capture a half-wave in the circumferential direction of the shell and would otherwise penalise buckling into a different mode, allows for a linear or nonlinear prediction of the critical buckling load associated with n. Even with this meshing penalisation approach however the FE results need to be post-processed in order to confirm that the desired mode has indeed occurred and the computed buckling resistance can be trusted. A different fully axisymmetric model needs to be considered for the axisymmetric buckling case corresponding to $n = 0$.

As thoroughly discussed in Sadowski *et al.* (2018), the panel analysis technique can be very inefficient and in some cases of poor solution quality, mostly due to numerical issues arising from the explicit modelling of the parasitic circumferential dimension of the shell. The additional complexity that comes with its implementation makes it an uninviting approach to the bifurcation analysis of axisymmetric shell problems, especially when compared with the alternative of directly including the circumferential harmonic n in the shell's finite element formulation. Numerical problems are additionally more likely to occur in systems of higher DOF counts, a consequence

of cumulative errors arising from finite-precision arithmetic operations that can either degrade the accuracy of the obtained solution or cause the analysis to be aborted. All of these issues have been visually summarised in an application of panel analysis technique by Sadowski *et al.* (2018) for the computation of nonlinear buckling loads corresponding to any competing circumferential number of waves n for cylinders under uniform meridional compression, as presented in 2.10. A wide variety of cylindrical lengths has been considered in this GNA exploration of critical buckling resistances, varying through the dimensionless Batdorf parameter Z, defined in Eq. 2.23 below. This extensively adopted parameterisation has been devised by Batdorf (1947) after the observation that a cylinder's buckling strength is dependent on both its radius-to-thickness ratio r/t and length-to-radius ratio L/r (Shen, 2017), a finding that was shared by Simitses (1996) on his review of studies on instability phenomena for cylindrical shells, considering finite-thickness effects.

$$Z = \frac{L^2\sqrt{1-\nu^2}}{rt} \tag{2.23}$$

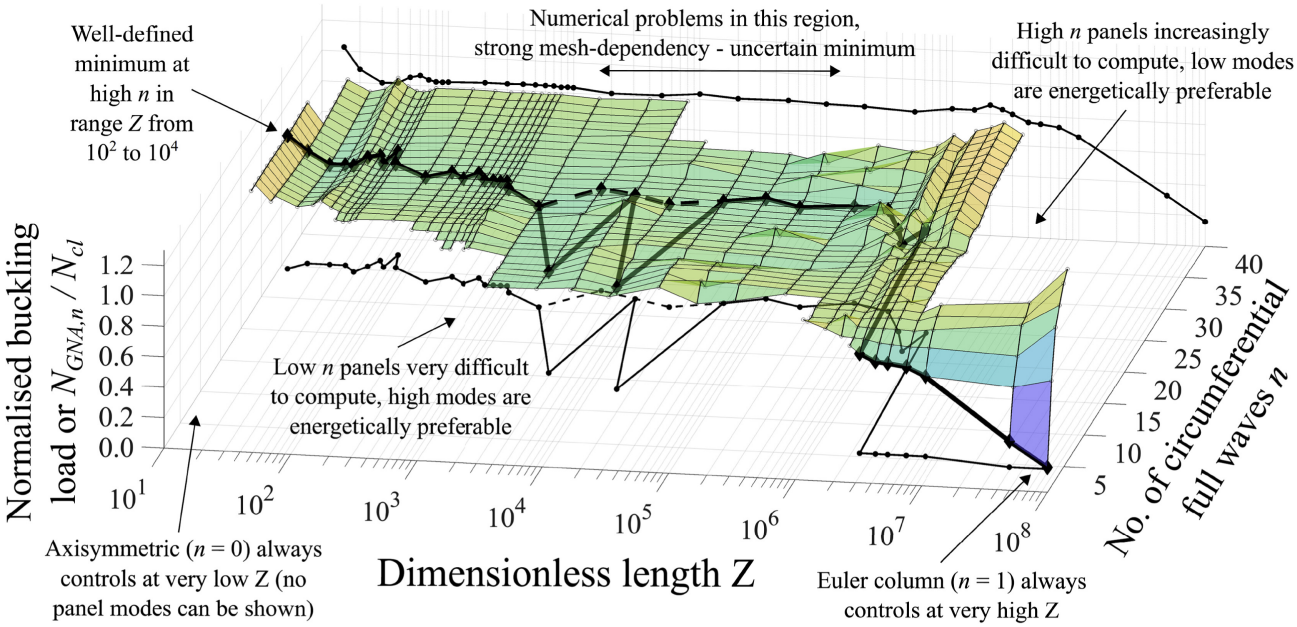


Figure 2.10: 3D surface plot of computed nonlinear buckling loads and mode wave numbers as a function of length, generated by Sadowski *et al.* (2018).

The 3D surface of Fig. 2.10 showcases the shortcomings of this involved modelling technique and highlights regions of numerically ill-conditioned behaviour, hindering the identification of any underlying relationship between the critical harmonic n and the dimensionless length of Eq. 2.23 Z. The additional consideration of potentially more than a hundred competing circumferential wavenumbers n as the cylinders become increasingly more slender (Teng & Rotter, 2004a) further adds to the infeasibility of the 'panel analysis' for the nonlinear prediction of critical buckling loads. The concluding statement of Sadowski *et al.* (2018), the significance of which is underpinned by the extensive effort of the authors to establish an efficient framework for this workaround, highlights the need for a more modern approach to the problem of bifurcation buckling for axisymmetric shell systems, one that involves an exact mathematical treatment to the nonlinear stability checks of axisymmetric shells.

As stated earlier, the necessary specialisation of the computational formulation required to accurately solve these problems was once commonplace within the research field of axisymmetric shell buckling. Before delving into a review of scientific software for the analysis of axisymmetric

shells and their history, it should be emphasised that only one of the following software is available through an unofficial (non-author) source in an unmaintained format, and with no exception none is publicly available in an executable or readily compilable version using programming environments and tools available in 2025. To the best of the author's knowledge, the list of legacy computational packages for the nonlinear analysis of axisymmetric shells is limited to the following three software, catalogued in no particular order.

- The INCA module developed by A. Combescure in the 1980s (Combescure & Garuti, 1983; Combescure, 1986) as part of the multidisciplinary CASTEM software (Combescure *et al.*, 1982) for the computational analysis of problems related to mechanical engineering applications. The COMU quasi-axisymmetric shell element, built on the principles of Marguerre's shallow shell theory (Debongnie, 1979) and written within the INCA module, allows for an updated Lagrangian approach to nonlinear problems and incorporates a Fourier modal description of circumferential physical values and displacements. A harmonic representation of the buckling displacement field allows for a good agreement of computational results and the analytical solutions of Koiter (1945) for cylinder under meridional compression (Combescure & Bastien, 1984). The INCA module has been primarily used for the stability analysis of cooling towers in the nuclear industry (as the CASTEM software was written for the French Atomic Energy Commissariat), employed in a number publications until the 2000s (e.g. see Baillis *et al.* (2000); Combescure & Pernette (1989); Combescure (1998); Michel *et al.* (2000)). With the CAST3M computational package being the formal evolution of the presently unavailable CASTEM software, the COMU element and the nonlinear axisymmetric capabilities associated with it do not seem to have made the move into the new version of the software (deduced through a search of the corresponding Github repository). An advanced formulation of the COMU element has been presented by Brun *et al.* (2008), using a total Lagrangian approach instead of the updated Lagrangian scheme originally employed, with the element now written in the CalPen3D suite (Sibeaud *et al.*, 2004) for 3D penetration simulations suitable for hardened materials. Unfortunately the COMU formulation is not at the shell analyst's disposal, as the CalPen3D software is not currently publicly available in any format.

- The FELASH (Finite Element Analysis of axisymmetric Shells) suite of advanced finite element-based programs (Rotter, 1989) developed by J.G. Teng and J.M. Rotter (Teng & Rotter, 1989a,b) in the late 1980s, with contributions from other authors involved in the nonlinear analysis of axisymmetric shells like P.T. Jumikis, Y.F. Luo and T. Hong. The modular internal organisation of the FELASH suite of computational packages allowed for several different kinds of analyses to utilise the same pre and post processing routines. The full list of individual programs and their purpose is given in the following Table 2.1:

  A variety of other modules are also briefly mentioned in the series of publications introducing this computational suite (Teng, 1999), like the NEPAC and EPSAC components, but not many details are shared towards their functionality. The NEPAS in particular component of FELASH has been extensively used in civil engineering nonlinear shells research (e.g. see Rotter & Teng (1989); Teng & Rotter (1992b); Teng & Lou (1997); Teng (1999); Gillie & Rotter (2002); Rotter (2006)). The FELASH suite regrettably never made its way to the wider shell research community, with all of its uses traced to be in collaboration with the original developers of the software.

  A new computer program called CHASH (Coupled Harmonics Analysis of SHells) was developed by T. Hong and J.G. Teng Hong & Teng (2002); Hong (2000) as an extension of the NEPAS program. CHASH was developed to permit post-buckling analysis for shells of revolutions considering mode switching and interaction, with a series of results presented

Program module	Functionality
PASHA	Preprocessing for Axisymmetric SHell Analysis
LEASH	Linear Elastic Analysis of Shells using Harmonics
LEBAD	Linear Elastic Buckling Analysis using Donnell (Donnell, 1935a) strain-displacement relations
LEBAS	Linear Elastic Buckling Analysis using Sanders (Sanders Jr, 1963) strain-displacement relations
LEBARJ	Linear Elastic Buckling Analysis using Rotter-Jumikis (Jumikis, 1987) strain-displacement relations
LEBAB	Linear Elastic Buckling Analysis with nonlinear Bending strains (Jumikis, 1987)
LEBACT	Linear Elastic Buckling Analysis with Combined Loads including Torsion (Teng & Rotter, 1989b)
NEBARJ	geometrically Nonlinear pre-buckling with Elastic non-symmetric bifurcation Buckling Analysis
NEPAS	geometrically Nonlinear Elastic-Plastic Analysis for bifurcation Stability
SUMP	SUMmation and Plotting post-processor

Table 2.1: Different components and their purpose within the FELASH suite (Rotter, 1989; Jumikis, 1987).

in Teng & Hong (2006); Hong & Teng (2008). This more recent computational package for the nonlinear analysis of axisymmetric shells has never been formally made publicly available and its use has been limited to the research works of its developers.

- The BOSOR (Bucking of Shells of Revolution) suite of advanced finite difference-based programs developed by D. Bushnell and his research group, widely used for computational shell buckling studies in the aerospace sector for many decades starting in the 1960s. Different editions of this software were distributed through the years, with the first one being the BOSOR4 (Bushnell, 1974), implementing a finite difference scheme (Bushnell *et al.*, 1971) for the nonlinear solution of axisymmetric shells. New editions of the BOSOR4 program like the BIGBOSOR4 and HUGEBOSOR4 were able to handle more complex scenarios for branched shell problems. The release of BOSOR5 soon followed (Bushnell, 1976), with the author stating that this new program was not made available as a new edition of the BOSOR4 computational package, since the modal vibration capability was not transferred from BOSOR4, nor could it handle non-axisymmetrically loaded shells. BOSOR5 included large pre-buckling deflections and creep capabilities, contributing significantly to its popularity and extensive use amongst the shell research community (Rotter & Teng, 1989; Rotter, 2006). An optimisation program was also released by the author of BOSOR4 and BOSOR5, capitalising on the capabilities of the first of these two programs to perform minimum weight design of axisymmetric shell structures (Bushnell, 1987) The source code for the different editions of the BOSOR suite appears to have been available for download until about 2021 from its author's personal website (*www.shellbuckling.com*), and is presently only publicly obtainable through a non-author unofficial Github repository, without any support provided.

- The FASOR (Field Analysis of Shells of Revolution) (Cohen, 1979, 1981b) program, developed as a second generation integrated version of the SRA system (Cohen, 1973), for the solution of orthotropic and anisotropic axisymmetric shells for the purposes and needs of the aerospace industry. This computational implementation of the field method for the

integration of shell equations (Cohen, 1974, 1976), derived on the basis of a boundary-value problem, functions like a 'meta-element' which relieves the user from discretisation concerns or the artificial segmentation associated with finite difference methods (Bushnell *et al.*, 1971; Cohen, 1979) and constitutes the second numerical tool in this list for the nonsymmetric bifurcation of axisymmetric shells that does not utilise the principles of the finite element method. The FASOR program has not been a recipient of as much attention by the shell research community as the other computational alternatives have drawn, with limited axisymmetric shell explorations by the software's developer (Cohen, 1981a; Cohen & Haftka, 1989) making use of this tool, as coded for the NASA agency. The source code or an executable version of the FASOR program has not been made available to the shell buckling research community.

Complementing the list of computational tools utilised in nonlinear stability investigations for shells of revolution are a series of commercial 3D finite element solvers (Almroth & Brogan, 1978; ABAQUS, 2022; ANSYS, 2022), with an established record of shell research articles published over the last decades. These software alternatives have become the sole option for numerical modelling of axisymmetric shell systems characterised by circumferential stress state uniformity when nonsymmetric stability considerations are for an accurate solution of the structural model. Unavoidably, all of these options are subject to the efficiency and precision considerations illustrated in Sadowski *et al.* (2018) and outlined earlier, highlighting the need for a modern and robust computational tool that can handle nonlinear axisymmetric shell buckling problems.

2.4 The capacity curve framework of EN 1993-1-6

The very high discrepancy between analytically derived solutions and experimental results for the critical buckling load of pressurised spherical shells, cylinders under meridional compression and other classical axisymmetric shell systems has lead design standard committees to establish corresponding rules on the basis of lab tests. Early efforts in the development of such standards were led by NASA and the aerospace industry due to the dire need for weight-critical structurally optimised solutions (Rotter, 1998; Arbocz & Starnes Jr, 2002), commonly found to be highly susceptible to elastic buckling. Design of aircraft fuselages was based on a lower-bound philosophy that accounts for uncertainties through the use of an empirical 'knockdown factor' (Teng, 1996; Arbocz & Starnes Jr, 2002; Teng & Rotter, 2004a), a methodology adopted on account of the representativeness of test specimens as credible equivalents to practical aerospace vehicles. These knockdown factors are established on the grounds of extensive experimental data spreads, like those presented in Figure 1.2 for cylinders under meridional compression, introducing empirical knowledge into the design process through a single scaling factor, to be multiplied with the perfect shell resistance.

Several limitations to design according to knockdown factors have led to recent reinvestment into their derivation, with a major portion of those efforts pioneered by the Shell Buckling Knockdown Factor (SBKF) Project (Hilburger, 2012). These limitations are not only of economic nature, as the lab tests of the past century do not reflect the quality of fabrication and material technologies that are the modern standard of aerospace shell construction, but they additionally correspond to the difficulty in assessing the pedigree of test data used in the development of knockdown factors and the negligence of boundary conditions and length effects on the generated formulae for the knockdown factors. The SBKF is now attempting to address these shortcomings through utilisation of numerical analysis tools, to be employed for the generation of data to be used as a 'virtual test'. A study of geometric sensitivities, material properties and structural details associated with the construction of aerospace shells (welds and joints, cutouts etc.) will

precede execution of these virtual tests, in order to establish the statistical distribution of these parameters. A very similar approach has been proposed for the replacement of experimentally obtained knockdown factors by Arbocz & Starnes Jr (2002), suggesting a Monte Carlo approach paired with FE estimations of load carrying capacity of the investigated shell model, a process that was recently implemented and proven to work by Sadowski et al. (2023).

Whilst the aerospace engineering community spearheaded research endeavours on translating shell buckling scientific knowledge into implementable relationships for the design of shell systems, the civil engineering discipline has effectively reduced utilisation of experimentally obtained design curves for two decades, incorporating the use of a dimensionless and scalable capacity curve framework that is generated on a purely computational basis. The European standard EN 1993-1-6 has adopted this novel construct for the design of shell structures from its original publication as an EN (following conversion from ENV, initiated by a Commission Mandate in 1998) in 2007 (EN 1993-1-6, 2007). The capacity curve framework lends itself to design according to three different methods of evaluating the shell's resistance based on varying levels of assumptions, conservativeness, and computational effort, as will be shown in the discussion of the present section. Even the completely computational approach of a full GMNIA, permitting a complete nonlinear exploration of the shell system with explicitly defined imperfections, can benefit from comparisons with capacity curves for loosely-related reference shell systems, providing a preliminary check and a measure of the differences between the resistance of the reference model and the actual shell. A brief history on the development of the capacity curves across different Standards may be additionally found in Sadowski & Filippidis (2025), with a focus on versional updates of the parameters that provide a characterisation of a reference shell system within the framework. As the theoretical background to the European Standard EN 1993-1-6 (2007) is rather extensive to be included in the Standard itself, a series of supporting books have been published to accompany its different versions, with the most recent being the fifth edition's second impression for *Buckling of Steel Shells, European Design Recommendations*, published by the ECCS Technical Committee 8 for Structural Stability and edited by J.M. Rotter and H. Schmidt (ECCS EDR5 (2013)).

The capacity curve framework offers an abstraction to complex nonlinear quasi-static structural responses, accounting for the effects of geometric and material nonlinearities, as well as their interaction and stability considerations. While the novelty of a capacity curve for structural systems does not rest solely with the EN 1993-1-6 developers, as they can be traced all the way back to the mid-eighteenth century (Rankine, 1866), their essential feature of providing two clearly defined limiting cases for material and stability failure accordingly has been capitalised by the shell research community to characterise their behaviour with respect to the shell's slenderness λ. The abstraction is not limited to these phenomena however, as the conceptualisation of a structural shell system through the capacity curve construct may additionally include geometric and material characteristics of the model, producing relationships that are impartial to specific model values but rather depend on relative features (Rotter, 1998; Doerich & Rotter, 2011b). An illustration of 'traditional' and 'modified' capacity curves is provided in Figure 2.11 for a generic shell system according to EN 1993-1-6, having adopted the notation of Sadowski & Filippidis (2025) for the dimensionless parameter $\psi = R_k/R_{cr}$ of the modified form.

The dimensionless resistance of the shell can now be calculated within the context of the capacity curve framework through the following relationships (EN 1993-1-6, 2025):

$$\chi = \begin{cases} \chi_h - \frac{\lambda}{\lambda_0}(\chi_h - 1) & \text{if } \lambda \leq \lambda_0 \text{ (fully plastic)} \\ 1 - \beta(\frac{\lambda - \lambda_0}{\lambda_p - \lambda_0})^\eta & \text{if } \lambda_0 < \lambda < \lambda_p \text{ (elastic-plastic)} \\ \frac{\alpha_G \alpha_I}{\lambda^2} & \text{if } \lambda_p \leq \lambda \text{ (elastic)} \end{cases} \tag{2.24}$$

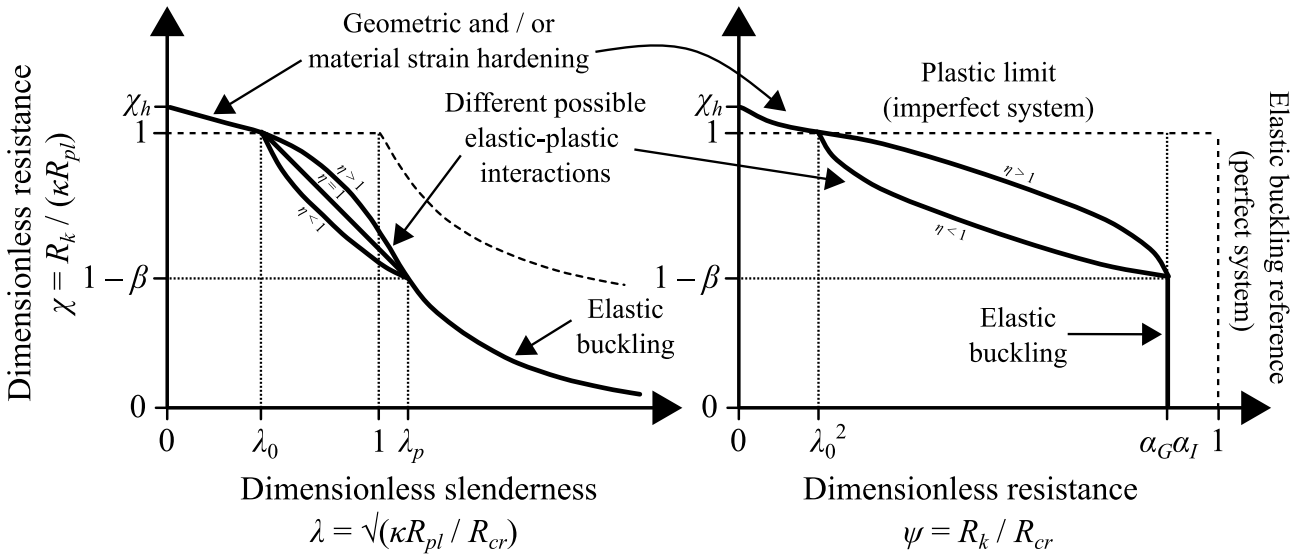


Figure 2.11: Schematic representation of the capacity curve framework used in EN 1993-1-6 (2025), in 'traditional' χ vs λ form (left) and 'modified' (Rotter) χ vs ψ form (right), as adapted from Sadowski & Filippidis (2025).

where

$$\chi = \frac{R_k}{\kappa R_{pl}} \tag{2.25}$$

$$\lambda = \sqrt{\frac{\kappa R_{pl}}{R_{cr}}} \tag{2.26}$$

$$\lambda_p = \sqrt{\frac{\alpha_G \alpha_I}{1-\beta}} \tag{2.27}$$

and

$$\eta = \eta_0 \left(\frac{\lambda_p - \lambda}{\lambda_p - \lambda_0}\right) + \eta_p \left(\frac{\lambda - \lambda_0}{\lambda_p - \lambda_0}\right) \tag{2.28}$$

together define the complete algebraic buckling resistance χ vs slenderness λ relationship in dimensionless terms (see Fig. 2.11 (left)). An alternative representation generated with the same data can be obtained in a dimensionless resistance space χ vs ψ, with the second of these parameters given as:

$$\psi = \frac{R_k}{R_{cr}} \tag{2.29}$$

A modified (or 'Rotter') (Rotter, 2005b,a) form of the capacity curve obtained in this manner, schematically illustrated in Fig. 2.11 (right), permits a different perspective for systems that buckle elastically and allows clear identification of the α_G and α_I parameters, representing the sensitivity of the shell structure to initial imperfections. A complete presentation of the parameters of the capacity curve framework and the two reference resistances that provide specialisation to a given system, their theoretical ranges, how they are established by computational analysis and their dependencies on geometric or material nonlinearities and imperfections is offered in Table 2.2. The background and first formal definition of early version of these parameters has been presented in Rotter (2002), generalising their conceptual development by Schmidt (1991). Those parameters marked with a † have a theoretical upper bound (Doerich & Rotter, 2011b; Rotter, 2011).

Entity	Interpretation	Geom. nonlin.	Mat. nonlin.	Imper -fections
α_G $\in [0, \infty)$	Effect of geometric nonlinearity on linear elastic buckling response of the perfect system. Computed as $\alpha_G = R_{GNA}/R_{LBA}$.	✓	✗	✗
α_I $\in [0, \infty)$	Effect of imperfection sensitivity on nonlinear elastic buckling response of the imperfect system. Computed as $\alpha_I = R_{GNIA}/R_{GNA}$.	✓	✗	✓
β $\in [0, 1]$	Identifies value of $1 - \chi$ at which plasticity first affects the nonlinear buckling resistance. Computed at $\lambda \equiv \lambda_p$ where R_{GMNIA}/R_{MNIA} and R_{GNIA}/R_{MNIA} first significantly diverge.	✓	✓	✓
η_0 $\in [0, \infty)$†	Describes curvature of $\chi(\lambda)$ near λ_0, gives strength of elastic-plastic interaction. Computed to fit $\chi = R_{GMNIA}/R_{MNIA}$ in the range $\lambda_0 \leq \lambda \leq \lambda_p$.	✓	✓	✓
η_p $\in [0, \infty)$†	Describes curvature of $\chi(\lambda)$ near λ_p, gives strength of elastic-plastic interaction. Computed to fit $\chi = R_{GMNIA}/R_{MNIA}$ in the range $\lambda_0 \leq \lambda \leq \lambda_p$.	✓	✓	✓
κ $\in [0, \infty)$	Effect of imperfection sensitivity on reference plastic collapse resistance of the imperfect system. Computed as $\kappa = R_{MNIA}/R_{MNA}$.	✗	✓	✓
λ_0 $\in [0, \infty)$	Identifies the 'squash limit' where full plasticity is attained. Computed as λ where $\chi = 1$.	✓	✓	✓
χ_h $\in [1, \infty)$	A simple representation of post-yield strain hardening reserves. Computed as conservative projected intersect of χ) at $\lambda = 0$.	✓	✓	✓
R_{cr} $\in [0, \infty)$	Reference elastic critical buckling resistance of the perfect system. Computed as $R_{cr} = R_{LBA}$.	✗	✗	✗
R_{pl} $\in [0, \infty)$	Reference plastic collapse resistance of the perfect system. Computed as $R_{pl} = R_{MNA}$.	✗	✓	✗

Table 2.2: Definitions and scope of parameters and resistances within the capacity curve framework of EN 1993-1-6 (2025), adopted from Sadowski & Filippidis (2025).

It should be emphasised that these parameters are oftentimes dependent on specific boundary conditions and loading combinations, applied on the base geometry of the shell, as the discussion of the following Section 2.4.4 highlights. In the absence of a clearly relatable reference system that has been fully characterised through the capacity curve construct, the first generation European Standard EN 1993-1-6 (2007) permitted the use of capacity curve parameters relating to meridionally compressed unstiffened cylinders on the basis that no shell buckling case can be imagined to be more sensitive than this classical axisymmetric shell problem (Rotter & Schmidt, 2013). The conservativeness of this statement has been shown to be inaccurate for cylinders of intermediate slenderness when subjected to uniform bending (Wang *et al.*, 2020; Sadowski & Filippidis, 2025) and it has consequently been amended to consider capacity curves for both of these fundamental loading scenarios in the second generation of EN 1993-1-6 (2025), encouraging engineers to consider the more conservative out of the two scenarios for design. Nevertheless, this shortcoming in appreciating the relevant criticality of some classic loading scenarios for the most studied axisymmetric shell geometry illustrates a need for more thorough

explorations of reference shell systems in order to assess the conservativeness of each scenario across a range of possible slendernesses.

2.4.1 Design through GMNIA

The capabilities of modern numerical solvers are exploited in this entirely computational estimation of the nonlinear elastic-plastic buckling resistance of practical shell structures. This constitutes the most intensive assessment of the load carrying capacity of a shell system, not only due to the extensive numerical examinations necessary to assess the different aspects of nonlinear behaviour and imperfection sensitivity for the shell to be designed, requiring a robust FE solver that can facilitate all of EN 1993-1-6 (2025) defined computational investigations, but also owing to the necessary modelling skills on the analyst's part to ensure the representativeness of the obtained solution for the system under consideration. To guarantee accuracy and reliability, design through a GMNIA is typically preceded by a sequence of increasingly sophisticated analyses, starting with a set of LA-LBA assessments to establish the elastic behaviour of the shell and its critical buckling load. An MNA identifies the shell's full plastic resistance, absent any strain-hardening material characteristics, while the subsequent GMNA step of this process aims to establish the elastic-plastic buckling strength of the nominally perfect geometry of the model. A series of GMNIAs on the basis of different forms of initial geometric deviations constitutes the last computational step of this process, seeking to determine the geometrically and materially nonlinear resistance of the shell system relevant to worst imperfection shape. This last set of GMNIA examinations of the shell structure is the most onerous out of computational processes necessary for this approach, not only due to the complexity of accurately establishing the strength of a numerical model when geometric and material nonlinearities are both included and potential interact, but also due to the ambiguity of the a priori selection of appropriate imperfection shapes out of all potential initial geometric deviation forms. Termination of a GMNIA and computation of the elastic-plastic buckling resistance of the imperfect structure R_{GMNIA} is determined as the lowest load factor at which either one of the following criteria C1-C3 are satisfied as the load-deformation curve of the shell is traced.

Criterion C1: Maximum load factor attained by the analysis during tracing of the equilibrium path, associated with limit point or plateauing behaviour (with a computational approach to establishing the maximum load factor associated with plateaus in equilibrium curves in the presence of plasticity presented in Doerich & Rotter (2011a)).

Criterion C2: Load factor at which instability phenomena are initiated, with the accurate and reliable detection of buckling being a separate issue for computational solvers (as the discussion of the next chapter indicates).

Criterion C3: Maximum tolerable deformation, where this occurs before a bifurcation buckling load has been reached on the equilibrium path. Utilisation of criterion C3 is necessary in structures that display hardening effects, either due to material or geometric behaviour (Rotter, 2005b) so that there is no clear maximum on the load-deformation curve of the shell structure.

Criterion C4: The load factor at which the equivalent stress at the most highly stressed point of the shell wall reaches the design value of yield stress. This criterion is secondary to the C1-C3 criteria just presented and only relevant to provide a safe estimate of the load carrying capacity when a material nonlinear analysis is unavailable in the numerical solver employed, permitting computational treatment through a GNIA. This approach can result in conservative estimates of the nonlinear buckling resistance of the shell, except from cases of very slender shells that buckle elastically, without any point on the shell surface reaching yield (ECCS EDR5 (2013)).

A final step is required after the nonlinear computational resistance R_{GMNIA} has been computed

when a shell is designed according to the EN 1993-1-6 (2025) Standard, corresponding to a calibration calculation with established results relatable to the structural shell system under consideration to check the precision of the GMNIA estimate of its strength. This comparative assessment of GMNIA's validity can be either through well documented test results or other sources of verified calculation, including the capacity curve framework of EN 1993-1-6 (2025) as previously outlined. The computationally evaluated resistance R_{GMNIA} is then combined with either available reference result to produce a calibration factor k_{GMNIA}, defined as:

$$k_{GMNIA} = \frac{R_{test}}{R_{GMNIA}} \quad \text{or} \quad \frac{R_{k,known}}{R_{GMNIA}} \tag{2.30}$$

which can be appropriately scale the GMNIA evaluated resistance of the shell to obtain a characteristic resistance R_k and subsequently a design resistance R_d as:

$$R_k = k_{GMNIA} \cdot R_{GMNIA} \quad \text{and} \quad R_d = \frac{R_k}{\gamma_{M1}} \tag{2.31}$$

with γ_{M1} being the partial factor in the context of the buckling ultimate limit state. The calibration value k_{GMNIA} needs to be within the range $0.8 < k_{GMNIA} < 1.2$ if a 'known value' is utilised, while for a test result the corresponding value of the calibration factor is limited to $k_{GMNIA} < 1.0$ (EN 1993-1-6, 2025). With concerns towards the incorporation of existing experimental results in the calibration step of the GMNIA methodology presented in Sadowski & Seidel (2023b), the alternative of employing an $R_{k,known}$ result appears to be a viable prospect to support a full computational approach on the design of shell structures. Owing to the limited availability of well documented reference solutions that can assist this EN 1993-1-6 (2025) design methodology, with the worked solution of the international 'round-robin' exercise in Sadowski & Seidel (2023b) contributing to this very short list, a need for established reference solutions that can facilitate even seemingly entirely numerical design approaches is necessary for engineers working with the European Standard.

2.4.2 Stress design

The Stress Design approach for the strength evaluation of a shell structure permits simple hand calculations for predicting its load carrying capacity, potentially without the need for any computational analyses. This method has been conceived on the basis of a uniform membrane stress state, a common scenario for some of the most fundamental load cases in cylindrical shells that have also been the subject of extensive experimental investigations (Schmidt, 2018). These three fundamental load cases, also termed as Primary Load Cases (Rotter, 2016b), correspond to uniform meridional stress, uniform circumferential stress and uniform in-plane shear stress throughout the cylinder. Meridionally compressive membrane stresses on cylinders result to relatively localised buckle formations, while uniform circumferential membrane stresses and uniform in-plane shear stresses can lead to buckles spread across the entirety of the meridian. Stress Design addresses all shell buckling phenomena as arising from a combination of the three Primary Load Cases in cylindrical shells (Greiner *et al.*, 2008), an approach that is based on the observation that most practical loading conditions produce locations of stress peaks that contain contributions of all three Primary Load Cases. An in-depth description and commentary of the foundations and background of the method in the context of the first generation of EN 1993-1-6 (2007) can be found in Greiner *et al.* (2008).

Application of the Stress Design method requires evaluation of the relative slenderness of the shell λ, estimated through Eq. 2.26. The elastic critical resistance of the shell is evaluated

as equal to the elastic critical buckling stress $R_{cr} = \sigma_{cr}$ that would initiate buckling on the corresponding shell system, with the classical elastic critical stress σ_{cl} of Eq. 2.15 as derived for cylinders under meridional compression, while the plastic resistance of the shell is taken to be equal to its fabrication material's yield stress $R_{pl} = f_y$. The characteristic resistance R_k of the shell can be subsequently calculated through the capacity curve framework for the reference shell system that most closely relates to the mechanics of the shell to be designed, in the form of a stress σ_{Rk}. Combination with the partial safety factor γ_{M1} produces a design stress σ_{Rd} which serves as a limit to the membrane stresses that can potentially have a destabilising effect or lead to yielding (Rotter, 2002, 2007, 2010b, 2016b; Doerich & Rotter, 2011b; Sadowski & Filippidis, 2025). The stress profile of the shell can be determined either on an analytical basis by considering well-established bending theory solutions for the problem under examination or through a computational LA result, with the equivalency of the two approaches outlined in Section 1.2.2.

An even more conservative approach may be employed by limiting stresses on the inner/outer surfaces of the shell wall to comply with the design value σ_{Rd}. Stress results from an LA can considerably underestimate the plastic collapse load of a ring-loaded cylinder when compared to the more accurately computed MNA result, even though this axisymmetric problem does not involve any high local stress peaks. The LA predictions can be as low as ~40% of $R_{pl,MNA}$ when the outer surfaces of the shell wall are checked on a first yield criterion basis, or ~80% when first membrane yield is considered (Doerich & Rotter, 2011a,b; Rotter, 2011).

While the Stress Design method offers a relatively swift and simplified approach for the design of a shell structure, it comes with considerable shortcomings that undermine the structural solution's economy. The concept of designing on the basis of a localised stress peak neglects the reality of rather complex stress states that can spread across finite regions of the shell before plastic collapse or buckling can occur Rotter (2011, 2016a). Interactions between these two nonlinear phenomena can not be accounted for through this approach, a scenario that can be very common in shells of intermediate slenderness where zones of plasticity may develop and lead to the rapid onset of a buckling failure mechanism. As extensive yielded regions can arise before the shell eventually buckles, or even develops additional plasticity zones that actually lead to a plastic collapse mechanism, the Stress Design approach can be significantly over-conservative for shell structures of practical interest. All of these shortcomings are the consequence of implicitly considering external loading patters and conditions through the stress they produce, a limitation that the following design alternatives are not subject to.

2.4.3 The LBA-MNA method

Design of shell structures through the LBA-MNA methodology, already introduced as an option in the first generation of the European standard with the status of an EN (EN 1993-1-6, 2007) but not being an option in earlier 'ENV' versions of the Eurocode (ENV 1993-1-6, 1999; Schmidt, 2000), offers the alternative of treating loading scenarios as design parameters to be tested. The method has been motivated by the extensive development and availability of FE software for the analysis of shells, with most of them offering a linear elastic eigenvalue check of the structural system through an LBA, as well as an MNA for the identification of its plastic collapse mechanism for an elastic perfectly plastic material law (EN 1993-1-6, 2025). Worked numerical examples of the LBA-MNA methodology for the design of shells according to EN 1993-1-6 are additionally presented in ECCS EDR5 (2013), written as a supporting document for the use of EN 1993-1-6 (2007).

The slenderness of the shell structure is now evaluated computationally by calculating the elastic critical buckling resistance as $R_{cr} = R_{LBA}$ and the plastic resistance as $R_{pl} = R_{MNA}$. A linear

elastic analysis of the shell may be utilised to provide an estimate of R_{pl} (Rotter & Schmidt, 2013) for preliminary design purposes or in cases where a full MNA is unavailable in the computational software employed. R_k is calculated through Eq. 2.25 for a capacity curve computed for a closely related reference system, providing an estimate of the load capacity by accounting for material nonlinearities and buckling events individually. This constitutes one of the major shortcomings of the LBA-MNA methodology for the design of shell structures, as interaction between these two major sources of nonlinearity for shell behaviour is ignored. Regions of the shell that may be critical for buckling events to occur may not be subject to the likelihood of developing an equally disastrous plastic failure zone and vice-versa. As a consequence, the LBA-MNA methodology can be seen as the combination of relatively disconnected responses of a shell structure that is under the same loading conditions (Rotter, 2016b), raising considerations and demanding verification towards the structural mechanics background of the approach.

In addition to the above concerns on the reliability of the LBA-MNA methodology, it should be emphasised that application of this approach heavily relies on the level of relatability of the shell to be designed compared to the reference system used for the generation of the adopted capacity curve. While a level of conservativeness for the Stress Design method is guaranteed on the basis of ignoring any nonlinear strength capacity while finite regions of plasticity or critical compressive stresses develop, the same does not apply to the LBA-MNA method which accounts for nonlinear aspects of the shell's response, even if done independently through different analyses, by explicitly designing for external loading patterns. As such, an intimate relationship between the reference system and the examined shell system is a prerequisite for a robust application of this purely computational methodology. Realistic combinations of external loading scenarios can therefore severely complicate application of the LBA-MNA approach, introducing a significant level of uncertainty in the process that does not guarantee either conservativeness or economic design. Additional considerations regarding application of the LBA-MNA methodology on multi-segment shell structures where zones prone to the detrimental effects of initial imperfections do not coincide with those found to be critical for instability phenomena during the LBA step are discussed in Schmidt (2002); Rotter & Schmidt (2013), outlining procedures to ensure the reliability and consistency of this approach.

2.4.4 The Reference Resistance Design method

The Reference Resistance Design (RRD) method (Rotter, 2013) represents the most recent alternative for the design of shell structures according to EN 1993-1-6 (2025), introduced into the European Standard through an amendment in 2017 as originally presented by Rotter with a series of publications (Rotter, 2016a,b, 2017) around the time of publication of the first generation of EN 1993-1-6 (2007). This methodology is an entirely algebraic approach to the design of shell structures that allows the analyst to accurately evaluate its resistance whilst fully accounting for nonlinear phenomena arising as the shell carries its loads and deforms. Contribution from potential interactions between material and geometric nonlinearities is additionally incorporated into this framework, an element of a shell's nonlinear response that is included in the LBA-MNA design approach through a similar manner.

As the RRD methodology relies on a full algebraic parametrisation of a reference shell system through a series of computational analyses that target different aspects of its nonlinear behaviour, it may only be applied to systems that have been reliably explored within the context of the capacity curve framework. The examination of cylindrical shell systems under global bending by Wang *et al.* (2020) represents a quintessential example of the extensive computational nature such an endeavour necessitates. Several reference shell systems could benefit from a similar thorough investigation, including stepped-wall tanks and silos, tanks and silos under wind

loading scenarios, stiffened and unstiffened corrugated shells, conical shells under external pressure, local loads on a shell wall, cylinders with openings and cutouts, buckling above local supports and many more (Rotter, 2016b), with several of these systems partially explored through FE simulations by Chen in his PhD thesis (Chen, 2011). Whilst Primary Load Cases are not included in this list of possible candidate reference systems, as capacity curves have already been generated for these three systems and an algebraic characterisation provided within Annex D of EN 1993-1-6 (2025), the modelling techniques with which they have been generated are subject to the discussion presented in Section 2.3 and the systems could therefore benefit from validation reruns through specialised axisymmetric FE solvers.

In contrast to the LBA-MNA methodology, the critical elastic buckling resistance R_{cr} and the full plastic failure resistance R_{pl} are evaluated through closed form relationships. These relationships may be either established on an analytical basis for systems that allow such an endeavour, such as for shell of revolution under the Primary Load Cases discussed earlier. In cases where this is not a realistic possibility however, these two characteristic resistances that constitute the anchors of the RRD method can be obtained through FE simulations. Closed-form relationships that relate these resistances to the physical parameters can be subsequently formulated through a fitting scheme.

2.4.5 On the generation of capacity curves

The meticulous nature of a reference shell system's characterisation through the construct of capacity curves requires a clear plan of an analysis hierarchy that would permit a research team to capture different aspects of its nonlinear response across a spectrum of considered slenderness. A sensible strategy for such a computational venture has been formally presented by Sadowski *et al.* (2017a) within the context of an exploration of cylindrical shells under global bending, describing different 'Levels' of parametric variations for the physical parameters of a shell structure as illustrated in Figure 2.12. This scheme permits an exhaustive GMNIA investigation to evaluate all capacity curve parameters described in Table 2.2 and obtain the desired full algebraic characterisation. However, it may be beneficial to perform independent sets of LBAs, MNAs and GNAs - GNIAs on different levels to isolate individual aspects of the systems nonlinear behaviour and reduce the amount of required GMNIAs to achieve the same result. As both LBAs and MNAs are performed on an ideal perfect structure, with no strain hardening considered when material nonlinearities are present (for MNAs), Levels 2 and earlier of the hierarchy presented in Figure 2.12 are irrelevant to their execution and subsequent calculation of relationships for R_{cr} and R_{pl}. In a similar manner, relationships for α_I can be obtained through a GNIA examination of the shell system in question with Level 1 (material hardening variation) ignored.

The full set of FE models and different analyses for the investigation of a reference shell system within the scope of the capacity curve construct aims to generate conservative formulae that relate its resistance R_k to its slenderness λ. For the purposes the slenderness variation, as defined through Eq. 2.26, different ratios of R_{pr}/R_{cr} need to be considered, from stocky models for which plastic collapse is expected to be critical ($R_{pl} << R_{cr}$) to rather slender shells for which elastic buckling will govern their response ($R_{pl} >> R_{cr}$). A common technique adopted for the variation of the slenderness as the dependent variable of the capacity curves framework is to consider different r/t ratios for the shell system (Doerich *et al.*, 2018; Fajuyitan & Sadowski, 2018; Wang *et al.*, 2020; Blazejewski, 2022), with lower values corresponding to stockier models and higher r/t ratios representing shells of considerable slenderness. However, an alternative to this technique has been proposed from the very early stages of introducing the RRD methodology to the shell research community by Rotter (2010a) where all geometric parameters describing

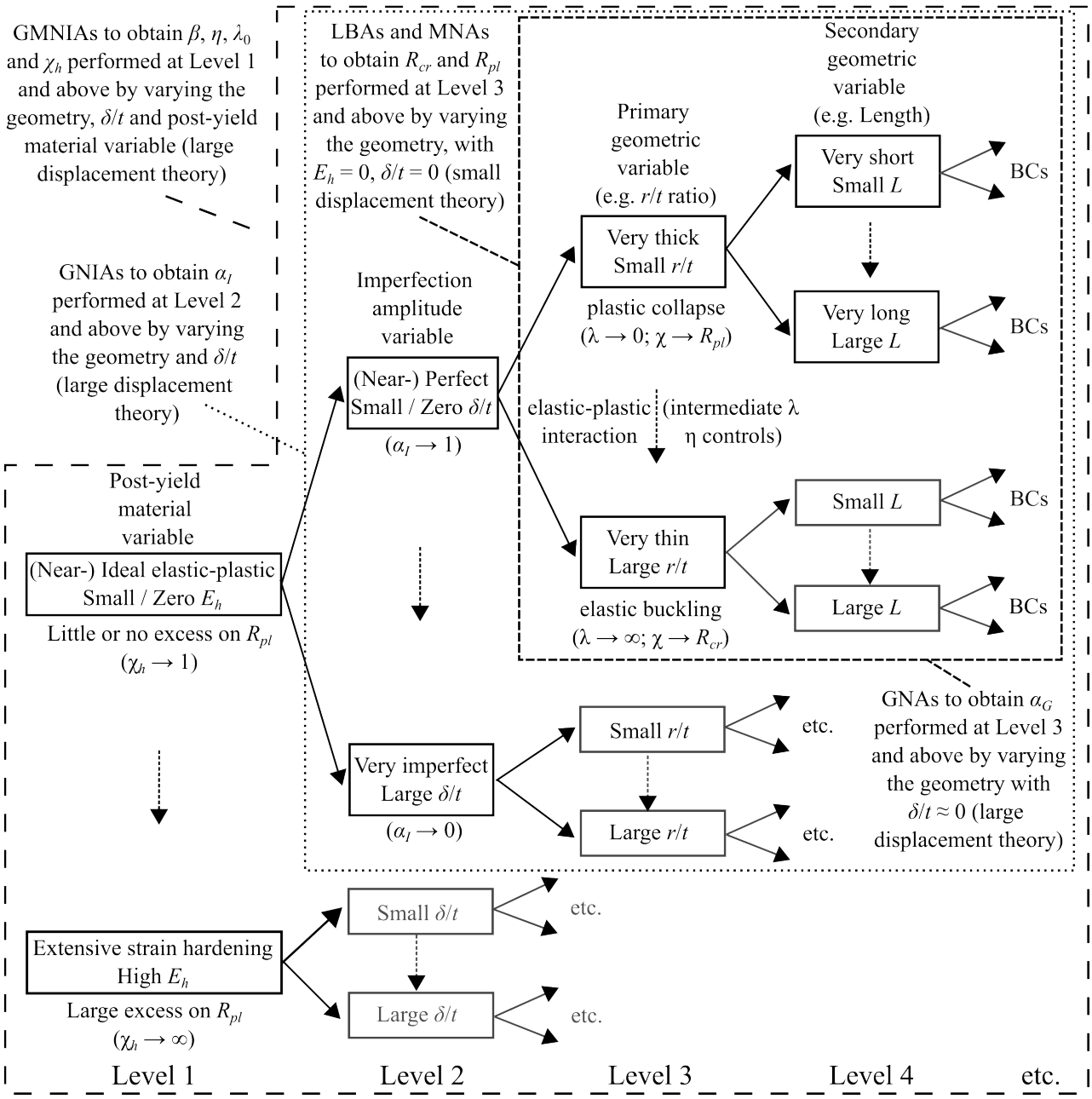


Figure 2.12: Analysis hierarchy to establish RRD parameters from system variables, adjusted from Sadowski *et al.* (2017a) for general shell reference systems.

the reference shell system remain constant. Variation of the fabrication material's yield stress f_y while the model's geometry remains unchanged keeps the elastic buckling resistance R_{cr} constant while generating different values for the full plastic resistance R_{pl}. Varying the slenderness λ through a variation of f_y allows geometrically nonlinear effects to remain constant for all models considered, reducing result interpretation needs to only those related to material nonlinearities. While this seems as a considerably beneficial approach to the computational investigation of a reference shell, the benefit of this scheme can itself hinder the integrity of the generated capacity curves as a complete abstraction of the shell system, since different geometrically nonlinear effects associated with r/t can have an influence on the overall shape of the produced capacity curve. An intimate relationship of the specific r/t ratio selected as the constant geometry on which the yield stress f_y will vary and the obtained capacity curve relationship is unavoidable, as will be illustrated in detail in Chapter 4.

Chapter 3

The AQUINAS-FE software

3.1 Motivation

The development of a versatile computational tool for the nonlinear bifurcation buckling analysis of axisymmetric shell problems has been greatly driven by the need for accurate and efficient generation of capacity curves, a construct that allows detailed explorations over an array of nonlinear mechanical responses for shell structures in the context of EN 1993-1-6 (2025). Distribution of specialised software between researchers was once commonplace, with the open-source computational packages being written from scholars active in the field of axisymmetric shell buckling having the needs of the wider scientific and design communities in mind. For the engineering discipline to fully benefit from the use of computational tools that support modern design standards, the shell research community needs to both question and reduce the use of black-box commercial FE solvers that not only place a paywall on computational approaches to facilitate further understanding but also on the scalability of numerical explorations through tokenisation systems that introduce financial considerations to parallelisation of computations. Investment into specialised tools appears to be a more profitable path for closer examination of reference shell systems to be possible, as is hinted by the surge of high quality publications on shell buckling within the decades after the release of the different BOSOR versions, FELASH, FASOR and INCA (with all of these packages now being out of circulation, as presented and discussed in section 2.3).

To amend the lack of availability of such research oriented computational tools (Teng & Song, 2001; Sadowski *et al.*, 2018), the MATLAB written FE solver AQUINAS has been recently released (Filippidis & Sadowski, 2023b) and communicated through the Eurosteel conference series (Filippidis & Sadowski, 2023a). The software is capable of tracing the equilibrium path of the shell, allowing for both geometrically and materially nonlinear effects to be accounted for as the shell deforms, detecting bifurcation into any circumferential mode $n \geq 0$ by treating the problem of axisymmetric shell buckling in its inherently 2D nature. AQUINAS is built using MATLAB's object-oriented programming capabilities, exposing multiple options for the definition of the objects through name-value pairs and permitting complete control over the solution quality of a shell problem. The full EN 1993-1-6 (2025) taxonomy of analysis types is natively supported, with an array of tools provided for the swift script modelling of axisymmetric shell problems in the context of each type of analysis.

Apart from the class definitions and analysis scripts, an extensive collection of over 30 examples can be found in the repository, serving not only as a guide for the generation of an axisymmetric shell problem in AQUINAS, but also as validation of the solution accuracy for a wide range of

meridional geometries and analysis types. The FE solution of the software is compared against analytical solutions wherever possible, but also against the results of other well-established computational tools (Bushnell, 1976; Teng & Rotter, 1989a,b; ABAQUS, 2022) that are able to perform axisymmetric shell analyses. The thoroughly documented library of example scripts may be regarded as a valuable resource on its own, as EN 1993-1-6 (2025) and EN 1993-1-14 (2025) now require the verification and validation of FE software used for the generation of thin-walled shell models. Further examples will be added with later releases of AQUINAS, extending the repository of reference solutions for axisymmetric shell problems.

The thin shell finite element formulation adopted for AQUINAS has been presented in the original articles by Teng & Rotter (1989a) *'Elastic-plastic large deflection analysis of axisymmetric shells'* and Teng & Rotter (1989b) *'Non-symmetric bifurcation of geometrically nonlinear elastic-plastic axisymmetric shells under combined loads including torsion'*. This element has been employed in the now unavailable FELASH suite of axisymmetric FE solvers with a successful track of application on the nonlinear analysis of axisymmetric shell structures (Teng & Rotter, 1989a,b; Rotter & Teng, 1989; Teng & Rotter, 1991, 1992b). Its independent interpolation field for the meridional curvature properties within an element provides an eventually more precise estimation of strain quantities, a very attractive feature for an FE formulation to be entrusted with detailed explorations into different types of nonlinear shell responses of structural forms where a high-quality curvature definition is critical. The reader may find that the contents of the first sections in this chapter are to an extent somewhat similar to those of the publication which this work is based upon. Nevertheless, the necessary definitions for the thin axisymmetric finite element shell formulation are presented here for completeness of the current work, with additional comments to elaborate on the details of the more complex steps where necessary. An attempt to adopt the European standard's EN 1993-1-6 (2025) notation is made throughout AQUINAS over any other nomenclature used in relevant literature, including the shell finite element publication of Teng & Rotter (1989a).

3.2 Geometric definition

The axisymmetric shell's geometry is defined in a cylindrical coordinate system by the radial and axial coordinates r and z as well as the meridional slope $d\phi/ds$. The characteristic geometry of the shell's meridian is illustrated in Figure 3.1, presented in an isoparametric system η for a two node element of length $2L$.

The nodal values of these geometric properties are then used to interpolate and compute the geometry along the element using Hermitian cubic functions as follows:

$$r = \sum_{i=1,2} N_{0i} r_i + N_{1i} \left(\frac{dr}{ds}\right)_i \tag{3.1a}$$

$$z = \sum_{i=1,2} N_{0i} z_i + N_{1i} \left(\frac{dz}{ds}\right)_i \tag{3.1b}$$

$$\left(\frac{d\phi}{ds}\right) = \sum_{i=1,2} N_{0i} \left(\frac{d\phi}{ds}\right)_i + N_{1i} \left(\frac{d^2\phi}{ds^2}\right)_i \tag{3.1c}$$

The element shape functions N_{0i} and N_{1i} for obtaining the interpolated geometric properties within an element are given as:

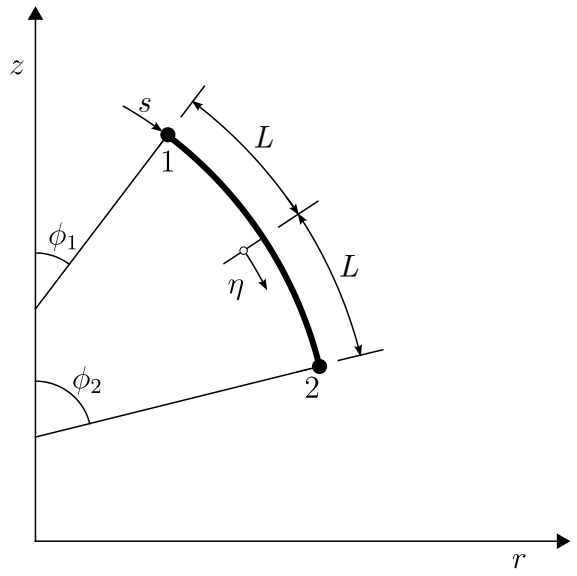


Figure 3.1: Meridional geometry of a curved shell finite element.

$$N_{01} = \frac{1}{4}(2 - 3\eta + \eta^3) \tag{3.2a}$$

$$N_{11} = \frac{L}{4}(1 - \eta - \eta^2 + \eta^3) \tag{3.2b}$$

$$N_{02} = \frac{1}{4}(2 + 3\eta - \eta^3) \tag{3.2c}$$

$$N_{12} = \frac{L}{4}(-1 - \eta + \eta^2 + \eta^3) \tag{3.2d}$$

where η is a dimensionless curvilinear meridional coordinate defined in terms of the curvilinear meridional coordinate s and the element's half-length L as:

$$\eta = \frac{2s - s_1 - s_2}{2L} \tag{3.3}$$

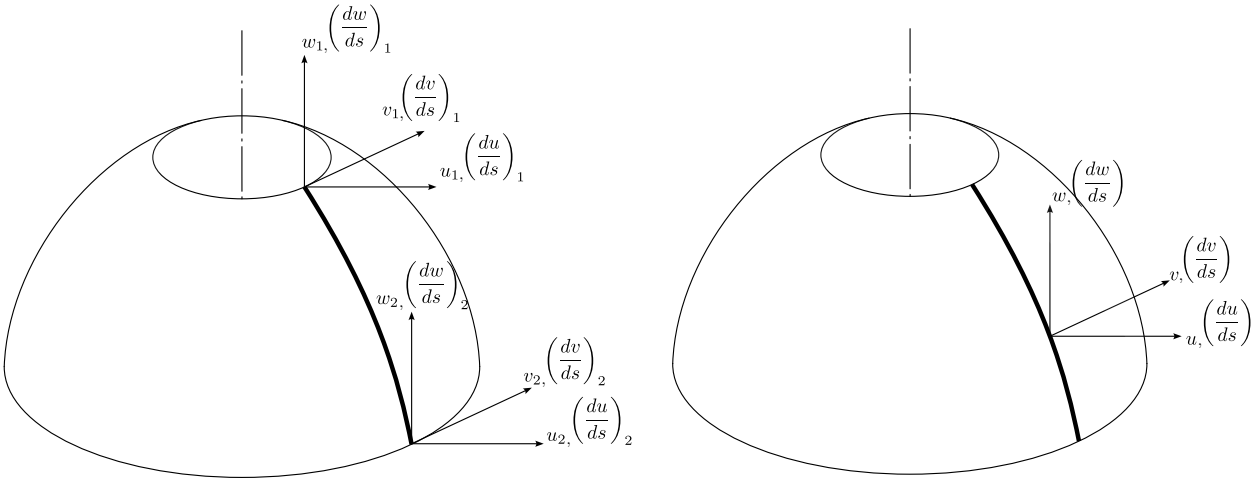
with the half-length of the element's meridian given as:

$$L = \frac{s_2 - s_1}{2} \tag{3.4}$$

A reader who looks into the original publication Teng & Rotter (1989a) may notice that the element's half-length L is not included in the equations N_{11} and N_{12} there. However, one can appreciate that interpolating derivatives of variables requires the element's length in order to scale said derivatives to the element's size (see Eqs (3.1a)-(3.1c)). The same principle is also considered in the presentation of the element's shape functions by Jumikis P.T. in his PhD thesis (Jumikis, 1987), one of the researchers that worked on developing the FELASH suite and the axisymmetric shell finite element of Teng & Rotter (1989a).

While the curvature of the shell's meridian could be obtained through differentiation of the Cartesian coordinates in Eqs (3.1a) - (3.1b), the curvature here is defined as an independent variable in Eq. (3.1c). This over-complete meridional geometry definition allows for a particularly stable and precise element, avoiding a consequent loss of accuracy in the strain matrix due to a

poor definition of meridional curvature.



(a) End node DOFs. (b) DOFs within an element.

Figure 3.2: Element Degrees of Freedom.

The Hermitian interpolation field is also adopted for obtaining the displacements, expressed in the global cylindrical coordinate system, along the meridian of an element based on the end-node Degrees Of Freedom (DOF). The end-node DOFs for all elements are u_i, $(\mathrm{d}u/\mathrm{d}s)_i$, v_i, $(\mathrm{d}v/\mathrm{d}s)_i$, w_i and $(\mathrm{d}w/\mathrm{d}s)_i$ as illustrated in Figure 3.2a. The displacement interpolation field within an element, as shown in Figure 3.2b, using the shape functions of Eqs (3.2a)-(3.2d), is given as:

$$u = \sum_{i=1,2} N_{0i} u_i + N_{1i} \left(\frac{du}{ds}\right)_i \tag{3.5a}$$

$$v = \sum_{i=1,2} N_{0i} v_i + N_{1i} \left(\frac{dv}{ds}\right)_i \tag{3.5b}$$

$$w = \sum_{i=1,2} N_{0i} w_i + N_{1i} \left(\frac{dw}{ds}\right)_i \tag{3.5c}$$

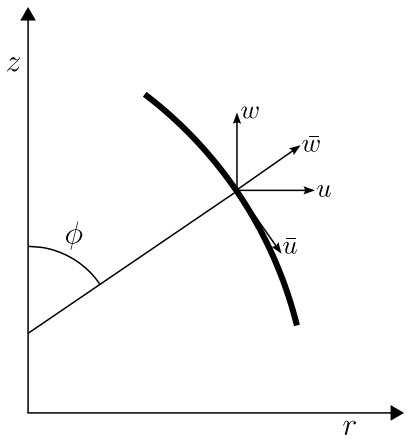


Figure 3.3: Local and global Degrees of Freedom.

Global displacements u, v and w are related to the corresponding local $\bar{u}$, $\bar{v}$ and $\bar{w}$ ones, also

defined in curvilinear coordinates, through a transformation matrix T:

$$\begin{Bmatrix} \bar{u} \\ \bar{v} \\ \bar{w} \end{Bmatrix} = \begin{bmatrix} \cos(\phi) & 0 & -\sin(\phi) \\ 0 & 1 & 0 \\ \sin(\phi) & 0 & \cos(\phi) \end{bmatrix} \begin{Bmatrix} u \\ v \\ w \end{Bmatrix} = [T] \begin{Bmatrix} u \\ v \\ w \end{Bmatrix} \tag{3.6}$$

The global cylindrical coordinate system is used for the definition of the element displacements. On the other hand, stresses and strains are expressed in the local curvilinear system of each element such that the transformation matrix of Eq. (3.6) must be used to obtain the displacements in the local coordinate system of the element. This transformation is implicitly applied with the use of the strain-displacement matrix $[B]$, which relates end-node displacements expressed in the global cylindrical coordinate system, to the strains at a dimensionless meridional coordinate η along the element.

In the present finite element formulation for axisymmetric shells, the displacement field is assumed to follow a symmetric Fourier series variation in the circumferential direction. The antisymmetric terms, also included in the original publication by Teng & Rotter (1989a), are here dropped since they are only relevant to describe the displacement field of shells under torsional effects, currently considered out of the scope of the software. Therefore, the circumferential displacements, only included the symmetric variation of the Fourier series, are given as:

$$u = \sum_{n=0}^{N} u_n \cos(n\theta) \tag{3.7a}$$

$$v = \sum_{n=0}^{N} v_n \sin(n\theta) \tag{3.7b}$$

$$w = \sum_{n=0}^{N} w_n \cos(n\theta) \tag{3.7c}$$

It should be noted that the notation used for a circumferential wave-number here is 'n', instead of the 'm' letter used in Teng & Rotter (1989a). This is done to adopt the notation used most often in classical texts on shell theory (though 'm' may also be encountered in some of them), but is also a decision based on the follow-up publication by Teng & Rotter (1989b), where the notation for a circumferential wave-number is changed from 'm' to 'n'.

The circumferential wave-number is embedded in the finite element formulation of this software, meaning that each stiffness matrix assembled corresponds to a specific wave-number and has an underlying assumption about the circumferential displacement field. For most tasks handled by the software, the axisymmetric wave-number ($n = 0$) is considered, with non-zero wave-numbers being only relevant for analyses including bifurcation checks.

3.3 Kinematic relations

Thin shell theory dictates that the strain state at any distance ζ normal to the reference surface of the shell, choosing to differentiate to the z notation employed in Teng & Rotter (1989a,b) to avoid confusion with the axial coordinate z, can be defined in terms of three membrane strains and three bending strain components. For the formulation of the shell element employed here it is considered that the shell's reference surface and its mid-surface coincide, hence the

normal coordinate ζ may take values in the range [-t/2,t/2] (where t is the thickness of the shell's meridian). The membrane strains and curvatures (bending strain components) that may be used to define the strain state at any point within the shell wall of an element are:

$$\{\epsilon\} = \{\epsilon^0_\phi, \epsilon^0_\theta, \gamma^0_{\phi\theta}, \kappa^0_\phi, \kappa^0_\theta, \kappa^0_{\phi\theta}\}^T \tag{3.8}$$

where the '0' superscript is used for indicating strains corresponding to the shell's mid-surface. The initial strains that the reader may notice to be included in the corresponding equation in Teng & Rotter (1989a) are here neglected as currently out of scope for the software. Transverse shear strain terms (relevant to a thick shell response) are also currently omitted from the formulation (with consideration of finite-thickness effects discussed in the derivational work of Chapter 6). The six strain terms of Eq. (3.8) may now be used to obtain the strains $\{\epsilon^\zeta\} = \{\epsilon^\zeta_\phi, \epsilon^\zeta_\theta, \gamma^\zeta_{\phi\theta}\}^T$ at any point ζ as:

$$\{\epsilon^\zeta\} = [Z]\{\epsilon\} \tag{3.9}$$

where the $[Z]$ matrix is given as:

$$[Z] = \begin{bmatrix} 1 & 0 & 0 & \zeta & 0 & 0 \\ 0 & 1 & 0 & 0 & \zeta & 0 \\ 0 & 0 & 1 & 0 & 0 & \zeta \end{bmatrix} \tag{3.10}$$

with ζ referring to the distance from shell's midsurface. The generalised strains of Eq. (3.8) can be separated into two parts, the linear $\{\epsilon_l\}$ components given as linear functions of the displacements, and the nonlinear $\{\epsilon_{nl}\}$ components given as quadratic relations of the displacements:

$$\{\epsilon\} = \{\epsilon_l\} + \{\epsilon_{nl}\} \tag{3.11}$$

where the linear and nonlinear strain vectors are:

$$\{\epsilon_l\} = \{\epsilon^0_{\phi l}, \epsilon^0_{\theta l}, \gamma^0_{\phi\theta l}, \kappa_{\phi l}, \kappa_{\theta l}, \kappa_{\phi\theta l}\}^T \tag{3.12a}$$

$$\{\epsilon_{nl}\} = \{\epsilon^0_{\phi l}, \epsilon^0_{\theta l}, \gamma^0_{\phi\theta l}, 0, 0, 0\}^T \tag{3.12b}$$

3.3.1 Linear strain-displacement relations

The linear strains $\{\epsilon_l\}$ of the shell's mid-surface, according to small deflection theory, are given as:

$$\epsilon^0_{\phi l} = \frac{\partial \bar{u}}{\partial s} + \frac{\partial \phi}{\partial s}\bar{w} \tag{3.13a}$$

$$\epsilon^0_{\theta l} = \frac{\cos\phi}{r}\bar{u} + \frac{1}{r}\frac{\partial \bar{v}}{\partial \theta} + \frac{\sin\phi}{r}\bar{w} \tag{3.13b}$$

$$\gamma^0_{\phi\theta l} = \frac{1}{r}\frac{\partial \bar{u}}{\partial \theta} - \frac{1}{r}\cos\phi\bar{v} + \frac{\partial \bar{v}}{\partial s} \tag{3.13c}$$

$$\kappa_\phi = \frac{\partial^2 \phi}{\partial s^2}\bar{u} + \frac{\partial \phi}{\partial s}\frac{\partial \bar{u}}{\partial s} - \frac{\partial^2 \bar{w}}{\partial s^2} \tag{3.13d}$$

$$\kappa_\theta = \frac{1}{r}\frac{\partial \phi}{\partial s}\cos\phi\bar{u} + \frac{1}{r^2}\sin\phi\frac{\partial \bar{v}}{\partial \theta} - \frac{\cos\phi}{r}\frac{\partial \bar{w}}{\partial s} - \frac{1}{r^2}\frac{\partial^2 \bar{w}}{\partial \theta^2} \tag{3.13e}$$

$$\kappa_{\phi\theta} = \frac{1}{r}\frac{\partial\phi}{\partial s}\frac{\partial\bar{u}}{\partial\theta} + \left(\cos\phi\frac{\partial\phi}{\partial s} - \frac{2}{r}\sin\phi\cos\phi\right)\frac{\bar{v}}{r} + \frac{\sin\phi}{r}\frac{\partial\bar{v}}{\partial s} + \frac{2}{r^2}\cos\phi\frac{\partial\bar{w}}{\partial\theta} - \frac{2}{r}\frac{\partial^2\bar{w}}{\partial s\partial\theta} \tag{3.13f}$$

While the resource cited in Teng & Rotter (1989a) for their derivation (Rotter & Jumikis, 1987) is presently inaccessible, their derivation may also be found in the PhD thesis of P.T. Jumikis Jumikis (1987). These linear strains can be found to be identical to those derived in the classical book *Stresses in Shells* by Flügge (1990) (Chapter 6.1.2 therein), as well as those of Reissner (Kraus, 1967; Seide, 1975) cited in the original publication Teng & Rotter (1989a).

3.3.2 Nonlinear strain-displacement relations

The nonlinear strain components $\{\epsilon_{nl}\}$ may be defined as quadratic functions of the shell's mid-surface pseudo-rotations. The reference provided for the derivation of the nonlinear strains in Teng & Rotter (1989a) is once again found to be the currently inaccessible report Rotter & Jumikis (1987), but the same derivation is also included in Jumikis (1987). The nonlinear strains are defined in terms of the pseudo-rotations β_1-β_6 as:

$$\epsilon^0_{\phi nl} = \frac{1}{2}(\beta_1^2 + \beta_2^2 + \beta_3^2) \tag{3.14a}$$

$$\epsilon^0_{\theta nl} = \frac{1}{2}(\beta_1^2 + \beta_2^2 + \beta_3^2) \tag{3.14b}$$

$$\gamma^0_{\phi\theta nl} = (\beta_1\beta_4 + \beta_2\beta_5 + \beta_3\beta_6) \tag{3.14c}$$

with the pseudo-rotations being:

$$\beta_1 = \frac{\partial\bar{w}}{\partial s} - \bar{u}\frac{\partial\phi}{\partial s} \tag{3.15a}$$

$$\beta_2 = \frac{\partial\bar{v}}{\partial s} \tag{3.15b}$$

$$\beta_3 = \frac{\partial\bar{u}}{\partial s} + \bar{w}\frac{\partial\phi}{\partial s} \tag{3.15c}$$

$$\beta_4 = \frac{1}{r}\left(\frac{\partial\bar{w}}{\partial\theta} - \bar{v}\sin\phi\right) \tag{3.15d}$$

$$\beta_5 = \frac{1}{r}\left(\frac{\partial\bar{v}}{\partial\theta} + \bar{w}\sin\phi + \bar{u}\cos\phi\right) \tag{3.15e}$$

$$\beta_6 = \frac{1}{r}\left(\frac{\partial\bar{u}}{\partial\theta} - \bar{v}\cos\phi\right) \tag{3.15f}$$

It should be noted that these relations hold for moderate rotations. The vector of pseudo-rotations Θ can now be defined as:

$$\{\Theta\} = \{\beta_1, \beta_2, \beta_3, \beta_4, \beta_5, \beta_6\}^T \tag{3.16}$$

and the matrix $[A]$ of pseudo-rotations as:

$$[A] = \begin{bmatrix} \beta_1 & \beta_2 & \beta_3 & 0 & 0 & 0 \\ 0 & 0 & 0 & \beta_4 & \beta_5 & \beta_6 \\ \beta_4 & \beta_5 & \beta_6 & \beta_1 & \beta_2 & \beta_3 \end{bmatrix} \tag{3.17}$$

It can be easily proven that the following relation holds for the nonlinear strains:

$$\{\epsilon_{nl}\} = \frac{1}{2}[\Omega]\{\Theta\} \tag{3.18}$$

where Ω is constructed as:

$$[\Omega] = [A^T, 0]^T \tag{3.19}$$

and 0 in the above relation is a 6-by-3 matrix with zero entries.

3.4 Constitutive relations

The J2 flow rule of plasticity has been implemented to model the nonlinear behaviour of materials, the yielding of which is determined according to the von Mises yield criterion. The J2 deformation theory of plasticity, presented in the second publication by Teng & Rotter (1989b) has not been implemented in AQUINAS since the pre-buckling configurations that would lead to elastic-plastic shear strains and stresses, such as those arising in axisymmetric shells under torsional effects that would require the determination of the effective shear modulus G_{ef}, are currently out of scope for the software. More complex expressions for the constitutive relations of an axisymmetric shell may be found in a subsequent publication by the same authors (Teng & Rotter, 1992a), presenting an element for the analysis of concrete shells that accounts for yielding of reinforcement bars and rigorously models the nonlinear behaviour of concrete by considering flexural, thermal and shrinkage cracking effects.

Isotropic hardening can be included through the definition of a nonlinear uniaxial stress-strain curve that will be used to determine the hardening parameter based on the value of the equivalent plastic strain of the material point. However, kinematic hardening effects are neglected in the current version of AQUINAS, mainly because they are, for the most part, only significant in cases where cyclic plasticity occurs. These cases are not currently studied by AQUINAS, which focuses at present on the monotonic applications of loads.

The von Mises yield criterion is defined as:

$$F(\sigma, k) = \bar{\sigma} - \sigma_y = 0 \tag{3.20}$$

with k being the hardening parameter and $\bar{\sigma}$ the equivalent von Mises stress:

$$\bar{\sigma} = \sqrt{\sigma_\phi^2 + \sigma_\theta^2 - \sigma_\phi \sigma_\theta + 3\tau_{\phi\theta}^2} \tag{3.21}$$

where the stresses in the meridional and circumferential directions are σ_ϕ and σ_θ respectively while $\tau_{\phi\theta}$ is the shear stress. The yield stress σ_y is given as a function of the plastic strains at any material point, which for isotropic hardening can be defined as:

$$\sigma_y = \sigma_{y0} + \int H' d\bar{\epsilon}_p \tag{3.22}$$

In Eq. (3.22) above, σ_{y0} is the material stress at the point of first yielding (zero plastic strain), while the plastic strain increment $\bar{\epsilon}_p$ is:

$$d\bar{\epsilon}_p = \frac{2}{\sqrt{3}}\sqrt{(d\epsilon^{\zeta}_{\phi p})^2 + (d\epsilon^{\zeta}_{\theta p})^2 + d\epsilon^{\zeta}_{\phi p} d\epsilon^{\zeta}_{\theta p} + (d\gamma^{\zeta}_{\phi\theta p})^2/4} \tag{3.23}$$

where $d\epsilon^{\zeta}_{\phi p}$, $d\epsilon^{\zeta}_{\theta p}$ and $d\gamma^{\zeta}_{\phi\theta p}$ are the meridional, circumferential and shear plastic strain increments respectively at any location ζ through the shell wall. The isotropic hardening parameter H', relating the elastic and tangent moduli of the material, is defined as:

$$H' = \frac{E E_t}{E - E_t} \tag{3.24}$$

Where the elasticity modulus E (Young's modulus) in Eq. (3.24) is constant throughout the analysis for a specific material point, the tangent modulues E_t may depend on the magnitude of the plastic strain $\bar{\epsilon}_p$ and be obtained through a uniaxial stress-strain curve as presented in Figure 3.4.

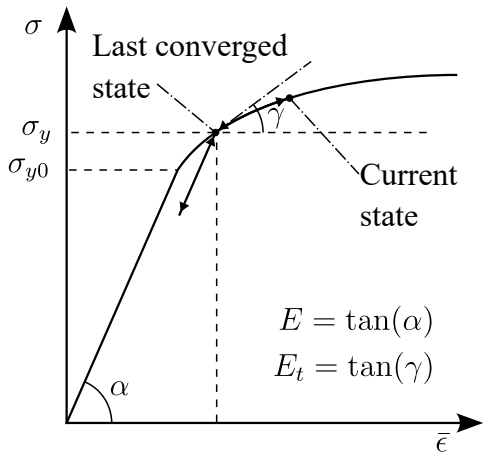


Figure 3.4: Uniaxial stress-strain curve and incremental plastic reversibility assumption.

The flow rule, as can be found in classical texts on plasticity (Crisfield, 1991; Simo & Hughes, 2006), is given as

$$d\{\epsilon_p\} = d\bar{\epsilon}_p \frac{\partial F}{\partial\{\sigma\}} = d\bar{\epsilon}_p \frac{3}{2\bar{\sigma}}\{s\} \tag{3.25}$$

with the vectors of plastic strains ϵ_p, stresses σ and deviatoric stresses s being:

$$\{\epsilon_p\} = \{\epsilon^z_{\phi p}, \epsilon^z_{\theta p}, \gamma^z_{\phi\theta p}\}^T \tag{3.26a}$$
$$\{\sigma\} = \{\sigma^z_{\phi}, \sigma^z_{\theta}, \tau^z_{\phi\theta}\}^T \tag{3.26b}$$
$$\{s\} = \{s^z_{\phi}, s^z_{\theta}, s^z_{\phi\theta}\}^T \tag{3.26c}$$

The deviatoric stresses s, which correspond to the difference between the total stress component σ and the hydrostatic stresses, are given as:

$$s_\phi = \frac{1}{3}(2\sigma_\phi - \sigma_\theta) \tag{3.27a}$$
$$s_\theta = \frac{1}{3}(2\sigma_\theta - \sigma_\phi) \tag{3.27b}$$
$$s_{\phi\theta} = 2\tau_{\phi\theta} \tag{3.27c}$$

An increment of the stress vector is then defined as:

$$d\{\sigma\} = [D_{ep}]d\{\epsilon^z\} \tag{3.28}$$

where the elastic-plastic modulus matrix $[D_{ep}]$ is:

$$[D_{ep}] = [D_e] - a[D_p] \tag{3.29}$$

The factor a in Eq. (3.29) is set to $a = 0$ for elastic material points, while $a = 1$ for plastic-hardening ones. The elastic rigidity matrix for plane stress conditions is given as:

$$[D_e] = \frac{E}{(1-\nu^2)} \begin{bmatrix} 1 & \nu & 0 \\ \nu & 1 & 0 \\ 0 & 0 & (1-\nu)/2 \end{bmatrix} \tag{3.30}$$

where E is the elastic modulus (Young's modulus) and ν is the Poisson ratio of the material. The plastic matrix component of Eq. (3.29) is then:

$$[D_p] = \frac{E}{(1-\nu^2)S_5} \begin{bmatrix} S_1S_1 & S_1S_2 & S_1(1-\nu)\tau_{\phi\theta} \\ S_1S_2 & S_2S_2 & S_2(1-\nu)\tau_{\phi\theta} \\ S_1(1-\nu)\tau_{\phi\theta} & S_2(1-\nu)\tau_{\phi\theta} & \tau_{\phi\theta}^2(1-\nu)^2 \end{bmatrix} \tag{3.31}$$

with the parameters S_1 to S_5 being:

$$S_1 = s_\phi + \nu s_\theta \tag{3.32a}$$
$$S_2 = s_\theta + \nu s_\phi \tag{3.32b}$$
$$S_3 = S_1 d\epsilon_\phi^z + S_2 d\epsilon_\theta^z + (1-\nu)\tau_{\phi\theta} d\gamma_{\phi\theta}^z \tag{3.32c}$$
$$S_4 = s_\phi^2 + s_\theta^2 + 2\nu s_\phi s_\theta + 2(1-\nu)\tau_{\phi\theta}^2 \tag{3.32d}$$
$$S_5 = \frac{2\bar{\sigma}^2(1-\nu)H'}{9G} + S_4 \tag{3.32e}$$

An increment of the equivalent plastic strains of a material point can be found to be:

$$d\bar{\epsilon}_p = \frac{2\bar{\sigma}}{3}\frac{S_3}{S_5} \tag{3.33}$$

The process for formulating $[D_{ep}]$ and $[D_p]$ of Eqs (3.29) - (3.31), as well as for computing an increment of the equivalent plastic strains of a material point, can be found in Chapter 6 *Basic plasticity* of Crisfield (1991) as well as other classical texts on plasticity (Simo & Hughes, 2006; Owen, 1980). Once the stresses at all material points across the thickness of the shell wall have been computed, the vector of generalised stress resultants $\{\Sigma\}$ can be integrated according to classical shell theory relations. The three membrane stress resultants and three bending stress resultants that comprise $\{\Sigma\}$ are

$$\{\Sigma\} = \{N_\phi, N_\theta, N_{\phi\theta}, M_\phi, M_\theta, M_{\phi\theta}\} \tag{3.34}$$

where N_ϕ and N_θ are the meridional and circumferential membrane stress resultants respectively, $N_{\phi\theta}$ is the in-plane membrane shear stress resultant (not to be confused with transverse shear), M_ϕ and M_θ are the bending stress resultants in the meridional and circumferential directions respectively while $M_{\phi\theta}$ is the twisting moment. An increment of generalised stress resultants can be related to an increment of reference surface strains of Eq. (3.11) through the tangent modulus matrix $[D_T]$ as

$$\{d\Sigma\} = [D_T]d[\{\epsilon\} - \{\epsilon_0\}] \tag{3.35}$$

with the tangent modulus $[D_T]$ given by:

$$[D_T] = \int_{-t/2}^{t/2} [Z]^T [D_{ep}][Z]dz \tag{3.36}$$

As can be seen from the relation above, in order to obtain the tangent modulus matrix $[D_T]$ the elastic-plastic modulus matrices $[D_{ep}]$ of Eq. (3.29) must be integrated across the thickness of the shell wall. This integration is carried out using Simpson's 1/3 rule, as advised in Teng & Rotter (1989a), but also most commonly encountered as the through thickness integration scheme when material nonlinearities are considered due to their discontinuous nature that invalidates the use of a Gauss-Legendre scheme (which assumes an n^{th} order polynomial behaviour).

3.5 Finite Element Formulation

With reference to Figure 3.2a, the end node DOFs vector of the axisymmetric shell element presented here is:

$$\{\delta\} = \left\{u_1, \left(\frac{\partial u}{\partial s}\right)_1, v_1, \left(\frac{\partial v}{\partial s}\right)_1, w_1, \left(\frac{\partial w}{\partial s}\right)_1, u_2, \left(\frac{\partial u}{\partial s}\right)_2, v_2, \left(\frac{\partial v}{\partial s}\right)_2, w_2, \left(\frac{\partial w}{\partial s}\right)_2\right\}^T \tag{3.37}$$

Adopting a total Lagrangian formulation, all quantities relate to the original undeformed geometry of the thin shell. The principle of virtual displacements yields:

$$\int_V d\epsilon^T \sigma dV = \Pi \tag{3.38}$$

with the work done by body forces q and external tractions p being equal to:

$$\Pi = \int \rho du^T q dV + \int du^T p dA \tag{3.39}$$

In the above relations, ϵ and σ are the vectors of Green strains and Piola-Kirchoff stresses respectively, ρ is the density of the body, u is the vector of displacements while dA and dV are the elements of surface area and volume respectively, referring to the undeformed configuration.

Following classical finite element theory concepts for the solution of nonlinear problems, the tangent stiffness matrix of the shell elements is split into the material and geometric stiffness components which, when added, formulate the tangent stiffness matrix of an element. The formulation of the individual stiffness components will be described in the following paragraphs.

Revisiting Eq. (3.11) and taking variations while accounting for the relation of Eq. (3.18), an increment of strain can be defined as:

$$d\{\epsilon\} = d\{\epsilon_l\} + \frac{1}{2}[\Omega]d\{\Theta\} + \frac{1}{2}d[\Omega]\{\Theta\} \tag{3.40}$$

Through substitution and differentiation, it can be proven that:

$$[\Omega]d\{\Theta\} = \{\Theta\}d[\Omega] \tag{3.41}$$

Hence, an increment of strain may be given as:

$$d\{\epsilon\} = d\{\epsilon_l\} + [\Omega]d\{\Theta\} \tag{3.42}$$

Observing Eq. (3.42) above, the increment of the linear strains $d\{\epsilon_l\}$ and the term $[\Omega]d\{\Theta\}$ will now need to be related to the nodal displacements of an element, $\{\delta\}$, in order to formulate the linear-nonlinear strain-displacement matrix $[B]$ and eventually compute the material stiffness of the shell element. The strain-displacement matrix $[B]$, used to relate a strain increment to a nodal displacement increment, is given as:

$$d\{\epsilon\} = [B]d\{\delta\} \tag{3.43}$$

Denoting as $[B_0]$ the strain-displacement matrix corresponding to the linear components of the strains, which is independent of the nodal displacements developing during the solution process, an increment of the linear strain can be found to be:

$$d\{\epsilon_l\} = [B_0]d\{\delta\} \tag{3.44}$$

Before going into the formulation of the strain-displacement matrix corresponding to nonlinear strains, it is important to note that a total Lagrangian formulation for thin shells has been adopted in Teng & Rotter (1989a), and consequently here, where all quantities relate to the initial undeformed configuration of the meridian. Hence, no updating of nodal positions should be expected by the reader when tracing the prebuckling axisymmetric state of the shell when geometrical nonlinearities are considered, and the only place where the nonlinear changes in the geometry are accounted for is through the nonlinear strain-displacement matrix.

A combination of Eqs (3.5), (3.6), (3.15) and (3.16) leads to:

$$\{\Theta\} = [G]\{\delta\} \tag{3.45}$$

with $[G]$ being an array of shape functions and their derivatives, relating the pseudo-rotations of Eq. (3.15) to the nodal displacement vector $\{\delta\}$. By taking variations in Eq. (3.45):

$$d\{\Theta\} = [G]d\{\delta\} \tag{3.46}$$

An increment of the nonlinear strain components can now be found as:

$$d\{\epsilon_{nl}\} = [B_L]d\{\delta\} \tag{3.47}$$

where the strain-displacement matrix $[B_L]$, relating the nonlinear strains increment $d\{\epsilon_{nl}\}$ to the nodal displacement vector $\{\delta\}$, can be obtained from Eqs. (3.42) and (3.46) as:

$$[B_L] = [\Omega][G] \tag{3.48}$$

The strain-displacement matrix $[B]$, relating the reference surface strains $\{\epsilon\}$, including both the linear and nonlinear components $\{\epsilon_l\}$ and $\{\epsilon_{nl}\}$ to the end node displacements $\{\delta\}$, is now defined from Eq. (3.42) as:

$$[B] = [B_0] + [B_L] \tag{3.49}$$

For a single element, Eq. (3.38) can be written as:

$$d\{\delta\}^T = \int [B]^T\{\Sigma\}dV = d\{\delta\}^T\{R\} \tag{3.50}$$

where $\{R\}$ is a vector of equivalent nodal forces because of body forces q and surface tractions p. The vector of virtual displacements $\{d\delta\}^T$ is arbitrary, hence the nonlinear equations for an element can be written as:

$$\{\Phi(\delta)\} = \{R\} - \int [B]^T\{\Sigma\}dV = 0 \tag{3.51}$$

The above expression for the vector of nodal residual forces $\{\Phi(\delta)\}$ will be the fundamental nonlinear equation for which a solution is sought, for problems where either material or geometric nonlinearities are to be considered. The assumption that the equivalent nodal forces $\{R\}$ are conservative is made for all that follows.

For a known increment of the total displacements δ_i, such that the residual forces are non-zero ($\Phi(\delta_i) \neq 0$), the value of Φ for an increment $\Delta\delta_i$ in δ_i can be expressed as a Taylor series expansion of Φ about δ_i:

$$\Phi(\delta_i + \Delta\delta_i) = \Phi(\delta_i)\left[\frac{\partial\Phi}{\partial\delta}\right]_{\delta=\delta_i}\Delta\delta_i + ... = 0 \tag{3.52}$$

Ignoring the second and higher order terms, a linear approximation of the residual force vector

with respect to the nodal displacement increments can be obtained as:

$$\{\Phi(\delta_i)\} = [K_T]\{\Delta\delta_i\} \tag{3.53}$$

In Eq. (3.52) above $[K_T]$ is the tangent stiffness matrix of the axisymmetric shell and is defined as:

$$[K_T] = -\left[\frac{\partial\Phi}{\partial\delta}\right]_{\delta=\delta_i} \tag{3.54}$$

Due to the truncation of the Taylor series of Eq. (3.52) just after the first order term, the solution obtained for $\Delta\delta_i$ will be only a linear approximation of the set of nonlinear equations. A series of iterations needs to be performed to obtain a solution of sufficient accuracy, most commonly adopting a Newton-Raphson scheme.

Through manipulation of Eq. (3.51), a relation for the tangent stiffness matrix $[K_T]$ can be obtained as:

$$-\frac{d\{\Phi\}}{d\{\delta\}} = \int [B]^T \frac{d\{\Sigma\}}{d\{\delta\}} dA + \int \frac{d[B]^T}{d\{\delta\}}\{\Sigma\} dA \tag{3.55}$$

Taking variations of Eq. (3.49), by considering Eq. (3.48), one may find that:

$$d[B]^t = d[B_L]^T = [G]^T[\Omega]^T \tag{3.56}$$

since $[B_0]$ only contains terms of shape functions and their derivatives, and therefore vanishes in a differentiation with respect to the nodal displacements. Substituting Eqs (3.35) and (3.56) into Eq. (3.55) leads to:

$$-\frac{d\{\Phi\}}{d\{\delta\}} = \int [B]^T[D_T][B] dA + \int [G]^T \frac{d[\Omega]^T}{d\{\delta\}}\{\Sigma\} dA \tag{3.57}$$

The terms in the second integrand can be rewritten in the form:

$$\frac{d[\Omega]}{d\{\Sigma\}} = [N_0]\frac{d\{\Theta\}}{d\{\delta\}} = [N_0][G] \tag{3.58}$$

where $[N_0]$ is a 6 x 6 matrix of membrane stress resultants, corresponding to the pseudo rotations according to the nonlinear strains $\{\epsilon_{nl}\}$ of Eqs (3.14), given as:

$$[N_0] = \begin{bmatrix} N_\phi & 0 & 0 & N_{\phi\theta} & 0 & 0 \\ 0 & N_\phi & 0 & 0 & N_{\phi\theta} & 0 \\ 0 & 0 & N_\phi & 0 & 0 & N_{\phi\theta} \\ N_{\phi\theta} & 0 & 0 & N_\theta & 0 & 0 \\ 0 & N_{\phi\theta} & 0 & 0 & N_\theta & 0 \\ 0 & 0 & N_{\phi\theta} & 0 & 0 & N_\theta \end{bmatrix} \tag{3.59}$$

Substituting Eq. (3.58) into Eq. (3.57) yields:

$$-\frac{d\{\Phi\}}{d\{\delta\}} = \int_A [B]^T [D_T][B] dA + \int_A [G]^T [N_0][G] dA \tag{3.60}$$

Since the variation of an element's residual forces with respect to its nodal displacements is equivalent to the tangent stiffness $[K_T]_e$, Eq. (3.60) leads to:

$$[K_T]_e = [\bar{K}]_e + [K_\sigma]_e \tag{3.61}$$

where:

$$[\bar{K}]_e = \int_A [B]^T [D_T][B] dA \tag{3.62a}$$

$$[K_\sigma]_e = \int_A [G]^T [N_0][G] dA \tag{3.62b}$$

The tangent stiffness matrix $[K_T]_e$ of an element is formed in Eq. (3.61) through the addition of two individual stiffness matrix components, the material stiffness $[\bar{K}]_e$, accounting for changes in element geometry through the nonlinear strain corresponding terms in the strain-displacement matrix of Eq. (3.49), and the geometric stiffness $[K_\sigma]_e$ which accounts for the effects of internal stresses in the stiffness of the element.

The tangent stiffness of the structure is assembled through the insertion of each element's stiffness terms in the appropriate cells of the global stiffness array, a common procedure in matrix structural analysis. Before going into the assembly of the global tangent stiffness matrix however, the end-node DOFs du/ds and dw/ds need to be statically condensed, in order to avoid connecting wrong variables at segment junctions with an abrupt change of meridional slope. The process of statically condensing these nodal DOFs is thoroughly presented in the following section.

3.5.1 Condensation of nodal variables

For shells with continuous meridional curvature, the six nodal DOFs of u_i, $(du/ds)_i$, v_i, $(dv/ds)_i$, w_i, $(dw/ds)_i$ Eq. (3.37) (6 per node, 12 per element) are indeed appropriate for use in the assembled global stiffness matrix. In cases however that there are sudden changes of slope between segments of the shell's meridian, associating the $(du/ds)_i$ and $(dw/ds)_i$ DOFs at the intersection can lead to errors in the analysis due to the excessive continuity that is imposed between elements, as illustrated in Figure 3.5.

For this reason, the $(du/ds)_i$ and $(dw/ds)_i$ nodal DOFs are disassociated between shell segments. These two nodal variables are first transformed according to the following relation:

$$\begin{Bmatrix} \beta_i \\ \gamma_i \end{Bmatrix} = \begin{bmatrix} -\sin\phi & -\cos\phi \\ \cos\phi & -\sin\phi \end{bmatrix} \begin{Bmatrix} (du/ds)_i \\ (dw/ds)_i \end{Bmatrix} \tag{3.63}$$

where β_i corresponds to the rotation and γ_i to the meridional stretching of node i. Once the transformation has been applied, the nodal DOFs γ and dv/ds are condensed out of the stiffness matrix of the element, before the global stiffness matrix is assembled.

At this point, it is important to note that a different procedure is adopted for condensing out the desired DOFs, depending on the type of the element's stiffness matrix the static condensation

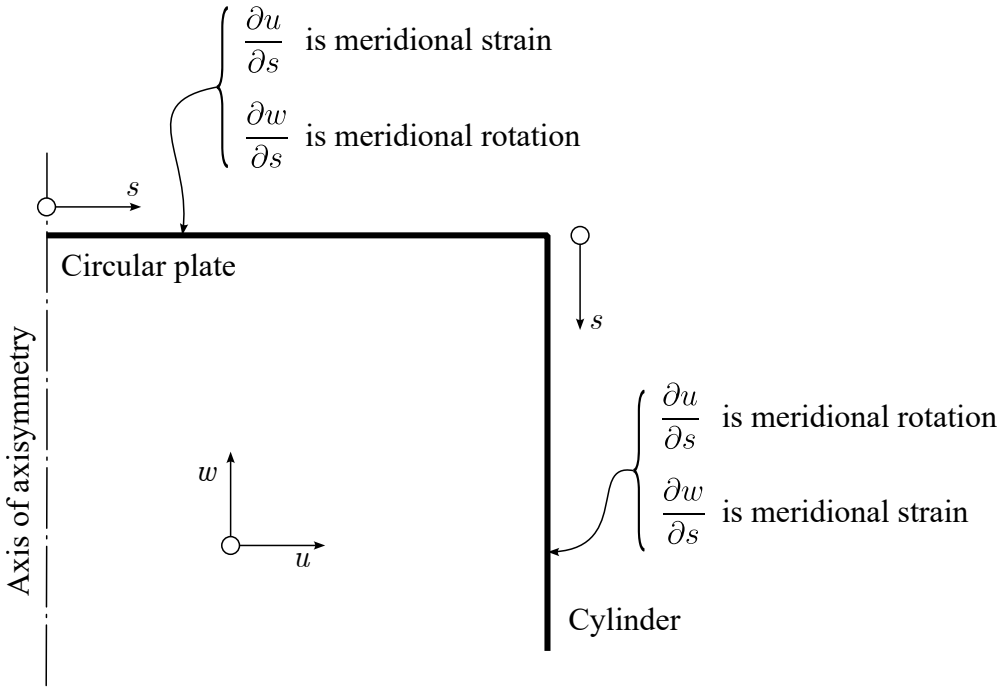


Figure 3.5: Segment intersection with discontinuous meridional curvature

is applied upon. For application in the tangent stiffness matrix, which in the absence of geometric nonlinearities in the analysis is indistinguishable from the element's material stiffness components, the process takes its classic form, presented in the 1st article by J.G. Teng and J.M. Rotter (Teng & Rotter, 1989a) and also most commonly found in matrix structural analysis textbooks. However, when the DOFs need to be condensed out from the geometric stiffness matrix, the steps and formulas need to be applied are considerably more complex, as outlined in Jumikis (1987).

In the case of the tangent stiffness, after the transformation of the nodal variables takes place, the $[K_T]_e$ matrix of the element is partitioned as presented in the following relation, where the remaining DOFs are denoted with a subscript a and the ones to be condensed out (i.e. nodal variables $(dv/ds)_i$ and γ) are denoted with a subscript b:

$$[K_T]_e\{d\delta\} = \begin{bmatrix} K_a & K_{ab} \\ K_{ab}^T & K_b \end{bmatrix} \begin{Bmatrix} d\delta_a \\ d\delta_b \end{Bmatrix} = \begin{Bmatrix} \Phi_a \\ \Phi_b \end{Bmatrix} \tag{3.64}$$

Expanding Eq. (3.64) above yields:

$$d\delta_b = K_b^{-1}[\Phi_b - K_{ab}^T d\delta_a] \tag{3.65}$$

Substituting $d\delta_b$ from Eq. (3.65) into Eq. (3.64) leads to:

$$K_{Tc} d\delta_a = \Phi_c \tag{3.66}$$

where K_{Tc} is the condensed stiffness matrix of the element, given as:

$$K_{Tc} = K_a - K_{ab} K_b^{-1} K_{ab}^T \tag{3.67}$$

and the condensed residual forces vector Φ_c of the element being:

$$\Phi_c = \Phi_a - K_{ab}K_b^{-1}\Phi_b \tag{3.68}$$

After application of Eqs (3.67) and (3.68), the condensed tangent stiffness matrix and residual force vector of the element may be obtained and used in the assembly of the global stiffness matrix and force vector of the axisymmetric shell model, hence the equilibrium equation of Eq. (3.53) for the displacements of the current load increment can now be solved for.

However, in the case of performing bifurcation checks for any competing circumferential modes, the γ and dv/ds DOFs need to be condensed out from both the material (which may or may not include the contribution of nonlinear strains) and the geometric stiffness matrices. As discussed in Jumikis (1987), the geometric (or stability) matrix of an element is in general not positive definite, and the procedure outlined above cannot be applied for its condensation due to the necessary inversion step of the process. Instead, the technique presented in Zienkiewicz & Taylor (2005) - Geradin (1971) is adopted, where the condensation is applied to the equilibrium equation as a whole. Splitting the material and geometric components of the element's stiffness matrix, the equilibrium equation is given as

$$[\bar{K} + K_\sigma]_e\{\delta\} = \{\Phi\} \tag{3.69}$$

where the notation of Teng & Rotter (1989a) for the material and geometric stiffness matrices, instead of Jumikis (1987), is used. The same reordering and partition of the DOFs in the element is performed, as in Eq. (3.64). It is assumed that the condensed out variables δ_a depend on the remaining DOFs δ_b through an auxiliary matrix $[L]$ so that:

$$\{\delta_b\} = [L]\{\delta_a\} \tag{3.70}$$

or

$$\{\delta\} = \begin{bmatrix} I \\ L \end{bmatrix} \{\delta_a\} \tag{3.71}$$

The assumption that the forces applied on the system perform the same amount of work on either the full or condensed system Zienkiewicz & Taylor (2005) is also made:

$$\{\Phi\}^T\{\delta\} = \{\Phi_c\}^T\{\delta_a\} \tag{3.72}$$

Substitution of Eq. (3.71) into Eq. (3.72) leads to:

$$\{\Phi\}^T \begin{bmatrix} I \\ L \end{bmatrix} \{\delta_a\} = \{\Phi_c\}^T\{\delta_a\} \tag{3.73}$$

which leads to the following relation for the condensed vector of nodal forces:

$$\{\Phi_c\} = \begin{bmatrix} I \\ L \end{bmatrix}^T \{\Phi\} \tag{3.74}$$

Substitution of Eqs (3.69) and (3.71) into Eq. (3.74) yields:

$$[K_{Tc}] = \begin{bmatrix} I \\ L \end{bmatrix}^T [\bar{K} + K_\sigma] \begin{bmatrix} I \\ L \end{bmatrix} \tag{3.75}$$

which may be rewritten as:

$$[K_{Tc}] = \begin{bmatrix} I \\ L \end{bmatrix}^T [\bar{K}] \begin{bmatrix} I \\ L \end{bmatrix} + \begin{bmatrix} I \\ L \end{bmatrix}^T [K_\sigma] \begin{bmatrix} I \\ L \end{bmatrix} \tag{3.76}$$

In order to obtain a relation between the condensed DOFs $\{\delta_a\}$ and $\{\delta\}$, it is assumed that the general pattern of deformation will follow that which would be obtained by imposing displacements $\{\delta_a\}$ on an otherwise unloaded structure (Jumikis, 1987), which by taking into account the partitioning of Eq. (3.64) gives:

$$[K_{ab}]^T \delta_a + [K_b]\{\delta_b\} = 0 \tag{3.77}$$

since the eliminated DOFs are unloaded, which in turn leads to:

$$\{\delta_b\} = -[K_b]^{-1}[K_{ab}]^T \delta_a \tag{3.78}$$

A relation for the $[L]$ matrix may now be obtained by comparing the above equation with Eq. (3.70):

$$[L] = -[\bar{K}_b]^{-1}[\bar{K}_{ab}]^T \tag{3.79}$$

Substitution of $[L]$ into the first term of Eq. (3.76) can be used to verify the relation for condensed tangent stiffness matrix of an element of Eq. (3.67). Partitioning the geometric stiffness matrix in the same manner the tangent stiffness was partitioned in Eq. (3.64), its condensed form may be obtained after substituting it and $[L]$ into the second term of Eq. (3.76), yielding:

$$\begin{aligned} [K_{\sigma c}] &= \begin{bmatrix} I \\ -\bar{K}_b^{-1}\bar{K}_{ab}^T \end{bmatrix}^T \begin{bmatrix} K_{\sigma,a} & K_{\sigma,ab}] \\ K_{\sigma,ab}^T & K_{\sigma b} \end{bmatrix} \begin{bmatrix} I \\ -\bar{K}_b^{-1}\bar{K}_{ab}^T \end{bmatrix}^T \\ &= [I - \bar{K}_{ab}^{-1}\bar{K}_b^{-T}] \begin{bmatrix} K_{\sigma,a} - K_{\sigma,ab}\bar{K}_b^{-1}\bar{K}_{ab}^T \\ K_{\sigma,ab}^T - K_{\sigma,b}\bar{K}_b^{-1}\bar{K}_{ab}^T \end{bmatrix} \\ &= K_{\sigma,a} - K_{\sigma,ab}\bar{K}_b^{-1}\bar{K}_{ab}^T - \bar{K}_{ab}\bar{K}_b^{-T}K_{\sigma,ab}^T + \bar{K}_{ab}\bar{K}_b^{-T}K_{\sigma,b}\bar{K}_b^{-1}\bar{K}_{ab}^T \end{aligned} \tag{3.80}$$

As a consequence of the material matrix $\bar{K}$ being symmetric, Eq. (3.80) may be rewritten as:

$$[K_{\sigma c}] = K_{\sigma,a} - K_{\sigma,ab}\bar{K}_b^{-1}\bar{K}_{ab}^T - (K_{\sigma,ab}\bar{K}_b^{-1}\bar{K}_{ab}^T)^T + \bar{K}_{ab}\bar{K}_b^{-1}K_{\sigma,b}\bar{K}_b^{-1}\bar{K}_{ab}^T \tag{3.81}$$

The grouping of the partitioned components in Eq. (3.81) allows for some additional saving in computational effort, in comparison to the form presented in Eq. (3.80), due to the third

term being the transpose of the second one. After condensing out the γ and dv/ds DOFs, the geometric stiffness matrix of the element can now be assembled into the global geometric stiffness matrix to be used for solving the eigenvalue problem for a given circumferential mode n, expressed as:

$$[\bar{K}_c + \lambda K_{\sigma c}]\{\phi\} = \{0\} \tag{3.82}$$

3.5.2 Recovery of nodal variables

Once the equilibrium equation of Eq. (3.66) has been solved for and the nodal variables remaining in the system after condensation have been computed, the full set of element DOFs need to be evaluated in order to determine the linear-nonlinear strain increments according to Eqs (3.13) and (3.14). This process is one of undoing the static condensation and obtaining the nodal variables that were eliminated from the stiffness matrix, which can be done through Eq. (3.65), using the same partitioned components of the tangent stiffness matrix.

It is important to note that at this point the element DOFs vector, just after having worked out the condensed out components, is still under the effect of the transformation of Eq. (3.63). The $(du/ds)_i$ and $(dw/ds)_i$ nodal variables can be found through multiplication with the transpose of the transformation matrix of Eq. (3.63), that is:

$$\begin{Bmatrix} (du/ds)_i \\ (dw/ds)_i \end{Bmatrix} = \begin{bmatrix} -\sin\phi & \cos\phi \\ -\cos\phi & -\sin\phi \end{bmatrix} \begin{Bmatrix} \beta_i \\ \gamma_i \end{Bmatrix} \tag{3.83}$$

As a consequence of the condensation process applied before the solution of the equilibrium equation, the derivatives of the displacements du/ds, dv/ds and dw/ds are discontinuous between elements meeting at a common node, as highlighted in Teng & Rotter (1989a). This results to 12 DOFs being necessary to define the deformed state of the shell rather than 6 per node. In turn, this may lead to discontinuities of the strain-stress fields across different elements of the shell's meridian.

In the case of bifurcation checks however there is no need to recover the nodal variables that were condensed out from the stiffness matrices, since the chief goal of the analysis is one of obtaining a number of eigenvalues for a competing circumferential mode n and there are no strains-stresses to be determined after a solution is obtained.

3.6 Software capabilities

AQUINAS has been designed to be a versatile and efficient Finite Element Analysis tool for solving linear or nonlinear axisymmetric shell problems. Having the productivity of its users in mind, it provides an array of tools for the generation of an axisymmetric shell problem, all of which can be accessed and programmed through a single MATLAB script. From different ways to define the meridional geometry of a shell segment to the optimisation procedures applied for identifying the critical circumferential mode n, it all starts with the generation of an AQUINAS object. In the following paragraphs, the capabilities of the software will be outlined with some hints and tips provided on the internal processes of AQUINAS.

3.6.1 Geometric definitions

Definition of an axisymmetric shell element in AQUINAS requires that the first and second derivatives of geometrical components be known at the nodes along the meridian of a segment, as can be appreciated from the FE formulation of Teng & Rotter (1989a). In order to reduce the analyst's effort for the computational modelling of a shell problem, these derivatives can be automatically evaluated at nodal positions for reference meridional geometries and their combinations.

An important point for all of the following geometric definitions is that the condition of axisymmetry of a shell problem the should not be violated under any circumstances, for nodes existing in the negative plane of radial coordinates. Failing to do so will result in an error in the construction of the segment object and the analysis will not proceed.

3.6.1.1 Plate segment geometry

One of the most basic types of axisymmetric shell geometry is that of a circular plate, with or without an opening at its centre. The definition of one is simple with the `'Plate'` option of a segment object (see the following chapter for available options of an `AQUINAS_Segment_Object`). Only the radial r and axial z coordinates of the plate's ends are required to fully define a segment, illustrated in Figure 3.6, while the derivatives of the meridional geometric components necessary for the formulation are given in Eq (3.84) below, to be computed at the nodal positions. It is important, for the optimal behaviour of the solver, for the *'top'* end of the plate segment to be the one closest to the axis of revolution.

$$\left(\frac{\partial r}{\partial z}\right)_i = \infty \tag{3.84a}$$

$$\left(\frac{\partial^2 r}{\partial z^2}\right)_i = 0 \tag{3.84b}$$

$$\left(\frac{\partial^3 r}{\partial z^3}\right)_i = 0 \tag{3.84c}$$

$$\left(\frac{\partial r}{\partial s}\right)_i = 1 \text{ if } r_{bot} > r_{top},\ -1 \text{ if } r_{bot} < r_{top} \tag{3.84d}$$

$$\left(\frac{\partial z}{\partial s}\right)_i = 0 \tag{3.84e}$$

$$\phi_i = 0 \tag{3.84f}$$

$$\left(\frac{\partial \phi}{\partial s}\right)_i = 0 \tag{3.84g}$$

$$\left(\frac{\partial^2 \phi}{\partial s^2}\right)_i = 0 \tag{3.84h}$$

3.6.1.2 Conical segment geometry

Perhaps the most encountered types of axisymmetric shell in real-life civil engineering applications, cylinders and cones can be easily and accurately defined with the aid of the `'Cone'` option of the segment object in AQUINAS. Due to the straight meridian of conical segments, as was the case with the plate segment earlier, the coordinates of just the two end points are

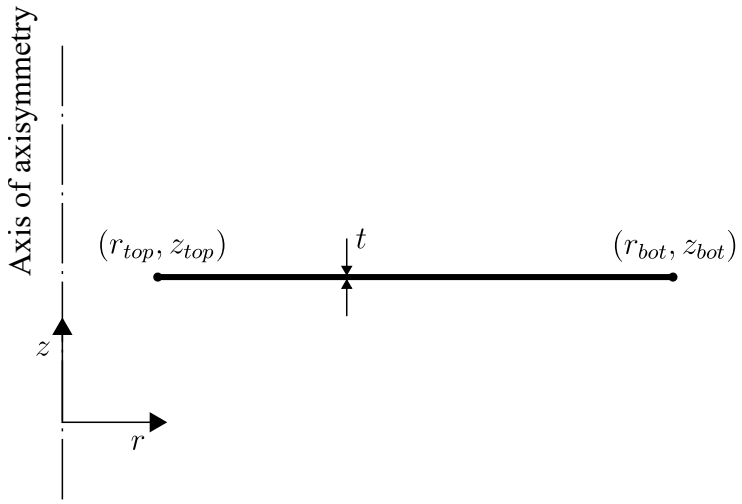


Figure 3.6: Meridional geometry definition of a plate segment.

sufficient for modelling of an axisymmetric cone problem as illustrated in Figure 3.7. Cylinders can be regarded as a special case of conical segments, where the radial coordinates of its top and bottom edges are equal i.e. $r_{top} = r_{bot}$.

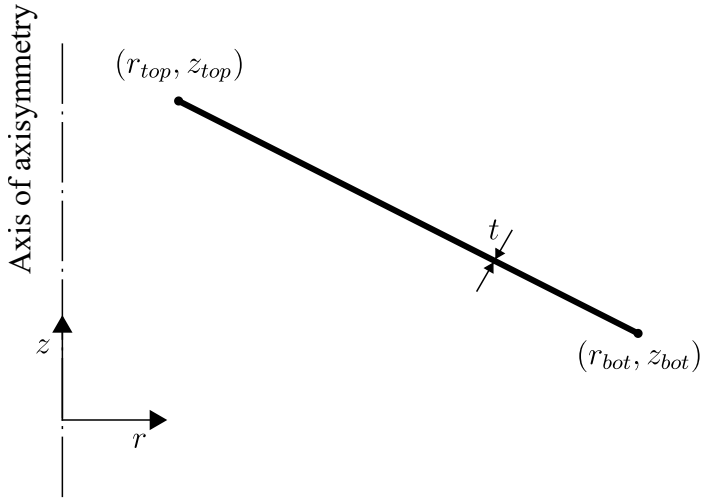


Figure 3.7: Meridional geometry definition of a conical segment.

The relationships that govern the geometric definition of a cone shell element, as coded in `AQUINAS_Segment_Object`, are given in Eq (3.85) below:

$$\left(\frac{\partial r}{\partial z}\right)_i = \frac{r_{bot} - r_{top}}{z_{bot} - z_{top}} \tag{3.85a}$$

$$\left(\frac{\partial^2 r}{\partial z^2}\right)_i = 0 \tag{3.85b}$$

$$\left(\frac{\partial^3 r}{\partial z^3}\right)_i = 0 \tag{3.85c}$$

$$\left(\frac{\partial r}{\partial s}\right)_i = 1 \text{ if } \left(\frac{\partial r}{\partial z}\right)_i \equiv \infty, \ \frac{-\left(\frac{\partial r}{\partial z}\right)_i}{\sqrt{1 + \left(\frac{\partial r}{\partial z}\right)_i^2}} \text{ otherwise} \tag{3.85d}$$

$$\left(\frac{\partial z}{\partial s}\right)_i = 0 \text{ if } \left(\frac{\partial r}{\partial z}\right)_i \equiv \infty, \frac{-1}{\sqrt{1+\left(\frac{\partial r}{\partial z}\right)_i^2}} \text{ otherwise} \tag{3.85e}$$

$$\phi_i = \frac{\pi}{2} - \tan^{-1}\left(-\left(\frac{\partial r}{\partial z}\right)_i\right) \tag{3.85f}$$

$$\left(\frac{\partial \phi}{\partial s}\right)_i = 0 \tag{3.85g}$$

$$\left(\frac{\partial^2 \phi}{\partial s^2}\right)_i = 0 \tag{3.85h}$$

3.6.1.3 Elliptical segment geometry

Not as common as cylindrical or conical shell segments, but still widely used owning to the efficient load bearing behaviour of their doubly curved surfaces or natural architectural beauty, spherical shells and ellipsoids are a fundamental form of axisymmetric shell structures that could not be missing from AQUINAS. The governing equation for the meridional geometry of an elliptical segment is provided in Eq. (3.86), where the reader may appreciate that the current software supports ellipses without the need for their centre to be on the origin of the radial/axial axes, but it does not currently support a rotated ellipse in the 2D modelling space. The governing equation is

$$\frac{(r-r_C)^2}{\rho_r^2} + \frac{(z-z_C)^2}{\rho_z} = 1 \tag{3.86}$$

where r_C and z_C are the coordinates of the centre of the elliptical segment, while $2\rho_r$ and $2\rho_z$ are the length and width of the full ellipse (even if the entire ellipse is not modelled). Spherical segments, which can be either fully closed spheres or truncated spherical caps, may be generated by setting the major and minor axes of the ellipse to be of equal length for $\rho_r = \rho_z$. The meridional geometric definition of an elliptical segment in AQUINAS is given in the following Figure 3.8. The radial and axial coordinates of the top (r_{top}, z_{top}) and bottom (r_{bot}, z_{bot}) edges of the shell segment can aid in defining truncated spherical or elliptical segments.

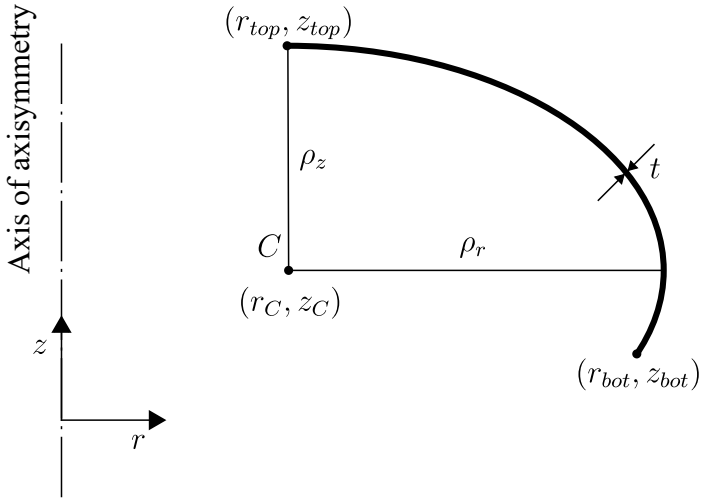


Figure 3.8: Meridional geometry definition of an elliptical segment.

The reader should be advised that meridional regions from both sides of an apex of an elliptical segment should not be modelled into the same object. Instead, two segments should be used,

meeting at a common node at the apex, each modelling a portion of the shell that has a meridional curvature of opposite sign (as measured from the axis of revolution). This is done for purely logistical reasons of AQUINAS' inner proceedings so that the same elliptical segment class can capture the behaviour of axisymmetric shells for both positive and negative Gaussian curvature, introduced in the following Eqs. 3.87 for the geometric components through the sign of the meridional curvature parameter κ_m.

The equations that fully describe the geometric components of a sphere or an ellipse are presented in Eqs (3.87), which have been derived having Eq. (3.86) as a starting point.

$$\left(\frac{\partial r}{\partial z}\right)_i = \kappa_m \frac{\rho_r}{\rho_z} \frac{z_C - z_i}{\sqrt{(z_C + \rho_z - z_i)(z_C - \rho_z + z_i)}} \tag{3.87a}$$

$$\left(\frac{\partial^2 r}{\partial z^2}\right)_i = -\kappa_m \frac{\rho_r \rho_z}{\sqrt{(z_C + \rho_z - z_i)(z_C - \rho_z + z_i)}^3} \tag{3.87b}$$

$$\left(\frac{\partial^3 r}{\partial z^3}\right)_i = -3\kappa_m \frac{\rho_r \rho_z (z_C - z_i)}{\sqrt{(z_C + \rho_z - z_i)(z_C - \rho_z + z_i)}^5} \tag{3.87c}$$

$$\left(\frac{\partial r}{\partial s}\right)_i = \begin{cases} 1 & \text{if } \left(\frac{\partial r}{\partial z}\right)_i \equiv \infty \\ -\frac{\left(\frac{\partial r}{\partial z}\right)_i}{\sqrt{1+\left(\frac{\partial r}{\partial z}\right)_i^2}} & \text{otherwise} \end{cases} \tag{3.87d}$$

$$\left(\frac{\partial z}{\partial s}\right)_i = \begin{cases} 0 & \text{if } \left(\frac{\partial r}{\partial z}\right)_i \equiv \infty \\ -\frac{1}{\sqrt{1+\left(\frac{\partial r}{\partial z}\right)_i^2}} & \text{otherwise} \end{cases} \tag{3.87e}$$

$$\phi_i = \frac{\pi}{2} - \tan^{-1}\left(-\left(\frac{\partial r}{\partial z}\right)_i\right) \tag{3.87f}$$

$$\left(\frac{\partial \phi}{\partial s}\right)_i = \begin{cases} \kappa_m \frac{\rho_z}{\rho_r^2} & \text{if } \left(\frac{\partial r}{\partial z}\right)_i \equiv \infty \\ \frac{\left(\frac{\partial z}{\partial s}\right)_i \left(\frac{\partial^2 r}{\partial z^2}\right)_i}{1+\left(\frac{\partial r}{\partial z}\right)_i^2} & \text{otherwise} \end{cases} \tag{3.87g}$$

$$\left(\frac{\partial^2 \phi}{\partial s^2}\right)_i = \begin{cases} 0 & \text{if } \left(\frac{\partial r}{\partial z}\right)_i \equiv \infty \\ -\left(\frac{\partial z}{\partial s}\right)_i \left(\frac{\left(\frac{\partial^3 r}{\partial z^3}\right)_i}{\sqrt{1+\left(\frac{\partial r}{\partial z}\right)_i^2}^3} - 3\left(\frac{\partial r}{\partial z}\right)_i \frac{\left(\frac{\partial^2 r}{\partial z^2}\right)_i^2}{\sqrt{1+\left(\frac{\partial r}{\partial z}\right)_i^2}^5} \right) & \text{otherwise} \end{cases} \tag{3.87h}$$

3.6.1.4 Three-point arc segment geometry

While spherical shells can be generated with the `'Ellipse'` options of the segment object, in some cases it is more convenient to generate their curved meridians as a circular arc passing through three non-collinear points. This can be achieved in AQUINAS using the `'3pointArc'` option, defined in conjunction with an additional input field for the radial and axial coordinates of the third point that the arc will pass through. This option can be very handy when it comes to scripting an axisymmetric shell problem quickly, without the need of evaluating the centre and radius of an arc, for which the analyst does know at least one additional point along with the top and bottom edges. There is no requirement that the third point defining the arc should be set midway along the meridian between the other two, but it does need to be at an axial coordinate lower than that of the top edge but higher than the bottom one. Once the segment

has been constructed, and the centre and radius of the implied circle on the 2D space of the meridian have been computed, the segment will be turned into an `'Ellipse'`, and be treated as such thereafter, using the derivatives of Eqs (3.87) for the formulation of the element's geometry.

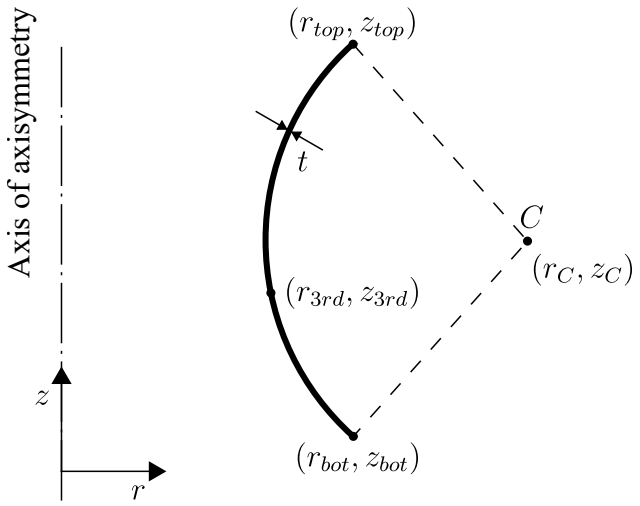


Figure 3.9: Meridional geometry definition of a circular arc segment defined through three points.

3.6.1.5 Interpolated segment geometry

An option encompassing all of the previous ones, as well as cases of more arbitrary meridians that cannot be categorised into any of the previously presented families of geometries, is that of a segment defined through an 'Akima interpolation' of a series of points. The `'Interp'` option will initiate the generation of such a segment that has to go through all of the provided point coordinates, fitting a piecewise polynomial of up to third order (cubic). The procedure applied is considerably different compared to that of the cubic spline, as it allows for a quick regression into a linear portion of the fitted line, without the oscillations in the neighbourhood near this transition that the spline algorithm is usually associated with. The mathematics of the Akima interpolation have been meticulously presented in *A New Method of Interpolation and Smooth Curve Fitting Based on Local Procedures* by Akima (1970), the formulation of which has been adopted here. It is important to note that the interpolation algorithm coded here has some minor differences compared to the modified Akima interpolation included with MATLAB's distribution (which could not be used as there are special cases that have to be handled here). The interpolated geometry of a segment is illustrated in Figure 3.10 below.

While the locations of the points provided for the generation of an interpolation does not have to coincide with the nodal ones, it should be done so whenever possible, to utilise the best performance attainable by the Akima interpolation algorithm implemented. It is important for the first node in the series to be the topmost one and the last one to be at the bottom. If this does not hold in the point series provided, it will be reversed internally with a warning message displayed to the command window to alert the user.

The interpolation results in a function of the radial coordinate r with respect to the axial coordinate z. This leads to a straightforward computation of all derivatives of r with respect to z. The remaining geometric derivatives may then be computed using the relationships of Eq. (3.87) for derivatives with respect to the arc coordinate S.

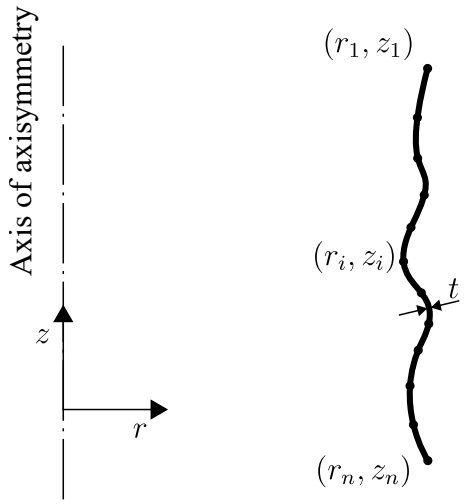


Figure 3.10: Meridional geometry definition of an interpolated segment, defined through a series of points.

3.6.2 Analysis types

The AQUINAS toolbox is presently capable of carrying out the following computational structural analyses as defined by EN 1993-1-6 (2025) on the strength and stability of metal shells, interpreted from the formal definitions of Section 1.2.2 into the fully computational context of the software as follows:

- LA: Linear elastic analysis to obtain the complete primary (membrane) and secondary (bending) stress state
- LBA: Linear bifurcation analysis to obtain the critical and near-critical bifurcation buckling eigenvalues and associated eigenmodes
- MNA: Materially nonlinear analysis to obtain the small-displacement plastic collapse mechanism
- GNA: Geometrically nonlinear elastic analysis to obtain the deformation and stress state assuming large deflections, and to detect axisymmetric limit point and / or potentially non-symmetric bifurcation buckling
- GMNA: Geometrically and materially nonlinear analysis which extends a GNA to include plasticity
- GNIA: Geometrically nonlinear elastic analysis which extends a GNA to include imperfections (primarily unintended geometric deviations of the shell midsurface)
- GMNIA: Geometrically and materially nonlinear analysis which extends a GMNA to include imperfections

By convention, LAs, LBAs, MNAs, GNAs and GMNAs are performed on a reference shell geometry defined by a 'perfect' midsurface assuming no imperfections of any kind, although a number of recent research works have undertaken 'LBIAs' (Sadowski *et al.*, 2018) and 'MNIAs' (Wang *et al.*, 2020) under special circumstances. All (G)(M)N(I)As are implemented in AQUINAS as incremental path-tracing analyses using the arc-length algorithm. Every bifurcation buckling check assumes an axisymmetric pre-buckling stress state.

3.6.3 Optimisation

The buckling strength of an axisymmetric shell may be identified as a function $F(n)$ of the circumferential full wave-number n associated with its bifurcation. Further capitalising on the capability of AQUINAS to explicitly obtain the buckling load for any mode n, a minimisation approach on $F(n)$ for the computation of the critical buckling resistance and circumferential mode can be established. This minimisation has to be performed in a computational manner, aiming at reducing the exhaustive evaluation of bifurcation loads corresponding to all competing harmonics for a specific shell problem.

The Surrogate Model Optimisation (SMO) algorithm has been employed in AQUINAS in order to perform this minimisation. While this is a machine learning algorithm that is included in the MATLAB (2022) Global Optimization Toolbox, the algorithm has been independently coded in AQUINAS, found in `AQUINAS_SO.m`, not only to reduce the number of dependencies for execution of the solver (since MATLAB toolboxes are not included in its basic distribution), but also in order to have full control over the parameters of the optimisation process.

A brief outline of the surrogate optimisation algorithm, as well as all of the parameters that govern its behaviour, is presented here. This section should not be viewed as a presentation of the surrogate optimisation process itself, but rather a description of the algorithm in the context of computing the critical bifurcation load and associated harmonic n in an efficient, less time consuming manner. The principles of *Engineering Design via Surrogate Modelling* by Sóbester *et al.* (2008), are adopted in the current implementation of the surrogate optimisation algorithm. The surrogate model is obtained through a Gaussian process regression scheme, as is the most popular case for such models, with a Radial Basis Function kernel being used for obtaining the covariance of the Gaussian process.

The chief concept of the surrogate modelling approach to the optimisation of an unknown function, in this case that of the bifurcation load with respect to the harmonic number n, is the application of the minimisation procedure on a substitute 'surrogate' function that approximates the original over a range of n values. This model can be obtained through computing the value of the $F(n)$ function for a few circumferential modes n and then fitting the approximate surrogate model on them through a Gaussian process. This stage can be thought of as the training of the surrogate model, with the bifurcation load acting as the dependent variable y and its associated harmonic n acting as the independent one x of the training range.

Training of the surrogate model is performed by computing one more bifurcation load for a circumferential mode n that the model is not already trained on. Deciding which harmonic should be used to enhance the surrogate model is done on the basis of an Expected Improvement (EI) function, as presented in Sóbester *et al.* (2008), that aims on maximising the accuracy of the prediction on the global minimum of the original function. The amount of improvement expected is evaluated based on the mean $\hat{y}(x)$ and variance $\hat{s}^2(x)$ of the surrogate model, given as:

$$E[I(x)] = (y_{min} - \hat{y}(x))\Phi\left(\frac{y_{min} - \hat{y}(x)}{\hat{s}(x)}\right) + \hat{s}\phi\left(\frac{y_{min} - \hat{y}(x)}{\hat{s}(x)}\right) \tag{3.88}$$

where $\Phi()$ is the cumulative distribution function and $\phi()$ is the probability density function.

The harmonic n corresponding to the maximum value of the EI function will be used as the new training data point in order to update the surrogate model. Once the maximum Expected Improvement is below some threshold tolerance, the surrogate optimisation has converged into a reasonable approximation of the original function. The minimum of the surrogate model

constitutes a prediction for the critical bifurcation load of the axisymmetric shell model. The surrogate optimisation algorithm may also be terminated by exhausting a number of iterations without achieving convergence of the surrogate model, in which case the already computed data will be used for an estimation of the critical bifurcation load.

In its most basic form, the lower and upper bounds of the training range for the surrogate models are kept constant throughout the optimisation process. This is not the case for the current implementation of the algorithm, as it may not be apparent how high of a circumferential wave-number n should be considered as competing for the bifurcation of thin axisymmetric shells. A way to deal with this issue could potentially be to consider an extremely high harmonic as the upper bound of the range. Such an approach has the major drawback of spending considerable computational time for training of the model over an extensive range of harmonics. Instead, the option is provided for a harmonic to be used as an initial upper bound, only to be updated if the surrogate model expects improvement toward the higher end of its training range. A step for expanding the upper bound of the range of competing harmonics will be used in such a case, the value of which can be set by the analyst before submission of an analysis.

It is not uncommon in Gaussian processes, when used in the context of machine learning algorithms, to have their hyper-parameters optimised as the surrogate model develops, so that the best possible approximation to the original function can be achieved. This technique is also applied here, with the optimisation of the hyper-parameters performed through a maximising process of the log marginal likelihood function, as per the algorithmic procedures presented in *Gaussian Processes for Machine Learning* by Williams & Rasmussen (2006). It is important to note that the step of hyper-parameter optimisation is an optional one in the overall course of the surrogate model training, and the hyper-parameters may be kept constant at their initial values, before entering the surrogate optimisation loop.

Once the surrogate model has been trained for the current loop of the optimisation process, and the non-compulsory operations of updating the upper bound of the training range or optimising the hyper-parameters have either been carried out or skipped, it is time to update the surrogate function itself, through a Gaussian Process Regression scheme, in preparation of the next iteration in the optimisation process. A Radial Basis Function (RBF) constitutes the most basic, but also popular, choice of a kernel for the Gaussian process for computing the covariance between points. The kernel will in turn help in the approximation of the 'true' function form between trained data points. For a more in depth presentation of the underlying mathematics of Gaussian processes, the interested reader is encouraged to examine the formulations of Williams & Rasmussen (2006) as a valuable and well established resource for such methods.

A practical example of the surrogate optimisation process in the context of computing the critical bifurcation load of an axisymmetric shell is illustrated in the following Figures 3.11 - 3.16. As showcased, there are two ways to approach the problem of evaluation of the linear bifurcation strength for a cylindrical shell under axial compression, a problem that will be further investigated in Appendix A while studying the results of `input_Example_LBA01.m`. The first, and rather laborious one, is the extensive computation of the eigenvalues (corresponding the bifurcation LPF for LBA problems) for all competing harmonics n. This approach gets increasingly expensive in computational time as the cylinders increase in slenderness. For a cylinder with an r/t ratio of 2000, the competing circumferential modes may go all the way up to a harmonic n of 61.

The alternative of using a surrogate model to perform the minimisation has considerable advantages, as only a fraction of the modes need to be actually processed through the FE solver of AQUINAS. Starting with an initial number of 8 data points to generate the surrogate model, the optimisation process is applied, gradually obtaining a better approximation of the true

eigenvalue distribution in the neighbourhood of its global minima. The 95% confidence intervals are also plotted, showing the 'confidence' of the Gaussian process's estimation. These intervals get closer to the mean distribution of the prediction, as more steps are taken in the optimisation process and the model is trained. Only a mere 13 modes are actually computed (with the axisymmetric one evaluated after convergence of the model), leading to a 78.7 % percent saving in FEA computational time.

This case also serves as a warning statement of the limitations of this machine learning algorithm. Even though the actual global minima is located, a second convex region exists for 'low' circumferential mode numbers, which is completely missed during the optimisation process. While this is of no severe consequence for the current investigation, the results of the Surrogate Model Optimisation process are not to be trusted blindly and a 'sanity check' should be performed at the end of the procedure, simply by plotting the distribution of computed buckling loads with respect to their circumferential harmonics n and checking for under-examined convex regions where a potential global minima could exist.

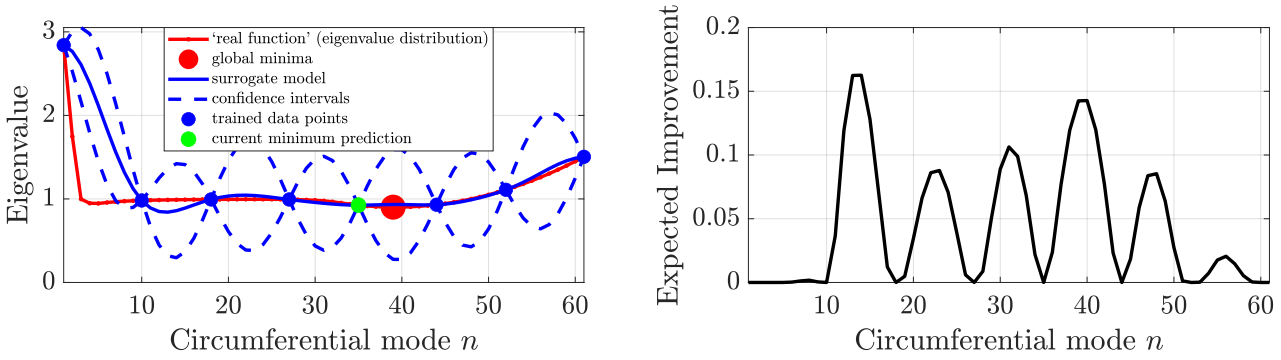


Figure 3.11: Initial training of surrogate model.

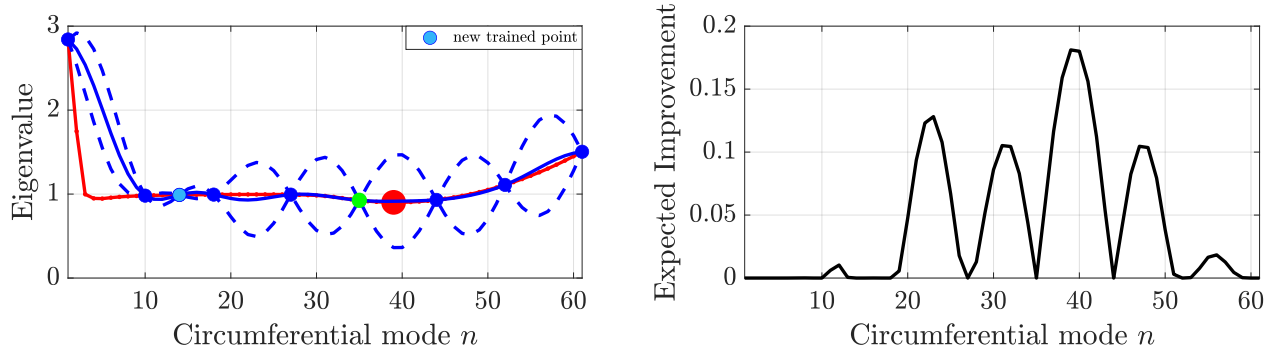


Figure 3.12: First training step in the surrogate optimisation process.

The flow of control for the surrogate optimisation algorithm, as coded in the `AQUINAS_SO.m` script, is presented in Figure 3.17, where the steps with a dashed line correspond to optional actions, that may or may not be undertaken in the process of training the surrogate model.

3.7 Software architecture

Submitting a linear or nonlinear analysis with AQUINAS is facilitated with MATLAB's object oriented programming capabilities. An understanding of the way to define different AQUINAS objects, as well as the purpose they serve in any type of analysis, is important to the successful solution of an axisymmetric shell problem. The name-value pairs, either necessary or optional,

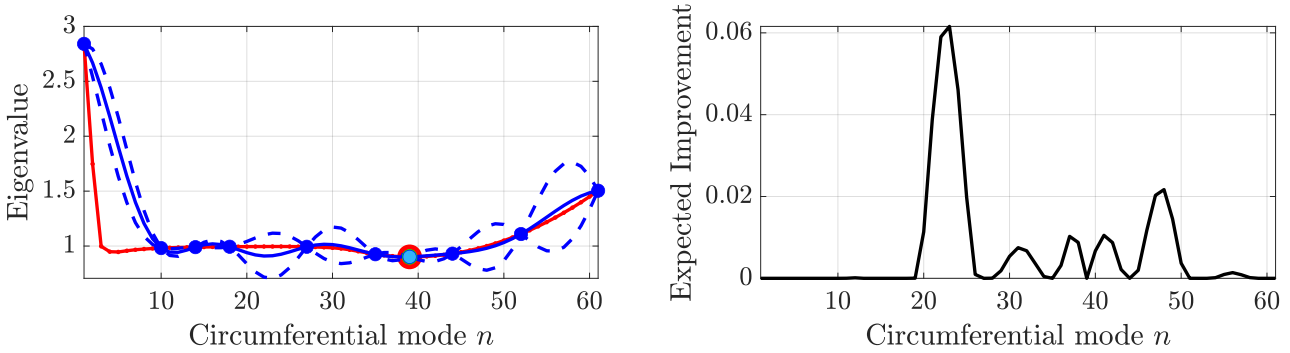


Figure 3.13: Second training step in the surrogate optimisation process.

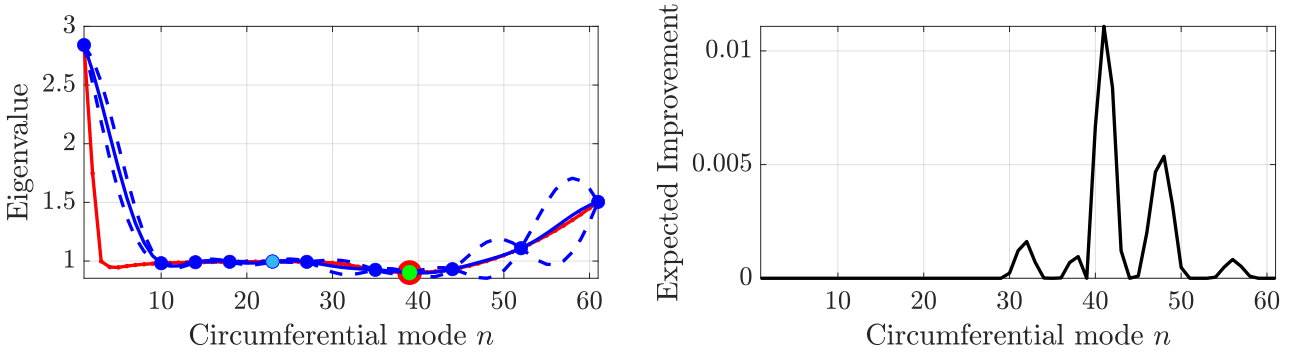


Figure 3.14: Third training step in the surrogate optimisation process.

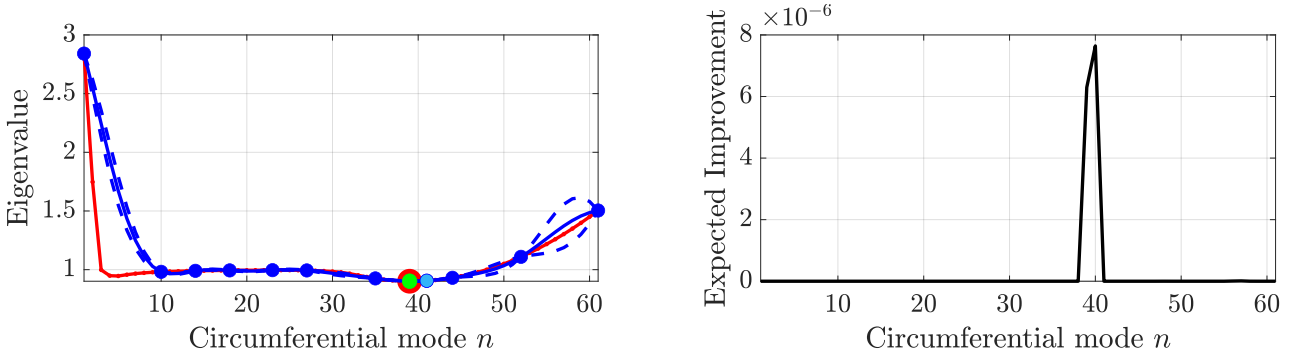


Figure 3.15: Fourth training step in the surrogate optimisation process.

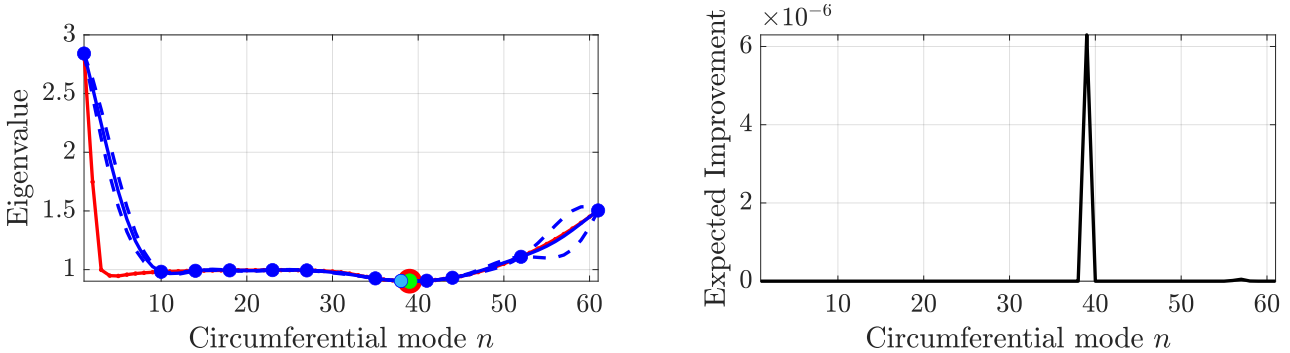


Figure 3.16: Fifth (and final) training step in the surrogate optimisation process.

for the generation of any object will be presented one by one with useful tips provided on the appropriate values that may be assigned to each.

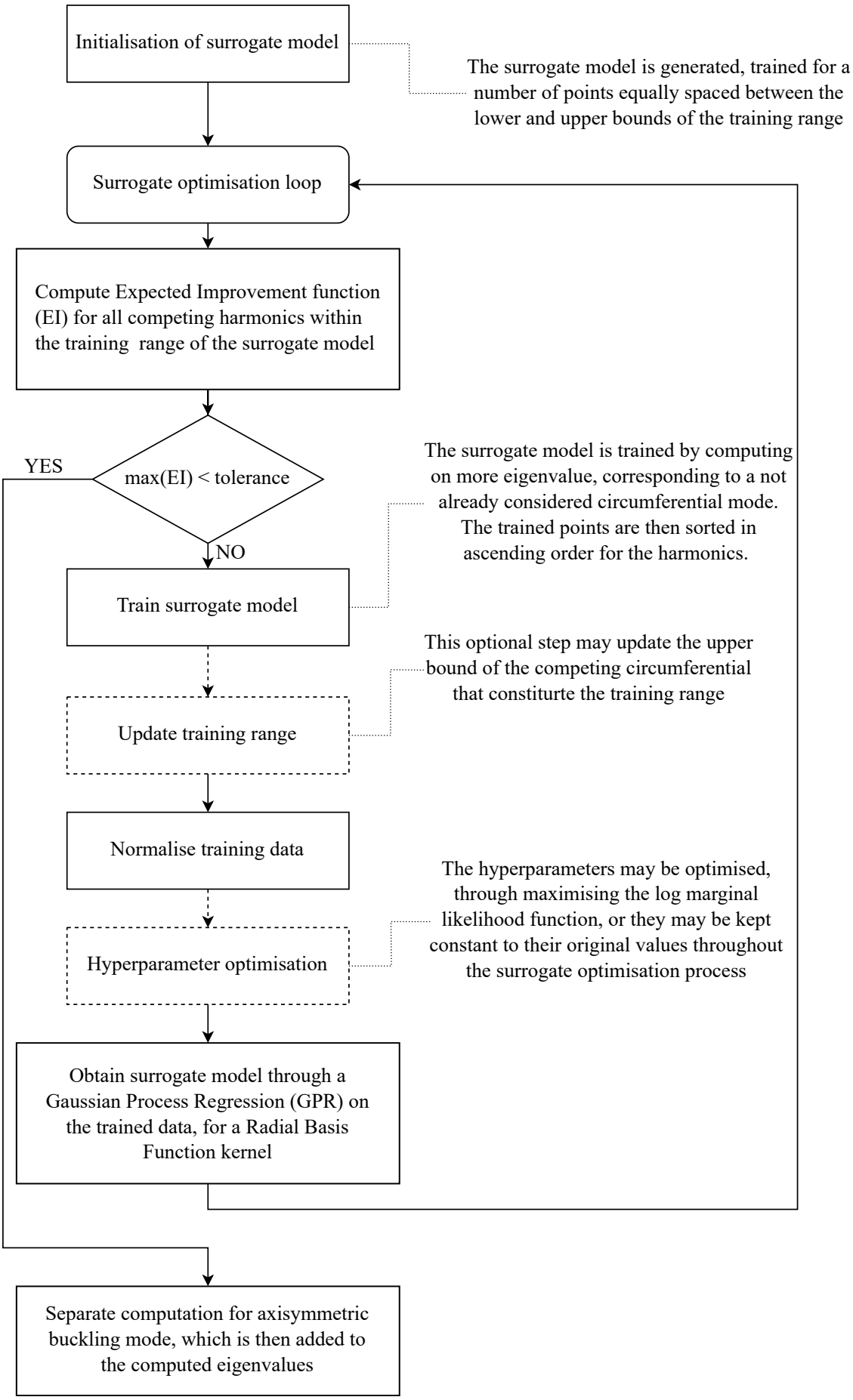


Figure 3.17: AQUINAS Surrogate Optimisation flowchart.

3.7.1 Flow of control in AQUINAS

Before going into the individual study of the available AQUINAS objects, the general software architecture will be briefly presented so that the reader may familiarise themselves with its internal proceedings and stages of an analysis. Flow of control within AQUINAS is outlined in Figure 3.18, where some distinct levels in the solution process may be identified. The user instantiates a suite of objects representing the geometry, loads, constraints, materials, solver settings and output requests, and submits these as a `varargin` (variable-length argument list) to the `AQUINAS_Protocol.m` function which acts as a central control pipeline through the software. A series of error checks are then performed in the master script `AQUINAS_Protocol` to ensure their combination actually defines an axisymmetric shell problem. The reader is cautioned that these error checks do not exhaust all possible cases of ill-defined objects or axisymmetric shell problems and the actual understanding of the objects, in the context of different analysis types, is valuable.

Having confirmed the appropriate definition of the necessary components for an analysis to be submitted, control is passed to the relevant script. Adopting the terminology of EN 1993-1-6 (2025), the different analysis scripts are `AQUINAS_LA.m`, `AQUINAS_LBA.m` and `AQUINAS_GMNA.m`. Geometric and material nonlinearities are taken into account in the same piece of code responsible for all nonlinear incremental types of analysis. While an interaction between `AQUINAS_GMNA.m` and `AQUINAS_LBA.m` may appear suspicious at first sight, the reader is reassured that this is just the name of the script and the current stress state of the shell is considered in the bifurcation checks performed on the last converged increment of a nonlinear analysis. `AQUINAS_SO.m` acts as a wrapper to either linear or nonlinear bifurcation checks with `AQUINAS_LBA.m` during a surrogate optimisation process (see Section 3.6.3).

The results of any analysis are then either organised in a structured output for the analyst to perform any post-processing and plotting in their master input scripts, or written into an ASCII text type of file to be processed at a later stage. This last capability is not entirely functional and currently under development (hence the dashed lines at the output level of Fig. 3.18), to be made available in a later release of AQUINAS.

3.7.2 Class descriptions

AQUINAS takes advantage of MATLAB's object oriented programming capabilities, using several different classes of objects for the analysis of an axisymmetric shell problem. Their assembly and organisation through `AQUINAS_Protocol` formulates a computationally defined shell model, to be processed by the appropriate AQUINAS script for the generation of the FE solution.

For all AQUINAS objects, the inputs parameters provided for their creation should be in name-value pairs. This allows for quickly testing the inputs, for both their type and value, using MATLAB's intrinsic argument validation tools. Any checks that cannot be handled through the argument validation functions are executed inside the constructor of each object, in case the potential issue corresponds to incompatible, missing or ill-defined name-value pairs for a single object definition, or in `AQUINAS_Protocol` if the error relates to incompatibilities between different AQUINAS objects for a given type of analysis. Failing any of these checks will lead to an error message and termination of execution. Warnings may also be generated in scenarios where the user needs to be alerted for model inconsistencies or numerical ill-behaviour during analysis execution.

The purpose that each AQUINAS class serves for every different type of analysis will be briefly outlined in the following paragraphs, with reference to some of the key, either mandatory or

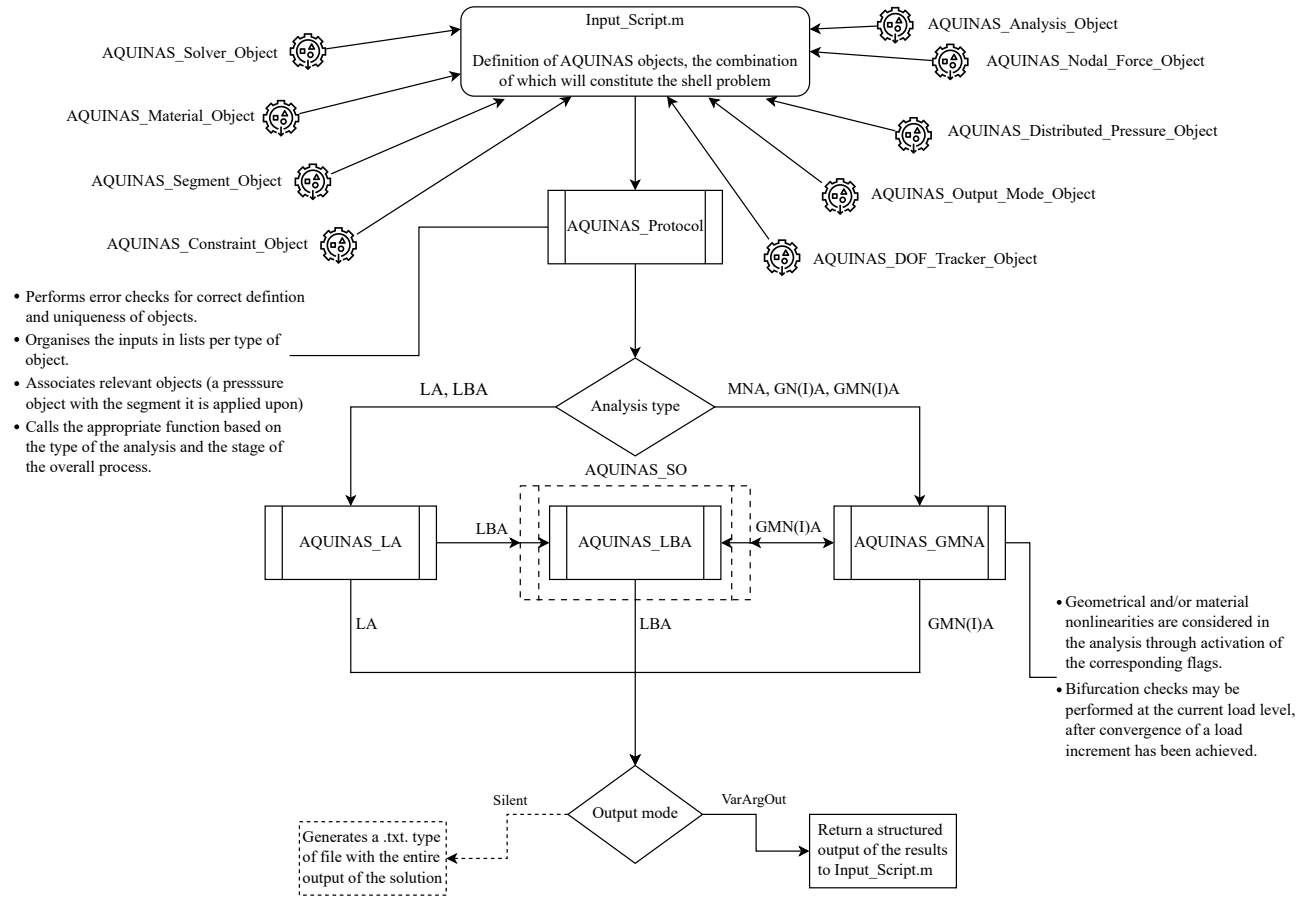


Figure 3.18: AQUINAS general flow of control diagram

optional, name-value pairs for object definition. Further information of considerably higher detail for every available name-value pair can be found in the publicly accessible AQUINAS-FE repository (Filippidis & Sadowski, 2023b), with explicit discussion on the values that each may take and defaults that will be assigned if definition is omitted.

AQUINAS Material Object

The `AQUINAS_Material_Object` is essential for defining an AQUINAS axisymmetric shell problem and an error message is inevitable if none is found. On top of the basic isotropic elastic parameters such as the Poisson ratio ν, Young's modulus E and shear modulus G, a complete stress-strain curve can be provided for the estimation of plastic characteristics of the material such as the yield stress and hardening parameters, allowing the same class definition to be utilised for both materially linear (elastic) or nonlinear (elastic-plastic) analyses. The input vectors σ_y and ϵ_p for the definition of the stress-strain curve can be either directly defined as 'True' or 'Cauchy' stresses and strains (discussed in Chapter 4.6 of (Crisfield, 1991)) or defined in engineering format and transformed within the constructor of the material object into their equivalent true format, according to the following relationships:

$$\sigma_{y,T} = \sigma_{y,E}(1 + \epsilon_{p,E})\epsilon_{p,T} = \ln(1 + \epsilon_{p,E}) \tag{3.89}$$

AQUINAS Segment Object

The 5 different types of axisymmetric shell segment definitions presented earlier in Section 3.6.1 can be modelled through the `AQUINAS_Segment_Object`, with different name-value pairs being relevant depending on the actual type of the segment. For the purposes of an axisymmetric shell problem modelling, geometric definition takes place in the 2D sub-space of positive radial

coordinates. The constructor of the object will potentially address base-level processing of the inputs, such as transformation of a `'3pointArc'` into an `'Ellipse'` segment, prior to communication with the rest of the software through `AQUINAS_Protocol`. Meridional discretisation is additionally controlled by assigning a total number of elements to be used for each `AQUINAS_Segment_Object`, with the option to define a graded mesh towards either or both edges of the meridian. The existence of at least one segment object is necessary for an analysis to be executed.

AQUINAS Nodal Force Object
For axisymmetric shells, computationally modelled in the 2D space with the necessary kinematic assumptions along their circumference, a nodal force corresponds to a line load evenly distributed in the circumferential direction. Defining such a force in AQUINAS is done by using the `AQUINAS_Nodal_Force_Object`, with minimal inputs required. For software architecture purposes, a nodal force may only be applied at the edge of a segment object. Therefore, the coordinates of the point where the force is applied must coincide with those of the edge of at least one segment object included in the analysis submission. In case this does not hold, an error will occur. In AQUINAS, the magnitude of the force object should be equal to that of the corresponding line load ([F/L] units), instead of the total force resultant ([F] units) that ABAQUS (2022) users may be familiar with. Any necessary scaling based on the radial position that the load is applied to will be taken care by AQUINAS internally. It should also be noted that the magnitude is a signed algebraic value and should be negative if the applied force does not share the same direction as the global $r - z$ axes. The definition of this object is optional, since a shell problem can be generated without a line load applied anywhere on the FE model.

AQUINAS Distributed Pressure Object
On top of using a nodal force object to define the loading conditions of the axisymmetric shell problem, the analyst has the option to define a distributed pressure along the meridian. The `AQUINAS_Distributed_Pressure_Object` may be used for defining a normal or tangential pressure (traction) in the meridional direction. The pressure is assumed to be uniform along the circumference of the shell, but may have any distribution along the meridian, provided that it can be defined through a function handle with respect to either the radial r, axial z or angular ϕ coordinate of the meridian.

AQUINAS Constraint Object
Boundary conditions and shell segment interactions alike are being handled by the constraint object in AQUINAS. The `AQUINAS_Constraint_Object` is responsible for generating appropriate Lagrange multiplier terms that will enrich the global stiffness matrix of the system to account for any kind of edge restraints, eccentrical connections between segments or ensuring connectivity of segments that share an edge point. If the constraint object corresponds to an eccentrical connection between segments, then the magnitude of said eccentricity will be computed on the fly by AQUINAS as the distance between the associated ends of the connected segments. Implementing boundary conditions with the method of Lagrange multipliers also allows for the definition of inclined roller restraints without the need for a nodal transformation matrix to be computed, as well as conditions that may be linear combinations of nodal DOFs. For the same reasons outlined in the `AQUINAS_Nodal_Force_Object`, a boundary condition constraint may only be applied at the edge of a segment.

Contrary to what may be expected for a constraint in an FE model, this is actually a potentially optional object in AQUINAS, depending on the specifics of the axisymmetric shell model explored. A computational shell problem may be submitted for analysis without any constraints and result to a robust solution process. As an example, a cylinder under the effect of two equal and opposing axial edge loads, with their cancelling-out vectors restricting axial rigid

body deformation modes while still inducing a state of compression along the meridian of the cylindrical shell, constitutes a problem that has been tested and solved with AQUINAS, even without the inclusion of constraints during the call to `AQUINAS_Protocol`. However, regardless of the possibility of being successful in dealing with ill-defined FE models, the author strongly recommends to ensure a sufficiently constrained model is submitted for analysis in order to avoid numerical issues during the solution process.

AQUINAS DOF Tracker Object
For purposes of output and post-processing, `AQUINAS_DOF_Tracker_Object` tracks the development of a specific DOF at any end of a segment object. The DOF to be tracked will also be used for visualising purposes of the nonlinear solution process (it being either a GNA, MNA or GMNA), if the corresponding option in the solver object is activated. The equilibrium path tracked will be stored for output and included in the structured result set of AQUINAS.

AQUINAS Output Mode Object
Even though an analysis submitted to `AQUINAS_Protocol` may be executed from start to finish without inclusion of an `AQUINAS_Output_Mode_Object`, the results will be inaccessible for the analyst to examine. Currently, there is just one option for output in AQUINAS, that of a structured collection of result data, while there is an additional mode under development that will allow results to be written in a .txt file format, to be accessed after completion of the analysis.

AQUINAS Analysis Object
A single `AQUINAS_Analysis_Object` has to be included in the model submission. This object carries the fundamental property `'type'`, which corresponds to the type of analysis to be executed, and guides `AQUINAS_Protocol` to make the necessary calls to the appropriate scripts. Apart from the `'type'` property, this object is also relevant to analyses executing bifurcation checks at some point in their runtime by providing information on the circumferential wavenumbers that need to be trialled and number of eigenvalues to be extracted for each.

AQUINAS Solver Object
The `AQUINAS_Solver_Object` serves as the backbone for any type of analysis, holding all required information to fine-tune the parameters that will determine the efficiency and accuracy of execution. General options such as the utilisation of pre-compiled MATLAB MEX binaries and number of processors to be employed for the parallel computation of element stiffness matrices, or even enabling informative console output to update the analyst on the progress of the solution process (at the cost of time needed for MATLAB to print a string on the console window, which can be a considerable portion of the total execution time if the model is relatively small) are decided through name-value pairs of this object. Task specific choices can also be made, corresponding to bifurcation checks, surrogate model optimisation and nonlinear analysis load incrementation, with a brief summary of their key characteristics that can be controlled with the `AQUINAS_Solver_Object` provided in the following paragraphs.

As the behaviour of the `eigs` MATLAB function for the solution of eigenvalue problems is strongly determined by parameters provided as inputs during its call, the solver object enables control over these options through equivalent name-value pairs that will be included in the `egis` call. Numerical tolerance for convergence of the implicitly restarted Arnoldi algorithm (Arnoldi, 1951; Sorensen, 1992), employed by MATLAB for the iterative computation of the eigenvalues of a sparse matrix system, strongly controls the accuracy of the eigenproblem results. As the material stiffness matrix $[K_m]$ is enhanced with Lagrange multiplier terms to account for mechanical boundary conditions of the axisymmetric shell problem, a similar procedure needs to be employed for the geometric stiffness matrix $[K_g]$ to ensure compatibility of the arrays for eigenvalue extraction. The magnitude of the Lagrange multiplier terms $C_{LM,g}$ to

be used in the $[K_g]$ matrix can lead to two eigenvalues equal to $-C_{LM,m}/C_{LM,g}$ that relate to the boundary conditions and are not meaningful in the context of a bifurcation buckling check, with the Lagrange multiplier terms of the material stiffness matrix usually being equal to unity $C_{LM,m} = 1$ for most constraints. A small enough value for $C_{LM,g}$ can ensure that these eigenvalues are both negative and of a regulated high absolute value, pushing them away from either the value of zero or one, around which the eigenvalue problem is solved for within the context of an LBA or a GNA/GMNA.

The load incrementation protocol adopted can make a significant difference in the step-wise tracing of the equilibrium curve. In AQUINAS load increments are either modulated through a constant Newton-Raphson incrementation scheme, where the only way to adjust the step size is through a cutback after a failed attempt to reach increment convergence, or through the more versatile and resilient arc-length method, able to properly adjust the step size around highly nonlinear regions of the equilibrium path. Two different implementations of the arc-length algorithm are offered, the single solution to the arc-length constraint method according to Ramm (1981) , which however only enforces this constraint on the first iteration within an increment and consequently can result in uneven steps and potentially numerical ill-behaviour of the method near limit-points (Fafard & Massicotte, 1993), or the modified-Riks (also found as Riks-Crisfield) implementation of the arc-length method (Riks, 1979; Crisfield, 1983). Whilst the latter ensures that the constraint equation is satisfied within every iteration through the solution of a quadratic form of the arc-length constraint, with the one corresponding to a closer 'angle' to the previous step selected as the method's solution, the roots of the constraint equation can potentially be complex numbers (Fafard & Massicotte, 1993) that cannot be meaningful in the context of a load incrementation scheme, resulting in necessary actions to abort further iterations and reattempt the increment after a cutback has been applied. Due to this complexity associated with the Riks-Crisfield approach to the arc-length algorithm, the strategy presented by Ramm (1981) is set as the default for cases where the arc-length method is employed. Relevant to both of these implementations is the adaptive scaling of the arc-length constraint, aiming to accelerate execution through larger increment sizes for near-linear stages of the solution process while at the same time refining the step for highly nonlinear regions or in the neighbourhood of limit-points. This scaling is performed according to the following relationship:

$$l_i = l_{i-1}\sqrt{J_d/J_{i-1}} \tag{3.90}$$

where l_{i-1} is the amplitude of the arc-length constraint used for the previous increment of the analysis, J_d is the desired number of iterations to achieve convergence for an applied load increment (with a default $J_d = 3$ that the AQUINAS user can possibly overwrite) and J_{i-1} being the number of iterations required to achieve convergence of the previous load increment (Crisfield, 1983; Teng & Rotter, 1989a,b).

3.7.3 Procedure descriptions

Having presented the architecture of the software, in a rather abstract manner, but also all of the available objects that may be defined as an axisymmetric shell problem is generated, it is time to discuss what is actually happening when an analysis is submitted with AQUINAS. As showcased in the flowchart of Figure 3.18, there are three basic analysis scripts that handle the linear or nonlinear solution process. Each of them will be outlined in the following sections, where the focus is on the considerably more complex `AQUINAS_GMNA.m` script, responsible for geometric and/or material nonlinear analyses.

3.7.3.1 AQUINAS LA

The most generic type of a FE solution, a Linear Analysis consists of a single analysis increment that only considers linear kinematics (small displacement theory) and purely elastic material law. Once the error checking and organising parts of `AQUINAS_Protocol.m` have been completed, a call is made to `AQUINAS_LA.m`. Inside this LA script, the material stiffness matrices of the element are computed and after the condensation process (see earlier Section 3.5.1) has been applied, the global stiffness matrix for the axisymmetric shell system is assembled, taking into account its sparsity patterns. This assembly may be done either through the relevant MATLAB scripts or pre-compiled C++ files, using MATLAB's MEX capability. The global stiffness matrix is enriched with the appropriate Lagrange multipliers terms to ensure the boundary conditions are applied to the model.

Once the equilibrium equation has been solved, the condensed-out DOFs of an element's nodes are recovered. Control is returned to `AQUINAS_Protocol`, where the midsurface strain and generalised stress resultants may now be computed. The inner-middle-outer fibre strains-stresses can also be evaluated from the relevant midsurface components. The results are organised in the way desired by the analyst as defined through an `AQUINAS_Output_Mode_Object`, and at this stage the analysis has successfully been completed.

3.7.3.2 AQUINAS LBA

Bifurcation analyses may be performed through a call to `AQUINAS_LBA.m`. The name of this script may be deceiving, as bifurcation is checked at the current stress state of the shell, as provided through an array of membrane stress resultants evaluated at the midsurface Gauss integration points along the elements. For an actual LBA to be executed, an LA will be submitted beforehand, so that the stress resultants have been computed and the linear bifurcation checks may be executed.

Both the material and geometric stiffness matrices need now be computed. If the bifurcation checks are performed as part of a geometrically nonlinear analysis, the nonlinear components of the strain-displacement matrix will also be considered in the formulation of the material stiffness of an element. The stiffness matrices will then be condensed, with the condensation process of the geometric stiffness being also described in the corresponding discussion of Section 3.5.1. Two global stiffness matrices are now formed, with the Lagrange multipliers added after multiplication with an input provided factor that ensures eigenvalues corresponding to the boundary conditions (where boundary conditions lead to additional rows-columns in the stiffness matrices) are positioned as far as possible from the load related ones. MATLAB's sparse eigenvalue solver `eigs` is employed in order to calculate the eigenvalues and corresponding eigenmodes of the shell problem. The eigenmodes will then not be put through the recovery process to obtain the full set of element nodal variables, as the computation of strains-stresses is not sensible in the context of a bifurcation analysis.

3.7.3.3 AQUINAS GNA - MNA - GMNA

A fully nonlinear analysis may be executed through a call to `AQUINAS_GMNA.m`. Geometric and material nonlinearities are included in the FE solution through appropriate boolean flags, based on the type of analysis that was submitted, evaluated before entering the main load incrementation loop.

Before proceeding with the exploration of the load bearing capacity development for an axisymmetric shell problem, on the way to its failure mode, certain operations are required to ensure the solution process runs as efficiently as possible. These include the initialisation of

storage arrays for the stiffness terms, strains and stresses, but also the computation of the nodal geometric properties of Eq. (3.1) so that they don't have to be re-calculated on every iteration of the process. If the user desires the visualisation of the nonlinear solution procedures, the corresponding MATLAB windows will be generated at this point. The total LPF achieved and number of load steps converged are set to zero.

Once all the necessary initialisations have been completed, the solution may now enter the main load incrementation loop. For each load step attempted some further initialisations need to be made, corresponding to the accumulated results within the step and auxiliary convergence related fields. A set of iterations is now attempted for each load increment, aiming at achieving convergence through minimisation of the residual forces in the shell model. To aid with the following discussion, the index i will be referring to the attempted load increment, while index j to the nonlinear iteration en route to convergence of load step i.

On the very first iteration j of an increment i, the tangent stiffness matrix of the axisymmetric shell model needs to be computed, as well as the externally applied force vector. The stiffness terms will not be evaluated on any subsequent iteration for the same load step, leading to a 'modified Newton-Raphson' kind of approach to the solution process. The element tangent stiffness matrices $[K_T]_e$ will include the effects of nonlinear strains on the strain-displacement matrix B of Eq. (3.49), as well as geometric stiffness terms $[K_\sigma]_e$ on $[K_T]_e$, if geometric nonlinearities are to be considered in the analysis. On the other hand, if the effects of material nonlinearities are to be included, the tangent modulus matrix $[D_T]$ for each Gauss station along the shell's meridian will need to be integrated according to Eq. (3.36). This integration is performed numerically, through the application of Simpson's 1/3 rule. The γ_i nodal variable will be condensed out of the stiffness matrix of each element according to Eq. (3.67), before assembly into the global tangent stiffness matrix. There is no need to condense out the $(\partial v/\partial s)_i$ nodal variable, as both the v and $\partial v/\partial s$ DOFs are set to zero by default in the purely axisymmetric pre-buckling path of the shell that AQUINAS aims to trace. Once the global stiffness matrix and force vector have been formulated for the current increment i, the reference solution may be obtained through the equilibrium equation as:

$$\{\delta_I\}_i = [K_T]_i^{-1}\{F_I\}_i \tag{3.91}$$

On subsequent iterations, the equilibrium equation is only solved for the vector of residual forces $\{\Phi\}_i^j$ in the system, with the correction to the displacement vector found by:

$$\{\Delta\delta_R\}_i^j = [K_T]_i^{-1}\{\Phi\}_i^j \tag{3.92}$$

If the arc-length method is to be used for the load incrementation, the change of the LPF will have to be evaluated after solution of the equilibrium equation. The vector of accumulated displacement $\{\Delta\delta_a\}_i^j$ for the current increment i will have to be updated, based on the displacement solution obtained on iteration j. The full set of element nodal degrees of freedom of Eq. (3.37) will also need to be recovered according to Eq. (3.65), and the transformation of Eq. (3.63) applied, with the circumferential ones still omitted due to the convention discussed above. As a final step before proceeding to the computation of the element's residual forces, the change in the nodal displacement magnitudes ζ is evaluated, for purposes of checking against a tolerance parameter to test for converge or divergence of the current load step i, as:

$$\zeta = \frac{(\Delta_i^j)^2 - (\Delta_i^{j-1})^2}{(\Delta_i^j)^2} \tag{3.93}$$

with Δ_i^j defined as follows:

$$\Delta_i^j = \sqrt{(u_i^j)^2 + (w_i^j)^2} \tag{3.94}$$

The midsurface strains $\{\epsilon\}$ along the shell's meridian may now be evaluated, at all available Gauss stations, according to Eq. (3.11). In an analysis where geometric nonlinearities are neglected, the nonlinear terms of Eq. (3.11), as given by Eq. (3.14), are omitted. The increment of the strain vector for iteration j is evaluated as the change from the previous strain state of the midsurface point.

If materially nonlinear effects are not included in the FE model, the computation of the stress resultants of Eq. (3.34) is a straight forward process, with the modulus matrix of Eq. (3.36) including only the elastic rigidity matrix $[D_e]$ of eq. (3.30). If plasticity is to be considered however in tracing the nonlinear behaviour of the shell, the through-thickness stress distribution for all Gauss points has to be computed in order to calculate the stress resultants. The first step in this process is to evaluate the strain increments for the iteration j across the fibres of the shell wall, as given by Eq. (3.9). For each of these material points the corresponding stress increment is to be evaluated, following the sub-incremental procedure outlined in Section 3.4. Once the stresses are found to be on the yield surface of the material, the stress resultants are evaluated by applying Simpson's 1/3 rule of integration for the through-thickness stations that were used.

The residual forces can now be evaluated as the difference between the externally applied forces with those that develop internally for each element. The condensation process is once again necessary in order to construct the global residual force vector. It is important to note that in the process of condensing the residual forces for every element the condensed tangent stiffness matrices are also calculated and the global stiffness matrix reformulated. Even though the stiffness terms themselves are not calculated again at this point, the global matrix $[K_T]$ that was set up in the first iteration of the increment cannot be used again, as the condensed element stiffness arrays are affected by the different force vectors used during the condensation. Omission of the intermediate step corresponding to re-application of the condensation step on pre-computed full tangent stiffness matrices $[K_T]_e$ for each element would lead to erroneous displacements in the process of recovering their full set of nodal displacement, as the force vector employed in Eq. 3.65 would represent externally applied loading rather than element residuals of the current convergence iteration.

If this is not the first iteration for the running load step, convergence of will be tested on the basis of comparing the maximum change in the ζ vector with a tolerance ζ_t. Divergence may also be tested by comparing with a tolerance ζ_d, and potentially abort the current increment attempt and apply cutbacks on the load (or arc-length) applied for the step. In the case that convergence is achieved bifurcation checks may be performed for a set of competing harmonics n, provided that geometric nonlinearities are included in the problem and the associated termination condition (controlled through the `AQUINAS_Solver_Object`) has been provided. Bifurcation checks may not be executed for an MNA in AQUINAS, as this is a counter-intuitive process that is not in accordance with the geometrically nonlinear nature of buckling. If any of the termination conditions provided has been satisfied the analysis process will be concluded and control will be returned to `AQUINAS_Protocol`.

The internal processes of `AQUINAS_GMNA` are presented in Figure 3.19. An attempt to distinguish steps that are specific to a geometrically or materially nonlinear solution is made, so that the reader may appreciate the way AQUINAS handles both types of nonlinearity within the same script.

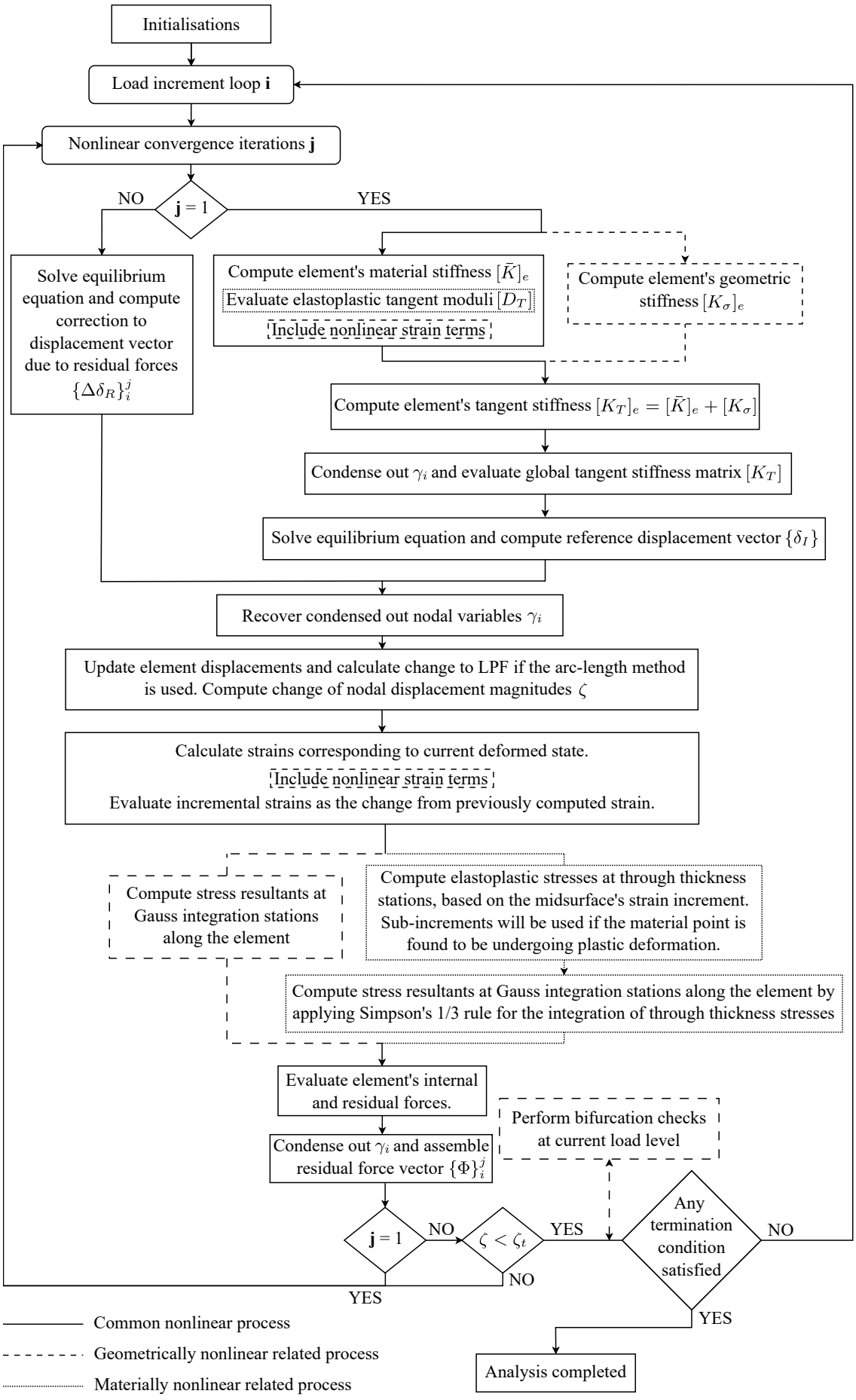


Figure 3.19: AQUINAS Geometrically and/or Materially Nonlinear Analysis flowchart.

3.8 Generation of capacity curves with AQUINAS-FE

With the novel Reference Resistance Design method introduced in Eurocode 3, as outlined in EN 1993-1-6 (2025) (also discussed in Rotter (2016a)), the engineer tasked with the design of a shell structure has the option of an entirely algebraic approach to compute its resistance. However, as discussed earlier in Section 2.4.4, the algebraic characterisation of each reference shell system requires the exploration of its response across different domains of mechanical behaviour, most commonly through the construct of a capacity curve. The analyst may then benefit from a conservative relationship that accounts for any nonlinear phenomena, without necessarily resorting to the strenuous execution of a GMNIA. The generation of a nominal capacity curve for unpressurised cylinders of varying slenderness and imperfections under axial compression with AQUINAS will be shortly presented. Accurate evaluation of the cylinders' ultimate resistance constitutes a very demanding computational task not only for AQUINAS, but for any FE software capable of a GMNIA, since very different nonlinear effects trigger the failure of the appreciably varying models as they advance through the slenderness spectrum. The dimensionless length of the cylindrical models to be considered in the present illustration is kept constant to a dimensionless Ω parameter, defined as:

$$\Omega = \frac{L}{r}\sqrt{\frac{t}{r}} \tag{3.95}$$

with the slenderness of the cylinders varying through a series of r/t ratios. Keeping $\Omega = 1$ and for a unit thickness t, the radius r is manually varied which in turn causes L to change. A BC1r boundary condition is considered at the base of all cylindrical models and a BC2r at their top edge, where the meridionally compressive edge load N is applied.

Two distinct imperfection shapes will be examined for a range of nominal imperfection amplitudes to illustrate the capabilities of AQUINAS. The cylinders' sensitivity to a mid-height weld depression imperfection shape (Rotter & Teng, 1989) will be investigated first, with the effect of an eigenmode affine imperfection shape obtained through an AQUINAS LBA for mode n = 0 to be subsequently explored.

3.8.1 Capacity curves for axially compressed cylinders with weld depression imperfections

A realistic imperfection shape that replicates the deviation from the perfect meridional geometry due to the anticlastic bending as the shell plates are rolled and the cooling deformations of a circumferential weld has been proposed by Rotter & Teng (1989). Direct access to the mathematical representation of a Type A weld allows for the generation of the meridional coordinates of the cylinder, providing an appealing imperfection form for computational exploration under various loading scenarios (Wang *et al.*, 2020; Sadowski *et al.*, 2023), with the deviation δ from the straight cylindrical geometry given as:

$$\delta = \delta_m e^{-\left(\frac{\pi|z-z_\delta|}{\Lambda}\right)}\left(\cos\left(\frac{\pi|z-z_\delta|}{\Lambda}\right) + \sin\left(\frac{\pi|z-z_\delta|}{\Lambda}\right)\right) \tag{3.96}$$

in which δ_m is the mathematical amplitude of the depression, z_δ the axial position of the weld and Λ is the thin shell theory linear bending half-wavelength, as defined in Eq. 2.14. It is crucial to distinguish between the mathematical amplitude of the imperfection δ_m (controlled by the analyst during modelling) and the code-compliant dimple tolerance amplitude δ_0 (verified on the

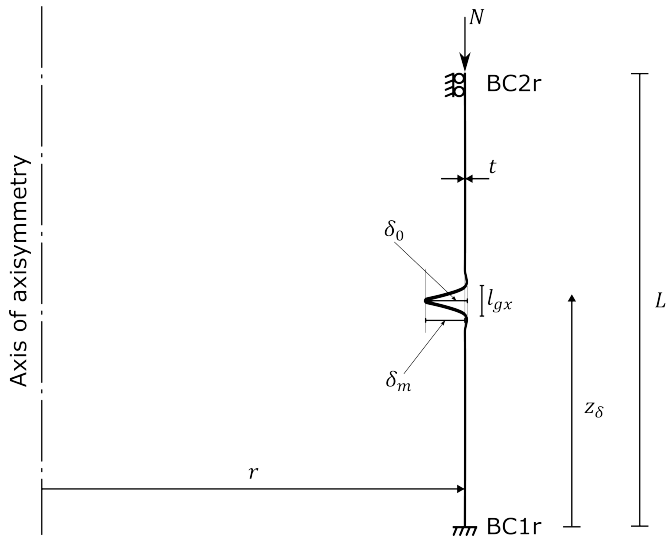


Figure 3.20: Exaggerated imperfect meridional geometry for a Type A weld depression imperfection.

completed physical structure), defined relative to an appropriate gauge length l_g as illustrated in Figure 3.20. For systems dominated by meridional compression this is set to $l_g = l_{gx}$ (EN 1993-1-6, 2025), given as:

$$l_{gx} = 4\sqrt{rt} \tag{3.97}$$

For a meaningful exploration of the sensitivity to different kinds of imperfection shapes for cylinders under meridional compression to be made, the mathematical amplitude δ_m which controls the geometric generation of the model needs to be calibrated as to achieve a target tolerance δ_0 of a specific magnitude (EN 1993-1-6, 2025; Sadowski & Seidel, 2023b). Example nominal GMNIA capacity curves for the δ_0 ratios examined here are presented in Fig. 3.21, where a strong imperfection sensitivity, exceptionally detrimental for cylinders of high slenderness, is evident. These results however are only a showcase of the capabilities of the AQUINAS toolbox and are not presented in the context of an imperfection sensitivity exploration. The native axisymmetric treatment of the pre-buckling stress state and the built-in consideration of different harmonic bifurcation buckling modes through the formulation of the element included in AQUINAS permitted a swift and unsupervised generation of FE results for the examination of this reference shell system, a process that has been fully utilised in the computational exploration of the next chapter.

The generation of a capacity curve typically requires an additional set of MNAs and LBAs for each model considered to evaluate the reference plastic R_{MNA} and critical elastic buckling R_{LBA} resistances. This step is omitted in the present exploration, as the reference system of an axially compressed cylinder has been thoroughly researched and analytical expressions for these resistances have been established on the basis of a thin shell theory stability result (with an important caveat on the accuracy of this result for stocky cylindrical models discussed in detail in Chapter 5), a simplification that has also been applied in a similar study (Wang *et al.*, 2020). The R_{MNA} result reference resistance can here be replaced with the squash load plastic resistance R_{pl}, corresponding to the load level that would cause meridional membrane yielding, while R_{LBA} can be replaced with the R_{cl} resistance relating to the critical elastic buckling load of Eq. 2.19.

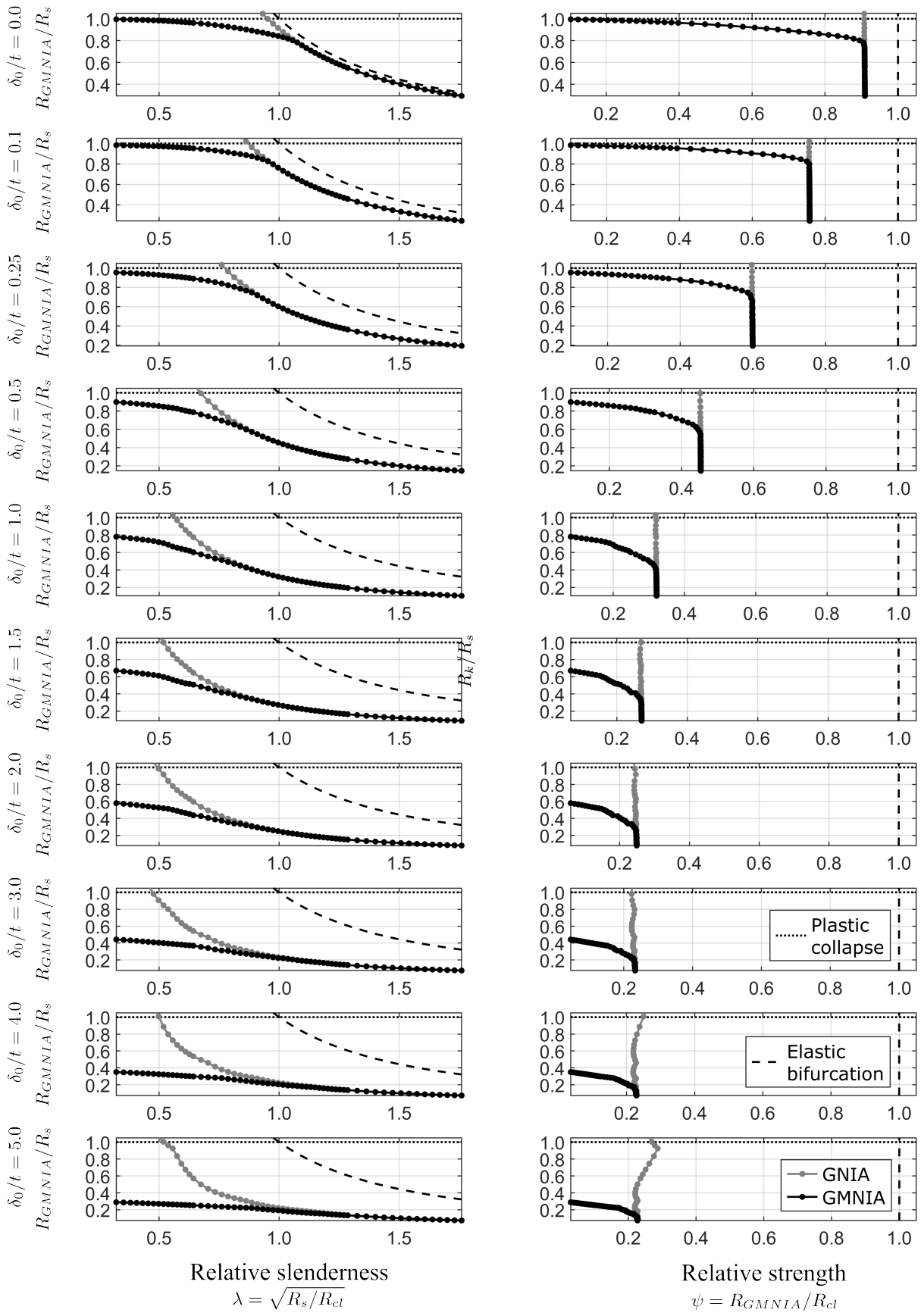


Figure 3.21: Dimensionless traditional (left) and modified 'Rotter' (right) nominal capacity curves for meridionally compressed cylinders with a midspan Type A weld depression imperfection shape.

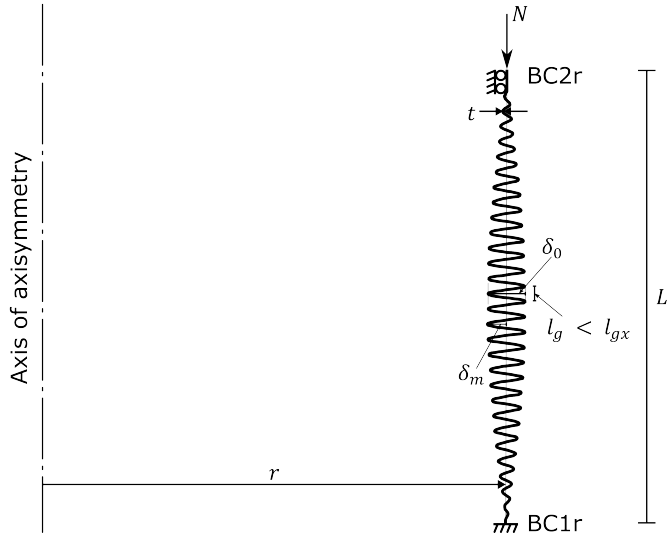


Figure 3.22: Exaggerated imperfect meridional geometry for an eigenmode affine imperfection shape.

3.8.2 Capacity curves for axially compressed cylinders with axisymmetric eigenmode affine imperfections

A second set of GMNIAs was performed to estimate the sensitivity of the axially compressed cylinders to an eigenmode-affine imperfection shape. Imperfections of this type are commonly considered by analysts in their FE models as unfavourable to the resistance of the structure, convenient in terms of implementation or simply in the absence of alternative shapes. This EN 1993-1-6 (2025) approved approach has been fully adopted and examined across several literature resources (Teng & Song, 2001; Song, 2002; Sadowski & Seidel, 2023a) relevant to the estimation of a cylindrical shell's load bearing capacity, not that much on the grounds of realism (i.e. representativeness of actual manufacturing processes) or proven worst conceivable deviations but rather on the assumption that imperfections assuming a shape corresponding to a critical mode superimposed on the perfect shell geometry would act as the most potent catalyst for the acceleration of instability phenomena. As the discussion of Section 2.1.3.1 has outlined, consideration of pre-buckling nonlinearities can alter the critical mode that an axisymmetric shell system may be susceptible to bifurcate into, producing an inconsistency in this approach as the mode predicted through an LBA may not be critical any more in the context of a GNIA or GMNIA investigation, a shortcoming that has been thoroughly examined and documented in Teng & Song (2001). A review of techniques and approaches in the selection of an appropriate imperfection shape is well beyond the scope of the present doctoral work however and the eigenmode affine imperfection shapes of Fig. 3.22 will be considered without questioning their validity.

For the present computational treatment, a perfect cylindrical model is submitted through an LBA to obtain the eigenmode shape corresponding to an axisymmetric mode ($n = 0$), normalised so that the maximum displacement degree of freedom is equal to unity. Calibration of the imperfection shape is slightly more complex in this scenario since the mathematical amplitude δ_m ($= 1$ due to the normalisation of the modal form) may not be positioned at the same meridional location as that of the dimple tolerance δ_0 in Figure 3.22, estimated from the outside of the cylinder with an appropriate gauge length l_{gx}. The fact that eigenmodes are sign reversible is accounted for by considering both possible modal configurations, and the one leading to the higher scaling factors for the imperfection shapes is considered for the GMNIA step of each model (Sadowski & Seidel, 2023a,b). This fully automated pipeline on the

generation of cylinders superimposed with eigenmode affine imperfection shapes is inevitably less computationally efficient when compared to models with weld depression imperfections due to the additional step of an LBA. This probes a discussion on the actual compensation that this scheme provides in terms of total time efficiency, as the time saved during the modelling stage by considering a more simple base geometry without the need to justify a selection of appropriate initial imperfections shapes may be eventually spent performing preliminary analyses to obtain a not entirely realistic or conservative imperfection profile.

In Figure 3.23 the GMNIA results of AQUINAS are presented for this second set of nonlinear analyses under eigenmode affine imperfections. The algebraic R_{pl} and R_{cl} resistances are once again used in place of the corresponding computational R_{MNA} and R_{LBA}. The shape of the nominal capacity curves for such deeply imperfect shells bears a strong resemblance with those computed for comparably highly imperfect cylinders under uniform bending by Wang *et al.* (2020) using ABAQUS.

All of the FE analyses were executed on a Red Hat Enterprise Linux 8.5 operating system over several days, running on the High Performance Computing cluster of the Imperial College London. The parallelisation of the assemblies was exploited by splitting the calculations through 64 CPUs. It can be appreciated that the computations for the full algebraic characterisation of this reference shell system are exhaustive, as a series of different dimensionless length parameters Ω and boundary conditions need also be considered. A 3D 'panel analysis' approach (Sadowski *et al.*, 2018) to perform the evaluation of these capacity curves would be excessively onerous and prohibitively time consuming. The strategy for setting up such an analysis hierarchy has already been outlined (Sadowski *et al.*, 2017a), a process that may be fully automated with the MATLAB API exposed by the AQUINAS software.

3.9 Concluding remarks

The development of the AQUINAS FE solver presented in this chapter addresses the absence of non-axisymmetric bifurcation buckling mode detection capabilities within the natively axisymmetric modelling space of commercial general purpose computational software. Whilst it has been widely known in the shell buckling research community that the load carrying capacity of thin axisymmetric shells characterised by a pre-buckling stress field of circumferential uniformity is often governed by instability phenomena associated with a harmonic distribution of modal displacements along the circumference of the shell system, the specialised mathematical treatment necessary for a numerical solution to be obtained has not found its way into 21^{st} century computational analysis software. Once commonplace in legacy codes such as BOSOR5 and FELASH, the particular formulation features necessary for identification of circumferentially harmonic bifurcation buckling modes have been incorporated into this open-source MATLAB written FE toolbox, programmed on the basis of EN 1993-1-6 (2025) definitions of analysis types as its internal software architecture indicates.

Ease of modelling is achieved through an abstract scripting API, permitting swift set-up of axisymmetric shell problems while advanced options remain accessible for modification to allow for a higher level of control over key solution parameters. Full scale parallelisation of any supported type of analysis is provided through pre-compiled C++ MEX binaries that can accelerate numerically intensive tasks by distributing computation of stiffness coefficients across any available cores, utilising the OpenMP API for multi-threaded numerical evaluations. This encourages deployment of AQUINAS into high-performance computing clusters for large parametric or sensitivity studies, presently tested on both Windows and Linux operating systems.

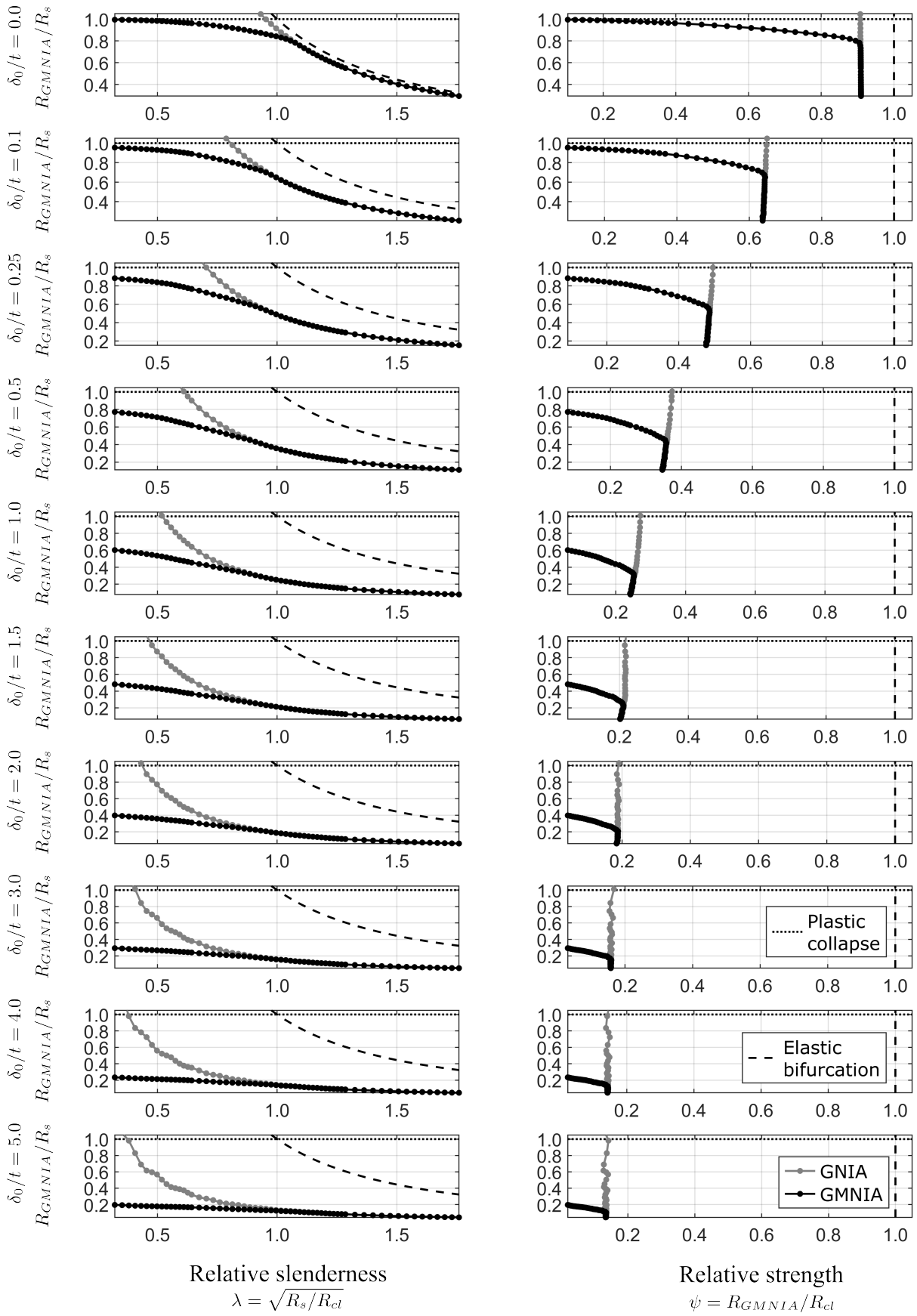


Figure 3.23: Dimensionless traditional (left) and modified 'Rotter' (right) nominal capacity curves for meridionally compressed cylinders with an eigenmode affine imperfection shape.

AQUINAS can be a powerful computational tool for any research related to the linear or nonlinear analysis of shells of revolution, as the presentation of the software in this chapter and the extensive list of solved axisymmetric shell problems in Appendix A illustrates, with the efficiency of its FE implementation compared thoroughly against ABAQUS in Appendix B within the scope of three different kinds of analysis. The aim is for its repository to be actively maintained and constantly updated, democratising availability of high-fidelity FE solvers for nonlinear bifurcation buckling analysis of axisymmetric shells and providing versions of the software that extend its capabilities and enrich the library of reference solution scripts. Limitations of its thin shell formulation will be highlighted in the following chapters, leading to a discussion regarding necessary further developments on its solver capabilities.

Chapter 4

On the generation of capacity curves for meridional compression and uniform bending

4.1 Motivation

Modern-era availability of computational resources has facilitated the employment of a partially numerical framework for the design of shell structures that has been found on the basis of a hand calculation approach (ECCS EDR5 (2013)), that of the LBA-MNA methodology as formally described in EN 1993-1-6 (2025). Rigorous and accurate estimations of a shell model's elastic critical buckling resistance R_{cr} and plastic collapse resistance R_{pl} can be obtained through LBA and MNA numerical simulations accordingly (even though the latter can be substituted by a lower bound estimate obtained through an LA (ECCS EDR5 (2013))), with the two resistances combined to provide an estimate of the shell system's dimensionless slenderness $\lambda = \sqrt{R_{pl}/R_{cr}}$. The characteristic resistance R_k of the shell system can subsequently be evaluated through the capacity curve framework of EN 1993-1-6 (2025) as it has been outlined earlier in Section 2.4 of the present document, incorporating the potential of a fully nonlinear GMNIA exploration of reference shell systems to determine a shell's load carrying capacity. Although Section 2.4.3 highlights potential pitfalls of the LBA-MNA methodology, the essential requirement of a complete algebraic characterisation of capacity curve parameters tied to a thoroughly examined reference shell system that is relatable to the shell model under design constitutes the main consideration during application of this approach. In the absence however of a clearly relatable reference shell system to support reliable application of the LBA-MNA design method, a 'default' set of capacity curve parameters (with their individual definition furnished in Table 2.2) needs to be identified if application of this approach is to be permitted. The first generation of the European Standard EN 1993-1-6 (2007) for the strength and stability of shell structures permitted utilisation of capacity curve parameters, corresponding to meridionally compressed cylindrical shells on the historical perception of their de-facto conservativeness as a critically imperfection sensitive shell system for elastic material response. The integrity of this premise has been questioned in computational investigations of the last decade, leading to important adjustments of relevant EN 1993-1-6 (2025) provisions as will be discussed shortly.

A recent computational investigation of cylindrical shells under uniform bending (Wang *et al.*, 2020) has highlighted a shortcoming in the provision of EN 1993-1-6 (2007) on the design of axisymmetric shells through the LBA-MNA approach where a clearly comparable reference shell system cannot be identified. Paragraph (11) of section 8.6.2 of EN 1993-1-6 (2007) explicitly

stated that in cases where it is difficult to establish appropriate values for the capacity curve parameters that will determine the resistance of the axisymmetric shell system to be designed, the corresponding values for a meridionally compressed unstiffened cylinder can be adopted. This statement is made on the basis of two underlying assumptions concerning the role of pre-buckling geometric nonlinearities in the estimation of a shell system's critical resistance as well as the method of assessing the plastic reference resistance (ECCS EDR5 (2013)). The mechanics of the shell system in question should guarantee limited impact of geometrically nonlinear behaviour on its pre-buckling response since cylindrical shells under uniform meridional compression only showcase a $10 \sim 15\%$ reduction of their critical elastic buckling resistance when these effects are considered. Additional guidance is provided for cases where the shell system is susceptible to snap-through buckling, a detrimental scenario that requires the incremental path-tracing capabilities of a GNA.

The second and more fundamental of these two underlying assumptions relates to the imperfection sensitivity of meridionally compressed cylindrical shells, which is found to considerably reduce the elastic buckling capacity, especially of highly slender cylinders. First generation of the European standard EN 1993-1-6 (2007) would combine the effect of both these assumptions into the α parameter of the capacity curve framework, later split into individual parameters α_G and α_I such that $\alpha = \alpha_G \alpha_I$ (see Table 2.2). The commentary in ECCS EDR5 (2013) highlights that due to the pre-buckling stress uniformity in cylinders under meridional compression there may be very little separation between the first yield load and the full plastic collapse load for stockier models, resulting in low values for the plastic range parameter β ($1 - \beta \approx 1$). It is thus recommended that in cases where the LA estimate of the plastic collapse load R_{pl} is marginally lower than the corresponding MNA result, the value of the β parameter should be appropriately increased to account for potential discrepancies between first yield and full plastic load resistances of the system. Special mention is made to moderately long bending dominated cylindrical systems, such as chimneys under wind loads, where first yield and fully plastic bending moments are largely separated (ECCS EDR5 (2013)).

An algebraic characterisation of cylinders under global bending and generation of parameters to be utilised in the context of the capacity curve framework of EN 1993-1-6 (2025) has been undertaken by Wang *et al.* (2020) for shells of varying slenderness, ranging from rather stocky 'short' cylinders to more slender 'long' models. With reference to the dimensionless length group parameters ω and Ω (provided again here for convenience):

$$\omega = \frac{L}{\sqrt{rt}} \tag{4.1}$$

and

$$\Omega = \frac{L}{r}\sqrt{\frac{t}{r}} \tag{4.2}$$

the four distinct domains of behaviour for nominally perfect ($\alpha_I = 1$) cylinders under uniform bending, identified during the computational exploration of Rotter *et al.* (2014), are described as:

Short domain: Fully restrained local buckling and ovalisation by edge boundary conditions, with limit point buckling occurring at a moment $M_k \gg M_{cr}$ (with $\alpha_G \gg 1$).

Medium domain: Local short-wave bifurcation buckling develops adjacent to the most compressed meridian at approximately $M_k \approx 0.9 M_{cr}$ (i.e., $\alpha_G \approx 0.9$). The $\sim 10\%$ reduction from M_{cr} results from pre-buckling amplification of the boundary conditions, as also observed under meridional compression. In this domain, the resistance is relatively inde-

pendent of r/t because ovalisation is restrained when the dimensionless length $\omega < 0.5(r/t)$ or $\Omega < 0.5$.

Transitional domain: With increasing length, ovalisation becomes more significant, causing a progressively nonlinear pre-buckling path. This leads to stiffness loss and premature local buckling on the flattened compressed meridian, where $M_k \ll 0.9M_{cr}$ (i.e., $\alpha_G \ll 0.9$). This regime is characterised using the dimensionless group Ω (defined in Eq. (3b)), beginning at $\Omega = 0.5$ or $\omega = 0.5(r/t)$.

Long domain: Ovalisation is fully developed and cylinders with lengths $\Omega \geq 7$ bifurcate elastically at an asymptotic moment $M_k \approx 0.5M_{cr}$ (corresponding to $\alpha_G \approx 0.5$).

The four distinct domains of length behaviour for this classical shell reference system are additionally visually illustrated through the scatter of FE results generated by Fajuyitan *et al.* (2015) for fully clamped or simply supported (pinned) boundary conditions at the edges of the perfect geometry cylindrical models. The computational findings of Wang *et al.* (2020) have supported the commentary provided by the European Recommendations ECCS EDR5 (2013) with regards to the underestimation of the β parameter, if the value corresponding to the case of uniform meridional compression was to be adopted instead of a more appropriately evaluated result for cylinders under bending.

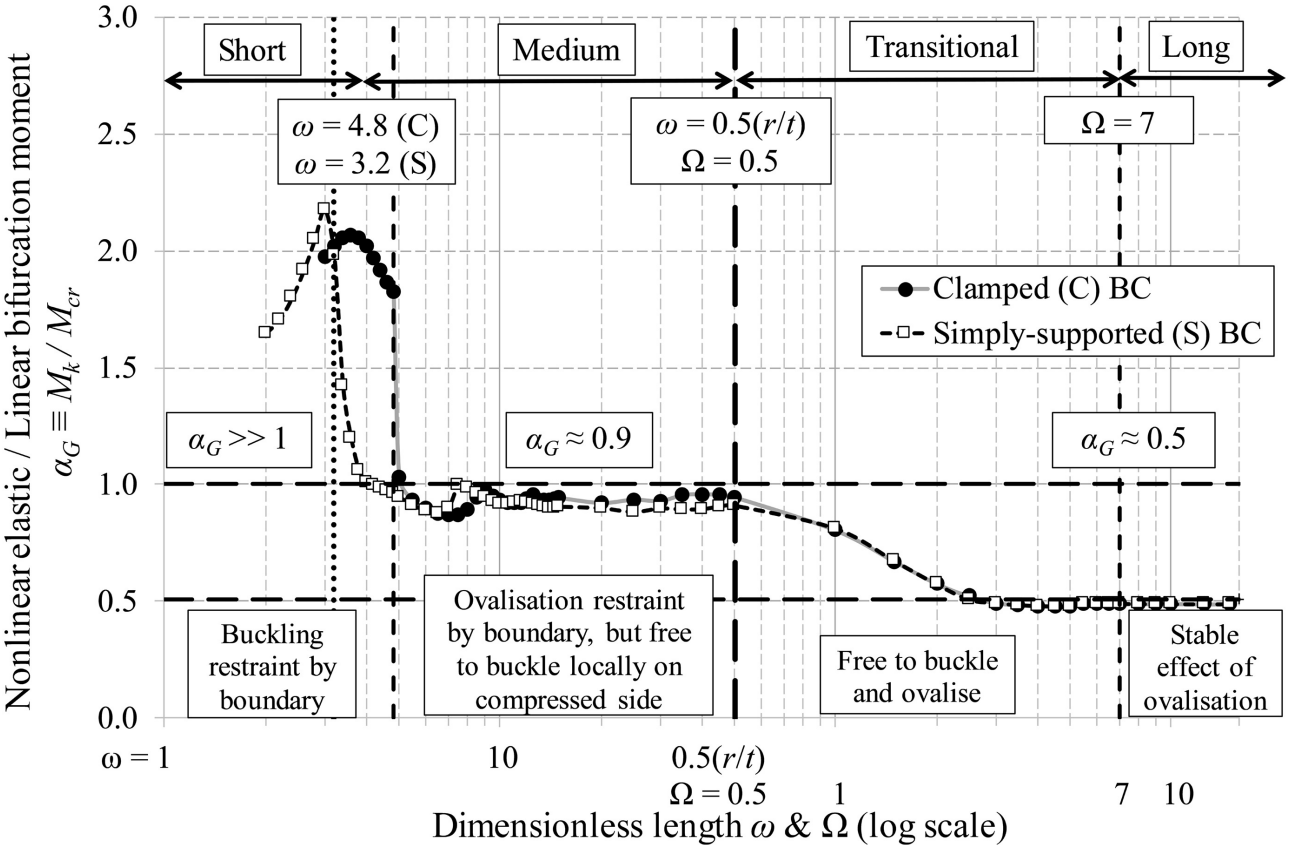


Figure 4.1: Computational illustration of the four length domains governing geometric nonlinearity in perfect elastic cylinders under uniform bending, as generated using ABAQUS by Fajuyitan *et al.* (2015).

With the second generation of the European Standard EN 1993-1-6 (2025) on the strength and stability of shell structures now available to the shell design community, this shortcoming has been formally amended through the corresponding guidelines relevant to the inclusion of Annex E capacity curve parameters for cylinders under bending in design cases where a clearly

identifiable reference shell system isn't available. This additional provision of adopting the most conservative set of capacity curve parameters between those provided for cylinders under meridional compression and cylinders under global bending, with a slenderness λ estimated through computational LBA and MNA assessments, ensures the integrity of this partially computational methodology for the design of shell structures. The disconnection of the algebraically characterised reference shell systems presently at an analyst's disposal through the corresponding annexes of EN 1993-1-6 (2025) with more practicable design shell systems, such as multi-segment towers under combined effects of bending, torsion and compression, is hence better treated through the improved conservativeness in the introduction of a 'default' case when the capacity curve framework is employed for assessment. Relationships for the characteristic resistance of meridionally compressed cylinders are provided through Annex D of EN 1993-1-6 (2025), with a visual comparison against those for uniform bending presented in Figure 4.2 for different classes of fabrication qualities, allowing a more direct appreciation of the conservativeness in evaluating the resistance of axisymmetric shell systems in the lack of a better correlated and already characterised reference shell system.

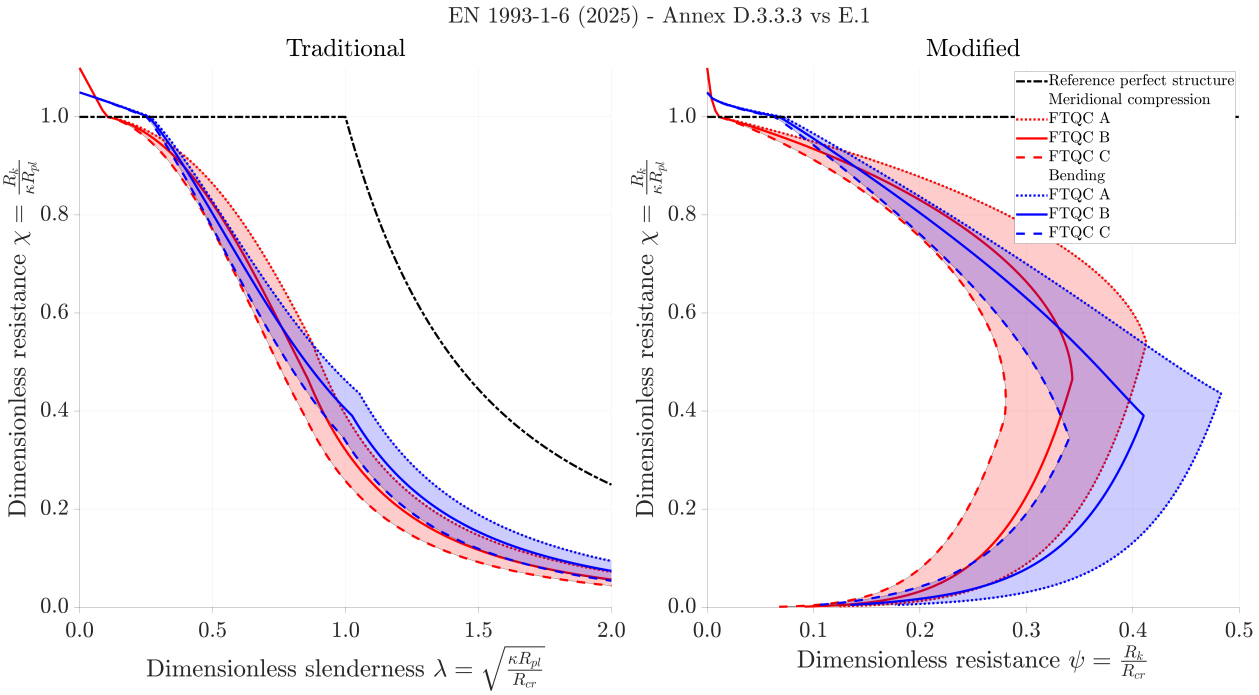


Figure 4.2: Comparison of capacity curves for cylindrical shells uniform meridional compression and uniform bending in EN 1993-1-6 (2025) in χ vs λ ('traditional' form, left) and in χ vs ψ ('modified' form, right), as presented in Sadowski & Filippidis (2025). The letters A, B and C respectively represent 'Excellent', 'High' and 'Normal' Fabrication Tolerance Quality Classes (FTQCs). Note that $\kappa = 1$ for meridional compression (red results) but $\kappa \neq 1$ for bending (blue results).

This chapter presents the extensive generation of FE results and associated challenges in an endeavour to provide a computational comparison on two of the most classical reference shell systems, cylinders under uniform meridional compression and cylinders under uniform bending, supporting justification of the relevant recent amendment in EN 1993-1-6 (2025) through a communicated peer-reviewed document. Comparison is limited to a dimensionless group $\Omega = 0.5$ for the purposes of focusing on a specific set of capacity curve parameters for cylinders of intermediate slenderness (α_G, α_I and β) at varying levels of imperfection amplitudes. This work constitutes only the second half of the research published in the *Journal of Constructional Steel Research*, since the historical review of relevant design standards and the de-facto perception of

meridionally compressed cylinders as the most conservative shell system to base design upon includes work to which the present author did not directly contribute. Emphasis is placed on the modelling and post-processing assessment of FE solutions, with a discussion on the quality of results generated by the different software employed.

4.2 Uniform meridional compression vs uniform bending: a computational justification

In an endeavour to provide a quantitative justification for the important amendment made to the 'default' capacity curve choice to be used for the LBA-MNA design method, implemented in EN 1993-1-6 (2025) and described in Section 2.4.3 earlier in this document, a series of computational capacity curves are presented and processed here for the two reference systems of a cylinder of medium length under uniform meridional compression and that under uniform bending. The study of this classical shell system under uniform meridional compression will precede that for uniform bending as has historically been the case, laying the foundations for the subject of shell buckling.

Modelling symmetry will be exploited in any instance that the corresponding shell mechanics permit for a reduction of time spent executing large-scale sweeps of FE models, without any adverse effect on the quality or numerical accuracy of the generated results. The techniques applied in the following sections have been extensively leveraged across a wide range of computational investigations, with cases where particular considerations require a full model to be examined unambiguously identified by Fajuyitan (2018) in the context of cylinders under global bending. These cases however are not relevant to the study of the present chapter, allowing for both circumferential and meridional symmetry reductions for uniform bending loading scenarios, while full pre-buckling axisymmetry is exploited for the analysis of cylinder under meridional compression, as discussed in the following section.

4.2.1 Natively axisymmetric finite element modelling of cylindrical shells under uniform meridional compression

The newly-developed AQUINAS (Filippidis & Sadowski, 2023b) finite element software was used to generate illustrative computational capacity curves for cylinders under uniform meridional compression. By removing an entire dimension's worth of parasitic degrees of freedom, AQUINAS considerably reduces execution times and increases solution quality when compared with 3D model equivalents (Sadowski *et al.*, 2018), but only for natively axisymmetric shell systems, a performance enhancing feature that will be fully utilised for the purposes of the computational venture at hand.

The axisymmetric modelling space of AQUINAS greatly simplifies the process of generating and submitting a model of a cylindrical shell under uniform meridional compression for analysis. The material properties used are consistent with those assumed so far ($E = 200$ GPa, $f_{yk} = 460$ MPa and $\nu = 0.3$). A dimensionless length of $\Omega = L/r\sqrt{t/r} = 0.5$ was assumed, representative of medium-length cylinders which undergo localised short-wave buckling modes that are essentially unaffected by end boundary conditions or long-shell 'Euler column' behaviour. Only half of the meridian's length $L/2$ was modelled for yet more efficiency, with meridional symmetry boundary conditions assumed at midspan where a single 'Type A' axisymmetric weld depression imperfection (Rotter & Teng, 1989) was located, and a BC2r boundary condition on the loaded edge which permits meridional displacement but not rotation about the circumferential axis (Fig. 4.3). The assumption of an axisymmetric idealised imperfection form does not preclude the

criticality of unsymmetrical bifurcation buckling modes, which indeed the AQUINAS toolbox was specifically developed to accurately and efficiently compute.

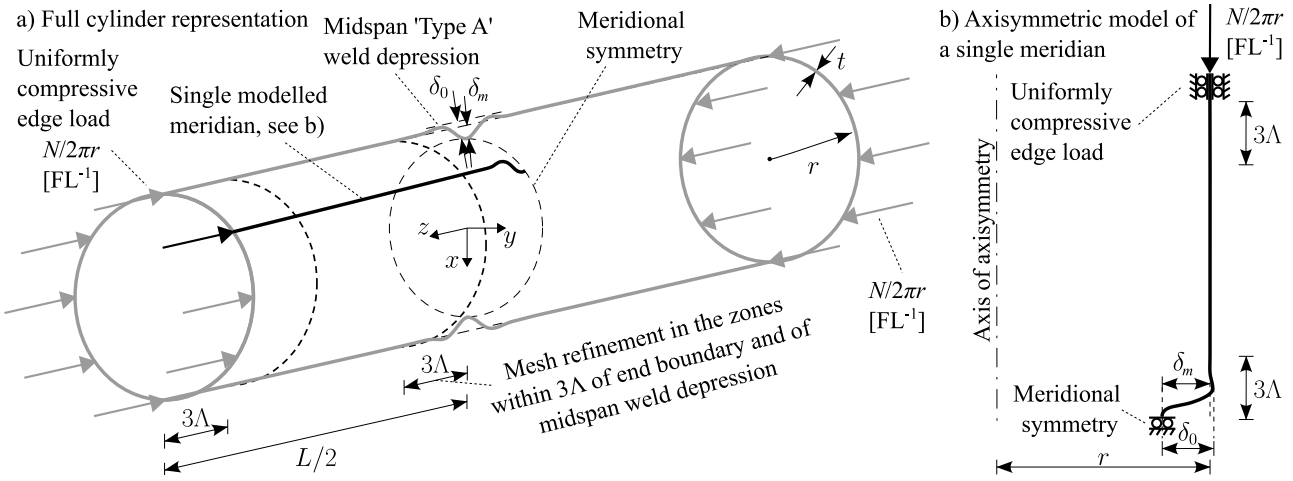


Figure 4.3: Natively axisymmetric finite element model of a medium-length imperfect cylinder under uniform meridional compression. The full cylinder in a) is shown with grey solid lines denoting complete represented geometry and black solid lines denoting actually modelled single meridian geometry in b) using AQUINAS.

Each capacity curve was generated at a constant imperfection amplitude δ_0/t by varying the r/t ratio from 70 to 700 in fine increments, assuming a unit thickness. The distributed edge load $N/2\pi r$ [FL^{-1}] was applied as:

$$N = \min(N_{pl}, N_{cl}) \text{ where } N_{pl} = 2\pi r t f_{yk} \text{ and } N_{cl} = \frac{2\pi E t^2}{\sqrt{3(1-\nu^2)}} \tag{4.3}$$

depending on λ. Low r/t simulations representative of very stocky cylinders were not performed, in part because this is not necessary to illustrate the phenomenon of Fig. 4.2 and in part because the AQUINAS element formulation is not currently extended to be appropriate for thick shells, as the discussion of Section 4.3.3 later on illustrates. Here δ_0 refers to the tolerance amplitude relative to a gauge of length $l_{gx} = 4\sqrt{rt}$ (compliant with EN 1993-1-6 (2025)) and should be differentiated from δ_m which is the mathematical amplitude controlling the 'Type A' weld depression model: the two are however closely related as $\delta_m \approx 0.98\delta_0$ (Sadowski & Seidel, 2023b). Values of δ_0/t were varied from a nominally perfect 0.001 to a highly imperfect 5.0, with each producing a separate computational capacity curve. The cylinder meridian had a refined discretisation within 3Λ of the loaded edge and the midspan weld depression where at least ten elements per Λ were employed (Λ being the linear meridional bending half-wavelength as defined in Eq. 4.4), with the mesh within the boundary layer caused by the loaded edge permitted to remain fully elastic to avoid premature buckling at this location due to localised surface yielding (Wang *et al.*, 2020). The Hermite cubic interpolation used in the Teng & Rotter (1989a,b) formulation independently for the element displacement field, its geometry and its meridional curvature ensure a particularly high-quality representation of the idealised imperfect geometry in AQUINAS. Approximately 450 GNIAs and 650 GMNIAs were performed in total with an implementation of the nonlinear arc-length solver by Ramm (1981) (although AQUINAS also offers an implementation of the arc-length algorithm by Crisfield (1983)).

$$\Lambda = \frac{\pi\sqrt{rt}}{[3(1-\nu^2)]^{1/4}} \tag{4.4}$$

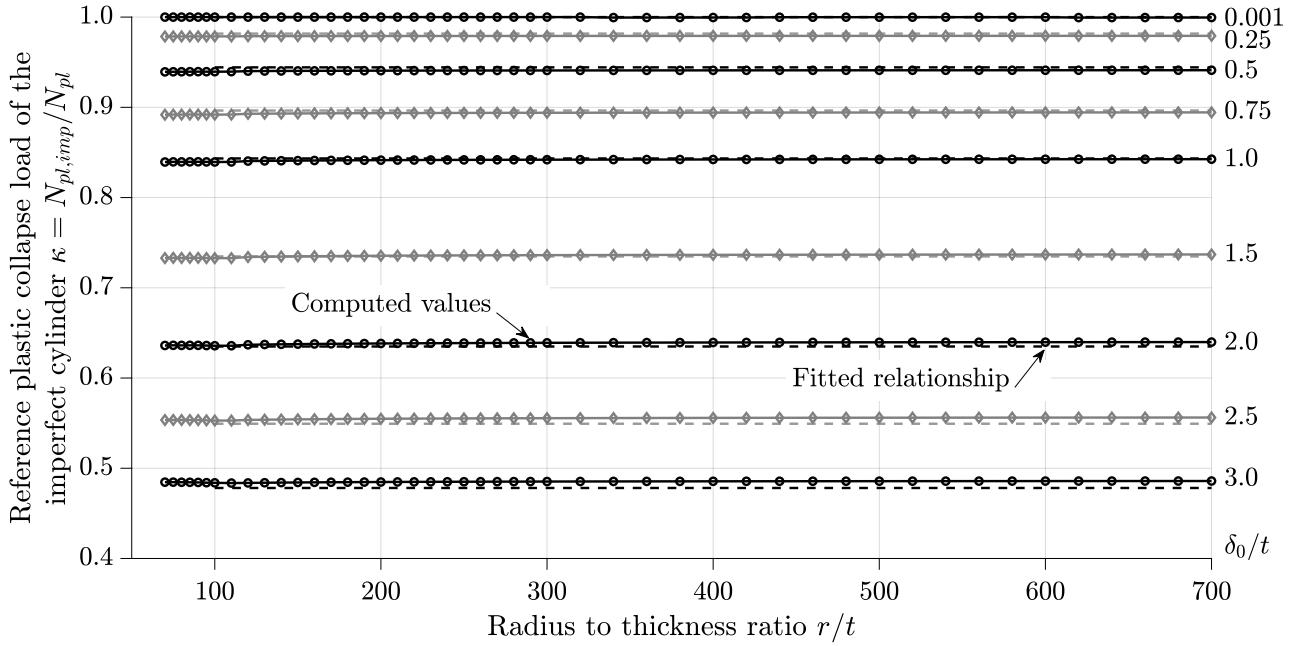


Figure 4.4: Variation of the $\kappa_{thin} = N_{pl,imp}/N_{pl}$ 'plastic imperfection sensitivity' relationship with r/t (which in fact shows independence) and δ_0/t for medium-length thin cylinders with $\Omega = 0.5$ and a midspan 'Type A' weld depression imperfection.

To permit a direct comparison between this system and uniform bending within the most general formulation of the capacity curve framework (Eq. 2.24), a tentative relationship for $\kappa_{thin} = N_{pl,imp}/N_{pl}$ (valid for thin cylinders under uniform meridional compression in the limit $r/t \to \infty$) is derived here through approximately 500 MNIA analyses, adopting the process presented in Wang *et al.* (2020). The values of $N_{pl,imp}$ (the plastic collapse load of the *imperfect* thin shell, sharing the same imperfection model as GMNIA) computed by MNIA are normalised by the value for the perfect thin shell $N_{pl} = Af_{yk}$ and plotted in Fig. 4.4 against the r/t ratios of the corresponding models, for imperfection amplitudes δ_0/t up to 3.0. For thin shells the κ relationship is shown to be invariant with r/t and the asymptotic relationship as $r/t \to \infty$ and may be characterised as follows:

$$\kappa_{thin} = 0.06 + \frac{0.94}{1 + 0.2(\delta_0/t)^{5/3}} \tag{4.5}$$

It is stressed however that this relationship is *not* currently codified in EN 1993-1-6 (2025) and is employed in this paper solely for illustration purposes. It is presented in Fig. 4.5 and compared against the corresponding relationship for uniform bending (Eq. 4.7 taken from (Wang *et al.*, 2020)) which, surprisingly, is more deleterious.

4.2.2 3D finite element modelling of cylinders under uniform bending

The commercial ABAQUS (2022) finite element software has an established history as the tool of choice in exploring the nonlinear buckling of thick or thin shell structures (Fajuyitan & Sadowski, 2018; Rotter *et al.*, 2014; Wang *et al.*, 2020; Fajuyitan, 2018; Sadowski & Rotter, 2013) and was used here to generate illustrative computational capacity curves for cylinders under uniform bending. A complete computational study was recently conducted by Wang *et al.* (2020) which forms the basis of the corresponding rule in Annex E.1 of EN 1993-1-6 (2025). The current study has independently recalculated a selection of these results for the purposes of generating a comparison with capacity curves for uniform meridional compression computed with AQUINAS.

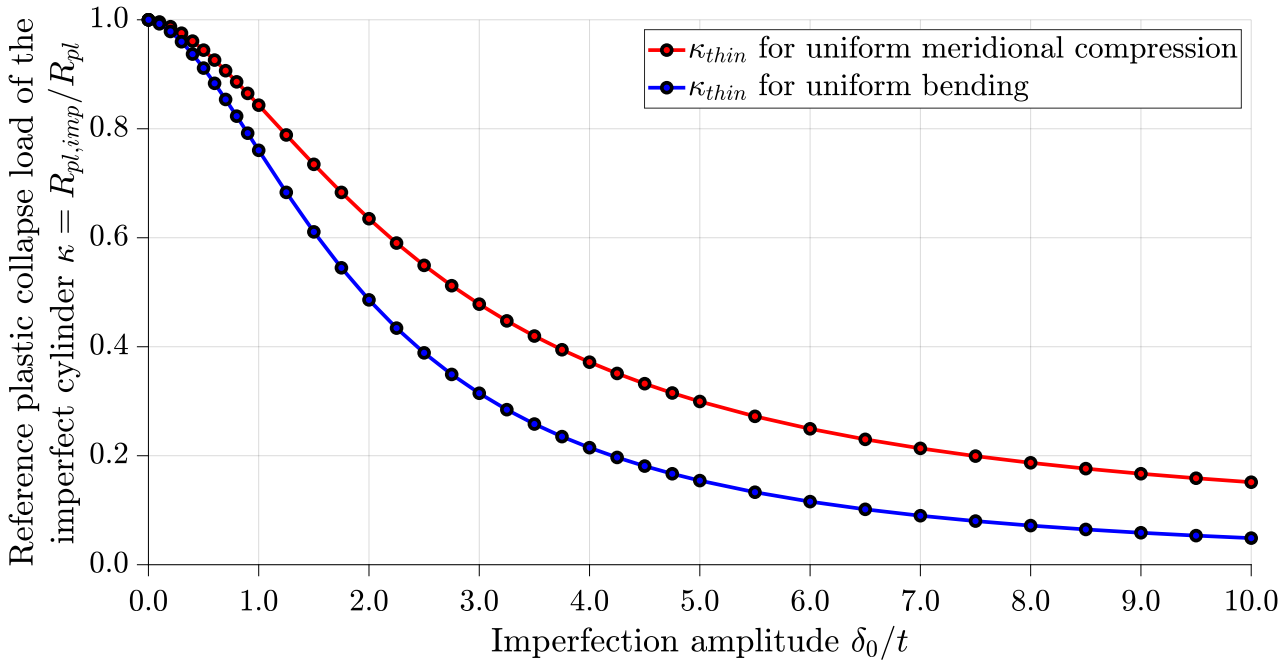


Figure 4.5: κ_{thin} for a thin cylinder under uniform meridional compression (as $N_{pl,imp}/N_{pl}$) and for one under uniform bending (as $M_{pl,imp}/M_{pl}$) representing 'plastic imperfection sensitivity' relationships for medium-length cylinders with a 'Type A' midspan weld depression imperfection.

The modelling techniques of a number of precursor studies (Sadowski & Rotter, 2013; Fajuyitan & Sadowski, 2018; Fajuyitan, 2018; Wang *et al.*, 2020) were adopted which assumed planes of meridional and circumferential symmetry leading to a quarter-cylinder model with details as illustrated in Fig. 4.6. Such modelling schemes have additionally been employed by independent FEA examinations of cylindrical shells (Guggenberger, 1995; Knebel & Schweizerhof, 1995; Goto & Zhang, 1999) for an assortment of loading scenarios, demonstrating the effectiveness of leveraging planes of symmetry in numerical simulations.

Two sets of GNIA and GMNIA analyses (approximately 650 of each) were performed to generate capacity curves for medium-length cylinders with $\Omega = 0.5$ under uniform bending, with r/t ratios varying from 10 to 700 at constant δ_0/t for an axisymmetric 'Type A' weld depression imperfection applied at the midspan varied from a nominally perfect 0.001 to a highly imperfect 5.0. The ABAQUS implementation of the Riks (1979) arc-length algorithm was used. The end moment M [FL] was applied as

$$M = \min(M_{pl}, M_{cl}) \text{ where } M_{pl} = (4r^2t + \frac{1}{3}t^3)f_{yk} \text{ and } M_{cl} = \frac{Ert^2\pi}{\sqrt{3(1-\nu^2)}} \tag{4.6}$$

depending on λ. Where the half-length $L/2$ of the cylinder exceeds the linear meridional bending half-wavelength Λ (Eq. 4.4) by a factor of 12, zones of mesh refinement are introduced near the boundary layer (to better capture bending effects here, although the material definition in this region was kept elastic to prevent premature buckling under high surface yielding) and near midspan (to better capture local buckling at the imperfection, see Fig. 4.6). The bilinear multi-purpose reduced integration S4R shell element was employed throughout, capable of modelling both thick and thin shell behaviour (Sadowski & Rotter, 2013) although the focus here is initially on the region of the capacity curve representing thin shells, following a resolution of at least 10 elements per Λ with an elastic boundary layer enforced near the loaded edge to avoid premature buckling in this location. For cylinders with a modelled half-length $L/2$ shorter

that 12Λ, a uniform mesh resolution was applied along their meridian.

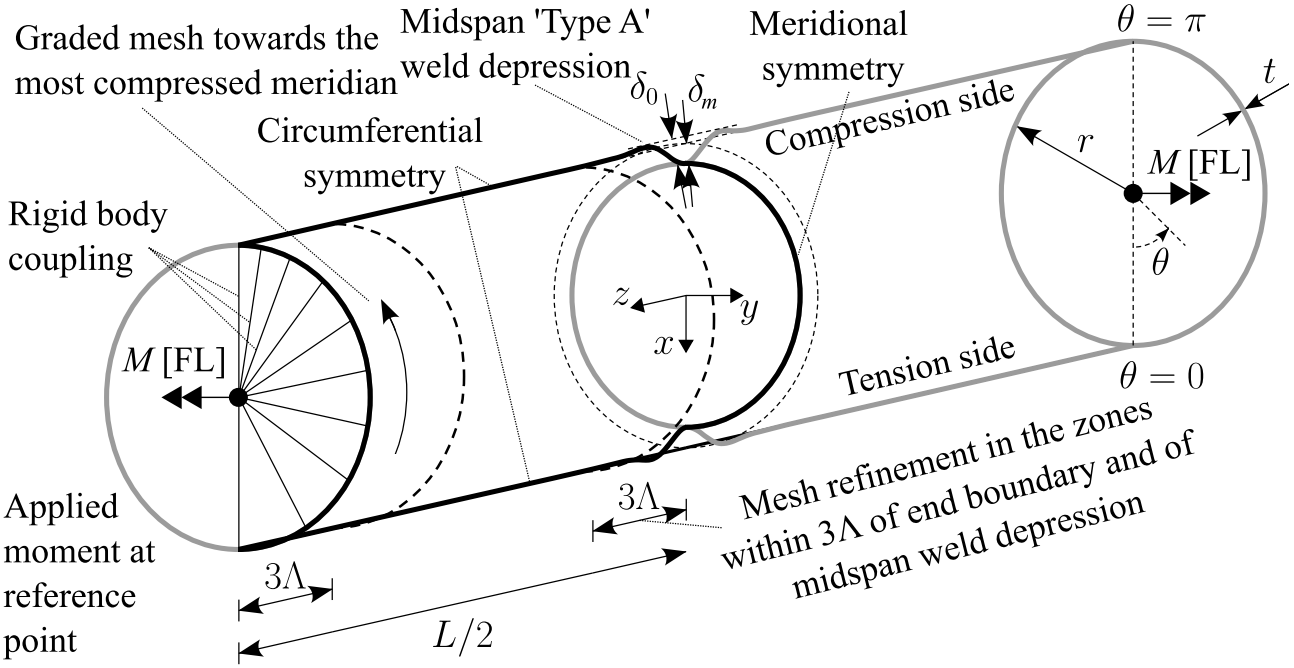


Figure 4.6: Quarter-shell finite element model of a medium-length imperfect cylinder under uniform bending. The full cylinder is shown with grey solid lines denoting complete represented geometry and black solid lines denoting actually modelled quarter-shell geometry using ABAQUS.

The proposed relationship for $\kappa_{thin} = M_{pl,imp}/M_{pl}$ of Wang *et al.* (2020) for thin shells was adopted here to permit a consistent illustration of the capacity curves for both systems under consideration in terms of the most complete formulation of the capacity curve framework (Eq. 2.24). This relates the full plastic moment of the *imperfect* cylinder $M_{pl,imp}$ to the perfect value for a thin shell $M_{pl} = 4r^2 t f_{yk}$ as:

$$\kappa_{thin} = 0.2 + \frac{0.8}{1 + 0.014(\delta/t)^{0.2} + 0.23(\delta/t)^2} \tag{4.7}$$

and is illustrated in Fig. 4.5 where it is shown to be a more deleterious relationship than the corresponding one for uniform meridional compression.

4.2.3 A comparison of the α_G, α_I and β capacity parameters for cylinders under uniform meridional compression vs uniform bending

The high performance computing cluster of Imperial College London was used throughout to efficiently generate all capacity curves for the two reference cylindrical shell systems introduced above. It is stressed that the computed capacity curves that follow are strictly *not* the same relationships that would be obtained using the algebraic form (Eq. 2.24) with the aid of the capacity parameters as currently codified in EN 1993-1-6 (2025) which contain additional conservative assumptions and simplifications.

An illustration of the capacity curves for both systems under nominally perfect conditions (negligible midspan imperfection with $\delta_0/t = 0.001$ for which $\kappa_{thin} \approx 1$) is given in Fig. 4.7 in both χ vs λ and χ vs ψ representations. The value of the dimensionless resistance χ (relative to the reference plastic collapse condition) at which plasticity first begins to have a significant affect

is identified by $1-\beta$. For either of the systems under consideration here, the theoretical value of $1-\beta$ can be obtained by considering simple beam theory as R_{el}/R_{pl}, where R_{el} is the resistance at first yield. For a thin circular hollow section (CHS) under a uniform axial (longitudinal if referring to a beam under compression model) force, the cross-sectional meridional stress state is uniform and the force at first yield is synonymous with that at complete cross-sectional yield, such that:

$$1-\beta=\frac{N_{el}}{N_{pl}}=\frac{2\pi rtf_{yk}}{2\pi rtf_{yk}}=1. \tag{4.8}$$

By contrast, for a thin CHS under bending the moment at first yield is significantly below that necessary to cause full plastification of the cross-section:

$$1-\beta=\frac{M_{el,thin}}{M_{pl,thin}}=\frac{\pi r^2tf_{yk}}{4r^2tf_{yk}}=\frac{\pi}{4}\approx 0.79. \tag{4.9}$$

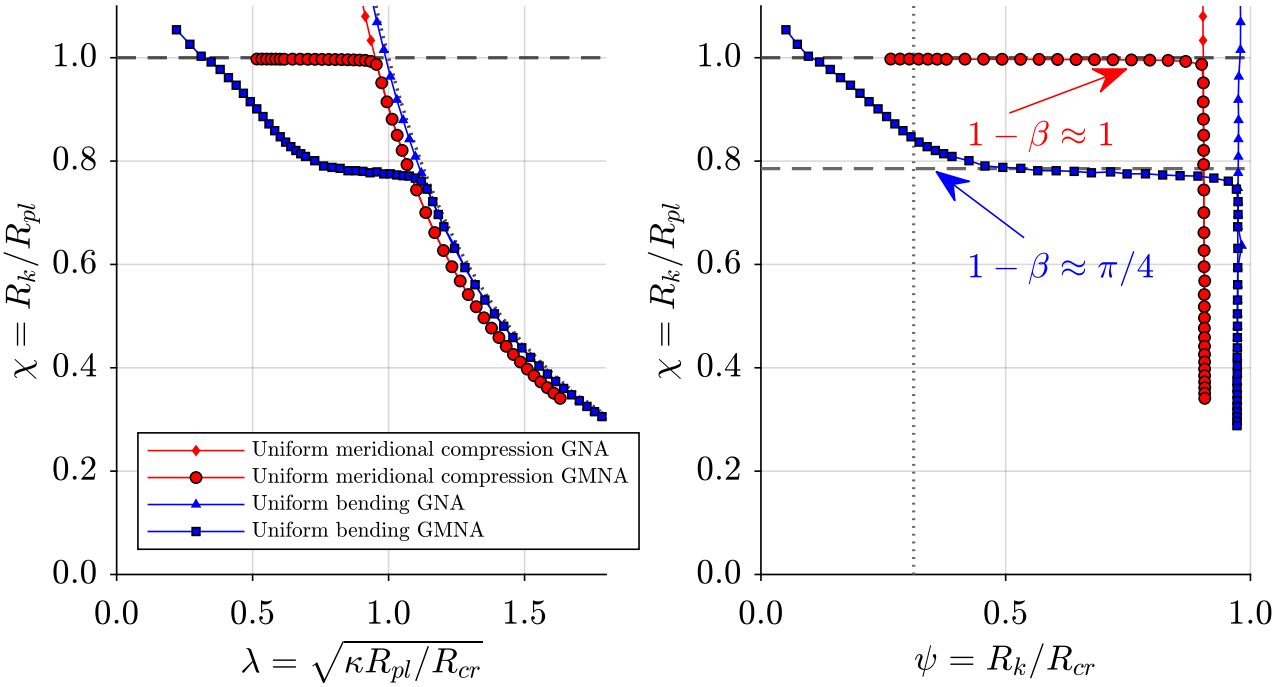


Figure 4.7: A comparison of computed capacity curves for nominally perfect ($\kappa \approx 1$) medium-length cylinders ($\delta_0/t = 0.001$, $\Omega = 0.5$) under uniform meridional compression (red, computed with AQUINAS) or uniform bending (blue, computed with ABAQUS).

In a like-for-like comparison of dimensionless capacity relationships for both systems expressed on the same axes, the curve for a cylinder under uniform bending must begin plastifying at a dimensionless resistance χ approximately 20% lower than the curve under uniform meridional compression, and the curve for uniform bending in the range $\lambda_0 < \lambda < \lambda_p$ should then fall mostly below that for uniform meridional compression. The curves shown in Fig. 4.7 computed with GMNA suggests that this is indeed the case over most of the intermediate slenderness range, and for this reason alone it is more conservative to specify the capacity curve for uniform bending as the 'default' relationship (say, for an LBA-MNA buckling check) in this slenderness range rather than the curve for uniform meridional compression as was done prior to EN 1993-1-6 (2025). It is reminded that the actual codified rule asks that the 'default' be the *minimum* χ of both capacity curves at any λ, since they do not share the same value of λ_p.

An interesting point of discussion concerns why the curve for uniform bending suggests that cylinders are affected so strongly by even very modest plastification of the circumference (represented in the codified capacity parameters by $\eta_p < 1$), and why a significant portion of this relationship in the intermediate slenderness region remains near-horizontal around the first yield moment. This 'first yield plateau' has been described in some depth in Wang *et al.* (2020), but the opportunity is taken here to supply additional insight in light of the striking contrast between both capacity curves. The variation in slenderness λ was achieved by varying the r/t ratio, with high r/t corresponding to high λ and thus the right-most parts of either curve. In the high slenderness region, both reference systems exhibit elastic short-wave buckling modes whose circumferential half-wavelengths are well defined and proportional to $\sqrt{rt}$. For uniform meridional compression, these are classical 'chequerboard' modes that are periodic around the circumference, while for uniform bending these are localised modes on the compressed side.

As r/t and λ both decrease towards the left-most parts of the capacity relationship, the individual short-wave buckles begin to cover a larger portion of the circumference $2\pi r$ since $\sqrt{rt}/r = \sqrt{t/r} \to \infty$ as $r/t \to 0$. However, in the vicinity of λ_p the cylinders are still quite thin with a localised critical buckling mode that still occupies only a small portion of the total circumference, such that even partial plastification of the circumference already implies a significant plastification of this very localised buckle (Fig. 4.8), and it is for this reason that the buckle forms very soon after first yield. As r/t decreases, both the circumferential extent of the plastification and the localised buckle grow at approximately similar rates leading to only a negligibly upward change in χ from the first yield moment and creating a 'plateau' around this value. As r/t drops further, the buckling mode eventually occupies most of the compressed circumference and ultimately transforms into a partial plastic hinge involving yielding on the tension side, which is when the curve begins to rise off the plateau towards $\chi = 1$.

A more complete set of computational capacity curves for both reference systems are presented in both formats in Fig. 4.9 for a varying imperfection amplitude. These illustrate that the 'first yield plateau' phenomenon persists for increasingly imperfect systems, ensuring that $1 - \beta$ is always lower for cylinders under uniform bending than under uniform meridional compression. By contrast, the elastic imperfection sensitivity continues to be more critical for uniform meridional compression as is evident by this system having the lower $\alpha_G\alpha_I$ product. The variation of both α_I (the relevant capacity parameter for $\lambda \geq \lambda_p$) and $1 - \beta$ (the relevant parameter for $\lambda_0 < \lambda < \lambda_p$) with δ_0/t is illustrated in Fig. 4.10, and illustrates why the 'default' capacity curves in EN 1993-1-6 (2025) have now been chosen more carefully as described earlier. The behaviour seen for $\delta_0/t \geq 4$ is out of scope of the present discussions but it is a consequence of increasingly imperfect shells exhibiting increasingly long-wave buckling modes which begin interacting with boundary conditions (e.g. see Figure 8 in Rotter & Teng (1989)).

4.3 On complications in the generation of computational capacity curves

The successful generation of a complete capacity curve places a particularly high demand on the finite element software, which must offer a high-quality plane stress shell element formulation supporting a correct (or at least accurate) doubly-curved geometry and finite strains capable of modelling nonlinear collapse with extensive yielding, elastic-plastic and entirely elastic bifurcation and limit-point buckling limit states, each of which is governed by different termination criteria (Sadowski *et al.*, 2017a) and is sensitive to different nonlinear solvers and different hyperparameters in different ways. A selection of the author's experiences in generating computational capacity curves for metal shell systems is shared here, in part to caution the

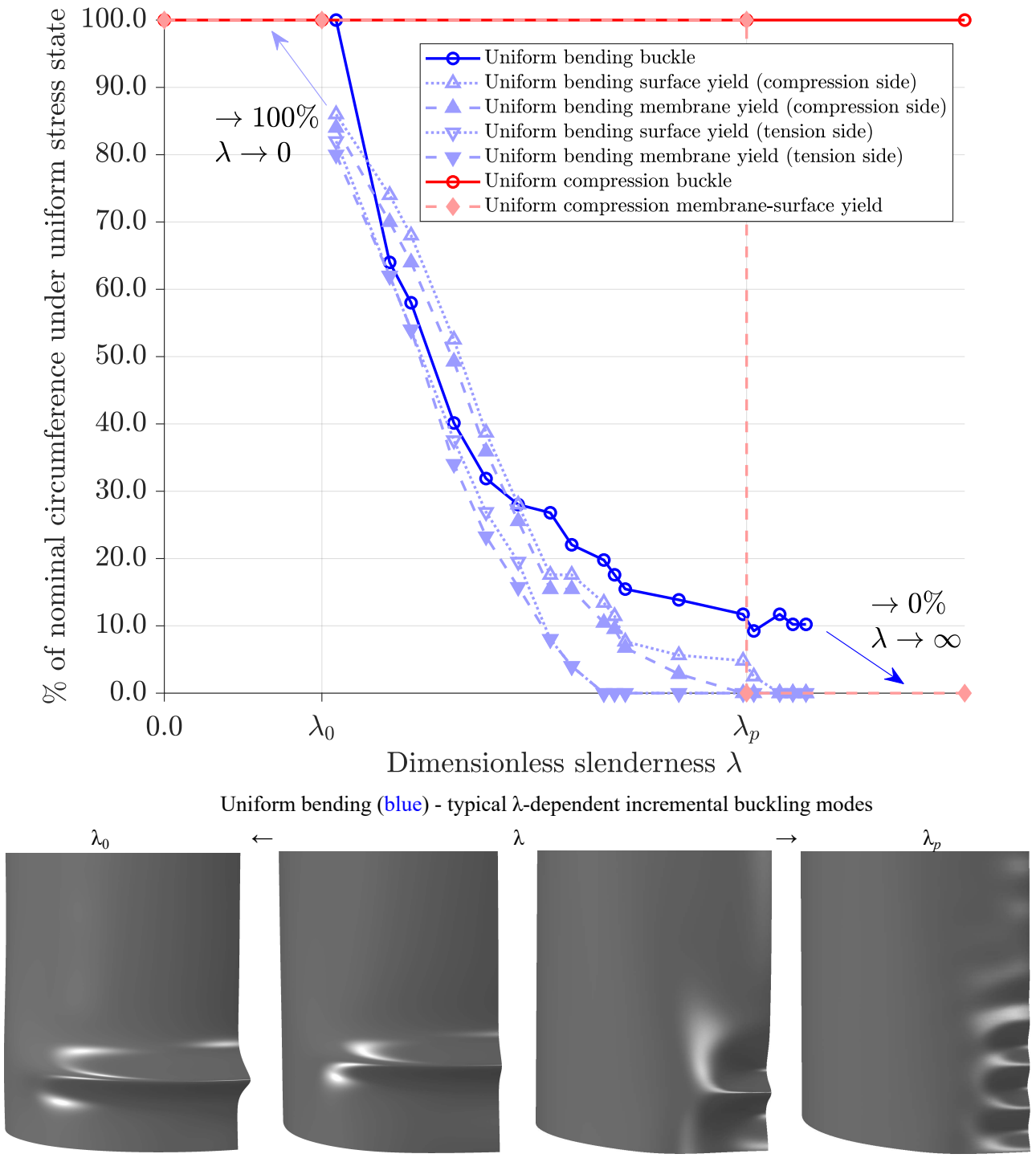


Figure 4.8: Portion of cylinders' circumferences under compression participating in critical buckling and compression or tension participating in yielding, with associated representative λ-dependent bifurcation or incremental buckling modes.

unwary against very subtle pitfalls which are easily made that can lead to seriously erroneous simulations, and in part to draw attention to what appears to be a worrying lack of ongoing development in core solver capabilities in the most popular commercial finite element software.

What follows employed a reference λ-dependent meshing scheme motivated by well-established mechanical and finite element analysis principles, already implemented in ABAQUS 2022 during the investigations of the α_I and $1-\beta$ relationships for medium-length cylinders under bending just presented (Figs 4.7 to 4.10) and now extended for implementation using ANSYS (2022)

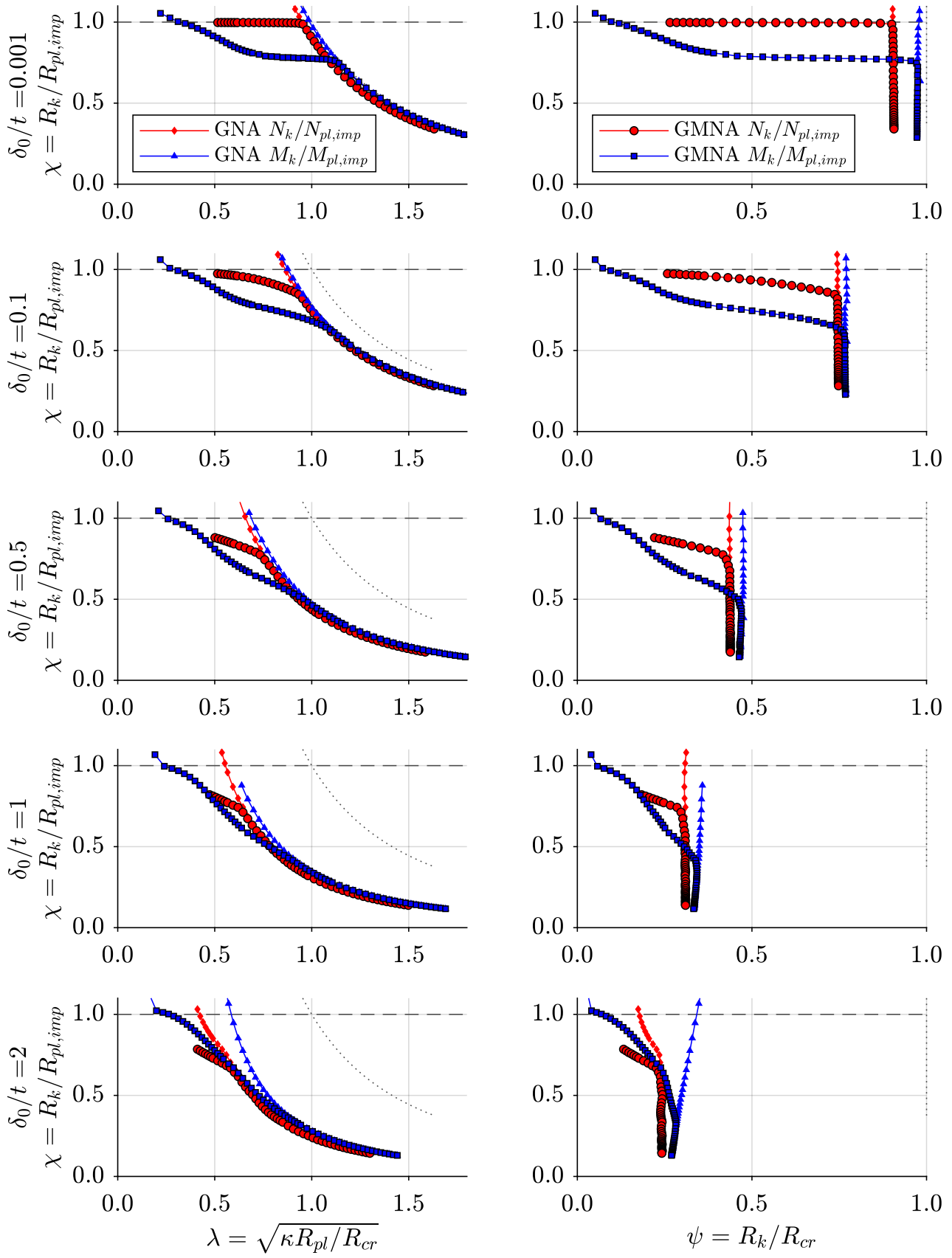


Figure 4.9: Dimensionless capacity curves for cylinders under uniform meridional compression (red) and uniform bending (blue) for a constant dimensionless group $\Omega = 0.5$ and varying imperfection amplitude δ_0/t.

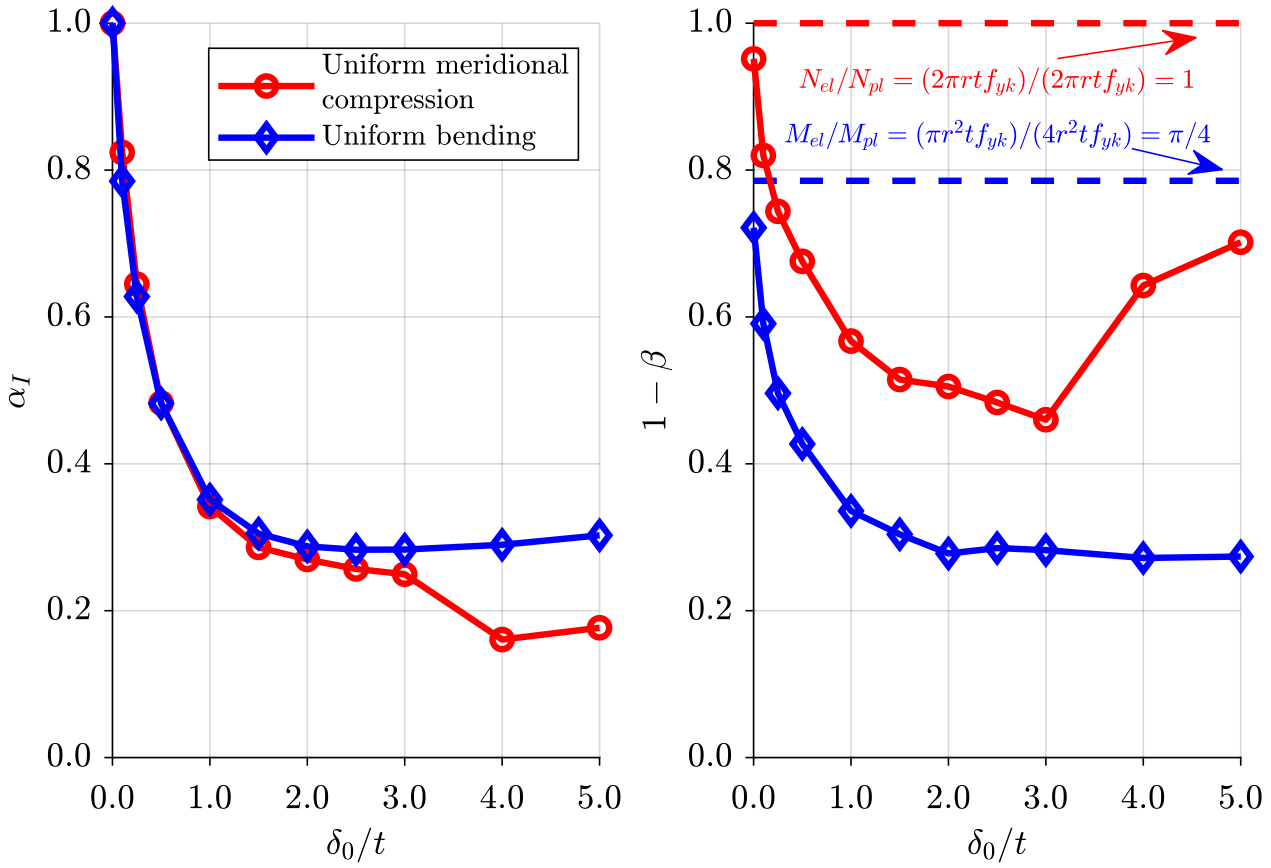


Figure 4.10: Computed 'elastic imperfection reduction' α_I and corresponding 'plastic range' $1-\beta$ parameters for varying imperfection amplitude δ_0/t.

under as similar a set of settings as was possible (which include the use of its arc-length solver (Forde & Stiemer, 1987)) to offer a comparison between the arguably two most popular and powerful commercial finite element codes. This reference scheme employed, circumferentially, 50 uniformly distributed (unit grading bias) bilinear elements (S4R in ABAQUS, SHELL181 with one Gauss point in ANSYS with MPC184 for rigid body constraints, see Fig. 4.6) for cylinders expected to develop considerable plasticity (i.e. when $M_{pl} < M_{cl}$, Eq. 4.6), but 75 elements with a grading bias gradually increasing up to a factor of 10 once local buckling is deemed to be the more critical condition (i.e. when $M_{cl} < M_{pl}$, Eq. 4.6). The meridional discretisation followed a similar pattern, with either 200 elements uniformly distributed along the modelled length if $L/2 < 12\Lambda$, or otherwise 100 elements in the middle region of the quarter-shell models and zones of refinement with 30 elements (10 elements per Λ) near the (elastic) loaded edge and the weld depression. For more slender shells such that $M_{cr} < M_{pl}$ a further refinement was applied, with 36 elements near the weld-depression zone and 120 along the middle region of the meridian (20% increase), aiming to better capture the expected localised buckles. A relatively coarse initial load step of 0.05 was used for the stockier models ($M_{pl} < M_{cl}$) predicted to reach a plateau in their equilibrium path, with the load step steadily reducing in size with increasing λ eventually attaining a value of 0.005 for cylinders expected to fail by elastic buckling ($M_{cr} < M_{pl}$). The effect of varying these modelling assumptions 'one at a time' will be scrutinised in the following section.

4.3.1 Sensitivity to initial conditions

The main theme in what follows is that the computed buckling load may be very sensitive to what are arguably only minor changes in the initial conditions which, concerningly, prevailing knowledge would suggest should only be *beneficial* to the buckling load prediction. For example, consider a selection of capacity curves for cylinders under uniform bending generated by varying r/t to vary the slenderness λ according to the reference meshing scheme exactly as just described except for one factor which is permitted to vary in a 'one-at-a-time' fashion. Four such factors were investigated. In the below the 'reference capacity curve' is the result from Fig. 4.7.

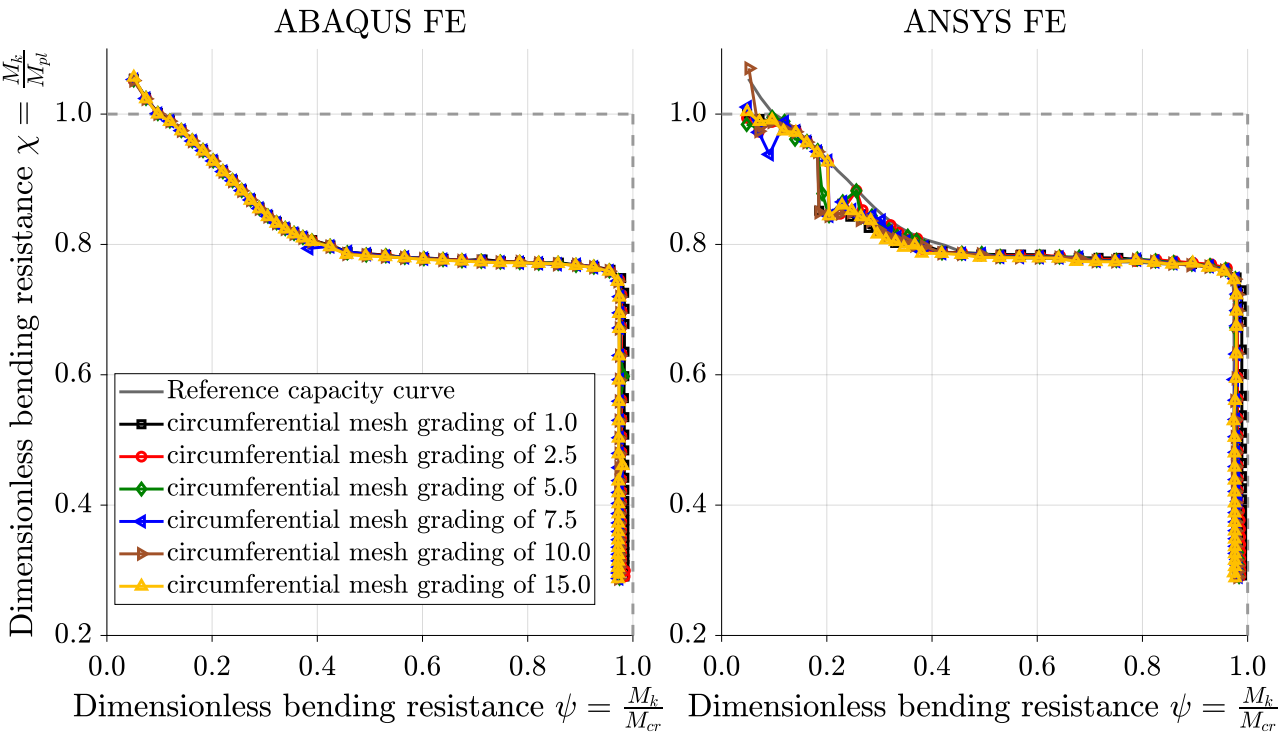


Figure 4.11: A comparison of computed capacity curves for nominally perfect cylinders under uniform bending in the 'modified' χ vs ψ format for constant *dof* counts but varying circumferential mesh gradings, compared against the reference capacity curve.

The first factor to be investigated was the circumferential mesh grading bias, varying from a value of 1.0 (no circumferential mesh bias with a uniform circumferential node spacing) to 15.0 (mesh highly biased to be concentrated near the compressed meridian) as shown in Fig. 4.11, without an overall increase in the total *dof* count at any λ. As the ultimate limit state is controlled by buckling on the most compressed meridian (Fig. 4.8), the buckling load prediction *should* improve as the mesh resolution of this region is increased locally in the buckling-critical region through the higher grading bias. This is indeed the case in the elastic (right-hand side) portion of the curve, where the increased bias reduces the stiffness of the mesh in the vicinity of the critical buckling region and leads to a more conservative (and correct) elastic bifurcation buckling load prediction. However, the elastic-plastic (left-hand side) portion of the curve as computed by ANSYS appears to exhibit several erroneous predictions suggesting a non-physical non-smooth χ vs. ψ relationship, predictions which clearly do *not* improve with local mesh refinement.

The second factor is the circumferential mesh resolution, varying from 25 to 100 elements around the circumference as shown in Fig. 4.12. The issue of non-physical elastic-plastic buckling predictions persists for ANSYS, and increasing the circumferential mesh resolution does not necessarily correct a non-physical result and may even degrade a previously-physical simulation.

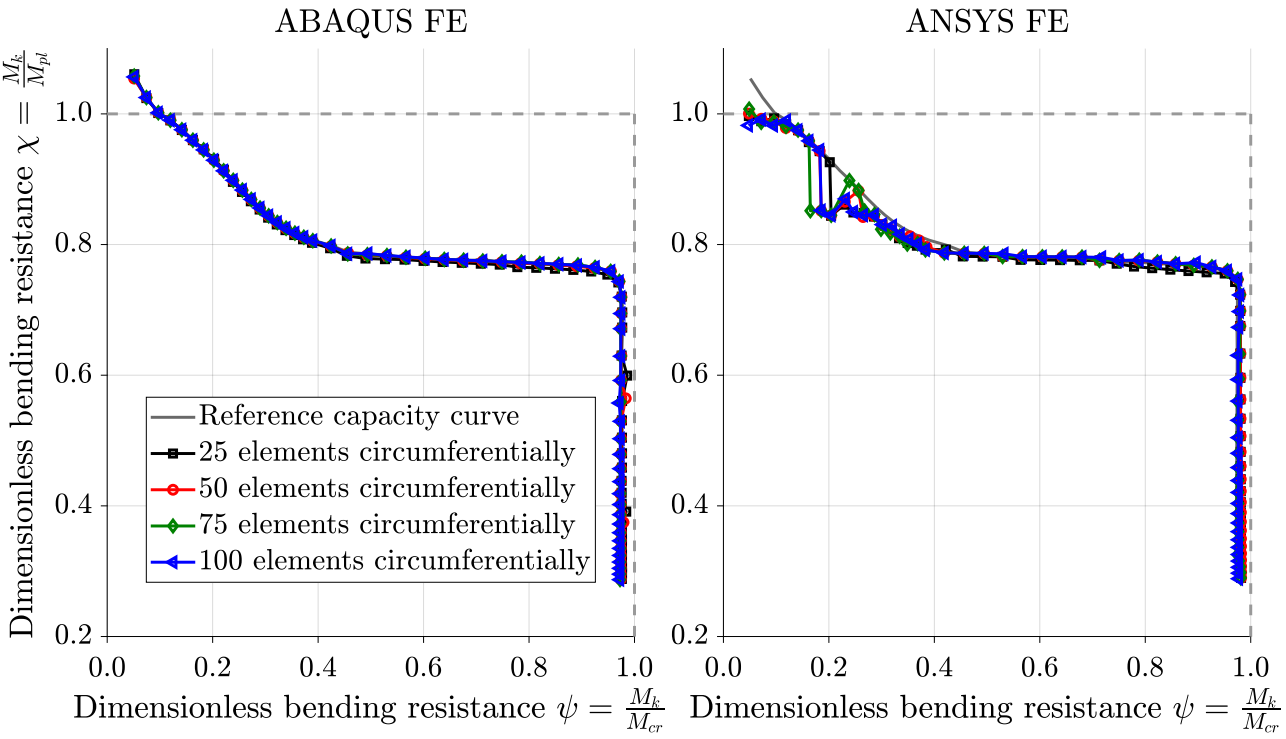


Figure 4.12: A comparison of computed capacity curves for nominally perfect cylinders under uniform bending in the 'modified' χ vs ψ format for an increasingly refined circumferential mesh resolution, compared against the reference capacity curve.

A similar phenomenon is seen if the meridional mesh resolution is treated as the (third) varying factor, assuming a uniform meridional meshing scheme for short cylinders where $L/2 < 12\Lambda$ and a three-part partitioned scheme for longer ones (a refined elastic boundary layer 3Λ from the loaded edge, and a refined critical buckling region 3Λ from midspan, see Fig. 4.6), varying as shown in Fig. 4.13.

The fourth and most alarming factor is the maximum load increment, here made to vary from 0.1 (10% of the applied reference moment at that slenderness, see Eq. 4.6) to 0.001 (0.1% thereof) as illustrated in Fig. 4.14. Reducing the maximum load increment, which would be expected to permit the solver to trace a higher-resolution pre-buckling equilibrium path and thus be more likely to accurately capture sharp bifurcation buckling events, leads to extremely incorrect elastic-plastic buckling predictions for both ABAQUS and ANSYS.

It is difficult to offer a definitive explanation for this behaviour given that the analyses are done with commercial software and no access to the core solver routines is possible. However, the one thing that each of the above comparisons has in common is that what *should* lead to an improved prediction (higher mesh resolution, reduced load increment) is also what causes the solver to perform more floating-point arithmetic, either by operating on a larger matrix system or by operating on an existing system more frequently. Either because this causes the numerical solution to accumulate more parasitic round-off error, or for some other reason, this appears to have a deleterious influence on solution quality and on the elastic-plastic buckling prediction in particular, perhaps because the latter involves yield surface state determination calculations which appear to be particularly numerically sensitive. This phenomenon is both under-explored and, for as long as the shell buckling discipline continues to use solely commercial solvers for its research needs, unfortunately largely beyond the analyst's control.

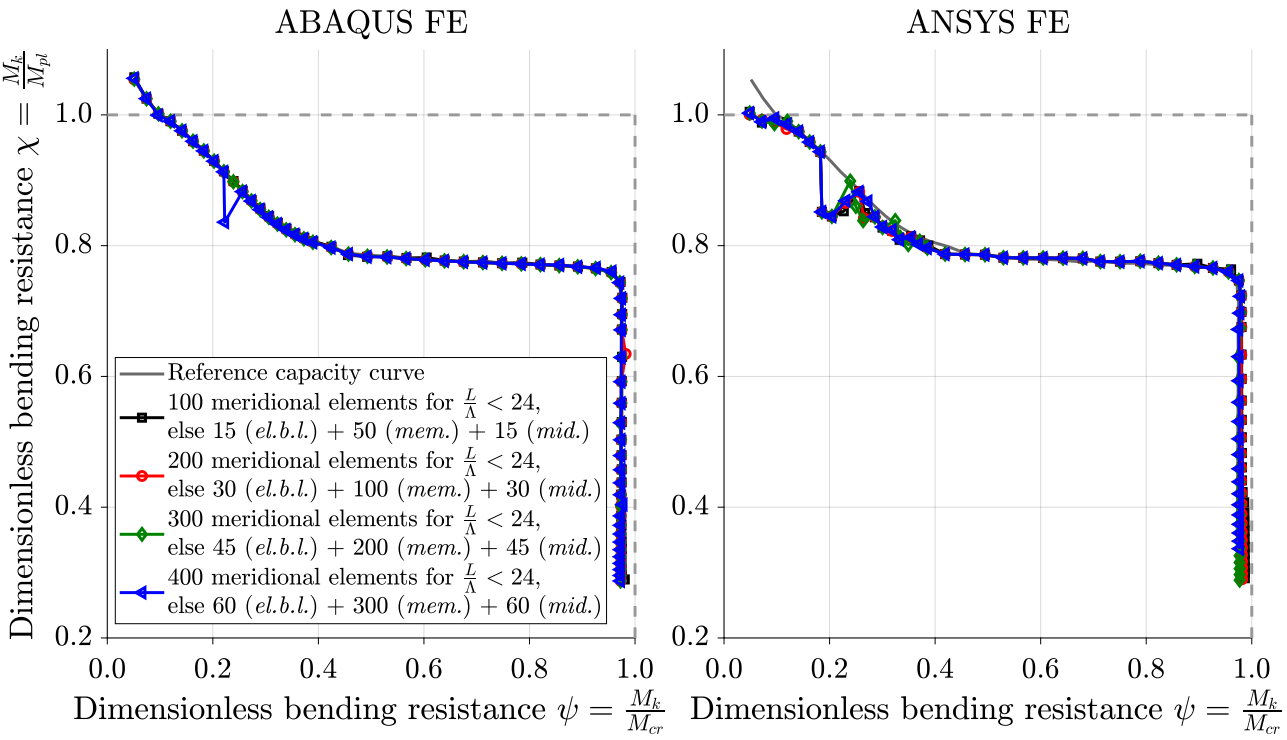


Figure 4.13: A comparison of computed capacity curves for nominally perfect cylinders under uniform bending in the 'modified' χ vs ψ format for an increasingly refined meridional mesh resolution, compared against the reference capacity curve.

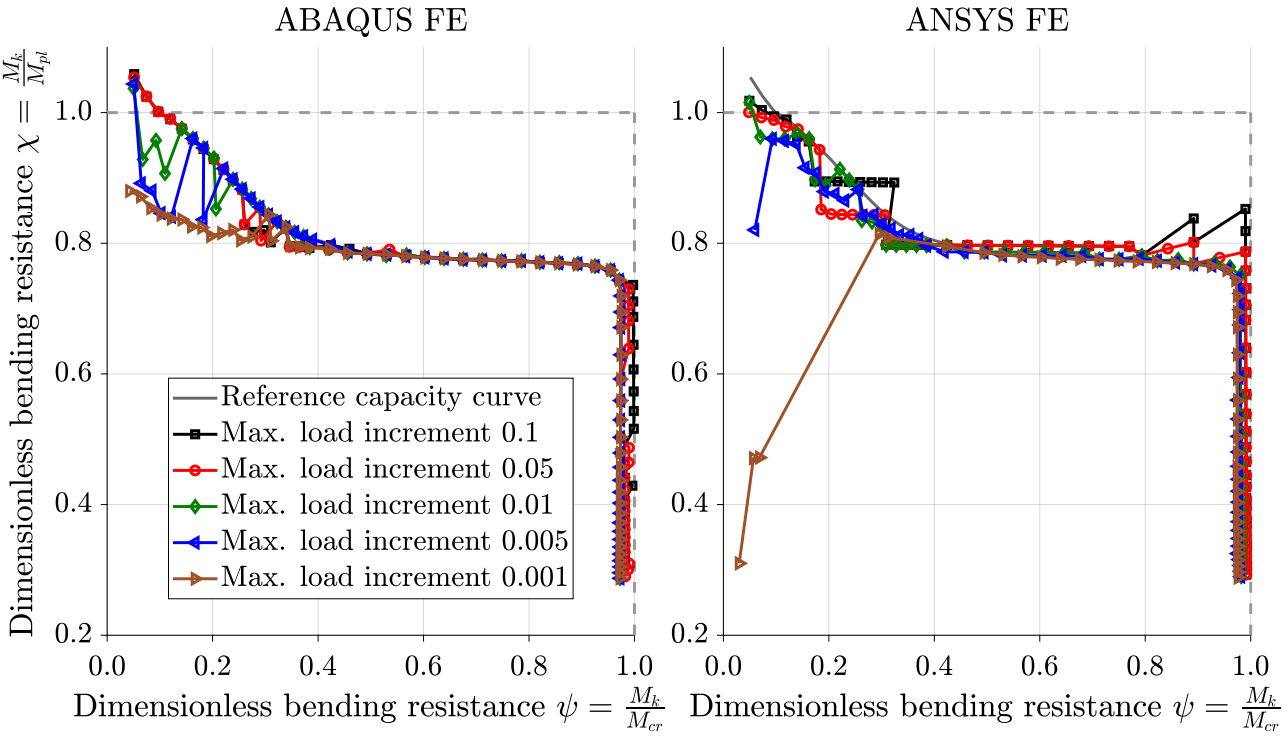


Figure 4.14: A comparison of computed capacity curves for nominally perfect cylinders under uniform bending in the 'modified' χ vs ψ format for increasingly fine max. load increments at constant mesh resolution, compared against the reference capacity curve.

4.3.2 Alternative generation strategy based on varying f_{yk}

It has been emphasised in a number of publications by J.M. Rotter (Rotter, 2007, 2010a, 2016b, 2017) on the evolution of the capacity curve framework for shell buckling that an alternative,

and from many aspects more advantageous, methodology to generate computational capacity curves involves varying the yield stress f_{yk} in order to vary the dimensionless slenderness λ. This may be motivated from Eq. 2.26 by realising that:

$$\lambda = \sqrt{\frac{\kappa R_{pl}}{R_{cr}}} \propto (\frac{r}{t})^a \sqrt{\frac{f_{yk}}{E}} \tag{4.10}$$

where $a > 0$ is some real scalar, since the two reference resistances R_{pl} and R_{cr} will always be linear in the yield strength f_{yk} and elastic modulus E respectively. Thus a varying λ may be achieved either by keeping the material properties constant and varying r/t as has frequently been done until now (here and in Chen *et al.* (2008); Wang *et al.* (2020)), but equally it may be achieved by keeping r/t constant and artificially varying f_{yk} (or indeed E) to even entirely physically unrealistic ranges (a successful example of this approach may be found in Doerich & Rotter (2008) for bracket-supported silos). While this means of generating theoretical capacity curves is entirely defensible on the grounds of mechanics and has the significant benefit of maintaining a genuinely constant geometry (L, r and t), geometric nonlinearity (α_G) and imperfection sensitivity (α_I) at all slendernesses as well as an invariant mesh, it is difficult to recommend it for the purposes of creating generic design curves for applications whose slendernesses are strongly correlated with the actual r/t and which then naturally occupy different regions of an r/t-dependent capacity relationship.

An example of capacity curves generated by varying f_{yk} for different constant r/t and nominally perfect cylinders under bending is presented in Fig. 4.15 below, obtained using ABAQUS. High-λ slender shells are achieved with exceptionally high values of f_{yk}, while low-λ stocky shells are achieved with values of f_{yk} approaching zero. A slightly different meshing scheme was adopted to that used previously (Fig. 4.6), where the meridian was meshed uniformly when it was relatively short such that $L/2 < 10\Lambda$, but cylinders longer than this had regions of refinement within 3Λ of the end (with an elastic material definition for the bending boundary layer to prevent premature buckling being triggered in this location) and within the midspan. By combining the definitions of the dimensionless length group $\Omega = \frac{L}{r}\sqrt{\frac{t}{r}}$ and the linear bending half-wavelength Λ (Eq. 4.4), it may be shown that:

$$\frac{L}{\Lambda} = \frac{[3(1-\nu^2)]^{1/4}}{\pi}\Omega\frac{r}{t} \approx 0.41\Omega\frac{r}{t} \tag{4.11}$$

for $\nu = 0.3$ such that for $\Omega = 0.5$ (medium-length non-ovalising cylinders), $L/2 < 10\Lambda$ if $r/t < 97.8$. From the perspective of computational efficiency, the smallest meshes are achieved for the thickest cylinders and the incentive when using varying f_{yk} to generate capacity curves would thus be to minimise r/t. However, capacity curves for $r/t < 97.8$ represent cylinders that are so short in terms of L/Λ that, according to the present meshing scheme, they undergo premature buckling within the elastic-plastic bending boundary layer which is manifest as a smoothening of the sharp $1-\beta$ point of the capacity curve. The curve for an exceptionally thick cylinder with $r/t = 10$ even significantly overestimates the elastic buckling resistance ($\psi > 1$), since the reference 'thin shell' M_{cl} result (Eq. 4.6) ignores the effect of transverse-thickness shear strains and is thus an increasingly stiff prediction for this reference resistance for low-r/t shells.

For thinner shells with $r/t \geq 100$, the sharp $1-\beta$ point is captured correctly but increasing r/t predicts that the 'first yield plateau' of resistances at $\chi \approx \frac{\pi}{4} \approx 0.79$ (Eq. 4.9) occurs over an increasingly wide range of λ. This is because at constant r/t the size of the critical buckle

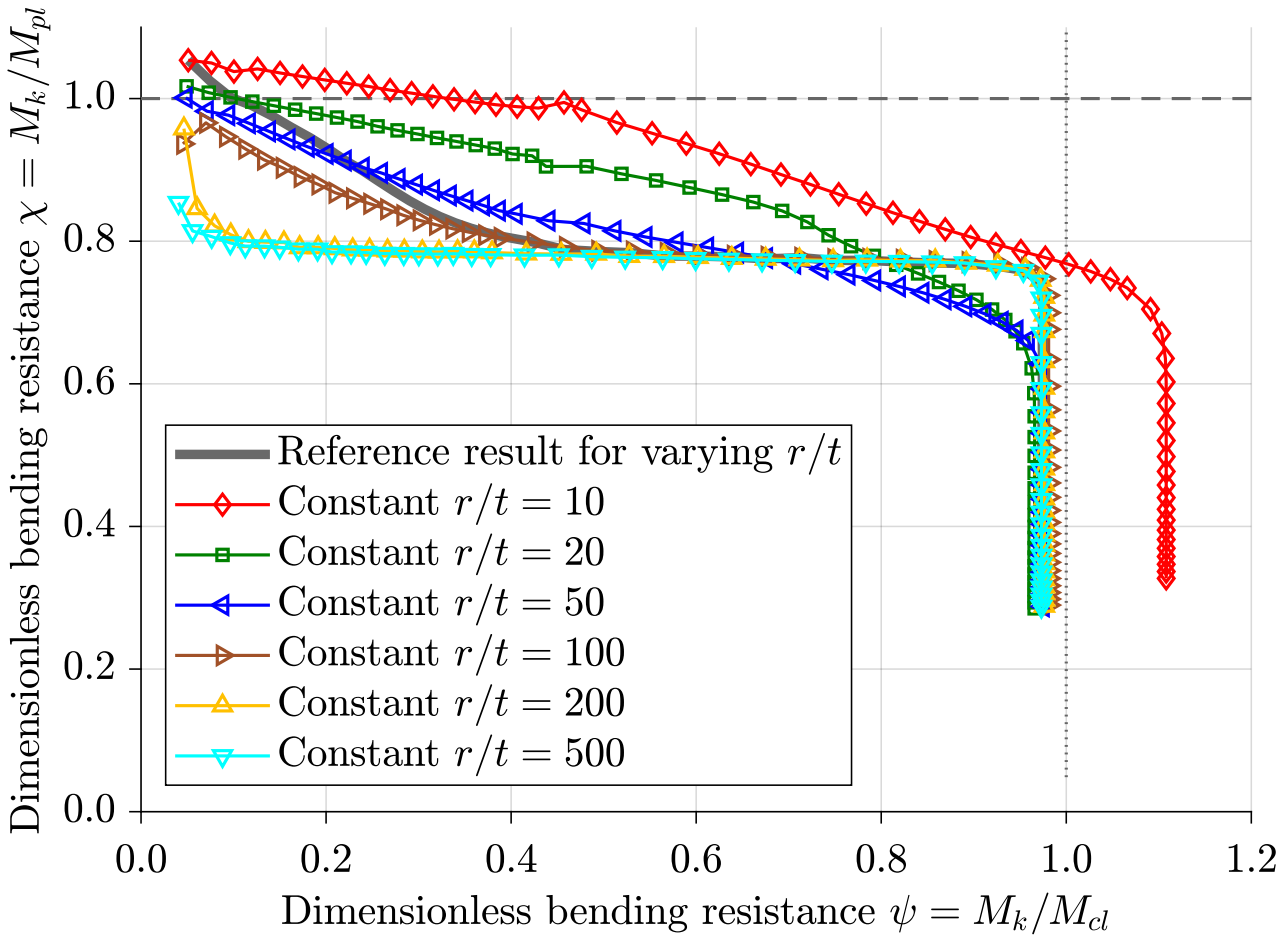


Figure 4.15: A comparison of computed capacity curves for nominally perfect cylinders under uniform bending in the 'modified' χ vs ψ format generated by varying f_{yk}, compared against the reference capacity curve generated by varying r/t.

relative to the circumference is now entirely invariant with λ, and as f_{yk} and λ both tend to zero the (increasingly small, with increasing r/t) portion of the circumference necessary to have yielded enough to fully enclose a critical buckle almost does not change at all. Unfortunately, as the constant r/t is increased further it becomes increasingly more difficult numerically to obtain acceptable solutions for very low λ values by varying f_{yk}, and it was not possible to obtain any results for $\chi \geq 1$ or estimates for λ_0. The Authors' recommendation is that this methodology is *not* applied for the generation of generic capacity curves for fundamental reference systems to allow specific structural applications to consume a buckling resistance that is representative of their characteristic r/t, and that it is reserved for specialised and genuinely fixed-geometry applications such as construction details or other localised components (e.g. Doerich & Rotter (2008)).

4.3.3 Limitations of the AQUINAS thin shell element formulation for low slenderness cylindrical shells

The preceding discussion of Section 4.2.1 suggested that the AQUINAS FE results for low r/t cylindrical shells under compression were entirely excluded after deemed unsuitable to describe the relationship of the dimensionless resistance χ against the slenderness λ of those models. While indeed the lack of a clearly identifiable λ_0 slenderness in the generated capacity curves (as the closer examination of results that shortly follows will illustrate to be the case) would not

interfere with the narrative and conclusions of this study, it is of paramount importance to the developers of AQUINAS for this scientific toolbox to be a reliable predictor of an axisymmetric shell's resistance across the full range of the slenderness spectrum, as has been reiterated at various points over this document. Estimation of a stockier cylindrical model's resistance through a GMN(I)A introduces considerable challenges to any computational software, from the incrementation algorithm implemented to the accuracy of elastoplastic strains integration and accumulation of numerical errors due to the inevitable approximations that convergence checks are accompanied by. Even if stability considerations are not critical for low slenderness cylinders under compression, geometrically nonlinear contributions to the stepwise evaluated strains can influence tracing of the equilibrium path and subsequent estimation of the cylinder's critical resistance R_k. A suitable set of nonlinear kinematics is therefore essential, even when the resistance of the cylinder R_k is expected to align with the full plastic resistance R_{pl}.

The natively axisymmetric model of Fig. 4.3 shall be revisited and submitted for a selection of MNAs and GMNAs, limited to r/t ratios that are associated with low slenderness cylindrical shells. Due to the finite length of those models L and its relationship with the bending half-wavelength Λ, partitioning of the edge and midspan weld depression boundary layers is omitted for all slendernesses considered, as for an $\Omega = 0.5$ and $r/t \in [10, 100]$ the corresponding ratios $L/2\Lambda \in [1.02, 10.2]$ do not permit a 3Λ partition at both ends of the half-modelled meridian $L/2$ for most of the cylindrical models. Early onset of plasticity effects in the compatibility bending boundary layer of the loaded edge can lead to premature buckling due to the softening of material stiffness in that neighbourhood, undermining the overall strength of the model (as discussed earlier in this chapter for both load cases, also addressed in Wang *et al.* (2020)). While such developments of material nonlinearities can potentially lead to erroneous estimations of the λ_0 slenderness at which the cylindrical models first achieve their full plastic resistance, the unsuitability of the AQUINAS solution for stocky models cannot be credited to this behaviour, as the comparative review with the ABAQUS (2022) software in Figure 4.16 illustrates.

Axisymmetric models generated through both AQUINAS and ABAQUS were submitted to three sets of analyses, an MNA with an elastic-perfectly plastic material law, as per the guidance of EN 1993-1-6 (2025), a GMNA with the same material law incorporated and a GMNA under the more realistic (Sadowski *et al.*, 2017b) bilinear stress-strain curve with 0.1% isotropic strain hardening. To allow for a direct comparison of the two numerical solutions, bifurcation checks in AQUINAS are restricted to only detect $n = 0$ axisymmetric buckling modes. The FE results presented in Fig. 4.16 show that in the absence of geometrical nonlinearities the two solvers are in relatively good agreement, accurately computing the full plastic resistance through their corresponding MNA solutions (n.b. the over-prediction of R_{pl} for the stockiest models considered reflects the influence of end boundary restraints in strengthening the cylindrical shell). Intuition would suggest that a GMNA with no strain hardening should provide ultimate resistance predictions relatively close to the MNA result for the thicker models, but to progressively diverge for increasing slendernesses and generate strength estimates of higher conservativeness. This is due to not only potential instability phenomena near the softened bending compatibility layer but also to the more pronounced geometrically nonlinear effects that an increase in cylinder slenderness is accompanied by. Whilst a similar behaviour is clearly observed in the AQUINAS results as the r/t ratios increase, there does not seem to be any agreement between the two nonlinear solutions for the stockier models. As the AQUINAS cylinders never attain their full plastic resistance R_{pl} for a dimensionless resistance $\chi = 1.0$, determination of a reasonable, physically interpretable value for the λ_0 slenderness becomes impossible. The introduction of isotropic strain hardening does not seem to provide enough of a stiffening effect for the GMNA solution to confidently intersect the $\chi = 1$ dimensionless resistance, whereas the axisymmetric solution of ABAQUS once again provides a reliable nonlinear evaluation of a cylinder's squash

load for $h = 0.1\%$. Introduction of material strain hardening into the modelling process leads to stiffening behaviour and higher resistance estimates for both solvers, as should be expected from any robust integration algorithm of strains in plasticity regardless of method implemented to do so (i.e. the sub-incremental approach for AQUINAS, while to the best of the present author's understanding ABAQUS uses a backwards Euler scheme).

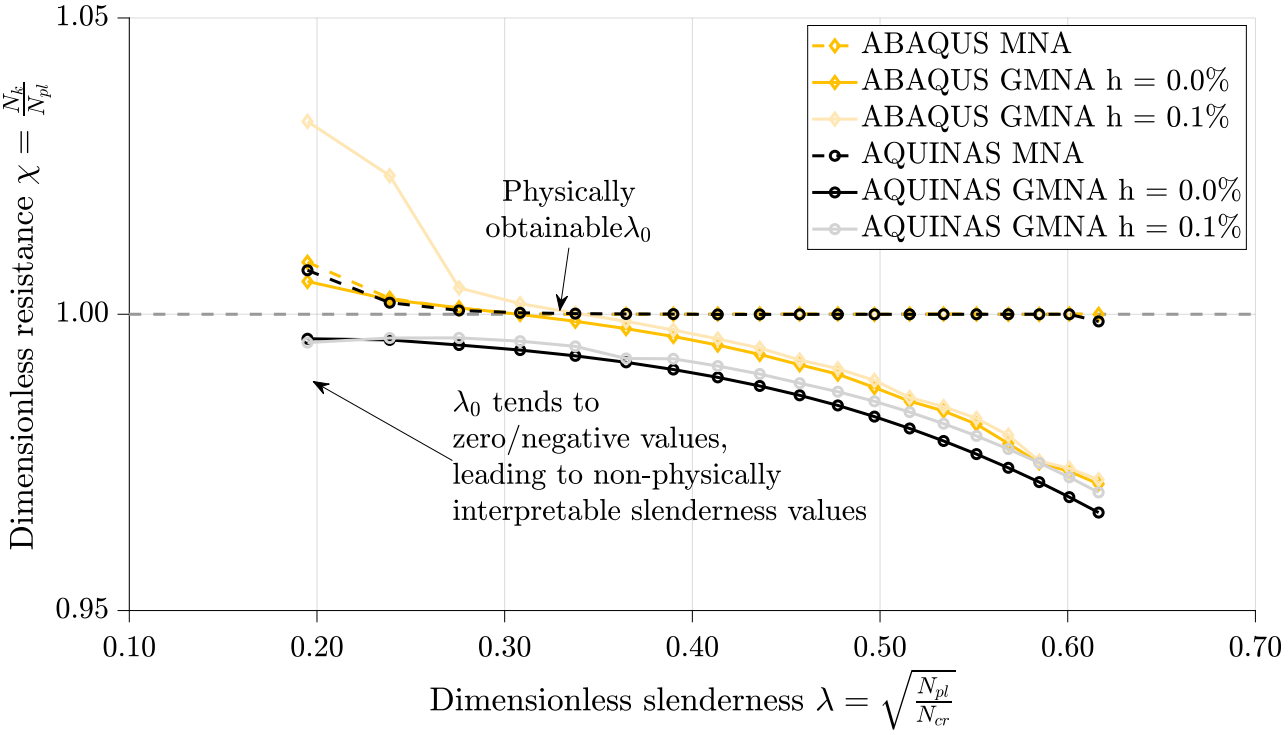


Figure 4.16: A comparison of computed capacity curves for nominally perfect cylinders under uniform meridional compression in the traditional χ vs λ format for fully axisymmetric shell models, with FE solutions obtained through ABAQUS and AQUINAS. Only axisymmetric buckling modes were permitted during the AQUINAS GMNA runs.

Interpretation of the capacity curve segments of Fig. 4.16 permits different perspectives on the underlying causes for these shortcomings and subsequent plans for further developments on the AQUINAS software. An obvious assessment of those results would dictate the inclusion of finite-thickness effects on the element's formulation, introduced through kinematic relationships. This observation is substantiated by the fact that discrepancies between AQUINAS and ABAQUS are more significant for the thicker and shorter models, with their pre-buckling response dominated by bending effects due to the relatively higher ratio of edge boundary layers Λ with respect to the overall length L, resulting in penetration of restraint compatibility bending boundary layers throughout the shell's meridian. As bending behaviour is accompanied by extensive shear stresses and strains, these contributions cannot be neglected for an error-free representation of the pre-buckling stress state. Nonlinear kinematic relations that include shear strain expressions need to be examined, additionally considering the impact of associated geometric stiffness coefficients that can potentially provide the necessary strengthening for the cylinders to reliably attain their full plastic resistance. An alternative interpretation needs to be taken into account however, as the accumulation of over-pronounced contributions of geometrically nonlinear strains could be responsible for the deterioration of the converged states and resultant solution accuracy. Finally, AQUINAS employs a Total Lagrangian (TL) scheme for the updating of its nonlinearly developing configurations, built around small strain increments and moderate rotations. The advantages and disadvantages of TL implementations have been outlined in Section 2.2.2.3 and discussed against other alternative options, but as the ABAQUS beam element formulations are

based on a corotational framework, with the axisymmetric shell elements SAX1/SAX2 being simple extensions of the B21/B22 elements, the inappropriateness of the TL scheme for specific types of problems needs to be examined.

A final note on the quality of the generated capacity curve through the ABAQUS explicitly axisymmetric modelling is crucial, especially after the critique on its sensitivity to initial modelling parameters of the previous section. In the absence of parasitic circumferential DOFs, the commercial FEA software reliably computes the load bearing capacity of the meridionally compressed cylindrical shells without showcasing any of the numerical ill-behaviour discussed in Section 4.3.1 or requiring model resubmissions. Whilst this could be attributed to the mechanics of the examined shell system, as the parametric exploration of Section 4.3.1 has been carried out on the basis of cylinders under bending, previous computational studies on meridionally compressed cylindrical shells have demonstrated similar characteristics (Sadowski *et al.*, 2018), with the presented GNA elastic resistances not conforming into a well defined smooth relationship with respect the number of circumferential waves n for each dimensionless length Z considered (as given by Eq. 2.23), also included for comparison in Section A.5.1. Appropriate modelling and treatment of axisymmetric shells does not necessarily guarantee solution accuracy, as axisymmetric wire models in ABAQUS have oftentimes required 'tweaking' with solution controls to circumvent path tracing difficulties and associated erroneous results during the author's experience with the software. Nevertheless, the major improvement in solution quality may be viewed as a testament to the importance of a suitable computational treatment for axisymmetric shell problems, a void in the modern era of FE solvers that AQUINAS aims to step into.

4.4 Conclusions

A detailed computational justification has been provided in the present chapter regarding the updated provision of EN 1993-1-6 for the 'LBA-MNA' buckling design method where the capacity curve for a cylinder under uniform meridional compression is not to be treated as the de-facto most conservative alternative in the lack of a more relevant reference system. The capacity curve parameters for cylinders under global bending are to be adopted as the 'default' set for models of intermediate slenderness, while cylinders under uniform meridional compression are to be still treated as the most conservative system for higher values of the dimensionless slenderness λ, with their critical resistance controlled by elastic instability phenomena. The justification relates to the mechanics of localised buckling under only partial plastification of the circumference and the fact that for a cylinder under bending the first yield moment is approximately 20% below the full plastic value M_{pl}.

The intricacies associated with the computational generation of capacity curves for even the most basic (but not trivial as the extensive ongoing research indicates) axisymmetric shell geometries, that of a circular cylindrical shell were thoroughly reviewed, with the two most well established commercial FE solvers employed in this endeavour. A selection of key modelling parameters relating to the discretisation and load incrementation were varied in an 'one-at-a-time' fashion in order to appreciate the effect each can have on the quality of the numerical solution. Neither commercial software was able to accurately determine the resistance of cylinders under bending consistently and without difficulties for all parametric sets, with ANSYS (2022) showcasing considerably higher result variability and sensitivity to modelling choices. Finer discretisation and smaller load increment have led to deterioration of computed results quality, an outcome that contradicts basic FE modelling intuition and requires further detailed investigations to assess the appropriateness of commercial 'black-box' computational software as tools that can

facilitate development and application of design standards. The results presented aim to not only warn analysts of the potential pitfalls in the usage of general FE solvers without post-processing solution scrutiny, but to also provide a critique on the performance of major high-end commercial packages that do not deliver the reliability and computational robustness their users expect.

The results of the AQUINAS axisymmetric shell solver are also subjected to the same level of scrutiny, with a critical inspection of squash load estimations for meridionally compressed cylinders in the presence of both geometric and material nonlinearities, considering a bilinear material law. Failure to attain the full plastic resistance through a GMNA for very stocky models contradicts not only intuition but also the results of the ABAQUS FE solver, hindering utilisation of the recently released software for the accurate estimation of capacity curve parameters in the range of low slenderness, stocky cylindrical shells. An extension to the finite element toolbox that can appropriately model the behaviour of such shells is therefore required for the AQUINAS toolbox to become the versatile solver originally intended, leading to the analytical and development works of the next chapters.

Chapter 5

Linear stress and bifurcation buckling analyses of shear-flexible axisymmetric cylindrical shells

5.1 Motivation

The thorough computational comparison of cylinders under meridional compression and uniform bending has drawn attention to the nonlinear characteristic resistance predictions of AQUINAS for the first of these two characteristic reference shell systems. As the discussion of Section 4.3.3 points out, the ultimate load carrying capacity of stocky cylinders under meridional compression is consistently underestimated by the AQUINAS solver in the presence of both material and geometric nonlinearities. The underestimation is of such significance that it does not permit the evaluation of a meaningful value for λ_0, as the full plastic resistance of the cylinder is never actually attained through a GMNA, even with inclusion of appropriate hardening effects on the material definition. This triggered an investigation of both computational and analytical natures to identify the underlying cause for this unintuitive behaviour, comprising comparisons with other axisymmetric FE solvers as well as a term-by-term examination of the linear and nonlinear kinematics employed into AQUINAS.

At first glance, the obvious limitation of the axisymmetric shell formulation described in Teng & Rotter (1989a,b) is the omission of finite-thickness effects on the strain-displacement relations. As shear strains are neglected in the explicitly thin shell linear and nonlinear kinematics of the element, its performance for a range of relatively thick, stocky cylindrical models is inevitably expected to deviate from its actual resistance. The extent of this deviation is however an unknown as it would rely on the shell theory utilised for the derivation of the load carrying capacity, or in the context of a nonlinear resistance prediction the computational description of its shell kinematics. Different alternatives for the strain-displacement relationships would include the widely employed kinematics of Reissner (1941), with appropriate extensions into the domain of nonlinear behaviour, as well as the equally popular description provided by Von Karman & Tsien (1939); Von Karman & Tsien (1941) and used in analytical explorations of composite laminated cylinders (Shen, 2017).

For AQUINAS to be a comprehensive well-rounded FE toolbox for the analysis of axisymmetric shells across a wide range of considered slendernesses, the decision was made to extend its formulation to account for finite-thickness effects, aiming to soon release an updated version with improved capabilities. Different stages of development necessitated the existence of different

benchmark results to establish the validity of the element definition in the context of various EN 1993-1-6 (2025) analysis procedures. Whilst an LA result is easily obtainable from first principles, even with the additional contribution of shear strains and stresses in the bending theory solution for a cylinder under meridional compression, a closed-form LBA result that related the critical bifurcation buckling load of the shell system to the number of circumferential waves n and meridional half-waves m associated with the buckling mode was not at all readily available in the relevant literature. To ensure verification of intermediate results in the development of a shear-flexible axisymmetric shell element, but also in order to provide a closed-form solution to an otherwise thoroughly studied stability problem for a fundamental reference shell system, a purely analytical venture into the linear bifurcation buckling of meridionally compressed cylinders was undertaken. The derivational work and obtained formulae produced during this work are presented in this chapter, with the stress analysis of cylinders under meridional edge loads and normal surface pressure preceding the exploration of stability phenomena under these two Primary Load Cases.

5.2 Introduction

A brief historic overview of developments on cylindrical shell theories that include finite-thickness effects on the shell response clearly indicates that the majority of recent publications considering such effects are relevant to composite shell-wall structures. New Functionally Graded Materials (FGM) have rekindled scientific interest into shear-flexible cylindrical shell theories, with the majority of new publications on the field studying stability phenomena in the context of laminated shells. As this is a study aiming to provide closed-form solutions for the problem of shear-deformable cylinder buckling as an extension of the classical work of Koiter (1945) if finite thickness effects were retained at the level of the adjacent equilibrium stage, a series of essential simplifications have been made to ensure success of this endeavour. These are clearly stated before any derivational work takes place, setting the scope and applicability of the obtained solutions, which does not include cross-ply laminates or any other kind of composite shell wall structure as they would make the analytical process adopted here unfeasible.

Several key results associated with the elastic stability of cylindrical shells and presented earlier in this document are reiterated in the current Chapter, not only for to aid on its conciseness but to also explicitly identify them as *thin shell theory* results through the use of an appropriate subscript. Equivalent thick shell theory are thus directly comparable, allowing a swift assessment of the derivational work.

5.2.1 Developments on shear-flexible shell theories for cylindrical shells

Stress patterns for axisymmetric cylindrical shells have been extensively studied for more than a century, with classical analytical works successfully capturing the bending behaviour of thin elastic cylinders under various loading conditions (Calladine, 1983; Timoshenko & Woinowsky-Krieger, 1959a; Flügge, 1990). The contribution of transverse shear effects on the bending theory solutions of slender cylindrical models is however most commonly neglected, with the relative slenderness usually expressed solely in terms of a radius r over thickness t ratio of the shell (Novozhilov, 1959).

Elastic thick-wall cylinder kinematics are commonly based on classical thin shell theories, enriched with the effect of transverse shear strains on the shell's deformation. A short review of the literature on shear-flexible cylindrical theories (Habip, 1965; Kapania, 1989) will point

out the two main approaches for the inclusion of transverse shear effects, the linear first-order shear deformation theory (FSDT) and the more advanced higher-order shear deformation theory (HSDT), involving nonlinear kinematic relations to describe the through thickness variation of shear strains. The advantages of linear transverse shear field kinematics associated with the FSDT approach have been utilised by Chandrashekhara & Pavan Kumar (1995) to perform a thorough comparison of classical cylindrical shell theories (Love, 1892; Donnell, 1935b; Sanders Jr, 1959; Flügge, 1990), appropriately modified to account for finite-thickness effects, on the problem of simply supported cylinders under radial loads. Variable thickness cylindrical shells were analysed using the FSDT by Ghannad *et al.* (2013) to obtain analytical solutions for clamped-clamped boundary conditions and normal pressure loading, evaluated through the matched asymptotic method of the perturbation theory. Analytical results were also obtained by Mahboubi Nasrekani & Eipakchi (2019) for cylinders of linearly varying thickness under axial and radial loads by adopting von Karman's kinematic relations and using the FSDT approach, considering buckling into fully axisymmetric modes.

The linear FSDT approach shall be adopted here for the transverse shear strain field relations. As will be shown later on, an algebraic bending theory solution for cylindrical shells under meridional compression and external pressure involves complex number arithmetic, an uninviting prospect for any analyst. However, the imaginary terms eventually reduce to numerically negligible quantities and may be ignored to yield entirely real-valued stress and displacement distributions. Programming languages such as Python which support complex arithmetic are perfect choices to implement the equations presented here, but it is illustrated in supplementary code released in the accompanying GitHub repository that even generic spreadsheet tools such as Excel that support complex number operations can be employed.

Closed-form expressions for the critical buckling load of deep beams under axial compression have been successfully derived and verified for over a century. The seminal work of Timoshenko & Gere (1961), commonly referenced in explorations of bifurcation loads for thick beams subject to compression, presents the two main approaches for the inclusion of transverse shear force effects on their analytical evaluation. Engesser's hypothesis (Engesser, 1891) assumes that the internal forces act normal to the undeformed cross-section of the beam on its perturbed configuration, while in Haringx's (Haringx, 1948) so-called 'modified approach' the stress resultants act on the cross-section after a correction due to shear effects has been applied. The seemingly more realistic approach of Haringx provides critical load predictions that are actually on the less conservative side (Ziegler, 1982; Blaauwendraad, 2010; Kardomateas & Dancila, 1997) and have been ultimately shown to be less accurate than their more simple equivalents obtained according to Engesser's hypothesis (Ziegler, 1982; Nanni & et al, 1971) for regular structural beam-column members.

The elastic buckling of thin isotropic cylinders has already posed significant challenges to the shell research community, mainly due to the coupling of meridional and circumferential stress fields that accompanies classical shell theory. A series of different analytical approaches have been presented over the years, varying in levels of approximations chosen to be appropriate for describing the pre-buckled state of the cylinder or its buckled mode. A considerable portion of these analytical efforts were focused on meridionally compressed cylinders, with three independent works (Lorenz, 1908; Timoshenko, 1910; Southwell, 1914) reaching the same result for the *classical elastic critical stress*:

$$\sigma_{cl} = \frac{E}{\sqrt{3(1-\nu^2)}}\frac{t}{r} \tag{5.1}$$

Donnell's theory (Donnell, 1935b), often referred to as *classical shell theory*, has provided a set of nonlinear strain-displacement relations that are commonly adopted or referenced in either analytical (Brush & Almroth, 1975; Koiter, 1945; Batdorf, 1947) or computational ventures (Teng & Rotter, 1989a,b) into the intricacies of cylinder buckling. With Donnell's expressions as a starting point, Koiter (1945) proceeded to show that the number of meridional half-wavelengths m and circumferential full-wavelengths n characterising the bifurcation modes of a cylinder under meridional compression may be found to form a circle after some minor variable transformations. This locus of m-n pairs, referenced as the 'Koiter circle' in related cylinder buckling literature (Brush & Almroth, 1975; Yamaki, 1984; Spagnoli, 2003; Sadowski *et al.*, 2018), can be expressed as:

$$\left(\bar{m}r - \sqrt{\frac{r}{t}}\sqrt[4]{\frac{3}{4}\left(1-\nu^2\right)}\right)^2 + n^2 = \frac{r}{t}\sqrt[2]{\frac{3}{4}\left(1-\nu^2\right)} \tag{5.2}$$

for a critical axial edge load of:

$$N_{m-n,thin} = \frac{Et^3}{12(1-\nu^2)}\left(\frac{\bar{m}^2r^2+n^2}{\bar{m}r^2}\right)^2 + \frac{Et}{r^2}\left(\frac{\bar{m}r^2}{\bar{m}^2r^2+n^2}\right)^2 \tag{5.3}$$

where definition of $\bar{m}$ is indifferent to a thin or thick shell theory approach, given as:

$$\bar{m} = \frac{m\pi}{L} \tag{5.4}$$

and L represents the cylinder's length. Minimisation of Eq. 5.3 with respect to the quantity $(\bar{m}^2r^2+n^2)^2/(\bar{m}^2r^2)$ eventually leads to a classical result for the bifurcation load $N_{cl,thin}$, which can be calculated as:

$$N_{cl,thin} = \sigma_{cl}t = \frac{E}{\sqrt{3(1-\nu^2)}}\frac{t^2}{r} \tag{5.5}$$

For the purposes of a realistic cylinder buckling mode, only integer values for the m-n parameters are eligible contenders in Eqs. 2.18-5.3, a consequence of their physical meaning as wavenumbers. It is not uncommon for very slender cylindrical shells to exhibit buckling near a hundred competing m-n pairs that are practically within 1% of the critical buckling load (Teng & Rotter, 2004b). Some notable nonlinear cylindrical shell theories that delve deeper into the complexities of large displacement behaviours are those of Sanders Jr (1963), Novozhilov (1959) and Flügge & Chou (1967), who, as is the case with his linear theory, makes significant effort for a detailed description of the shell's behaviour.

It is perhaps unsurprising that the analytical endeavours for closed-form expressions of the critical elastic buckling load for shear-flexible cylindrical shells are infrequent (Simitses, 1996; Geier & Singh, 1997; Soldatos, 1986; Yang & Kuo, 1992). While thicker cylinders behaving elastically are at first glance less common in structural engineering (see next paragraph for an important caveat), they find greater application in the fields of aerospace or ocean engineering. Composite materials are frequently employed for the fabrication of an optimal load carrying assembly, leading to numerous publications on the stability of shear-flexible laminated composite cylinders originating from these two fields of engineering (Simitses, 1996). The extensive work of Kardomateas on the bifurcation of orthotropic thick cylindrical shells (Kardomateas & Philobos, 1995; Kardomateas & Dancila, 1997) has yielded valuable analytical results in the form of reference curves, rather than closed-form expressions, mainly due to the dependence on a determinant problem on a per case basis.

Analytical efforts on the derivation of the critical elastic buckling resistance of cylinders under fundamental loads are often conjoined with a series of simplifying assumptions related to the pre-buckling deformation of the shell. A condition of pure membrane stress state is commonly considered to approximate the pre-buckling stress field to sufficient accuracy (Donnell, 1935b; Koiter, 1945; Brush & Almroth, 1975), for medium-length cylinders at least. The seminal work of Yamaki (1984) treats the pre-buckling stress field to a higher degree of accuracy by considering bending effects imposed on the cylinder by essential boundary conditions, with an additional comparison of the critical buckling resistance predictions according to different shell theories. A linearised approach to the closed-form derivation of buckling loads is the established norm in the shell research community (Yamaki, 1984; Brush & Almroth, 1975; Koiter, 1945), as a more accurate large displacement pre-buckling state of the cylinder would require iterative schemes to trace a nonlinear interaction between a stepwise increasing load and the shell deformations (Brush & Almroth, 1975). In scenarios where large displacements were considered (Fischer, 1963; Stein, 1964) a finite difference approach aided in the evaluation of the critical load through a determinant problem. As the constant strive for accuracy in the academic world has led to a desire for nonlinear pre-buckling effects to be retained in the estimation of critical buckling loads, but also owning to the rapid developments in scientific software employing the finite element method, computer aided predictions of buckling loads have superseded mathematical derivations for the stability of shells. Recent summative works on the developments of cylindrical shell buckling (Teng, 1996; Schmidt, 2000; Edlund, 2007) show a clear preference for finite element results rather than closed-from analytical solutions, since these are generally thought to be intractable. While a geometrically nonlinear approach to the pre-buckling state of a cylinder shows a 10% reduction to the prediction of the critical elastic bifurcation buckling load for thin cylinders under meridional compression (Teng & Rotter, 2004b), there is still room for analytical linearised results to serve as reference solutions and provide a swift non-computational estimate to the buckling resistance of cylindrical shells.

5.2.2 A case for closed-form elastic critical buckling predictions for shear-flexible cylinders under meridional compression

Inclusion of finite-thickness effects and contributions from non-shallow shell theory provides a more flexible (and thus more conservative) prediction of the elastic critical bifurcation buckling reference load R_{cr} of a cylinder with low r/t, in that $R_{cr,thin} > R_{cr,thick}$. This has consequences for the definition of the dimensionless slenderness of a shell $\lambda = \sqrt{R_{pl}/R_{cr}}$ in the European Standard for the design of shell structures EN 1993-1-6 (2025), where R_{cr} has hitherto always been de-facto treated as $R_{cr,thin}$ in the absence of routine closed-form expressions for (or routine computational evaluations through Linear Bifurcation Analyses (LBAs) of) $R_{cr,thick}$. However, the dimensionless characteristic buckling resistance $\chi = R_k/R_{pl}$ of the cylinder may be overpredicted if only a thin-walled slenderness is used for a shell where finite-thickness effects should not be neglected (such as for tubular support structures, piles, chimneys or other low-slenderness shells of modern industrial importance), as:

$$\lambda_{thin} = \sqrt{R_{pl}/R_{cr,thin}} < \sqrt{R_{pl}/R_{cr,thick}} = \lambda_{thick} \tag{5.6}$$

such that the corresponding dimensionless buckling resistance $\chi(\lambda_{thin}) > \chi(\lambda_{thick})$, although this overprediction is usually minor.

A related but more pressing issue arises during the development of EN 1993-1-6 (2025) capacity curves themselves, which begin with parametric finite element (FE) simulations populating a curve in the χ vs λ ('traditional' form) or χ vs $\psi = R_k/R_{cr}$ ('modified' or 'Rotter' form) to

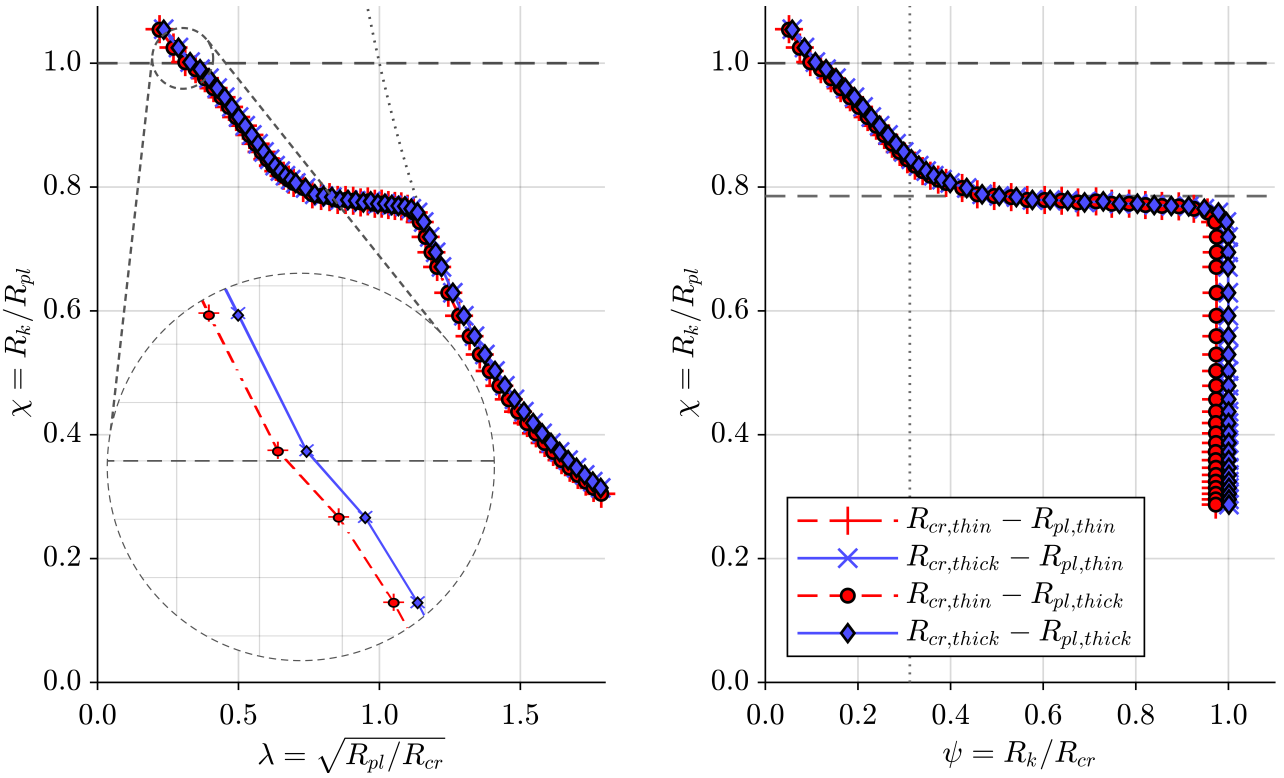


Figure 5.1: A comparison of characteristic (left) and modified (right) computed capacity curves for nominally perfect ($\kappa \approx 1$) medium-length cylinders under uniform bending, normalised against a thin shell theory critical buckling resistance $R_{cr,thin}$ or a non-shallow finite-thickness shell theory $R_{cr,thick}$ prediction.

allow for algebraic characterisation in terms of eight capacity parameters (Sadowski & Filippidis, 2025). The numerical values of these parameters will clearly depend not only on the computed finite element buckling resistances, but also on the assumed R_{cr} and R_{pl} reference resistance expressions which are used to normalise the former for expression in these two dimensionless planes. The accuracy with which finite thickness effects are captured by either assumed reference resistance then directly (and primarily) influence the capacity parameters most relevant to predominantly plastic buckling behaviour at *low* slendernesses (χ_h, η_0, λ_0 and κ, see (Sadowski & Filippidis, 2025) for full discussion), rather than those relevant for classically 'thin' high-slenderness shells (α_G, α_I, β and η_p) where thick-shell effects are negligible and the reference resistances reduce to the thin-walled result. To illustrate this, a recently computed set of FE results for cylinders under uniform bending Sadowski & Filippidis (2025) are first normalised by $R_{cr,thin}$ (using the classical formula of Eq. 5.1 combined with the thin-walled elastic section modulus) as:

$$R_{cr,thin} \equiv M_{cr,thin} \approx W_{el,thin}\sigma_{cl} = \frac{E}{\sqrt{3(1-\nu^2)}}\pi r t^2 \tag{5.7}$$

and then by $R_{cr,thick}$ using a version of Eq. 5.1 for shear-flexible cylinders (derived later in this manuscript, see Appendix C) and a thick-walled elastic section modulus as:

$$R_{cr,thick} \equiv M_{cr,thick} \approx W_{el,thick}\sigma_{cr,thick} = \left(\frac{4r^2+t^2}{4r+2t}\right)\pi r t \sigma_{cr,thick}. \tag{5.8}$$

Both equations assume the 'local buckling hypothesis' for a cylinder under bending, details of which may be found in Rotter et al. Rotter *et al.* (2014). The corresponding equations for the reference plastic collapse condition are $R_{pl,thin} = 4r^2t\sigma_y$ and $R_{pl,thick} = (4r^2t + t^3/3)\sigma_y$ respectively.

Figure 5.1 illustrates the differences in interpretation that different assumptions for R_{pl} and R_{cr} *can* have. For the specific system of a cylinder under uniform bending, a thin-walled vs thick-walled version of R_{pl} has only a negligible outcome on the interpretation of the capacity curve, but the same is not true for thin-walled vs. thick-walled versions of R_{cr}. In the zoomed region, it is shown that a thin-walled R_{cr} expression leads to an estimate for the 'squash limit relative slenderness' λ_0 (the slenderness at which the full plastic resistance $\chi = 1$ is attained) of ~ 0.316, while a thick-walled version of this expression leads to an estimate of ~ 0.33. If this is thought to be a negligible difference, then it should be stressed that these λ_0 differences correspond to differences in $d/(t\epsilon^2)$ of ~ 8, which is just under half the distance between Class 1, 2 and 3 $d/(t\epsilon^2)$ boundaries for circular hollow sections as per 1993-1-1 (2005). The author is informed by his supervisor that smaller differences than this have led to lengthy discussions in Eurocode 3 committees, and Fig. 5.1 encapsulates the motivation for deriving more accurate reference results for the linear-elastic reference buckling resistances of finite-thickness cylinders under fundamental load conditions to support a reliable use of the EN 1993-1-6 capacity curve formulation.

5.3 Stress analysis of finite-thickness elastic isotropic cylindrical shells under the combined action of meridional edge load and normal pressure

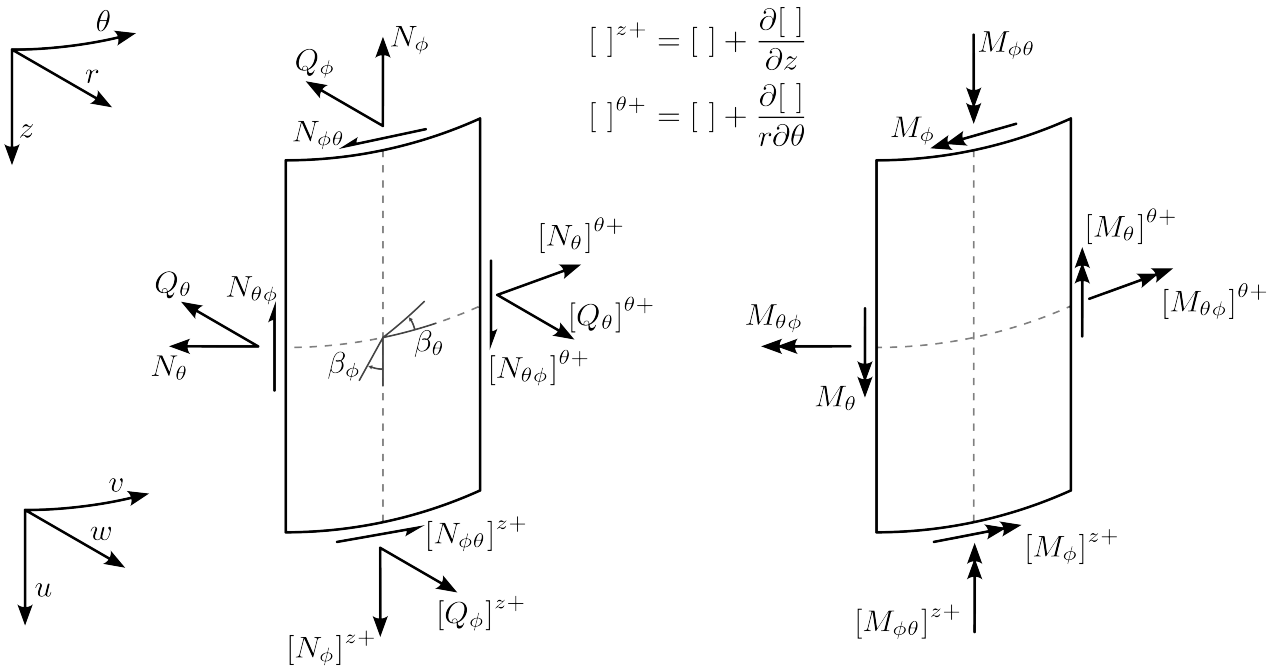


Figure 5.2: Cylindrical shell system

5.3.1 Kinematic relations

The following kinematic relations are based on Green's strain tensor for shells (Green & Zerna, 1992) and have been specialised for the case of a cylinder (Jumikis, 1987; Teng & Rotter,

1989a). This specialisation allows for considerable simplifications, with the meridional angle set to $\phi = \pi/2$ (clockwise, measuring from the axis of axisymmetry) and the midsurface's radial coordinate being constant and equal to the circumferential radius of curvature ($r = r_\theta$), while the radius of meridional curvature tends to infinity ($r_\phi \to \infty$). With reference to the conventions presented in Fig. 5.2, the full set of midsurface strains and curvatures for a finite-thickness cylindrical shell may be written as follows:

Membrane strains

$$\epsilon_\phi = \frac{\partial u}{\partial z} \tag{5.9a}$$

$$\epsilon_\theta = \frac{w}{r} + \frac{1}{r}\frac{\partial v}{\partial \theta} \tag{5.9b}$$

Shear strains

$$\gamma_{\phi\zeta} = \frac{\partial w}{\partial z} + \beta_\phi \tag{5.10a}$$

$$\gamma_{\theta\zeta} = \frac{1}{r}\frac{\partial w}{\partial \theta} - \frac{v}{r} + \beta_\theta \tag{5.10b}$$

$$\gamma_{\phi\theta} = \gamma_{\theta\phi} = \frac{1}{r}\frac{\partial u}{\partial \theta} + \frac{\partial v}{\partial z} \qquad \textit{(in-plane)} \tag{5.10c}$$

Curvatures

$$\kappa_\phi = \frac{\partial \beta_\phi}{\partial z} \tag{5.11a}$$

$$\kappa_\theta = \frac{1}{r}\frac{\partial \beta_\theta}{\partial \theta} \tag{5.11b}$$

$$\kappa_{\phi\theta} = \kappa_{\theta\phi} = \frac{1}{2}\left(\frac{1}{r}\frac{\partial \beta_\phi}{\partial \theta} + \frac{\partial \beta_\theta}{\partial z}\right) \tag{5.11c}$$

The strains and curvatures of Eqs. 5.9-5.11 are identical to those presented in reference shell theory textbooks (Calladine, 1983; Brush & Almroth, 1975), with the exception of the arguably more complete and complex theory derived from first principles by Flügge's 'Stresses in Shells' (Flügge, 1990), when the assumption of thin shell theory is applied:

$$\beta_\phi \approx -\frac{\partial w}{\partial z} \tag{5.12a}$$

$$\beta_\theta \approx -\frac{1}{r}\frac{\partial w}{\partial \theta} + \frac{v}{r} \tag{5.12b}$$

The additional definitions for the meridional and circumferential transverse shear strains of Eqs. 5.10 are essential to the derivation of a thick cylinder bending theory solution. It should be emphasised that the positive sign of the rotations β_ϕ and β_θ in Eqs. 5.10 stems from the convention corresponding to their positive direction, as illustrated in Fig. 5.2.

5.3.2 Constitutive relations

According to classical bending shell theory (Calladine, 1983; Flügge, 1990; Timoshenko & Woinowsky-Krieger, 1959a), with additional considerations for transverse shear effects and the

simplifications of Assumption 3, the full set of membrane, bending and shear stress resultants for a cylinder may be expressed as:

Membrane stress resultants:

$$N_\phi = C(\epsilon_\phi + \nu\epsilon_\theta) \tag{5.13a}$$
$$N_\theta = C(\epsilon_\theta + \nu\epsilon_\phi \tag{5.13b}$$
$$N_{\phi\theta} = N_{\theta\phi} = C\frac{1-\nu}{2}\gamma_{\phi\theta} \tag{5.13c}$$

Bending stress resultants:

$$M_\phi = D(\kappa_\phi + \nu\kappa_\theta) \tag{5.14a}$$
$$M_\theta = D(\kappa_\theta + \nu\kappa_\phi) \tag{5.14b}$$
$$M_{\phi\theta} = M_{\theta\phi} = D(1-\nu)\kappa_{\phi\theta} \tag{5.14c}$$

Transverse shear stress resultants:

$$Q_\phi = kGt\gamma_\phi \tag{5.15a}$$
$$Q_\theta = kGt\gamma_\theta \tag{5.15b}$$

where the extensional stiffness C, flexural stiffness D and shear modulus G are defined as:

$$C = \frac{Et}{1-\nu^2} \tag{5.16a}$$
$$D = \frac{Et^3}{12(1-\nu^2)} \tag{5.16b}$$
$$G = \frac{E}{2(1+\nu)} \tag{5.16c}$$

for an elastic isotropic material. The shear correction factor is set to $k = 5/6$ (Cowper, 1966), appropriate for rectangular cross-sections, an assumption that is valid for both sides of an infinitesimal element $dz\,rd\theta$ which is used for the derivations of the cylindrical shell theory (Mirsky & Herrmann, 1958; Chandrashekhara & Pavan Kumar, 1995).

5.3.3 Equilibrium equations for axisymmetric cylinders

Only a handful of the force terms and their increments displayed in Fig. 5.2 will participate in the equilibrium equations for a (pre-buckling) stress state characterised by circumferential axisymmetry which characterises many lower slenderness reference shell systems of industrial importance. Any derivatives with respect to the circumferential angle θ may be ignored, as they would violate the axisymmetric stress state, together with transverse shear forces Q_θ and in-plane shear terms. The circumferential degrees of freedom v and β_θ are also assumed to be zero.

Summation of forces along the radial r and axial z axes, referring to the undeformed configuration of Fig. 5.2, with the reductions on the equilibrium equations outlined above, yields:

$$\frac{\partial N_\phi}{\partial z} = 0 \tag{5.17a}$$

$$r\frac{\partial Q_\phi}{\partial z} - N_\theta + rp = 0 \tag{5.17b}$$

while equilibrium along the circumferential axis θ leads to an identity for the case of axisymmetry. Application of the same simplifications results in two more identities for the moment equilibrium about the radial r and axial z axes, while summation of moments about the circumferential axis θ gives:

$$\frac{\partial M_\phi}{\partial z} - Q_\phi = 0 \tag{5.18}$$

5.3.4 System of equations

Substitution of the kinematic relations of Eqs. 5.9-5.11 into the constitutive relations of Eqs. 5.13-5.15, after application of reductions arising from the condition of circumferential stress uniformity, produces the following generalised stress resultants:

$$N_\phi = C(\epsilon_\phi + \nu\epsilon_\theta) = C\left(\frac{\partial u}{\partial z} + \nu\frac{w}{r}\right) \tag{5.19a}$$

$$N_\theta = C(\epsilon_\theta + \nu\epsilon_\phi) = C\left(\frac{w}{r} + \nu\frac{\partial u}{\partial z}\right) \tag{5.19b}$$

$$M_\phi = D\kappa_\phi = D\frac{\partial \beta_\phi}{\partial z} \tag{5.19c}$$

$$M_\theta = \nu D\kappa_\phi = \nu D\frac{\partial \beta_\phi}{\partial z} \tag{5.19d}$$

$$Q_\phi = kGt\gamma_\phi = kGt\left(\frac{\partial w}{\partial z} + \beta_\phi\right) \tag{5.19e}$$

while the $N_{\phi\theta}$, $M_{\phi\theta}$, Q_θ stress resultants are equal to zero due to the condition of axisymmetry. A further substitution of the now updated constitutive relations with the kinematics of the shell system into the reduced equilibrium equations of Eqs. 5.17 and 5.18 yields:

$$C\left(\frac{\partial^2 u}{\partial z^2} + \frac{\nu}{r}\frac{\partial w}{\partial z}\right) = 0 \tag{5.20a}$$

$$rkGt\left(\frac{\partial^2 w}{\partial z^2} + \frac{\partial \beta_\phi}{\partial z}\right) - C\left(\frac{w}{r} + \nu\frac{\partial u}{\partial z}\right) + rp = 0 \tag{5.20b}$$

$$D\frac{\partial^2 \beta_\phi}{\partial z^2} - kGt\left(\frac{\partial w}{\partial z} + \beta_\phi\right) = 0 \tag{5.20c}$$

Integration of Eq. 5.20a with respect to the z coordinate introduces a constant to the equation for meridional force equilibrium, representing a natural boundary condition (BC) N_z for the meridional membrane stress resultant N_ϕ to be set equal to at the loaded edge of the cylinder:

$$C\left(\frac{\partial u}{\partial z} + \frac{\nu}{r}w\right) = N_z \tag{5.21}$$

Solving for the first derivative of u from Eq. 5.21 and substituting into Eq. 5.20b allows for partial decoupling of the system of Eqs. 5.20, which now only includes terms in the normal displacement w and meridional rotation β_ϕ. The partially decoupled set of equations may be written as:

$$rkGt\frac{\partial^2 w}{\partial z^2} + rkGt\frac{\partial \beta_\phi}{\partial z} - \frac{C(1-\nu^2)}{r}w - \nu N_z + rp = 0 \tag{5.22a}$$

$$D\frac{\partial^2 \beta_\phi}{\partial z^2} - kGt\left(\frac{\partial w}{\partial z} + \beta_\phi\right) = 0 \tag{5.22b}$$

5.3.5 Solution of the homogeneous problem for a thick cylinder

The system of second order linear ordinary differential equations (ODEs) in Eqs. 5.22 governs the bending behaviour of a cylinder under the combined action of a meridional force N_z and normal pressure p. The solution of this system allows for the computation of stress patterns along the meridian of the cylinder. In compliance with the general mathematical treatment for ODE systems of this nature, the homogeneous part of these equations will be isolated and solved for, neglecting any terms that do not include the degrees of freedom (DOFs) w and β_ϕ. The computation of a particular solution will follow and complete the expressions for the displacement field along the meridian of the cylinder.

5.3.5.1 Reduction into first order linear system of ODEs

Due to the nature of the problem, a substitution of variables is required in order to transform the system of second order linear ODEs into a first order one. Let:

$$w_a = w \tag{5.23a}$$

$$w_b = \frac{\partial w}{\partial z} \tag{5.23b}$$

$$\beta_{\phi,a} = \beta_\phi \tag{5.23c}$$

$$\beta_{\phi,b} = \frac{\partial \beta_\phi}{\partial z} \tag{5.23d}$$

Hence:

$$w_b = w_a' \tag{5.24a}$$

$$\beta_{\phi,b} = \beta_{\phi,a}' \tag{5.24b}$$

The homogeneous part of the original system can now be rewritten as:

$$rkGtw_b' + rkGt\beta_{\phi,b} - \frac{C(1-\nu^2)}{r}w_a = 0 \tag{5.25a}$$

$$D\beta_{\phi,b}' - kGtw_b - kGt\beta_{\phi,a} = 0 \tag{5.25b}$$

Solving for the now first order derivatives of the system w_b' and $\beta_{\phi,b}'$ leads to:

$$w_b' = \frac{C}{kGt}\frac{1-\nu^2}{r^2}w_a - \beta_{\phi,b} \tag{5.26a}$$

$$\beta_{\phi,b}' = \frac{kGt}{D}w_b + \frac{kGt}{D}\beta_{\phi,a} \tag{5.26b}$$

The homogeneous part of the system may now be expressed in matrix form:

$$\begin{Bmatrix} w'_a \\ w'_b \\ \beta'_{\phi,a} \\ \beta'_{\phi,b} \end{Bmatrix} = \begin{bmatrix} 0 & 1 & 0 & 0 \\ \frac{C}{kGt}\frac{1-\nu^2}{r^2} & 0 & 0 & -1 \\ 0 & 0 & 0 & 1 \\ 0 & \frac{kGt}{D} & \frac{kGt}{D} & 0 \end{bmatrix} \begin{Bmatrix} w_a \\ w_b \\ \beta_{\phi,a} \\ \beta_{\phi,b} \end{Bmatrix} \tag{5.27}$$

5.3.5.2 Characteristic equation for the homogeneous problem

The matrix form of the system allows for the extraction of the characteristic equation through the solution of the eigenvalue problem:

$$|A - \Lambda I| = \begin{vmatrix} -\Lambda & 1 & 0 & 0 \\ \frac{C}{kGt}\frac{1-\nu^2}{r^2} & -\Lambda & 0 & -1 \\ 0 & 0 & -\Lambda & 1 \\ 0 & \frac{kGt}{D} & \frac{kGt}{D} & -\Lambda \end{vmatrix} = 0 \tag{5.28}$$

Computation of the above determinant, allows for the characteristic equation to be found as:

$$r^2\Lambda^4 - \frac{2(1+\nu)}{k}\Lambda^2 + \frac{12(1-\nu^2)}{t^2} = 0 \tag{5.29}$$

where the membrane and bending stiffnesses, as well as the shear modulus, have been substituted for according to Eqs. 5.16. The quartic characteristic equation is found to be quadratic in Λ^2, allowing for the root finding problem to be approached in a classical quadratic equation fashion. The discriminant of the 'quadratic' form can be evaluated to be:

$$\Delta = \frac{4(1+\nu)^2}{k^2} - 4r^2\frac{12(1-\nu^2)}{t^2} \tag{5.30}$$

For reasonable values of the above parameters and for $r/t > 1$ (but not necessarily $r/t \gg 1$) the discriminant Δ is negative, therefore the two Λ^2 roots will be:

$$\Lambda^2 = \frac{1+\nu}{kr^2} \pm i\frac{1}{r^2}\sqrt{\frac{(1+\nu)^2}{k^2} - 12(1-\nu^2)\left(\frac{r}{t}\right)^2} \tag{5.31}$$

In turn, the four Λ roots of the quartic characteristic equation can be evaluated as:

$$\Lambda = \pm\sqrt{\frac{1+\nu}{kr^2} \pm i\frac{1}{r^2}\sqrt{\frac{(1+\nu)^2}{k^2} - 12(1-\nu^2)\left(\frac{r}{t}\right)^2}} \tag{5.32}$$

The real and imaginary parts of these roots can be isolated as follows:

$$\begin{aligned} \Lambda_1 &= \ \ a + ib \\ \Lambda_2 &= \ \ a - ib \\ \Lambda_3 &= -a + ib \\ \Lambda_4 &= -a + ib \end{aligned} \tag{5.33}$$

where the positive real parameters a and b are defined as:

$$a = \frac{1}{\sqrt{2}r}\sqrt{\sqrt{12(1-\nu^2)\left(\frac{r}{t}\right)^2} + \frac{1+\nu}{k}} \tag{5.34a}$$

$$b = \frac{1}{\sqrt{2}r}\sqrt{\sqrt{12(1-\nu^2)\left(\frac{r}{t}\right)^2} - \frac{1+\nu}{k}} \tag{5.34b}$$

5.3.5.3 Eigenvectors for the matrix system of the homogeneous problem

The matrix system $[A - \Lambda_j I]$ can be readily shown to be singular, as the Λ_j parameters with $j = 1, 4$ correspond to the roots of the Eq. 5.28 eigenvalue problem. Due to the singularity of the matrix system, there is an infinite number of eigenvector solutions $\{\phi_j\}$ such that:

$$[A - \Lambda_j I]\{\phi_j\} = \{0\} \tag{5.35}$$

where the $\{\phi_j\}$ eigenvector is given as:

$$\{\phi_j\} = \begin{Bmatrix} w_{a,j} \\ w_{b,j} \\ \beta_{a,j} \\ \beta_{b,j} \end{Bmatrix} \tag{5.36}$$

To allow for a sensible solution, let $w_{a,j} = 1$ for all Λ_j roots. The j^{th} eigenvector of Eq. 5.35 then becomes:

$$\{\phi_j\} = \begin{Bmatrix} w_{a,j} \\ w_{b,j} \\ \beta_{a,j} \\ \beta_{b,j} \end{Bmatrix} = \begin{Bmatrix} 1 \\ \Lambda \\ \frac{kGt\Lambda}{kGt - D\Lambda^2} \\ \frac{kGt\Lambda^2}{kGt - D\Lambda^2} \end{Bmatrix} \tag{5.37}$$

5.3.5.4 Displacement field solution for the homogeneous problem

The normal displacement w and meridional rotation β_ϕ fields that satisfy the homogeneous problem of Eq. 5.22:

$$w = C_1 e^{\Lambda_1 z} + C_2 e^{\Lambda_2 z} + C_3 e^{\Lambda_3 z} + C_4 e^{\Lambda_4 z} \tag{5.38a}$$

$$\beta = \beta_{a,1} C_1 e^{\Lambda_1 z} + \beta_{a,2} C_2 e^{\Lambda_2 z} + \beta_{a,3} C_3 e^{\Lambda_3 z} + \beta_{a,4} C_4 e^{\Lambda_4 z} \tag{5.38b}$$

Expansion of the Λ_j roots in the above expression can lead to:

$$\begin{aligned} w = {} & C_1 e^{az}(\cos(bz) + i\ \sin(bz)) + C_2 e^{az}(\cos(bz) - i\ \sin(bz)) \\ & + C_3 e^{-az}(\cos(bz) + i\ \sin(bz)) + C_4 e^{-az}(\cos(bz) - i\ \sin(bz)) \end{aligned} \tag{5.39a}$$

$$\begin{aligned} \beta = {} & \beta_{a,1} C_1 e^{az}(\cos(bz) + i\ \sin(bz)) + \beta_{a,2} C_2 e^{az}(\cos(bz) - i\ \sin(bz)) \\ & + \beta_{a,3} C_3 e^{-az}(\cos(bz) + i\ \sin(bz)) + \beta_{a,4} C_4 e^{-az}(\cos(bz) - i\ \sin(bz)) \end{aligned} \tag{5.39b}$$

The half-wavelength for the shear-flexible bending theory solution may now be found as:

$$\lambda_{thick} = \frac{\pi}{b} = \frac{\pi\sqrt{2}r}{\sqrt{\sqrt{12(1-\nu^2)\left(\frac{r}{t}\right)^2} - \frac{1+\nu}{k}}} \tag{5.40}$$

It can be readily shown that the relationship for the bending half-wavelength of Eq. 5.40 quickly reduces to the corresponding thin shell theory result as the r/t ratio in the denominator increases and overshadows the shear correction factor quantity:

$$\frac{\lambda_{thick}}{\lambda_{thin}} = \frac{\pi\sqrt{2}r}{\frac{\sqrt{\sqrt{12(1-\nu^2)\left(\frac{r}{t}\right)^2} - \frac{1+\nu}{k}}}{\pi\sqrt{rt}}} = \frac{1}{\sqrt{1 - \frac{t}{r}\frac{1+\nu}{k\sqrt{12(1-\nu^2)}}}} > 1 \tag{5.41}$$

An equivalent reduction may also be achieved for high values of the k factor, essentially 'enforcing' a thin shell theory to the finite-thickness approach adopted here. Closer examination of Eq. 5.41 additionally indicates that the inclusion of transverse shear effects on the cylinders deformation permits the bending boundary layers to cover a larger portion of the shell's meridian, owing to their increased flexibility.

5.3.6 Particular solution to the inhomogeneous problem for a thick cylinder

A particular solution for the normal displacement w and meridional rotation β can be found through membrane theory (Heyman, 1977) as:

$$w_m = \frac{pr^2}{tE} - \frac{N_z \nu r}{tE} \tag{5.42}$$

and

$$\beta_m = 0 \tag{5.43}$$

As is always the case with displacement field solutions produced through membrane theory, they cannot satisfy essential boundary conditions relating to restraints of the displacements or rotations on the cylinder's edges.

5.3.7 Bending theory solution to cylinder under meridional edge load and normal pressure

The particular solution to the displacements may now be added to the field computed for the homogeneous part of Eqs. 5.39, yielding the general solution to the ODE system:

$$\begin{aligned} w = {} & C_1 e^{az}(\cos(bz) + i\ \sin(bz)) + C_2 e^{az}(\cos(bz) - i\ \sin(bz)) \\ & + C_3 e^{-az}(\cos(bz) + i\ \sin(bz)) + C_4 e^{-az}(\cos(bz) - i\ \sin(bz)) + \frac{pr^2}{tE} - \frac{N_z \nu r}{tE} \end{aligned} \tag{5.44a}$$

$$\begin{aligned} \beta = {} & \beta_{a,1} C_1 e^{az}(\cos(bz) + i\ \sin(bz)) + \beta_{a,2} C_2 e^{az}(\cos(bz) - i\ \sin(bz)) \\ & + \beta_{a,3} C_3 e^{-az}(\cos(bz) + i\ \sin(bz)) + \beta_{a,4} C_4 e^{-az}(\cos(bz) - i\ \sin(bz)) \end{aligned} \tag{5.44b}$$

The last step in producing a thick shell bending theory solution is the evaluation of the unknown constants C_j. These four unknowns require four essential boundary conditions for their calculation, two at each end of the cylinder. Arrangement into a matrix system for the calculation of the C_j unknowns has been formally outlined elsewhere (Rotter & Sadowski, 2012), with the process being indifferent to the shell theory utilised for the derivation of said unknowns.

Computation of the normal displacement w and meridional rotation β_ϕ allows in turn for the

evaluation of the meridional displacement u at any point along the cylinder. Integration with respect to the meridional coordinate z on Eq. 5.21, which was used for the elimination of the $\partial u/\partial z$ derivative, can lead to the following solution of the meridional displacement u:

$$\begin{aligned} u =& u_c + z\frac{N_z}{C} - \frac{\nu}{r}\Bigg(\frac{C_1}{\Lambda_1}e^{az}(\cos(bz) + i\ \sin(bz)) + \frac{C_2}{\Lambda_2}e^{az}(\cos(bz) - i\ \sin(bz)) \\ &+ \frac{C_3}{\Lambda_3}e^{-az}(\cos(bz) + i\ \sin(bz)) + \frac{C_4}{\Lambda_4}e^{-az}(\cos(bz) - i\ \sin(bz)) + z\frac{pr^2}{tE} - z\frac{N_z\nu r}{tE}\Bigg) \end{aligned} \tag{5.45}$$

with the integration constant u_c chosen such that it satisfies a boundary condition at either end of the cylinder. Strains and stresses can now be readily calculated at any point using the displacement and rotation fields of Eqs. 5.44-5.45 and their derivatives, providing a full stress resultant profile for shear-flexible cylinders.

Unlike the displacement field expressions for thin shell bending theory, in Eqs. 5.44-5.45 the exponent az does not match the bz quantity in the sine and cosine terms. Consequently, the finite-thickness expressions for u, w and β cannot be rearranged in a way that would allow for the imaginary portions to be eliminated. However, numerical results illustrate that the imaginary part of these seemingly complex solutions can be found to be negligible, within reasonable tolerance levels for machine precision. This finding can be reproduced even with a common spreadsheet implementation of the present section's finite-thickness solution, as is shown in the accompanying GitHub repository files.

5.4 Linear bifurcation buckling of cylindrical shells under uniform meridional compression and uniform external pressure

The exact range of applicability, in terms of geometric properties, for shallow or non-shallow shell theories is not well explored in the relevant literature, notwithstanding the analytical comparisons of different shell theories that fall within these two categories (Brush & Almroth, 1975; Wilson Wong & Weaver, 2006). Across theoretical resources exploring the additional intricacies of non-shallow shell theory, otherwise encountered as 'deep' shell theory, it is commonly recognised that a shallow theory is not sufficient for shells with large curvatures (small r/t) or when normal displacements w are significant relative to the wall's thickness. Wilson Wong & Weaver (2006) make use of the dimensionless length parameter L', first introduced by Calladine (1983), to define ranges where different shallow and non-shallow shell theories (Donnell, 1935b; Loo, 1957; Love, 1892; Sanders Jr, 1959; Flügge, 1990) may be most accurate. As some of these are strictly shallow shell theories, while others are not, the work in Wilson Wong & Weaver (2006) may be seen as an attempt to define the set of L' parameters for which non-shallow theory terms should be taken into account. It is additionally recognised that for cylindrical models where non-shallow effects may be relevant, the contribution of transverse shear strains can potentially be non-negligible (Calladine, 1983), an interconnectedness that the present unified approach will attempt to deal with concurrently.

Before delving into the derivation of a linearised system of stability equations for shear-flexible cylinders, the terms associated with non-shallow shell theory shall be identified, isolating the additional layer of complexity that is introduced when compared with classical Donnell thin shell theory. Quantities that are not commonly neglected in shallow shell theory are multiplied

with a boolean integer operator δ, such that:

$$\delta = \begin{cases} 0 & \text{for shallow shell theory} \\ 1 & \text{for non-shallow shell theory} \end{cases} \tag{5.46}$$

Using the δ operator, the circumferential transverse shear strain $\gamma_{\theta\zeta}$ may be rewritten as:

$$\gamma_{\theta\zeta} = \frac{1}{r}\frac{\partial w}{\partial \theta} - \delta\frac{v}{r} + \beta_\theta \tag{5.47}$$

since a thin shallow shell theory would dictate that $\beta_\theta \approx -\frac{\partial w}{\partial \theta}$ instead of the approximation presented in Eq. 5.12b. With the exception of relationships corresponding to finite-thickness effects through the shell wall, the stability theory of what follows is largely based on the buckling theory textbook *Buckling of bars, plates and shells* by Brush & Almroth (1975), for both shallow / Donnell theory as well as non-shallow shell behaviour. Equilibrium of forces along the meridional z, circumferential θ and radial r axes in the perturbed state of the cylinder, with the displacement and rotation conventions illustrated in Fig. 5.2, produces:

$$r\frac{\partial N_\phi}{\partial z} + \frac{\partial N_{\theta\phi}}{\partial \theta} = 0 \tag{5.48a}$$

$$r\frac{\partial N_{\phi\theta}}{\partial z} + \frac{\partial N_\theta}{\partial \theta} + \delta Q_\theta = 0 \tag{5.48b}$$

$$\begin{aligned} &\frac{\partial Q_\theta}{\partial \theta} + r\frac{\partial Q_\phi}{\partial z} - N_\theta + rN_\phi\frac{\partial^2 w}{\partial z^2} + N_{\phi\theta}\left(\frac{\partial^2 w}{\partial z \partial \theta} - \delta\frac{\partial v}{\partial z}\right) \\ &+ N_{\theta\phi}\frac{\partial^2 w}{\partial \theta \partial z} + N_\theta\left(\frac{1}{r}\frac{\partial^2 w}{\partial^2 \theta} - \delta\frac{1}{r}\frac{\partial v}{\partial \theta}\right) + \delta p\left(w + \frac{\partial v}{\partial \theta}\right) + rp = 0 \end{aligned} \tag{5.48c}$$

while summation of moments about the meridional z and circumferential θ axes yields:

$$\frac{\partial M_\theta}{\partial \theta} + r\frac{\partial M_{\phi\theta}}{\partial z} - rQ_\theta = 0 \tag{5.49a}$$

$$r\frac{\partial M_\phi}{\partial z} + \frac{\partial M_{\theta\phi}}{\partial z} - rQ_\phi = 0 \tag{5.49b}$$

The reader may notice that the rotations β_ϕ and β_θ, used to express the rise of additional force equilibrium terms in the deformed configuration of the shell, have been replaced by equivalent displacement derivatives in Eq. 5.48c, when compared to their original form in Brush & Almroth (1975). While this may appear as a counter-intuitive action on a study of shear-flexible cylinders, it is dictated by Engesser's hypothesis on the stability equations.

Moment equilibrium about the radial axis r yields once more an identity of self-equilibrating sets of moments, as was the case in Eq. 5.18. As a consequence of Assumption 3, there shall be no differentiation between the in plane shear terms $N_{\phi\theta}$ and $N_{\theta\phi}$ (Eq. 5.13c), or the twisting moments $M_{\phi\theta}$ and $M_{\theta\phi}$ (Eq. 5.14c).

5.4.1 Adjacent equilibrium criterion

A mathematically equivalent method to the minimum potential energy criterion, the adjacent equilibrium criterion is commonly employed in analytical explorations relating to loss of stability in structures. Its implementation on critical bifurcation buckling load investigations allows the discovery of possible equilibrium configurations in a slightly deformed configuration of the

cylinder, expressed as:

$$u = u_0 + u_1 \tag{5.50a}$$
$$v = v_0 + v_1 \tag{5.50b}$$
$$w = w_0 + w_1 \tag{5.50c}$$
$$\beta_\phi = \beta_{\phi,0} + \beta_{\phi,1} \tag{5.50d}$$
$$\beta_\theta = \beta_{\theta,0} + \beta_{\theta,1} \tag{5.50e}$$

where quantities with a 0 subscript refer to the fundamental pre-buckling state of the cylinder, while a subscript of 1 denotes small increments to the displacements and rotations for the shell to reach its perturbed (buckled) configuration.

An essential simplification for analytical ventures of this nature to be successful in generating closed-form solutions is the adoption of linear kinematics to express the strains at any point along the shell wall, ignoring quadratic or higher order terms from Green's strain tensor that can be a source of nonlinearity in this effort (Brush & Almroth, 1975; Jumikis, 1987). The kinematic relations of Eqs. 5.9-5.11 may hence be adopted once more to express the internal state of the shell, leading to what is known as a linear form of the stability equations. As a consequence, strains, stresses and stress resultants can be expressed in a similar manner to Eqs. 5.50, with terms having a 0 subscript being in equilibrium with the externally applied loads.

Meridional rotations of the shell wall in its fundamental equilibrium configuration are neglected, assuming a pure axisymmetric membrane stress state as characteristic of the pre-buckling state, a simplification that is frequently applied in analytical thin shell theory buckling developments. Thus, any terms relating to the rotations $\beta_{\phi,0}$, $\beta_{\theta,0}$, or derivatives of any order to the displacements u_0, v_0, w_0, may be eliminated. Summation of the forces and moments of Eqs. 5.48-5.49 in the adjacent equilibrium state, after elimination of externally applied loads and terms only containing quantities with a 0 subscript (as they refer to an equilibrating fundamental configuration of the shell), leads to:

$$r\frac{\partial N_{\phi,1}}{\partial z} + \frac{\partial N_{\phi\theta,1}}{\partial \theta} = 0 \tag{5.51a}$$
$$r\frac{\partial N_{\phi\theta,1}}{\partial z} + \frac{\partial N_{\theta,1}}{\partial \theta} + \delta Q_{\theta,1} = 0 \tag{5.51b}$$
$$\begin{aligned}&\frac{\partial Q_{\theta,1}}{\partial \theta} + r\frac{\partial Q_{\phi,1}}{\partial z} - N_{\theta,1} + rN_{\phi,0}\frac{\partial^2 w_1}{\partial z^2} \\ &+ N_{\theta,0}\left(\frac{1}{r}\frac{\partial^2 w_1}{\partial^2 \theta} - \frac{1}{r}\frac{\partial v_1}{\partial \theta} + \delta\frac{w_1}{r} + \delta\frac{1}{r}\frac{\partial v_1}{\partial \theta}\right) = 0\end{aligned} \tag{5.51c}$$
$$\frac{\partial M_{\theta,1}}{\partial \theta} + r\frac{\partial M_{\phi\theta,1}}{\partial z} - rQ_{\theta,1} = 0 \tag{5.51d}$$
$$r\frac{\partial M_{\phi,1}}{\partial z} + \frac{\partial M_{\phi\theta,1}}{\partial z} - rQ_{\phi,1} = 0 \tag{5.51e}$$

where in-plane shear stress resultants $N_{\phi\theta,0}$ have also been eliminated due to the axisymmetric nature of pre-buckling deformations for destabilising meridional and/or external pressure loading. Thus, the only terms surviving into the expressions for equilibrium in the perturbed configuration referring to quantities of the fundamental state are the membrane stress resultants $N_{\phi,0}$ and $N_{\theta,0}$, since all others have either been ignored or excluded for being connected to a state of equilibrium.

A limitation of the analytical approach for the linearised critical bifurcation load predictions

is the a priori consideration of the edge restraints, embedded into the functional form of the buckling modes. In direct analogy to the mathematical treatment of thin cylinder buckling, a doubly harmonic displacement field is assumed to characterise the bifurcation modes of the cylinder once buckling occurs (Donnell, 1935b; Koiter, 1945). Unfortunately, the nature of the bifurcation problem for shear-flexible cylinders does not readily allow for the reductions that the equivalent thin shell theory approach benefits from, expressing equilibrium in the perturbed configuration only in terms of the normal displacement w. Decoupling the equilibrium Eqs. 5.48-5.49, even partially, appears to be an impractical task when transverse shear effects are included. Hence, all five degrees of freedom need to be retained, with appropriate sine and cosine terms to account for the edge boundary conditions. A pinned-pinned condition (BC2f-BC2f if referring to EN 1993-1-6 (2025) or S3-S3 if using Yamaki's BC definitions (Yamaki, 1984)) is assumed for the edge restraints hereafter, an arrangement also adopted for the thin shell critical load derivations (Donnell, 1935b; Koiter, 1945; Brush & Almroth, 1975). The harmonic displacement fields may now be expressed as:

$$u_1 = U_1 \cos(\bar{m}z)\cos(n\theta) \tag{5.52a}$$
$$v_1 = V_1 \sin(\bar{m}z)\sin(n\theta) \tag{5.52b}$$
$$w_1 = W_1 \sin(\bar{m}z)\cos(n\theta) \tag{5.52c}$$
$$\beta_{\phi,1} = B_{\phi 1} \cos(\bar{m}z)\cos(n\theta) \tag{5.52d}$$
$$\beta_{\theta,1} = B_{\theta 1} \sin(\bar{m}z)\sin(n\theta) \tag{5.52e}$$

with the capital quantities U_1 to $B_{\theta 1}$ representing the amplitude of the bifurcation modes. Substitution of the above harmonic field into Eqs. 5.9-5.11, and consequent substitution into the constitutive relations of Eqs. 5.13-5.15 and adjacent equilibrium Eqs. 5.51, eventually yields:

$$\cos(\bar{m}z)\cos(n\theta)\frac{Et}{r(1-\nu^2)}\Bigg(-U_1\bar{m}^2r^2 + \frac{\bar{m}r(V_1n(1+\nu)+2\nu W_1)}{2} + \frac{n^2(1-\nu)U_1}{2}\Bigg) = 0 \tag{5.53a}$$

$$\sin(\bar{m}z)\sin(n\theta)\frac{Et}{2r(1-\nu^2)}\Bigg(-V_1\bar{m}^2r^2(1-\nu) + r(\delta kt(1-\nu)B_{\theta 1} + U_1\bar{m}n(1+\nu)) - \delta kt(1-\nu)(V_1+nW_1) - 2n^2V_1 - 2nW_1\Bigg) = 0 \tag{5.53b}$$

$$\sin(\bar{m}z)\cos(n\theta)\Bigg(\frac{kEt^2}{2r(1+\nu)}\left(-\delta nV_1 - n^2W_1 + rnB_{\theta 1} - r^2\bar{m}^2W_1 - r^2\bar{m}B_{\phi 1}\right) + \frac{Et}{r(1-\nu^2)}\left(\nu r\bar{m}U_1 - nV_1 - W_1\right) - r\bar{m}^2W_1N_{\phi,0} - \frac{nV_1+n^2W_1}{r}N_{\theta,0} + \delta\frac{nV_1+W_1}{r}N_{\theta,0}\Bigg) = 0 \tag{5.53c}$$

$$\sin(\bar{m}z)\sin(n\theta)\frac{Et^2}{24r(1-\nu^2)}\Bigg(r\left(12k(1-\nu)(\delta V_1+nW_1) + t(1+\nu)\bar{m}nB_{\phi 1}\right) - B_{\theta 1}\left((1-\nu)r^2(12k+t\bar{m}^2)+2tn^2\right)\Bigg) = 0 \tag{5.53d}$$

$$\cos(\bar{m}z)\cos(n\theta)\frac{Et^2}{2r(1-\nu^2)}\Bigg(k(\nu-1)r^2(\bar{m}W_1+B_{\phi 1})-\frac{tr^2\bar{m}^2}{6}B_{\phi 1} - \frac{t(1-\nu)n^2}{12}B_{\phi 1}+\frac{(1+\nu)trn\bar{m}}{12}B_{\theta 1}\Bigg)=0 \tag{5.53e}$$

For a non-trivial solution to exist, such that the above equations may hold regardless of the meridional coordinate z or circumferential coordinate θ, the determinant of an array comprising coefficients of the bifurcation amplitude variables U_1 to $B_{\theta 1}$ needs to be equal to zero. Unlike the eigenvalue problem of Eq. 5.28, this determinant is that of a dense 5x5 array, as can be seen below:

$$\frac{Et}{r(1-\nu^2)}\begin{vmatrix} \frac{n^2(1-\nu)}{2}-r^2\bar{m}^2 & \frac{(1+\nu)rn\bar{m}}{2} \\ \frac{r(1+\nu)n\bar{m}}{2} & -\frac{2n^2+(1-\nu)(\delta kt+r^2\bar{m}^2)}{2} \\ \nu r\bar{m} & -n-n\frac{(1-\nu)kt}{2}-\frac{(1-\delta)(1-\nu^2)nN_{\theta,0}}{Et}\ ... \\ 0 & \frac{\delta(1-\nu)krt}{2} \\ 0 & 0 \end{vmatrix}$$

$$\begin{matrix} \nu r\bar{m} \\ -\frac{2n+\delta(1-\nu)ktn}{2} \\ ...-1-\frac{(1-\nu)kt(n^2+r^2\bar{m}^2)}{2}-\frac{r(1-\nu^2)(r^2\bar{m}^2N_{\phi,0}+N_{\theta,0}(n^2-\delta))}{Etr}\ ... \\ \frac{(1-\nu)krtn}{2} \\ \frac{(\nu-1)ktr^2\bar{m}}{2} \end{matrix} \tag{5.54}$$

$$\begin{vmatrix} 0 & 0 \\ 0 & \frac{\delta(1-\nu)ktr}{2} \\ ... \quad -\frac{(1-\nu)ktr^2\bar{m}}{2} & \frac{(1-\nu)ktrn}{2} \\ \frac{(1+\nu)rt^2n\bar{m}}{24} & \frac{(\nu-1)tr^2(12k+t\bar{m}^2)-2t^2n^2}{24} \\ \frac{12(\nu-1)ktr^2-2t^2r^2\bar{m}^2-(1-\nu)t^2n^2}{24} & \frac{(1+\nu)t^2rn\bar{m}}{24} \end{vmatrix}=0$$

Aiming to obtain an accurate analytical solution through a manageable and time-efficient work

pipeline, the author has utilised the mathematical programming capabilities of Maple (2022) to ensure the quality of the produced closed-form solutions. By setting $N_{\theta,0}$ and $N_{\phi,0}$ in turn equal to zero and solving the determinant of Eq. 5.54 one may obtain predictions of the bifurcation load $N_{m-n,thick}$ of cylinders under uniform meridional compression and $p_{m-n,thick}$ of cylinders under uniform external pressure, given as $p_{m-n,thick} = N_{\theta|m-n,thick}/r$ for a pure membrane pre-buckling stress state. Closed-form expressions for $N_{m-n,thick}$ are presented in Appendix C.1 while those for $p_{m-n,thick}$ may be found in Appendix C.2.

A considerably reduced form for the critical bifurcation load under meridional compression may be obtained by ignoring terms relating to non-shallow shell theory. This allows for an analytical result for shear-flexible, yet shallow, cylinders defined as:

$$N_{m-n,thick} = -tE\left(\frac{\bar{m}^2r^2}{(\bar{m}^2r^2+n^2)^2} + \frac{t}{2(\nu+1)}\frac{k(\bar{m}^2r^2+n^2)^2}{\bar{m}^2r^2\frac{6kr^2(1-\nu)}{t} + \bar{m}^2r^2(\bar{m}^2r^2+n^2)}\right) \tag{5.55}$$

The above relationship for $N_{m-n,thick}$ is considerably more manageable compared to the extensive formulae of Appendix C, though less accurate for stocky cylinders, as will be illustrated shortly. Nevertheless, it does offer itself as a validation check on the derivations correctness, reducing to the Donnell theory result as $k \to \infty$:

$$\begin{aligned}\lim_{k\to\infty} N_{m-n,thick} &= \lim_{k\to\infty} -tE\left(\frac{\bar{m}^2r^2}{(\bar{m}^2r^2+n^2)^2} + \frac{t}{2(\nu+1)}\frac{k(\bar{m}^2r^2+n^2)^2}{\bar{m}^2r^2\frac{6kr^2(1-\nu)}{t} + \bar{m}^2r^2(\bar{m}^2r^2+n^2)}\right) \\ &= -tE\left(\frac{\bar{m}^2r^2}{(\bar{m}^2r^2+n^2)^2} + \frac{t}{2(\nu+1)}\frac{(\bar{m}^2r^2+n^2)^2}{\bar{m}^2r^2\frac{6r^2(1-\nu)}{t}}\right) = N_{m-n,thin}\end{aligned} \tag{5.56}$$

Importantly, it hints at an unfortunate lack of a 'clean' minima topology for the various competing $m-n$ pairs, as an equivalent Koiter circle for the shallow finite-thickness result only presents itself for considerably more slender cylinders.

5.5 Examples

A series of selected examples are presented here illustrating the thick cylindrical shell theory just derived. After a display of linear stress analysis results for meridional compression and uniform external pressure, a demonstration of linearised predictions for the critical bifurcation load of various cylindrical models follow. Computational results are included where possible, for additional verification.

In all that follows, the material parameters of the cylinders are kept constant, with a Poisson ratio of $\nu = 0.3$ and a Young's modulus of $E = 2 \cdot 10^5\ N/mm^2$. The boundary conditions classification scheme of EN 1993-1-6 (2025) is adopted for the definition of edge restraints, with Yamaki's equivalents additionally used as a reference (Yamaki, 1984). Characterisation of the cylinder length is made in a dimensionless manner in terms of a group ω, as defined earlier in this document by Eq. 4.1.

The linear elastic stress analysis examples of the next section have been implemented in both Python scripts and Excel spreadsheet form, included in the accompanying GitHub repository `https://github.com/AchilleasF/RSPA-ThickCylinders`. Python functions for the shear-flexible prediction of the bifurcation buckling load of cylinders under meridional compression or external pressure may also be found in the repository.

5.5.1 Linear elastic stress analysis examples for shear-flexible axisymmetric cylinders

Owning to the principles of superposition that linear elasticity allows for, the individual study of a cylindrical system under either uniform meridional compression or uniform external pressure illustrates the theory's correctness for combinations of these two load cases while showcasing the discrepancies between thin and thick analytical shell theories and results obtained computationally from the well-established ABAQUS (2022) finite element software.

For the stress analysis comparisons to be meaningful and any discrepancies between thin and thick cylindrical shell theories to be made apparent, a very low $r/t = 5$ ratio is chosen for both loading scenarios accompanied by a unit thickness. Geometric definition of the following models is concluded by a dimensionless group $\omega = 5$. Even according to thin shell theory, the material and geometric parameters used for the stress analysis examples here lead to a normalised length ratio of $L/\lambda_{thin} = 2.05$. The thick theory bending half-wavelength λ_{thick} of Eq. 5.40 has been found to be always higher than its thin theory equivalent, thus ensuring interaction of the $2\lambda_{thick}$ bending boundary layers.

5.5.1.1 Cylinder under uniform meridional compression

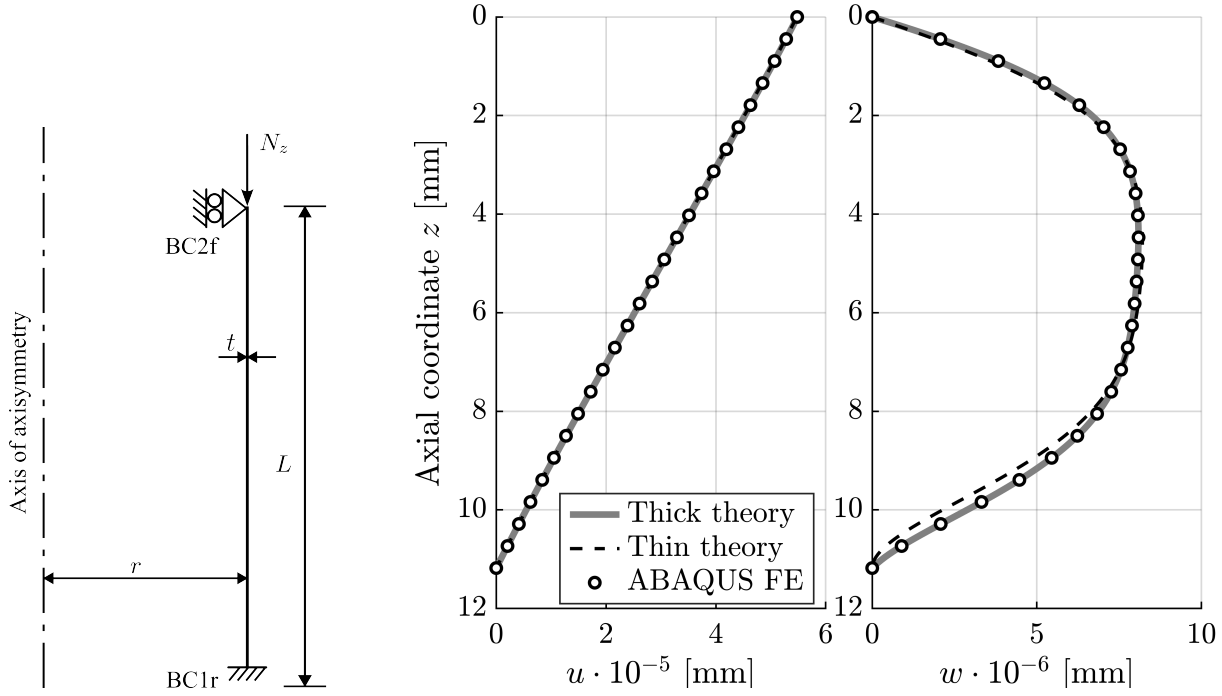
A cylinder under uniform meridional compression (introduced via a compressive meridional edge load) constitutes the first example presented here. The generating meridian with its loading and BCs is illustrated in its axisymmetric space in Fig. 5.3a, with the corresponding analytical and computational displacement fields in Fig 5.3b. A unit compressive edge load $N_z = -1\ N/mm$ is applied on its top end, with the negative sign owning to the convention for membrane stress resultants being positive under external loading. The present derivations offer a more flexible cylinder deformation pattern due to the inclusion of shear strain effects in the formulation, as displayed in Fig. 5.3b. More pronounced deflection profiles are commonly associated with higher strain energy outputs and hence closer estimates of the ideal continuum behaviour of a mechanical body. A very close agreement between the thick shell solution with reference finite element results is presented in Fig. 5.3b for the u and w displacement profiles and in Fig. 5.4 for the meridional and circumferential stress patterns.

5.5.1.2 Cylinder under uniform external pressure

The displacement field of Eqs. 5.44-5.45 additionally allows for a finite-thickness solution to the problem of a cylinder under normal pressure. A unit external pressure $p = -1\ N/mm^2$ is applied on the cylinder of Fig. 5.5a. The more flexible solution of the thick cylindrical theory is in agreement with the ABAQUS FE displacements (Fig. 5.5b) and stresses (Fig. 5.6). As was the case with the bending half-wavelength λ of Eq. 5.40, the solutions for both loadcases considered here quickly reduced to their thin shell theory equivalents, either naturally by increasing the r/t aspect ratio of the models or by enforcing a thin theory through values of $k \to \infty$.

5.5.2 Linearised stability analysis for shear-flexible cylinders

Solution of the determinant problem of Eq. 5.54 allows for the elastic critical buckling loads to be computed for two of the most important reference shell systems, a cylinder under meridional compression and under external pressure individually. As was the case with the stress analysis examples presented earlier, the inclusion of transverse shear force effects on the cylinders' mathematical representation results in a more flexible behaviour, that ultimately leads to consistently lower critical bifurcation buckling load predictions. Very low r/t ratios will be adopted were possible to highlight the conservativeness of the present approach for stockier



(a) System geometry. (b) Meridional u and normal w displacement profiles.

Figure 5.3: Cylinder under uniform meridional compression.

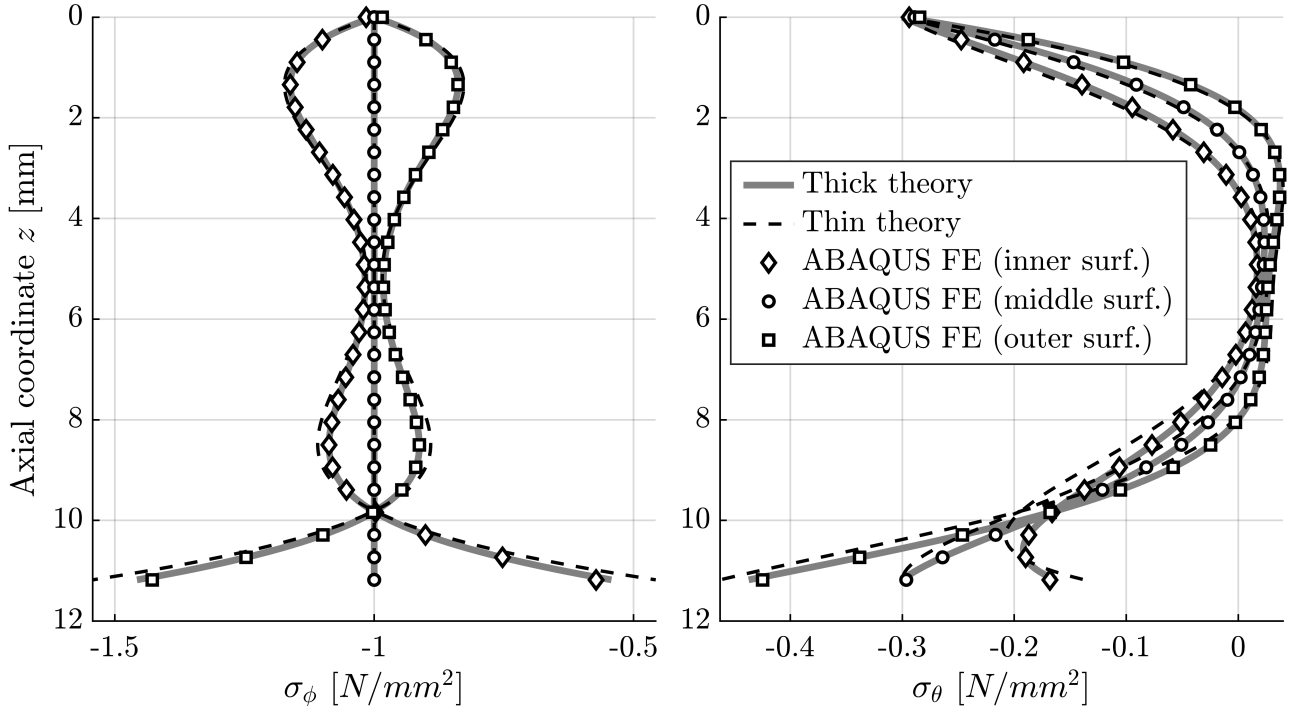
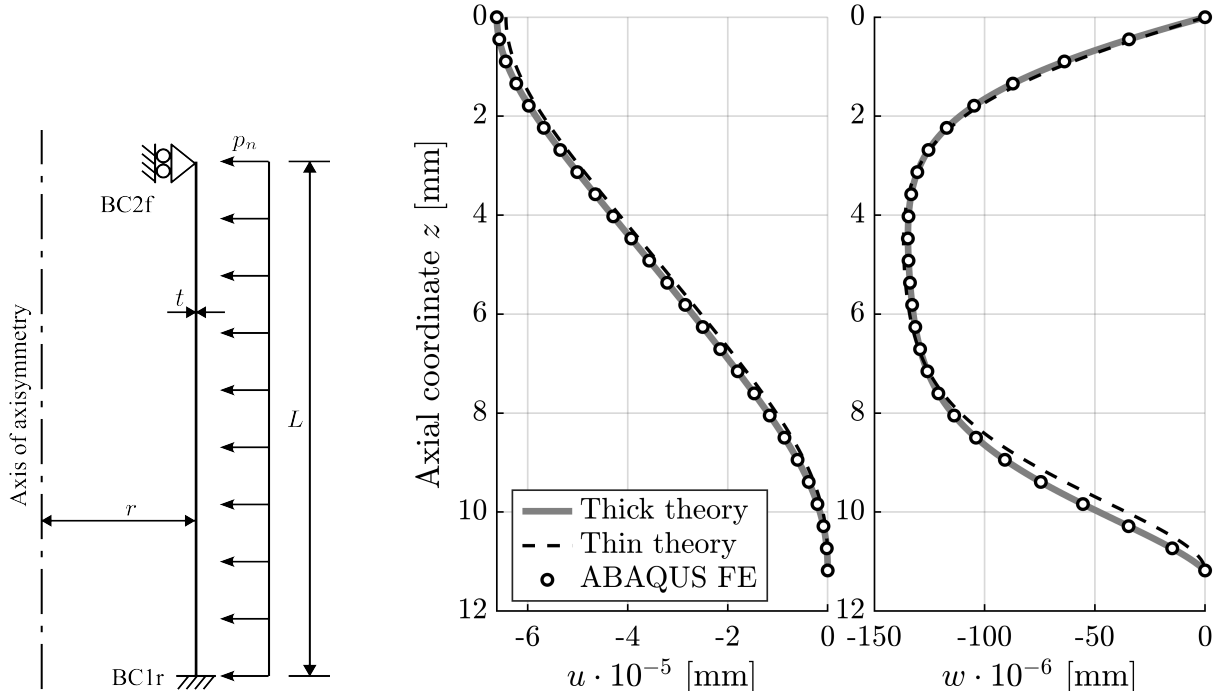


Figure 5.4: Meridional (left) and circumferential (right) axisymmetric stress patterns for a cylinder under uniform meridional compression.

models, while paying equal attention to more slender models and ensuring that the results tend to their thin shell theory counterparts as r/t increases.

5.5.2.1 Bifurcation buckling of cylinders under uniform meridional compression

A direct comparison between thin and thick cylindrical shell theories cannot be a sufficient metric on the validity of the latter, as the two are supposed to diverge for stockier models but



(a) System geometry. (b) Meridional u and normal w displacement profiles.

Figure 5.5: Cylinder under uniform external pressure.

the extent of these discrepancies is currently unknown. As an amendment to these ramifications in the verification process, finite element results are included in the comparisons, allowing for external sources of critical load predictions. ABAQUS offers a handful of axisymmetric shell elements for the modelling of a cylinder under meridional compression, with the general-purpose thick or thin SAX1 element being considered good candidates. However, ABAQUS does not allow for non-symmetric bifurcation modes to be explored on its 2D axisymmetric models, a shortcoming that limits the applicability of ABAQUS axisymmetric shell elements to be used as a point of reference for the thick cylinders' behaviour to only fully axisymmetric $n = 0$ buckling modes. The alternative of the 'panel technique' (Sadowski *et al.*, 2018) for the computation of non-symmetric modes shall not be employed here, mainly due to its laborious nature that stems from the inclusion of parasitic DOFs in the 3D modelling space for what is inherently a mathematically 2D problem.

The recently released AQUINAS toolbox for the nonsymmetric bifurcation buckling analysis of thin axisymmetric shells assumes a harmonic displacement field similar to that of Eqs. 5.52. It additionally allows for different restraints to be assigned at the exposed edges of the shell during the pre-buckling stress analysis step and the subsequent eigenvalue computations. A closer approximation to the analytical shell theories can be achieved in this manner, as appropriate BCs during the pre-buckling step can ensure a uniform membrane pre-buckling stress state for the cylinder, without the need to be carried on to the buckling step. For this to be achieved, the BCs for the pre-buckling stage are assumed to be a free edge at the loaded end and a meridional support $w = 0$ at the base of the cylinder. A BC2f-BC2f is assumed for the buckling step, as implied by the harmonic field of Eqs. 5.52. The same result may be also achieved in ABAQUS by differentiating boundary conditions as *stress perturbation only* or *buckling mode calculation only*.

The formulae presented in Appendix C are examined in the following investigation of critical load predictions for cylinders of varying slenderness for a handful of dimensionless groups ω, as illustrated in Fig. 5.7. To allow for a consistent comparison, only axisymmetric modes $n = 0$ are

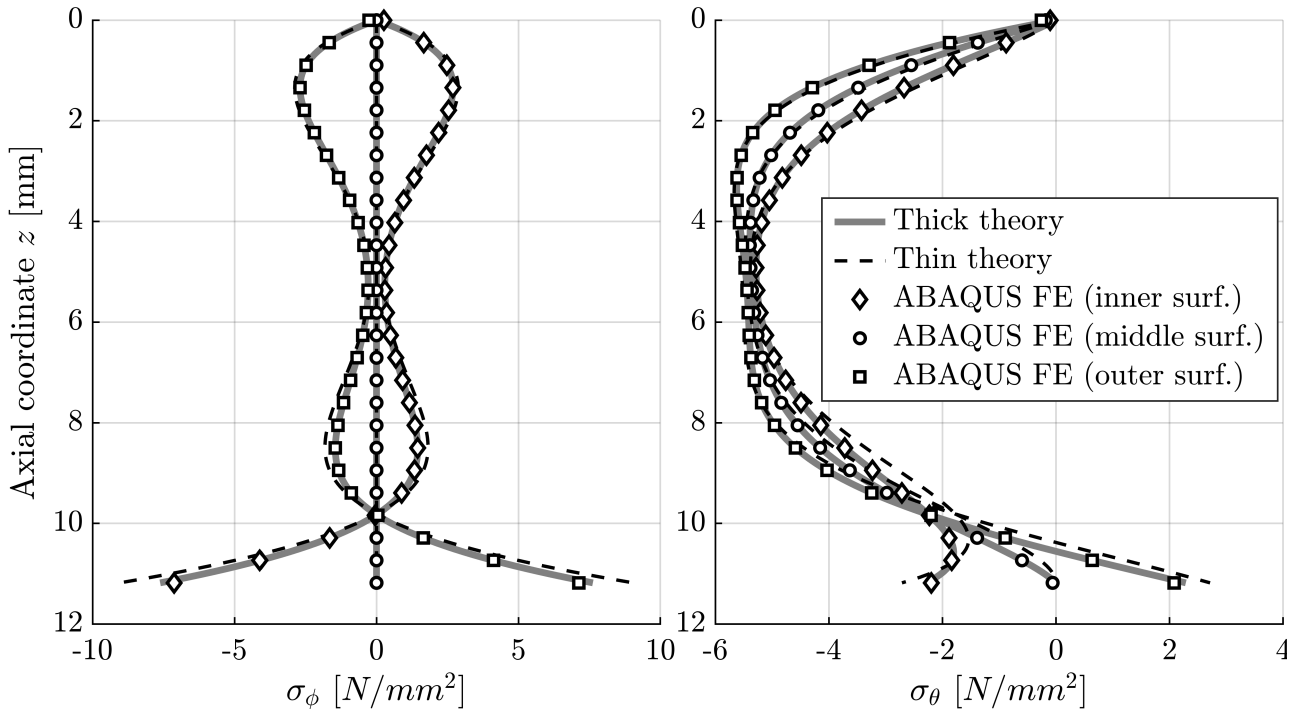


Figure 5.6: Meridional (left) and circumferential (right) axisymmetric stress patterns for a cylinder under uniform external pressure.

trialled in this initialled screening of the thick cylindrical theory, regardless of the meridional half-wavelength m that would be critical. It is evident that the expressions of Appendix C are in close agreement with those computationally obtained using the thick or thin ABAQUS SAX1 element for every r/t ratio considered. The thin only FE formulation of AQUINAS falls short on its predictions for the stockier models, showcasing however an increasing divergence for lower r/t ratios due to the non-shallow shell theory effects included in the strain-displacement fields of its formulation. It should also be noted that the analytical thin theory result of Fig. 5.7 does not fall exactly at 1.0 because the axisymmetric mode that is enforced on these curves is not necessarily the one that leads to the critical load $N_{cl,thin}$ of Eq. 5.5, a relationship that additionally assumes continuous values for the critical $m-n$ pairs.

A fuller exploration of the bifurcation loads N_{m-n} associated with each competing harmonic $m-n$ pair is displayed in Fig. 5.8. The two theories progressively diverge as higher wavenumbers are considered, for both the meridional and circumferential directions. Bifurcation patterns that are of a 'wavier' nature are physically associated with higher bending strain energy outputs once buckling occurs, which as may be expected are accompanied by an analogous quantity of shear strain energy. This effect can be captured by the present shear-flexible theory, leading to predictions that are lower estimates for the bifurcation load, regardless of whether or not they refer to critical wavenumber pairs.

As was highlighted in the discussion following the determinant problem of Eq. 5.54, a closed-form minimisation of the $N_{m-n,thick}$ (Eq. C.1) is not possible due to the complexity and range of terms included in the relationship of Appendix C. The lack of a meaningful minima on the surface of bifurcation loads for finite-thickness cylinders can be also graphically deduced from closer inspection of Fig. 5.8. Tracing the 'valley' of the thick shell theory surface numerically towards the left-hand side of the curve, from higher to lower meridional half-waves numbers m, the critical bifurcation load is found to be steadily decreasing, unfortunately making it impossible to establish a minimised $N_{cl,thick}$ analytically in closed form.

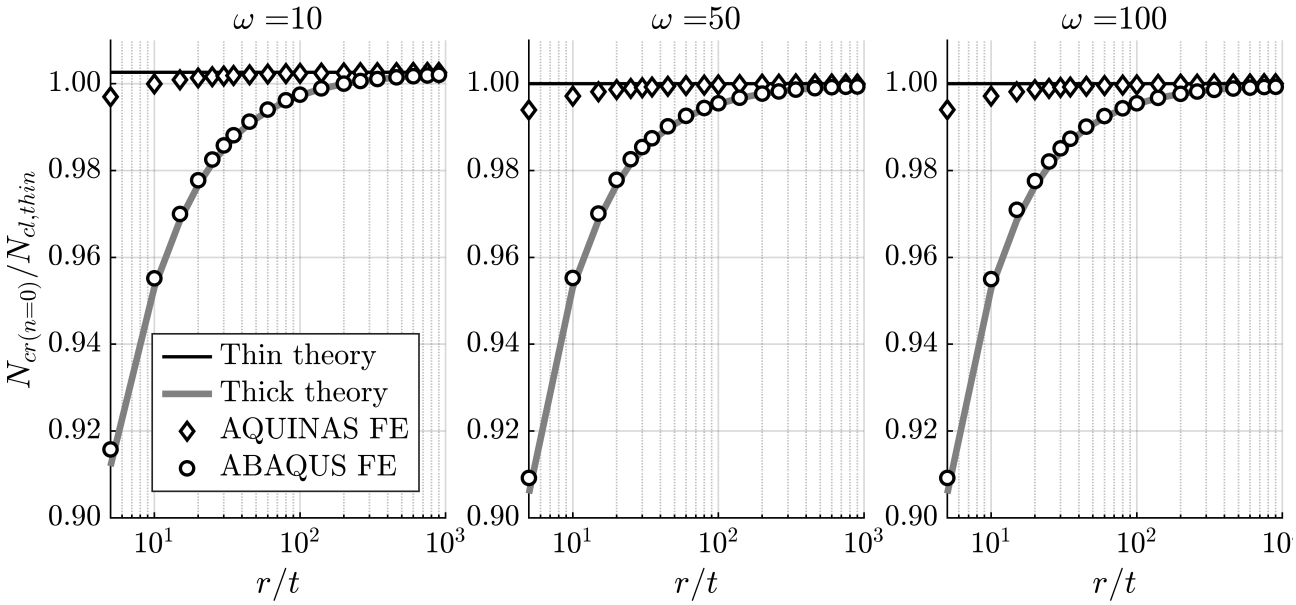


Figure 5.7: Normalised critical loads for cylinders under uniform meridional compression, considering only axisymmetric modes.

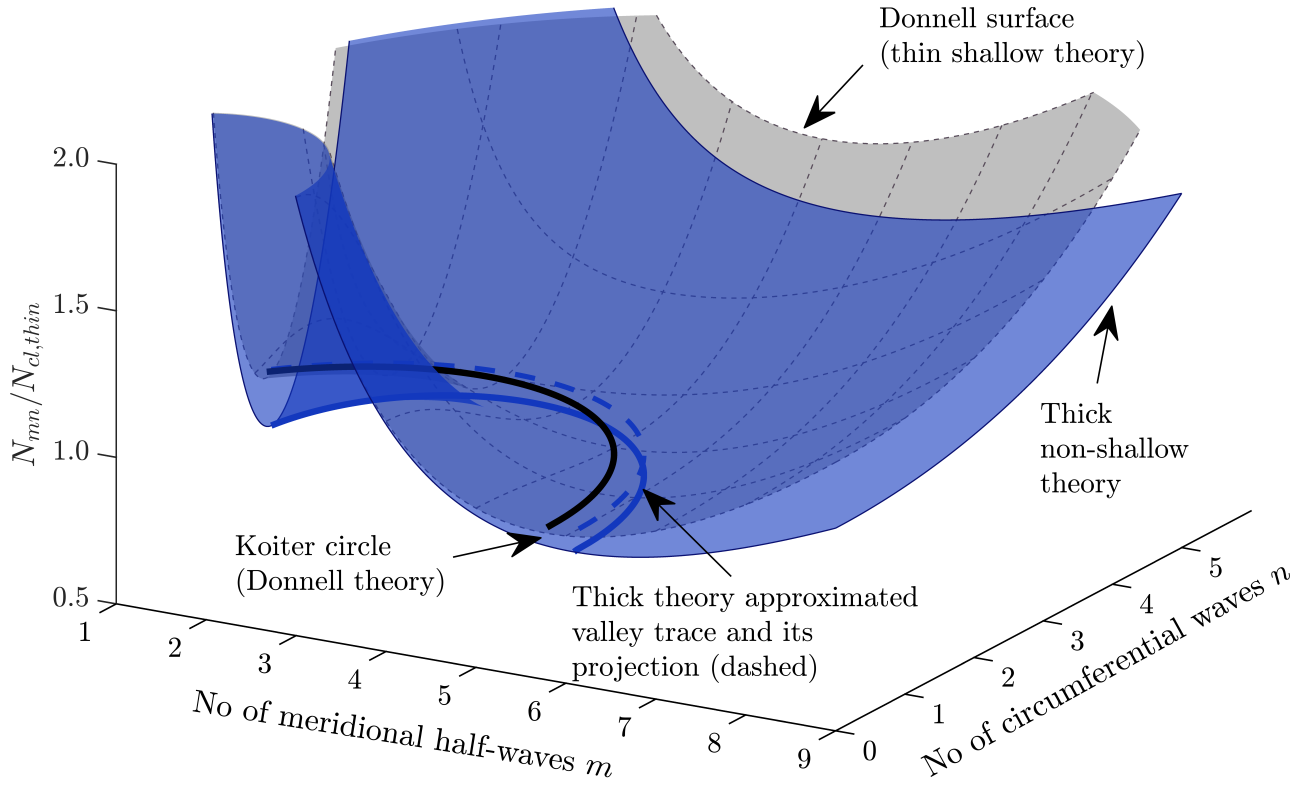


Figure 5.8: Surfaces of analytically evaluated loads with respect to the $m-n$ pairs for a cylinder under uniform meridional compression, according to thin and thick cylindrical shell theories.

Whilst no equivalent topology to that of the Koiter circle can be identified for the thick theory surface, where all $m-n$ would be simultaneously critical for the cylinder to bifurcate into, the projection of the valley of said surface can be roughly approximated by a circle in the $\bar{m}-n$ space. The radius of that circle may be computed by considering an axisymmetric mode $n=0$

and differentiating Eq. C.1 with respect to $\bar{m}$, yielding the following relationship:

$$\rho_{thick} = \frac{\sqrt{-3k(\nu^2 + \sqrt{3}kr\sqrt{1-\nu^2}\,(\nu-1)-1)}}{\sqrt{-2t(\nu + 3k^2r^2\,(\nu-1)+1)}} \tag{5.57}$$

A circle that is centred at (ρ_{thick}, 0) and has a radius ρ_{thick} in $\bar{m} - n$ space traces the base of the thick shell theory 'valley' (with the appropriate transformations applied in Fig. 5.8 to go from $\bar{m} - n$ space to $m - n$ space), leading to ever-reducing critical bifurcation edge loads when moving counter-clockwise along it. Further processing of this empirically fitted result allows for the axisymmetric mode's meridional half-wavelength $\lambda_{axi,thick}$, to be derived as:

$$\lambda_{axi,thick} = \frac{\pi}{\rho_{thick}} = \frac{\pi\sqrt{-2t(\nu + 3k^2r^2\,(\nu-1)+1)}}{\sqrt{-3k(\nu^2 + \sqrt{3}kr\sqrt{1-\nu^2}\,(\nu-1)-1)}} \tag{5.58}$$

while the square 'chequerboard' buckling mode pattern's circumferential $\lambda_{\theta,thick}$ and meridional $\lambda_{\phi,thick}$ half-wavelengths for $\bar{m} = n$ are:

$$\lambda_{\phi,thick} = \lambda_{\theta,thick} = 2\frac{\pi}{\rho_{thick}} = 2\frac{\pi\sqrt{-2t(\nu + 3k^2r^2\,(\nu-1)+1)}}{\sqrt{-3k(\nu^2 + \sqrt{3}kr\sqrt{1-\nu^2}\,(\nu-1)-1)}} \tag{5.59}$$

These results can be shown to reduce to their corresponding thin shell theory half-wavelengths as $k \to \infty$ from above through a method similar to Eq. 5.56.

5.5.2.2 Bifurcation of cylinders under uniform external pressure

For stocky cylinders under external pressure, neglecting the additional effect of a centrally directed pressure as the shell wall deforms in the circumferential direction while buckling occurs already substantially overestimates the critical load by up to 25% (Brush & Almroth, 1975), a shortcoming of classical Donnell theory (Xue *et al.*, 2013). This already introduces two very different families of thin shell theories, especially for cylinders where the critical mode involves just two full-waves along the circumference of the shell, with the effect of centrally directed pressure in the buckled state of the shell being included in the non-shallow version of Eqs. 5.48 stability system.

As the starting point for the thick shell theory presented here is Donnell's theory, the results are only valid for circumferential harmonics $n \geq 2$ (Brush & Almroth, 1975). A graphical comparison of critical external pressures is shown in Fig. 5.9 for a handful of r/t ratios that characterise considerably stockier cylindrical shell models. The $r/t = 100$ ratio is kept in Fig. 5.9 as a point of reference with the original (Brush & Almroth, 1975), rather than a meaningful evaluation of the different theories considered. Comparison with analytical non-shallow thin shell theory solutions exhibits a very good agreement for cylinders as thick as $r/t = 50$, with the predictions of the critical harmonic being indifferent to the inclusion of finite-thickness effects. The analytical results only begin to deviate from their non-shallow thin theory counterparts for $r/t = 10$ and normalised $L \leq \pi r$ lengths on the left hand-side of the curve, suggesting that the inclusion of transverse shear force effects on the stability of pressurised cylinders predominantly affect very short and stocky models. These deviations are even more pronounced for an $r/t = 5$ ratio, suggesting that finite-thickness effects should not be ignored for very thick cylinders under pressure.

As an additional source of validation, FE results have once more been considered. Full 3D ABAQUS cylindrical models under external pressure were used, with the boundary conditions

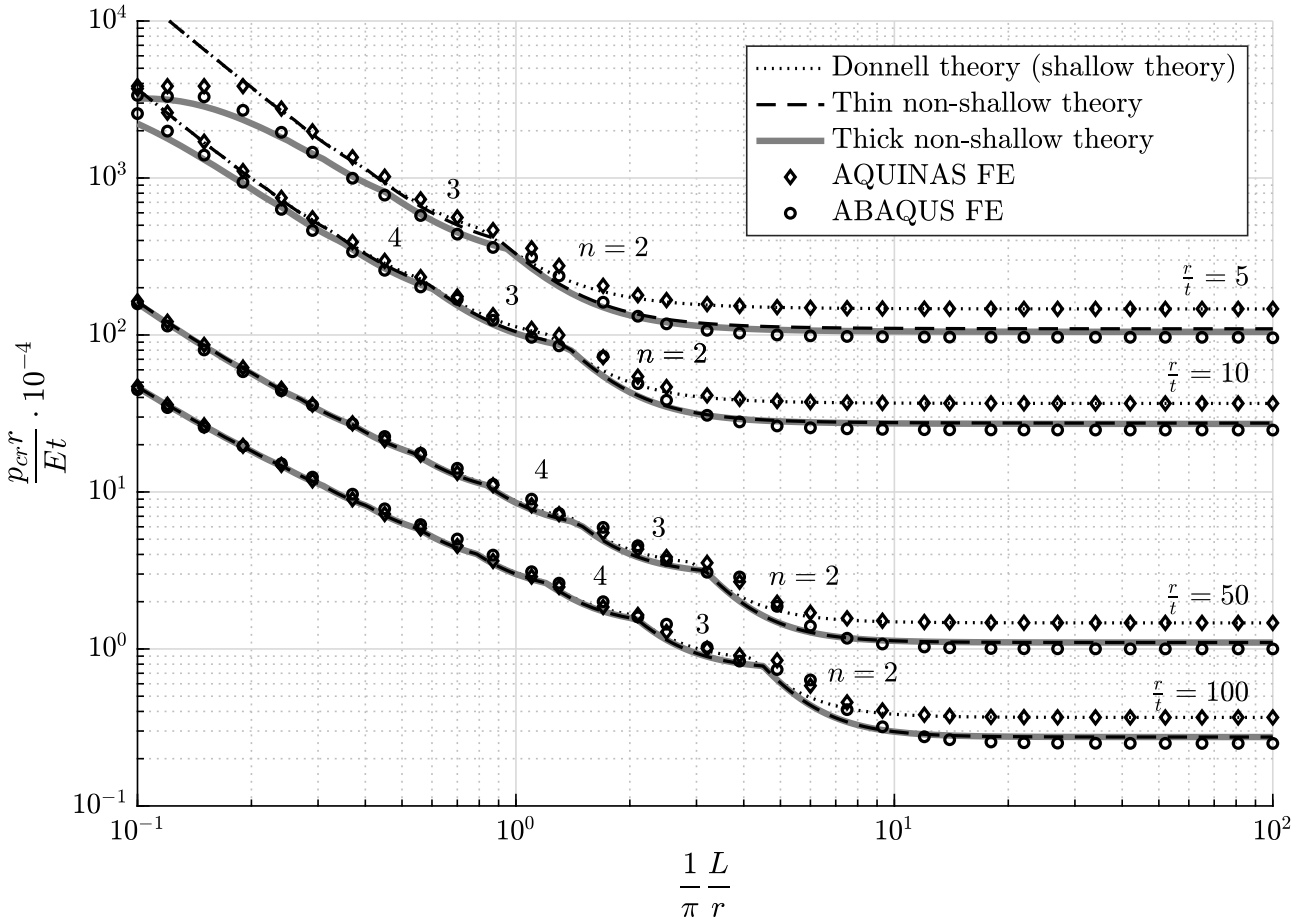


Figure 5.9: Normalised critical bifurcation pressures p_{cr} for selected r/t ratios and varying lengths for any possible combinations of $m - n$ wavenumbers.

for stress perturbation or buckling mode calculation being selected on a basis that ensures a pure membrane pre-buckling stress but also reflects the assumptions made in the harmonic displacement field of Eqs. 5.52. An equal set of natively axisymmetric AQUINAS models were considered, with the same technique applied in the previous section for the pre-buckling stress state also adopted here. It may be seen that the analytical results of the derivations presented for shear-flexible cylinders best match those of a full, thick or thin, ABAQUS FE analysis. Despite AQUINAS' non-shallow formulation for the strain-displacement field being aligned with the kinematic relations presented earlier, with the rotations of Eqs. 5.12 considered instead of the transverse shear strains in Eqs. 5.10, its results are unable to capture the effect of centrally directed pressure in the buckled configuration of the cylinder. As a consequence, AQUINAS shows a better agreement with Donnell's shallow theory results in Fig. 5.9 for long tubes. Additionally, it is evident from the lowest $r/t = 5$ ratio considered that its strictly thin shell FE formulation (Teng & Rotter, 1989a,b) is not appropriate for the analysis of such short and stocky models, a range of shells that the AQUINAS toolbox has not yet been extended to cover.

While differentiation of the relationships in Appendix C is intractable, it is empirically evident that a single meridional wave $m = 1$ always leads to the most conservative prediction for the buckling pressure $p_{cr,thick}$, as is the case for thin shell theory.

5.6 Conclusions

Analytical closed-form expressions have been derived for finite-thickness shear-flexible cylinders under two fundamental axisymmetric loadcases, meridional compression and external pressure. The inclusion of transverse shear strains in the kinematic relationships of Green's strain tensor leads to a more flexible behaviour and therefore a closer approximation to the cylinder's functioning as an ideal continuum body. Effects of the present, shear-flexible theory for cylindrical shells gradually diminish and can eventually be ignored as the slenderness of the models increases, most commonly through their radius over thickness r/t ratio. A thin shell theory can additionally be enforced on the expressions derived here by assuming that the shear correction factor k tends to infinity.

Equilibrium on the undeformed configuration of the cylinder, after simplifications concerning the pure axisymmetric state of the cylinder have been applied, leads to a second order linear system of ODEs, involving the meridional displacement u, normal displacement w and meridional rotation β_ϕ. This system can only be partially uncoupled, after the displacement u has been eliminated, but cannot be reduced to a single equation that only involves the normal displacement w, as was the case with thin shell theory. Consequently, a solution to the homogeneous part is obtained through an eigenvalue problem, with membrane theory providing a particular solution that completes the bending theory finite-thickness solution. The finite-thickness bending half-wavelength λ is found to be reducible to its thin cylindrical shell theory equivalent as $k \to \infty$, while for a regular value of $k = 5/6$ bending boundary effects are found to penetrate deeper along the cylinder's meridian. The unknown coefficients of the displacement field can be evaluated through application of boundary conditions to the model.

A linearised form of the elastic stability expressions can be obtained by considering equilibrium of the shell in a slightly perturbed configuration. It is natural for a theory that refers to relatively stocky models to additionally include terms relating to non-shallow shell theory, further complicating the derivation process. Application of the adjacent equilibrium criterion yields a stability problem whose solution requires a doubly harmonic displacement field that satisfies the edge boundary conditions. Computing the critical bifurcation edge load or external pressure for shear-flexible cylinders once again relies on the evaluation of a determinant. The complexity and format of the closed-form relationships obtained does not allow for a topological construct equivalent to the 'Koiter circle' for thick cylinders, a consequence of including both transverse shear force effects and non-shallow shell theory terms.

The results of the formulae presented for $N_{m-n|thick}$ and $p_{m-n|thick}$ consistently provide conservative estimates for the buckling loads of these two important reference shell systems, with the magnitude of the discrepancies between thin and thick theories becoming negligible as the models become more slender. Development of EN 1993-1-6, or of other standards concerned with the design of cylindrical shells under these fundamental loading scenarios, may benefit from the results presented here: a stiffer thin shell theory result becomes progressively unconservative for stockier shells, a feature that is currently not easily corrected for in the EN 1993-1-6 capacity curve used for buckling strength verifications except through ad-hoc empirical modifications.

Chapter 6

Challenges in the development of a shear-flexible axisymmetric shell element

6.1 Motivation

After the analytical intermission of the previous chapter, the focus of the present document is once again shifted into the computational treatment and exploration of axisymmetric shell structures, to be examined in the context of the capacity curve framework of EN 1993-1-6 (2025). The nonlinear thin shell formulation adopted for AQUINAS proved unsuitable for the evaluation of a physically interpretable slenderness λ_0 for which a cylinder under meridional compression attains its full plastic resistance R_{pl} through a GMNA, as the results and discussion of Section 4.3.3 have illustrated. Considering the stockiness of cylindrical shells in the range of slendernesses at which a model is expected to fail through a predominantly plastic collapse mode, a logical starting point for extending the capabilities of the MATLAB scientific toolbox is the inclusion of finite-thickness effects on the linear and nonlinear kinematics of the coded finite element.

The success of the commercial computational software ABAQUS (2022) for numerically determining the value of the λ_0 slenderness parameter for meridionally compressed cylinders has only reinforced prior convictions on the importance of explicitly defined shear strains and stresses in a path tracing analysis of thick walled shells, owing to the thick or thin shell formulation of the SAX1/SAX2 elements. With these two axisymmetric shell elements being simple extensions of the planar B21/B22 beam elements through the inclusion of hoop strains and stresses as formally stated in the documentation of the commercial solver, literature resources relating to their formulation (Budiansky, 1963; Rodal & Witmer, 1979) will be examined in an effort to reproduce axisymmetric squash load evaluations through the derivation presented here. The simplicity of the interpolation order and programming implementation, as understood by the author through his experience with the SAX1/SAX2 elements in ABAQUS and a study of the corresponding theoretical guide sections, present an appealing case for a potential new formulation to be adopted as an update to the already released MATLAB toolbox (Filippidis & Sadowski, 2023b). Nevertheless, axisymmetric shell and beam finite elements from alternative resources will also be examined, provided that they are properly documented with a plethora of references to support their implementation, prioritising open-source computational tools over any black-box solvers.

A reproduction of the analytical elastic results for both stress analysis and linear bifurcation buckling analysis presented in the previous chapter will be a natural first step into the verification of any finite element formulation to take place in the following sections. Comparisons will be extended to different axisymmetric shell geometries, examining the reliability of the proposed element across different models and loading scenarios, with FE solutions from the commercial ABAQUS (2022) solver included in the validation process. The success of any produced derivation will be determined based on its accuracy for the generation of capacity curves for cylinders under meridional compression with an emphasis on low slenderness models, as the formulatory nature of this study aims to amend the shortcoming of the AQUINAS software and establish its versatility and reliability across a wider range of axisymmetric shell problems.

6.2 Approaches and scope of development

Two distinct options are available to determine the future of the newly released software. The discussion on the validity and implementation feasibility of these alternatives will be the main focus of the present section, considering the pros and cons from both a developer's and an analyst's point-of-view. It is essential to identify potential shortcomings of an individual approach that can hinder utilisation in the context of a geometrically nonlinear incremental analysis, as the element to be eventually employed in AQUINAS will be expected to reliably predict the strength of a wide assortment of axisymmetric shell geometries and load cases.

6.2.1 Extension of the AQUINAS element formulation

An approach of significant appeal for the introduction of computational capabilities for shear-flexible shells into the AQUINAS solver could involve the enhancement of the Teng & Rotter (1989a,b) finite element formulation to incorporate shear strains and stresses. Augmentation of the meridionally cubic interpolation field to account for finite thickness effects without complete redevelopment of the element mechanics would leverage all prior software functionality with minimal alterations to its overall architecture and internal procedures, promoting maintenance and reducing testing requirements upon further releases of the FE toolbox. The kinematic relationships of Eqs. 3.13 and Eqs. 3.14 would be retained, with the exception of strains relating to derivatives of the normal to the shell wall displacement $\bar{w}$ that would now be expressed in terms of the meridional rotation β_ϕ, as Assumption 5 (see Section 2.1.1) would not be relevant any more. Introduction of shear strains and stresses would require minor alterations to the computation and treatment of residual forces in the context of nonlinear analyses, but would otherwise leave the most complex internal procedures unaffected.

Disassociation of $\partial\bar{w}/\partial s$ and β_ϕ introduces a new challenge in the formulation of such an element, as their equivalency is inherently assumed through the interpolation field of Eqs. 3.5, employing the Hermitian cubic shape functions of Eqs. 3.2 for the derivation of an MITC axisymmetric shell element. Disruption of this equivalency through the inclusion of shear strain terms would result in an interpolation field that cannot utilise $\partial\bar{w}/\partial s$ derivatives, rendering adoption of regular Hermitian cubics unfeasible. Naturally, shear-flexible finite elements are established on the basis of independent interpolation fields for translational and rotational DOFs (Zienkiewicz *et al.*, 1977; Cook, 1982), commonly of the same order even though Tessler & Dong (1981) has provided arguments against this technique and suggestions towards using polynomials for interpolation of the rotational field of exactly one order lower than those used for transverse displacements, without any of these schemes blending the two for the evaluation of the element's deformed reference surface/axis. An alternative to the independent interpolation of $\bar{w}$ and β_ϕ can however be found in relevant literature, leveraging the characteristics of cubic Hermitian shape

functions to retain a mixed interpolation field. A Timoshenko beam finite element for the static and dynamic analysis of frame structures with interdependent polynomials for the transverse and rotational DOFs has been presented by Friedman & Kosmatka (1993), isolating bending and shear behaviours of an element through a stiffness parameter ψ, responsible for scaling the associated terms of the interpolation field to describe element kinematics. Similar concepts for a parametrised interdependent interpolation field where later adopted by several other classical formulatory works (Reddy, 1997; Edem, 2006). The ψ ratio of bending over shear stiffnesses is herein expressed in the context of axisymmetric shells, substituting the beam width that the corresponding relationship in Friedman & Kosmatka (1993) requires for calculating the beam cross-sectional area A and its second moment of area I with an infinitesimal circumferential length of $r\,d\theta$, readily cancelling out from both the numerator and denominator of the following expression and resulting in a dependency to the shell wall thickness t, the element length L (not to be confused with the element half-length L used throughout Chapter 3) and the elastic material properties.

$$\psi = \frac{1}{L^2}\left(\frac{Et^2}{kG}\right) \tag{6.1}$$

Shape functions that isolate bending and shear behaviour within an element can then be defined in an isoparametric space, appropriately adjusted from the general description of Friedman & Kosmatka (1993). The notation has additionally been altered to the one adopted throughout the current document, with reference to the element geometry system of Figure 3.1.

$$[N_{\bar{w}}] = \begin{bmatrix} \dfrac{1}{4(1+\psi)}\Big\{\eta^3 - 2\eta\psi - 3\eta + 2\psi + 2\Big\} \\ \dfrac{L}{4(1+\psi)}\Big\{\eta^3 - \eta^2\psi - \eta^2 - \eta + \psi + 1\Big\} \\ \dfrac{1}{4(1+\psi)}\Big\{-\eta^3 + 3\eta + 2\eta\psi + 2\psi + 2\Big\} \\ \dfrac{L}{4(1+\psi)}\Big\{\eta^3 + \eta^2\psi + \eta^2 - \eta - \psi - 1\Big\} \end{bmatrix} \tag{6.2}$$

$$[N_{\beta_\phi}] = \begin{bmatrix} \dfrac{3}{2L(1+\psi)}\Big\{\eta^2 - 1\Big\} \\ \dfrac{1}{4(1+\psi)}\Big\{3\eta^2 - 2\eta\psi - 2\eta + 2\psi - 1\Big\} \\ \dfrac{3}{2L(1+\psi)}\Big\{1 - \eta^2\Big\} \\ \dfrac{1}{4(1+\psi)}\Big\{3\eta^2 + 2\eta + 2\eta\psi + 2\psi - 1\Big\} \end{bmatrix} \tag{6.3}$$

such that normal to the shell surface displacements $\bar{w}$ and meridional rotations β_ϕ are then interpolated within an element as:

$$\begin{Bmatrix} \bar{w} \\ \beta_\phi \end{Bmatrix} = \begin{bmatrix} [N_{\bar{w}}]^T \\ [N_{\beta_\phi}]^T \end{bmatrix} \begin{Bmatrix} \bar{w}_1 \\ \beta_{\phi 1} \\ \bar{w}_2 \\ \beta_{\phi 2} \end{Bmatrix} \tag{6.4}$$

The magnitude of the ψ parameter scales the corresponding interpolation fields of Eqs. 6.2 and 6.3 to different polynomial orders, as is visually illustrated in Figure 6.1. For bending dominated interpolation fields, corresponding to low values of the ψ stiffness ratio, the element shape functions readily reduce to the Hermitian cubics employed in Teng & Rotter (1989a), provided in Eqs. 3.2 and notated as N_H in Fig 6.1 (n.b. in the context of the finite element formulation presented in Chapter 3, the interpolation is applied on nodal displacements and their first derivatives with respect to the meridional coordinate s instead of the rotational DOF β_ϕ). In scenarios where shear behaviour is important to describe the response of the element and its contribution cannot be neglected, higher values of ψ reduce the polynomial order of both $N_{\bar{w}}$ and N_{β_ϕ}, with an interpolation field for normal displacement $\bar{w}$ that is linear with respect to the nodal translational DOFs $\bar{w}_i$ and quadratic with respect to nodal rotational DOFs $\beta_{\phi i}$, while the interpolation field for the meridional rotation β_ϕ is now linear in terms of nodal rotations $\beta_{\phi i}$ and does not depend on nodal translations $\bar{w}_i$.

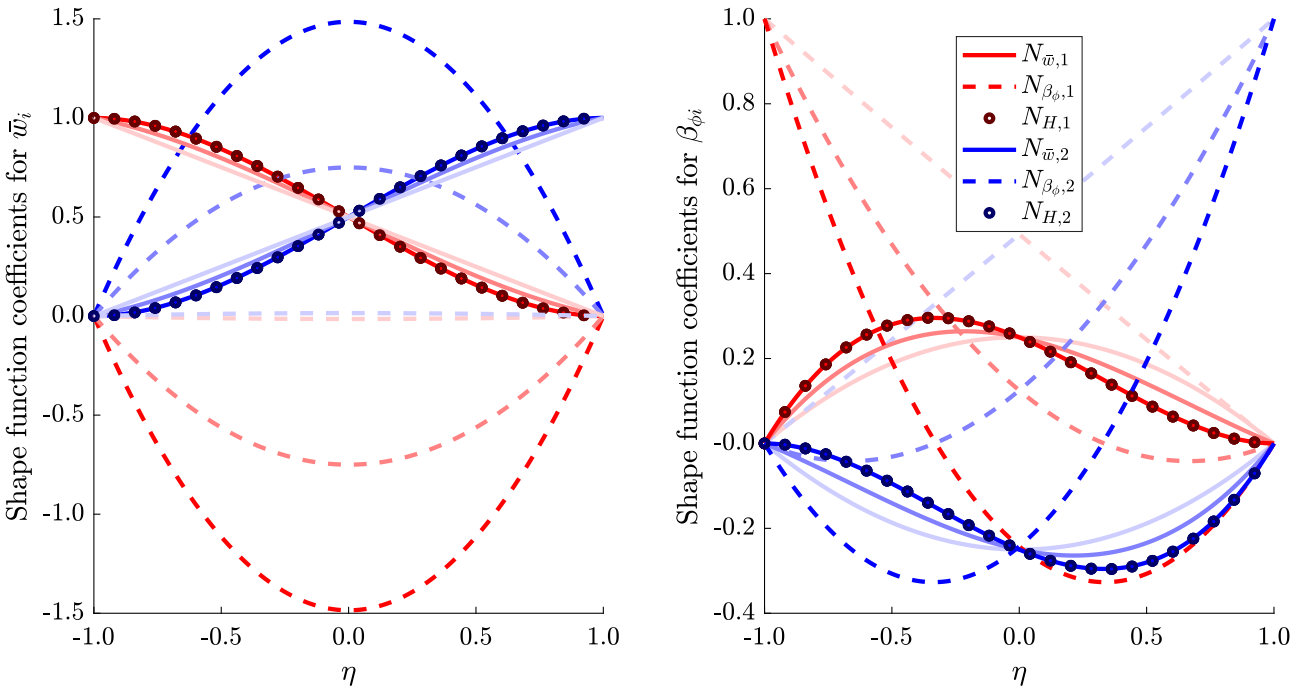


Figure 6.1: Shape functions for the interpolation of normal displacement $\bar{w}$ (left) and meridional rotation β_ϕ (right) fields for varying amplitudes of the ψ parameter. Solid lines are associated to interpolation fields utilising the nodal translational DOF $\bar{w}$ while dashed lines utilise the nodal rotational DOF β_ϕ, as per Eq. 6.4. Higher colour transparency corresponds to higher values for the ψ stiffness ratio, representing considerably shear-flexible elements, while more opaque colours correspond to more slender elements that match regular Hermitian cubic shape functions as $\psi \to 0$.

The formulation of Teng & Rotter (1989a,b) is built upon a cubic interpolation of the displacement field and its first derivatives, expressed in the global coordinate system illustrated in Figures

3.2 and 3.3. Explicit evaluation of midsurface strains-stresses and stiffness matrices as a function of DOFs in the global coordinate system benefits from the elimination of intermediate transformation steps and the computational time accompanied with them. The essential treatment that this particular formulation requires for suppressing continuity of local meridional displacement derivatives $\partial\bar{u}/\partial s$ and association of only meridional rotations β_ϕ (termed as just β within Chapter 3 and Teng & Rotter (1989a,b)) between elements is handled through a precise isolated transformation of global displacement derivatives $\partial u/\partial s$ and $\partial w/\partial s$ prior to static condensation of the stiffness matrix. Efficiency however comes at the expense of ease in extending the formulation to incorporate additional effects at the level of kinematic relationships, as evidenced by the author's own experience. The lack of a clearly identifiable normal and meridional displacement when the element interpolation field of Eqs. 3.5 is employed hinders adoption of the previously presented shape functions of Eqs. 6.2 and 6.3, a field that is only valid for the representation of bending and shear behaviour kinematics. Incorporation of these for the description of displacements that are responsible for membrane stretching of the shell's midsurface can severely deteriorate solution accuracy, as the order of the shape function polynomials now depends on the ψ ratio of bending over shear stiffnesses. The workaround of only assuming the interpolation field of Eqs. 6.2 and 6.3 for normal displacements and meridional rotations while still utilising the Hermitian cubics of Eqs. 3.2 for meridional displacements unfortunately does not present itself due to the adopted global coordinate system description of fundamental element quantities, rendering an extension of the AQUINAS element impractical on the basis of the formulation provided by Teng & Rotter (1989a,b). To the best of the author's knowledge, an alternative to the inclusion of finite-thickness effects for mixed interpolation elements utilising Hermitian cubic shape functions does not exist in a conveniently available format across the relevant literature, and as such the augmentation of the formulation presented in Chapter 3 has been abandoned.

6.2.2 Derivation and implementation aspects for a new axisymmetric shell element

Whilst the element of Teng & Rotter (1989a,b) does not offer itself to the implementation of strategic enhancements to ensure reliable treatment of stockier axisymmetric shell models, it is of paramount importance to the developers of the AQUINAS software for its FE solver to be an accurate predictor of a shell's load bearing capacity across the entire slenderness spectrum. Consequently, a new element shall be considered as an addition to the already released MATLAB toolbox, aiming to transform AQUINAS into a computational suite containing different options for nonlinear examinations of axisymmetric shell mechanics. Any candidate element formulation needs to satisfy a certain list of criteria before eventually being coded into the AQUINAS solver, with a summary of the desirable features it must possess outlined in the following checklist.

- *Inclusion of finite-thickness effects into axisymmetric shell kinematics.*
  Shear strains and associated stresses shall be retained in the kinematics description of the axisymmetric shell element to be programmed into AQUINAS, with meridional shear behaviour derived on the basis of principles adopted in shear-flexible beam elements. Circumferential transverse shear strains will additionally be included in the formulation to ensure finite-thickness effects are considered during nonsymmetric buckling modes.

- *Nonsymmetric bifurcation into a prescribed harmonic mode n.*
  As the main motive for the development of AQUINAS, appropriate detection of bifurcation buckling into nonsymmetric modes characterised by a harmonic description of the modal displacement field along the circumference of the axisymmetric shell is an essential feature for any FE formulation to be employed. Due to the lack of such a shear-flexible formulation

being readily available in the existing shell literature, the corresponding aspects of the Teng & Rotter (1989a); Jumikis (1987) derivation shall be fused into an axisymmetric shell formulation that includes finite-thickness effects.

- *Geometrically nonlinear configuration updating through a Total Lagrangian scheme.*
  Minimal alteration of the main procedural pipelines in AQUINAS dictates adoption of an element formulation that is built on the basis of a Total Lagrangian framework for the updating of the geometrically nonlinear configuration of the shell. It will be revealed that this constitutes more of a limitation rather than a feature of the implemented finite element, as later discussion and examination of results will illustrate.

- *Seamless integration into the AQUINAS FE toolbox with minimal changes on its software architecture.*
  Not only to minimise programming work and accelerate deployment of an updated AQUINAS version, to be made available after appropriate documentation through its official GitHub repository, a harmonious implementation of any new FE formulation will promote maintenance of the software during potential future releases.

- *Implementation simplicity that permits further formulation extensions, should the need arise.*
  The lack of readily available ground to include additional effects and advanced concepts in the already programmed finite element has highlighted the struggles associated with coding a new formulation, essentially from scratch, as the AQUINAS software has been built around the Teng & Rotter (1989a) element, catering to its needs without facilitating the development and testing of any marginally different formulations. Consequently, the opportunity to invest in coding a simple, versatile element that can easily be enhanced with various computational characteristics in the future will be utilised, attempting to establish a development foundation for the open-source toolbox.

Compatibility with pre-existing general functionality programmed in AQUINAS already eliminates any axisymmetric solid continuum formulations available in shell literature, owing not only to nodal placement and order but also to strain and stress quantities that need to be computed and traced for in order to fully describe the deformed state of the element. Procedures relating to the step-wise integration of elastoplastic strains, as discussed in Section 3.4 have been developed on the basis of plane stress material behaviour, completely invalidated once through-thickness stresses σ_ζ are non-negligible for an explicit computational rendering of a shell wall with axisymmetric solids. Through-thickness integration requirements, even for a relatively simple linear elastic analysis further complicates potential utilisation of an axisymmetric continuum element. Consequently, formulations such as those presented by Oden & Key (1970); Mitchell *et al.* (1971); Wood & Zienkiewicz (1977); Surana (1982) are inevitably excluded from any further consideration, preventing AQUINAS from acquiring an element similar to the CAX family of axisymmetric solids (ABAQUS, 2022).

Axisymmetric shell elements are not impervious to shear-locking phenomena, commonly associated with low-order shear-flexible finite elements failing to predict near-zero shear strain fields in scenarios where bending behaviour dominates the response of a thin shell. Various techniques of alleviating the excessive stiffening associated with shear-locking behaviour have been presented and discussed by several authors (Hughes *et al.*, 1977; Tessler, 1986; Tessler & Spiridigliozzi, 1988; Zienkiewicz *et al.*, 1971), with reduced integration schemes and inclusion of a penalty relaxation parameter on the shear stress resultant being popular alternatives to achieve a better shear energy approximation of thin shell structures. The first of these approaches has been shown to be effective in the context of a two-node linear axisymmetric shell element (Zienkiewicz *et al.*, 1977), ensuring that stiffness associated with shear behaviour is permitted

to be singular as the element becomes increasingly thin, and will therefore be adopted for the linear interpolation element that shall be formulated in the following sections.

6.3 Principles of finite element formulation

Since the simple axisymmetric shell element presented by Zienkiewicz *et al.* (1977) is limited to linear elastic stress analysis solutions, geometric stiffness contributions to the tangent stiffness matrix as well as material stiffness coefficients relating to the development of nonlinear strains will be derived following regular principles associated with the finite element method (Zienkiewicz & Taylor, 2005; Crisfield, 1991). In doing so however, an effort will be made to not repeat steps of the process that have already been presented in Chapter 3 or have been thoroughly documented in other works, but rather provide a concise description of the fundamental characteristics and key assumptions accompanying the present formulation. A step-by-step derivation of the shear-flexible kinematic framework for the element will precede construction of the finite element formulation, providing details on the interpolation of nodal DOFs and the necessary transformations that the element has to undergo prior to assembly and solution of equilibrium or eigenvalue equations.

6.3.1 Derivation of shear-flexible axisymmetric shell strains

The approach employed by Jumikis and Rotter for the derivation of their nonlinear axisymmetric shell theory (Rotter & Jumikis, 1987; Teng & Rotter, 1989a,b) will be adopted herein as the starting point of the shear-flexible finite element formulation, as presented in Jumikis (1987). The thinness assumptions that typically justify neglecting shear strains in kinematic relationships will not be utilised here, allowing for a broader range of characteristic slenderness to be appropriately modelled for bending dominated axisymmetric shell structures. Derivational steps prior to the definition of the Gauss-Codazzi relations for an axisymmetric shell may be found in Section 3.2 of Jumikis (1987). A similar strategy for the geometric description of the shell's deformed state is also employed in the kindred doctoral work of Hong (2000), extending the capabilities of the original FE formulation by permitting mode-switching and interaction of modes in the post-buckling branch of the equilibrium curve.

The conventions employed for the displacement field used to represent the deformed state of the shell are visually summarised in Figure 6.2, with three interrelated systems identified and the differences between global and local DOFs already discussed to some detail in previous sections (also in Appendix A). As the element formulation outlined in this section is to be included in the AQUINAS solver, an effort is made to work with respect to the conventions of Teng & Rotter (1989a), inevitably resulting in discrepancies with classical shell theory (see early discussion of Chapter 3), as well as the analytical work of the previous chapter.

The relative position of two points P and P' located within the shell wall can be described through the vector joining them as:

$$PP' = dl_0 = ds\hat{s} + rd\theta\hat{\theta} + d\zeta\hat{\zeta} \tag{6.5}$$

where $\hat{s}$, $\hat{\theta}$ and $\hat{\zeta}$ are unit vectors in the meridional, circumferential and normal directions of the axisymmetric shell, with the associated u_ϕ, u_θ and u_ζ translations illustrated in Figure 6.2. If the first of these points P undergoes a displacement $\hat{u}$, with the corresponding vector defined as:

$$\hat{u} = u_\phi\hat{s} + u_\theta\hat{\theta} + u_\zeta\hat{\zeta} \tag{6.6}$$

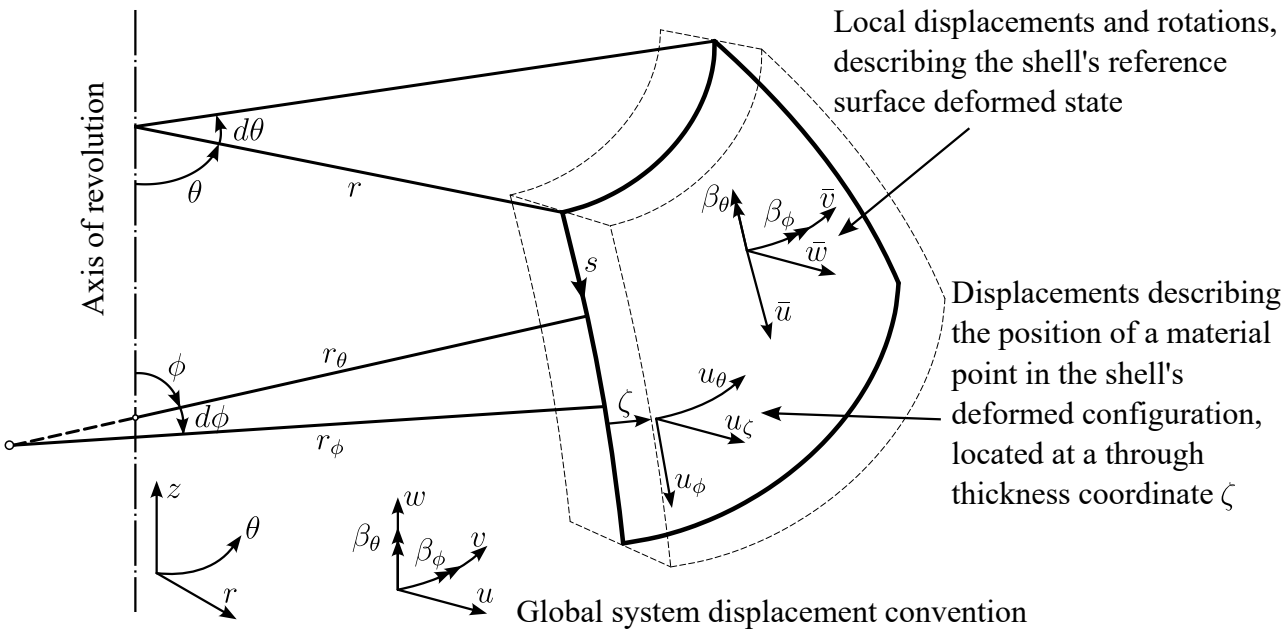


Figure 6.2: Axisymmetric shell system, illustrating the different conventions for the displacements and rotations used to describe its deformed geometry.

then the vector describing the updated position of the point P' is given as:

$$\hat{u'} = \hat{u} + \frac{\partial \hat{u}}{\partial s} ds + \frac{\partial \hat{u}}{\partial \theta} d\theta + \frac{\partial \hat{u}}{\partial \zeta} d\zeta \tag{6.7}$$

leading to the following expression for the new length between points P and P' in the deformed configuration of the shell:

$$dl = dl_0 + \frac{\partial \hat{u}}{\partial s} ds + \frac{\partial \hat{u}}{\partial \theta} d\theta + \frac{\partial \hat{u}}{\partial \zeta} d\zeta \tag{6.8}$$

The Gauss-Codazzi relations (Szwabowicz & Pietraszkiewicz, 2004; Ciarlet, 2008) for the unit vectors $\hat{s}$, $\hat{\theta}$ and $\hat{\zeta}$ have been formally established in the doctoral thesis of Jumikis (1987), and will be employed here after minor notational alterations to the format provided therein in order to facilitate exploration of deformations for the axisymmetric shell structure. Any spatial derivatives omitted in the following set of Eqs. 6.9 are equal to zero as a consequence of the orthogonality of the chosen unit vector system and considerations of model axisymmetry.

$$
\begin{aligned}
\frac{\partial \hat{\zeta}}{\partial s} &= \frac{\partial \hat{\zeta}}{\partial \phi}\frac{\partial \phi}{\partial s} = (\cos\phi, -\sin\phi)\frac{\partial \phi}{\partial s} = \hat{s}\frac{\partial \phi}{\partial s} \\
\frac{\partial \hat{s}}{\partial s} &= \frac{\partial \hat{s}}{\partial \phi}\frac{\partial \phi}{\partial s} = (-\sin\phi, -\cos\phi)\frac{\partial \phi}{\partial s} = -\hat{n}\frac{\partial \phi}{\partial s} \\
\frac{\partial \hat{\theta}}{\partial \theta} &= (-\cos\theta, -\sin\theta) = -\hat{r} = -\hat{n}\sin\phi - \hat{s}\cos\phi \\
\frac{\partial \hat{r}}{\partial \theta} &= (-\sin\theta, \cos\theta) = \hat{\theta} \\
\frac{\partial \hat{\zeta}}{\partial \theta} &= \sin\phi\frac{\partial \hat{r}}{\partial \theta} = \sin\phi\hat{\theta} \\
\frac{\partial \hat{s}}{\partial \theta} &= \cos\phi\frac{\partial \hat{r}}{\partial \theta} = \cos\phi\hat{\theta}
\end{aligned}
\tag{6.9}
$$

Differentiation of the Gauss-Codazzi relations along the ϕ, θ and ζ directions of the axisymmetric shell system, as illustrated in Figure 6.2, and rearrangement into a matrix format produces the following vectorised expression for the length dl between the two points examined in the deformed state of the shell.

$$
\begin{aligned}
dl &= \begin{bmatrix}
1 + \dfrac{\partial u_\zeta}{\partial \zeta} & \dfrac{\partial u_\zeta}{\partial s} - u_\phi\dfrac{\partial \phi}{\partial s} & \dfrac{1}{R}\left(\dfrac{\partial u_\zeta}{\partial \theta} - u_\theta\sin\phi\right) \\
\dfrac{\partial u_\phi}{\partial n} & 1 + \dfrac{\partial u_\phi}{\partial s} + u_\zeta\dfrac{\partial \phi}{\partial s} & \dfrac{1}{R}\left(\dfrac{\partial u_\phi}{\partial \theta} - u_\theta\cos\phi\right) \\
\dfrac{\partial u_\theta}{\partial \zeta} & \dfrac{\partial u_\theta}{\partial s} & 1 + \dfrac{1}{R}\left(\dfrac{\partial u_\theta}{\partial \theta} + u_\zeta\sin\phi + u_\phi\cos\phi\right)
\end{bmatrix}
\begin{Bmatrix} d\zeta \\ ds \\ rd\theta \end{Bmatrix} \\
&= \begin{bmatrix}
1 + e_{\zeta\zeta} & e_{\zeta\phi} & e_{\zeta\theta} \\
e_{\phi\zeta} & 1 + e_{\phi\phi} & e_{\phi\theta} \\
e_{\theta\zeta} & e_{\theta\phi} & 1 + e_{\theta\theta}
\end{bmatrix}
\begin{Bmatrix} d\zeta \\ ds \\ rd\theta \end{Bmatrix} = [A]\begin{Bmatrix} d\zeta \\ ds \\ rd\theta \end{Bmatrix}
\end{aligned}
\tag{6.10}
$$

leading to the following expression for the change of a squared element's length:

$$
dl^2 - dl_0^2 = \begin{Bmatrix} d\zeta & ds & rd\theta \end{Bmatrix}\left[A^TA - I\right]\begin{Bmatrix} d\zeta \\ ds \\ rd\theta \end{Bmatrix}
\tag{6.11}
$$

with $[I]$ being a 3-by-3 identity matrix. Strains ϵ at any point through the shell wall may now be defined according to Green's strain tensor (Green & Zerna, 1992) as:

$$
[\epsilon] = \frac{1}{2}[A^TA - I] = \begin{bmatrix}
\epsilon_{\zeta\zeta} & \epsilon_{\zeta\phi} & \epsilon_{\zeta\theta} \\
\epsilon_{\phi\zeta} & \epsilon_{\phi\phi} & \epsilon_{\phi\theta} \\
\epsilon_{\zeta\theta} & \epsilon_{\phi\theta} & \epsilon_{\theta\theta}
\end{bmatrix}
\tag{6.12}
$$

in which the individual strain quantities are defined through the following relationships, with the $[A]$ matrix implicitly defined through Eq. 6.10. The strains at the point P' in the deformed

configuration can therefore be evaluated as:

$$\epsilon_{\zeta\zeta} = e_{\zeta\zeta} + \frac{1}{2}(e_{\zeta\zeta}^2 + e_{\phi\zeta}^2 + e_{\zeta\theta}^2) \tag{6.13a}$$

$$\epsilon_{\phi\phi} = e_{\phi\phi} + \frac{1}{2}(e_{\zeta\phi}^2 + e_{\phi\phi}^2 + e_{\phi\theta}^2) \tag{6.13b}$$

$$\epsilon_{\theta\theta} = e_{\theta\theta} + \frac{1}{2}(e_{\zeta\theta}^2 + e_{\phi\theta}^2 + e_{\theta\theta}^2) \tag{6.13c}$$

$$\epsilon_{\zeta\phi} = \epsilon_{\phi\zeta} = \frac{e_{\zeta\phi}}{2} + \frac{e_{\phi\zeta}}{2} + \frac{1}{2}(e_{\zeta\zeta}e_{\zeta\phi} + e_{\phi\zeta}e_{\phi\phi} + e_{\zeta\theta}e_{\phi\theta}) \tag{6.13d}$$

$$\epsilon_{\zeta\theta} = \epsilon_{\theta\zeta} = \frac{e_{\zeta\theta}}{2} + \frac{e_{\theta\zeta}}{2} + \frac{1}{2}(e_{\zeta\zeta}e_{\zeta\theta} + e_{\phi\zeta}e_{\phi\theta} + e_{\zeta\theta}e_{\theta\theta}) \tag{6.13e}$$

$$\epsilon_{\phi\theta} = \epsilon_{\theta\phi} = \frac{e_{\phi\theta}}{2} + \frac{e_{\theta\phi}}{2} + \frac{1}{2}(e_{\zeta\phi}e_{\zeta\theta} + e_{\phi\phi}e_{\phi\theta} + e_{\phi\theta}e_{\theta\theta}) \tag{6.13f}$$

where the e_{ij} terms are given as:

$$e_{\zeta\zeta} = \frac{\partial u_\zeta}{\partial \zeta} \tag{6.14a}$$

$$e_{\phi\phi} = \frac{\partial u_\phi}{\partial s} + u_\zeta \frac{\partial \phi}{\partial s} \tag{6.14b}$$

$$e_{\theta\theta} = \frac{1}{r}\left(\frac{\partial u_\theta}{\partial \theta} + u_\zeta \sin\phi + u_\phi \cos\phi\right) \tag{6.14c}$$

$$e_{\zeta s} = \frac{\partial u_\zeta}{\partial s} - u_\phi \frac{\partial \phi}{\partial s} \tag{6.14d}$$

$$e_{\zeta\theta} = \frac{1}{r}\left(\frac{\partial u_\zeta}{\partial \theta} - u_\theta \sin\phi\right) \tag{6.14e}$$

$$e_{\phi\zeta} = \frac{\partial u_\phi}{\partial \zeta} \tag{6.14f}$$

$$e_{\phi\theta} = \frac{1}{r}\left(\frac{\partial u_\phi}{\partial \theta} - u_\theta \cos\phi\right) \tag{6.14g}$$

$$e_{\theta\zeta} = \frac{\partial u_\theta}{\partial \zeta} \tag{6.14h}$$

$$e_{\theta\phi} = \frac{\partial u_\theta}{\partial s} \tag{6.14i}$$

For a linear variation of displacements through the shell wall according to Assumption 3 (as given in Section 2.1.1) and consistent with the Love-Kirchhoff assumptions, the effect of varying radii through-thickness of the shell is omitted. Displacements at any point can then be expressed as a linear combination of the displacements $\bar{u}$ - $\bar{v}$ - $\bar{w}$ and rotations β_ϕ- β_θ of the shell's midsurface as follows:

$$u_\phi = \bar{u} + \zeta \frac{\partial u_\phi}{\partial \zeta} = \bar{u} + \zeta \beta_\phi \tag{6.15a}$$

$$u_\theta = \bar{v} + \zeta \frac{\partial u_\theta}{\partial \zeta} = \bar{v} + \zeta \beta_\theta \tag{6.15b}$$

$$u_\zeta = \bar{w} + \zeta \frac{\partial u_\zeta}{\partial \zeta} = \bar{w} \tag{6.15c}$$

where the reduction $\partial u_\zeta / \partial \zeta = 0$ readily follows from the negligible normal strain ϵ_ζ assumption, one of the main simplifications of shell theory associated with Assumption 1 for $\sigma_\zeta = 0$ as discussed in Chapter 2. Substitution of Eqs. 6.15 into the expressions of Eqs. 6.14 for the coefficients of Green's strain tensor lead to the strain-displacement relations for the axisymmetric shell, with the linear and nonlinear parts of the kinematics identified and individually presented in the following sections.

6.3.1.1 Linear kinematics

The above relationships can now be used to express the strains of the shell wall in terms of the midsurface displacements and rotations. Isolating linear parts of the strain expressions given in Eqs. 6.13, with the quadratic terms of those equations corresponding to nonlinear behaviour as the shell deforms, produces the following kinematic relations for a doubly-curved axisymmetric shell after substitution of Eqs. 6.15 into Eqs. 6.14 for the through-thickness variation of displacement u_ϕ, u_θ and u_ζ:

Linear membrane strains

$$\epsilon_{\phi,l} = \frac{\partial \bar{u}}{\partial s} + \bar{w} \frac{\partial \phi}{\partial s} \tag{6.16a}$$

$$\epsilon_{\theta,l} = \frac{\cos \phi}{r} \bar{u} + \frac{1}{r} \frac{\partial \bar{v}}{\partial \theta} + \frac{\sin \phi}{r} \bar{w} \tag{6.16b}$$

$$\gamma_{\phi\theta,l} = \frac{1}{r} \frac{\partial \bar{u}}{\partial \theta} - \frac{\cos \phi}{r} \bar{v} + \frac{\partial \bar{v}}{\partial s} \tag{6.16c}$$

Linear curvatures

$$\kappa_{\phi,l} = \frac{\partial \beta_\phi}{\partial s} \tag{6.17a}$$

$$\kappa_{\theta,l} = \frac{1}{r} \left(\frac{\partial \beta_\theta}{\partial \theta} + \cos \phi \beta_\phi \right) \tag{6.17b}$$

$$\kappa_{\phi\theta,l} = \frac{\partial \beta_\theta}{\partial s} + \frac{1}{r}\left(\frac{\partial \beta_\phi}{\partial \theta} - \cos\phi\beta_\theta\right) \tag{6.17c}$$

Linear transverse shear strains

$$\gamma_{\phi\zeta,l} = \beta_\phi - \bar{u}\frac{\partial \phi}{\partial s} + \frac{\partial \bar{w}}{\partial s} \tag{6.18a}$$

$$\gamma_{\theta\zeta,l} = \beta_\theta + \frac{1}{r}\left(\frac{\partial \bar{w}}{\partial \theta} - \sin\phi\bar{v}\right) \tag{6.18b}$$

where the engineering shear strains of Eqs. 6.18 are given as twice Green's tensorial strain components of Eqs. 6.13. Whilst membrane stretching strain expressions are consistent with those derived for the purposes of the original AQUINAS formulation, curvature terms are now explicitly defined with respect to meridional β_ϕ and circumferential rotations β_θ, with the linear shear strains of Eqs. 6.18 functioning as a link between meridional and circumferential variations of the normal displacement $\bar{w}$ and those rotations (Zienkiewicz *et al.*, 1977).

6.3.1.2 Nonlinear kinematics

After substitution of the translational DOFs of Eqs. 6.15 in the relationships of Eqs. 6.14 for the evaluation of Green's strain tensor in Eq. 6.10, quantities that do not vary linearly with respect to the unknown kinematic variables in the local system of the shell (as illustrated in Figure 6.2) can be arranged into expressions for the nonlinear stretching, shearing and bending (curvatures) strains of the shell's midsurface. As was the case for the linear kinematics of the previous section, disassociation of rotations with first derivatives of the normal displacements produces an additional set of two nonlinear transverse shear strain relations, defined by means of 'pseudo rotations' (Jumikis, 1987) as follows:

Nonlinear membrane strains

$$\epsilon_{\phi,nl} = \frac{1}{2}\left(\beta_1^2 + \beta_2^2 + \beta_3^2\right) \tag{6.19a}$$

$$\epsilon_{\theta,nl} = \frac{1}{2}\left(\beta_4^2 + \beta_5^2 + \beta_6^2\right) \tag{6.19b}$$

$$\gamma_{\phi\theta,nl} = \beta_1\beta_4 + \beta_2\beta_5 + \beta_3\beta_6 \tag{6.19c}$$

Nonlinear curvatures

$$\kappa_{\phi,nl} = \beta_1\beta_7 + \beta_2\beta_8 + \beta_3\beta_9 \tag{6.20a}$$

$$\kappa_{\theta,nl} = \beta_4\beta_{10} + \beta_5\beta_{11} + \beta_6\beta_{12} \tag{6.20b}$$

$$\kappa_{\phi\theta,nl} = \frac{1}{2}\left(\beta_1\beta_{10} + \beta_2\beta_{11} + \beta_3\beta_{12} + \beta_4\beta_7 + \beta_5\beta_8 + \beta_6\beta_9\right) \tag{6.20c}$$

Nonlinear shear strains

$$\gamma_{\phi\zeta,nl} = \beta_\phi\beta_3 + \beta_\theta\beta_2 \tag{6.21a}$$

$$\gamma_{\theta\zeta,nl} = \beta_\phi\beta_6 + \beta_\theta\beta_5 \tag{6.21b}$$

with the β_1-β_{12} pseudo rotations defined as:

$$\beta_1 = \frac{\partial \bar{w}}{ds} - \bar{u}\frac{\partial \phi}{ds} \tag{6.22a}$$

$$\beta_2 = \frac{\partial \bar{v}}{ds} \tag{6.22b}$$

$$\beta_3 = \frac{\partial \bar{u}}{ds} + \bar{w}\frac{\partial \phi}{ds} \tag{6.22c}$$

$$\beta_4 = \frac{1}{r}\left(\frac{\partial \bar{w}}{\partial \theta} - \bar{v}\sin\phi\right) \tag{6.22d}$$

$$\beta_5 = -\frac{1}{r}\left(\frac{\partial \bar{v}}{\partial \theta} + \bar{u}\sin\phi + \bar{w}\cos\phi\right) \tag{6.22e}$$

$$\beta_6 = -\frac{1}{r}\left(\frac{\partial \bar{w}}{\partial \theta} - \bar{v}\cos\phi\right) \tag{6.22f}$$

$$\beta_7 = -\beta_\phi\frac{\partial \phi}{ds} \tag{6.22g}$$

$$\beta_8 = \frac{\partial \beta_\theta}{ds} \tag{6.22h}$$

$$\beta_9 = \frac{\partial \beta_\phi}{\partial s} \tag{6.22i}$$

$$\beta_{10} = -\frac{1}{r}\beta_\theta\sin\phi \tag{6.22j}$$

$$\beta_{11} = \frac{1}{r}\left(\frac{\partial \beta_\theta}{\partial \theta} + \beta_\phi\cos\phi\right) \tag{6.22k}$$

$$\beta_{12} = \frac{1}{r}\left(\frac{\partial \beta_\phi}{\partial \theta} - \beta_\theta\cos\phi\right) \tag{6.22l}$$

As could be expected, nonlinear membrane strains are found to be identical to those corresponding to an explicitly thin shell theory formulation (Teng & Rotter, 1989a,b), obtained after application of the full set of Kirchhoff assumptions on the quantities of Eqs. 6.14, as transverse shear kinematics do not interfere with stretching modes of the shell surface. Nonlinear curvatures are however affected due to Assumption 5 (see Section 2.1.1) not being applied for the reduction of kinematic relationships, easily demonstrated through a comparison with the associated thin shell theory expressions found in Section 3.2 of Jumikis (1987) where pseudo rotations can be defined through variations of translational DOFs of the shell's midsurface instead of directly referring to rotations β_ϕ and β_θ.

6.3.2 Formulation of the axisymmetric finite element

Whilst the linear and nonlinear strain-displacement relationships derived for the axisymmetric shell element in the previous sections permit the kinematic description of a doubly-curved shell, the conscious choice to reduce the geometric modelling accuracy of the element is made with the

intention to reduce programming complexity at early stages of development. Any geometry will therefore be approximated through piecewise linear straight segments, a modelling technique that was critiqued in the discussion of Section 2.2.2. As the first major computational task to determine the present formulation's success will be the generation of capacity curves for cylinders under meridional compression in an attempt to establish a physically interpretable λ_0 slenderness parameter, interpolation of meridional curvature between nodes will not be a contributing factor to numerical results accuracy. However, even in scenarios of smoothly curved shells such as spheres or ellipses, displacement profiles of sufficient precision with only a small number of straight elements can be obtained, as an example of the following section shall illustrate. This observation is aligned with the findings reported in the kindred publication of Zienkiewicz *et al.* (1977) that has formulated the basis of the present element construction, showcasing a good track of computational solutions for stress analysis problems. The efficiency, mostly expressed in computational cost-effectiveness, of the single-curved SAX1 element in ABAQUS (2022) further supports this approach, with a better approximation of elaborate meridional geometries through higher discretisation always being an available option.

Nullification of meridional curvature $\partial\phi/\partial s$ substantially simplifies the kinematic relations of the axisymmetric shell element, as can be observed through a study of the linear and nonlinear strain-displacement expressions of Eqs. 6.16 - 6.21. Intricacies associated with meridional geometry interpolation fields are also reduces, with the radial r and axial z coordinates interpolated within an element as:

$$r = \sum_{i=1,2} N_i r_i \tag{6.23a}$$

$$z = \sum_{i=1,2} N_i z_i \tag{6.23b}$$

where $r_1 - r_2$ and $z_1 - z_2$ are the nodal coordinates of the element and shape functions N_1 and N_2 are defined through the linear Lagrange polynomials:

$$N_1 = \frac{1-\eta}{2} \tag{6.24a}$$

$$N_2 = \frac{1+\eta}{2} \tag{6.24b}$$

Unlike the cubic Hermitian shape functions of Eqs. 3.2, the interpolation field of Eqs. 6.24 provides a low order approximation of nodal variables without exploiting their variations for the evaluation of quantities within an element. An analogously simple interpolation field can now be defined for local element DOFs:

$$\bar{u} = \sum_{i=1,2} N_i \bar{u}_i \tag{6.25a}$$

$$\bar{v} = \sum_{i=1,2} N_i \bar{v}_i \tag{6.25b}$$

$$\bar{w} = \sum_{i=1,2} N_i \bar{w}_i \tag{6.25c}$$

$$\beta_\phi = \sum_{i=1,2} N_i \beta_{\phi i} \tag{6.25d}$$

$$\beta_\theta = \sum_{i=1,2} N_i \beta_{\theta i} \tag{6.25e}$$

As the same global system conventions employed for the thin shell formulation already coded in AQUINAS, as those have been described in Chapter 3, have been the basis for the system illustrated in Figure 6.2, the transformation process will naturally share its details with the corresponding expression presented in Eq. 3.6, including two additional entries for the now explicitly interpolated nodal rotations β_ϕ and β_θ:

$$\begin{Bmatrix} \bar{u} \\ \bar{v} \\ \bar{w} \\ \beta_\phi \\ \beta_\theta \end{Bmatrix} = \begin{bmatrix} \cos\phi & 0 & -\sin\phi & 0 & 0 \\ 0 & 1 & 0 & 0 & 0 \\ \sin\phi & 0 & \cos\phi & 0 & 0 \\ 0 & 0 & 0 & 1 & 0 \\ 0 & 0 & 0 & 0 & 1 \end{bmatrix} \begin{Bmatrix} u \\ v \\ w \\ \beta_\phi \\ \beta_\theta \end{Bmatrix} = [T] \begin{Bmatrix} u \\ v \\ w \\ \beta_\phi \\ \beta_\theta \end{Bmatrix} \tag{6.26}$$

After transformation of nodal quantities into the global coordinate system, assumption of a harmonic distribution field for the native treatment of nonsymmetric bifurcation buckling modes can finally be incorporated into the formulation of the element, obtained after compatibility considerations relating to the variations of displacements and rotations with respect to θ as:

$$u = \sum_{n=0}^{N} u_n \cos(n\theta) \tag{6.27a}$$

$$v = \sum_{n=0}^{N} v_n \sin(n\theta) \tag{6.27b}$$

$$w = \sum_{n=0}^{N} w_n \cos(n\theta) \tag{6.27c}$$

$$\beta_\phi = \sum_{n=0}^{N} \beta_{\phi n} \cos(n\theta) \tag{6.27d}$$

$$\beta_\theta = \sum_{n=0}^{N} \beta_{\theta n} \sin(n\theta) \tag{6.27e}$$

6.3.2.1 Constitutive relationships

Elastic-plastic material behaviour is still approximated through the plane stress material law presented earlier in Section 3.4, after appropriate adjustments to the rigidity matrices to account for shear strain terms. Handling nonlinear material behaviour through a plane stress law may be viewed as contradictory to the notion of finite-thickness effects included in the present formulation, as transverse shear strains through the shell would theoretically necessitate a full 3D continuum material model for the accurate integration of elastoplastic strains. This is however consistent with treatment of transverse shear strains as not to invoke plasticity effects in the response of shell elements found in numerical solvers, both open-source (Taylor, 1987) and commercial (ABAQUS, 2022), but also across general shell element formulations incorporating finite thickness effects (Simo & Kennedy, 1992; Eberlein & Wriggers, 1999). The same strategy

will be utilised in the present axisymmetric shell element formulation, not only to capitalise on simple constitutive relationships that improve numerical efficiency but also to avoid the introduction of a new material plasticity algorithm into AQUINAS. The elastic-plastic tangent modulus matrix $[D_{ep}]$ will therefore still be constructed as defined by Eq. 3.29, albeit with suitable modifications to accommodate the additional shear strain terms. These changes relate to the attachment of an additional row and column with zero entries on the plastic part $[D_p]$ of the $[D_{ep}]$ matrix, turning it into a 4-by-4 array, while the elastic rigidity matrix is now given as:

$$[D_e] = \frac{E}{(1-\nu^2)} \begin{bmatrix} 1 & \nu & 0 & 0 \\ \nu & 1 & 0 & 0 \\ 0 & 0 & (1-\nu)/2 & 0 \\ 0 & 0 & 0 & k(1-\nu)/2 \end{bmatrix} \tag{6.28}$$

Hence, the tangent modulus matrix $[D_T]$ can now be integrated through the thickness of the shell by applying Simpson's 1/3 integration rule in a similar process to the one presented earlier in Chapter 3, resulting in an 8-by-8 matrix $[D_T]$:

$$[D_T] = \int_{-t/2}^{t/2} [Z]^T [D_{ep}][Z] dz \tag{6.29}$$

with appropriate adaptations to the $[Z]$ matrix of Eq. 3.10 to accommodate integration of shear stresses and computation of the corresponding stress resultants:

$$[Z] = \begin{bmatrix} 1 & 0 & 0 & z & 0 & 0 & 0 & 0 \\ 0 & 1 & 0 & 0 & z & 0 & 0 & 0 \\ 0 & 0 & 1 & 0 & 0 & z & 0 & 0 \\ 0 & 0 & 0 & 0 & 0 & 0 & 1 & 1 \end{bmatrix} \tag{6.30}$$

It is important to note that the matrix form of the constitutive relations presented in this section assumes a unified approach for the rectification of the constant through-thickness distribution of actually parabolic transverse shear strains profile with respect to the coordinate ζ through the use of the same shear correction factor k for both meridional $\gamma_{\phi\zeta}$ and circumferential $\gamma_{\theta\zeta}$ shear strains. This is justified on the basis of near rectangular cross-section when considering a infinitesimal shell panel $ds \cdot rd\theta$, but also by reflecting upon an equivalent full 3D shell modelling scenario where general quadrilateral shell elements would apply the same shear correction factor on both normal to the midsurface facets (Hughes *et al.*, 1977). Membrane, bending and shear stress resultants can now be integrated in a similar fashion across the same material points used for tracing elastic-plastic strain development for materially nonlinear analyses or be readily evaluated as $\{\Sigma\} = [D_T]\{\epsilon\}$ when plasticity effects are ignored, producing the following 8 stress resultants for shear-flexible axisymmetric shells:

$$\{\Sigma\} = \{N_\phi, N_\theta, N_{\phi\theta}, M_\phi, M_\theta, M_{\phi\theta}, Q_\phi, Q_\theta\} \tag{6.31}$$

6.3.2.2 Formulation and assembly of stiffness matrices

Excluding the fundamental characteristic of the Teng & Rotter (1989a) axisymmetric shell element formulation, that of defining stiffness matrices in the global coordinate system already at the level of computing individual stiffness coefficients without any need for transformation matrices to be computed (apart from those applied in the process of static condensation, as

discussed earlier), the corresponding process adopted for the present element is largely similar. This is inline with the development objectives set out at the beginning of this derivational work, permitting exploitation of already established functionality in AQUINAS. An element's tangent stiffness matrix is split into material stiffness $[\bar{K_m}]_e$ and geometric stiffness $[\bar{K_g}]_e$ components, expressed in the local system of the element:

$$[\bar{K_T}]_e = [\bar{K_m}]_e + [\bar{K_g}]_e \tag{6.32}$$

with the material and geometric stiffness matrices evaluated as:

$$[\bar{K_m}]_e = \int_A [B]^T [D_T][B] dA \tag{6.33a}$$

$$[\bar{K_g}]_e = \int_A [G]^T [N_0][G] dA \tag{6.33b}$$

where $[G]$ is a 12-by-10 array that relates nodal DOFs in the element's local system to pseudo rotations as:

$$\{\Theta\} = [G]\{\bar{\delta}\} \tag{6.34}$$

with $\{\Theta\}$ being a vector containing pseudo rotations β_1-β_{12} and $\{\bar{\delta}\}$ a vector comprising local DOFs in the following order:

$$\{\delta\} = \{\bar{u_1}, \bar{v_1}, \bar{w_1}, \beta_{\phi 1}, \beta_{\theta 1}, \bar{u_2}, \bar{v_2}, \bar{w_2}, \beta_{\phi 2}, \beta_{\theta 2}\} \tag{6.35}$$

Integration of individual stiffness parts along the meridian is performed at weighted Gauss-Legendre stations, while circumferential integration is carried out by leveraging trigonometric identities. The determinant of the Jacobian for the isoparametric space is found equal to the element's half length, completing numerical integration of the linear element. Single point Gauss-Legendre integration is considered in the meridional direction for the purposes of under-integrating shear behaviour related stiffness coefficients (Zienkiewicz *et al.*, 1977), ensuring that shear locking effects can be avoided. The strain-displacement matrix $[B]$, necessary for accumulating strains corresponding to small increments of nodal displacement and rotations but also required for computation of material stiffness matrices $[\bar{K_m}]_e$, is once more deconstructed into its linear $[B_l]$ and nonlinear $[B_{nl}]$ components, with the minor notational differences of adopting a subscript l instead of 0 for the linear part and a subscript nl instead of L for the nonlinear, given as:

$$[B] = [B_l] + [B_{nl}] \tag{6.36}$$

where the linear part $[B_l]$ can be formulated through the kinematics of section 6.3.1.1 and is provided in Appendix D, while the nonlinear component $[B_{nl}]$ of the strain-displacement matrix is found as:

$$[B_{nl}] = [\Omega][G] \tag{6.37}$$

with the derivational steps in obtaining Eq. 6.37 provided in Section 3.5 and also presented in Jumikis (1987). The terms of the $[G]$ matrix are provided alongside those of $[B_l]$ in Appendix D, where a description of the $[N_0]$ array containing the stress resultant terms of the $\{\Sigma\}$ vector of

Eq. 6.31 to include their destabilising effects on the element geometric stiffness matrix. The $[\Omega]$ matrix, comprising pseudo rotations β_1-β_{12} to determine nonlinear strain increments according to the expressions of Eqs. 6.19 - 6.21, defined is such a way that:

$$\{\epsilon_{nl}\} = \frac{1}{2}[\Omega]\{\Theta\} \tag{6.38}$$

where $\{\epsilon\}$ is a vector of nonlinear membrane, bending and transverse shear strain quantities in the same order presented in Section 6.3.1.2. $[\Omega]$ can be organised in terms of arrays $[A_m]$, $[A_b]$ and $[A_s]$ as:

$$[\Omega] = \left[[A_m]^T, [A_b]^T, [A_s]^T\right]^T \tag{6.39}$$

where the individual matrices responsible for nonlinear membrane, bending and shear behaviour are formulated as:

$$[A_m] = \begin{bmatrix} \beta_1 & \beta_2 & \beta_3 & 0 & 0 & 0 & 0 & 0 & 0 & 0 & 0 & 0 \\ 0 & 0 & 0 & \beta_4 & \beta_5 & \beta_6 & 0 & 0 & 0 & 0 & 0 & 0 \\ \beta_4 & \beta_5 & \beta_6 & \beta_1 & \beta_2 & \beta_3 & 0 & 0 & 0 & 0 & 0 & 0 \end{bmatrix} \tag{6.40}$$

$$[A_b] = \begin{bmatrix} \beta_7 & \beta_8 & \beta_9 & 0 & 0 & 0 & \beta_1 & \beta_2 & \beta_3 & 0 & 0 & 0 \\ 0 & 0 & 0 & \beta_{10} & \beta_{11} & \beta_{12} & 0 & 0 & 0 & \beta_4 & \beta_5 & \beta_6 \\ \beta_{10} & \beta_{11} & \beta_{12} & \beta_7 & \beta_8 & \beta_9 & 0 & 0 & 0 & 0 & 0 & 0 \end{bmatrix} \tag{6.41}$$

$$[A_s] = \begin{bmatrix} 0 & 2\beta_\theta & 2\beta_\phi & 0 & 0 & 0 & 0 & 0 & 0 & 0 & 0 & 0 \\ 0 & 0 & 0 & 0 & 2\beta_\theta & 2\beta_\phi & 0 & 0 & 0 & 0 & 0 & 0 \end{bmatrix} \tag{6.42}$$

Selective omission of any component $[A_m]$, $[A_b]$ or $[A_s]$ through substitution with an array of equal size comprising zero entries can result in complete exclusion of the associated nonlinear strain components in the evaluation of the strain-displacement matrix $[B]$, even though application of this strategy on the $[A_m]$ part of Eq. 6.39 contradicts all relevant literature resources that prioritise nonlinear membrane strains over all other strain terms in their geometrically nonlinear formulations, including Teng & Rotter (1989a,b). Transformation of the stiffness matrices into the global system of Figure 6.2 can subsequently be applied according to the following expression:

$$[K_T]_e = [T]_e^T [\bar{K_T}]_e [T]_e \tag{6.43}$$

where the element transformation matrix $[T]_e$ is evaluated by considering the transformation of Eq. 6.26 at both nodes as $[T]_1$ - $[T]_2$, leading to:

$$[T]_e = \begin{bmatrix} [T]_1 & [0] \\ [0] & [T]_2 \end{bmatrix} \tag{6.44}$$

with [0] in this context being a 5-by-5 array of all zero entries. Further FE implementation details of the formulation presented herein are omitted to avoid repetition of with the corresponding

descriptions of Chapter 3. Meridional and through-thickness integration is performed in the same manner employed for the Teng & Rotter (1989a) formulation, albeit with just a single Gauss-Legendre integration point along the meridian, whilst circumferential integration is handled through trigonometric identities (Jumikis, 1987).

6.4 Examination of shear-flexible computational solutions and discussion

Comparisons between different shell theories have been carried out to some extent through doctoral studies (Jumikis, 1987; Hong, 2000) relating to the original formulation of the double curved axisymmetric shell element (Teng & Rotter, 1989a,b) coded into AQUINAS, assessed against finite element formulations based on the theories of Novozhilov (Novozhilov, 1959, 1999), Reissner (Reissner, 1941), DMV (Donnell, 1935b; Mushtari, 1938a,b; Vlasov, 1944) and Sanders (Sanders Jr, 1959, 1963). The present chapter will not delve into such comparisons for the element derived, only including external FE solutions as a contrast against different computational approximations for the linear and nonlinear analysis of axisymmetric shells. It should be emphasised though that currently the element described in the following sections is not programmed into the AQUINAS toolbox (Filippidis & Sadowski, 2023b), as a consequence of its architectural characteristics revolving around the MITC element of Teng & Rotter (1989a). Even though the formulation is not included in the scientific software for the time being, its results will still be referred to as *AQUINAS (thick)* to reflect the intention of extending the capabilities of the toolbox, with *AQUINAS (thin)* corresponding to the existing cubic, explicitly thin axisymmetric shell element already released in the first version of the AQUINAS solver.

6.4.1 Linear elastic stress analysis results

Capitalising on the analytical cylindrical shell results of the previous chapter that account for finite-thickness effects on the bending theory solution of displacement and stress profiles along their meridian, the two scenarios of cylinders under meridional compression and external pressure will constitute the first set of tests for evaluating the performance of presently described shear flexible derivation. As the element corresponds to a singly-curved axisymmetric shell formulation, a straight meridian model presents a suitable baseline assessment of its LA solution. A curved meridian model, such as that of a truncated spherical part under radial edge loads that will be explored shortly after, will provide a good measurement of not only the shear-flexible element's accuracy but also its ability to approximate non-straight meridians through reasonable mesh resolutions.

6.4.1.1 Cylinder under uniform meridional compression

The cylindrical shell model of Section 5.5.1.1 will now be revisited, assuming the same geometric characterisation and boundary conditions to scale discrepancies between thin and thick shell theory solutions for illustrations purposes. ABAQUS results will be excluded from the comparison momentarily, as the corresponding finite-thickness analytical results of the previous chapter have already been shown to be in good agreement with the computational solutions of the commercial solver for both load cases examined. With the geometry already displayed in Figure 5.3a, the unit compressive meridional edge load N_z results in the meridional $\bar{u}$ and normal $\bar{w}$ displacement fields presented in Figure 6.3, where the adopted convention has now been changed to that of the present axisymmetric shell element system with reference to the local displacements of Figure 6.2 corresponding to the transformation of Eq. 6.26, instead of their classical shell theory definitions

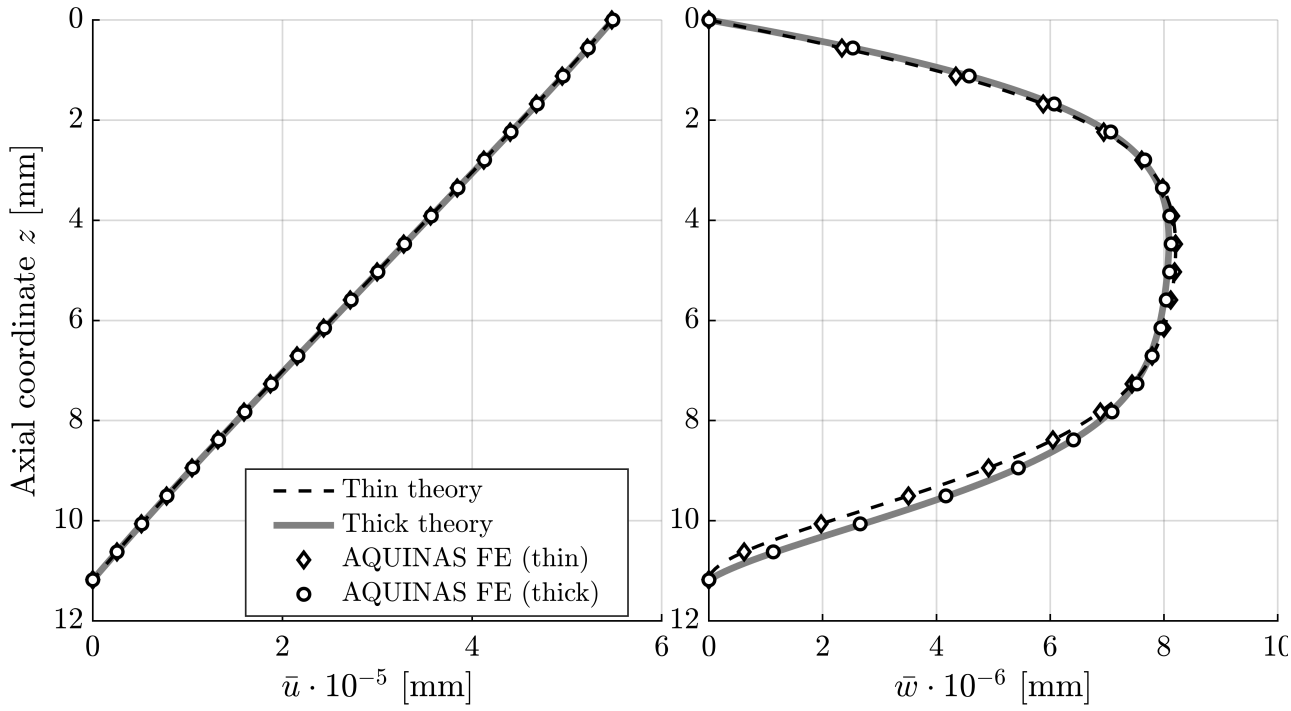


Figure 6.3: Meridional $\bar{u}$ and normal $\bar{w}$ axisymmetric displacement profiles for a cylinder under uniform meridional compression.

employed in the previous chapter. Whilst the thin axisymmetric shell element programmed in AQUINAS has already been tested in Chapter 3 and the accompanying LA section of Appendix A, its results are included in the present comparison as a reference solution. Both thin and thick AQUINAS elements showcase strong agreement with the corresponding analytically evaluated results. The stress profiles of Figure 6.4 add to the credibility of AQUINAS as a trustworthy tool for the analysis of shear-flexible axisymmetric shell systems.

6.4.1.2 Cylinder under uniform normal pressure

In a similar approach for the examination of a cylindrical shell under external pressure, the analytical solution derived in the previous chapter and presented in Section 5.5.1.2 will constitute an accurate comparison benchmark. Geometric definition of the problem has been offered in Figure 5.5 and will not be repeated, focusing attention on the computational approximations of the displacement field and evaluated stress profiles along the meridian of the externally pressurised cylinders. Once more, both thin and thick FE results are in alignment with analytically evaluated distributions, as is exhibited in Figures 6.5 and 6.6, furnishing another favourable assessment for the validity of the linearly interpolated axisymmetric shell element discussed herein.

6.4.1.3 Spherical part under radial edge load

A more challenging but necessary evaluation test for the present singly-curved axisymmetric shell formulation is examined in this section, inspired from an analytical example studied in the seminal work of Flügge (1990). The same stress analysis problem has been a part of AQUINAS' examples library (Filippidis & Sadowski, 2023b) and can be found in Section A.2.5, exploring the behaviour of the cubic element that leverages measures of meridional curvature $\partial\phi/\partial s$ and its variation with respect to s to provide an independent interpolation scheme of curvature characteristics instead of their implicit evaluation through other geometric components, ensuring accurate strain measures at Gauss points (Teng & Rotter, 1989a). Negligence of all kinematic

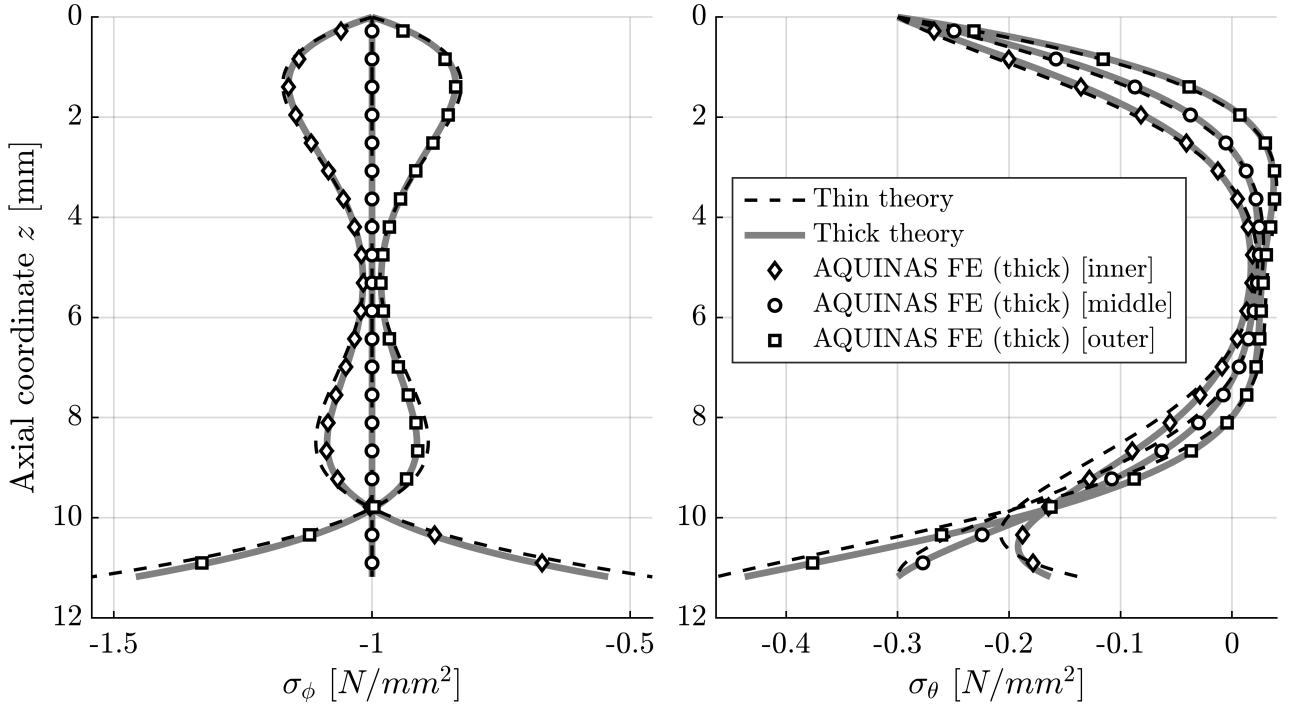


Figure 6.4: Meridional (left) and circumferential (right) axisymmetric stress patterns for a cylinder under uniform meridional compression.

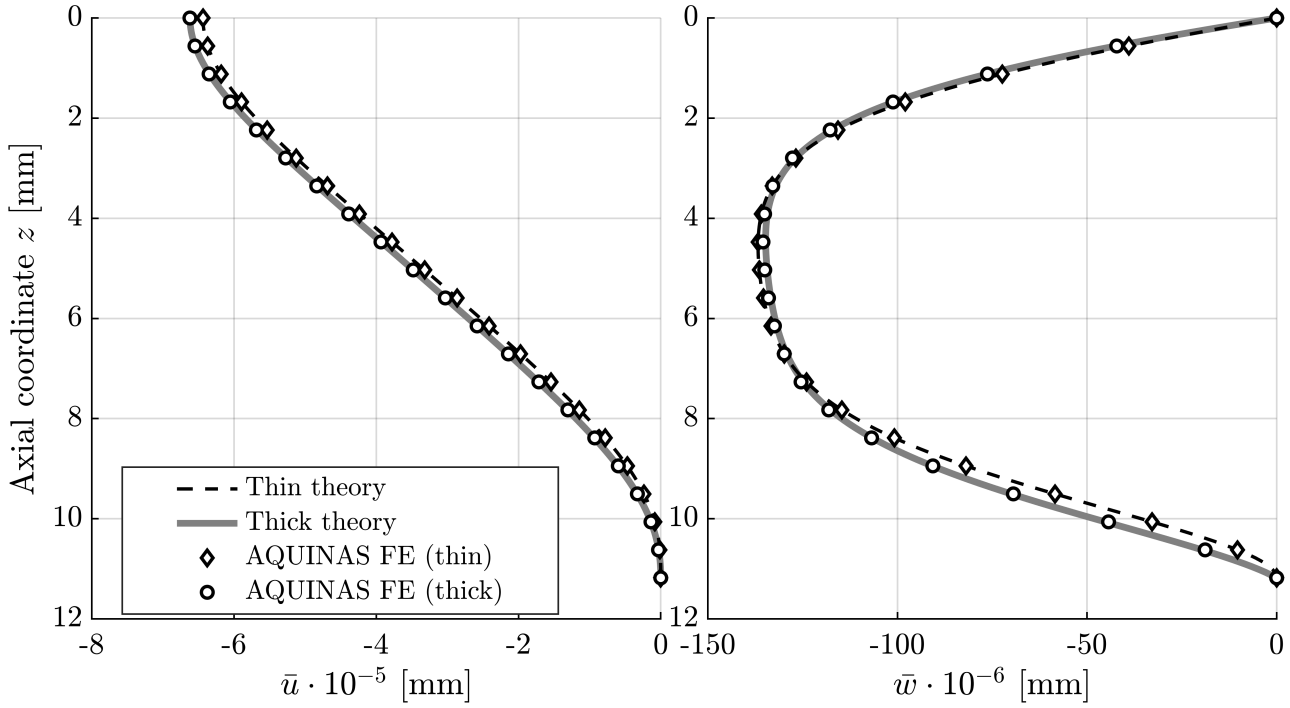


Figure 6.5: Meridional $\bar{u}$ and normal $\bar{w}$ axisymmetric displacement profiles for a cylinder under uniform external pressure.

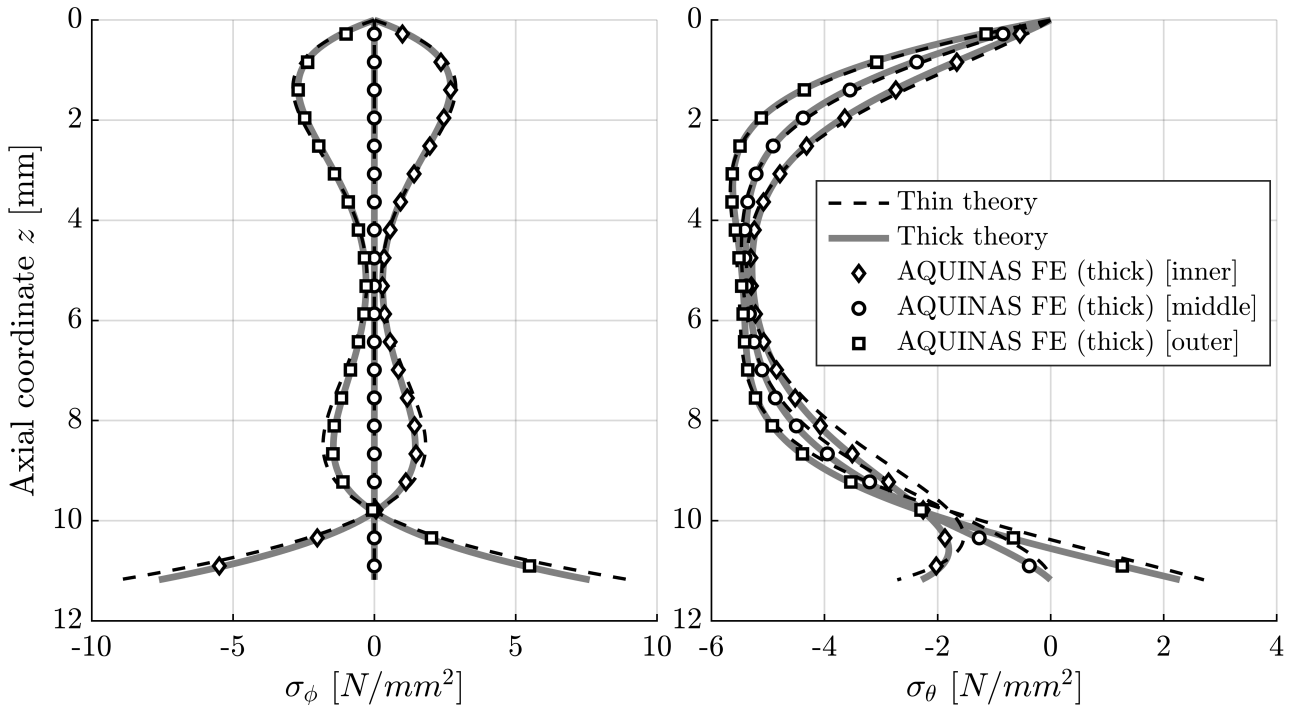


Figure 6.6: Meridional (left) and circumferential (right) axisymmetric stress patterns for a cylinder under uniform external pressure.

components that relate to meridional curvature aspects will inevitably result in degradation of the numerical solution accuracy that an element is capable of, but will additionally place a challenge on geometric modelling approximation of doubly-curved axisymmetric shells, as the discussion of 2.2.2 outlines.

The truncated spherical part of a total angular span 2α is illustrated in Figure 6.7, with the plane of meridional symmetry capitalised through suitable boundary conditions at the equator of the shell, reducing modelling requirements. As the present chapter is focused on the behaviour of axisymmetric shells where the inclusion of finite-thickness effects can be a contributing factor on the computational solution's validity, the geometric aspects of the meridian are slightly altered compared to those adopted in Section A.2.5, but also the original presentation of this problem in Flügge (1990), to scale the significance of shear strains and stresses as part of the spherical part's bending response. Hence, the r_ϕ/t ratio is decreased from 15 to 5, with $r = 5.0\ mm$ and $t = 1.0\ mm$, while the half-model angle α is doubled such that now $\alpha = 20°$, anticipating that the meridian's increased length will pronounce bending response effects. For a unit magnitude of the radial edge load $H = 1\ N/mm$, radial u and axial w displacement profiles expressed in the global coordinate system of Fig. 6.2 are displayed in Figure 6.8, obtained through both analytical and computational resources. The thin shell theory solution of Flügge (1990) and FE results of AQUINAS for an explicitly thin axisymmetric shell element are not in good agreement in this case due to the dependence of the analytical derivations on the κ factor, defined as:

$$\kappa^4 = 3(1-\nu^2)\frac{r_\phi^2}{t^2} - \frac{\nu^2}{4} \tag{6.45}$$

with additional terms in the series being necessary for values of κ not close to the one assumed through the problem definition of `input_Example_LA05.m`. The formulation of AQUINAS is therefore a more representative solution for thin shell behaviour, absent any finite-thickness effects. On the other hand, the two shear-flexible computational results of ABAQUS (2022) and

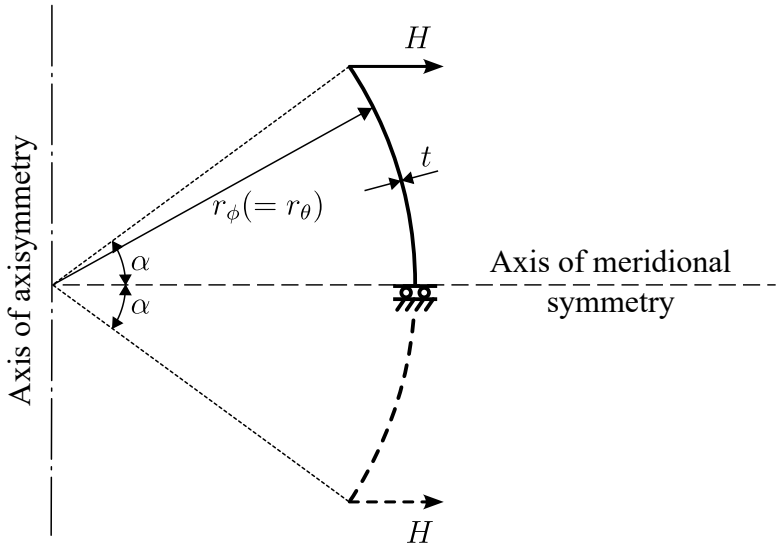


Figure 6.7: Axisymmetric spherical part model under a radially outwards edge load, exploiting meridionally symmetry through appropriate boundary conditions.

AQUINAS (thick) appear to be in great agreement, with only 20 of the previously described elements used against a 100 of SAX1 thick or thin axisymmetric shell elements employed in ABAQUS, not due to any shortcoming of the commercial software's formulation but rather to remove any considerations of numerical accuracy unrelated to the underlying kinematics of the SAX1 element from the comparison. A solution of similar accuracy could also be obtained with just 10 AQUINAS (thick) element, but as the economy of the linearly interpolated element is already substantial compared to the original and more elaborate AQUINAS formulation Teng & Rotter (1989a), there does not appear a reason to delve into a discussion on the precision of coarser mesh resolutions.

As the analytical solution of Flügge (1990) appears to be unsuitable for the resulting κ parameter of the problem after alteration of its geometric characteristics, comparison with a thin shell result will be fully resorted to the AQUINAS (thin) FE solution. On that basis, meridional σ_ϕ and circumferential σ_θ stress profiles are exhibited in Figure 6.9. Discrepancies between thin and thick shell formulations are not as visually pronounced as was the case with the distribution of displacements presented earlier, whilst comparison of AQUINAS (thick) and ABAQUS profiles adds to the consensus of the present axisymmetric shell element's appropriateness for the analysis of shear flexible models.

6.4.2 Linear elastic bifurcation buckling analysis results for axisymmetric and nonsymmetric modes

With the brief but encouraging comparison of LA results for the shear-flexible element now concluded, attention will be shifted again on the key formulation feature that has motivated the development of AQUINAS in the first place, detection of bifurcation buckling modes into circumferential harmonics n. The destabilising effects of membrane and shear stress resultants will be retained during evaluation of geometric stiffness coefficients, while destabilising moment effects will be neglected as they have been found to be only relevant for specific categories of axisymmetric shell problems that would not buckle in their absence (Jumikis, 1987). Inclusion of finite thickness effects will not only have consequences on the formulation of geometric stiffness matrices but shall also alter the pre-buckling bending response of any stocky axisymmetric shell system, leading to different membrane stress resultant profiles along the meridian of the shell

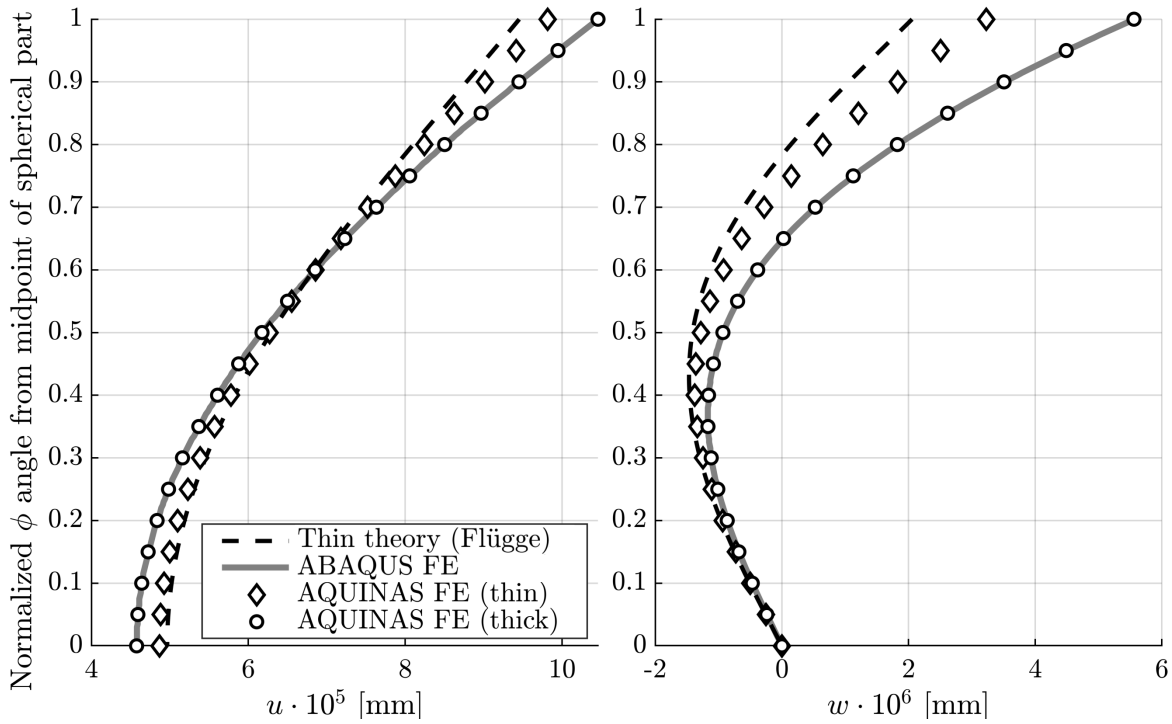


Figure 6.8: Global radial u and axial w axisymmetric displacement profiles for a spherical part under a radial edge load with respect to a normalised ϕ angle distance from a midspan plane of meridional symmetry.

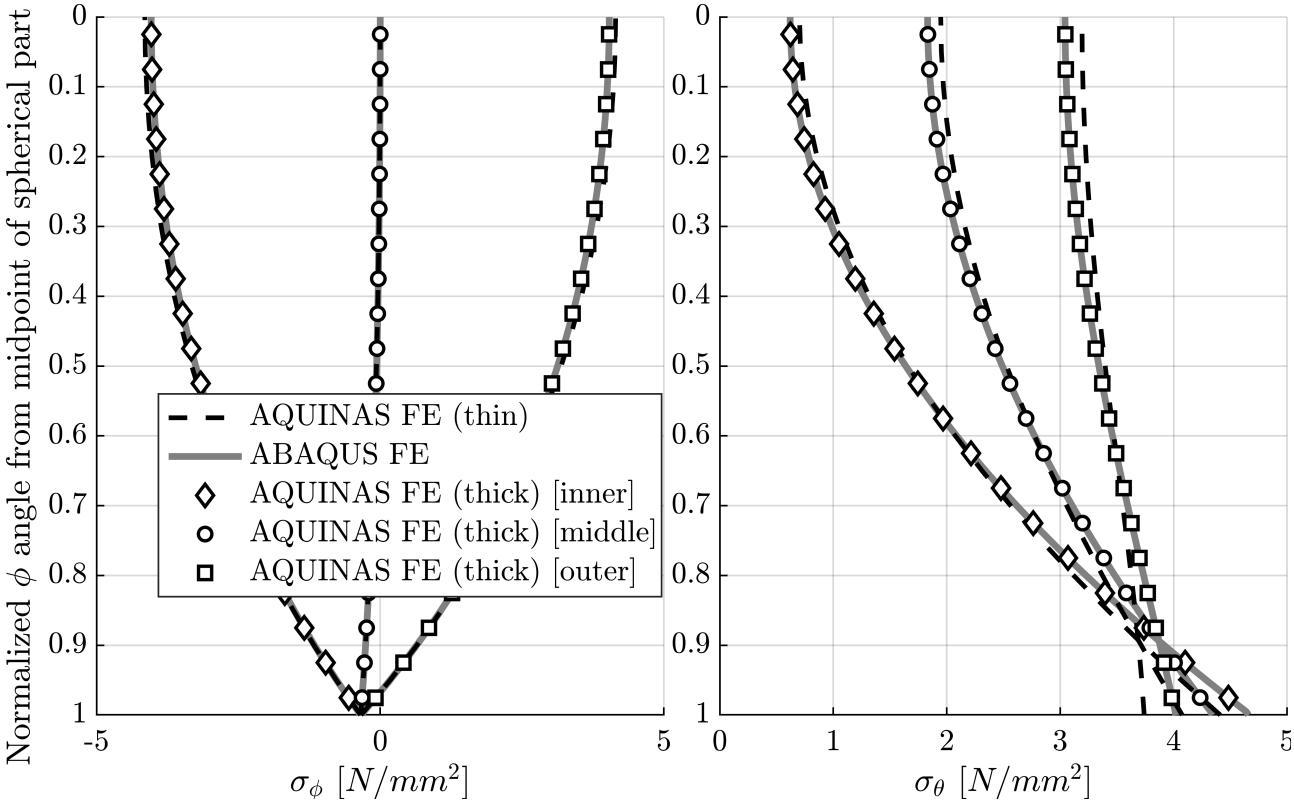


Figure 6.9: Meridional (left) and circumferential (right) axisymmetric stress patterns for a spherical part under a radial edge load with respect to a normalised ϕ angle distance from a midspan plane of meridional symmetry.

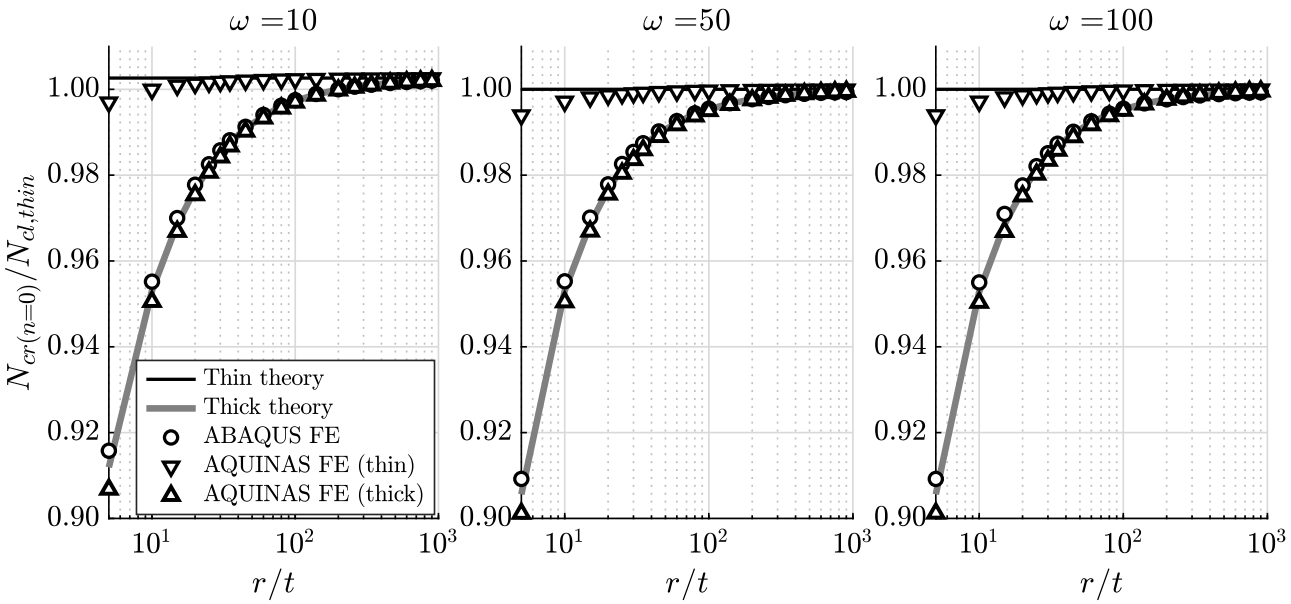


Figure 6.10: Computational and analytical predictions of critical buckling loads for cylinders under uniform meridional compression, considering only axisymmetric modes.

and a two-fold influence on buckling load estimations.

As was the case with the LA problems of the previous section, the analytical results of Chapter 5, established as a reliable validation reference through comparisons with ABAQUS (2022) FE generated critical buckling load predictions, will be employed for the assessment of LBA solutions computed through the present shear-flexible axisymmetric shell element. Cylindrical shells will monopolise benchmark tests, with computational results from both ABAQUS and the thin formulation of AQUINAS included to illustrate the differences in element assumptions across different ranges of slenderness. Suitable boundary conditions associated with the pre-buckling analysis step of the LBA shall ensure a pure membrane stress state, while a different set of restraints activated during stability checks will approximate the harmonic circumferential distribution of the modal displacement field described by Eqs. 5.52.

6.4.2.1 Axisymmetric buckling of cylinders under uniform meridional compression for varying dimensionless groups ω and r/t ratios

A full reproduction of the numerically evaluated elastic buckling loads associated with only axisymmetric modes for $n = 0$ will constitute the first step in the validation process, allowing for a comparison that momentarily neglects in-plane shear strains and twisting curvature terms as well as DOFs and variations related to a circumferential description of the buckling mode. Finite element model organisation strategy is entirely similar to that employed for the evaluation of Figure 5.7 related results, examining a wide range of r/t ratios for three dimensionless ω groups, as demonstrated in Figure 6.10. LBA predictions associated with the stockiest cylinders considered are actually even more flexible than estimations obtained through the Appendix C formulae, providing conservative evaluations for the critical elastic buckling loads of this classical shell system. Progressively increasing model slenderness leads to agreement of all comparative resources, either analytical or computational in nature, suggesting that this shear-flexible formulation can be a reliable element for thick or thin axisymmetric shell systems. Complete agreement with AQUINAS (thin) results can also be achieved by a numerically high enough value for the shear coefficient k (Cowper, 1966), an artificial enforcing of a thin shell theory result that was also relevant in the context of the preceding chapter's analytical solutions.

6.4.2.2 Nonsymmetric bifurcation buckling of cylinders under external pressure

Verification benchmarks will now progress to fully nonsymmetric bifurcation buckling modes, investigating the elastic critical buckling load estimations obtained through the AQUINAS (thick) formulation for cylindrical shells under external pressure. The modelling techniques described for the natively axisymmetric shell models of AQUINAS in Section 5.5.2.2, referenced as AQUINAS (thin) herein, facilitate a pure pre-buckling membrane stress state to allow direct comparison with the expressions of Appendix C and other theoretical resources (Brush & Almroth, 1975). Examination of the FE results exhibited in Figure 6.11 indicates that inclusion of finite-thickness effects in a computational approximation of the present stability problem leads to estimates in good agreement with buckling load evaluations obtained through the full 3D ABAQUS modelling space, utilising the general purpose S4 element, although this agreement progressively deteriorates for the characteristic dimensionless lengths $L/(r\pi)$ considered in Figure 6.11. The eventual regression into the AQUINAS (thin) FE predictions indicates that the lack of computational aspects related to omission of follower effects on the applied loads are still pertinent for relatively slender cylindrical models. The corresponding analytical thick non-shallow estimation on the basis of Appendix C.2 formulae accurately captures the influence of centrally directed pressure in the adjacent equilibrium state of the elastic stability problem, permitting complete agreement with ABAQUS (2022) where both thin and thick AQUINAS formulations are shown to be limited. This shortcoming may only be amended through explicit consideration of load stiffness components in the element stiffness matrices (not to be confused with the geometric stiffness part of Eq. 6.32), a deformation dependent feature that while included in the general shell formulations of ABAQUS and has been demonstrated to have significant effects on pressurised shell systems (Iwata *et al.*, 1991) is not currently prioritised for development and immediate releases of the AQUINAS software.

6.4.3 Materially nonlinear stress analysis performance of linearly interpolated element

Whilst formulation of the present shear flexible element has been driven by the need for accurate estimations of the load bearing capacity for low slenderness axisymmetric shell systems, the simplicity of its interpolation field and overall element description is anticipated to provide an advantageous basis for the implementation of plasticity algorithms (Crisfield, 1991). Due to the lack of any computational schemes that could violate continuity of plastic flow between elements, such as the transformation and subsequent static condensation of nodal variables relating to midsurface stretching of elements $\partial\bar{u}/\partial s$ (Teng & Rotter, 1989a), materially nonlinear behaviour is expected to provide more intuitive continuous stress states for regions where yielding has occurred. Adoption of a single-point Gauss-Legendre integration strategy for evaluation of stiffness matrices along the element's meridian will ensure that introduction of plasticity effects at any through-thickness Simpson integration stations shall not invalidate the assumption of a continuous polynomial interpolation field for in-element stresses. Higher order polynomials are inevitably imprecise for the interpolation of materially discontinuous element fields when multi-point Gauss-Legendre integration is applied, a notion that has been considered by the author as one of the drawbacks associated with the element coded into AQUINAS during programming of its MNA functionality, especially when contrasted against the integration strategies of the SAX1 (ABAQUS, 2022) or SHELL208 (ANSYS, 2022) elements of commercial computational solvers.

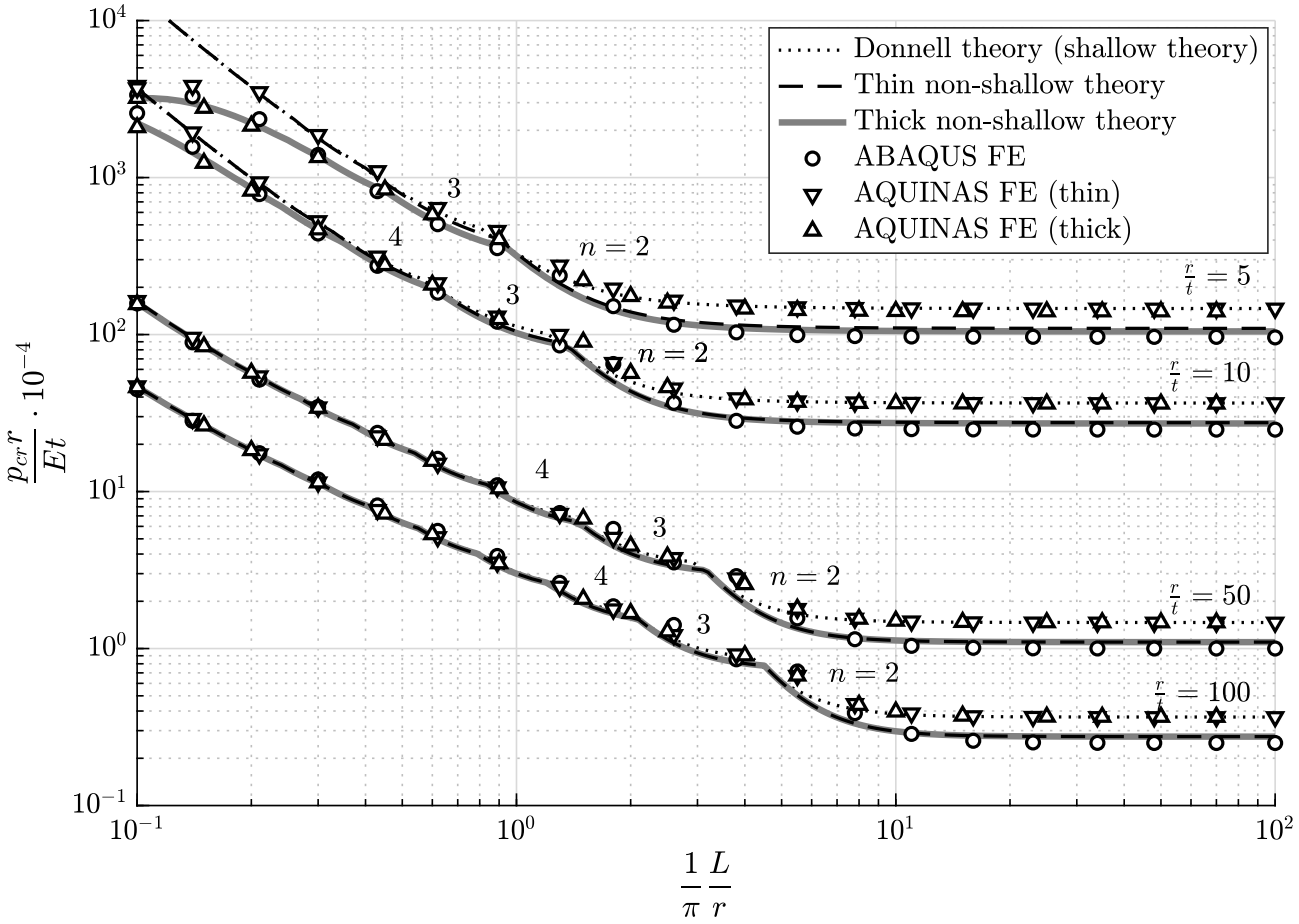


Figure 6.11: Computational predictions of critical bifurcation pressures p_{cr} for selected r/t ratios and varying lengths for any possible combinations of $m - n$ wavenumbers, compared against various analytically obtained theoretical results.

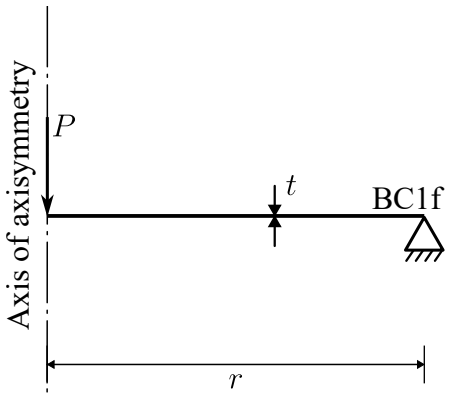


Figure 6.12: Circular plate under an axial concentrated force, applied on the axis of axisymmetry.

6.4.3.1 Circular plate under an axial concentrated force at its centre

To examine the reliability of the presently constructed element in the context of a materially nonlinear analysis, but to also formally provide tangible proof for all of the above claims, one of the more problematic MNA benchmarks included in the first release of AQUINAS (Filippidis & Sadowski, 2023b) will now be revisited. `input_Example_MNA02.m` studies the development of bending stress resultants along the meridian of a simply-supported circular plate under a concentrated axial force applied on its centre, coinciding with the model's axis of axisymmetry as is illustrated in Figure 6.12. As bending stress resultants first peak at the centre of the circular plate, consideration of plasticity effects results in the development of yielded zones that progressively spread from the axis of revolution towards the supported edge of model and from material points on the outer surface fibres of the plate towards its mid-surface. Since the circular plate is under a state of pure bending, membrane stress resultants are effectively negligible throughout the analysis until full plastification of the model has been achieved and the corresponding equilibrium path plateaus asymptotically for a value of the concentrated force $P = 2\pi M_p$.

Whilst the described behaviour is indeed captured by AQUINAS in the corresponding MNA benchmark script, discussed in Section A.4.2, an examination of the meridional M_ϕ and circumferential M_θ bending stress resultants presented in Figures A.55 - A.56 clearly exhibits the irregular patterns of their distribution along the meridian of the plate, increasing in severity with further plastification of the plate. At the time of documenting this behaviour in the corresponding manual of the AQUINAS software, the unevenness of their distribution has been attributed by the author to application of the static condensation strategy employed in (Teng & Rotter, 1989a,b) and its detrimental consequences to the continuity of DOF terms across elements, without however any further computational justification due to the unavailability of an alternative formulation. Comparison with stress patterns obtained from ABAQUS would not constitute proof enough to support such claims, owing to the black-box nature of the solver and the possibility of potential internal post-processing of its results to ensure smoothness of stress distributions, whilst the progression of the corresponding bending stress resultants as presented in Teng & Rotter (1989a) hinted to a shortcoming in the programming of AQUINAS rather than the formulation itself.

Material and geometric characteristics describing the circular plate model are retained in the remodelling of this seemingly simple axisymmetric shell problem, this time through a discretisation employing the linearly interpolated shell element formulated in this chapter. With the edge of the plate located at a radial coordinate $r = 10.0\ mm$ and a unit thickness $t = 1.0\ mm$, the model undoubtedly qualifies for a thick plate characterisation at an $r/t = 10$ ratio even with

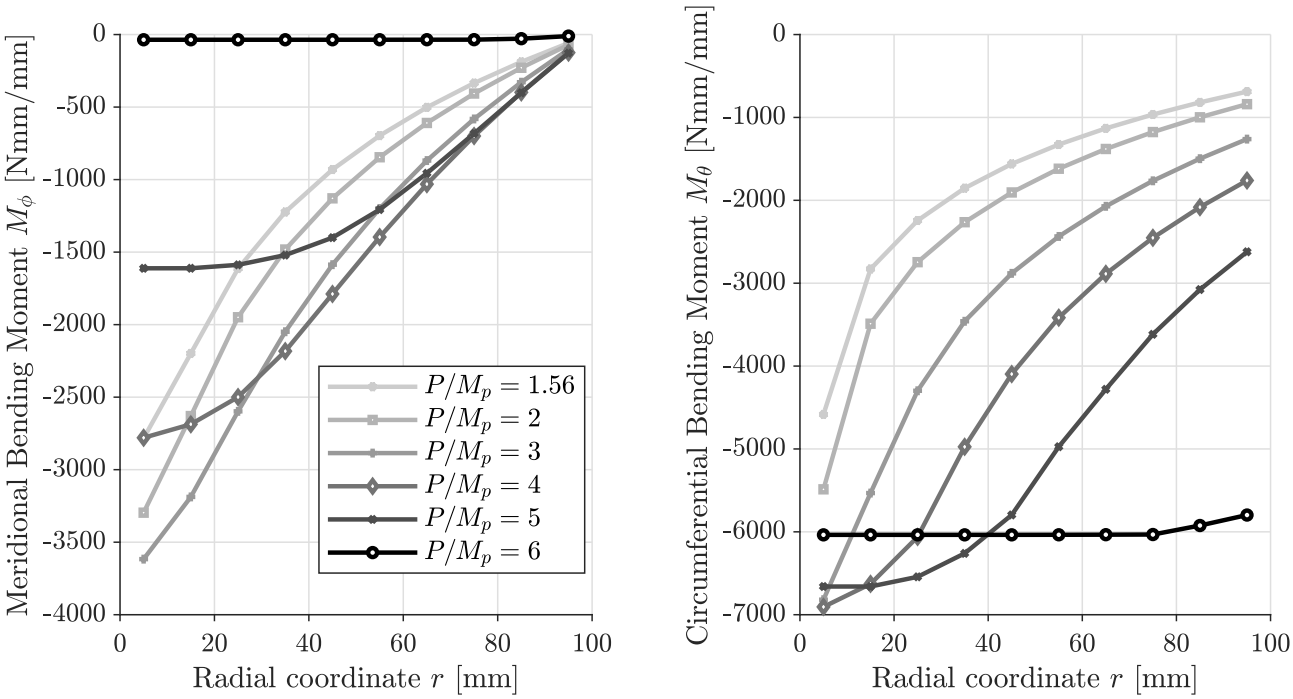


Figure 6.13: Simply-supported circular plate bending under an axial force applied at the axis of revolution.

the more austere criteria of Kraus (1967). Consequently, inclusion of finite thickness effects will result in increased flexibility and earlier onset of plasticity effects, leading to a reduction to the load P at which the full plastic resistance of the plate under bending is attained, even if only through an asymptotic plateau. With transverse shear behaviour assumed to be entirely elastic as a simplification to permit a plane stress material law to be utilised, this reduction is limited to 0.9% of the corresponding thin shell prediction, as evaluated through the existing AQUINAS coded element. Nevertheless, examination of meridional M_ϕ and circumferential M_θ bending stress resultant progression during a stepwise incrementation of the applied force P in Figure 6.13 indicates that static condensation of nodal could indeed be held responsible for the lack of consistency in their meridional distribution. In the absence of any methods that can violate the continuity of the DOF field, stress resultants computed at the integration points of each elements retain the anticipated features of a smooth distribution along the meridian of an axisymmetric system.

It should finally be noted that lower predictions of bending stress resultants near the centre of the circular plate are not a consequence of any underestimation or shear-flexibility effects but rather reflects the position of Gauss-Legendre integration points employed. For both the exploration of `input_Example_MNA02.m` and the present reproduction of those results through a thick shell element formulation, a rather coarse mesh resolution of a total of 10 elements was adopted, ensuring direct comparison with the presentation of the problem by Teng & Rotter (1989a), even though the cubic interpolation field of the corresponding element allows for a better approximation of the circular plate's bending response (but also at a higher computational cost). Hence, utilisation of 3-4 integration points in the meridional direction of the element, according to the suggestions of Jumikis (1987), inevitably places evaluation of bending stress resultants closer to the axis of axisymmetry and facilitates evaluation of higher peaks for both bending stress resultants as a comparison of Figure 6.13 and Figures A.55 - A.56 suggests, at least for the early elastic stages of the analysis where static condensation does not affect their meridional profile quality. The distributions computed herein can be shown to otherwise have the correct development tendencies, with circumferential bending resisting the entirety of the

applied force once yielding zones have penetrated the full shell wall thickness and meridional components of bending stress resultants reducing to zero.

6.4.4 Capacity curve computation and solution quality scrutiny for the shear-flexible axisymmetric shell element

Despite the particular computational achievements and alignment with solution expectations of increased flexibility and extended penetration of bending effects along the meridian of an axisymmetric shell, success of the finite element formulation discussed herein will ultimately be determined on an evaluation of capacity curves for cylindrical shells under meridional compression. Calculation of a physically interpretable and accurate λ_0 parameter, representing the slenderness of the shell system at which the full plastic resistance R_{pl} has been attained as presented in Table 2.2. Precise estimation of the squash load for this seemingly simple reference axisymmetric shell system in the presence of geometric nonlinearities has already proved an impractical objective for the purely thin shell theory kinematics of the Teng & Rotter (1989a,b) finite element description, resulting in negative λ_0 values, not allowing a full characterisation of this classical shell problem in the context of the capacity curve framework. In the hopes of having amended this shortcoming through inclusion of finite thickness effects on both linear and nonlinear shell kinematics for the element, attention of the present section will be swiftly turned towards a computational comparison of capacity curves within the same scope of the examination presented in Section 4.3.3.

6.4.4.1 GMNA examination of nominally perfect stocky cylinders under meridional compression

Exceptionally stocky cylindrical shells under meridional compression should reliably achieve load carrying capacities meeting or exceeding the system's squash load R_{pl} in the presence of material hardening effects. Geometric softening effects arising from negative stiffness contributions associated with destabilising stress states should be limited and controlled, owing to significantly high ratios of characteristic resistances R_{pl}/R_{cl} for cylinders of low slenderness, indicating that plasticity considerations will dictate the evaluation of the critical load without the severe geometric nonlinearities that can be detrimental for the shell structure's integrity at load levels near the critical elastic buckling load R_{cl} having sufficiently developed. Additional model aspects relating to the proximity of edge constraints for very short cylinders can have a compounding effect on surpassing the full plastic resistance R_{pl}, a common theme across different classical shell systems (Fajuyitan, 2018). With edge restraints for the cylindrical models of Section 4.3.3 being as restrictive as possible (i.e. a BC1r condition at their base and BC2r at their loaded edge, as illustrated in Figure 4.3, instead of a potentially more relaxed BC1f and BC2f at these two ends that would permit a higher degree of freedom for meridional deformations to develop), equilibrium paths are expected to progress confidently above load levels corresponding to the system's squash load.

With the same set of geometric characterisation and material parameters considered in the preceding computational venture of Section 4.3.3, albeit with modelling drawbacks relating to early onset of plasticity effects near the loaded edge of the cylinder facilitated by bending dominated boundary layers, MNA and GMNA assessments that employ the AQUINAS thick axisymmetric shell element are undertaken. A swift review of the corresponding results exhibited in Figure 6.14 clearly suggests that the present derivational endeavour has not been a successful one. Whilst the shear-flexible formulation appears to be capable of producing the physically interpretable value for the λ_0 slenderness that has constituted the main aim of this Chapter, the stockiest model considered for an $r/t = 10$ barely manages to reach its full plastic resistance R_{pl},

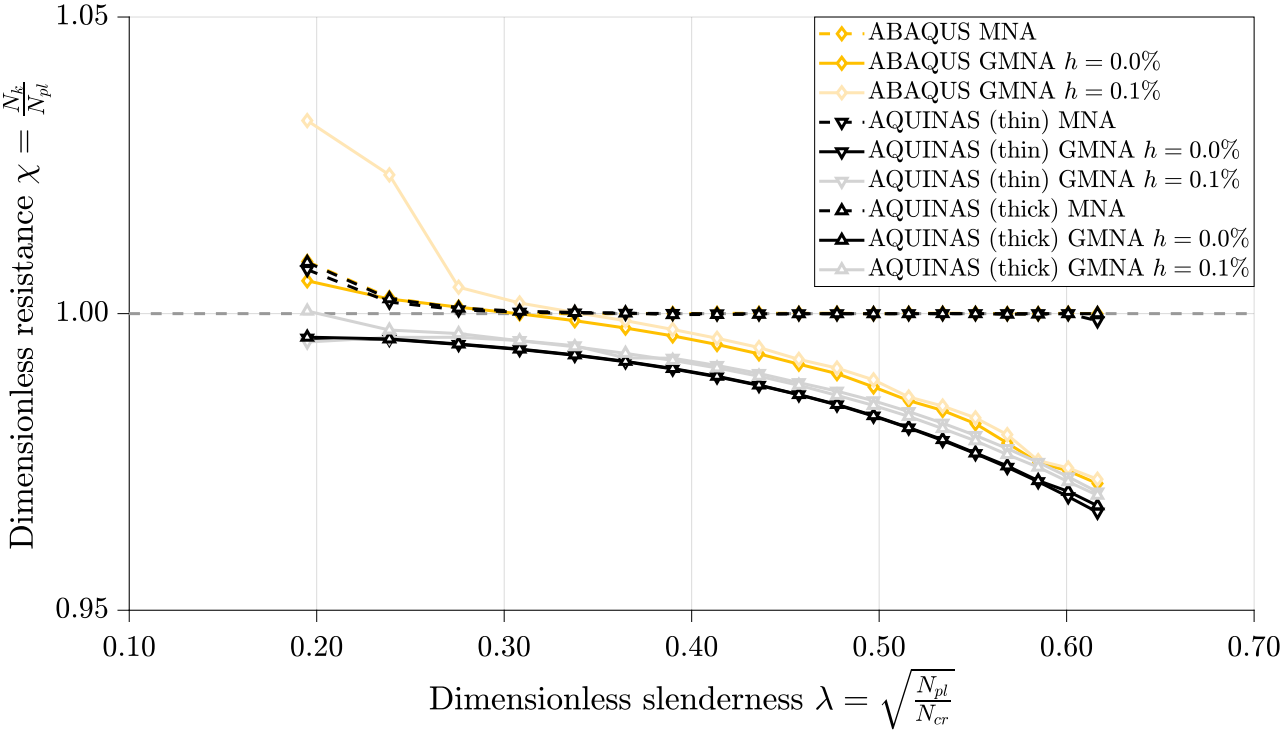


Figure 6.14: A comparison of computed capacity curves for nominally perfect cylinders under uniform meridional compression in the traditional χ vs λ format for fully axisymmetric shell models, with FE solutions obtained through ABAQUS and AQUINAS explicitly thin and thick element formulations. Only axisymmetric buckling modes were permitted during the AQUINAS GMNA runs.

leading to an achievement of questionable quality as over-restraining needs to also be taken into account in the examination of these capacity curves. The beneficial effects of closely positioned restraints impeding the development of mechanics that can lead to the collapse of the stockiest cylinders is appropriately demonstrated by the ABAQUS axisymmetric FE solution included in these plots, where all analyses corresponding to ratios $r/t \leq 20$ can attain a dimensionless resistance χ at least equal to unity, but also from the set of MNAs employing both thin and thick AQUINAS formulations associated with the same low slenderness range of r/t values, illustrating the robustness of the materially nonlinear algorithm utilised for both elements. With computational strategies pertaining to plasticity effects found to properly treat the problem of elastoplastic strain integration, even with the ad-hoc handling of transverse shear strains as not contributing to stresses traversing the yield surface according to a von Mises criterion (Crisfield, 1997), attention is once more redirected to the geometrically nonlinear aspects of the formulation.

To allow for a comprehensive comparison of different FE formulations relevant to the solution of axisymmetric shell structures, even if through the more general scope of a 3D modelling space, a series of GNAs will be executed for the stockiest of the cylinders considered in the capacity curve of Figure 6.14, that of an $r/t = 10$. As material nonlinearities will not be present in this investigation, the meridionally compressive edge load will be adjusted to reflect the load level at which elastic buckling is expected to occur, as provided by Eq. 2.19. Apart from equilibrium paths obtained through the AQUINAS formulations, a fully axisymmetric ABAQUS model utilising the reliable SAX1 element and two 3D shell panels discretised through the reduced integration general shell elements S4R and S4R5 are submitted for nonlinear analysis, with all 5 models being subject to the same solution control parameters relating to the load incrementation

scheme (even though the AQUINAS implementation of the arc-length solver has been shown to not be entirely identical to the equivalent ABAQUS algorithm). A brief review of Figure 6.15b suggests that the different shell formulations can result in critical load predictions of significant discrepancies, without a definitive estimate of the cylinder's load carrying capacity being readily available. The differences in these path-tracing solutions do not affect the GMNA FE result necessary for the construction of capacity curves, owing to the limited development of geometric nonlinearities at the early stages of the analysis, but it is evidently clear that both AQUINAS formulations are experiencing softening effects associated with geometrically nonlinear behaviour to a higher degree. The additional observation of the stiffening effect associated with solutions employing the SAX1 and S4R element formulations, leading to parts of the path tracing procedure where the stiffness is even higher than the initial elastic stiffness slope while the S4R5 general shell element stays closer to the AQUINAS solutions up to some load level without demonstrating a similar behaviour, indicates that there is a key computational feature that is not in common between these elements.

To further isolate and study the different aspects of these formulations, an assortment of computational examinations on this low slenderness system have been carried out. An intriguing result is illustrated in Figure 6.15b, where meridional and circumferential responses are completely decoupled by considering the impractical value of $\nu = 0.0$ for the material's Poisson's ratio. In the absence of a normal pressure or any radial line loads acting on the cylinder, circumferential strains and stresses remain numerically negligible throughout the analysis, effectively reducing the response of all shell models to one that could potentially be obtained through a simple planar beam model under the action of a compressive along its longitudinal axis (for example the axisymmetric shell formulation SAX1 of ABAQUS (2022) readily reduces to the B21 beam element). By only considering meridional membrane action as a source of geometric nonlinearity and completely ignoring bending and shear components of the shell's response, this comparison was intended to provide a baseline of agreement between the different shell element formulations. Nonetheless, solution conformity was limited to the two AQUINAS axisymmetric elements but was now also extended to the S4R5 element, strengthening the conviction that the similarities illustrated in Figure 6.15a were due to an underlying formulation characteristic. On the other hand, all other sources of FE generated equilibrium paths demonstrate stiffening effects associated with geometric nonlinearities, with the SAX1 element behaviour appearing to be in complete sync with the strongly stiffening response obtained through an S4R discretised panel model.

While this result appears to be counter-intuitive, as an axially compressed structural member would be expected to progressively exhibit higher deflections for constant increments to the applied loading, the stiffening features across different shell formulations, including the continuum axisymmetric ABAQUS element CAX4R but also an axisymmetric shell solution acquired through the SHELL208 element in ANSYS (2022), does not seem to be coincidental. Indeed, a pattern can be identified by browsing the corresponding theory guide pages of the computational solvers, as all FE generated results with a stiffening behaviour in the presence of geometric nonlinearities are obtained by employing elements based on a *finite membrane strain* nonlinear shell formulations, while softening responses are associated with *small strain* nonlinear shell formulations, including both AQUINAS elements. Explicit statements are made from both ABAQUS and ANSYS on their corresponding documentation pages for element formulations being in accordance with either geometrically nonlinear approach.

Finite strain shell formulations, either general or of an axisymmetric nature, have been introduced early in the development of FEM theory through the pioneering work of Argyris, later reinstated in a series of publications (Argyris *et al.*, 1978, 1979), but also promoted through the work of several authors (Hughes & Carnoy, 1983; Simo *et al.*, 1988; Crisfield & Tan, 2001; Klinkel &

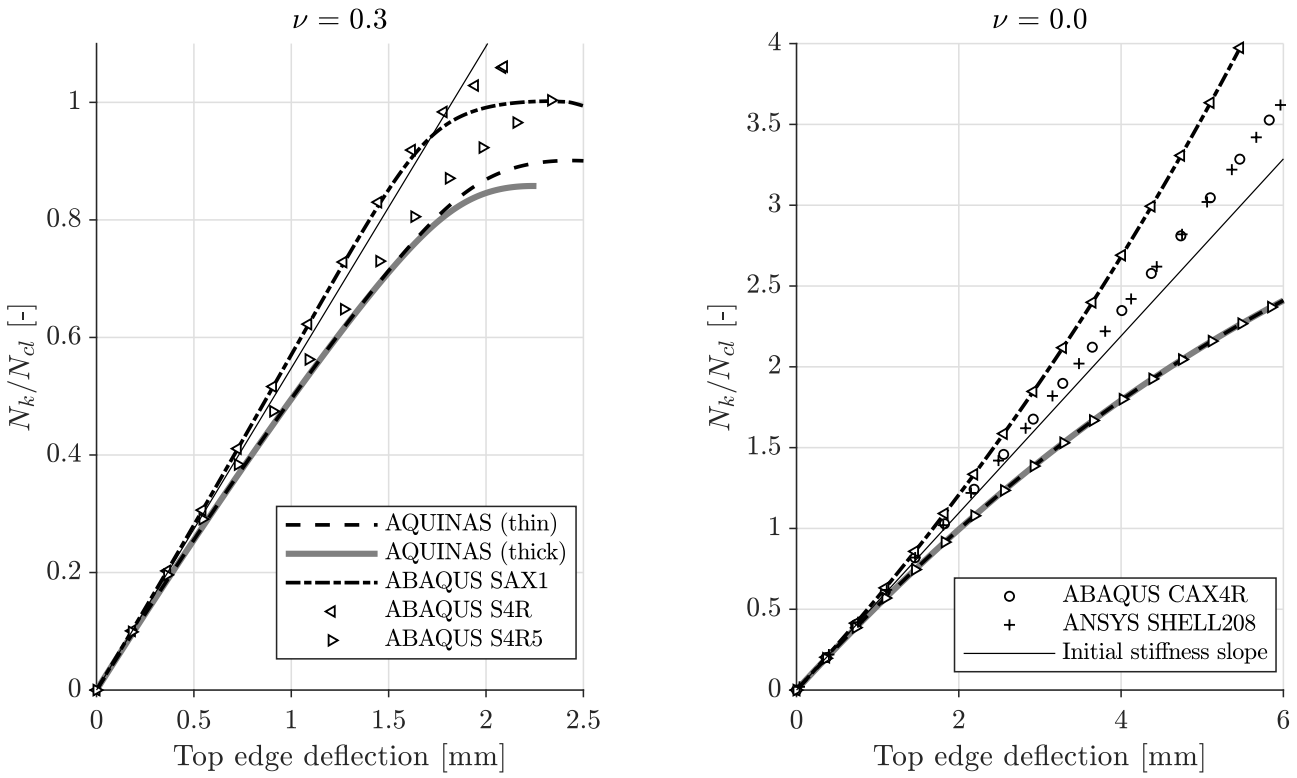


Figure 6.15: Equilibrium paths for stocky meridionally compressed cylindrical shell according to different finite element formulations, considering a Poisson's ratio of $\nu = 0.3$ corresponding to structural steel on the left sub-figure (a) and an unrealistic for civil engineering shell applications Poisson's ratio $\nu = 0.0$ on the right sub-figure (b).

Govindjee, 2002). Full nonlinear strain-displacement behaviour can be better approximated by retaining quadratic terms in displacement and rotational expressions, a shortcoming of small strain theory that truncates kinematic expressions by omitting corresponding higher order terms. As is evidently clear from recent literature resources on shell Simo *et al.* (1988); Crisfield & Moita (1996); Ibrahimbegovic (1997); Crisfield & Tan (2001) or more generic 3D beams (Jelenić & Crisfield, 1999; Crisfield & Jelenić;, 1999) and planar continua (Crisfield & Moita, 1996) formulations, but also through a survey of the dedicated ABAQUS documentation pages on the description of available shell finite elements, corotational frameworks are often leveraged as the basis of their derivation, excluding rigid-body motions from the deformational response by embedding a rotating local frame at the element level, enabling higher precision of estimated strain measures within that frame (Crisfield, 1997). Examination of these formulations reveals their mathematical and conceptual complexity, making an axisymmetric shell finite element adaptation a daunting task.

An equally interesting remark can be made through a re-examination of 6.15b and the observation that the axisymmetric solid result generated through a CAX4R in ABAQUS (2022) coincides with the SHELL208 axisymmetric shell solution in ANSYS (2022). Even though this comparison ignores considerable features of shell behaviour through a Poisson's ratio $\nu = 0.0$ and loading condition choices, the complete agreement between them but not with any of the other path-tracing solutions promotes a further study of the background theory guide provided by ANSYS, as an axisymmetric shell element would be expected to be aligned with other shell formulations of similar underlying assumptions rather than a continuum axisymmetric model. This computational agreement can be attributed to the formulatory approach adopted in the construction of SHELL208 element, as the corresponding page's reference to the article by Ahmad *et al.* (1970), describing a general 3D shell element that explicitly renders and integrates

the thickness of the shell wall, indicates that this axisymmetric shell element is essentially a degenerated shell formulation as discussed in Section 2.2.2.

6.4.4.2 The effect of incompressible cross-sections on the load carrying capacity of cylinders under meridional compression

Recognising the complexity of developing a full finite membrane strain formulation in the later stages of the present doctoral work, an attempt was made to isolate and only implement specific features relating to the conceptual strategies adopted in the context of 'geometrically exact' treatments. One such feature that could potentially justify the geometric stiffening behaviour illustrated in Figure 6.15b involves the omission of the fibre inextensibility condition (Hughes & Carnoy, 1983; Simo *et al.*, 1988), relevant to one of the simplifications associated with shell theory and implicitly corresponding to Assumption 1 (as defined in Section 2.1.1). Scaling of the shell wall thickness as a consequence of Poisson effects induced by membrane straining modes could result in thicker cross sections that would naturally increase the overall stiffness of the element. These Poisson effects arise due to the plane stress conditions leveraged in the constitutive relationships of the shell's material, leading to the following expression for the normal stretching strain ϵ_ζ of the shell wall for $\sigma_\zeta = 0$ as:

$$\epsilon_\zeta = -\frac{\nu}{1-\nu}(\epsilon_\phi + \epsilon_\theta) \tag{6.46}$$

Whilst a positive scaling of the shell thickness for a meridionally compressed cylinder could explain the increase in stiffness coefficients during an incremental GNA, utilisation of a Poisson's ratio $\nu = 0.0$ for the analyses of Figure 6.15 contradicts the development of fibre extensibility effects according to Eq. 6.46, as the thickness should remain constant. Indeed, an independent definition for a Poisson's ratio relating to cross-sectional scaling can be found by browsing through the modelling windows and solution parameters of ABAQUS (2022), termed as *effective Poisson's ratio* and assumed to take values within the range of -1.0 and 0.5 as stated in the corresponding pages of the documentation pages discussing this parameter in the context of beam elements. Adopting the notation ν_{eff} for an unassociated with constitutive relations Poisson's ratio, being only relevant to the evaluation of fibre extensibility, a scaling parameter f may be defined as:

$$f = [(1+\epsilon_\phi)(1+\epsilon_\theta)]^{\frac{-\nu_{eff}}{1+\nu_{eff}}} \tag{6.47}$$

where a value of $\nu_{eff} = 0.0$ corresponds to a constant thickness throughout the analysis while $\nu_{eff} = 0.5$ represent a thickness incompressibility condition. Augmenting the AQUINAS shear-flexible shell formulation with the scaling factor f of Eq. 6.47 and considering the 'extremes' of either constant thickness or incompressible cross-sectional behaviour (i.e. extremes in the context of structural steel, as an effective Poisson's ratio $\nu_{eff} = -1.0$ would not be representative of this material), the capacity curve generation of Figure 6.14 is undertaken once more in the hopes of obtaining a computational result that confidently permits evaluation of the slenderness λ_0. With the FE AQUINAS (thick) solution displayed in Figure 6.16, it is clear that incorporation of only a single aspect associated with finite membrane strain formulations constitutes a half-measure and cannot ultimately provide the extra stiffening effect that the element needs for the analysis of stocky meridionally compressed cylinders. Even though capacity curves for incompressible behaviour $\nu_{eff} = 0.5$ reliably provides GMNA strength estimates that are higher the corresponding for ν_{eff} for both stain hardening parameters considered, this strength increase is limited and cannot be accounted as a prime factor in the robust performance of the SAX1 element for numerical load carrying predictions.

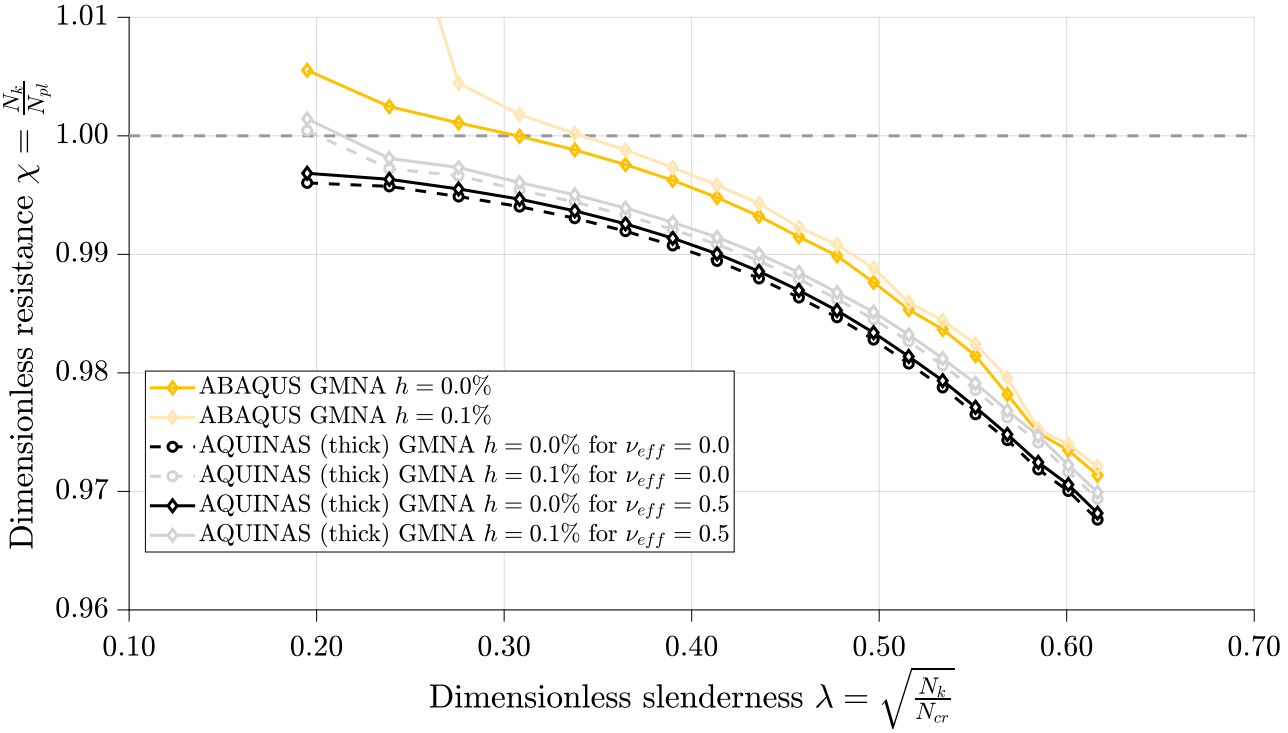


Figure 6.16: A comparison of computed capacity curves for nominally perfect cylinders under uniform meridional compression in the traditional χ vs λ format for fully axisymmetric shell models, with FE solutions obtained through the AQUINAS thick formulation examining the effects of incompressible cross-sectional behaviour. Only axisymmetric buckling modes were permitted during the AQUINAS GMNA runs.

6.5 Concluding remarks

The challenges in extending the axisymmetric shell element coded into AQUINAS to account for finite-thickness effects have been presented, focusing on the main aspects of the formulation that do not allow for a simple and manageable process of applying enhancements. Adjustable shape functions that can suitably scale bending or shear characteristics of the interpolation field depending on a stiffness ratio parameter ψ have been employed across several works for the inclusion of finite-thickness effects, with these shape functions readily reducing to cubic Hermitian polynomials for significantly slender models. Explicit definition of shell kinematics on a global coordinate system hinders incorporation of an interpolation field described in this manner, as shape functions that could change in order of interpolating polynomials depending on the ratio of bending and shear stiffnesses would additionally be utilised for meridional displacements, inappropriately altering polynomials associated with membrane stretching terms. Consequently, since the original explicitly thin shell formulation of AQUINAS cannot be suitably augmented for the analysis of shear-flexible axisymmetric shell structures, a new element was constructed as a conceptual blend of established formulations, not limited only to axisymmetric shells but also considering planar beam and general shell element features. The derived element is expected to not only reliably predict the load carrying capacity of stocky axisymmetric shell models but also lead to minimal architectural changes during its programming into AQUINAS, as well as provide a simple formulatory basis to potentially facilitate further extensions in the future.

The theoretical basis of the element's strain-displacement relations can be traced to the definition of Green's strain tensor, as this has been stated in the kindred doctoral work of (Jumikis, 1987).

Transverse shear strain are retained in the kinematics of the axisymmetric shell, resulting in a disconnection of both meridional β_ϕ and circumferential β_θ rotations with the corresponding first variations of the normal displacement $\bar{w}$. Linear and nonlinear kinematics are briefly compared against the equivalent expressions in the Teng & Rotter (1989a) formulation, with terms relating to membrane straining modes found to be in agreement, while curvatures are now expressed strictly through rotational terms. Application of this kinematic framework on a linearly interpolated two node axisymmetric shell element produces a simple base for the formulation in a local coordinate system, with the processes employed for the intermediate steps before evaluation of stiffness coefficients being in accordance with those corresponding to the already programmed thin shell element, limiting implementation modifications in AQUINAS. Material behaviour associated with transverse shear stresses is assumed to remain elastic, allowing for a plane stress constitutive law to be leveraged for the integration of elastoplastic strains without shear stresses contributing to a von Mises yield surface criterion.

A series of benchmark examples have been provided to examine the behaviour of the constructed finite element across a range of EN 1993-1-6 (2025) types of analyses. Stress analysis results are aligned with the shear-flexible analytical solutions of the preceding chapter, but also match ABAQUS FE results for a non-straight meridian axisymmetric shell problem, that of a spherical part under a radial edge load. Comparisons are extended to elastic critical buckling load predictions through LBAs, where once more tests employ the analytical stability results for cylinders under meridional compression and external pressure derived in the previous chapter. A more accurate estimate of the bifurcation buckling load can be obtained through inclusion of finite-thickness effects, considering both fully axisymmetric modes but also bifurcation into nonsymmetric harmonics n, a key formulation feature that has motivated development of AQUINAS in the first place. A single MNA example, that of a circular plate under a concentrated axial force applied at its centre, demonstrating that the single Gauss-Legendre integration scheme permits the constructed element to retain its computational integrity in the context of a materially nonlinear analysis, providing justification for the numerical ill-behaviour encountered in the corresponding example of the original AQUINAS release.

Computational competence of the constructed shear-flexible axisymmetric shell element is eventually determined on the basis of capacity curve generation for cylinders under meridional compression. Whilst the lack of a clearly identifiable positive value for the slenderness parameter λ_0 when FE predictions employed the AQUINAS thin shell element of Teng & Rotter (1989a,b) does not extend to the AQUINAS thick shell formulation derived in Section 6.3, the accuracy of an evaluated λ_0 parameter through the curves for low slenderness cylindrical shell models of Section 6.4.4 is highly questionable, as a comparison with the corresponding ABAQUS generated results employing an SAX1 element. A closer examination of GNA equilibrium paths for the stockiest model considered at an $r/t = 10$, computed through an assortment of different axisymmetric and general shell formulation, indicated that the underlying cause for these discrepancies rests in the nonlinear kinematics framework employed for the FE formulation. Finite membrane strain based elements demonstrated the development of geometric stiffening effects, clearly illustrated in a scenario where the model's Poisson's ratio is set to zero and decouples meridional and circumferential resisting mechanisms for the shell structure, while small strain nonlinear formulations appear to have a progressive softening behaviour that undermines their load carrying capabilities. Commonly implemented through utilisation of corotational frameworks for the accurate evaluation of straining modes without potential artificial strains relating to large rigid body rotations, as discussed in the review of nonlinear updating schemes of Section 2.2.2.3, finite membrane strains formulations appear to be necessary for the reliable evaluation GMNA resistances for very stocky cylindrical shells as well as for a wider range of low slenderness axisymmetric shell systems.

Chapter 7

Research outcomes and prospects for further research

It has been the aim of the present doctoral research to not only provide a detailed discussion of recent developments in the field of computational techniques for the analysis of axisymmetric shell structures, but also to re-raise awareness of key formulation aspects concerning the bifurcation buckling analysis of shell systems under a circumferentially uniform pre-buckling stress state. In doing so, different nonlinear characteristics of axisymmetric shell behaviour were explored, in ventures of both numerical and analytical nature, producing open-source tools that can support further development of the European Standard EN 1993-1-6 (2025). One of the most classical shell systems commonly encountered in civil engineering structural solutions due to its simplicity and optimised shape has received particular attention, that of circular cylindrical shells, studied for a wide range of geometric parametrisations. The outcomes of this research work will be summarised in this chapter, identifying areas that further scientific efforts can progress the field of axisymmetric shell buckling.

7.1 Research outcomes

Development of the AQUINAS software for the analysis of thin axisymmetric shell problems constitutes the pillar of the research work presented herein, motivated by the absence of computational capabilities by otherwise well-established commercial FE solvers pertaining to the detection of nonsymmetric bifurcation buckling modes as part of their axisymmetric shell modelling functionalities. Description of modal deformations through a harmonic distribution of displacements and rotations around the circumference of the shell has been an integral part of computational packages shared within the research community, regrettably not finding themselves into the 21^{st} century in an executable format due to either lack of maintenance or never being formally released in an open-source format. AQUINAS' release through a communicated GitHub repository amends this lack of specialised computational tools in the shell buckling research community by introducing an efficient MATLAB toolbox able to perform the full taxonomy of EN 1993-1-6 (2025) analyses. Its efficiency is further highlighted through utilisation of pre-compiled MEX binaries written in C++ that permit parallelisation of specific numerical processes through the OpenMP API, speeding up computation of stiffness coefficients and residual force terms by employing any number of available computer cores. The extensive list of example scripts and abstract object-oriented programming interface of the software ensure an intuitive and swift modelling experience for first-time users while also providing a fully customisable set of solution controls through name-value pair arguments for more proficient

analysts. Detailed documentation of both software options and procedures but also of benchmark models definition, their analytical intricacies and corresponding FE results scrutiny is furnished through the accompanying manual, to be found in the repository of this computational package.

The parallelisation traits of the AQUINAS toolbox were leveraged in the entirely computational venture of comparing FE generated capacity curves for two of the most classical axisymmetric shell systems available, cylinders under uniform meridional compression and global bending. This comparative examination of the two shell systems was performed for the purposes of providing a comprehensive justification for a research amendment made to the European standard for the strength assessment of shell structures, rectifying prior EN 1993-1-6 (2007) provisions considering meridionally compressed cylinders as the de-facto most conservative case for the evaluation of resistance parameters in the context of the capacity curve framework, absent any more relatable axisymmetric systems. An assortment of geometric parameters were considered for both systems to facilitate this investigation, varying the slenderness of the shell models through their characteristic r/t ratio while maintaining length dimensionality for a constant group $\Omega = 0.5$. Influence of initial imperfections was accounted for through a midspan Type A weld depression, assimilating a realistic imperfection shape that has been shown to be critical for the structural integrity of cylindrical shell systems rather than resorting to eigenmode affine imperfections, commonly chosen by analysts on a-priori notions of computational behaviour without tangible scientific proof. Scrutiny of GMNA strength assessments for cylinders under bending demonstrated that adoption of capacity curve parameters relating to meridionally compressed cylinders can actually overestimate the nonlinear strength of the system in the range of intermediate slendernesses, resulting in unreliable structural design of axisymmetric systems. The generation of FE results was impeded by numerical issues encountered during the solution of general shell models with ABAQUS, exhibiting high sensitivity to initial modelling conditions pertaining to discretisation and load incrementation. A parametric study was subsequently performed, additionally incorporating results from an equivalent set of analyses executed through ANSYS, to thoroughly document these computational problems as a point of caution in unquestionably accepting solutions from well-esteemed commercial software. Concurrently, the extensive generation of FE results for meridionally compressed cylinders by AQUINAS has led to identification of the thin, small strain shell formulation's shortcomings in GMNA predictions of the load carrying capacity for very stocky cylinders. The natively axisymmetric models of the toolbox failed to generate solutions where cylinders can attain their full plastic resistance, owing to the nature of its nonlinear kinematics description as was later discovered, leading to the evaluation of slenderness parameters λ_0 that are not physically interpretable in the context of the capacity curve framework.

To furnish a theoretical result for comparison purposes in the process of developing a robust axisymmetric shell element that includes finite-thickness effects, a comprehensive derivational study on the linear stress and bifurcation buckling behaviour of shear-flexible cylindrical shells under the axisymmetric loading conditions of meridional compression and external pressure was undertaken. By incorporating transverse shear strains into the strain-displacement relationships, the analytical solutions presented significantly improve result accuracy for stocky cylinders, where classical thin shell theory assumptions tend to be non-conservative. The derived closed-form expressions reflect a smooth transition from thick to thin shell behaviour as the slenderness ratio r/t increases, with the influence of terms associated with shear-flexible responses progressively diminishing for thinner shells. The stress analysis problem definition involves a second-order system of linear ODEs that cannot be fully decoupled, eventually producing expressions for the meridional displacement and rotational field that depend on the evaluation of constants associated with edge restraints. Calculation of these constants requires tools capable of handling basic arithmetic operations on complex numerics, even though the resulting deformation field

does not include imaginary numbers. Notably, bending boundary half-wavelengths Λ and associated effects were shown to penetrate deeper into the structure in shear-flexible models, a structural behaviour aspect that is associated with closer approximation of the more accurate continuum body description for a structural system. Stability results illustrated a similar pattern, where the inclusion of finite-thickness effects for the adjacent equilibrium state of the shell leads to more conservative estimates for the critical elastic buckling resistance of both cylindrical shell systems. Non-shallow terms have additionally enhanced the nonlinear kinematic description of the shell, permitting very good agreement with sophisticated ABAQUS FE results at the expense of extensive and elaborate formulae for the critical buckling load predictions for each considered load case. The thin shell formulation of AQUINAS is shown to substantially overestimate the corresponding buckling resistances as a consequence of its underlying strain-displacement assumptions, constituting one more reason for the introduction of a shear-flexible formulation. For both stress analysis and linear bifurcation buckling estimations, the analytical solutions derived can effectively be reduced to equivalent thin shell theory results through artificially high values for the shear correction factor k, enforcing a condition of negligible shear strains.

The computational struggles of the thin small strain formulation of AQUINAS were revisited in the preceding chapter, focusing on the development of a shear flexible axisymmetric shell element in the hopes of amending the limitations of its FE estimations exhibited in Chapter 4. With a brief investigation of enhancement possibilities available for the mixed-interpolation cubic field associated with the formulation of Teng & Rotter (1989a), the decision was made to proceed with the construction of a new element as a combination of key aspects corresponding to different formulations on the basis of a linear interpolation field of nodal variables. Starting from Green's strain tensor, kinematic components relevant to shear strain expressions were retained, producing relations where midsurface rotations and first variations of normal displacements are decoupled, leading to a formulation comprising 5 nodal DOFs. Transverse shear strains were assumed to be uninvolved in the development of plasticity behaviour as modelled through plane stress constitutive relations, allowing the corresponding functionality of AQUINAS to remain unaltered once this element is fully incorporated into its solver. Stress analysis and linear bifurcation buckling results were in good agreement with the theoretical solutions of Chapter 5 but also with the general purpose shell elements of ABAQUS, for both axisymmetric and 3D shell formulations. The linear interpolation field of the element permitted smooth progression of plasticity zones in an examination of the materially nonlinear bending response of a circular plate under a concentrated axial force, demonstrating that the irregular patterns of meridional M_ϕ and circumferential M_θ bending stress resultants were a consequence of static condensation procedures applied as part of the Teng & Rotter (1989a) formulation, preventing continuity of meridional membrane strains between elements. Computational success of the constructed element is eventually determined through an examination of capacity curves for meridionally compressed cylinders, aiming to produce a physically interpretable value for λ_0 in the low slenderness range of this reference shell system. Whilst such a value was indeed obtained through the shear-flexible element described, the accuracy of that result was questionable as a comparison with axisymmetric shell results from ABAQUS illustrated. A closer examination including different shell element formulations indicated that persistence of this shortcoming even after inclusion of finite thickness effects was a consequence of underlying nonlinear kinematic details. In particular, a finite membrane strain description of shell kinematics permitted a stiffening behaviour to develop for elements corresponding to this large strains nonlinear framework, an effect that contrasted the progressively softening response of small strain formulations, including both thick and thin AQUINAS element descriptions. Commonly associated with corotational frameworks for the nonlinear deformed configuration updating of an element's geometry while excluding any artificial straining modes relating to rigid body rotations, incorporation of finite membrane strain kinematics appears to be necessary for the accurate estimation of a low-slenderness

axisymmetric shell's resistance through a GMNA computational assessment.

7.2 Further research prospectives

Due to the broad scope of this research field in both theoretical background as well as computational strategies employed, suggestions on further research inevitably will comprise of both analytical endeavours but also numerical methods for the analysis of axisymmetric shells, always with the development and facilitation of design standards in mind. With the second generation of Eurocode for the strength and stability of shell structures EN 1993-1-6 (2025) released to the engineering community as of May 2025, FE assisted design of steel structures, an approach formerly restricted to the design of steels shells as determined through EN 1993-1-6 (2007), now has its own dedicated standard to dictate appropriate practices in computer aided engineering (EN 1993-1-14, 2025). This highlights the necessity for well-documented open-source tools that can reliably generate FEA estimations of an axisymmetric shell systems resistance, a need that AQUINAS aims to meet.

Further developments and updates are however essential if the recently released MATLAB written computational shell solver is to be successful in being a robust predictor of a shell's strength in the presence of both material and geometric nonlinearities, for slender but also stocky axisymmetric models. Notably, as the comparative venture of Chapter 4 has revealed and the formulatory work of Chapter 6 additionally demonstrated, the limitations of the thin small strain shell formulation adopted during first release of the software make it unsuitable for the analysis of very stocky axisymmetric shells in the context of a GMNA. With finite thickness effects not being solely responsible for this shortcoming, it is important to extend the computational capabilities of AQUINAS with the inclusion of a finite element built on the basis of finite membrane strain kinematics, permitting the necessary geometric stiffening effects to develop as a consequence of deformations inducing membrane straining. The nonlinear framework introduced through the corotational approach (Crisfield, 1997) appears to be a suitable candidate for processes relating to updates of the deformed configuration for such formulations, as both general shell elements (Simo *et al.*, 1988; Ibrahimbegovic, 1997) and beam elements (Jelenić & Crisfield, 1999; Crisfield & Jelenić;, 1999) found in relevant literature employing finite strain kinematics are based upon. Additional element modifications associated with finite strain theories, such as considerations of fibre extensibility during incremental loading of a shell structure can improve the geometric exactness of the element. The strategy for the derivation of this critically important for the future of AQUINAS formulation is not easily identifiable, since a degeneration approach could be applied on 3D shells to produce an axisymmetric element, but analogously an enhancement of a planar beam with terms pertaining to circumferential behaviour could potentially lead to the same element description, with reference to the discussion of Section 2.2.2. In any scenario, further considerations relating to the augmentation of the circumferential description of the displacement field with harmonic trigonometric distributions will be necessary, allowing evaluation of stiffness matrices for an a-priori assumed number of circumferential waves n and permitting detection of nonsymmetric bifurcation buckling modes for circumferentially uniform pre-buckling stress states.

With EN 1993-1-6 (2025) assisted design in mind, the undertaking of extensive computational explorations for the full characterisation of reference shell systems in the context of the capacity curve framework is essential. Several key such systems are now ripe for such a characterisation to take place (Rotter, 2016b), allowing implementation of both partly computational LBA-MNA and solely algebraic RRD methodologies to be promoted through the introduction of capacity curve parameters for more reference cases in appropriate Annexes of the European Standard.

Whilst utilisation of the AQUINAS software is limited to problems of circumferentially uniform pre-buckling stress states, its efficient solution capabilities could be leveraged for specific parts of such studies, among others the analysis of spherical caps with dimple imperfections where AQUINAS could perform all simulations considering the nominally perfect geometry of these models, with a more general FE solver like ABAQUS executing investigations of imperfection sensitivities for shapes that violate the axisymmetric conditions of the system. Introduction of uniform torsion handling functionalities in AQUINAS, a load case that the formulation of Teng & Rotter (1989a) permits and has been described in detail in Teng & Rotter (1989b), would further extend the scope of its competency for computational ventures on the generation of capacity curves. Combinations of loading scenarios could also be considered, examining the behaviour of cylinders under the combined effect of normal pressure, meridional compression and torsion being such an example. Furthermore, once the accurate treatment of both stocky and slender shell systems has been established in AQUINAS, a thorough investigation of length effects for cylinders under meridional compression to the same level of detail produced by Fajuyitan (2018) would be beneficial to the shell buckling discipline.

The derivational work of Chapter 5 for the evaluation of the elastic critical buckling load of shear-flexible cylinders under uniform meridional compression and external pressure has shown that there is still room for analytical endeavours in the 21^{st} century. Employment of FSDT principles and the mathematical programming environment of Maple (2022) could be further leveraged to improve theoretical understanding of instability phenomena in low slenderness shell structures. A prime opportunity for such an exploration can be identified in the analytical work of Zoelly (1915) for the critical buckling load of full closed spheres under external pressure. Introduction of finite thickness effects and re-derivation of the elastic buckling bifurcation load in an approach similar to that adopted for cylindrical shells could produce a valuable theoretical result for these systems, albeit with the simplification of a uniform membrane pre-buckling stress state still necessary. Moreover, re-examination of the cylindrical shell problem of Chapter 5 through the scope of a more complete Flügge shell theory, where the influence of changes in the radius of curvature r at different coordinates ζ through the shell wall is incorporated into the shell kinematics (with reference to Assumption 3), would result in an even more accurate estimation of the buckling resistance for very stocky cylinders, since the corresponding theory (Flügge, 1990) has been highlighted as the most complete for very thick shells (Jumikis, 1987) (even though strain-displacement expressions are notoriously complicated and can potentially hinder achievement of an analytical result).

The numerical sensitivity of ABAQUS during generation of FE results for cylindrical shells under bending, only reproduced through a similar effort utilising the computational capabilities of ANSYS, has highlighted the need of the shell buckling research community to move away from black-box commercial FE solvers as a discipline, restricting feasibility of more advanced projects that would require source code modifications but also placing paywall barriers on scholarly endeavours, with ABAQUS additionally setting financial limitations to extensive parallelisation of numerical simulations through a system of tokenisation. For shell researchers, and subsequently the shell design community, to fully profit from computer aided production of solutions for a variety of shell problems, further endeavours focused on the development of open-source tools similar to AQUINAS are necessary, capable of high precision analysis of both axisymmetric but also general shell structures.

Bibliography

1993-1-1, E. (2005) *"Eurocode 3: Design of Steel Structures. Part 1-1: General rules and rules for buildings"*. Comité Européen de Normalisation (CEN), Brussels.

ABAQUS (2022) *Commercial Finite Element Software and Documentation*. Dassault Systèmes Simulia Corp, United States.

Acharya, A. (2000) *A nonlinear generalization of the Koiter-Sanders-Budiansky bending strain measure*. International Journal of Solids and Structures, 37 (39), 5517–5528. doi:10.1016/S0020-7683(99)00231-0.

Ádány, S. & Schafer, B.W. (2025a) *Application of the Finite Tube Method for the analysis of tubular members: Buckling length, signature curve*. Thin-Walled Structures, 212, 113171. doi:10.1016/j.tws.2025.113171.

Ádány, S. & Schafer, B.W. (2025b) *Finite Tube Method for buckling analysis of tubular members using Fourier-approximation for the displacements*. Thin-Walled Structures, 206, 112672. doi:10.1016/j.tws.2024.112672.

Ahmad, S., Irons, B.M. & Zienkiewicz, O.C. (1970) *Analysis of thick and thin shell structures by curved finite elements*. International Journal for Numerical Methods in Engineering, 2 (3), 419–451. doi:10.1002/nme.1620020310.

Akima, H. (1970) *A New Method of Interpolation and Smooth Curve Fitting Based on Local Procedures*. J. ACM, 17 (4), 589–602. doi:10.1145/321607.321609.

Al Lawati, H. (2017) *Buckling of axially compressed cylindrical shells under different conditions*. Ph.D. thesis, The University of Edinburgh.

Al Lawati, H., Al Balushi, A. & Al Habsi, A. (2023) *Length and Boundary Condition Effects in the Buckling of Cylinders Under Different Load Combinations*. ce/papers, 6 (3-4), 1773–1779. doi:10.1002/cepa.2750.

Almroth, B.O. (1966) *Influence of edge conditions on the stability of axially compressed cylindrical shells.* AIAA Journal, 4 (1), 134–140. doi:10.2514/3.3396.

Almroth, B.O. & Brogan, F. (1978) *The STAGS computer code*. Technical Report NASA-CR-2950, NASA.

Amdahl, G.M. (1967) *Validity of the single processor approach to achieving large scale computing capabilities*. In Proceedings of the April 18-20, 1967, spring joint computer conference, pp. 483–485.

ANSYS (2022) *ANSYS Mechanical*. ANSYS, Inc., United States.

Arbocz, J. (1968) *Buckling of conical shells under axial compression.* Technical Report NASA-CR-1162, NASA.

Arbocz, J. & Hol, J. (1993) *Shell stability analysis in a computer aided engineering (CAE) environment.* In 34th Structures, Structural Dynamics and Materials Conference. La Jolla, CA, U.S.A. doi:10.2514/6.1993-1333.

Arbocz, J. & Starnes Jr, J. (2002) *Future directions and challenges in shell stability analysis.* Thin-Walled Structures, 40 (9), 729–754. doi:10.1016/S0263-8231(02)00024-1.

Argyris, J. (1964) *Recent Advances in Matrix Methods of Structural Analysis.* p. 187.

Argyris, J., Balmer, H., Doltsinis, J., Dunne, P., Haase, M., Kleiber, M., Malejannakis, G., Mlejnek, H.P., Müller, M. & Scharpf, D. (1979) *Finite element method — the natural approach.* Computer Methods in Applied Mechanics and Engineering, 17-18, 1–106. doi:10.1016/0045-7825(79)90083-5.

Argyris, J., Dunne, P., Haase, M. & Orkisz, J. (1978) *Higher-order simplex elements for large strain analysis — natural approach.* Computer Methods in Applied Mechanics and Engineering, 16 (3), 369–403. doi:10.1016/0045-7825(78)90108-1.

Arnoldi, W.E. (1951) *The principle of minimized iterations in the solution of the matrix eigenvalue problem.* Quarterly of applied mathematics, 9 (1), 17–29. doi:10.1090/qam/42792.

Aron, H. (1874) *Das Gleichgewicht und die Bewegung einer unendlich dünnen, beliebig gekrümmten elastischen Schale.* Journal für die reine und angewandte Mathematik, 1874 (78), 136–174. doi:10.1515/crll.1874.78.136.

Baillis, C., Jullien, J. & Limam, A. (2000) *An enriched 2D modelling of cooling towers.: Effects of real damage on the stability under self weight and on the strength under wind pressure.* Engineering Structures, 22 (7), 831–846. doi:10.1016/S0141-0296(98)00138-2.

Batdorf, S.B. (1947) *A simplified method of elastic-stability analysis for thin cylindrical shells.* Technical Report NACA-TN-1341, NACA.

Bathe, K.J. (2006) *Finite element procedures.* Klaus-Jurgen Bathe.

Bathe, K.J. & Bolourchi, S. (1979) *Large displacement analysis of three-dimensional beam structures.* International Journal for Numerical Methods in Engineering, 14 (7), 961–986. doi:10.1002/nme.1620140703.

Bathe, K.J. & Dvorkin, E.N. (1985) *A four-node plate bending element based on Mindlin/Reissner plate theory and a mixed interpolation.* International Journal for Numerical Methods in Engineering, 21 (2), 367–383. doi:10.1002/nme.1620210213.

Bathe, K.J., Ramm, E. & Wilson, E.L. (1975) *Finite element formulations for large deformation dynamic analysis.* International journal for numerical methods in engineering, 9 (2), 353–386.

Blaauwendraad, J. (2010) *Shear in Structural Stability: On the Engesser–Haringx Discord.* Journal of Applied Mechanics, 77 (3), 031005. doi:10.1115/1.3197142.

Blaauwendraad, J. & Hoefakker, J.H. (2014) *Semi-Membrane Concept Theory for Circular Cylindrical Shells*, pp. 161–172. Springer Netherlands, Dordrecht. doi:10.1007/978-94-007-6701-0_10.

Blanco, M.I. (2009) *The economics of wind energy.* Renewable and Sustainable Energy Reviews, 13 (6), 1372–1382. doi:10.1016/j.rser.2008.09.004.

Blazejewski, P. (2022) *Development of a Procedure for the Determination of the Buckling Resistance of Steel Spherical Shells according to EC 1993-1-6.* Materials, 15 (1). doi:10.3390/ma15010025.

Boyez, A. (2019) *Towards an improved computational method of analysis for multi-segment shells of revolution.* Ph.D. thesis, Imperial College London.

Boyez, A., Sadowski, A. & Izzuddin, B. (2017) *A novel 'boundary layer' finite element for the efficient analysis of thin cylindrical shells.* Computers & Structures, 182, 573–587. doi:10.1016/j.compstruc.2016.10.016.

Boyez, A., Sadowski, A. & Izzuddin, B. (2018) *A boundary layer finite element for thin multi-strake conical shells.* Thin-Walled Structures, 130, 535–549. doi:10.1016/j.tws.2018.05.019.

Brun, M., Combescure, A., Baillis, C., Limam, A. & Buzaud, E. (2008) *Simulations of the penetration of limestone targets using two-dimensional multimodal Fourier analysis.* International Journal of Impact Engineering, 35 (4), 251–268. doi:10.1016/j.ijimpeng.2007.02.004.

Brush, D.O. & Almroth, B.O. (1975) *Buckling of bars, plates, and shells.* McGraw-Hill.

Budiansky, B. (1959) *Buckling of clamped shallow spherical shells.* Technical report, HARVARD UNIV CAMBRIDGE MA.

Budiansky, B. (1963) *On the 'best' first-order linear shell theory.* The Prager Anniversary Volume-Progress in Applied Mechanics.

Bushnell, D. (1973) *Finite-Difference Energy Models versus Finite-Element Models: Two Variational Approaches in One Computer Program.* In Numerical and Computer Methods in Structural Mechanics (Edited by S.J. Fenves, N. Perrone, A.R. Robinson & W.C. Schnobrich), pp. 291–336. Academic Press. doi:10.1016/B978-0-12-253250-4.50018-X.

Bushnell, D. (1974) *Stress, stability and vibration of complex, branched shells of revolution.* Computers & Structures, 4 (2), 399–424. doi:10.1016/0045-7949(74)90066-2.

Bushnell, D. (1976) *B0S0R5 - program for buckling of elastic-plastic complex shells of revolution including large deflections and creep.* Computers & Structures, 6 (3), 221–239. doi:10.1016/0045-7949(76)90034-1.

Bushnell, D. (1987) *PANDA2—Program for minimum weight design of stiffened, composite, locally buckled panels.* Computers & Structures, 25 (4), 469–605. doi:10.1016/0045-7949(87)90267-7.

Bushnell, D. (1989) *Computerized buckling analysis of shells*, volume 9 of *Mechanics of Elastic Stability.* Springer.

Bushnell, D. (2020) *Shell buckling bibliography.* https://shellbuckling.com/papers/shellbucklingrefs.pdf https://shellbuckling.com/papers/shellbucklingrefs2.pdf. Accessed: 2025-05-03.

Bushnell, D., Almroth, B. & Brogan, F. (1971) *Finite-difference energy method for nonlinear shell analysis.* Computers & Structures, 1 (3), 361–387. doi:10.1016/0045-7949(71)90020-4.

Calladine, C. (1983) *Theory of shell structures.* Cambridge university press.

Cantin, G. & Clough, R.W. (1968) *A curved, cylindrical-shell, finite element.* AIAA Journal, 6 (6), 1057–1062. doi:10.2514/3.4673.

Castro, S.G., Zimmermann, R., Arbelo, M.A., Khakimova, R., Hilburger, M.W. & Degenhardt, R. (2014) *Geometric imperfections and lower-bound methods used to calculate knock-down factors for axially compressed composite cylindrical shells.* Thin-Walled Structures, 74, 118–132. doi:10.1016/j.tws.2013.08.011.

Chandrashekhara, K. & Pavan Kumar, D. (1995) *Assessment of shell theories for the static analysis of cross-ply laminated circular cylindrical shells.* Thin-Walled Structures, 22 (4), 291–318. doi:10.1016/0263-8231(94)00039-3.

Chapelle, D. & Bathe, K. (1998) *Fundamental considerations for the finite element analysis of shell structures.* Computers & Structures, 66 (1), 19–36. doi:10.1016/S0045-7949(97)00078-3.

Chen, L. (2011) *Buckling of circular steel cylindrical shells under different loading conditions.* Ph.D. thesis, The University of Edinburgh.

Chen, L., Doerich, C. & Rotter, J.M. (2008) *A study of cylindrical shells under global bending in the elastic-plastic range.* Steel Construction: Design and Research, 1 (1), 59–65.

Cheung, Y.K. & Tham, L. (1997) *The finite strip method.* CRC press. doi:10.1201/9781003068709.

Chryssanthopoulos, M.K. (1989) *Probabilistic buckling analysis of stringer-stiffened cylinders.* Ph.D. thesis, Imperial College London, London.

Chryssanthopoulos, M.K., Baker, M.J. & Dowling, P.J. (1991a) *Imperfection Modeling for Buckling Analysis of Stiffened Cylinders.* Journal of Structural Engineering, 117 (7), 1998–2017. doi:10.1061/(ASCE)0733-9445(1991)117:7(1998).

Chryssanthopoulos, M.K., Baker, M.J. & Dowling, P.J. (1991b) *Statistical Analysis of Imperfections in Stiffened Cylinders.* Journal of Structural Engineering, 117 (7), 1979–1997. doi:10.1061/(ASCE)0733-9445(1991)117:7(1979).

Ciarlet, P.G. (2008) *A brief introduction to mathematical shell theory.* In Classical and Advanced Theories of Thin Structures: Mechanical and Mathematical Aspects (Edited by A. Morassi & R. Paroni), pp. 111–185. Springer Vienna, Vienna. doi:10.1007/978-3-211-85430-3_5.

Cohen, G.A. (1973) *Computer analysis of ring stiffened shells of revolution.* Technical Report NASA-CR-2085, NASA.

Cohen, G.A. (1974) *Numerical Integration of Shell Equations Using the Field Method.* Journal of Applied Mechanics, 41 (1), 261–266. doi:10.1115/1.3423238.

Cohen, G.A. (1976) *Analysis of multicircuit shells of revolution by the field method.* Computer Methods in Applied Mechanics and Engineering, 8 (3), 301–318. doi:10.1016/0045-7825(76)90020-7.

Cohen, G.A. (1979) *FASOR—A second generation shell of revolution code.* Computers & Structures, 10 (1), 301–309. doi:10.1016/0045-7949(79)90099-3.

Cohen, G.A. (1981a) *Buckling of laminated anisotropic shells including transverse shear deformation.* Computer Methods in Applied Mechanics and Engineering, 26 (2), 197–204. doi:10.1016/0045-7825(81)90094-3.

Cohen, G.A. (1981b) *FASOR — a program for stress, buckling and vibration of shells of revolution.* Advances in Engineering Software (1978), 3 (4), 155–162. doi:10.1016/0141-1195(81)90013-9.

Cohen, G.A. & Haftka, R.T. (1989) *Sensitivity of buckling loads of anisotropic shells of revolution to geometric imperfections and design changes.* Computers & Structures, 31 (6), 985–995. doi:10.1016/0045-7949(89)90283-6.

Combescure, A. (1986) *Static and dynamic buckling of large thin shells: Design procedure, computation tools, physical understanding of the mechanisms.* Nuclear Engineering and Design, 92 (3), 339–354. doi:10.1016/0029-5493(86)90130-5.

Combescure, A. (1998) *Simplified prediction of creep buckling of cylinders under external pressure. Part 1: finite element validation.* European Journal of Mechanics - A/Solids, 17 (6), 1021–1036. doi:10.1016/S0997-7538(98)90507-1.

Combescure, A. & Bastien, R. (1984) *Computation of buckling of imperfect cylinder under axial compression.* Technical report, CEA Centre d'Etudes Nucleaires de Saclay.

Combescure, A. & Garuti, G. (1983) *A new periodic imperfect quasi axisymmetric shell element.* Technical report, CEA Centre d'Etudes Nucleaires de Saclay.

Combescure, A., Hoffmann, A. & Pasquet, P. (1982) *The CASTEM finite element system.* In Finite element systems: a handbook (Edited by C.A. Brebbia), pp. 115–125. Springer. doi:10.1007/978-3-662-07229-5_8.

Combescure, A. & Pernette, E. (1989) *Linear and nonlinear buckling of discrete supported cooling towers using special axisymmetric shell elements.* Nuclear Engineering and Design, 111 (2), 217–225. doi:10.1016/0029-5493(89)90208-2.

Cook, W.A. (1982) *A finite element model for nonlinear shells of revolution.* International Journal for Numerical Methods in Engineering, 18 (1), 135–149. doi:10.1002/nme.1620180112.

Cowper, G.R. (1966) *The shear coefficient in Timoshenko's beam theory.* Journal of applied mechanics, 33 (2), 335–340. doi:10.1115/1.3625046.

Crabtree, C.J., Zappalá, D. & Hogg, S.I. (2015) *Wind energy: UK experiences and offshore operational challenges.* Proceedings of the Institution of Mechanical Engineers, Part A, 229 (7), 727–746. doi:10.1177/0957650915597560.

Crisfield, M. (1983) *An arc-length method including line searches and accelerations.* International journal for numerical methods in engineering, 19 (9), 1269–1289.

Crisfield, M. (1991) *Non-linear Finite Element Analysis of Solids and Structures*, volume 1. John Wiley and Sons.

Crisfield, M. (1997) *Non-Linear Finite Element Analysis of Solids and Structures: Advanced Topics*, volume 2. John Wiley & Sons, Inc.

Crisfield, M. & Moita, G. (1996) *A unified co-rotational framework for solids, shells and beams.* International Journal of Solids and Structures, 33 (20), 2969–2992. doi:10.1016/0020-7683(95)00252-9.

Crisfield, M. & Tan, D. (2001) *Large-strain elasto-plastic shell analysis using low-order elements.* Engineering Computations, 18 (1/2), 255–286.

Crisfield, M.A. & Jelenić;, G. (1999) *Objectivity of strain measures in the geometrically exact three-dimensional beam theory and its finite-element implementation.* Proceedings of the Royal Society of London. Series A: Mathematical, Physical and Engineering Sciences, 455 (1983), 1125–1147. doi:10.1098/rspa.1999.0352.

De Borst, R. (1991) *The zero-normal-stress condition in plane-stress and shell elastoplasticity.* Communications in Applied Numerical Methods, 7 (1), 29–33. doi:10.1002/cnm.1630070105.

Debongnie, J. (1979) *Physical interpretation and generalization of Marguerre's shallow shell theory.* International Journal of Engineering Science, 17 (4), 387–399. doi:10.1016/0020-7225(79)90075-2.

Doerich, C. & Rotter, J. (2011a) *Accurate determination of plastic collapse loads from finite element analyses.* Journal of pressure vessel technology, 133 (1).

Doerich, C. & Rotter, J.M. (2008) *Behavior of cylindrical steel shells supported on local brackets.* ASCE Journal of Structural Engineering, 134 (8), 1269–1277.

Doerich, C. & Rotter, J.M. (2011b) *Generalised capacity curves for stability and plasticity: Application and limitations.* Thin-Walled Structures, 49 (9), 1132–1140. doi:10.1016/j.tws.2011.04.005.

Doerich, C., Vilnay, M. & Rotter, J.M. (2018) *Strength determination for band-loaded thin cylinders.* Advances in structural engineering, 21 (16, SI), 2454–2465. doi:10.1177/1369433218787715.

Donnell, L.H. (1935a) *A New Theory for the Buckling of Thin Cylinders Under Axial Compression and Bending.* Transactions of the American Society of Mechanical Engineers, 56 (8), 795–806. doi:10.1115/1.4019867.

Donnell, L.H. (1935b) *Stability of thin-walled tubes under torsion.* Technical Report NACA-TR-479, NACA.

Donnell, L.H. & Wan, C.C. (1950) *Effect of Imperfections on Buckling of Thin Cylinders and Columns Under Axial Compression.* Journal of Applied Mechanics, 17 (1), 73–83. doi:10.1115/1.4010060.

Dumir, P., Gandhi, M. & Nath, Y. (1984) *Axisymmetric static and dynamic buckling of orthotropic shallow spherical caps with flexible supports.* Acta Mechanica, 52 (1), 93–106.

Dvorkin, E.N. & Bathe, K.J. (1984) *A continuum mechanics based four-node shell element for general non-linear analysis.* Engineering computations, 1 (1), 77–88. doi:10.1108/eb023562.

Eberlein, R. & Wriggers, P. (1999) *Finite element concepts for finite elastoplastic strains and isotropic stress response in shells: theoretical and computational analysis.* Computer Methods in Applied Mechanics and Engineering, 171 (3), 243–279. doi:10.1016/S0045-7825(98)00212-6.

Eckstein, U., Krätzig, W.B. & Wittek, U. (1979) *Wirklichkeitsnahe Grenzbeullasten von Rotationsschalen unterschiedlicher Gauss'scher Flächenkrümmung.* Inst. für Konstruktiven Ingenieurbau, Ruhr-Univ., Bochum.

Edem, I.B. (2006) *The Exact Two-Node Timoshenko Beam Finite Element Using Analytical Bending and Shear Rotation Interdependent Shape Functions.* International Journal for Computational Methods in Engineering Science and Mechanics, 7 (6), 425–431. doi:10.1080/15502280600826381.

Edlund, B.L.O. (2007) *Buckling of metallic shells: Buckling and postbuckling behaviour of isotropic shells, especially cylinders.* Structural Control and Health Monitoring, 14 (4), 693–713. doi:10.1002/stc.202.

Edmondson, A.J. (1970) *Solution of shell problems by finite difference method.* Nuclear Engineering and Design, 11 (2), 208–216. doi:10.1016/0029-5493(70)90144-5.

Elias, Z.M. (1972) *Mixed finite element method for axisymmetric shells.* International Journal for Numerical Methods in Engineering, 4 (2), 261–277. doi:10.1002/nme.1620040211.

EN 1993-1-14 (2025) *"Eurocode 3: Design of Steel Structures. Part 1-14: Design assisted by finite element analysis" Submitted for Formal Vote and has status FprEN at the time of submission of this document, although it will very likely fully published as an EN sometime in 2025.* Comité Européen de Normalisation (CEN), Brussels.

EN 1993-1-6 (2007) *Eurocode 3: Design of steel structures–part 1-6: Strength and stability of shell structures.* Comité Européen de Normalisation (CEN), Brussels.

EN 1993-1-6 (2025) *"Eurocode 3: Design of Steel Structures. Part 1-6: Strength and Stability of Shell Structures".* Comité Européen de Normalisation (CEN), Brussels.

Engesser, F. (1891) *Die knickfestigkeit gerader stäbe.* W. Ernst & Sohn.

ENV 1993-1-6 (1999) *"Eurocode 3: Design of steel structures, Part 1. 6: General rules - Supplementary rules for the strength and stability of shell structures".* Comité Européen de Normalisation (CEN), Brussels.

Evkin, A. (2023) *Sensitivity and uncertainty propagation in buckling of spherical shells under external pressure.* Thin-Walled Structures, 190, 110978. doi:10.1016/j.tws.2023.110978.

Evkin, A., Kolesnikov, M. & Prikazchikov, D.A. (2017) *Buckling of a spherical shell under external pressure and inward concentrated load: Asymptotic solution.* Mathematics and Mechanics of Solids, 22 (6), 1425–1437. doi:10.1177/1081286516635872.

Fadaei, S., Afagh, F.F. & Langlois, R.G. (2024) *A Survey of Numerical Simulation Tools for Offshore Wind Turbine Systems.* Wind, 4 (1), 1–24. doi:10.3390/wind4010001.

Fafard, M. & Massicotte, B. (1993) *Geometrical interpretation of the arc-length method.* Computers & structures, 46 (4), 603–615.

Fajuyitan, O.K. (2018) *Length effects in elastic imperfect cylindrical shells under uniform bending.* Ph.D. thesis, Imperial College London.

Fajuyitan, O.K. & Sadowski, A.J. (2018) *Imperfection sensitivity in cylindrical shells under uniform bending.* Advances in Structural Engineering, 21 (16), 2433–2453. doi:10.1177/1369433218804928.

Fajuyitan, O.K., Sadowski, A.J. & Rotter, J.M. (2015) *A study of imperfect cylindrical steel tubes under global bending and varying support conditions.* In Proc., 8th Int. Conf. on Advances in Steel Structures, DECivil/IST/UL, pp. 22–24.

Felippa, C. & Haugen, B. (2005) *A unified formulation of small-strain corotational finite elements: I. Theory.* Computer Methods in Applied Mechanics and Engineering, 194 (21), 2285–2335. doi:10.1016/j.cma.2004.07.035. Computational Methods for Shells.

Feng, J. & Shen, W.Z. (2017) *Design optimization of offshore wind farms with multiple types of wind turbines*. Applied Energy, 205, 1283–1297. doi:10.1016/j.apenergy.2017.08.107.

Filippidis, A. & Sadowski, A. (2023a) *A MATLAB finite element toolbox for the efficient nonlinear analysis of axisymmetric shells*. ce/papers, 6 (3-4), 1735–1740. doi:10.1002/cepa.2355.

Filippidis, A. & Sadowski, A.J. (2023b) *Modern analysis of axisymmetric shells with AQUINAS: A MATLAB finite element toolbox*. SoftwareX, 23, 101434. doi:10.1016/j.softx.2023.101434.

Fischer, G. (1963) *Über den Einfluss der gelenkigen Lagerung auf die Stabilität dünnwandiger Kreiszylinderschalen unter Axiallast und Innendruck*. Z. Flugwiss., 11, 111–119.

Flügge, W. (1990) *Stresses in shells*. Springer Science & Business Media, 2nd edition.

Flügge, W. & Chou, S. (1967) *Large-Deformation Theory of Shells of Revolution*. Journal of Applied Mechanics, 34 (1), 56–58. doi:10.1115/1.3607668.

Forde, B.W. & Stiemer, S.F. (1987) *Improved arc length orthogonality methods for nonlinear finite element analysis*. Computers & structures, 27 (5), 625–630.

Forsberg, K. () *An evaluation of finite difference and finite element techniques for analysis of general shells*. Proc. of IUTAM Symp. on High Speed Computing of Elastic Structures.

Friedman, Z. & Kosmatka, J. (1993) *An improved two-node timoshenko beam finite element*. Computers & Structures, 47 (3), 473–481. doi:10.1016/0045-7949(93)90243-7.

Galletly, G.D., Kyner, W.T. & Moller, C.E. (1961) *Numerical Methods and the Bending of Ellipsoidal Shells*. Journal of The Society for Industrial and Applied Mathematics, 9, 489–513.

Geier, B. & Singh, G. (1997) *Some simple solutions for buckling loads of thin and moderately thick cylindrical shells and panels made of laminated composite material*. Aerospace science and technology, 1 (1), 47–63. doi:10.1016/S1270-9638(97)90023-7.

Geradin, M. (1971) *Error bounds for eigenvalue analysis by elimination of variables*. Journal of Sound and Vibration, 19 (2), 111–132.

Ghannad, M., Rahimi, G.H. & Nejad, M.Z. (2013) *Elastic analysis of pressurized thick cylindrical shells with variable thickness made of functionally graded materials*. Composites Part B: Engineering, 45 (1), 388–396. doi:10.1016/j.compositesb.2012.09.043.

Gillie, M. & Rotter, J. (2002) *The effects of patch loads on thin-walled steel silos*. Thin-Walled Structures, 40 (10), 835–852. doi:10.1016/S0263-8231(02)00028-9.

Goto, Y. & Zhang, C. (1999) *Plastic Buckling Transition Modes in Moderately Thick Cylindrical Shells*. Journal of Engineering Mechanics, 125 (4), 426–434. doi:10.1061/(ASCE)0733-9399(1999)125:4(426).

Gould, P.L. & Basu, P.K. (1977) *Geometric Stiffness Matrices for the Finite Element Analysis of Rotational Shells*. Journal of Structural Mechanics, 5 (1), 87–105. doi:10.1080/03601217708907307.

Grafton, P. & Strome, D. (1963) *Analysis of axisymmetrical shells by the direct stiffness method*. AIAA Journal, 1 (10), 2342–2347. doi:10.2514/3.2064.

Green, A. & Zerna, W. (1992) *Theoretical elasticity*. Dover Civil and Mechanical Engineering, 2nd edition.

Greiner, R. & Derler, P. (1995) *Effect of imperfections on wind-loaded cylindrical shells.* Thin-Walled Structures, 23 (1), 271–281. doi:10.1016/0263-8231(95)00016-7.

Greiner, R., Schmidt, H. & Rotter, J.M. (2008) *Rules for the buckling limit state assessment using stress design.* In Buckling of Steel Shells-European Design Recommendations, pp. 147–165. ECCS-European Convention for Constructional Steelwork.

Guggenberger, W. (1995) *Buckling and postbuckling of imperfect cylindrical shells under external pressure.* Thin-Walled Structures, 23 (1), 351–366. doi:10.1016/0263-8231(95)00022-6.

Gupta, A.K. (2015) *Efficient Wind Energy Conversion: Evolution to Modern Design.* Journal of Energy Resources Technology, 137 (5), 051201. doi:10.1115/1.4030109.

Habip, L. (1965) *A review of recent work on multilayered structures.* International Journal of Mechanical Sciences, 7 (8), 589–593. doi:10.1016/0020-7403(65)90014-7.

Haringx, J. (1948) *On highly compressible helical springs and rubber rods and their application for vibration-free mountings, I.* Philips research reports, 3, 401–449.

Harris, L.A., Suer, H.S., Skene, W.T. & Benjamin, R.J. (1957) *The Stability of Thin-Walled Unstiffened Circular Cylinders Under Axial Compression Including the Effects of Internal Pressure.* Journal of the Aeronautical Sciences, 24 (8), 587–596. doi:10.2514/8.3911.

Heyman, J. (1977) *Equilibrium of shell structures.* Oxford Engineering Science Series.

Hilburger, M. (2012) *Developing the next generation shell buckling design factors and technologies.* In 53rd AIAA/ASME/ASCE/AHS/ASC Structures, Structural Dynamics and Materials Conference, p. 1686. Honolulu, Hawaii, U.S.A. doi:10.2514/6.2012-1686.

Hilburger, M.W. (2020) *Buckling of thin-walled circular cylinders.* Technical Report NASA/SP-8007-2020/REV 2, NASA.

Hoff, N.J. (1955) *Thin Circular Conical Shells Under Arbitrary Loads.* Journal of Applied Mechanics, 22 (4), 557–562. doi:10.1115/1.4011154.

Hoff, N.J. (1966) *The effect of the edge conditions on the buckling of thin-walled circular cylindrical shells in axial compression.* In Applied Mechanics: Proceedings of the Eleventh International Congress of Applied Mechanics Munich (Germany) 1964, pp. 326–331. Springer.

Hong, T. (2000) *Nonlinear, buckling and postbuckling analysis of shells of revolution.* Ph.D. thesis, Hong Kong Polytechnic University.

Hong, T. & Teng, J. (2002) *Non-linear analysis of shells of revolution under arbitrary loads.* Computers & Structures, 80 (18), 1547–1568. doi:10.1016/S0045-7949(02)00109-8.

Hong, T. & Teng, J. (2008) *Imperfection sensitivity and postbuckling analysis of elastic shells of revolution.* Thin-Walled Structures, 46 (12), 1338 – 1350. doi:10.1016/j.tws.2008.04.001.

Huang, N.C. (1964) *Unsymmetrical buckling of thin shallow spherical shells.* Journal of Applied Mechanics, 31.

Hughes, T.J. & Carnoy, E. (1983) *Nonlinear finite element shell formulation accounting for large membrane strains.* Computer Methods in Applied Mechanics and Engineering, 39 (1), 69–82. doi:10.1016/0045-7825(83)90074-9.

Hughes, T.J.R., Taylor, R.L. & Kanoknukulchai, W. (1977) *A simple and efficient finite element for plate bending.* International Journal for Numerical Methods in Engineering, 11 (10), 1529–1543. doi:10.1002/nme.1620111005.

Hutchinson, J. (1965) *Axial buckling of pressurized imperfect cylindrical shells.* AIAA Journal, 3 (8), 1461–1466. doi:10.2514/3.3169.

Hutchinson, J.W. (2016) *Buckling of spherical shells revisited.* Proceedings of the Royal Society A: Mathematical, Physical and Engineering Sciences, 472 (2195), 20160577.

Ibrahimbegovic, A. (1997) *Stress Resultant Geometrically Exact Shell Theory for Finite Rotations and Its Finite Element Implementation.* Applied Mechanics Reviews, 50 (4), 199–226. doi:10.1115/1.3101701.

Ifayefunmi, O. (2014) *A survey of buckling of conical shells subjected to axial compression and external pressure.* Journal of Engineering Science and Technology Review, 7, 182–189.

Ismail, M., Mahmud, J. & Jailani, A. (2023) *Buckling of an imperfect spherical shell subjected to external pressure.* Ocean Engineering, 275, 114118. doi:10.1016/j.oceaneng.2023.114118.

Iwata, K., Tsukimori, K. & Kubo, F. (1991) *A symmetric load-stiffness matrix for buckling analysis of shell structures under pressure loads.* International Journal of Pressure Vessels and Piping, 45 (1), 101–120. doi:10.1016/0308-0161(91)90047-6.

Jelenić, G. & Crisfield, M. (1999) *Geometrically exact 3D beam theory: implementation of a strain-invariant finite element for statics and dynamics.* Computer Methods in Applied Mechanics and Engineering, 171 (1), 141–171. doi:10.1016/S0045-7825(98)00249-7.

Jones, R.E. & Strome, D.R. (1966) *Direct stiffness method analysis of shells of revolution utilizing curved elements.* AIAA Journal, 4 (9), 1519–1525. doi:10.2514/3.3729.

Jumikis, P. (1987) *Stability problems in silo structures.* Ph.D. thesis, Department of Civil and Mining Engineering, University of Sydney.

Kalnins, A. (1964) *Analysis of Shells of Revolution Subjected to Symmetrical and Nonsymmetrical Loads.* Journal of Applied Mechanics, 31 (3), 467–476. doi:10.1115/1.3629664.

Kapania, R.K. (1989) *A Review on the Analysis of Laminated Shells.* Journal of Pressure Vessel Technology, 111 (2), 88–96. doi:10.1115/1.3265662.

Kardomateas, G. & Dancila, D. (1997) *Buckling of moderately thick orthotropic columns: comparison of an elasticity solution with the Euler and Engesser/Haringx/Timoshenko formulae.* International Journal of Solids and Structures, 34 (3), 341–357. doi:10.1016/S0020-7683(96)00020-0.

Kardomateas, G.A. & Philobos, M.S. (1995) *Buckling of thick orthotropic cylindrical shells under combined external pressure and axial compression.* AIAA journal, 33 (10), 1946–1953. doi:10.2514/3.12750.

Key, S.W. & Krieg, R.D. (1973) *Comparison of Finite-Element and Finite-Difference Methods.* In Numerical and Computer Methods in Structural Mechanics (Edited by S.J. Fenves, N. Perrone, A.R. Robinson & W.C. Schnobrich), pp. 337–352. Academic Press. doi:10.1016/B978-0-12-253250-4.50019-1.

Kirchhoff, G. (1850) *Über das Gleichgewicht und die Bewegung einer elastischen Scheibe.* Journal für die reine und angewandte Mathematik (Crelles Journal), 1850 (40), 51–88.

Klinkel, S. & Govindjee, S. (2002) *Using finite strain 3D-material models in beam and shell elements*. Engineering Computations, 19 (3), 254–271.

Knebel, K. & Schweizerhof, K. (1995) *Buckling of cylindrical shells containing granular solids*. Thin-Walled Structures, 23 (1), 295–312. doi:10.1016/0263-8231(95)00018-9. Buckling Strength of Imperfection-sensitive Shells.

Koga, T. & Hoff, N.J. (1969) *The axisymmetric buckling of initially imperfect complete spherical shells*. International Journal of Solids and Structures, 5 (7), 679–697. doi:10.1016/0020-7683(69)90088-2.

Koiter, W. (1945) *On the stability of elastic equilibrium*. Ph.D. thesis, Delft University.

Koiter, W. (1963) *The effect of axisymmetric imperfections on the buckling of cylindrical shells under axial compression*. Mechanics, pp. 265–279.

Koiter, W. (1969) *Non linear buckling problem of a complete spherical shell under uniform external pressure, Parts I, II, III & IV*. Proceedings of the koninklijke nederlandse akademie van wetenschappen series b-physical sciences, 72 (2), 106.

Koiter, W.T. (1966) *On the nonlinear theory of thin elastic shells*. Proc. Koninkl. Ned. Akad. van Wetenschappen, Series B, 69, 1–54.

Koiter, W.T. & Simmonds, J.G. (1973) *Foundations of shell theory*. In Theoretical and Applied Mechanics (Edited by E. Becker & G.K. Mikhailov), pp. 150–176. Springer Berlin Heidelberg, Berlin, Heidelberg.

Kraus, H. (1967) *Thin Elastic Shells*. John Wiley and Sons, 1st edition edition.

Krauthammer, T. & Ventsel, E. (2001) *Thin plates and shells: theory, analysis and applications*. CRC Press. doi:10.1201/9780203908723.

Kunz, K.S. (1957) *Numerical Analysis*. McGraw-Hill Book Company Inc., New York.

Liu, W.K., Law, E., Lam, D. & Belytschko, T. (1986) *Resultant-stress degenerated-shell element*. Computer Methods in Applied Mechanics and Engineering, 55 (3), 259–300. doi:10.1016/0045-7825(86)90056-3.

Loo, T. (1957) *An extension of Donnells equation for a circular cylindrical shell*. Journal of the Aeronautical Sciences, 24 (5), 390–391.

Loo, T.T. (1954) *Effects of large deflections and imperfections on the elastic buckling of cylinders under torsion and axial compression*. In Proceedings of the 2nd US national congress on applied mechanics, pp. 345–357.

Lorenz, R. (1908) *Buckling of a cylindrical shell under axial compression*. J. Zeitschrift des Vereines Deutscher Ingenieure, 52, 1706–1713. doi:10.1016/0020-7403(65)90050-0.

Love, A.E.H. (1892) *A treatise on the mathematical theory of elasticity*. Cambridge University Press, Cambridge, UK.

Love, A.E.H. & Darwin, G.H. (1888) *The small free vibrations and deformation of a thin elastic shell*. Philosophical Transactions of the Royal Society of London. (A.), 179, 491–546. doi:10.1098/rsta.1888.0016.

Lu, Y., Khan, Z.A., Alvarez-Alvarado, M.S., Zhang, Y., Huang, Z. & Imran, M. (2020) *A Critical Review of Sustainable Energy Policies for the Promotion of Renewable Energy Sources*. Sustainability, 12 (12). doi:10.3390/su12125078.

Mahboubi Nasrekani, F. & Eipakchi, H. (2019) *Analytical solution for buckling analysis of cylinders with varying thickness subjected to combined axial and radial loads*. International Journal of Pressure Vessels and Piping, 172, 220–226. doi:10.1016/j.ijpvp.2019.03.036.

Maple (2022) *Maple 2022*. Maplesoft, a division of Waterloo Maple Inc., Waterloo, Ontario.

Marguerre, K. (1950) *Knick- und Beulvorgänge*. In Neuere Festigkeitsprobleme des Ingenieurs: Ausgewählte Kapitel aus der Elastomechanik (Edited by K. Marguerre), pp. 189–249. Springer Berlin Heidelberg, Berlin, Heidelberg. doi:10.1007/978-3-662-01208-6_6.

MATLAB (2022) *version 9.12.0 (R022a)*. The MathWorks Inc., Natick, Massachusetts.

Michel, G., Limam, A. & Jullien, J. (2000) *Buckling of cylindrical shells under static and dynamic shear loading*. Engineering Structures, 22 (5), 535–543. doi:10.1016/S0141-0296(98)00132-1.

Mirecki, A., Roboam, X. & Richardeau, F. (2007) *Architecture Complexity and Energy Efficiency of Small Wind Turbines*. IEEE Transactions on Industrial Electronics, 54 (1), 660–670. doi:10.1109/TIE.2006.885456.

Mirsky, I. & Herrmann, G. (1958) *Axially Symmetric Motions of Thick Cylindrical Shells*. Journal of Applied Mechanics, 25 (1), 97–102. doi:10.1115/1.4011695.

Mitchell, R., Woolley, R. & Fisher, C. (1971) *Formulation and experimental verification of an axisymmetric finite-element structural analysis*. NBS Journal of Research, 3 (4), 155–163.

Murray, D.W. & Wilson, E.L. (1969) *Finite-Element Large Deflection Analysis of Plates*. Journal of the Engineering Mechanics Division, 95 (1), 143–165. doi:10.1061/JMCEA3.0001073.

Mushtari, K.M. (1938a) *Certain generalizations of the theory of thin shells*. Izv. Fiz. Mat. Ob-va. Pri Kaz. Un-te, 11 (8), 28–56.

Mushtari, K.M. (1938b) *On the stability of cylindrical shells subjected to torsion*. Trudy Kazanskego aviatsionnugo inatituta, 2.

Naghdi, P.M. (1973) *The Theory of Shells and Plates*. In Linear Theories of Elasticity and Thermoelasticity: Linear and Nonlinear Theories of Rods, Plates, and Shells (Edited by C. Truesdell), pp. 425–640. Springer Berlin Heidelberg, Berlin, Heidelberg. doi:10.1007/978-3-662-39776-3_5.

Nanni, J. & et al (1971) *Das eulersche knickproblem unter berucksichtigung der querkrafte*. Zeitschrift fur Angewandte Mathematik und Physik, 22, 156–185. doi:10.1007/BF01624060.

Niordson, F.I. (1985) *The Donnell-Mushtari-Vlasov Theory*. In Shell Theory, volume 29 of *North-Holland Series in Applied Mathematics and Mechanics*, pp. 353–362. North-Holland. doi:10.1016/B978-0-444-87640-9.50021-6.

Noor, A.K. & Stephens, W.B. (1973) *Comparison of finite-difference schemes for analysis of shells of revolution*. Technical Report NASA-TN-D-7337, NASA.

Novozhilov, V.V. (1959) *The theory of thin shells*. Noordhoff.

Novozhilov, V.V. (1999) *Foundations of the nonlinear theory of elasticity*. Courier Corporation.

Oden, J. & Key, J. (1970) *Numerical analysis of finite axisymmetric deformations of incompressible elastic solids of revolution.* International Journal of Solids and Structures, 6 (5), 497–518. doi:10.1016/0020-7683(70)90027-2.

Oliver, J. & Onate, E. (1984) *A total lagrangian formulation for the geometrically nonlinear analysis of structures using finite elements. Part I. Two-dimensional problems: Shell and plate structures.* International Journal for Numerical Methods in Engineering, 20 (12), 2253–2281. doi:10.1002/nme.1620201208.

Owen, D.R.J. (1980) *Finite elements in plasticity, theory and practice.* Pineridge press.

Penny, R.K. (1961) *Symmetric Bending of the General Shell of Revolution by Finite Difference Methods.* Journal of Mechanical Engineering Science, 3 (4), 369–377. doi:10.1243/JMES_JOUR_1961_003_049_02.

Pflueger, A. (1937) *Stability of thin conical shells.* Ingenieur-Archiv, 8 (3).

Pircher, M. (2004) *Medium-Length Thin-Walled Cylinder under Wind Loading—Case Study.* Journal of Structural Engineering, 130 (12), 2062–2069. doi:10.1061/(ASCE)0733-9445(2004)130:12(2062).

Pircher, M., Guggenberger, W. & Greiner, R. (2001) *Stresses in Elastically Supported Cylindrical Shells under Wind Load and Foundation Settlement.* Advances in Structural Engineering, 4 (3), 159–167. doi:10.1260/1369433011502453.

Punera, D. & Kant, T. (2019) *A critical review of stress and vibration analyses of functionally graded shell structures.* Composite Structures, 210, 787–809. doi:10.1016/j.compstruct.2018.11.084.

Qiao, C., Liu, L. & Pasini, D. (2020) *Elastic thin shells with large axisymmetric imperfection: from bifurcation to snap-through buckling.* Journal of the Mechanics and Physics of Solids, 141, 103959. doi:10.1016/j.jmps.2020.103959.

Radkowski, P.P., Davis, R.M. & Bolduc, M.R. (1962) *Numerical Analysis of Equations of Thin Shells of Revolution.* ARS Journal, 32 (1), 36–41. doi:10.2514/8.5944.

Ramm, E. (1981) *Strategies for tracing the nonlinear response near limit points.* In Nonlinear Finite Element Analysis in Structural Mechanics: Proceedings of the Europe-US Workshop Ruhr-Universität Bochum, Germany, July 28–31, 1980, pp. 63–89. Springer.

Rankine, W.J.M. (1866) *Useful rules and tables.* Charles Griffin & Company, London.

Reddy, J. (1997) *On locking-free shear deformable beam finite elements.* Computer Methods in Applied Mechanics and Engineering, 149 (1), 113–132. doi:10.1016/S0045-7825(97)00075-3. Containing papers presented at the Symposium on Advances in Computational Mechanics.

Reddy, J. & Liu, C. (1985) *A higher-order shear deformation theory of laminated elastic shells.* International Journal of Engineering Science, 23 (3), 319–330. doi:10.1016/0020-7225(85)90051-5.

Reissner, E. (1941) *A New Derivation of the Equations for the Deformation of Elastic Shells.* American Journal of Mathematics, 63 (1), 177–184. doi:10.2307/2371288.

Riks, E. (1979) *An incremental approach to the solution of snapping and buckling problems.* International Journal of Solids and Structures, 15 (7), 529–551. doi:10.1016/0020-7683(79)90081-7.

Rodal, J. & Witmer, E. (1979) *Finite-strain large-deflection elastic-viscoplastic finite-element transient response analysis of structures*. Technical Report NASA-CR-159874, NASA.

Rotter, J. (1989) *The FELASH suite of programs for the analysis of axisymmetric shells*. In Proceedings of the fourth international conference on civil and structural engineering computing, vols 1 & 2 (Edited by B. Topping), pp. 323–328. City Univ London, Dept Civil Engn, Civil Comp press, Edinburgh.

Rotter, J. (2002) *Shell buckling and collapse analysis for structural design: the new framework of the European Standard*. In New Approaches to Structural Mechanics, Shells and Biological Structures, Eds. Drew H.R. and Pellegrino S., pp. 355–378. Kluwer Academic.

Rotter, J. (2005a) *The practical design of shell structures exploiting different methods of analysis*. In 8th Conference on Shell Structures, Theory and Applications, pp. 71–83. Taylor & Francis.

Rotter, J. (2005b) *Stability and plasticity in structural analysis: A new conceptual framework*. In Fourth International Conference on Advances in Steel Structures (Edited by Z. Shen, G. Li & S. Chan), pp. 1815–1826. Elsevier Science Ltd, Oxford. doi:10.1016/B978-008044637-0/50271-7.

Rotter, J. (2007) *A framework for exploiting different computational assessments in structural design*. In Proc. Sixth International Conference on Steel and Aluminium Structures, 6th ICSAS, volume 7.

Rotter, J. (2013) *Design of shells using reference resistances*. In Amend. AM-1-6-2013-05 to EN 1993-1-6, Approv. CEN TC250 SC3.

Rotter, J. (2016a) *The new method of Reference Resistance Design for shell structures*. Proc. SDSS, pp. 623–630.

Rotter, J. & Jumikis, P. (1987) *Nonlinear strain-displacement relations for thin shells of revolution*. School of Civil and Mining Engineering, University of Sydney.

Rotter, J. & Sadowski, A. (2012) *Cylindrical shell bending theory for orthotropic shells under general axisymmetric pressure distributions*. Engineering Structures, 42, 258–265. doi:10.1016/j.engstruct.2012.04.024.

Rotter, J.M. (1990) *Local collapse of axially compressed pressurized thin steel cylinders*. Journal of Structural Engineering, 116 (7), 1955–1970.

Rotter, J.M. (1998) *Development of Proposed European Design Rules for Buckling of Axially Compressed Cylinders*. Advances in Structural Engineering, 1 (4), 273–286. doi:10.1177/136943329800100404.

Rotter, J.M. (2006) *Elephant's foot buckling in pressurised cylindrical shells*. Stahlbau, 75 (9), 742–747. doi:10.1002/stab.200610079.

Rotter, J.M. (2010a) *The New Framework for Shell Buckling Design and the European Shell Buckling Recommendations Fifth Edition*. Journal of Pressure Vessel Technology, 133 (1), 011203. doi:10.1115/1.4002565.

Rotter, J.M. (2010b) *The New Framework for Shell Buckling Design and the European Shell Buckling Recommendations Fifth Edition*. Journal of Pressure Vessel Technology, 133 (1), 011203. doi:10.1115/1.4002565.

Rotter, J.M. (2011) *Shell buckling design and assessment and the LBA-MNA methodology.* Stahlbau, 80 (11), 791–803. doi:10.1002/stab.201101491.

Rotter, J.M. (2016b) *Advances in understanding shell buckling phenomena and their characterisation for practical design.* In Recent Progress in Steel and Composite Structures: Proceedings of the XIII International Conference on Metal Structures (ICMS2016, Zielona Góra, Poland, 15-17 June 2016), volume 2007, p. 3. CRC Press. doi:10.1201/b21417-3.

Rotter, J.M. (2017) *Challenges and their resolution in both philosophy and process to exploit advanced computation in shell structure design.* In Shell Structures: Theory and Applications Volume 4, pp. 41–50. CRC Press.

Rotter, J.M., Sadowski, A.J. & Chen, L. (2014) *Nonlinear stability of thin elastic cylinders of different length under global bending.* International Journal of Solids and Structures, 51 (15), 2826–2839. doi:10.1016/j.ijsolstr.2014.04.002.

Rotter, J.M. & Schmidt, H. (2013) *Buckling of Steel Shells: European Design Recommendations.* European Convention for Constructional Steelwork (ECCS), Brussels, 5th edition. Revised Second Impression.

Rotter, J.M. & Teng, J.G. (1989) *Elastic stability of cylindrical shells with weld depressions.* Journal of Structural Engineering, 115 (5), 1244–1263.

Sadowski, A., Pototschnig, L. & Constantinou, P. (2018) *The 'panel analysis' technique in the computational study of axisymmetric thin-walled shell systems.* Finite Elements in Analysis and Design, 152, 55–68. doi:10.1016/j.finel.2018.07.004.

Sadowski, A. & Rotter, J. (2011) *Steel silos with different aspect ratios: I — Behaviour under concentric discharge.* Journal of Constructional Steel Research, 67 (10), 1537–1544. doi:10.1016/j.jcsr.2011.03.028.

Sadowski, A.J., Fajuyitan, O.K. & Wang, J. (2017a) *A computational strategy to establish algebraic parameters for the Reference Resistance Design of metal shell structures.* Advances in Engineering Software, 109, 15–30. doi:10.1016/j.advengsoft.2017.02.012.

Sadowski, A.J. & Filippidis, A. (2025) *The capacity curve framework of EN 1993-1-6 (2025): Cylindrical shells under uniform meridional compression vs uniform bending.* Journal of Constructional Steel Research, 225, 109167. doi:10.1016/j.jcsr.2024.109167.

Sadowski, A.J., Morata, M.T., Kathirkamanathan, L., Seidel, M. & Rotter, J.M. (2023) *On the existing test dataset of isotropic cylindrical metal shells under axial compression and the design of modern metal civil engineering shells.* Structural Safety, 102, 102285. doi:10.1016/j.strusafe.2022.102285.

Sadowski, A.J. & Rotter, J.M. (2013) *Solid or shell finite elements to model thick cylindrical tubes and shells under global bending.* International Journal of Mechanical Sciences, 74, 143–153.

Sadowski, A.J., Rotter, J.M., Stafford, P.J., Reinke, T. & Ummenhofer, T. (2017b) *On the gradient of the yield plateau in structural carbon steels.* Journal of Constructional Steel Research, 130, 120–130. doi:10.1016/j.jcsr.2016.11.024.

Sadowski, A.J. & Seidel, M. (2023a) *8-MW wind turbine tower computational shell buckling benchmark. Part 1: An international 'round-robin' exercise.* Engineering Failure Analysis, 148, 107124. doi:10.1016/j.engfailanal.2023.107124.

Sadowski, A.J. & Seidel, M. (2023b) *8-MW wind turbine tower computational shell buckling benchmark. Part 2: Detailed reference solution.* Engineering Failure Analysis, 148, 107133. doi:10.1016/j.engfailanal.2023.107133.

Salvadori, M.G. (1951) *Numerical Computation of Buckling Loads by Finite Differences.* Transactions of the American Society of Civil Engineers, 116 (1), 590–624. doi:10.1061/TACEAT.0006570.

Samuelson, L. & Eggwertz, S. (1992) *Shell Stability Handbook.* CRC Press, 1st edition. doi:10.1201/9781482296716.

Sanchez, M.L., Pimenta, P.M. & Ibrahimbegovic, A. (2023) *A simple geometrically exact finite element for thin shells—Part 1: statics.* Computational Mechanics, 72 (6), 1119–1139. doi:10.1007/s00466-023-02339-2.

Sanders Jr, J.L. (1959) *An Improved Fisrt-Approximation Theory for Thin Shells.* NASA Tech. Rep., 1.

Sanders Jr, J.L. (1963) *Nonlinear theories for thin shells.* Quarterly of Applied Mathematics, 21 (1), 21–36.

Schmidt, H. (1991) *The German code DIN 18800 Part 4: Stability of shell-type steel structures, design philosophy and practical applications.* Buckling of Shell Structures, on Land, in the Sea and in the Air, pp. 265–269.

Schmidt, H. (2000) *Stability of steel shell structures: General Report.* Journal of Constructional Steel Research, 55 (1), 159–181. doi:10.1016/S0143-974X(99)00084-X.

Schmidt, H. (2002) *Beulsicherheitsnachweise für Schalen nach DIN 18800-4, E-DASt-Richtlinie 017 und DINV ENV 1993-1-6.* Stahlbau-Kalender, pp. 291–342.

Schmidt, H. (2018) *Two decades of research on the stability of steel shell structures at the University of Essen (1985–2005): Experiments, evaluations, and impact on design standards.* Advances in Structural Engineering, 21 (16), 2364–2392. doi:10.1177/1369433218756273.

Schmidt, H. & Krysik, R. (1991) *Towards recommendations for shell stability design by means of numerically determined buckling loads.* Buckling of Shell Structures, on Land, in the Sea and in the Air, London.

Seide, P. (1956) *Axisymmetrical Buckling of Circular Cones Under Axial Compression.* Journal of Applied Mechanics, 23 (4), 625–628. doi:10.1115/1.4011410.

Seide, P. (1975) *Small Elastic Deformations of Thins Shells.* Springer Dordrecht, 1st edition edition.

Seide, P. & Weingarten, V.I. (1961) *On the Buckling of Circular Cylindrical Shells Under Pure Bending.* Journal of Applied Mechanics, 28 (1), 112–116. doi:10.1115/1.3640420.

Shen, H.S. (2017) *Postbuckling Behavior of Plates and Shells.* World Scientific. doi:10.1142/10208.

Sibeaud, J., Delmas, A. & T., L. (2004) *CalPen3d.* In 21st International Symposium on Ballistics, 19 - 12 April 2004, Adelaide Convention Centre (Edited by N. Burman, J. Anderson & G. Katselis), pp. 418–426. Defense Science and Technology Organisation, Adelaide, Australia.

Simitses, G.J. (1996) *Buckling of moderately thick laminated cylindrical shells: a review.* Composites Part B: Engineering, 27 (6), 581–587. doi:10.1016/1359-8368(95)00013-5.

Simo, J. & Kennedy, J. (1992) *On a stress resultant geometrically exact shell model. Part V. Nonlinear plasticity: formulation and integration algorithms.* Computer Methods in Applied Mechanics and Engineering, 96 (2), 133–171. doi:10.1016/0045-7825(92)90129-8.

Simo, J.C., Fox, D.D. & Rifai, M.S. (1988) *Formulation and Computational Aspects of a Stress Resultant Geometrically Exact Shell Model.* In Computational Mechanics (Edited by S.N. Atluri & G. Yagawa), pp. 751–759. Springer Berlin Heidelberg, Berlin, Heidelberg.

Simo, J.C. & Hughes, T.J. (2006) *Computational inelasticity*, volume 7. Springer Science & Business Media.

Singer, J. (1965) *Buckling of circular conical shells under uniform axial compression.* AIAA Journal, 3 (5), 985–987. doi:10.2514/3.3042.

Singer, J., Arbocz, J. & Weller, T. (2002) *Buckling experiments: experimental methods in buckling of thin-walled structures, volume 2: shells, built-up structures, composites and additional topics*, volume 2. John Wiley & Sons.

Sóbester, A., Forrester, A. & Keane, A. (2008) *Engineering design via surrogate modelling: a practical guide.* John Wiley & Sons.

Soldatos, K.P. (1986) *On thickness shear deformation theories for the dynamic analysis of non-circular cylindrical shells.* International journal of solids and structures, 22 (6), 625–641. doi:10.1016/0020-7683(86)90027-2.

Soldatos, K.P. (1999) *Mechanics of Cylindrical Shells With Non-Circular Cross-Section: A Survey.* Applied Mechanics Reviews, 52 (8), 237–274. doi:10.1115/1.3098937.

Song, C.Y. (2002) *Buckling of cylindrical shells under non-uniform stress states.* Ph.D. thesis, Hong Kong Polytechnic University (Hong Kong).

Sorensen, D.C. (1992) *Implicit Application of Polynomial Filters in a k-Step Arnoldi Method.* SIAM Journal on Matrix Analysis and Applications, 13 (1), 357–385. doi:10.1137/0613025.

Southwell, R.V. (1914) *V. On the general theory of elastic stability.* Philosophical Transactions of the Royal Society of London. Series A, Containing Papers of a Mathematical or Physical Character, 213 (497-508), 187–244. doi:10.1098/rsta.1914.0005.

Spagnoli, A. (2001) *Different buckling modes in axially stiffened conical shells.* Engineering Structures, 23 (8), 957–965. doi:10.1016/S0141-0296(00)00112-7.

Spagnoli, A. (2003) *Koiter circles in the buckling of axially compressed conical shells.* International Journal of Solids and Structures, 40 (22), 6095–6109.

Spagnoli, A. & Chryssanthopoulos, M. (1999) *Elastic buckling and postbuckling behaviour of widely-stiffened conical shells under axial compression.* Engineering Structures, 21 (9), 845–855. doi:10.1016/S0141-0296(98)00036-4.

Speicher, G. & Saal, H. (1991) *Numerical calculation of limit loads for shells of revolution with particular regard to the applying equivalent initial imperfection.* Buckling of Shell Structures, on Land, in the Sea, and in the Air, pp. 466–475.

Stein, M. (1964) *The influence of prebuckling deformations and stresses on the buckling of perfect cylinders.* Technical Report NASA-TR-R-190, National Aeronautics and Space Administration.

Stolarski, H., Belytschko, T. & Lee, S.H. (1995) *A review of shell finite elements and corotational theories.* Computational Mechanics Advances, 2 (2), 125 – 212.

Stricklin, J.A., Navaratna, D.R. & Pian, T.H.H. (1966) *Improvements on the analysis of shells of revolution by the matrix displacement method.* AIAA Journal, 4 (11), 2069–2072. doi:10.2514/3.3854.

Surana, K. (1982) *Geometrically nonlinear formulation for the axisymmetric shell elements.* International Journal for Numerical Methods in Engineering, 18 (4), 477–502.

Szwabowicz, M.L. & Pietraszkiewicz, W. (2004) *Determination of the deformed position of a thin shell from surface strains and height function.* International Journal of Non-Linear Mechanics, 39 (8), 1251–1263. doi:10.1016/j.ijnonlinmec.2003.07.003.

Tani, J. & Yamaki, N. (1970) *Buckling of truncated conical shells under axial compression.* AIAA Journal, 8 (3), 568–571. doi:10.2514/3.5709.

Taylor, R.L. (1987) *FEAP - A finite element analysis programm.*

Teng, J. (1999) *Nonlinear and buckling analysis of complex branched shells of revolution.* In Computational Mechanics in Structural Engineering (Edited by F.Y. Cheng & Y. Gu), pp. 309–324. Elsevier Science Ltd, Oxford. doi:10.1016/B978-008043008-9/50062-4.

Teng, J. & Hong, T. (1998) *Nonlinear thin shell theories for numerical buckling predictions.* Thin-walled structures, 31 (1), 89–115. doi:10.1016/S0263-8231(98)00014-7.

Teng, J. & Hong, T. (2006) *Postbuckling analysis of elastic shells of revolution considering mode switching and interaction.* International Journal of Solids and Structures, 43 (3), 551–568. doi:10.1016/j.ijsolstr.2005.06.060.

Teng, J. & Rotter, J. (1991) *Plastic buckling of rings at steel silo transition junctions.* Journal of Constructional Steel Research, 19 (1), 1–18.

Teng, J. & Rotter, J. (1992a) *Geometrically and materially nonlinear analysis of reinforced concrete shells of revolution.* Computers & Structures, 42 (3), 327–340. doi:10.1016/0045-7949(92)90029-Y.

Teng, J. & Rotter, J.M. (1992b) *Buckling of Pressurized Axisymmetrically Imperfect Cylinders under Axial Loads.* Journal of Engineering Mechanics, 118 (2), 229–247. doi:10.1061/(ASCE)0733-9399(1992)118:2(229).

Teng, J. & Song, C. (2001) *Numerical models for nonlinear analysis of elastic shells with eigenmode-affine imperfections.* International Journal of Solids and Structures, 38 (18), 3263–3280. doi:10.1016/S0020-7683(00)00222-5.

Teng, J.G. (1996) *Buckling of Thin Shells: Recent Advances and Trends.* Applied Mechanics Reviews, 49 (4), 263–274. doi:10.1115/1.3101927.

Teng, J.G. & Lou, Y.F. (1997) *Post-collapse bifurcation analysis of shells of revolution by the accumulated arc-length method.* International Journal for Numerical Methods in Engineering, 40 (13), 2369–2383. doi:10.1002/(SICI)1097-0207(19970715)40:13<2369::AID-NME168>3.0.CO;2-8.

Teng, J.G. & Rotter, J.M. (1989a) *Elastic-plastic large deflection analysis of axisymmetric shell.* Computers & Structures, 31 (2), 211–233. doi:10.1016/0045-7949(89)90227-7.

Teng, J.G. & Rotter, J.M. (1989b) *Non-symmetric bifurcation of geometrically nonlinear elastic-plastic axisymmetric shells under combined loads including torsion.* Computers & Structures, 32 (2), 453–475. doi:10.1016/0045-7949(89)90056-4.

Teng, J.G. & Rotter, J.M. (2004a) *Buckling of thin metal shells.* CRC Press.

Teng, J.G. & Rotter, J.M. (2004b) *Buckling of thin metal shells.* CRC Press.

Tennyson, R.C. & Muggeridge, D.B. (1969) *Buckling of axisymmetric imperfect circular cylindrical shells underaxial compression.* AIAA Journal, 7 (11), 2127–2131. doi:10.2514/3.5568.

Tessler, A. (1986) *Shear deformable bending elements with penalty relaxation.* Finite Element Methods for Plate and Shell Structures, 1, 266–290.

Tessler, A. & Dong, S. (1981) *On a hierarchy of conforming timoshenko beam elements.* Computers & Structures, 14 (3), 335–344. doi:10.1016/0045-7949(81)90017-1.

Tessler, A. & Spiridigliozzi, L. (1988) *Resolving membrane and shear locking phenomena in curved shear-deformable axisymmetric shell elements.* International Journal for Numerical Methods in Engineering, 26 (5), 1071–1086. doi:10.1002/nme.1620260506.

Thompson, J.M.T. (1961) *The elastic instability of spherical shells.* Cambridge University.

Timoshenko, S. & Gere, J. (1961) *Theory of elastic stability.* Dover Civil and Mechanical Engineering, 2nd edition.

Timoshenko, S. & Woinowsky-Krieger, S. (1959a) *Theory of plates and shells.* McGraw-hill, 2nd edition.

Timoshenko, S. & Woinowsky-Krieger, S. (1959b) *Theory of plates and shells.* Engineering Societies Monographs.

Timoshenko, S.P. (1910) *Einige stabilitätsprobleme der elastizitätstheorie.* Zeitschrift für Mathematik und Physik, 58 (4), 337–385.

United Nations Framework Convention on Climate Change (2015) *The Paris Agreement.* In Paris Climate Change Conference. Paris.

Van der Neut, A. (1932) *De elastische stabiliteit van den dunwandigen bol.* Ph.D. thesis, Delft University.

Vlasov, V. (1944) *Basic differential equations in general theory of elastic shells.* Prikladnaia Matematika I Mekhanika, 8.

Von Karman, T. & Tsien, H.S. (1939) *The Buckling of Spherical Shells by External Pressure.* Journal of the Aeronautical Sciences, 7 (2), 43–50. doi:10.2514/8.1019.

Von Karman, T. & Tsien, H.S. (1941) *The Buckling of Thin Cylindrical Shells Under Axial Compression.* Journal of the Aeronautical Sciences, 8 (8), 303–312. doi:10.2514/8.10722.

Wagner, H., Hühne, C. & Janssen, M. (2020) *Buckling of cylindrical shells under axial compression with loading imperfections: An experimental and numerical campaign on low knockdown factors.* Thin-Walled Structures, 151, 106764. doi:10.1016/j.tws.2020.106764.

Wagner, H., Hühne, C. & Niemann, S. (2018) *Robust knockdown factors for the design of spherical shells under external pressure: Development and validation.* International Journal of Mechanical Sciences, 141, 58–77. doi:10.1016/j.ijmecsci.2018.03.029.

Wang, J., Fajuyitan, O.K., Orabi, M.A., Rotter, J.M. & Sadowski, A.J. (2020) *Cylindrical shells under uniform bending in the framework of Reference Resistance Design.* Journal of Constructional Steel Research, 166, 105920. doi:10.1016/j.jcsr.2019.105920.

Weingarten, V.I., Seide, P. & Peterson, J.P. (1968) *Buckling of thin-walled circular cylinders.* Technical Report NASA-SP-8007, NASA.

Williams, C.K. & Rasmussen, C.E. (2006) *Gaussian processes for machine learning.* MIT press Cambridge, MA.

Wilson Wong, K. & Weaver, P. (2006) *Prediction of Local, Global Buckling and Their Interactions on Thin Circular Cylindrical Shells.* 47th AIAA/ASME/ASCE/AHS/ASC Structures, Structural Dynamics, and Materials Conference. doi:10.2514/6.2006-1788.

Wood, R.D. & Zienkiewicz, O. (1977) *Geometrically nonlinear finite element analysis of beams, frames, arches and axisymmetric shells.* Computers & Structures, 7 (6), 725–735.

Xu, Z., Gardner, L. & Sadowski, A.J. (2017) *Nonlinear stability of elastic elliptical cylindrical shells under uniform bending.* International Journal of Mechanical Sciences, 128-129, 593–606. doi:10.1016/j.ijmecsci.2017.05.022.

Xue, J., Yuan, D., Han, F. & Liu, R. (2013) *An extension of Karman–Donnell's theory for non-shallow, long cylindrical shells undergoing large deflection.* European Journal of Mechanics - A/Solids, 37, 329–335. doi:10.1016/j.euromechsol.2012.08.004.

Yamaki, N. (1984) *Elastic stability of circular cylindrical shells.* North-Holland.

Yamaki, N., Otomo, K. & Matsuda, K. (1975) *Experiments on the postbuckling behavior of circular cylindrical shells under compression.* Experimental mechanics, 15, 23–28. doi: 10.1007/BF02318521.

Yang, H., Saigal, S. & Liaw, D. (1990) *Advances of thin shell finite elements and some applications—version I.* Computers & Structures, 35 (4), 481–504. doi:10.1016/0045-7949(90)90071-9. Special Issue: Frontiers in Computational Mechanics.

Yang, H.T.Y., Saigal, S., Masud, A. & Kapania, R.K. (2000) *A survey of recent shell finite elements.* International Journal for Numerical Methods in Engineering, 47 (1-3), 101–127. doi:10.1002/(SICI)1097-0207(20000110/30)47:1/3<101::AID-NME763>3.0.CO;2-C.

Yang, I. & Kuo, W. (1992) *Generic buckling of thick orthotropic cylindrical shells.* The Aeronautical Journal, 96 (958), 313–318. doi:10.1017/S0001924000025732.

Yuan, K. & Liang, C. (1989) *Nonlinear analysis of an axisymmetric shell using three noded degenerated isoparametric shell elements.* Computers & Structures, 32 (6), 1225–1239. doi: 10.1016/0045-7949(89)90300-3.

Zamani Nejad, M., Jabbari, M. & Hadi, A. (2017) *A review of functionally graded thick cylindrical and conical shells.* Journal of Computational Applied Mechanics, 48 (2), 357–370. doi:10.22059/jcamech.2017.247963.220.

Zhu, Y., Liu, W., Guan, W., Lv, H., Zhao, M. & Zhang, J. (2022) *Buckling pressure of imperfect spherical shell damaged by concentrated impact load.* International Journal of Pressure Vessels and Piping, 200, 104810. doi:10.1016/j.ijpvp.2022.104810.

Ziegler, H. (1982) *Arguments for and against Engesser's buckling formulas.* Ingenieur-Archiv, 52 (1-2), 105–113. doi:10.1007/BF00536318.

Zienkiewicz, O. & Taylor, R. (2005) *The finite element method for solid and structural mechanics*. Elsevier.

Zienkiewicz, O.C., Bauer, J., Morgan, K. & Onate, E. (1977) *A simple and efficient element for axisymmetric shells*. International Journal for Numerical Methods in Engineering, 11 (10), 1545–1558. doi:10.1002/nme.1620111006.

Zienkiewicz, O.C., Taylor, R.L. & Too, J.M. (1971) *Reduced integration technique in general analysis of plates and shells*. International Journal for Numerical Methods in Engineering, 3 (2), 275–290. doi:10.1002/nme.1620030211.

Zoelly, R. (1915) *Ueber ein knickungsproblem an der kugelschale*. Ph.D. thesis, ETH Zürich.

Appendix A

Axisymmetric shell problem examples library of AQUINAS

A.1 Introduction

AQUINAS comes with an extensive example library of 'input' files which take the form of simple MATLAB `.m` files. They are intended to act in part as tutorials in how various analyses and problems can be set up and solved, and in part as a repository of verification and validation exercises to establish the correctness of the software.

In what follows, two complementary classification schemes for axisymmetric shell edge boundary conditions will be used, that of Yamaki (1984) and EN 1993-1-6 (2025) presented in Tables A.1 - A.2 and A.3 respectively. The reader is cautioned that the notation used here is specialised for the current finite element formulation, where u and w are the nodal displacements in the radial r and axial z directions respectively. This is different to notation typically adopted in the algebraic shells literature, where w and u are the shell midsurface displacements in the normal and meridional directions respectively. It is equally important to state that while both in the work of Yamaki and in EN 1993-1-6 the boundary conditions are expressed in terms of local degrees of freedom (normal-meridional displacements), AQUINAS only allows the definition of boundary conditions in the global system (global radial-axial directions), as most commonly encountered in FE software.

Table A.1: Classification of shell clamped boundary conditions from Yamaki Yamaki (1984)

Clamped BC	Restrictions
C1	$\bar{u} = v = \bar{w} = 0, \frac{d\bar{w}}{ds} = 0$
C2	$\bar{u} = \bar{w} = 0, \frac{d\bar{w}}{ds} = 0, N_{\phi\theta} = 0$
C3	$v = \bar{w} = 0, \frac{d\bar{w}}{ds}0, = N_{\phi} = 0$
C4	$\bar{w} = 0, \frac{d\bar{w}}{ds} = 0, N_{\phi} = N_{\phi\theta} = 0$

There is however a way to restrict a local DOF of the shell's meridian with the options provided in the `AQUINAS_Constraint_Object`. Before going into the necessary process for such a boundary condition to be defined, the reader is the reminded of the transformations that associate the global and local DOFs of Figure 3.3. As presented in Teng & Rotter (1989a):

Table A.2: Classification of shell simply supported boundary conditions from Yamaki (1984)

Simply Supported BC	Restrictions
S1	$\bar{u} = v = \bar{w} = 0, \frac{d^2\bar{w}}{ds^2} = 0$
S2	$\bar{u} = \bar{w} = 0, \frac{d^2\bar{w}}{ds^2} = 0, N_{\phi\theta} = 0$
S3	$v = \bar{w} = 0, \frac{d^2\bar{w}}{ds^2} = 0, N_{\phi} = 0$
S4	$\bar{w} = 0, \frac{d^2\bar{w}}{ds^2} = 0, N_{\phi} = N_{\phi\theta} = 0$

Table A.3: Classification of shell boundary conditions from EN 1993-1-6 (2025)

BC code	Simple term	Restrictions
BC1r	Clamped	$\bar{u} = v = \bar{w} = 0, \beta = 0$
BC1f	-	$\bar{u} = v = \bar{w} = 0, \beta \neq 0$
BC2r	-	$v = \bar{w} = 0, \beta = 0, \bar{u} \neq 0$
BC2f	Pinned	$v = \bar{w} = 0, \bar{u} \neq 0, \beta \neq 0$
BC3r		$\bar{u} = v = \bar{w} \neq 0, \beta = 0$
BC3f	Free edge	$\bar{u} = v = \bar{w} \neq 0, \beta \neq 0$

$$\begin{Bmatrix} \bar{u} \\ \bar{v} \\ \bar{w} \end{Bmatrix} = \begin{bmatrix} cos(\phi) & 0 & -sin(\phi) \\ 0 & 1 & 0 \\ sin(\phi) & 0 & cos(\phi) \end{bmatrix} \begin{Bmatrix} u \\ v \\ w \end{Bmatrix} = [T] \begin{Bmatrix} u \\ v \\ w \end{Bmatrix} \tag{A.1}$$

Similar relations can also be found in Annex D of EN 1993-1-6 (2025). Taking into account the above Eq. A.1, the analyst can define a boundary condition in the local system by providing the left hand side parameters of the corresponding relation. These left hand side parameters will then be added to the stiffness matrix of the problem, hence the desired relation will be considered during solution of the equilibrium problem. For example, in order to restraint the local degree of freedom $\bar{u}$ it is enough to create a constraint object that links the global u and w DOFs with LHS factors equal to $cos(\phi)$ and $-sin(\phi)$ respectively, while leaving the RHS factor at its default value of zero. In code, this would look like:

```
ubarConstraint = AQUINAS_Constraint_Object('coordR',r,'coordZ',z,...
                 'dofs',{'u','w'},'coeffLHS',[cos(phi),-sin(phi)]);
```

It should be highlighted that the notation of EN 1993-1-6 (2025) will be adopted to define the axisymmetric shell problems, over any symbols used in relevant resources, at least for the cylindrical and conical models examined (with an effort made to also use the notation for other models, wherever applicable). Details on the discretisation of the axisymmetric shell problems may be found on the individual MATLAB example scripts, included in the distribution of AQUINAS. Most of the examples presented here require seconds to run, some take minutes while a handful (e.g. LBA05, GNA01, GNIA01, GNIA02, GMNA01 and GMNA02) may take significantly longer.

A.2 LAs

AQUINAS can accurately and efficiently execute linear elastic analyses (LAs) for a variety of multi-segment axisymmetric shell geometries. Due to the axisymmetric nature of the expected solution, the circumferential degree of freedom v is omitted from the analysis, allowing for a reduction in the computational effort. Once an LA has been completed, the analyst is able to view and extract for post-processing the degrees of freedom, the strains and curvatures, the stresses and the membrane and bending stress resultants, all expressed at the nodes of the shell segments.

The LA results of AQUINAS are put to the test through comparison with various trustworthy solutions, either algebraic, found in relevant literature on the mechanics of thin shells, or computational ones obtained through available scientific software. Over the following sections of this appendix, unless explicitly mentioned otherwise, the material that the axisymmetric shells are made of is steel, with a Young's modulus of $E = 200000\, N/mm^2$ and a Poisson's ratio of $\nu = 0.3$. Due to the axisymmetric nature of the LA solutions, the circumferential degree of freedom is zero by default and will therefore be omitted.

A.2.1 Example LA01: Thin cylinder under meridional compression and internal pressure

The first LA example is that of a cylindrical shell subject to meridional compression and uniform internal pressure which may be found in the script `input_Example_LA01.m`. A BC1r / C1 boundary condition is considered at the base edge of the cylinder and a BC2f / S3 condition at the top edge. The cylinder is under the effect of an meridionally compressive edge load of magnitude $N = 1000.0\, N/mm$ and of internal pressure $p_n = 1.0\, N/mm^2$. Its height and radius are $L = 500.0\, mm$ and $r = 500.0\, mm$ respectively, while the shell wall has a thickness of $t = 5.0\, mm$. The geometry of the problem is also presented in Figure A.1.

The finite element solution is compared against an algebraic bending and membrane theory solution for thin axisymmetric shells as detailed most accessibly in Rotter & Sadowski (2012) though also elsewhere (Flügge, 1990; Timoshenko & Woinowsky-Krieger, 1959b). A brief but insightful comparison of the stresses between AQUINAS and the analytical solutions, obtained through both membrane and bending theories, is presented in the following Figures A.2 - A.3. By running the input script the reader can also view a comparison of the radial and meridional displacements or the strains arising in the cylinder, or even for another set of material properties and loading of their choice.

A.2.2 Example LA02: Thin cylinder with midsurface eccentricity under meridional compression and internal pressure

This second LA example builds up on the previous cylindrical shell problem by introducing an eccentricity along the mid-height of the meridian, testing the software's capability to analyse eccentrically connected segments, in the `input_Example_LA02.m` script. A BC1f boundary condition is considered at the bottom edge of the cylindrical shell and a BC2f at the top. The cylinder is under the effect of an meridionally compressive edge load $N = 300.0\, N/mm$, applied at its top edge, and internal pressure $p_n = 1.0\, N/mm^2$. Its total length is $L = 500.0\, mm$ and the shell wall is of thickness $t = 1\, mm$. The eccentrical connection, of magnitude $e = 1.0\, mm$, is located at the mid-height of the cylinder's meridian, leading to a radius of $r_B = 100.0mm$ for the bottom half and of $r_T = r_B - e = 99\, mm$ for the top one. The geometry of this

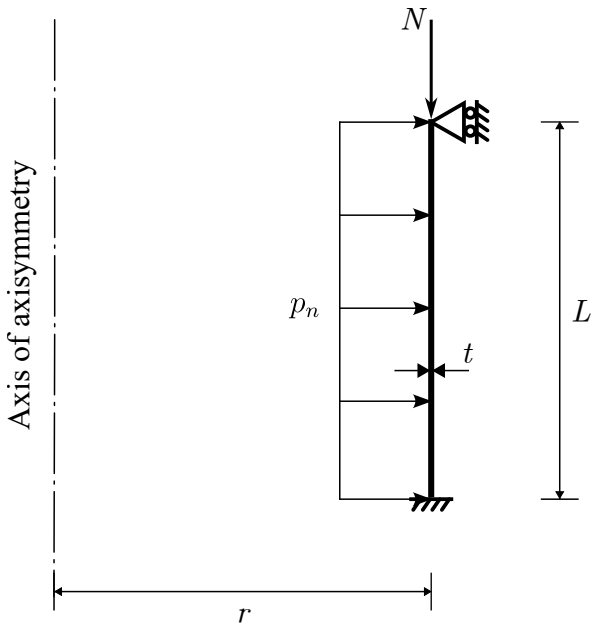


Figure A.1: LA01 - System diagram.

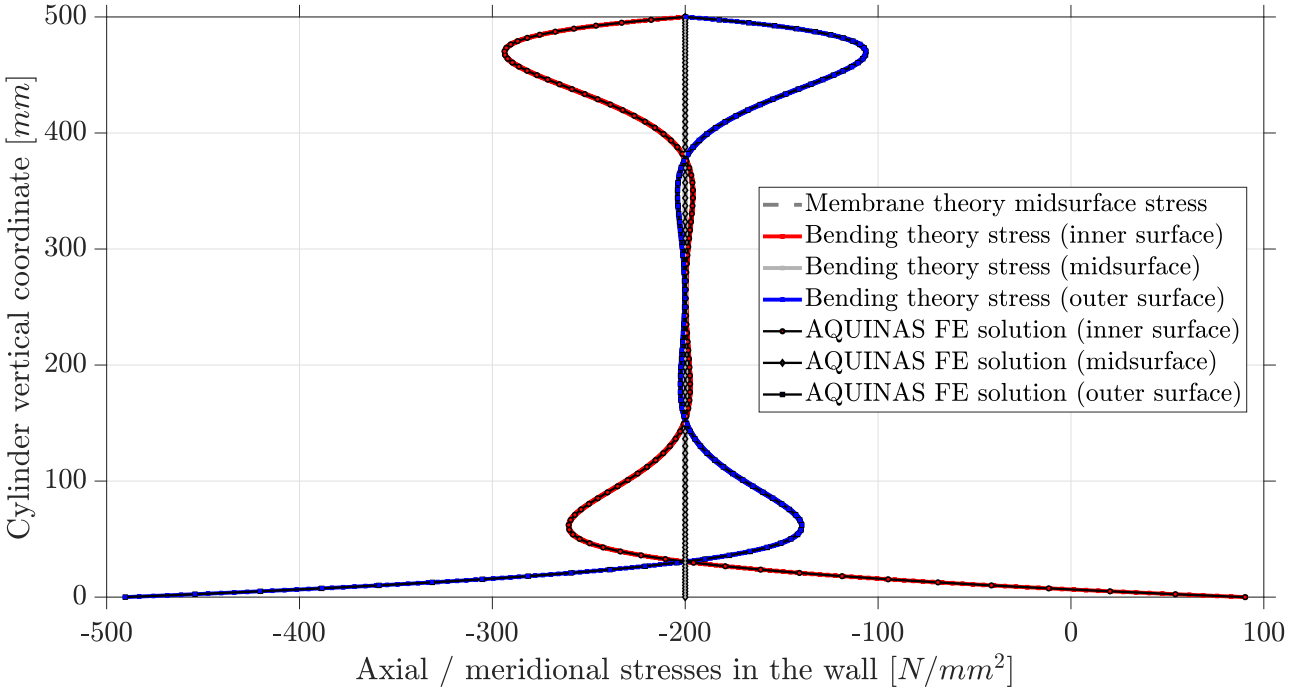


Figure A.2: LA01 - Comparison of meridional stresses in the inner, middle and outer surface of the shell wall.

axisymmetric shell problem can be seen in Figure A.4, where the eccentricity is exaggerated to aid understanding.

The finite element solution is once again compared against an analytical bending and membrane theory solution for thin axisymmetric shells based on the shell theory principles presented in Rotter & Sadowski (2012); Flügge (1990); Timoshenko & Woinowsky-Krieger (1959b). The inner-middle-outer surface meridional and circumferential stresses of AQUINAS are plotted against the corresponding analytical results in Figures A.5 - A.6. By running the input script the reader may also examine a full comparison of the radial and axial displacements, meridional or circumferential strains developing in the cylinder, or perhaps for another set of material,

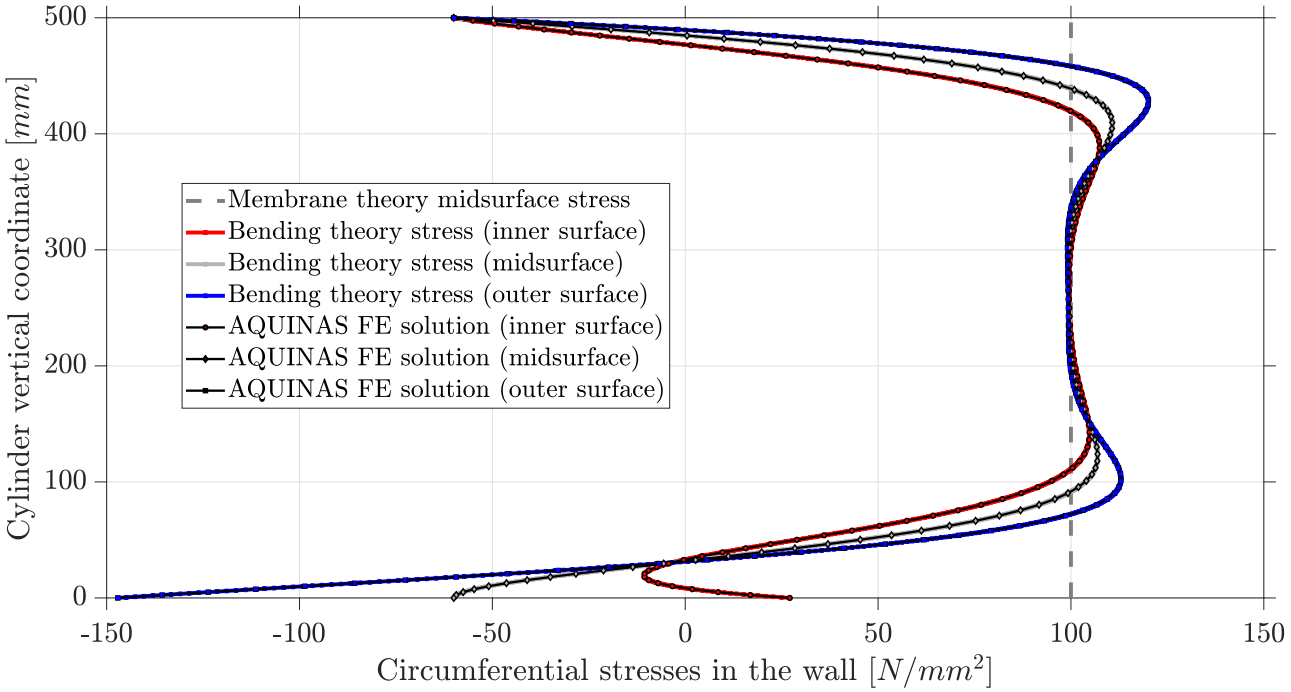


Figure A.3: LA01 - Comparison of circumferential stresses in the inner, middle and outer surface of the shell wall.

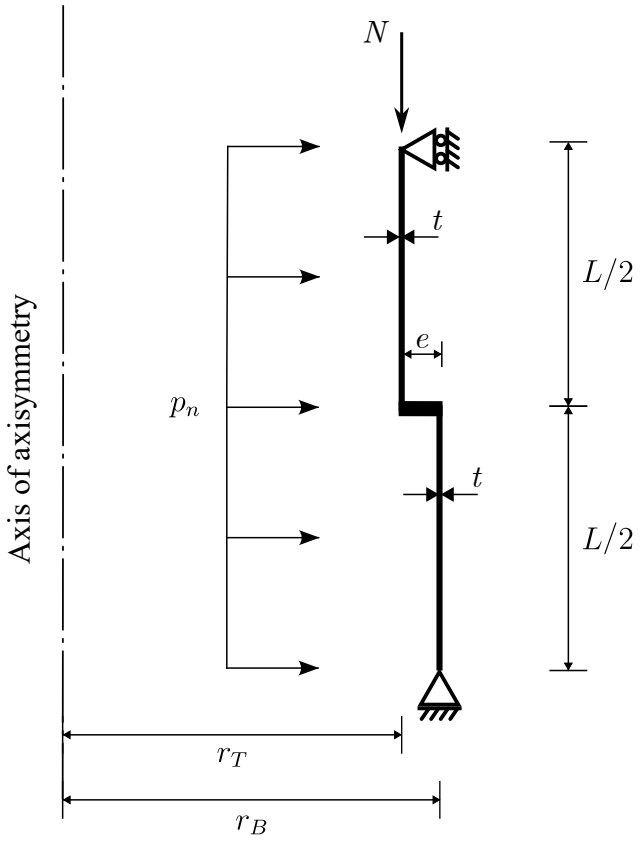


Figure A.4: LA02 - System diagram.

geometric or loading properties of their choice.

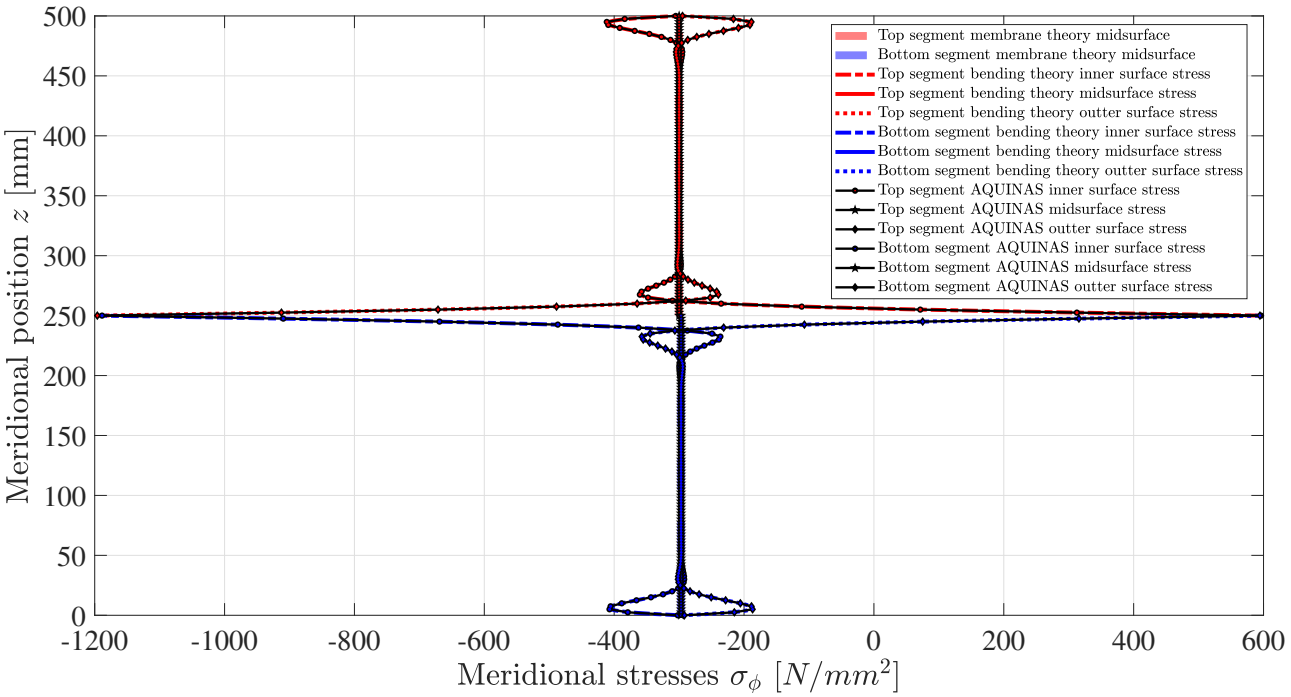


Figure A.5: LA02 - Comparison of meridional stresses in the inner, middle and outer surface of the shell wall.

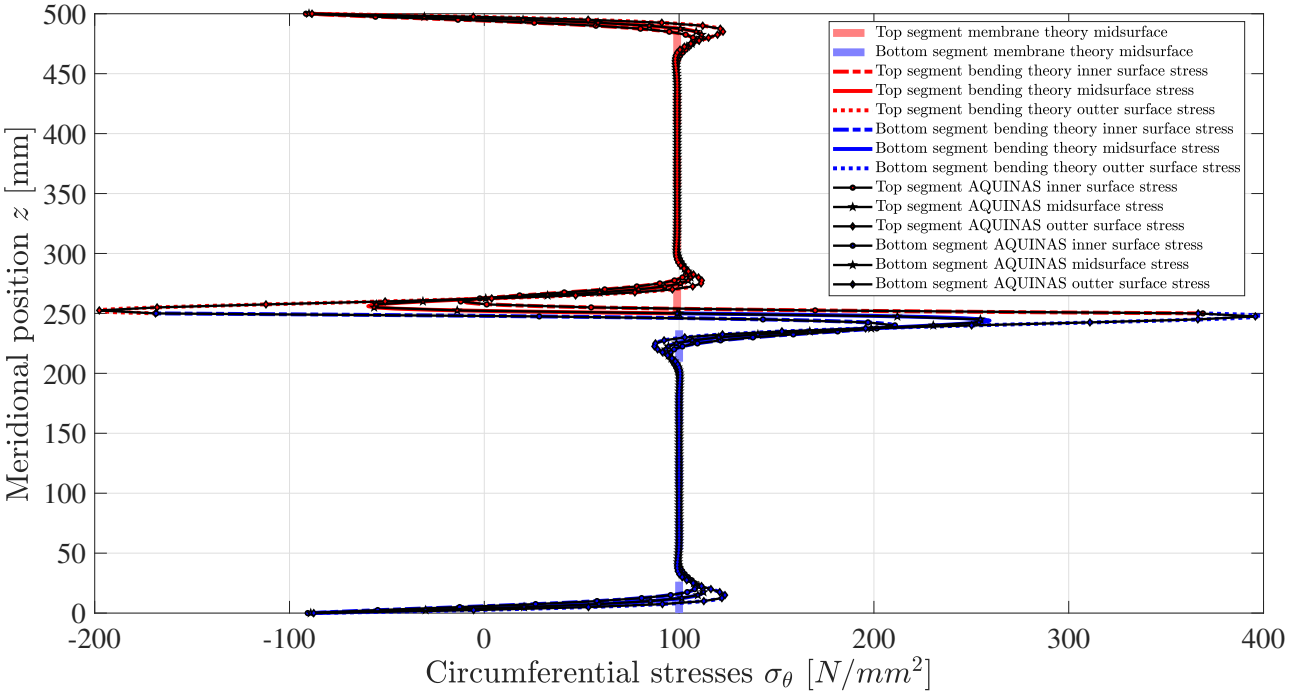


Figure A.6: LA02 - Comparison of circumferential stresses in the inner, middle and outer surface of the shell wall.

A.2.3 Example LA03: Multi-strake cylindrical silos with step-wise varying thickness under nonlinear loading

The linear elastic response of five different cylindrical isotropic silos under nonlinear pressure and traction distributions is investigated and compared against the work of Boyez *et al.* (2017). The five silos have different height over diameter (H/D) aspect ratios and number of segments along their meridian. The segments have an integer wall thickness that increases towards the

base of the silos. The geometries of the five silos are presented in Figure A.7, with the lengths of the different segments of the meridian summarized in Table A.4. The silos serve as storage units for granular solid which exerts a nonlinear normal pressure p_n and a frictional traction p_z, where the distribution that these loading patterns follow depend on the H/D ratio of the silos. A Jansen or modified Reimbert axisymmetric pressure distribution is used to model the loading of the silos. The interested reader may find a more in depth discussion on these pressure distributions, as well as the individual parameters that govern their variation along the meridians of the silos, in Sadowski & Rotter (2011).

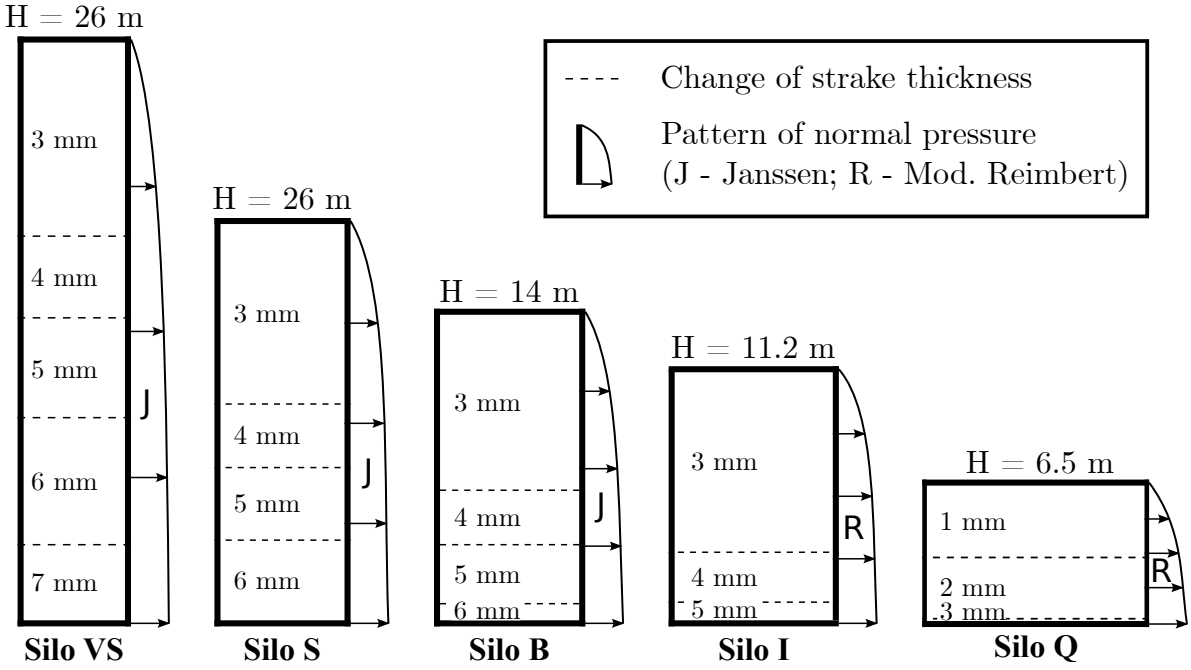


Figure A.7: LA03 - System diagram.

Table A.4: LA03 - Length h and thickness t of cylindrical segments

Silo VS $D = 5.0\,m$		Silo S $D = 6.0\,m$		Silo B $D = 6.8\,m$		Silo I $D = 7.6\,m$		Silo Q $D = 10.0\,m$	
t	h	t	h	t	h	t	h	t	h
3	8800								
4	3600	3	8200	3	8000				
5	4400	4	2800	4	2400	3	8200	1	3300
6	5600	5	3200	5	2600	4	2200	2	2700
7	3600	6	3800	5	1000	5	800	3	500

It is important to note that the CSBL element, as developed by Boyez *et al.* (2017) and used for the LAs of the silos in that reference, can accurately model up to a quadratic pressure per element due to the nature of the shape functions adopted. Taking into account that there is just one CSBL element to model each segment (one of the benefits of the corresponding formulation) of the silos, some discrepancies are expected (the reader is reminded that pressures in AQUINAS are split into trapezoids per element, but more than one elements are used per segment). These discrepancies will be more or less subtle depending on how close the original distribution function and the quadratic fit are. Some key stress results are presented in Figures A.8 - A.9, where the good agreement between the two computational approaches is illustrated.

More result plots regarding the displacements, strains or curvatures can be generated by running the `input_Example_LA03.m` script.

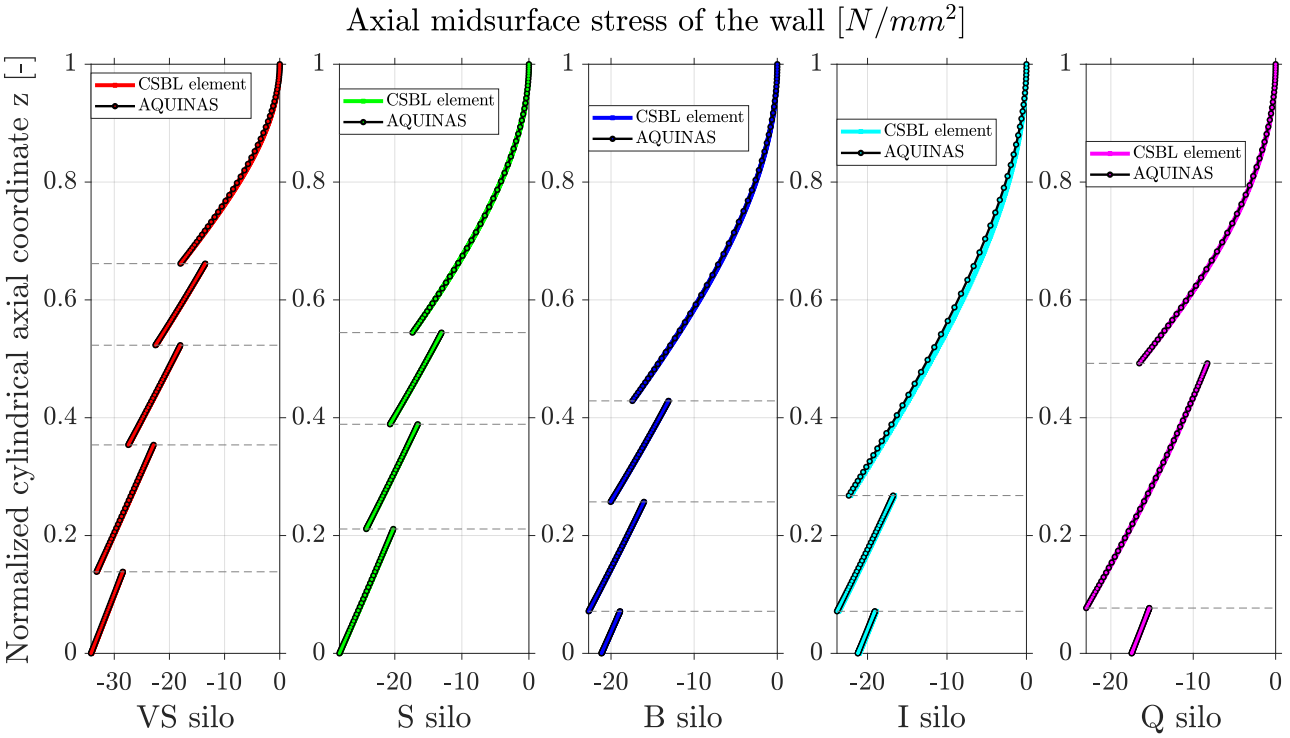


Figure A.8: LA03 - Comparison of midsurface meridional stresses of the shell wall.

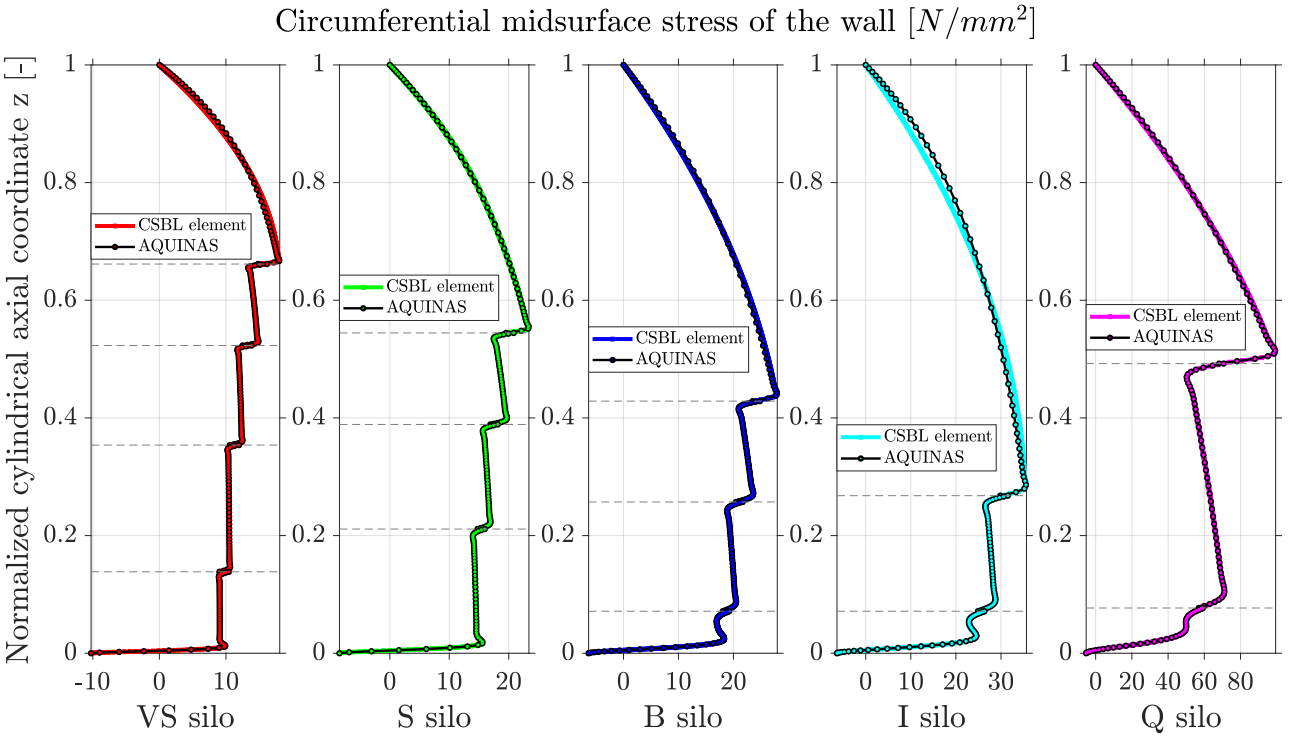


Figure A.9: LA03 - Comparison of midsurface circumferential stresses of the shell wall.

A.2.4 Example LA04: Conical shell under axial uniform pressure

In this LA example, as presented in the `input_Example_LA04.m` script, the FE results of a conical shell under unit axial (vertical) uniform axisymmetric pressure $q = 1.0\ N/mm^2$ are

compared against corresponding membrane and bending theory analytical solutions. The cone is closed at its apex, with the half apex angle being $\alpha = 30°$. The meridian of the cone has a length of $L = 200\,mm$ with a BC1f - S2 support applied at its base ($u = w = 0$ equivalent to $\bar{u} = \bar{w} = 0$), while the wall of the axisymmetric shell has a thickness of $t = 5\,mm$. The geometric properties of the cone are presented in Figure A.10.

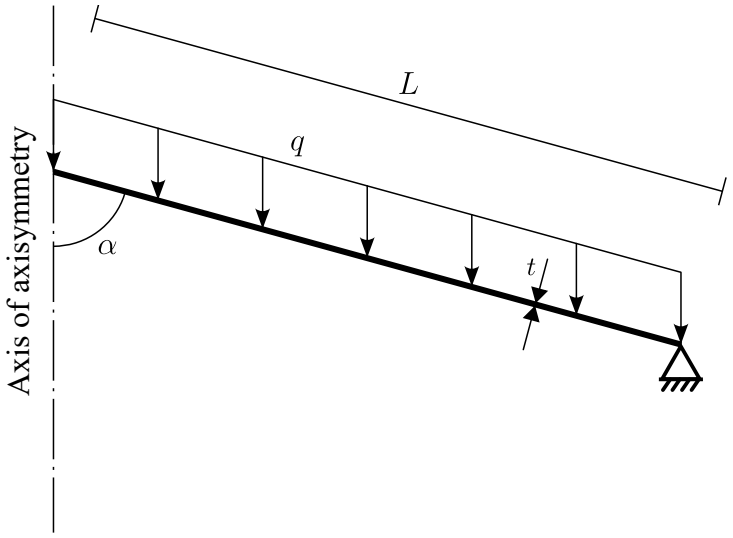


Figure A.10: LA04 - System diagram.

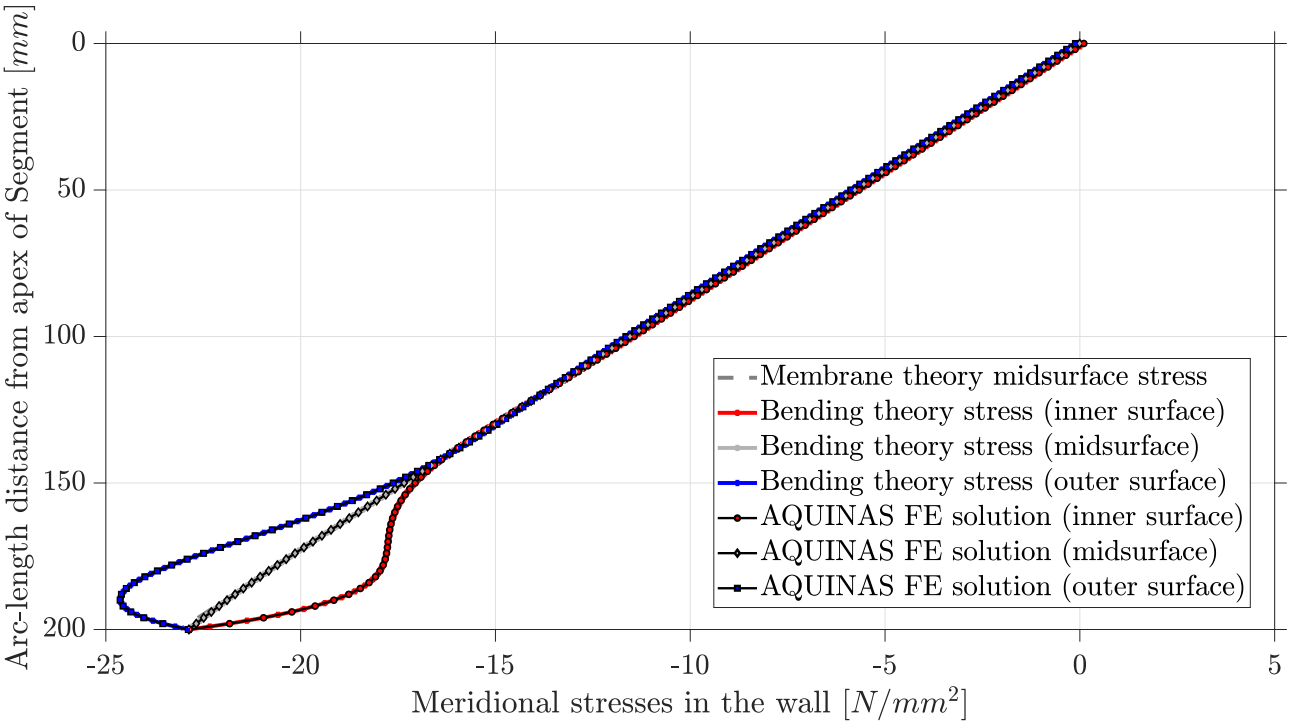


Figure A.11: LA04 - Comparison of inner, middle and outer surface meridional stresses of the conical shell wall.

The membrane and bending theory analytical solutions used for comparison purposes here can be found in Article 133 of Timoshenko & Woinowsky-Krieger (1959b). The inner, middle and outer surface stresses of the cone are displayed in Figures A.11 - A.12 where the AQUINAS FE results show a great agreement with the bending theory analytical solution. The membrane

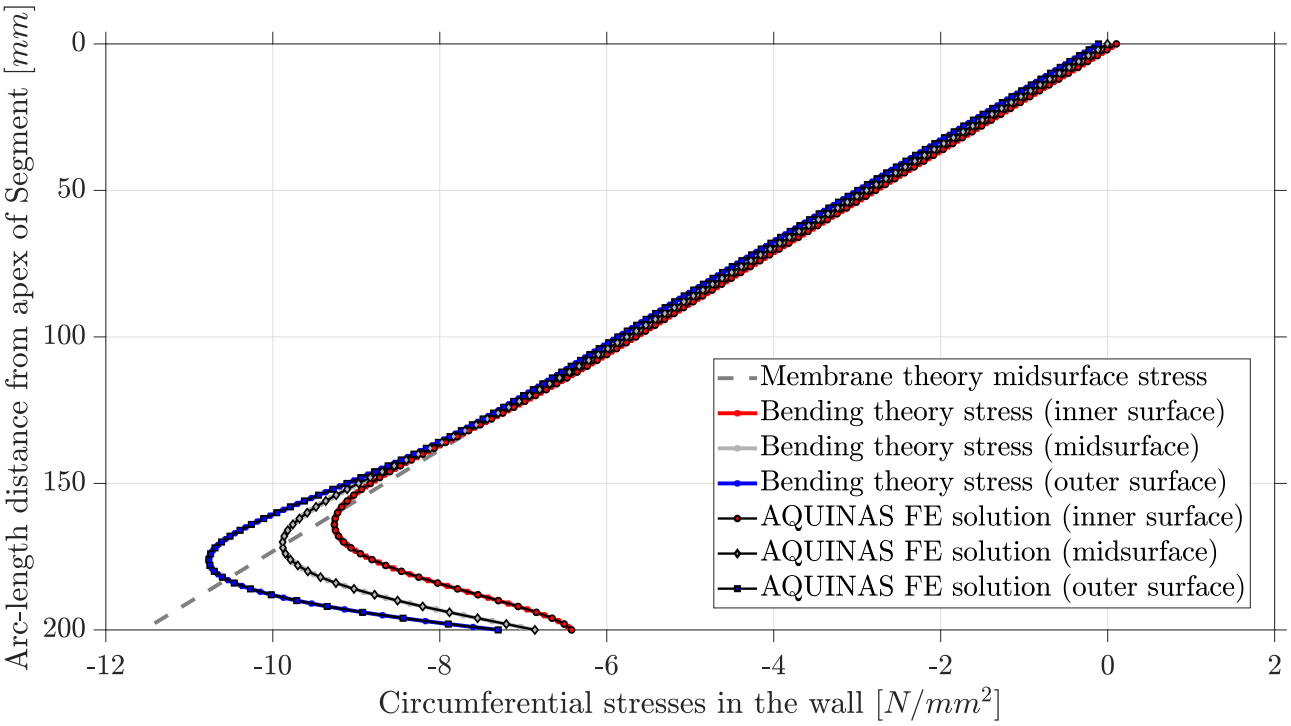


Figure A.12: LA04 - Comparison of inner, middle and outer surface circumferential stresses of the conical shell wall.

theory results are also included, despite the considerable deviations from the more accurate bending theory solution near the exposed edge of the shell, where bending effects are dominant.

A.2.5 Example LA05: Spherical shell segment with an outward radial edge load

The first LA example of an axisymmetric shell without a straight meridian is that of a spherical segment subjected to a radial edge load H. The analytical membrane and bending theory solutions, used for comparison purposes with AQUINAS' results, can be found in *'Stresses in Shells'* by Flügge (1990). The same parameters of the problem used in the book (radius of the sphere, thickness of the wall etc.) are also adopted in the `input_Example_LA05.m` script, with the only exception that [mm] are used as length units and [N] for force. The spherical zone, truncated at both ends, is symmetric about the horizontal axis with a total angle span of 2α, where $\alpha = 10°$. Taking into account the horizontal symmetry of the problem, only the upper half of the meridian is modelled, with appropriate boundary conditions at its base. The radius of the spherical segment is $a = 381.0\,mm (= 15.0\,in.)$ and the shell wall has a thickness of $t = 25.4\,mm (= 1.0\,in.)$ (n.b. a different set of geometric parameters for this doubly-curved axisymmetric shell model have been examined in the context of the finite-thickness formulation of Chapter 6). A unit line load H is applied at both truncated ends of the axisymmetric shell. The geometry of the spherical shell is displayed in Figure A.13, while a brief comparison of the meridional and circumferential stress results is made in g Figures A.14 - A.15.

A.2.6 Example LA06: Spherical cap subjected to uniform vertical pressure

It is interesting to also explore the response of a different kind of axisymmetric spherical shell, though one that is commonly encountered in real life problems, that of a spherical cap under

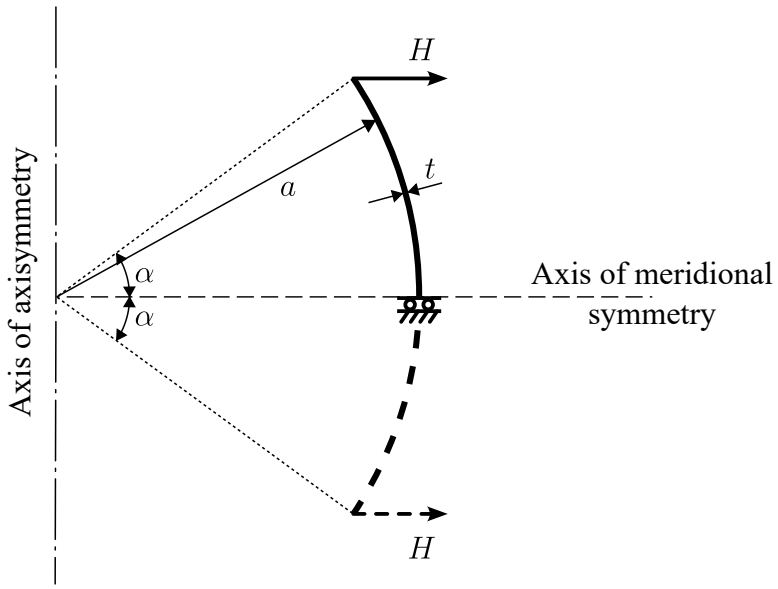


Figure A.13: LA05 - System diagram.

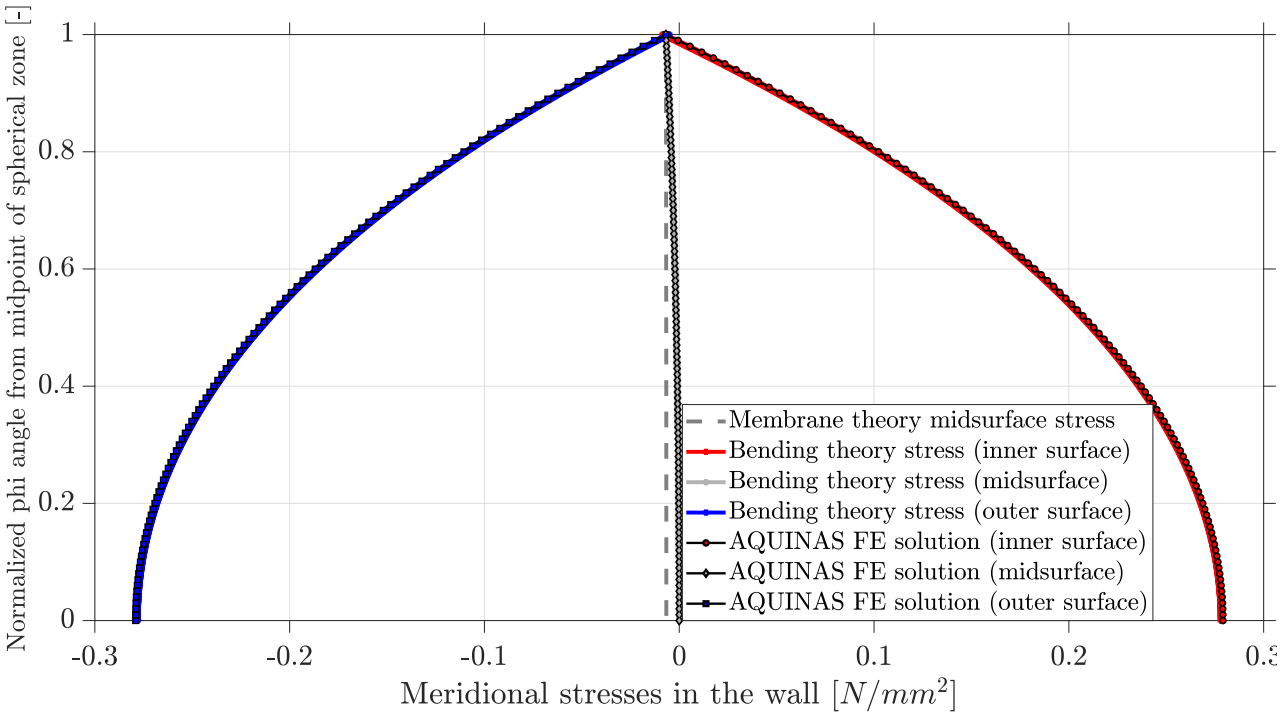


Figure A.14: LA05 - Comparison of inner, middle and outer surface meridional stresses of the spherical zone.

uniform vertical pressure. This problem closely relates to the spherical cap 'hats' used in silo containers. The spherical cap considered here has an angle span of 2α, where $\alpha = 10°$, and a radius of $a = 500.0\,mm$. The wall of the spherical cap has a thickness of $t = 1.0\,mm$ and a uniform vertical pressure (similar to the effect of the self-weight) is applied along its meridian. The geometry of the spherical cap and the pressure that is applied on it are displayed in Figure A.16.

An analytical solution has also been coded in the example script `input_Example_LA06.m` for comparison with the AQUINAS LA results. The membrane and bending theory solutions there are taken from Flügge (1990), where a similar problem is considered. It is important to note

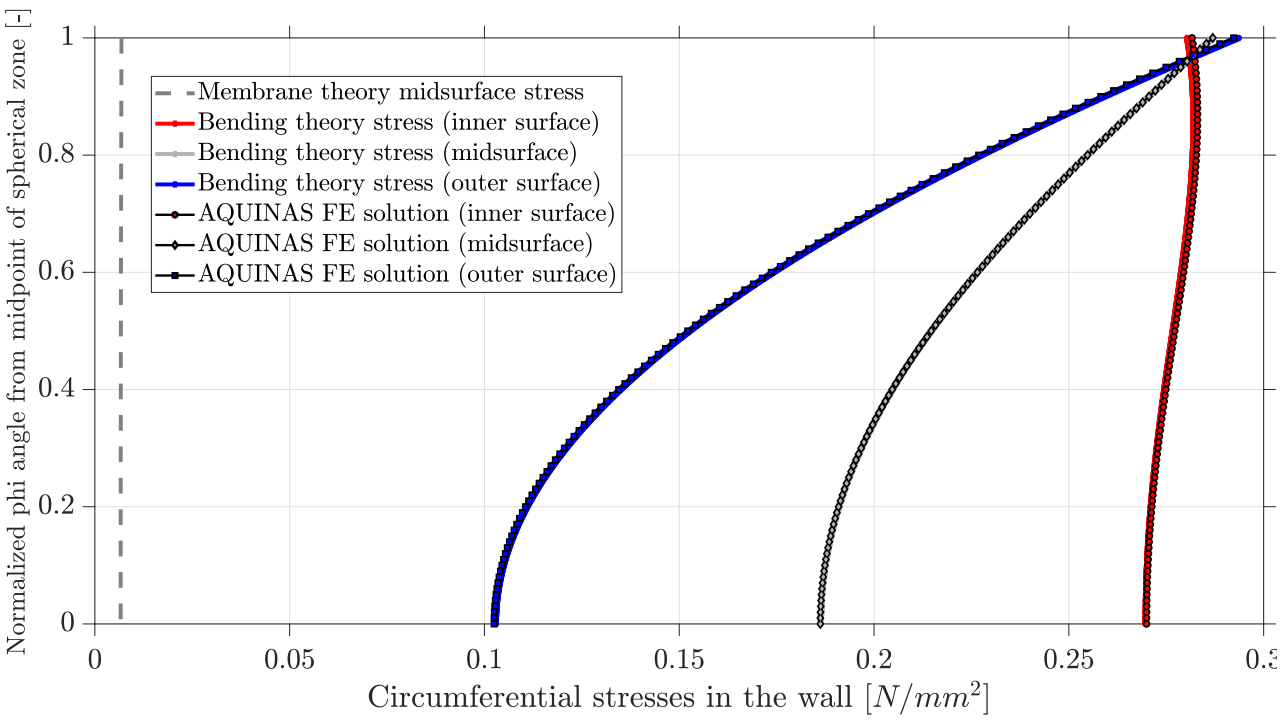


Figure A.15: LA05 - Comparison of inner, middle and outer surface circumferential stresses of the spherical zone.

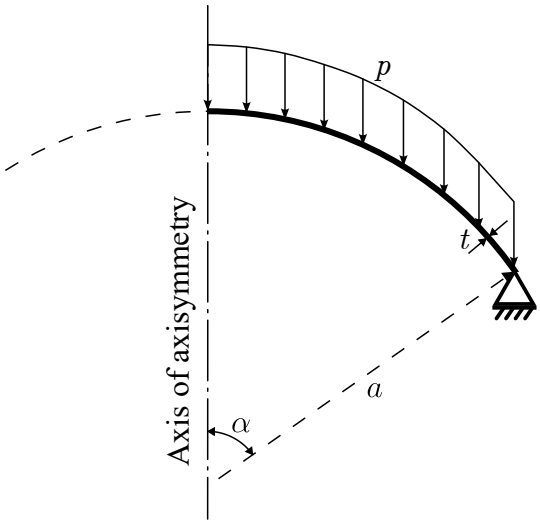


Figure A.16: LA06 - System diagram.

however that in the problem discussed there the Poisson's ratio used is equal to $nu = 0$, in contrast to the Poisson's ratio considered in all of the examples of this appendix, including this one, of $nu = 0.3$. Hence, if comparison with the results in the book by W. Flügge is intended, a minor alteration is in order. A brief presentation of the meridional and circumferential stresses is given in Figures A.17 - A.18. More results or different combinations of the input parameters can be examined by running the example script `input_Example_LA06.m`.

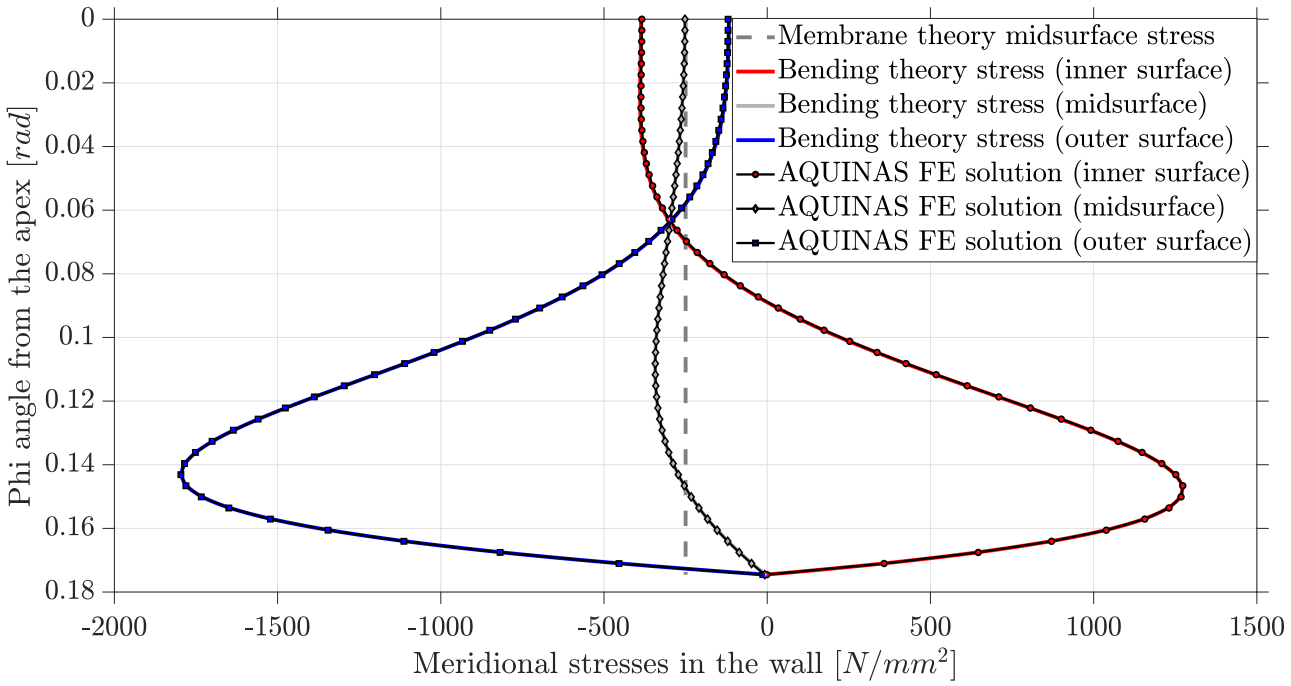


Figure A.17: LA06 - Comparison of inner, middle and outer surface meridional stresses of the spherical cap.

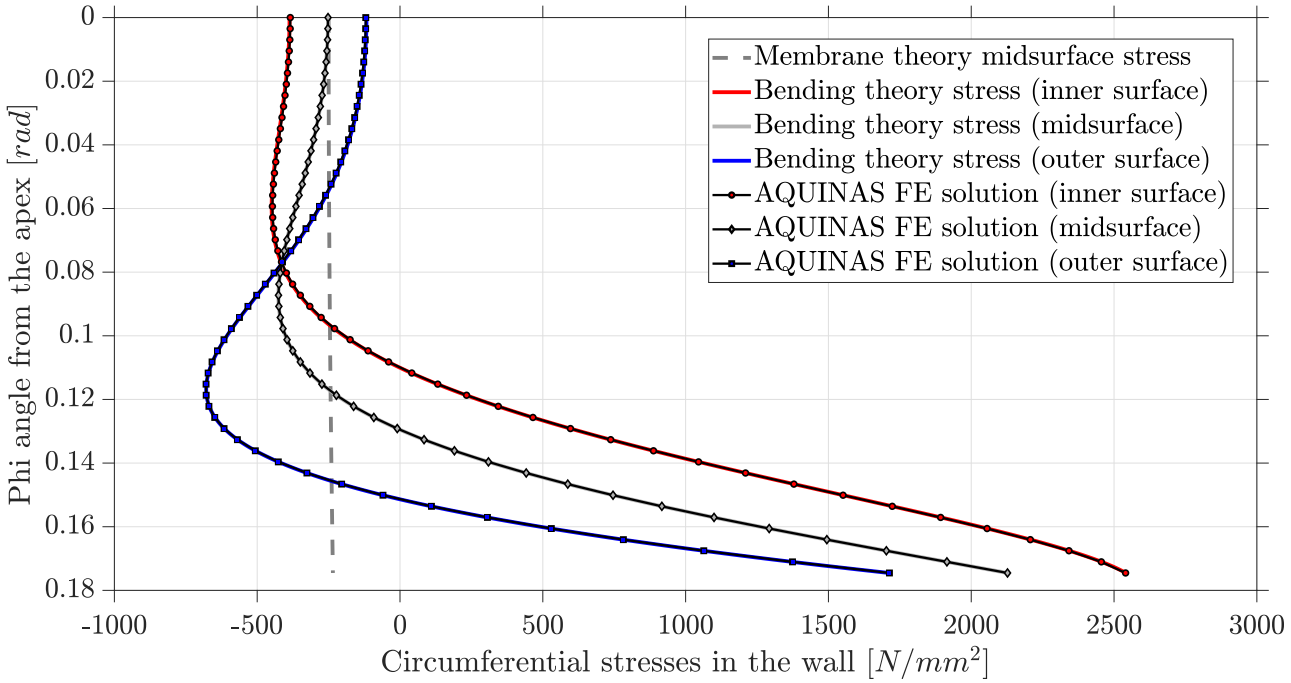


Figure A.18: LA06 - Comparison of inner, middle and outer surface circumferential stresses of the spherical cap.

A.2.7 Example LA07: LA of a thin elliptical shell cap under uniform pressure

In order to fully test the capability of AQUINAS to analyse elliptical shell segments, a simplification of which are the axisymmetric spherical shell problems of the two previous examples, the LA of a thin elliptical shell cap under uniform compression is examined in `input_Example_LA07.m`. The upper half of the ellipse that is modelled here has a meridional displacement restraint at

its bottom edge. Its geometry is defined by its major and minor radius, $a = 1000.0\,mm$ and $b = 500.0\,mm$ accordingly, while the shell wall has a thickness of $t = 1.0\,mm$. The normal internal pressure applied has a unit magnitude of $p = 1.0\,N/mm^2$. The definition of this axisymmetric shell problem is illustrated in Figure A.19.

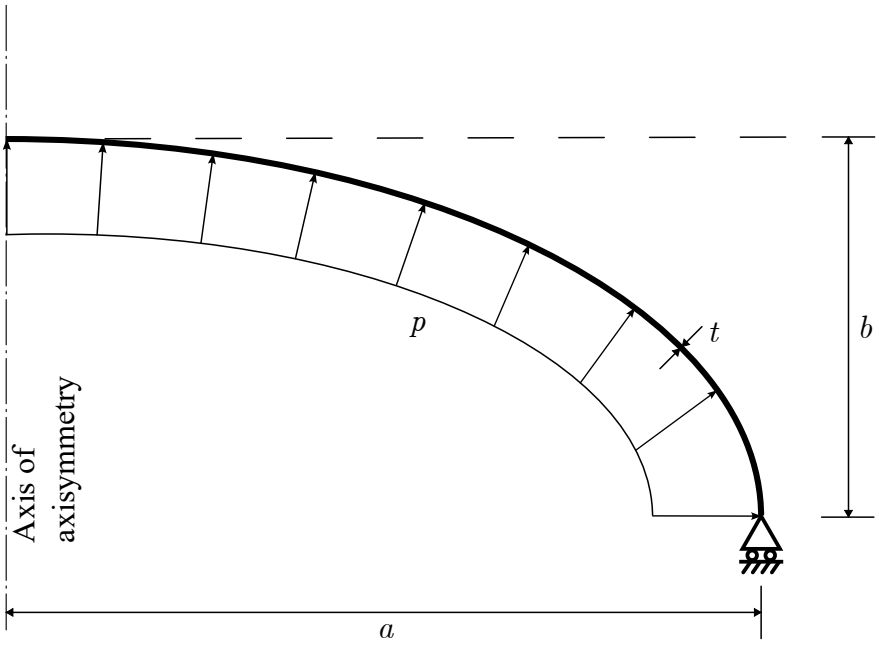


Figure A.19: LA07 - System diagram.

Due to the complexity of a potential bending theory analytical solution in this case, only a membrane theory algebraic solution is provided for reference. The membrane theory results can be found in Chapter *'2.2.2.2 Boiler End'* of *'Stresses in Shells'* by Flügge (1990). Instead, the AQUINAS FE results are compared against those of another FE software (ABAQUS, 2022). Its results for the problem definition described above are stored in `input_Example_LA07.csv` and will not be regenerated for different geometric, material or loading inputs in the corresponding script. Hence, a user who is interested in a comparison with any of the properties altered will only have the membrane theory results readily available, and may have to compute their own ABAQUS (or any other axisymmetric FE solver) solution for the problem if they seek a particular answer to this example. The stress results for the inner, middle and outer fibre of the shell wall are presented in Figures A.20 - A.21, where the good agreement between AQUINAS and ABAQUS can be appreciated, as well as with the membrane theory solution for the region of the shell's meridian that is sufficiently distant from the bending boundary layer of the ellipsoid's edge.

A.2.8 Example LA08: LA of a thin ogival shell under self weight pressure

There are two ways to define an ogival in AQUINAS. The analyst can either use the `'Ellipse'` option of the segment object and provide a centre for the ellipse (in this case sphere) that has a negative radial coordinate (behind the axis of axisymmetry), or use the `'3pointArc'` option and have as input 3 points along the curved meridian of the shell. In `input_Example_LA08.m` the `'3pointArc'` option was employed. The ogival's meridional curvature radii is $a = 1000.0\,mm$ while its truncation angle is $\phi_0 = 20°$. A meridional displacement restraint applied at its base. A unit self weight loading $q = 1.0\,N/mm^2$ is considered along the meridian of the shell, defined

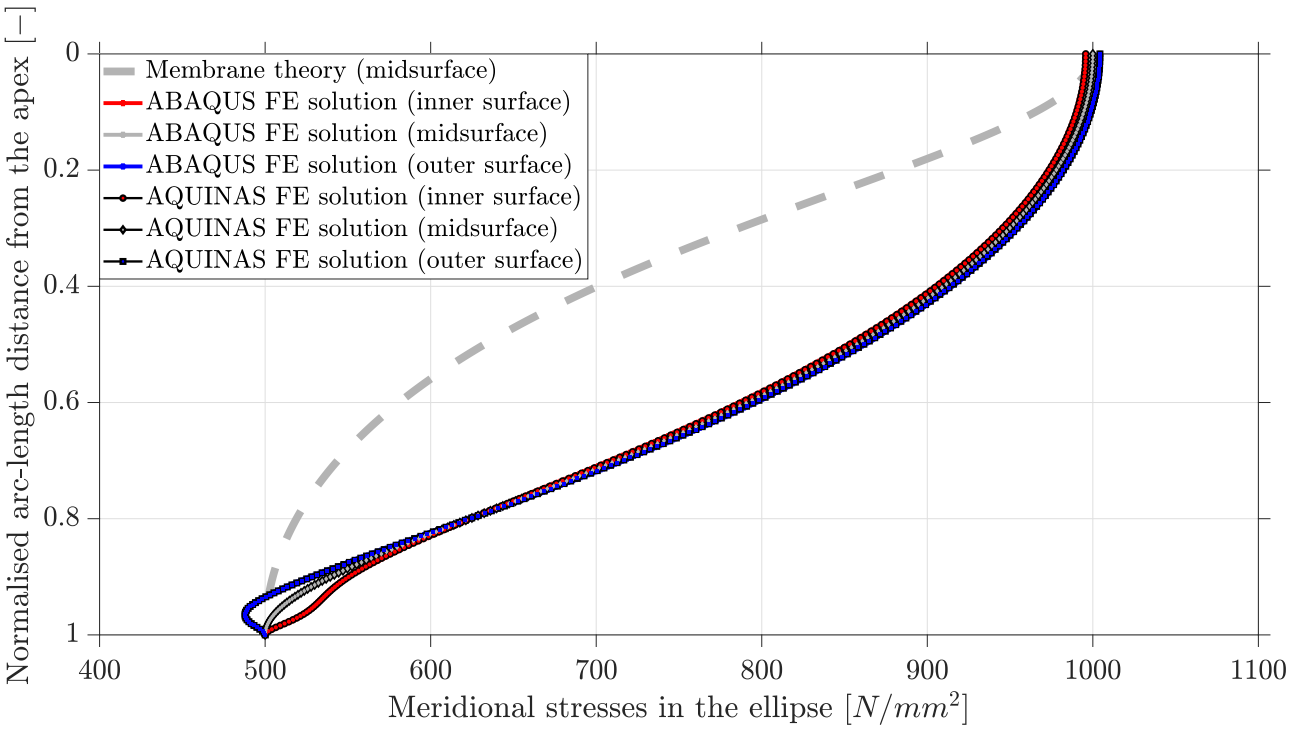


Figure A.20: LA07 - Comparison of inner, middle and outer surface meridional stresses of the spherical cap.

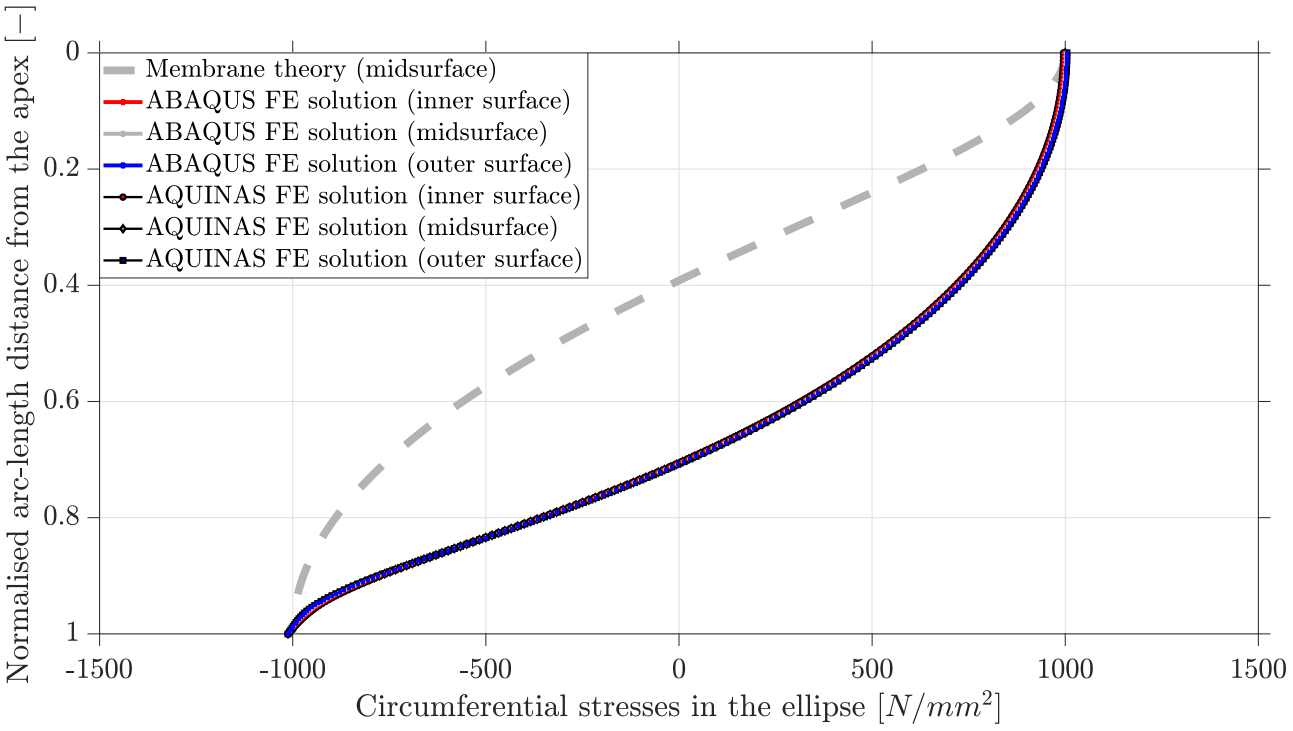


Figure A.21: LA07 - Comparison of inner, middle and outer surface circumferential stresses of the spherical cap.

as a combination of a normal pressure and traction (tangential pressure) that vary along the meridian of the shell. This shell problem is displayed in Figure A.22.

Once again, the stresses throughout the shell wall obtained from AQUINAS and ABAQUS are compared against each other, as well as the corresponding membrane theory results, in Figures A.23-A.24. The algebraic solution coded in the `input_Example_LA08.m` script is obtained from

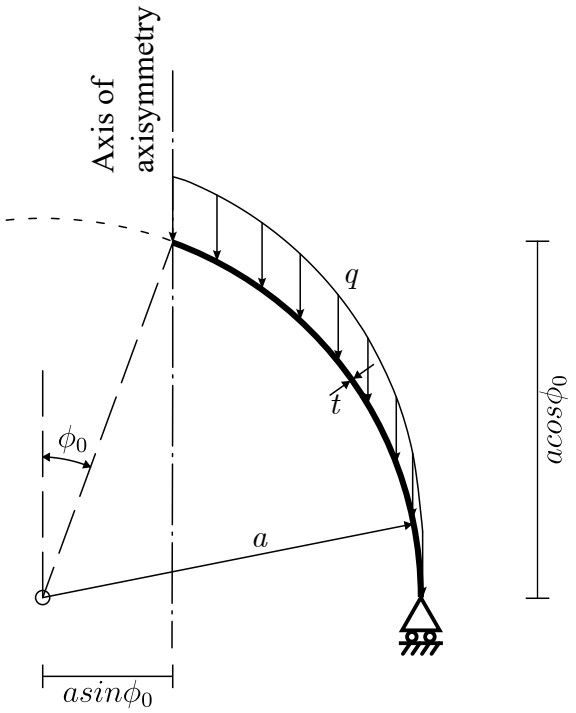


Figure A.22: LA08 - System diagram.

Chapter *2.2.2.3 Pointed Shells* of *'Stresses in Shells'* by Flügge (1990). More comparison plots may be generated by running the input script, while for different values of the input variables presented here only the membrane theory solution can be expected to still be valid.

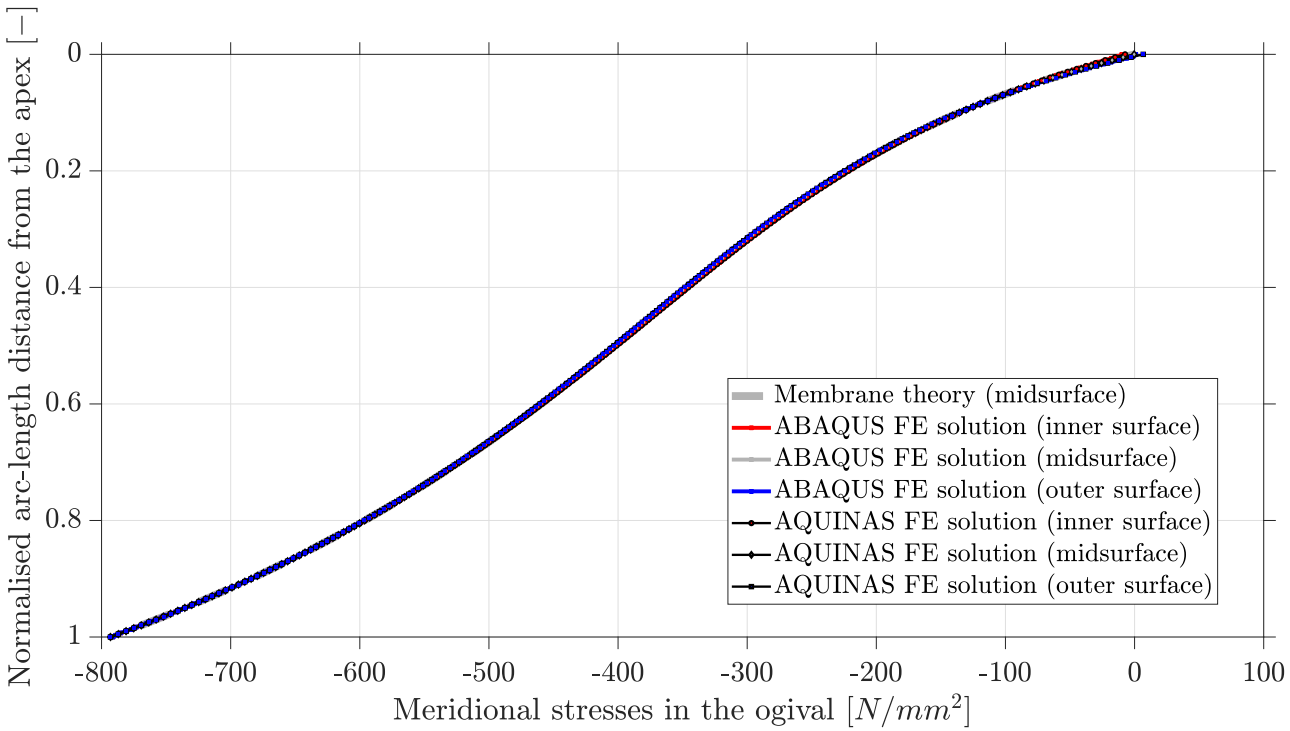


Figure A.23: LA08 - Comparison of meridional stresses in the inner, middle and outer surface of the shell wall.

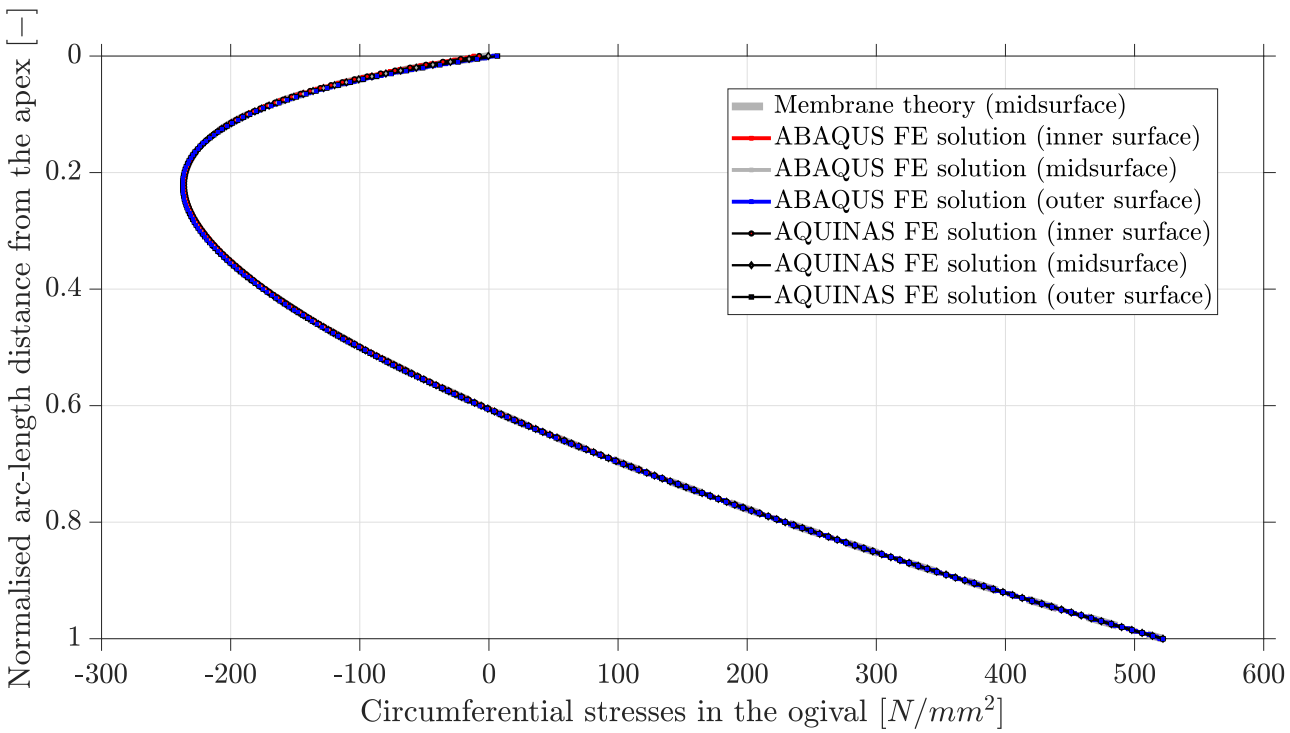


Figure A.24: LA08 - Comparison of circumferential stresses in the inner, middle and outer surface of the shell wall.

A.2.9 Example LA09: LA of a thin hyperboloid under an axial edge load

AQUINAS is also able to accurately model and analyse shell segment with negative meridional curvature, such as the hyperboloid of this LA example. The meridian is constructed with the use of the *'3pointArc'* option, with a total height of $h = 1000.0\,mm$ and a radius that ranges from $r_{edge} = 1000.0\,mm$ at the edges to $r_{in} = 750.0\,mm$ at the point closest to the axis of revolution. The axisymmetric hyperboloid has a BC1r - C1 boundary condition applied at its base, while the top edge is completely free, with an edge load $N = 1000.0\,N/mm$ acting axially downwards. The shell wall has a thickness of $t = 1.0\,mm$. The geometry of this shell problem is presented in Figure A.25.

In this example only an FE comparison with ABAQUS was attempted, owning to the scarcity of relevant axisymmetric shell problems in classic literature resources. The inner-middle-outer surface stress distributions along the hyperboloid's meridian are plotted for the two FE solvers in Figures A.26-A.27, adding to the cases where AQUINAS demonstrates good agreement with the established numerical analysis software.

A.2.10 Example LA10: LA of a thin multi-segment shell under normal pressure

The multi-segment shell of this LA example is inspired by the corresponding axisymmetric shell problem presented in *Equilibrium of shell structures* by Heyman (1977). While a membrane theory solution is presented in Heyman (1977), the shortcomings of the approach are acknowledged as there are evidently incompatibilities of circumferential stresses at shell junctions. The meridian of the pressure vessel modelled in `input_Example_LA10.m` consists of spherical caps, toroidal and barrel sections, and is symmetric about the equator of the axisymmetric shell, as can be appreciated from Figure A.28. For the FE modelling of the probably most demanding

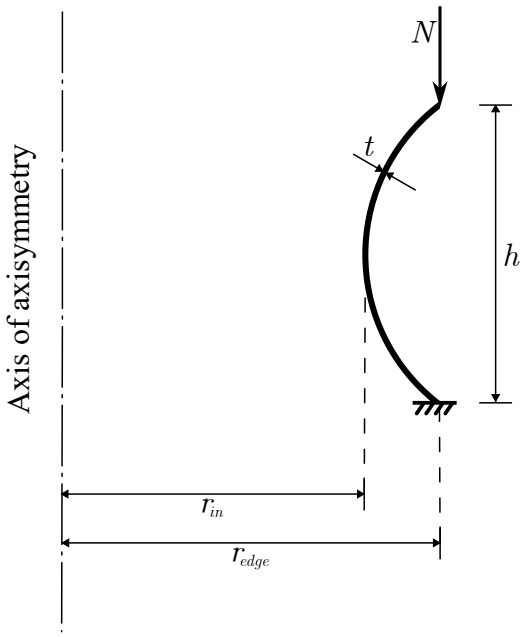


Figure A.25: LA09 - System diagram.

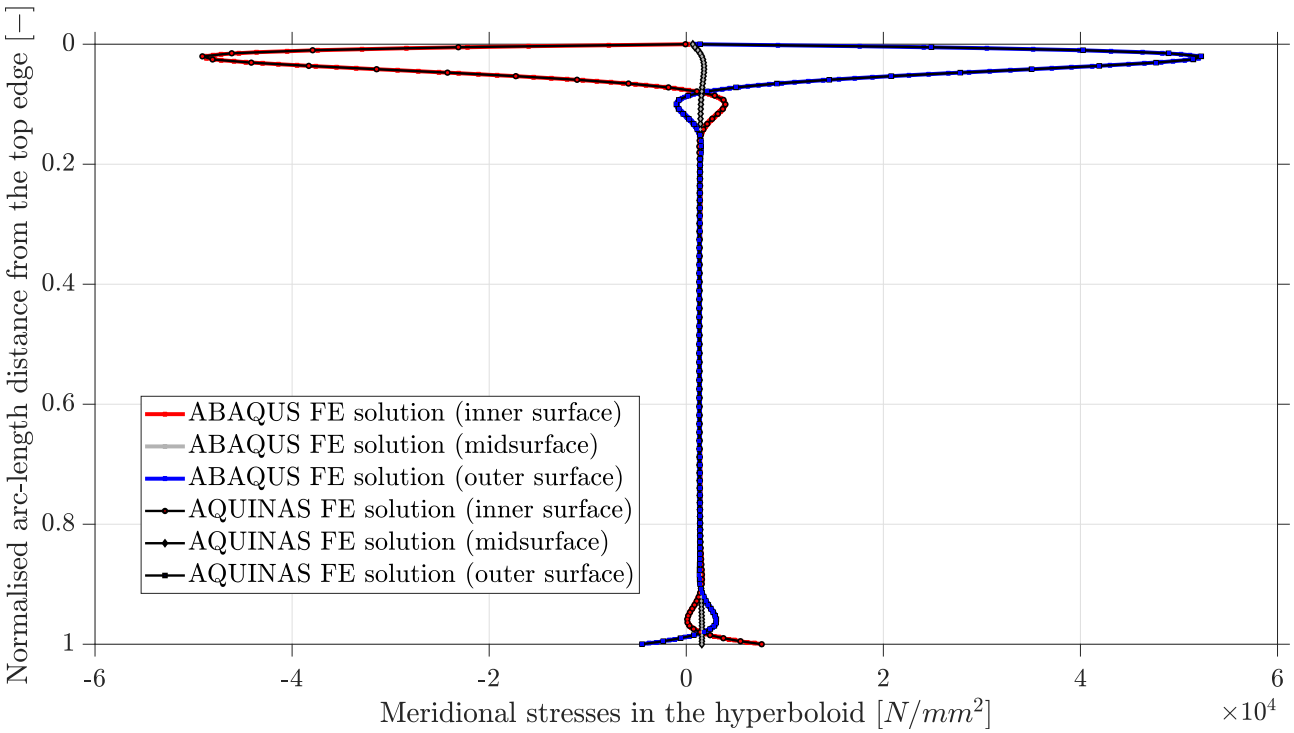


Figure A.26: LA09 - Comparison of meridional stresses in the inner, middle and outer surface of the shell wall.

LA problem thus far, the a reference radius parameter is set to $a = 200.0\,mm$ and the thickness of the shell wall at $t = 1.0\,mm$. The angle α can be found to be $\alpha = 24.3°$ (Heyman, 1977) from basic geometry considerations. A unit internal pressure $p = 1\ N/mm^2$ is considered, with the plane of meridional symmetry utilised to reduce the required discretisation for a computational solution of adequate quality to be obtained.

Due to the inability of a membrane theory solution to accurately describe the stress distribution along the shell's meridian, and the overall complexity of the problem that makes the prospect of a bending theory solution rather uninviting, a computationally obtained distribution of the

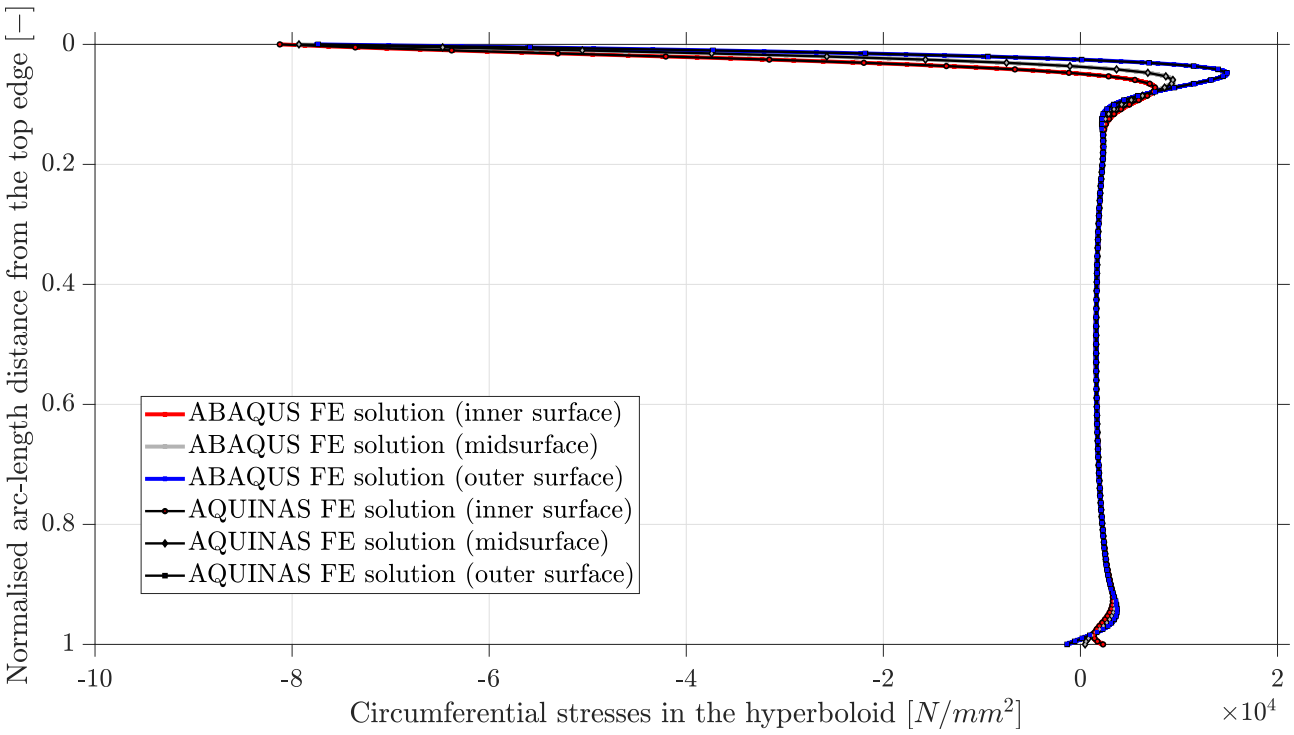


Figure A.27: LA09 - Comparison of circumferential stresses in the inner, middle and outer surface of the shell wall.

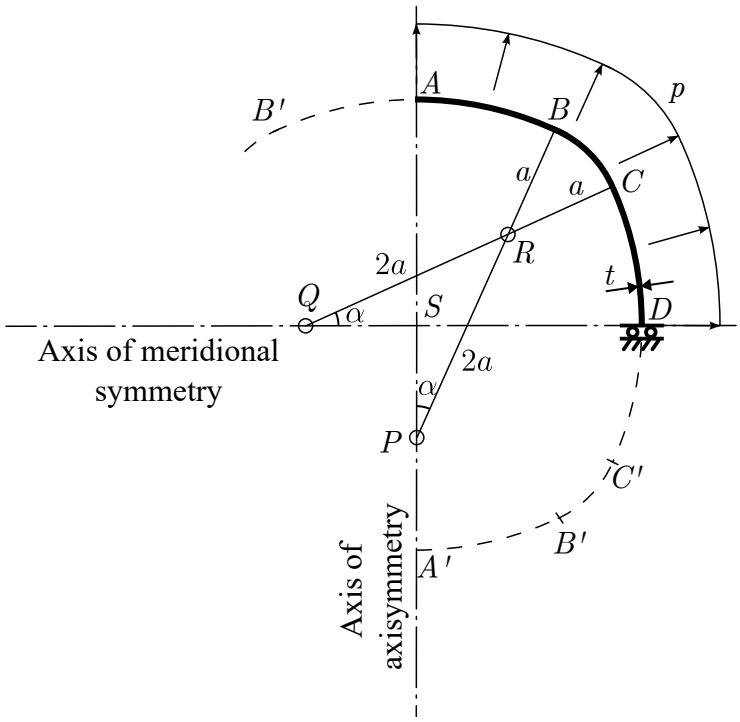


Figure A.28: LA10 - System diagram.

stresses, through submission of an ABAQUS (2022) model, will be used for comparison with the AQUINAS results. The meridional and circumferential stress distributions are displayed in Figures A.29 - A.30, where the reader may appreciate the significance of the bending boundary layers between junctions of the pressure vessel, but also another perfect agreement between the two FE solutions. The membrane theory solution is also presented in Table A.5, specialised for the specific a reference radius and p pressure used in the current implementation, as obtained

from Table 2.1 of Heyman (1977). The reader can visually compare these with the mid-surface results of Figures A.29 - A.30 as a further cross check of the validity of the AQUINAS solution.

Table A.5: LA10 - Meridional and circumferential membrane stress resultants at the shell junctions, obtained from Table 2.1 of Heyman (1977), with reference to Figure A.28.

Point	A	B^-	B^+	C^-	C^+	D
r_ϕ [mm]	600	600	600	380	380	400
r_θ [mm]	600	600	200	200	600	600
N_ϕ [N/mm]	300	300	300	190	190	200
N_θ [N/mm]	300	300	300	20	260	$266.\bar{6}$

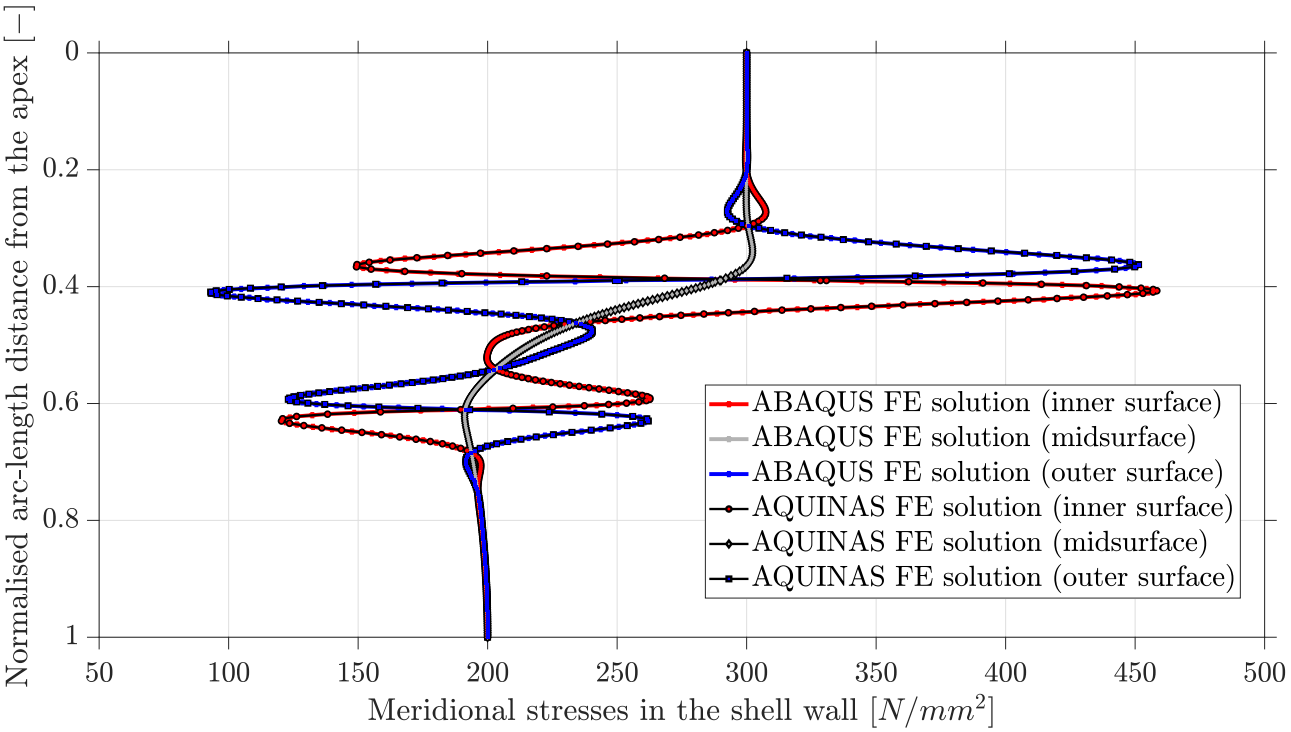


Figure A.29: LA10 - Comparison of meridional stresses in the inner, middle and outer surface of the shell wall.

A.2.11 Example LA11: Thin circular plate with clamped edges under uniform pressure

AQUINAS also provides the option for an explicit definition of an axisymmetric circular plate segment. The FE results obtained with the use of such a segment are tested in this LA example, where the focus is on a circular plate subjected to a uniform unit pressure. The ends of the plate are clamped, with no hole considered at the its centre. Its outer edge has a radius of $r = 50.0\,mm$ and its thickness is $t = 1.0\,mm$. The geometry of the plate, as well as the pressure applied, are presented in the following Figure A.31. Comparison is made with a bending theory analytical solution, found in Timoshenko & Woinowsky-Krieger (1959b). There is no point in a membrane theory for this example since there is no radial / meridional force acting on the plate and hence it only resists the uniform normal pressure through bending. Once more, stress results are presented in Figures A.32 - A.33 to illustrate the excellent agreement between the analytical solution and AQUINAS, while more can be found by running the `input_Example_LA11.m` script.

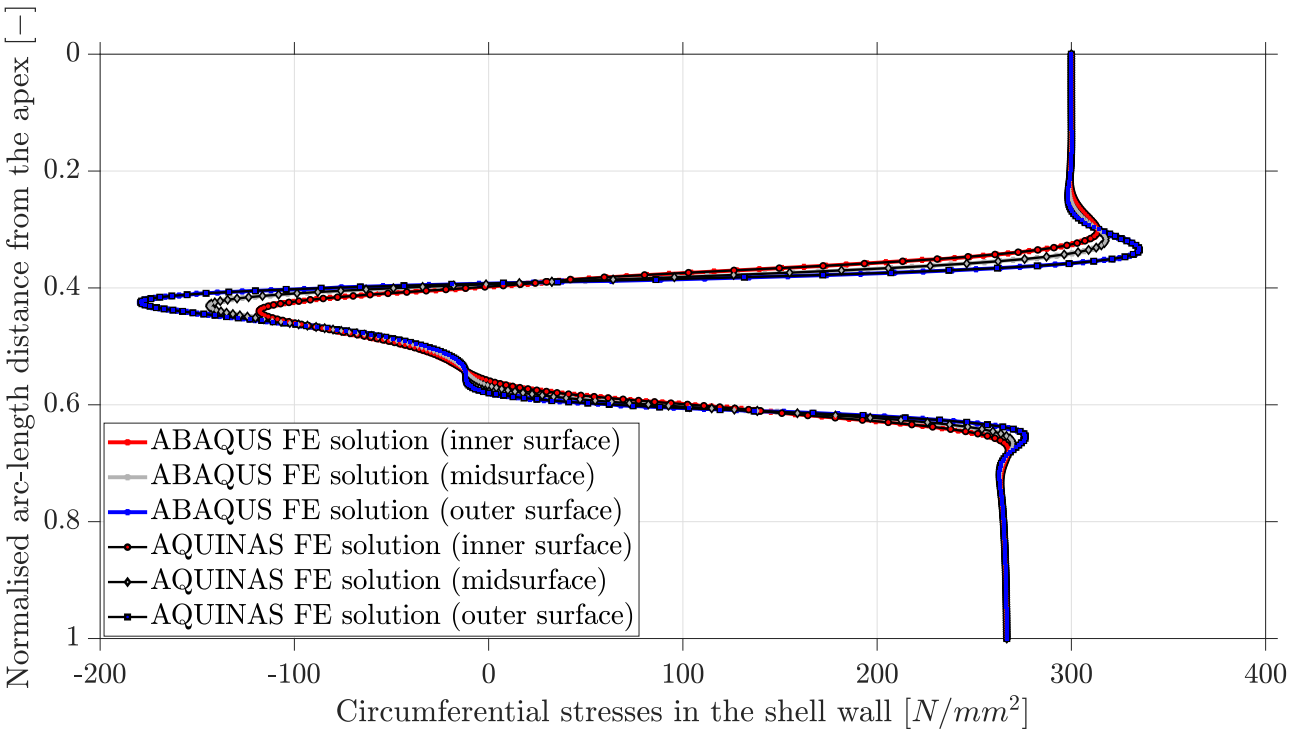


Figure A.30: LA10 - Comparison of circumferential stresses in the inner, middle and outer surface of the shell wall.

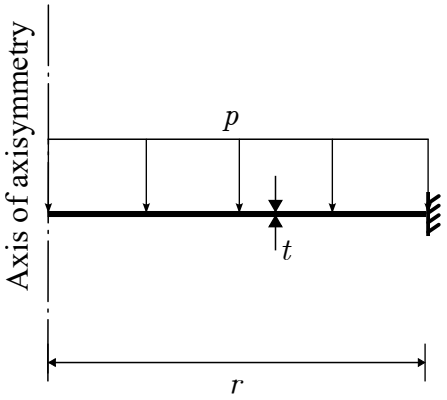


Figure A.31: LA11 - System diagram.

A.2.12 Example LA12 : LA of a thin toroid shell with uniform internal pressure

This LA example can be found in `input_Example_LA12.m`, where the focus is on a thin toroid under uniform internal pressure. The geometry of this doughnut shell problem is illustrated in Figure A.34.

The meridional radius of the shell is $a = 500.0\,mm$ and is centre is located at a radial coordinate of $r_c = 2000.0\,mm$. The bottom apex of the circular closed meridian has BC2f - S3 boundary condition and a unit normal internal pressure $p_n = 1.0\,N/mm^2$ is uniformly distributed along the shell's meridian. The shell wall has a uniform thickness $t = 1.0\,mm$.

ABAQUS is employed for one more time to generate the necessary results that will allow a visual comparison with AQUINAS. The meridional and circumferential stress distributions can be examined in Figures A.35-A.36 below, allowing the reader to appreciate the solid performance of AQUINAS throughout each of these LA examples. Deformed shape and strain results may

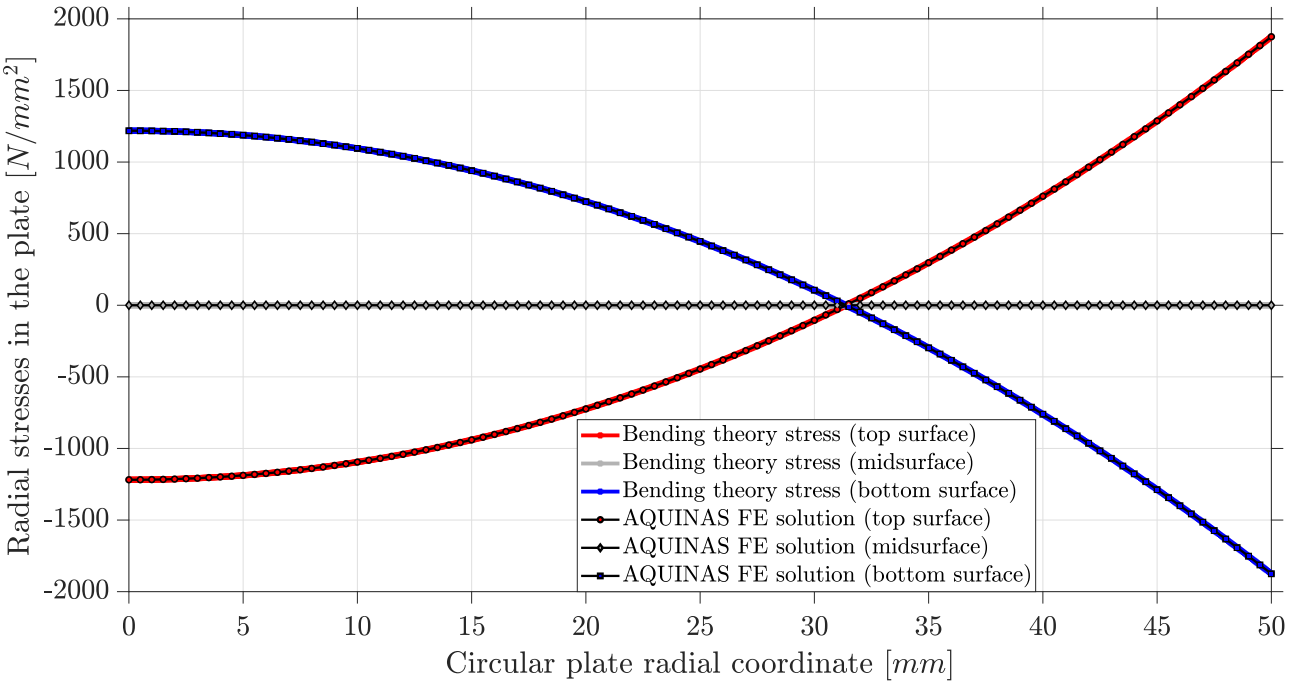


Figure A.32: LA11 - Comparison of top, middle and bottom surface radial stresses of the circular plate.

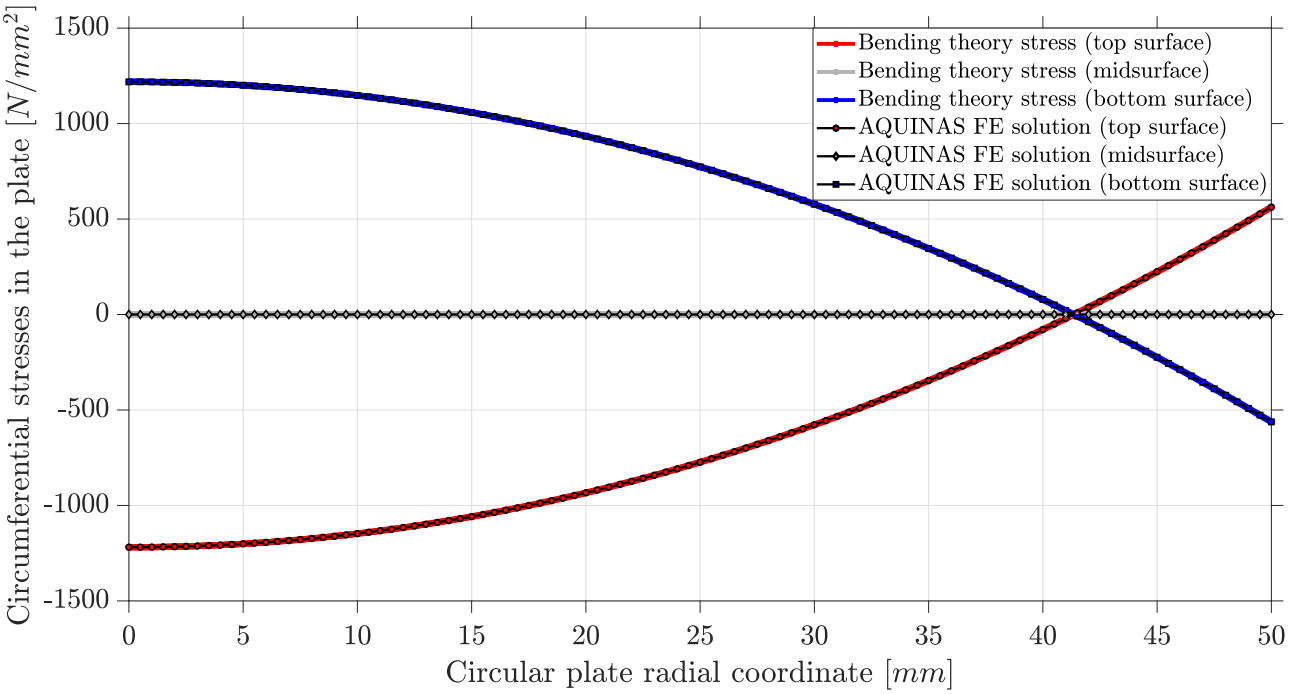


Figure A.33: LA11 - Comparison of top, middle and bottom surface circumferential stresses of the circular plate.

be generated by running the input script `input_Example_LA12.m`.

A.3 LBAs

The chief motivation for the development of AQUINAS has been the accurate and efficient identification of the unsymmetrical bifurcation buckling mode for axisymmetric shell problems.

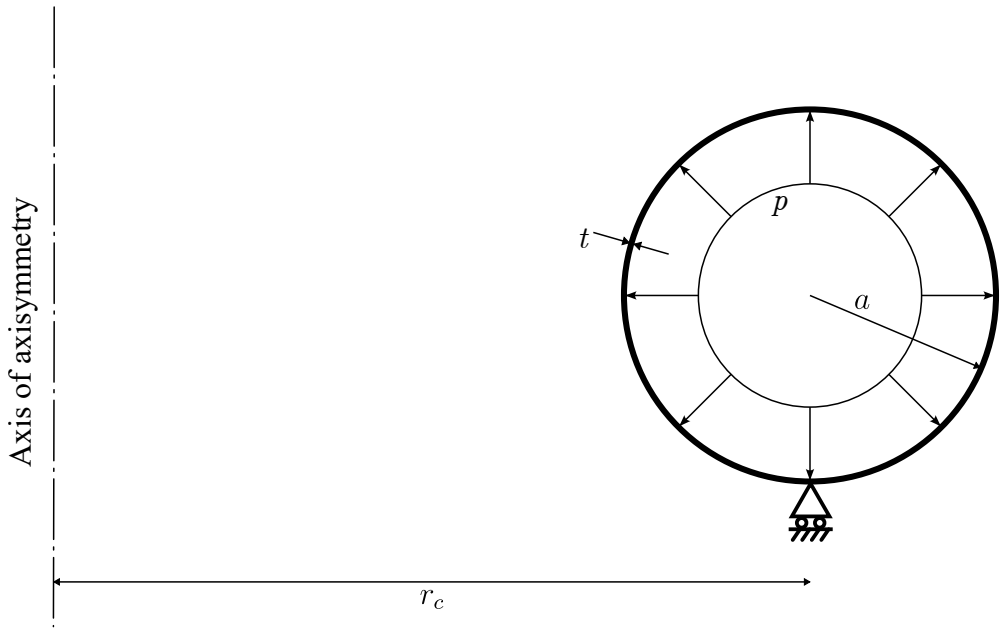


Figure A.34: LA12 - System diagram.

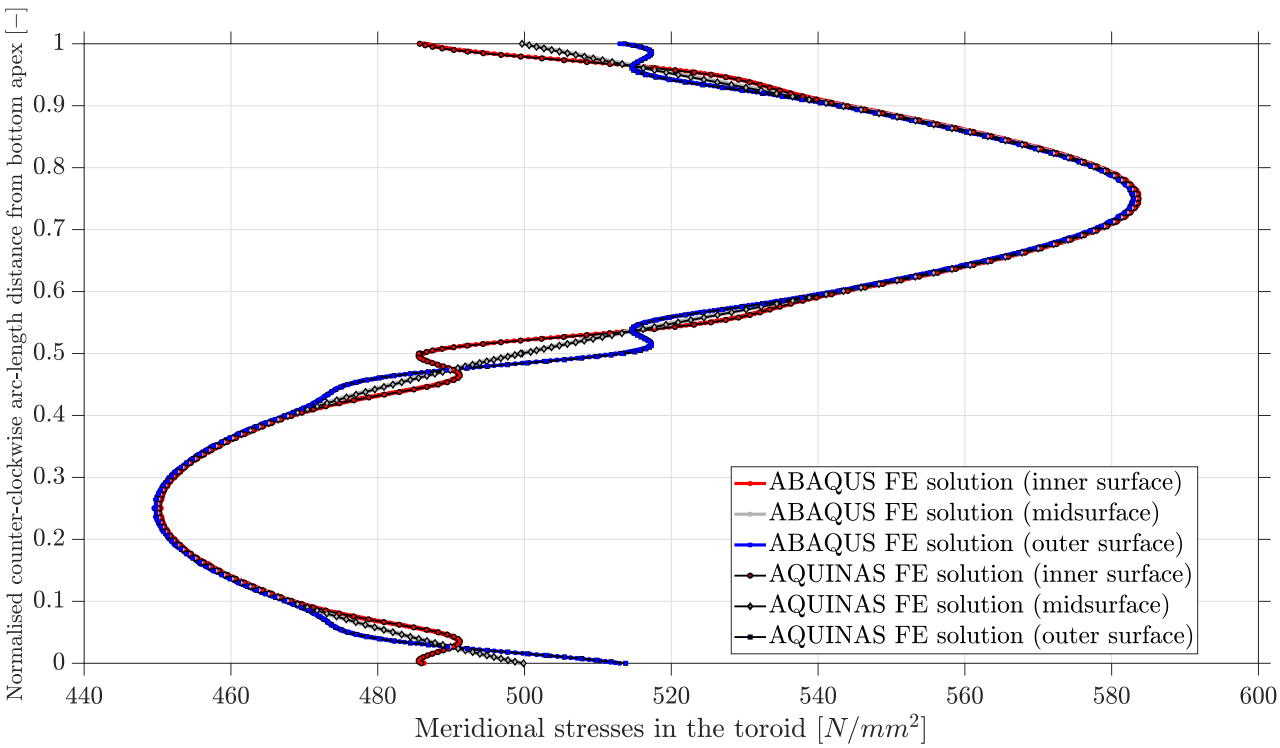


Figure A.35: LA12 - Comparison of circumferential stresses in the inner, middle and outer surface of the shell wall.

The LA examples of the previous section have generated confidence in the correctness of the geometric definition of shell meridians and calculations of strains-stresses in AQUINAS. The present section proceeds to the more demanding computational procedures of the software, the bifurcation analyses of axisymmetric shells. Unless stated otherwise the material considered is steel, with a Young's modulus of $E = 200000\ N/mm^2$ and a Poisson's ratio of $\nu = 0.3$.

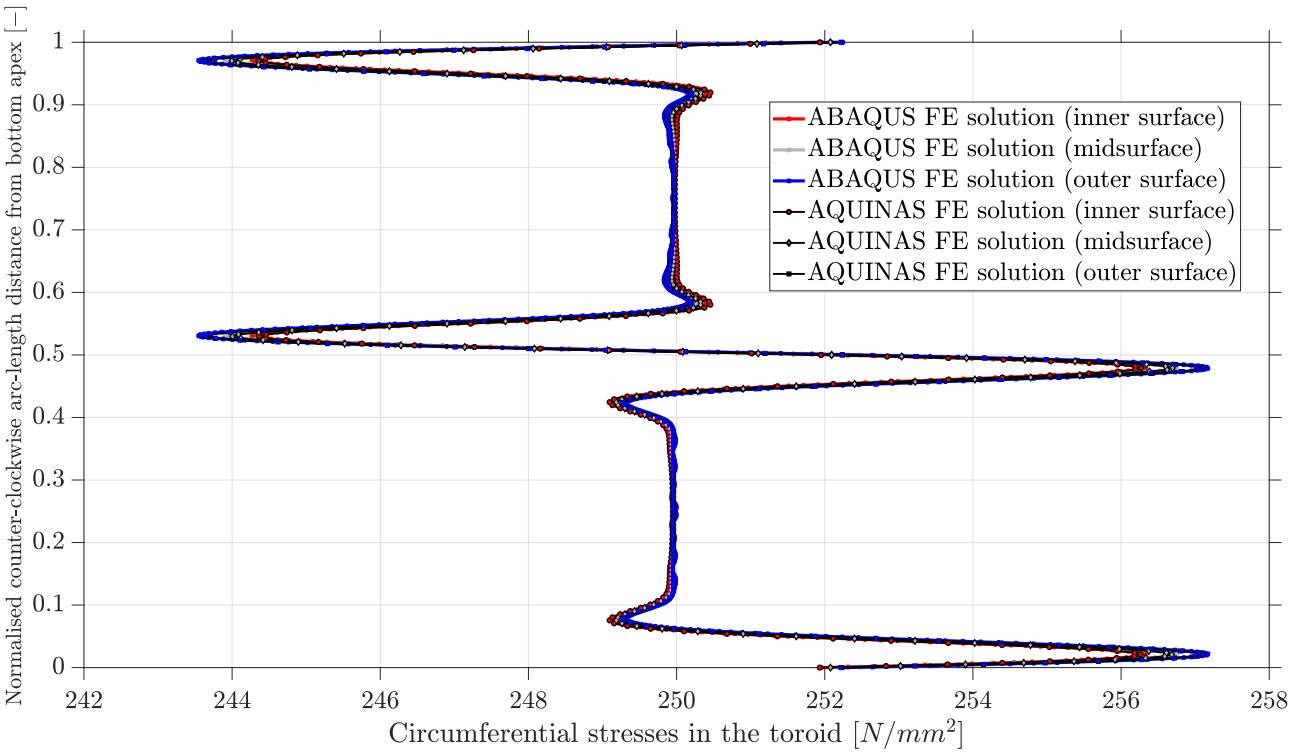


Figure A.36: LA12 - Comparison of circumferential stresses in the inner, middle and outer surface of the shell wall.

A.3.1 Example LBA01: LBA of a thin cylindrical shells of varying length under uniform meridional compression

In this LBA example, the response of thin unpressurised cylindrical shells under uniform compression is examined. The cylinders are of varying length, characterised by a dimensionless parameter Ω, as provided earlier in this document through Eq. 4.2. An meridionally compressing edge load N_{cl} is applied at the top edge of the cylinders, the magnitude of which is related to the classical elastic critical stress σ_{cl} for the bifurcation of cylinders under meridional compression, given in Eq. 2.15 as part of the review provided on cylindrical shell buckling. The derivation of the classical elastic critical stress σ_{cl} has been based on a uniform membrane pre-buckling stress state. This however does not hold in the current example, due to the restraint applied for the radial displacement u at both ends of the cylinder. A BC2f boundary condition is applied at the top edge of the cylinder and a BC1f at its base. While the length of the cylinders vary, their radius and thickness is set to $r = 500.0\,mm$ and $t = 1.0\,mm$ accordingly, leading to an r/t ratio of 500. The geometry, loading and boundary conditions of the cylinder are presented in Figure A.37. Several values of the Ω parameter are explored, from rather short ones, where plate-like buckling is expected to be critical, to very long tubes that behave like a column, with the Euler buckling load being very close to the FE prediction by AQUINAS. The critical buckling loads computed, normalised by the classical buckling load of Eq. (2.19) for all values of Ω considered, are plotted in Figure A.38.

It may be appreciated that the good agreement between the analytically derived buckling loads and the FE results of AQUINAS. Medium-length cylinders showcase a critical bifurcation edge load that is equal to the classical value of Eq. (2.19). Even though the condition of a uniform pre-buckling membrane stress state is violated with the edge restraints applied, the effect of this violation is negligible due to how short the bending boundary layers span in a medium-length cylinder. In cases where the cylinders can be characterised as either very short or very long, the

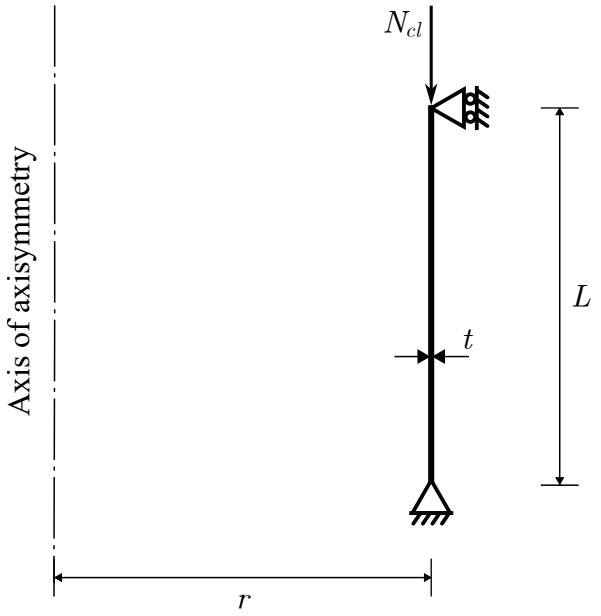


Figure A.37: LBA01 - System diagram.

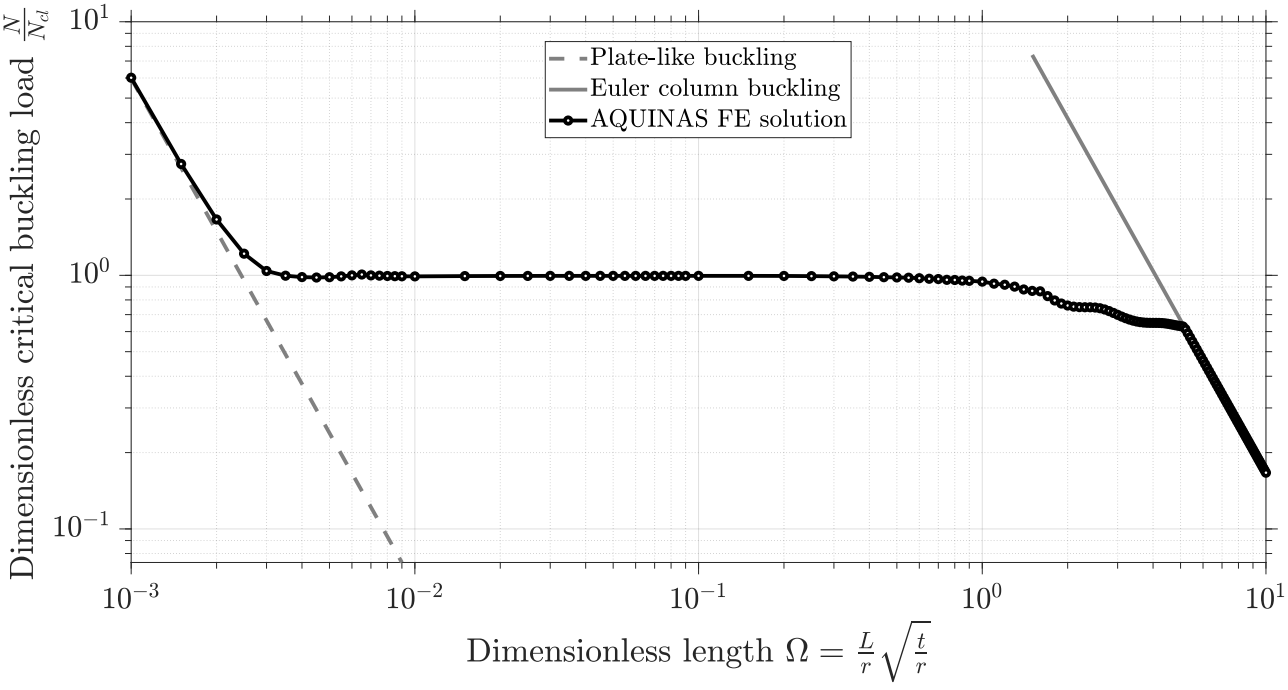


Figure A.38: LBA01 - Development of critical bifurcation load with respect to the dimensionless length parameter Ω.

critical bifurcation loads are consistent with the theoretical values of plate and Euler column buckling accordingly.

On top of the critical bifurcation loads, and their corresponding circumferential modes, AQUINAS may also output the Load Proportionality Factor that will cause buckling into any circumferential mode n. Capitalising on this feature, the user can obtain curves that showcase the development of the critical buckling load with respect to the harmonic number n, or in cases where there is a set of parametrised models, as is here with the dimensionless length parameter Ω, surfaces like the one of the following Figure A.39.

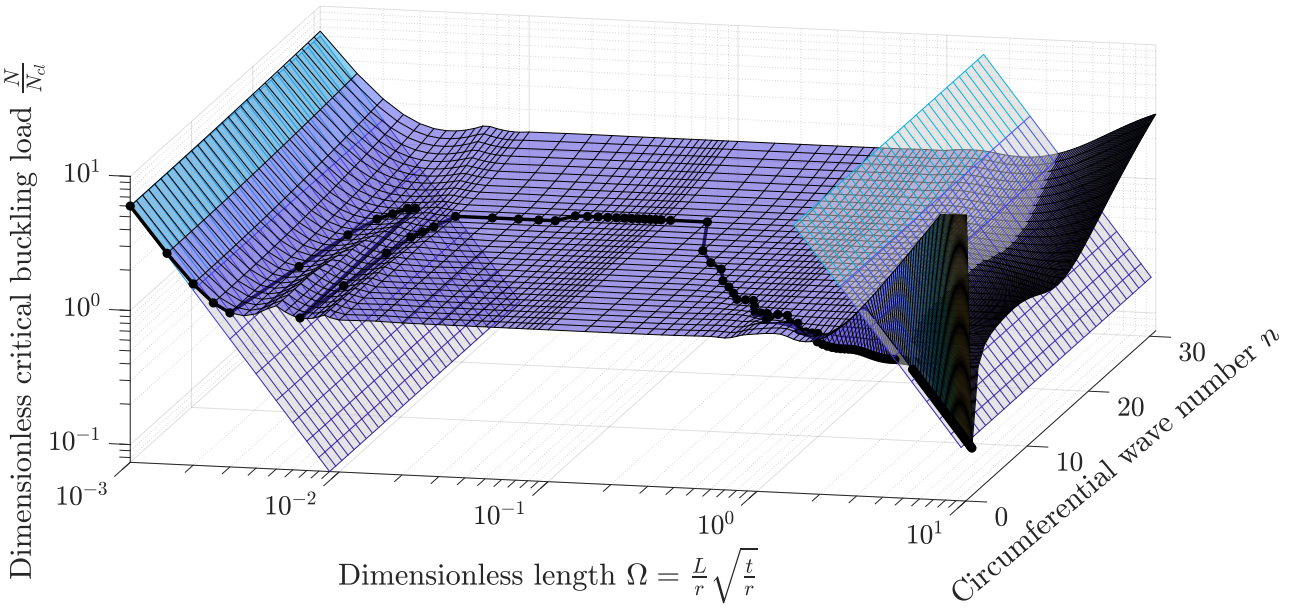


Figure A.39: LBA01 - Buckling loads for various values of the dimensionless length parameter Ω and circumferential modes n.

If the optimisation option is enabled, with AQUINAS employing its surrogate model optimisation algorithm, the 3D surface of Figure A.39 will not be displayed at the end of the analysis, since only a select few circumferential modes are trialled per Ω. The reader may wish to run the `input_Example_LBA01.m` script, potentially exploring a wider range of length parameters or r/t ratios or performing any other parametric study.

A.3.2 Example LBA02: LBA of a thin cylinder under meridional compression and direct comparison with the Koiter circle

This second LBA example serves as a continuation of the first one, investigating the locus of circumferential full waves n and meridional half waves m for the bifurcation modes corresponding to elastic buckling load N_{cl} of Eq. (2.19). This locus has been found in Koiter (1945) to be a circle, termed as the 'Koiter circle' in shell buckling related literature and briefly described in Eq. 2.18 of Section 2.1.3.2. The equation for the Koiter circle can be simplified for the material properties used here ($E = 200000\ N/mm^2$, $\nu = 0.3$) in the following form (Sadowski *et al.*, 2018):

$$(m\frac{\pi}{L}r)^2 + n^2 - 1.818r\sqrt{\frac{r}{t}}(m\frac{\pi}{L}) \approx 0 \tag{A.2}$$

In Figure 4 of Sadowski *et al.* (2018) it is illustrated that the bifurcation loads $N_{m,n}$ increase the further the corresponding m-n pair is from the Koiter circle, both in terms of their analytically obtained value or FE computed one. This result is reproduced in Figure A.40, where the source of computationally obtained critical buckling loads is AQUINAS. The single cylinder considered here is of length $L = 1000.0\ mm$ and shares the rest of its geometric properties, as well as loading and boundary conditions, with the cylinders of `input_Example_LBA01.m`, as displayed in Figure A.37.

It should be noted that while determining the circumferential mode n that the cylinder is bifurcating into in AQUINAS is a straightforward process, since n is explicitly included in the formulation of the stiffness matrices for the eigenvalue problem of Eq. (3.82), the number

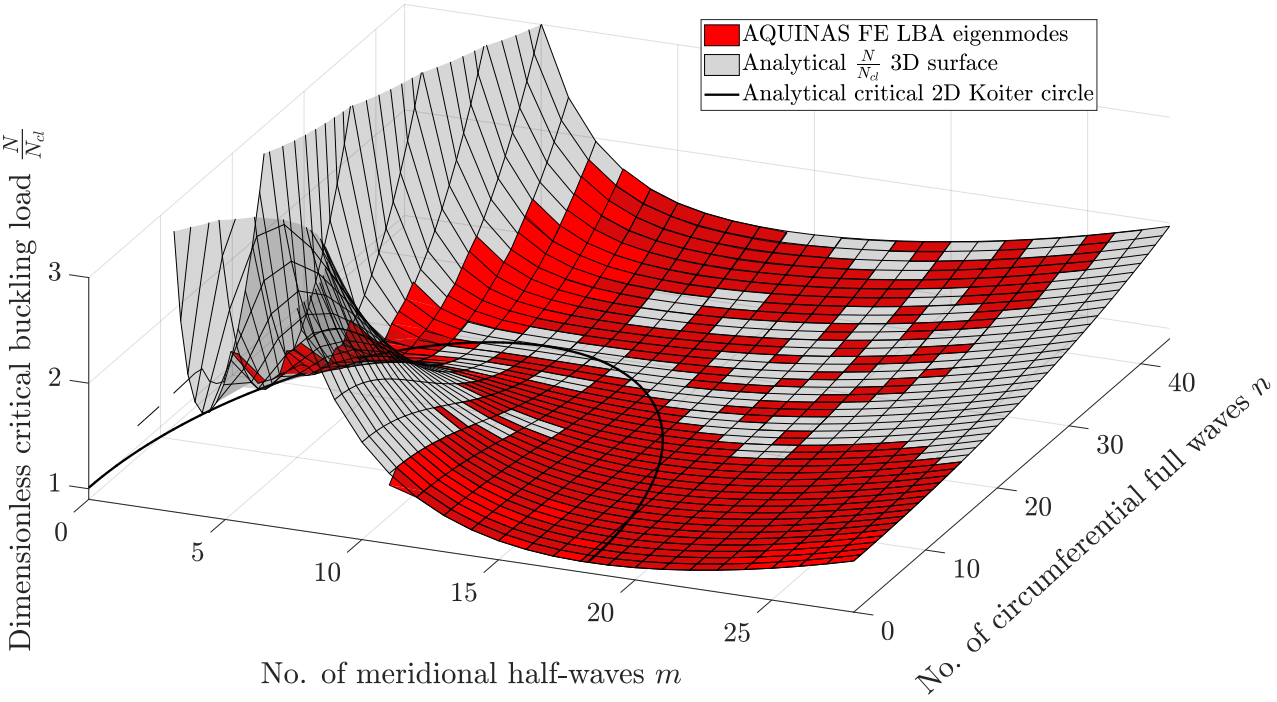


Figure A.40: LBA02 - Analytically and computationally obtained buckling loads $N_{m,n}$ for a cylinder under meridional compression.

of meridional half waves m is obtained through a post-processing fitting of harmonics on the computed eigenmodes for each n. As such, a level of error in this automated fitting is inevitable and can lead to meridional-half waves m being unrepresented for a circumferential harmonic n in Figure A.40, even for pairs that would fall very close to the Koiter circle of Eq. (A.2).

A.3.3 Example LBA03: LBA of a thin cylindrical shell under uniform lateral pressure

Having established the appropriate behaviour of the linear bifurcation solver in AQUINAS for cylinders under meridional compression, it is time to move on to another regularly encountered case in shell buckling literature, that of cylinders under uniform external normal pressure. An analytical solution for the bifurcation loads of the cylinders is also present for comparison purposes here, coded in `input_Example_LBA03.m` based on the formulations of the classical shell buckling textbook *'Elastic Stability of Circular Cylindrical Shells'* of Yamaki (1984). It is important to note that the analytical derivations of the bifurcation pressure associated with a circumferential mode in Yamaki (1984) are preformed on the basis of a uniform membrane pre-buckling stress state along the meridian of the cylinders, regardless of the boundary conditions that would be considered for the bifurcation checks themselves. Assuming different boundary conditions for the pre-buckling/buckling states of axisymmetric shell problems is a technique often encountered in literature resources of the past, usually due to the obvious reduction of the problem's complexity through omission of the bending effects near the edges. While it can be appreciated that this is not a very realistic approach to the design of axisymmetric shells against buckling, as it would be rather unlikely for the restraints applied to a shell to change just before is buckles, the capability to handle different cases of boundary conditions for different states of the shell's response has been added to AQUINAS, for the software to have all the necessary tools for a direct comparison with established textbook solutions. Several cylinders are examined, with their radius and thickness being constant at $r = 1000.0\,mm$ and $t = 1.0\,mm$, and their length L varying according to the Batdorf parameter:

$$Z = \sqrt{1-\nu^2}\frac{L^2}{rt} \tag{A.3}$$

Critical buckling pressure results for a few combinations of boundary conditions are displayed in Yamaki (1984), using the terminology of Tables A.1 and A.2. Here, only the C1-C1 (equivalent to a BC1r condition) case for the bifurcation modes is considered for all of the Batdorf parameters trialled, with the `input_Example_LBA03.m` script being readily extensible to explore any alternative combination of boundary conditions for the cylinders. The classical elastic critical buckling pressure, applied on the meridian of the cylindrical models, can be found to be (Teng & Rotter, 2004a)

$$p_{cl} = 0.92E\frac{r}{\sqrt{rtZ/sqrt(1-\nu^2)}}\left(\frac{t}{r}\right)^2 \tag{A.4}$$

where Z here is the Batdorf parameter of Eq. (A.3) and does not refer to the axial coordinate of the shell's meridian of Eq. (3.1b).

The geometry and boundary-loading conditions of the cylindrical shells are illustrated in Figure A.41, where as discussed above different restraints are applied for the pre-buckling stress state and the buckling modes. Only an axial restraint ($w = 0$) is applied at the base of the cylinders in order to allow for the axisymmetric models to deform without introducing bending behaviour for compatibility purposes at the edges, allowing a uniform pre-buckling stress state to develop.

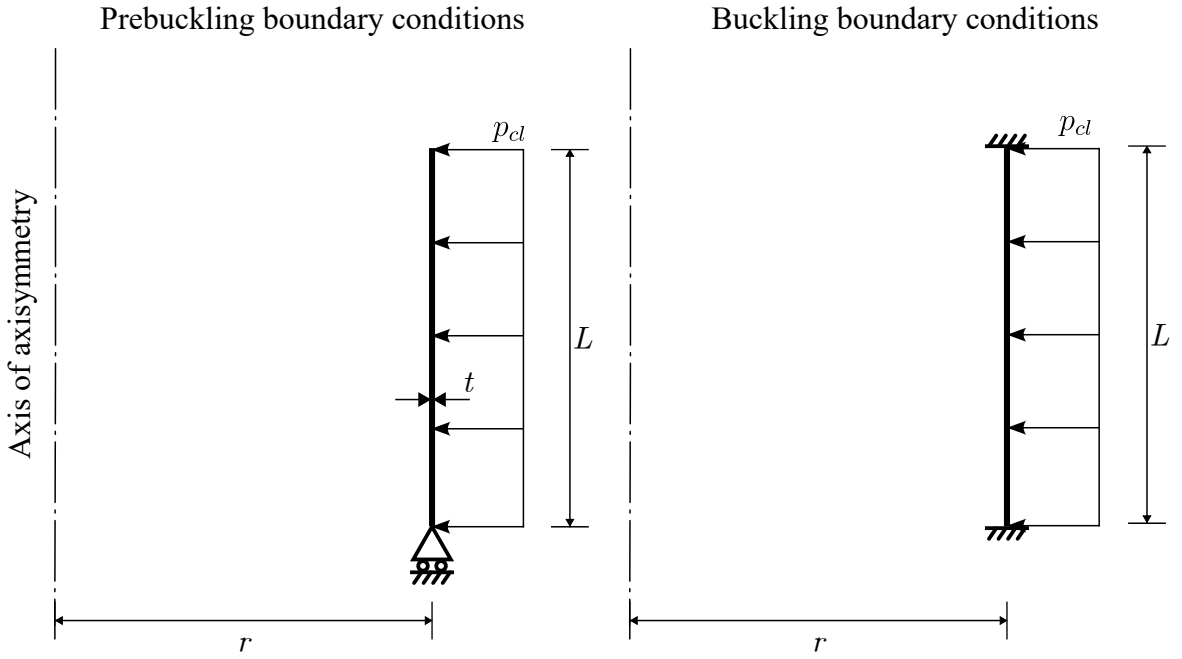


Figure A.41: LBA03 - System diagram.

In Figure A.42 the analytically derived critical bifurcation pressure and the associated circumferential mode n of Yamaki (1984) is shown to have an excellent agreement with the corresponding computationally obtained results from AQUINAS, with Yamaki's k_p and β parameters being adopted for this comparison. The critical buckling pressure p_{cr} normalised by the classical result for cylinders under external pressure p_{cl} of Eq. (A.4) is also plotted against the ω parameters (see Eq. 4.1) that are equivalent to the Batdorf ones considered for this example in Figure A.43. A benefit of the capability of AQUINAS to obtain an eigenvalue for any circumferential mode

to be considered is the computation of a surface of results, showcasing the development of the pressure and associated harmonic n that would lead to bifurcation as the cylinders increase in height, through a value of the dimensionless parameter Ω. This third plot may only be generated though by disabling the surrogate optimisation option, as only a select few harmonic's are trialled when the minimisation algorithm is enabled. While in Yamaki (1984) only the critical pressure and mode is presented, the derivations have been coded in the script to obtain a result for any circumferential mode of interest, allowing for a further comparison in this 3D surface space of Figure A.44. A reader who examines the `input_Example_LBA03.m` script can appreciate how complex these derivations actually are, even with the simplification of a uniform pre-buckling stress state, making the analytical approach completely impracticable for the design of cylinders under normal pressure.

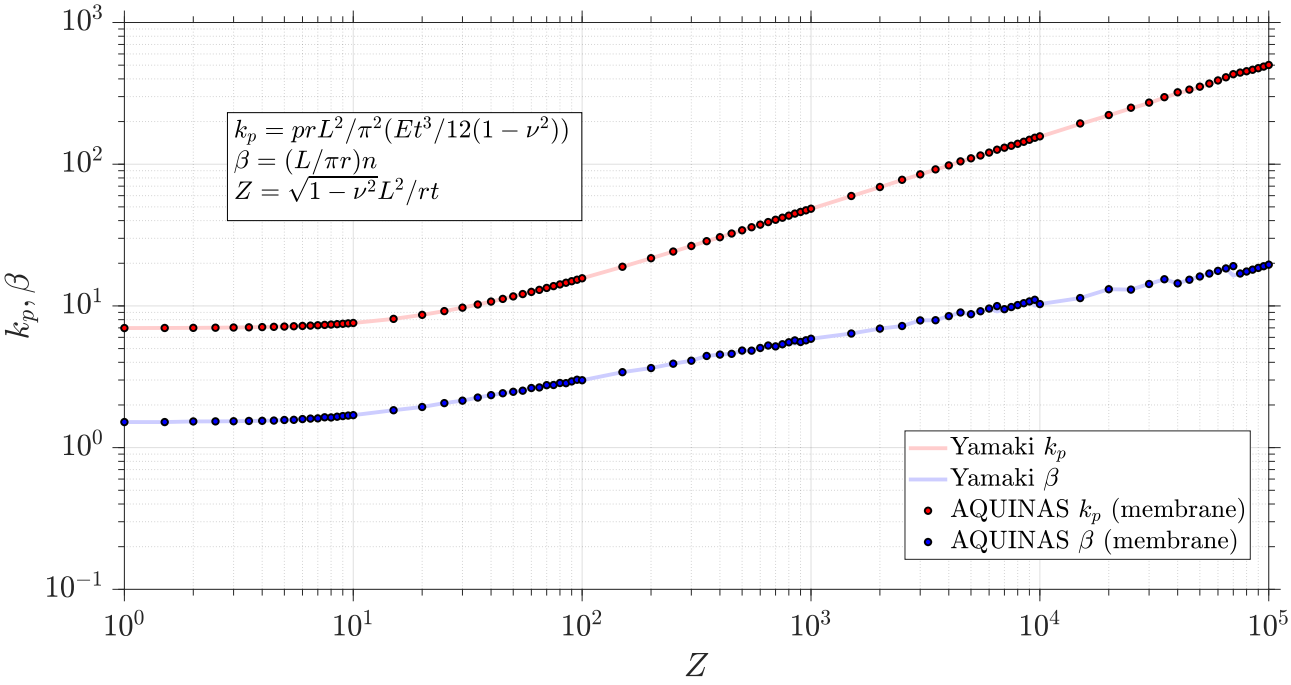


Figure A.42: LBA03 - Variation of k_p and β with the Batdorf parameter Z for a C1-C1 boundary condition case.

A.3.4 Example LBA04: Koiter ellipse for a thin truncated cone under uniform axial compression

A computational investigation of the bifurcation loads and modes for truncated conical shells under an axially compressive stress state in Spagnoli (2003) has shown that the locus of circumferential full waves n against meridional half waves m can be approximated by an ellipse, when these are plotted in a dimensionless $\bar{\beta}_c$-$\bar{\beta}_m$ space. The dimensionless wave-numbers are defined in Spagnoli (2003) as

$$\bar{\beta}_m = \frac{\bar{\lambda}}{\bar{l}_m} \tag{A.5a}$$

$$\bar{\beta}_c = \frac{\bar{\lambda}}{\bar{l}_c} \tag{A.5b}$$

where

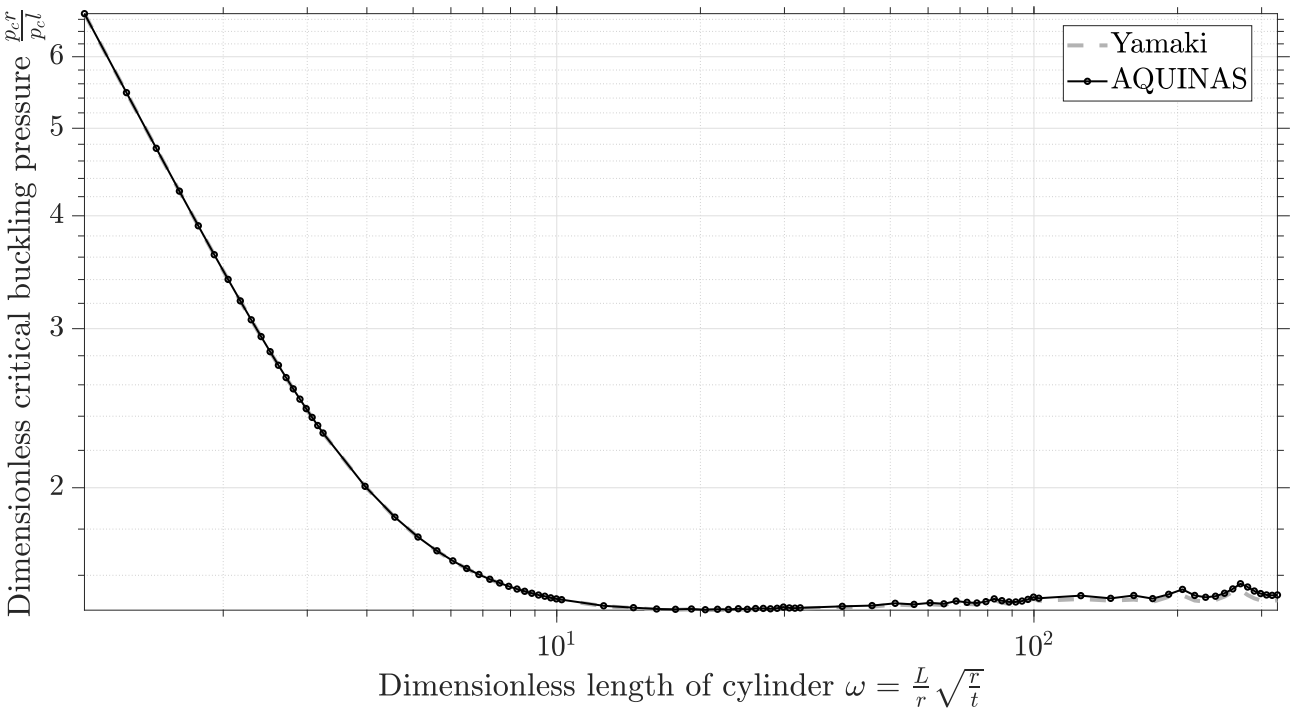


Figure A.43: LBA03 - Development of critical buckling pressure ratio p_{cr}/p_{cl} with respect to the dimensionless length parameter Ω.

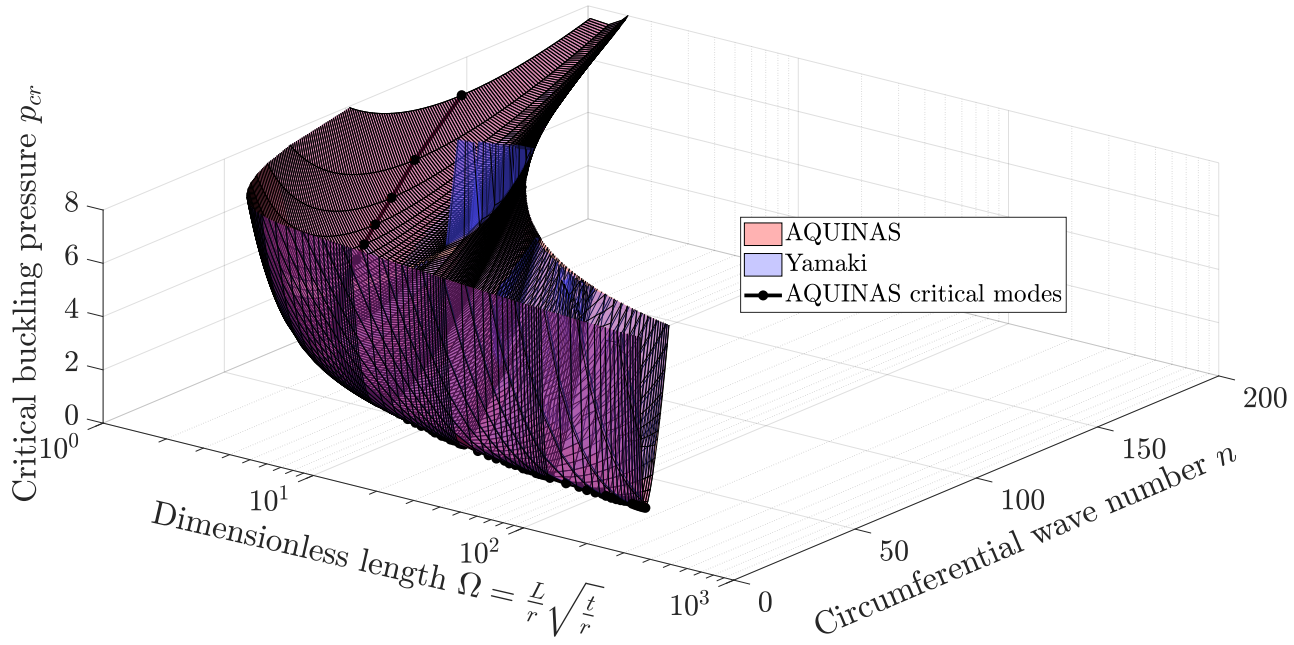


Figure A.44: LBA03 - Buckling pressures for various values of the dimensionless length parameter Ω and circumferential modes n.

$$\bar{l}_m = \frac{L}{m} \tag{A.6a}$$

$$\bar{l}_c = \frac{\pi\bar{\rho}}{n} \tag{A.6b}$$

and

$$\bar{\lambda} = \frac{\pi}{\sqrt[4]{3(1-\nu^2)}}\sqrt{\bar{\rho}t} \tag{A.7}$$

The $\bar{\lambda}$ parameter corresponds to the average half-wavelength according to the linear bending theory for cones, with $\bar{\rho}$ being the average radius of curvature. The derivations of the equations that will eventually lead to the elliptical locus for the dimensionless wave-numbers $\bar{\beta}_c$ and $\bar{\beta}_m$ may be found in Spagnoli (2003).

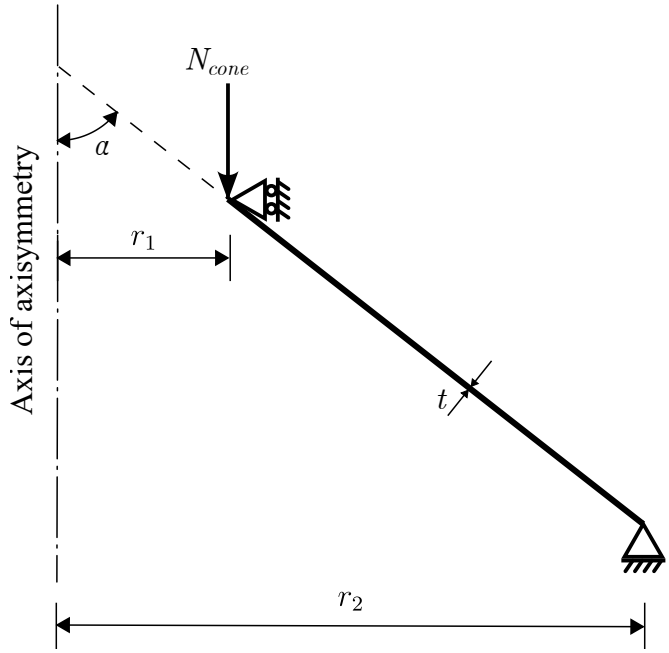


Figure A.45: LBA04 - System diagram.

For each run of `input_Example_LBA04.m`, the LBA of a single truncated conical shell under axial compression is executed, with the results then post-processed in order to obtain the meridional half wave-number m. The cones are characterised from their tapering angle α which can vary from $\alpha = 0°$, for a cone that is essentially a cylinder, up to $\alpha = 90°$ for a plate-like cone. The shell wall has a constant thickness of $t = 1.0\,mm$, while the inner (top) edge of the conical segment has a radius of $r_1 = 1000.0\,mm$. The meridian of the cone has a length of $L = 3000.0\,mm$, which can be used to compute the radial and axial coordinates of the outer (bottom) edge of the segment as a function of the tapering angle α. A BC1f restraint is applied at the outer edge of the cone and a BC2f at the top, with the circumferential DOF v restrained at both ends. The reader is cautioned that the notation used in Spagnoli (2003) is not the one adopted by AQUINAS and care should be exercised in interpreting the boundary conditions. The classical buckling compressive axial edge load, applied at the top edge of the cone, is derived on the basis of a membrane pre-buckling state and is given as:

$$N_{cone} = \frac{Et^2}{r_1\sqrt{3(1-\nu^2)}}\cos^2\alpha \tag{A.8}$$

The geometric definition for this LBA example is illustrated in Figure A.45, while in Figure A.46 the AQUINAS FE results are plotted in the dimensionless wave-number space and compared against the Koiter ellipse locus for a tapering angle of $\alpha = 15°$. While the agreement may seem good but not ideal here, it should be noted that the calculation of the meridional half wave-number m is done through a fitting of harmonic, equally spaced waves, running along the meridian

of the cones. This is a scheme that can lead to rather accurate computations for cylinders under axial compression (see `input_Example_LBA01.m`), but is only a rough approximation in the case of cones where the meridional half waves are generally not equally spaced. An even better agreement can be observed if the meridional half waves are manually counted one by one, a process that is much more strenuous compared to the automated approximation used here. Additionally, running this example may take some time.

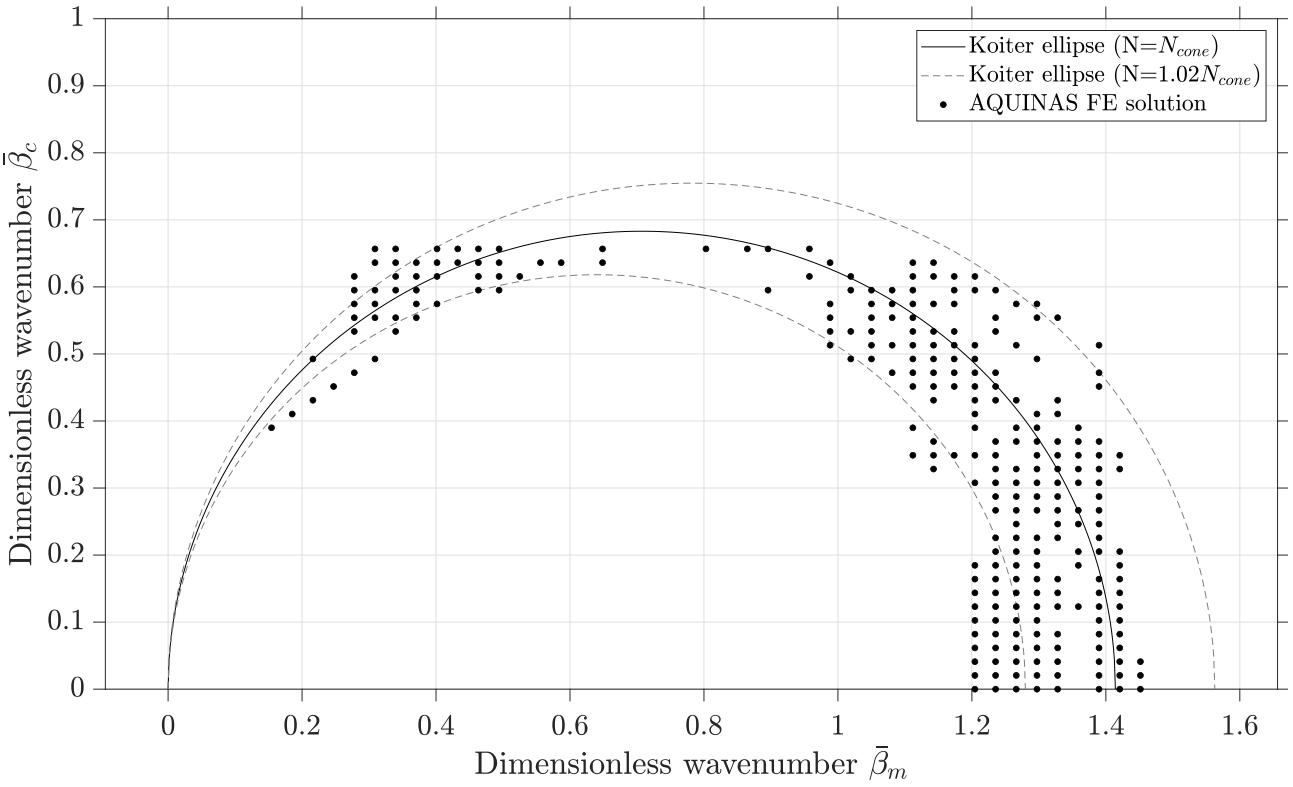


Figure A.46: LBA04 - Locus of simultaneous buckling modes with $N \leq 1.02N_{cone}$ for a cone with a tapering angle $\alpha = 15°$ in the $\bar{\beta}_m$ - $\bar{\beta}_c$ dimensionless wave-number space.

A.3.5 Example LBA05: Bifurcation modes of a thin spherical shell under uniform external pressure

Moving on to the LBA of axisymmetric shell problem with curved meridians, the circumferential and meridional modes of thin spherical shells under uniform external pressure are explored in `input_Example_LBA05.m`. As discussed by Hutchinson in *'Buckling of spherical shells revisited'* Hutchinson (2016), the bifurcation modes of closed spheres under external pressures may be described through the spherical harmonics S_{mn}, given as

$$S_{nm} = \cos(m\omega)P_n^m(sin\theta) \tag{A.9}$$

where P_n^m is the associated Legendre function of degree n and order m. The reader is cautioned that the notation used for this example, as adopted from Hutchinson (2016), should not be confused with the number of meridional half-waves m and circumferential full waves n used throughout AQUINAS, but instead they refer to the associated Legendre polynomials. The meridional angle θ is zero at the equator of the spheres, and ω is used for the circumferential angle (not to be confused with the dimensionless group of Eq. 4.1). While the order m of P_n^m is equivalent to the circumferential wave-number, the degree n should not be viewed as

a parameter equivalent to the meridional wave-number. The $\sin(m\omega)$ term is omitted in this example, as antisymmetric bifurcation terms are not included in AQUINAS' FE formulation (see corresponding discussion in Chapter 3).

The buckling modes for spherical shells of different radius over thickness ratios are examined, running from an $r/t = 50$ up to $r/t = 2000$ with the shell wall being kept at a unit thickness $t = 1.0mm$. The classical elastic buckling pressure p_{cl} Hutchinson (2016) is applied, given by

$$p_{cl} = \frac{2E}{\sqrt{3(1-\nu^2)}} \left(\frac{t}{r_\theta}\right)^2 \tag{A.10}$$

for which the degree n of the associated Legendre function can be found from:

$$n(n+1) = \sqrt{12(1-\nu^2)}\frac{r}{t} \tag{A.11}$$

Both the degree n and the order m are restricted to be of integer nature Hutchinson (2016), with $(0 \leq m \leq n)$. An axial displacement w restraint is applied at the base of the spheres, while the circumferential displacement v is restrained at both apexes. The geometry of this spherical shell problem is presented in Figure A.47.

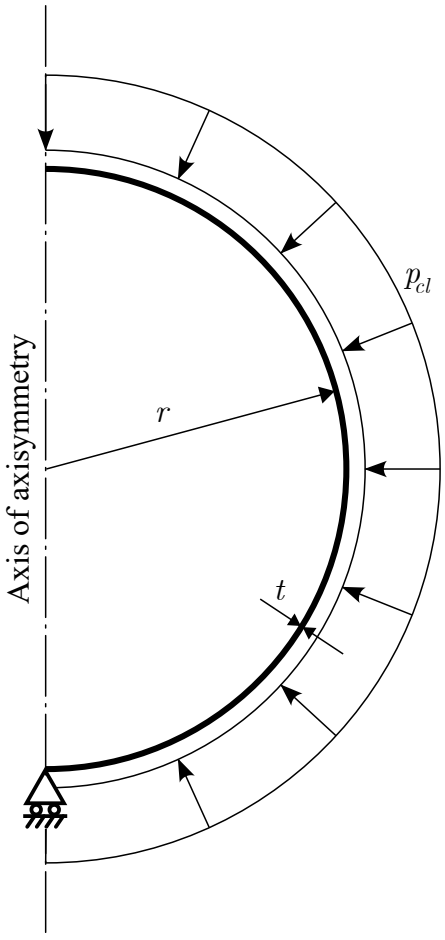


Figure A.47: LBA05 - System diagram.

The bifurcation modes obtained for each r/t ratio from AQUINAS are then post-processed in order to identify which spherical harmonic of Eq. (A.9) best fits the mode, and determine the degree n and order m of the Legendre polynomial. The normalised critical pressure, as well

as the degree of the associated Legendre polynomial obtained from the FE solution here, are plotted and compared against the classical theory presented in Hutchinson (2016) in Figures A.48 and A.49. An additional figure can be obtained if the Surrogate Model Optimisation option is disabled, where the 3D surface of degrees n and order m for every r/t ratio are computed and showcased in Figure A.50.

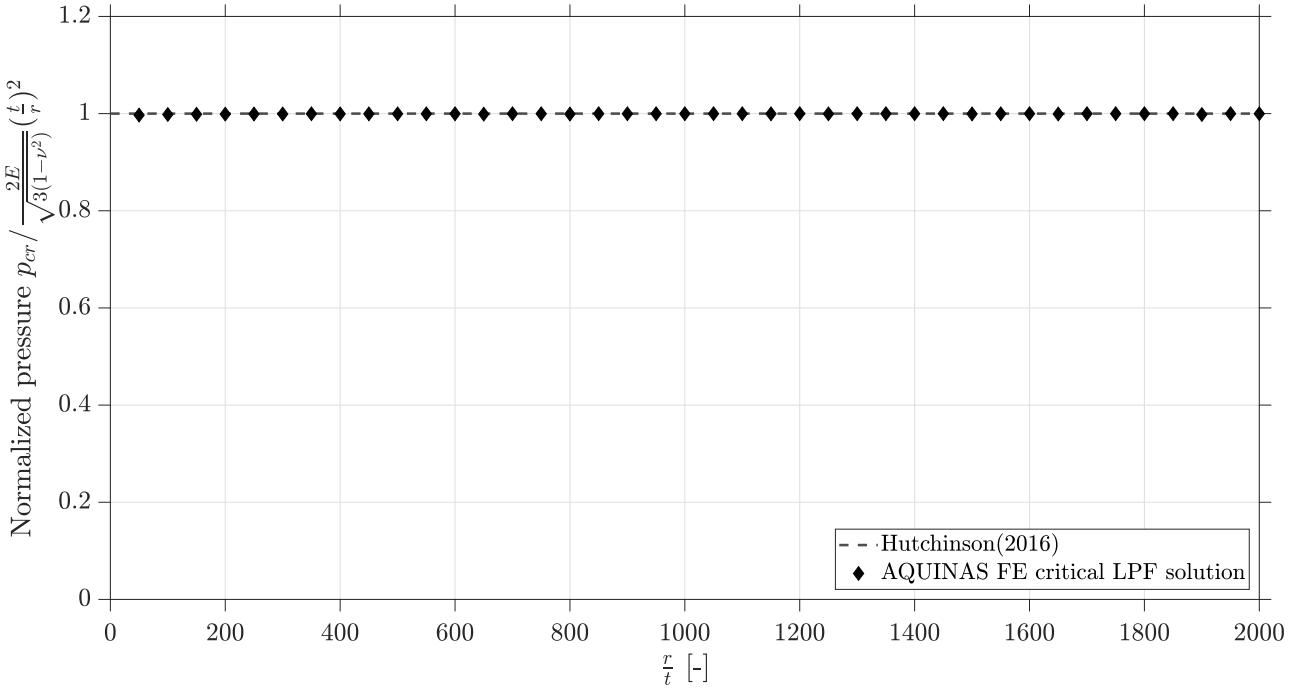


Figure A.48: LBA05 - Normalised critical bifurcation pressure for varying r/t ratios of full spherical shells.

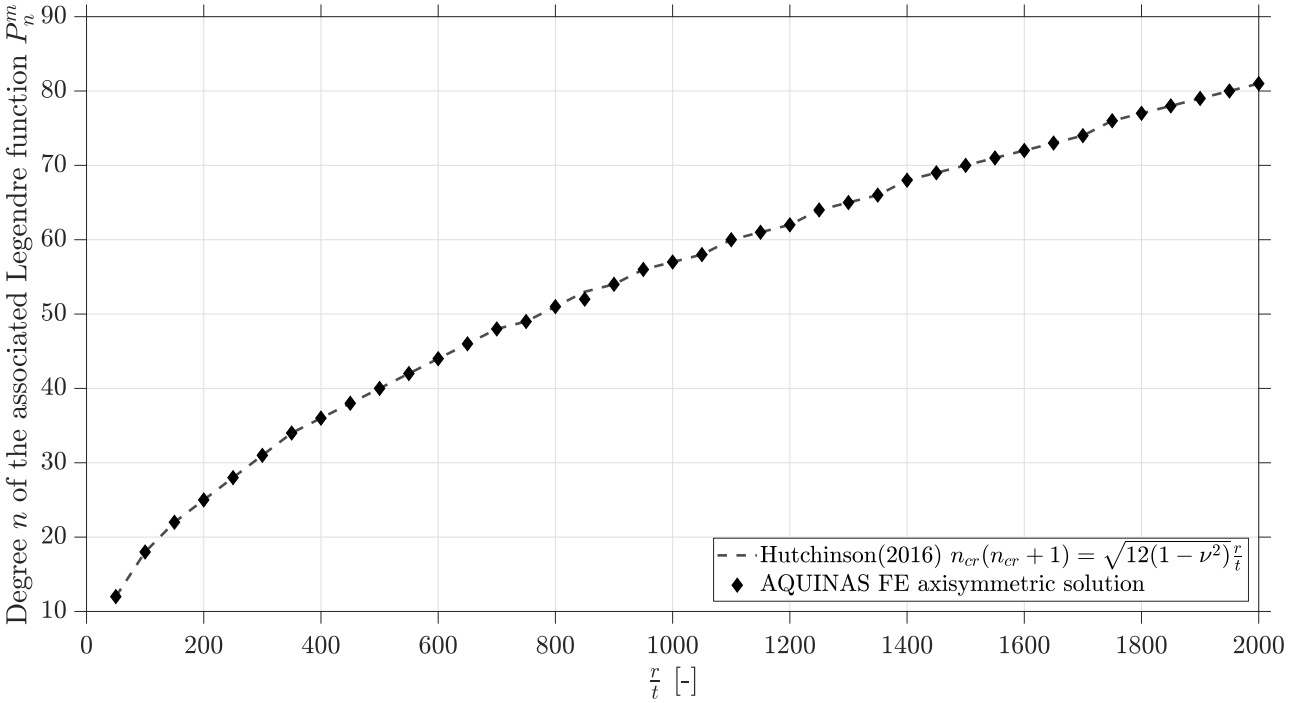


Figure A.49: LBA05 - Critical circumferential mode for varying r/t ratios of full spherical shells under external pressure.

The LBA results of AQUINAS seem to very accurately predict not only the critical pressure

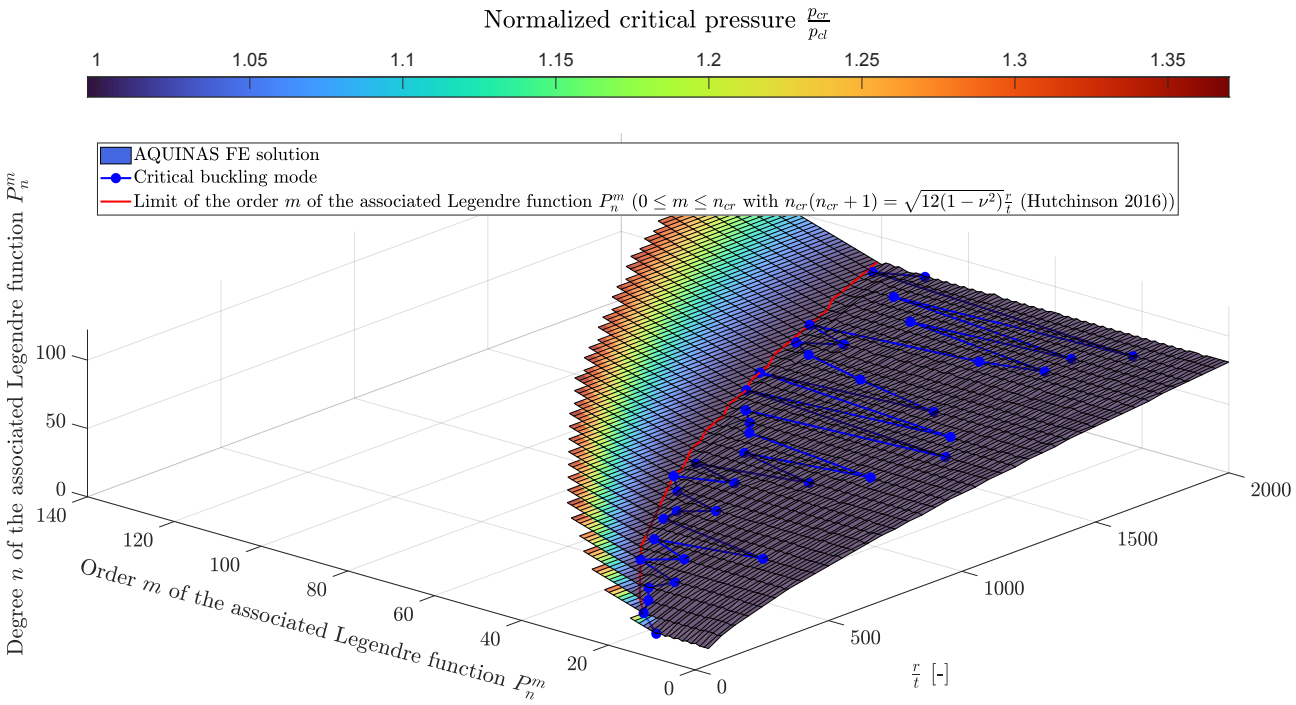


Figure A.50: LBA05 - Order m and degree n of associated Legendre polynomials for spheres of varying r/t ratios under external pressure.

p_{cr}, but also the bifurcation modes. The reader should not be alarmed if on consecutive runs of `input_Example_LBA05.m`, with and without the surrogate optimization algorithm employed, the order m (circumferential mode) is found to vary, as this is a consequence of all the competing circumferential modes essentially coexisting at the same load level (provided they refer to an order m that is less than the degree n of the associated Legendre polynomial).

A.4 MNAs

Axisymmetric shells may exhibit yielding, either local or global, as they are incrementally loaded to failure. Neglecting the effects of geometric nonlinearities, an MNA (as this type of analysis has been defined in Section 1.2.2 in the context of EN 1993-1-6 (2025)) may be executed with AQUINAS through the `AQUINAS_GMNA` script, following the procedure presented in Section 3.7.3.3. The stresses are computed on the through thickness fibres of the shell wall, checking for yielding of each individual point. In the case that elastic trial stress increment for a material point is found to be outside the yield surface, the corresponding strain increment will be applied through sub-increment that will allow the integration of the elastic-plastic strains. A correction will be applied at the end of the sub-increments that will bring the stresses closer to the yield surface, within a specified tolerance.

A series of examples will be presented in this section, exploring the materially nonlinear behaviour of axisymmetric shells models. The computed elastic-plastic stress distributions can be found to develop in an irregular pattern, especially in the case of a circular plate under bending for `input_Example_MNA02.m`. While this is the case, the Load Proportionality Factor (LPF) that leads to a plastic collapse mechanism seems to be accurately predicted, even for this second MNA problem. As stated in the beginning of the current manual, AQUINAS is meant to be an active, ongoing project with constant updates in its repository. The oscillating stress distributions that are currently computed for axisymmetric shells deep into plasticity constitute a chief reason for such an update, to be addressed at a later release of AQUINAS.

A.4.1 Example MNA01: MNA of a thin cylinder under uniform meridional compression

A cylindrical shell model will be once again used as the first benchmark to present the AQUINAS FE results, in this case in the challenging domain of materially nonlinear analyses. The cylinder under investigation has a radius $r = 1000.0\,mm$ and its total length is set to $L = 1000.0\,mm$, with a shell wall of unit thickness $t = 1.0\,mm$. A BC2f / S3 restraint is applied at its top edge and a BC1f / S1 at its base. An elastic perfectly plastic material is considered, with a yield stress $f_y = 250\,N/mm^2$. Its elastic properties are identical to those used in previous examples ($E = 200000.0\,N/mm^2$ and $\nu = 0.3$). The compressive line edge load N applied at the top end of the shell is incremented using the arc-length method, as plasticity gradually extends from the bending boundary layers of the cylinder to the membrane region of its meridian. The geometry and boundary conditions are presented in Figure A.51.

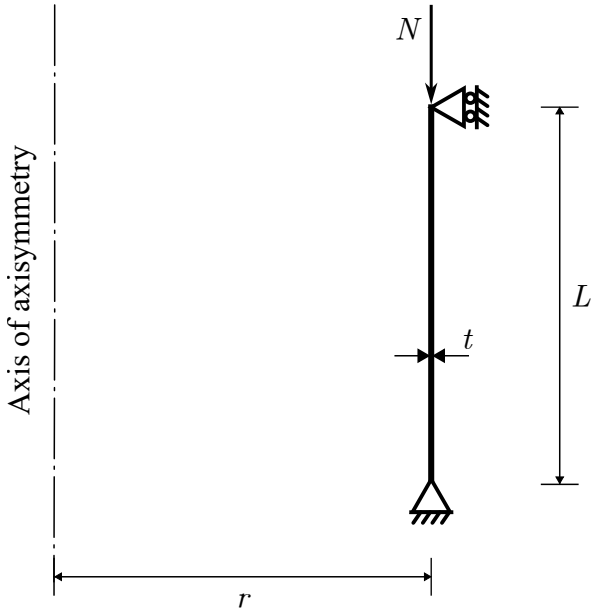


Figure A.51: MNA01 - System diagram.

For this example there is no external source of comparison, as the validity of the resulting equilibrium path can be assessed on intuition alone. A purely elastic behaviour is to be expected of the cylinder until the von Mises stress at any of the material points used for tracking plasticity in the shell wall crosses the yield surface. This will mark the onset of plasticity, leading to a plateauing behaviour for the cylinder where it continues to deform for very small changes in the line load N applied. For the elastic-perfectly plastic material that is considered for the present model, the plateau in the equilibrium path should correspond to an edge line load of $N = f_y t$. This exact behaviour is illustrated in Figure (A.52) through the equilibrium path for the cylinder under compression as obtained from an AQUINAS MNA. It may be appreciated that both the initial elastic behaviour and the plastic plateau of the cylindrical shell model, deep into which yielding has spread across the entirety of the shell's meridian and the arc-length increments applied are associated with minimal changes of the LPF.

A.4.2 Example MNA02: MNA of a simply-supported circular plate under concentrated load

This MNA example serves to illustrate the ability of AQUINAS to predict another axisymmetric shell's strength, but also as a demonstration of the occasional ruggedness of the stress

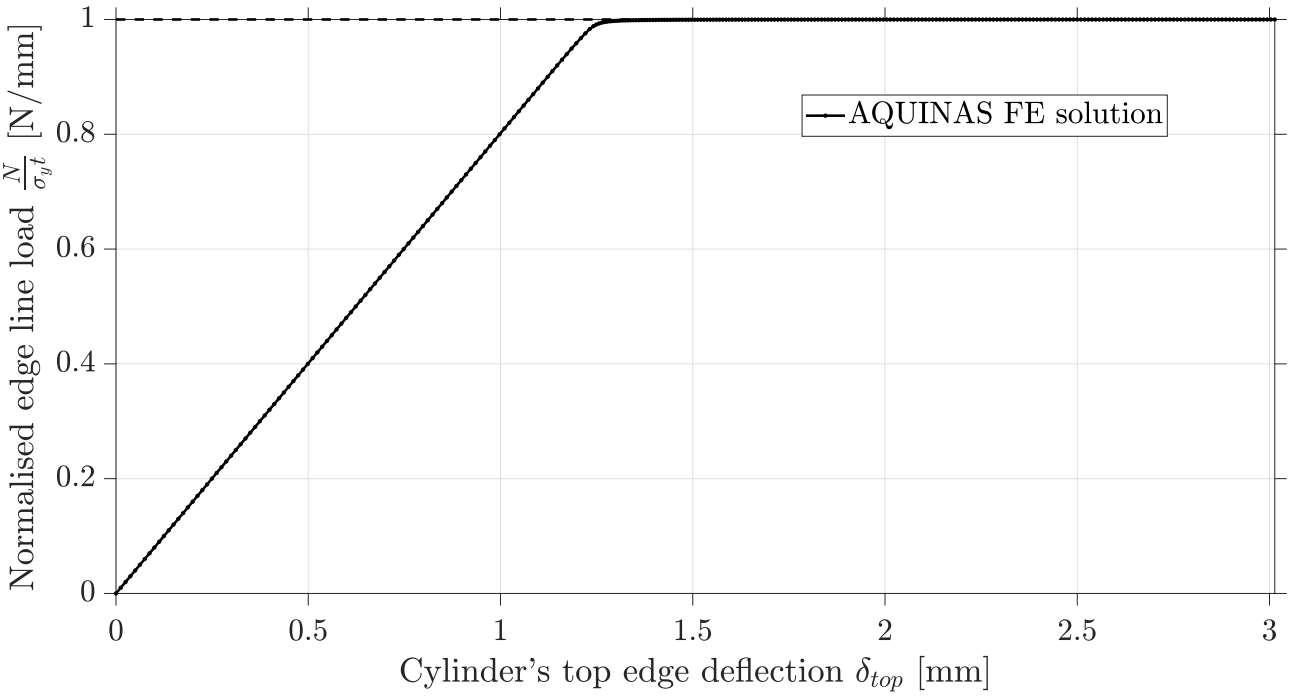


Figure A.52: MNA01 - Top edge deflection equilibrium path for a thin unpressurised cylinder under meridional compression.

distributions obtained deep into plasticity.

The model under investigation is a circular plate of radius $r = 100.0\,mm$ with a shell wall of thickness $t = 10.0\,mm$. The material is once again elastic perfectly plastic, with its yield stress set to $f_y = 250\,N/mm^2$. A BC1f boundary condition is applied at the edge of the plate, as can be seen in Figure A.53 where the geometry of this materially nonlinear shell problem is illustrated.

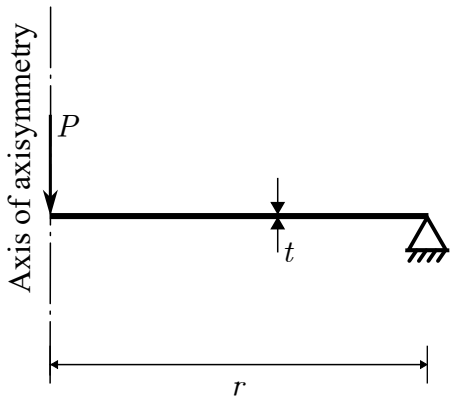


Figure A.53: MNA02 - System diagram.

The equilibrium response of the circular plate's centroid is presented in Figure A.54, illustrating a similar nonlinear and slowly plateauing behaviour that can be seen in Figure 4 of Teng & Rotter (1989a), the source publication of the AQUINAS FE toolbox. Plasticity spreads from the centre of the plate towards its BC1f edge, with the middle fibre of the cross section remaining completely unstressed for every integration station along the meridian. Larger deformations occur as the plate is fully yielded and the externally applied concentrated force asymptotically tends to $P = 2\pi M_p$. While this first result is very promising for the implementation of the AQUINAS' materially nonlinear solution process, the distributions of the bending stress resultants M_ϕ and

M_θ appears to be irregular, as the reader may observe from Figures A.55 - A.56. As yielding spreads across the meridian of the circular plate, 'residual' bending stress resultants arise where elements meet, with this effect being considerably more significant towards the centre of the axisymmetric shell model. This behaviour does not seem to occur in Teng & Rotter (1989a), where the bending stress resultant distributions are smooth, even deep into plasticity where the plate has fully yielded, with the author's interpretation of this result and its underlying causes provided in Section 6.4.

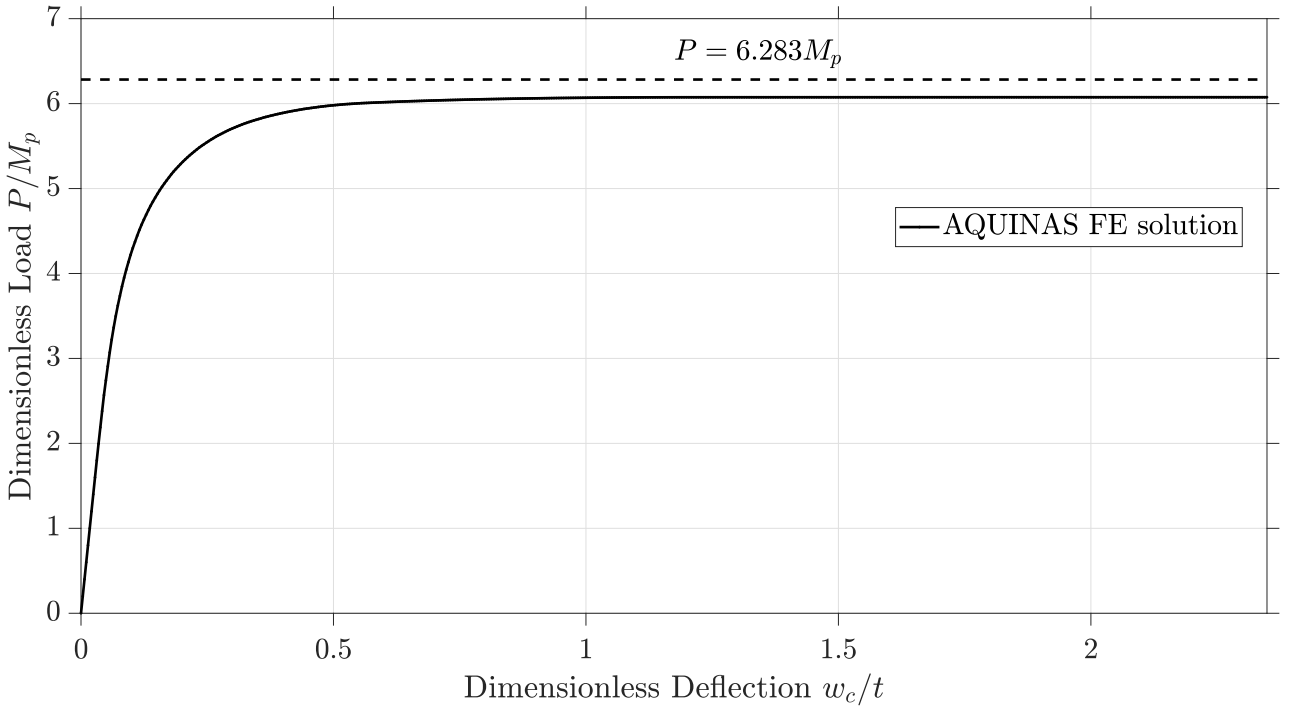


Figure A.54: MNA02 - Dimensionless deflection equilibrium path of circular plate's centroid w_c.

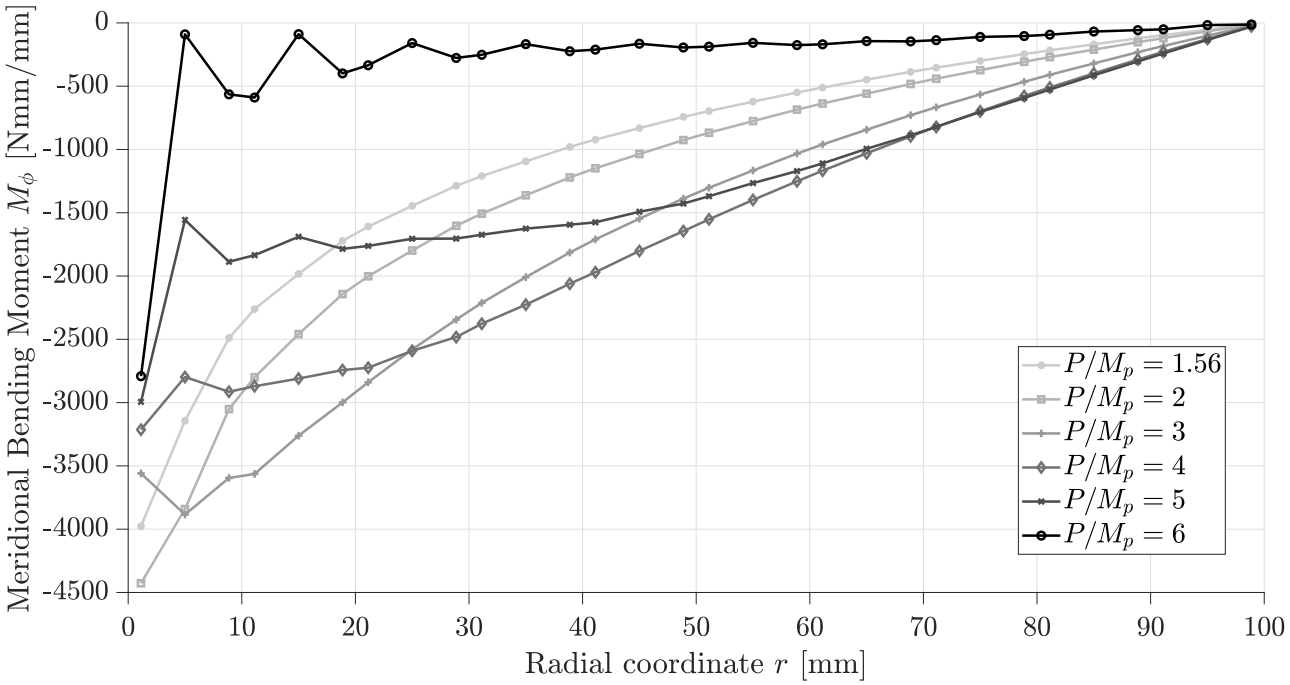


Figure A.55: MNA02 - Development of meridional membrane stress resultants M_ϕ.

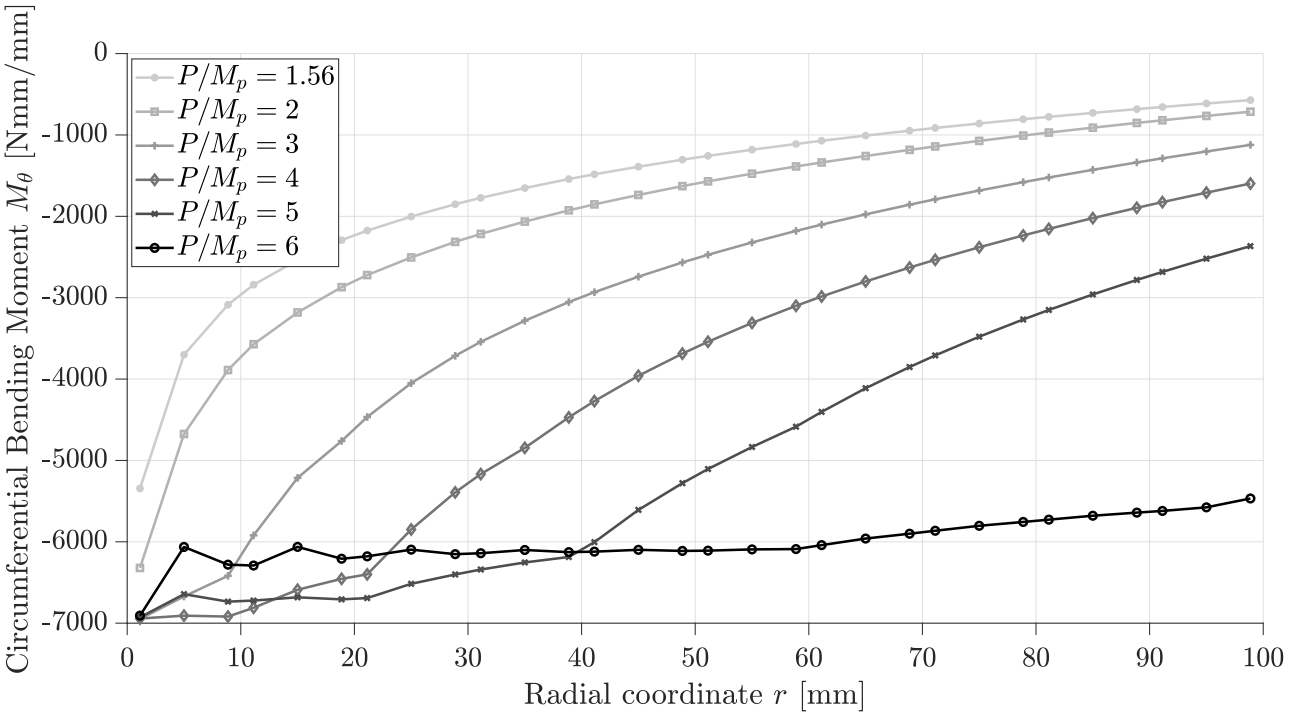


Figure A.56: MNA02 - Development of circumferential membrane stress resultants M_θ.

A.4.3 Example MNA03: MNA of a clamped spherical caps under uniform external pressure

In `input_Example_MNA03.m`, the limit loads of spherical caps under external pressure are obtained for a series of meridional angle spans ϕ_0. The shell wall is of unit thickness $t = 1.0\,mm$ for all of the spherical models with their radius of meridional curvature set to $r = 12.5\,mm$. A BC1r - C1 boundary condition is applied at the edge of the spherical caps, as illustrated in Figure A.57.

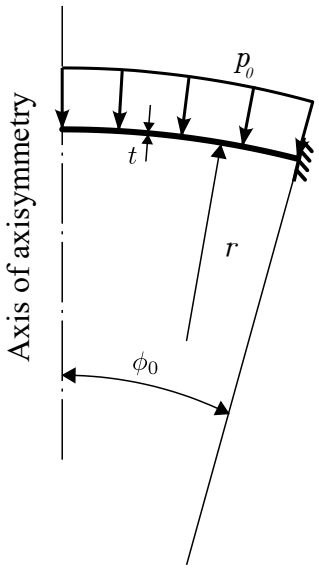


Figure A.57: MNA03 - System diagram.

The material is characterised by a yield stress of $f_y = 250\ N/mm^2$, with no strain hardening considered. Comparison is made with the limit loads obtained through digitisation from Teng and Rotter (1989a) Teng & Rotter (1989a), computed with the same underlying shell formulation.

The reader may appreciate the good agreement between the FE solutions, as presented in Table A.6, subject to the quality of a digitisation process.

Table A.6: MNA03 - Limit loads of clamped spherical caps under uniform pressure.

ϕ_0	Teng & Rotter (1989a)	AQUINAS
15°	75.897	77.65
20°	56.296	53.587
30°	43.077	43.173
40°	41.937	41.359
50°	41.026	40.669
60°	41.026	40.353

A.5 GNAs

The inherently nonlinear load bearing response of thin axisymmetric shells is analysed in AQUINAS through the master script `AQUINAS_GMNA.m`, responsible for the execution of both geometrically and materially nonlinear analyses. In this section, the equilibrium paths of axisymmetric FE shell models are explored, with the added consideration of geometrical nonlinearities as they are incrementally loaded to failure. The effects of geometrical nonlinearities as they bifurcate into a circumferential mode n will also be investigated, since the critical circumferential harmonic, associated with the lowest buckling load, may change as the analysis progresses and the shell models stress and deform.

As a special case of GNAs, GNIAs of shells will also be examined in the following section, with the imperfect shape of the shell's meridian being modelled through the segment object rather than being defined as a perturbation shape at the level of submitting an analysis. With analytical results being scarce on the topic, the focus will be on comparisons with established computational solutions in relevant literature.

A.5.1 Example GNA01: GNA of thin cylindrical shells under uniform meridional compression

Thin cylinders under axial compression are once again put to the test, in the form of a benchmark example, with the aim of establishing the accuracy of geometrically nonlinear solutions with AQUINAS. Cylinders of various lengths, parametrised with respect to the Batdorf parameter of Eq. (A.3) are submitted for a GNA that aims at computing the nonlinear buckling load, as well as the associated circumferential mode n.

All of the cylinders have a constant radius $r = 1000.0\,mm$ and thickness of $t = 1.0\,mm$. A BC2f-S3 boundary condition is applied at the top edge of the cylinders and a BC1f-S1 at their base. An edge load of magnitude equal to the buckling load of Eq. (2.19) is applied at their top edge. The geometry, loading and boundary conditions of the cylinders are identical to those of LBA01 as illustrated in Figure A.37. Comparison is made with results obtained through the 'panel analysis' technique , with ABAQUS (2022) being the FE solver of choice by the analysts in Sadowski *et al.* (2018). Axisymmetric shell models, that may only bifurcate into a zeroth harmonic mode $n = 0$, are also included in the comparison, as well as analytical ones based on the derivations of Yamaki (1984). As a consequence of Yamaki's solutions assuming a meridional symmetry of the boundary conditions, which is not the case for the cylinders analysed in AQUINAS or in Sadowski *et al.* (2018), they are treated as an upper-lower bound for

the computationally obtained for the critical buckling loads N_{GNA} computed. The comparison for the range of Batdorf parameters considered is shown in Figure A.58.

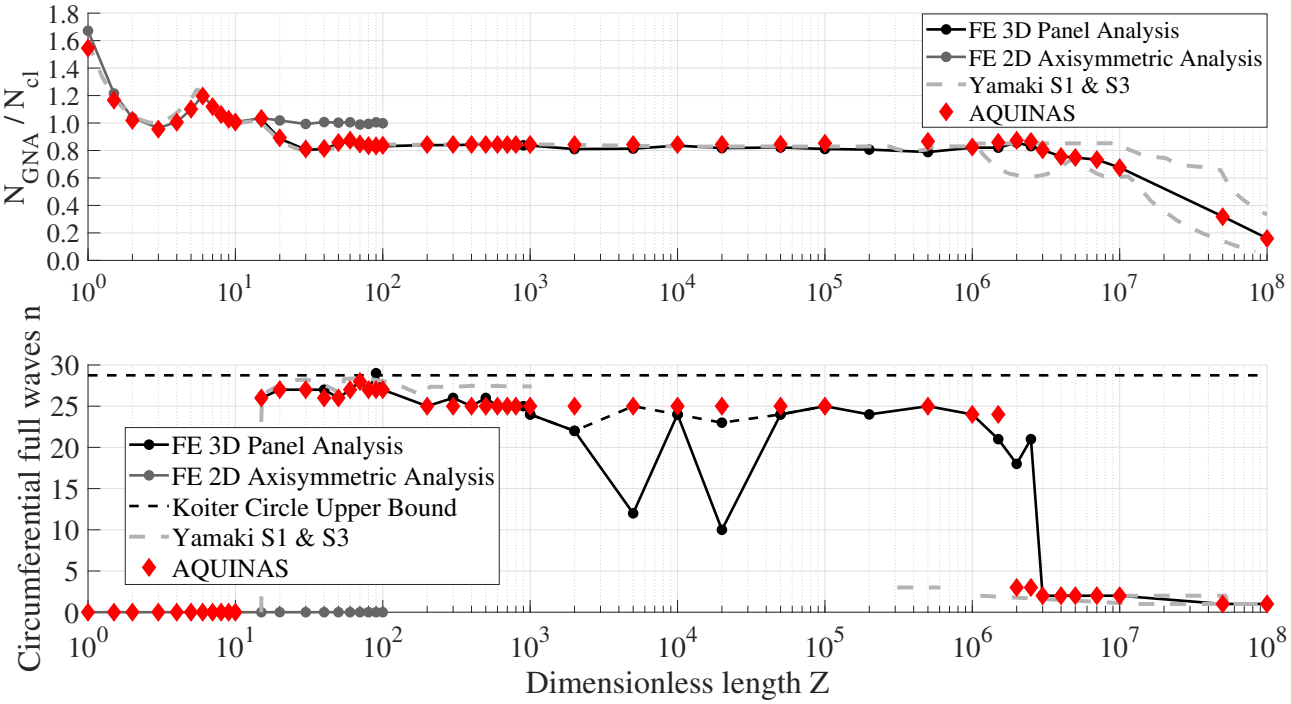


Figure A.58: GNA01 - Comparison of geometrically nonlinear critical bifurcation loads and associated circumferential modes for cylinders of varying length under axial compression.

The reader may appreciate that the predictions made by AQUINAS for the critical buckling load N_{GNA} and the associated circumferential mode n fall very close to those of the rest of the results included in the comparison. As discussed earlier, Yamaki's S1 and S3 solutions serve as upper-lower limits for the S1-S3 models analysed by AQUINAS, and indeed the FE computed results keep within all available bounds. Furthermore, AQUINAS illustrates a robust behaviour in the medium-length range of cylinders, where as explained in Sadowski *et al.* (2018) the 'panel analysis' technique faces numerical problems. A further exploration of how the bifurcation loads related to competing circumferential modes n develop alongside the Batdorf parameters Z is presented in Figure A.59, obtained using the capability of AQUINAS to consistently obtain an eigenvalue for a trialled harmonic n. The reader is cautioned however at this point that any AQUINAS result other than the one associated with the actually critical harmonic n for each cylindrical model is an estimate rather than a computation. AQUINAS will terminate the nonlinear analysis at the first bifurcation event, which corresponds to an eigenvalue equal to unity for any of the trialled circumferential modes. Hence, while AQUINAS has traced the nonlinear path of the axisymmetric shell model all the way to bifurcation into a specific mode with an eigenvalue of one, the rest of the competing harmonics have a higher associated eigenvalue. This result can be viewed as kind of a modified LBA, where the equilibrium path for the shell is traced up to some non-critical load level. As is the case with LBA results, the further the eigenvalue is from unity the higher the potential error in the critical load level prediction. Nevertheless, the reader can appreciate that for the most part of the surface presented in Figure A.59, the bifurcation loads predicted for the non-critical modes are reasonably close to the harmonic computed as critical, validating to some extent the estimations presented these surfaces. The AQUINAS surface is smooth for all Batdorf parameters analysed, a result that was only obtained due to the inclusion of the circumferential mode n into the FE formulation.

As is always the case with the example scripts presented in the current document, the reader

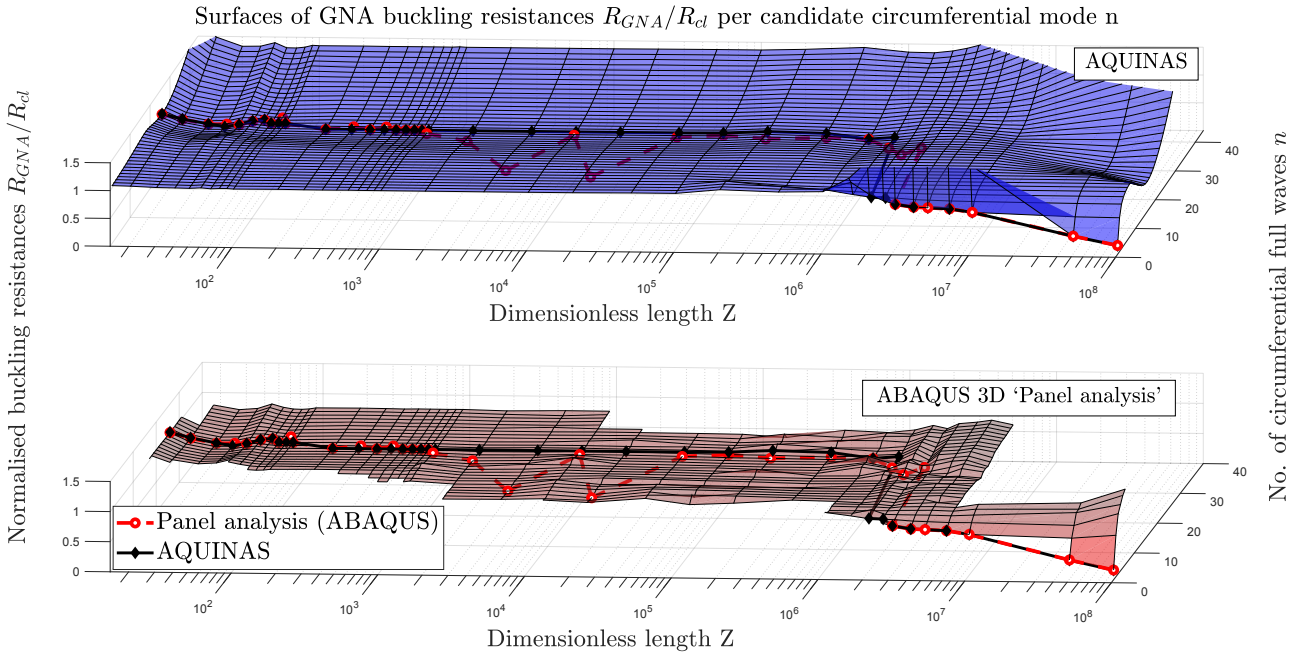


Figure A.59: GNA01 - Automated identification of the critical geometrically nonlinear GNA bifurcation buckling load for a thin cylindrical shell under uniform meridional compression as a function of the Batdorf dimensionless length parameter Z, with comparison against the 3D 'panel models' from ABAQUS.

may wish to run the script for themselves and examine the solution, or perhaps alter some of the parameters that define these cylindrical shell problems. Caution should be exercised in interpreting the generated plots if any of the parameters are altered, since the results included for comparison are loaded from a `.csv` file for the geometry, loading and boundary conditions discussed here. Additionally, running this example may take some time.

A.5.2 Example GNA02: GNA of the Belleville spring

An example that makes direct comparison with results presented in the publication from which AQUINAS shell formulation originates (Teng & Rotter, 1989a), `input_Example_GNA02.m` explores the equilibrium path of the Belleville spring. The snap-through behaviour of the conical shell structure assesses the nonlinear Riks solver in AQUINAS, as it has to identify the limit point and then trace the descending portion of the equilibrium path all the way until the stiffness turns positive again. The Belleville spring, which essentially is a shallow conical shell with its apex truncated, has an outer edge radius of $r_1 = 7.62\,cm$ and an inner one of $r_2 = 2.54\,cm$. The shell wall has a thickness of $t = 0.508\,cm$ and the height of the conical segment is $h = 1.27\,cm$. The material does not share its properties exactly with the steel material considered thus far, with its modulus of elasticity being $E = 2.1 \cdot 10^3\ kg/cm^2$ (Poisson's ratio is still $\nu = 0.3$). A vertical line load N is applied at the top/inner edge of the spring, the base of which is fully clamped. The geometry, loading and boundary conditions are displayed in Figure A.60.

The equilibrium path for the inner edge deflection δ obtained from AQUINAS is compared in Figure A.61 against the data points from Surana (1982) and the FE solution from Teng & Rotter (1989a), both digitised from the latter source. Great agreement is illustrated between the AQUINAS solution and Teng & Rotter (1989a), a consequence of the two FE software sharing the same shell formulation, and the discrepancies with the results of Surana (1982) that were

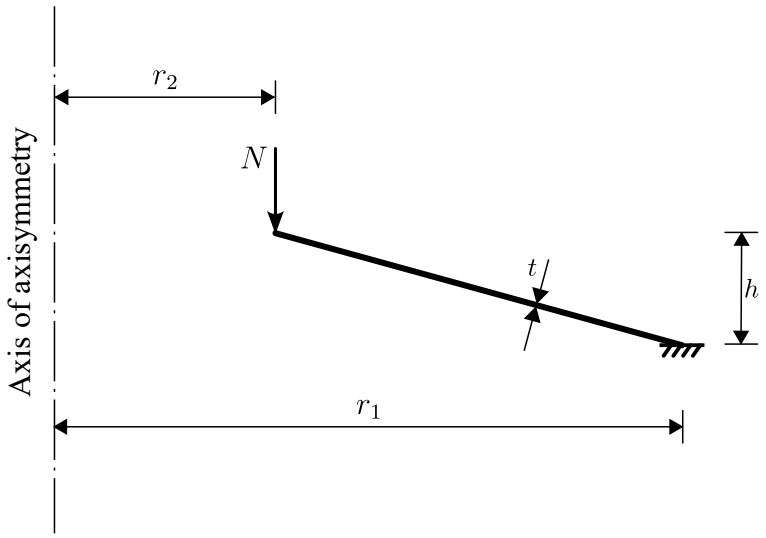


Figure A.60: GNA02 - System diagram.

observed in Teng & Rotter (1989a) also occur here.

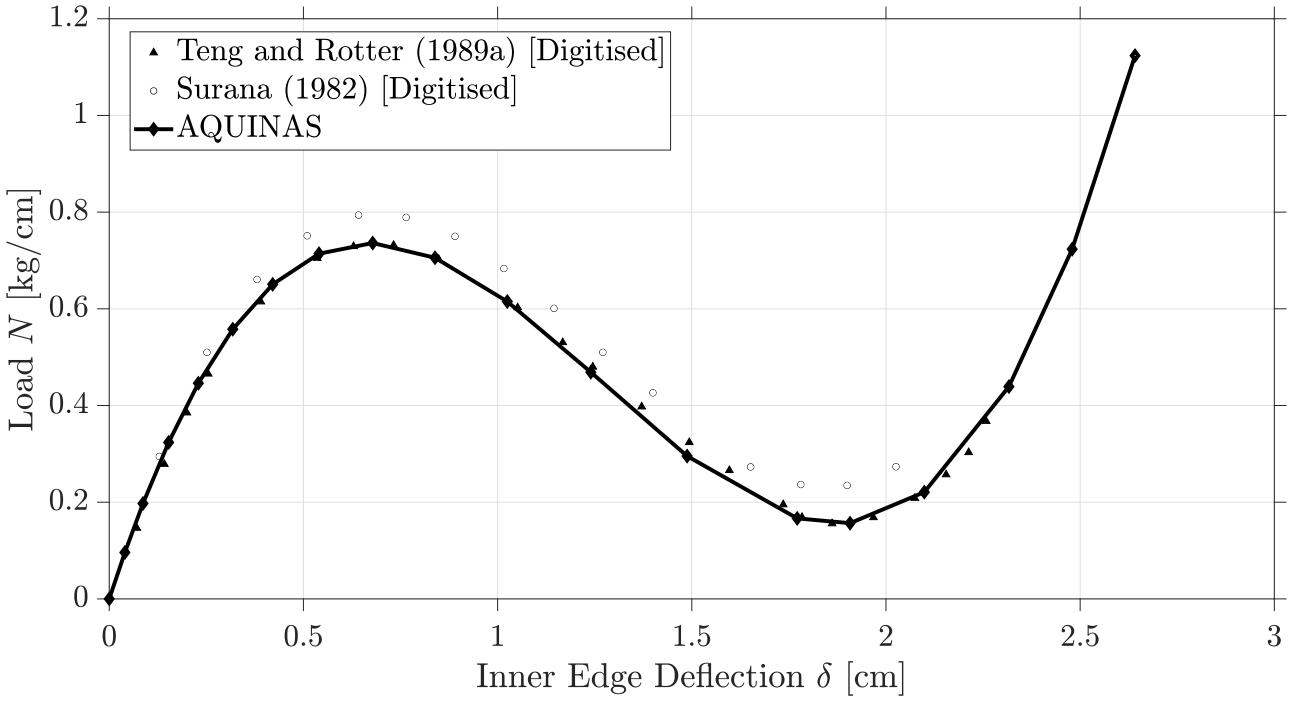


Figure A.61: GNA02 - Equilibrium path for the Belleville spring.

A.5.3 Example GNA03: GNA of a thin spherical cap under uniform external pressure

After exploring a couple of geometrically nonlinear analyses of axisymmetric shells with straight meridians, it is time to move on to doubly-curved shells. In `input_Example_GNA03.m`, the load-deflection path of a spherical cap's apex deflection under the effect of uniform external normal pressure is examined. The definition of this nonlinear shell problem is illustrated Figure A.62.

Comparison is once again made with the FE results from Teng & Rotter (1989a), but also from the established solution of Bathe *et al.* (1975), both obtained through digitisation from

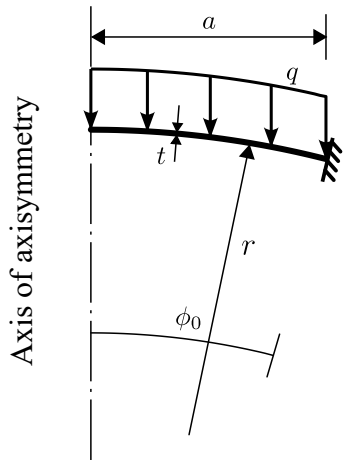


Figure A.62: GNA03 - System diagram.

Teng & Rotter (1989a). The spherical cap has a radius of $r = 2540.0\,mm$ and a thickness of $t = 12.7\,mm$, with its outer edge located at a meridional angle of $\phi_0 = 7.1°$. The material used in this GNA example is slightly different from the one used in most of the previous examples, with its Young's modulus being $E = 207000\,N/mm^2$ and its Poisson's ratio still set at $\nu = 0.3$. A BC1r boundary condition is applied at its edge. The excellent agreement between AQUINAS and both FE solutions is illustrated in Figure A.63.

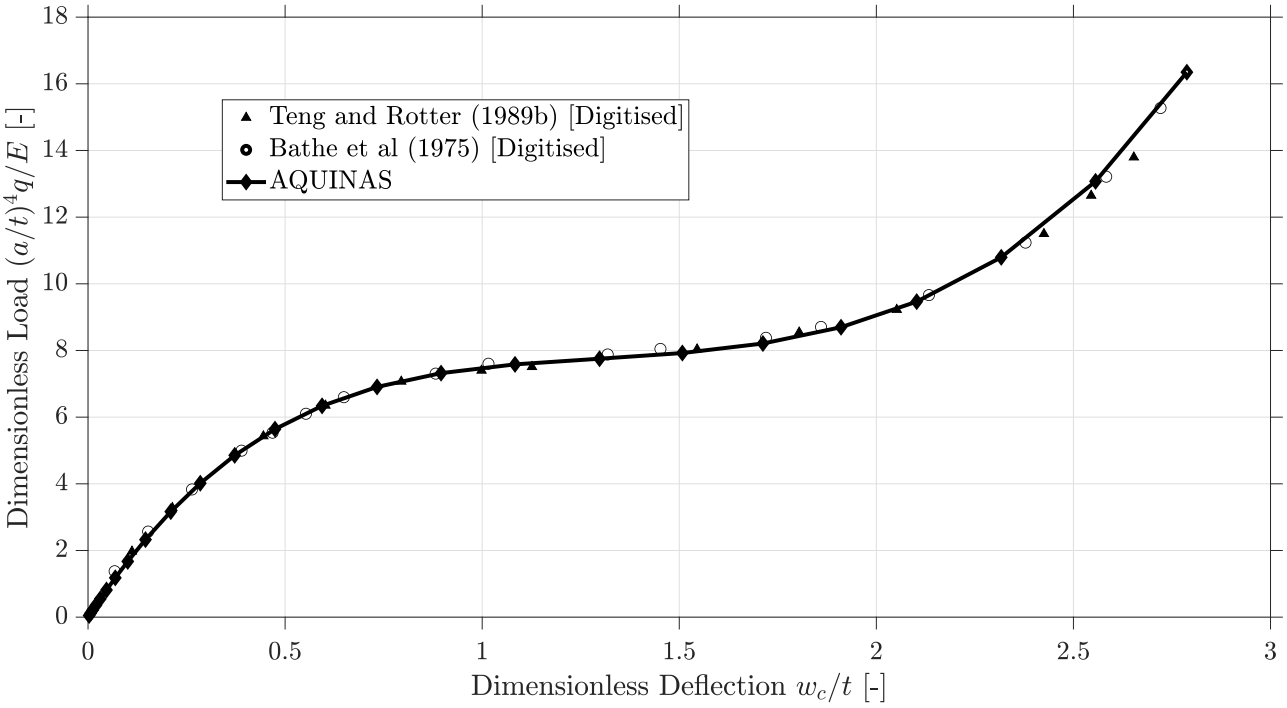


Figure A.63: GNA03 - Equilibrium path for apex deflection of shallow spherical cap under external

A.5.4 Example GNA04: GNA of a ring-loaded thin spherical cap

Another benchmark test that makes direct comparison with results from the source Teng & Rotter (1989a) of the AQUINAS shell formulation, `input_Example_GNA04.m` explores the equilibrium path of a ring-loaded thin spherical cap apex's deflection as illustrated in Figure A.64.

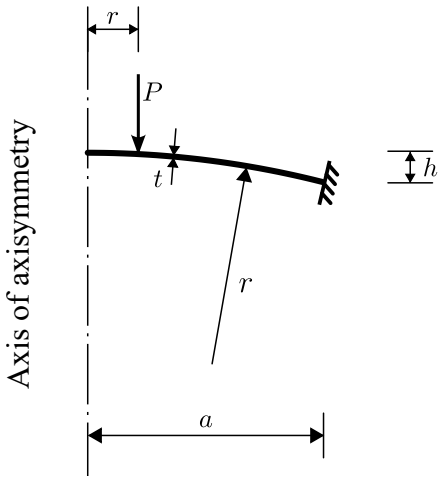


Figure A.64: GNA04 - System diagram.

Two load cases are considered, one where the load P is applied directly at the apex of the spherical cap ($r = 0$, concentrated load) and a second one where the load is applied as a ring load a distance $r = 0.42a$, where a is the projection of the spherical cap to the radial coordinate axis. The radius and thickness of the spherical cap's meridian are set to $r = 4.758\,in$ and $t = 0.01576\,in$ accordingly, while the projection a of the cap into the radial axis is $a = 0.9\,in$. The edge of the spherical cap is fully clamped. The two load-deflection paths of the spherical cap's apex deflection w_c are presented in Figure A.65. Comparison is made not only with the FE results of the source publication Teng & Rotter (1989a), but also with the computational solution of Wood & Zienkiewicz (1977). All three approaches seem to be in perfect agreement, for both the load cases considered, regardless of whether a limit point is observed on the equilibrium path of the spherical cap.

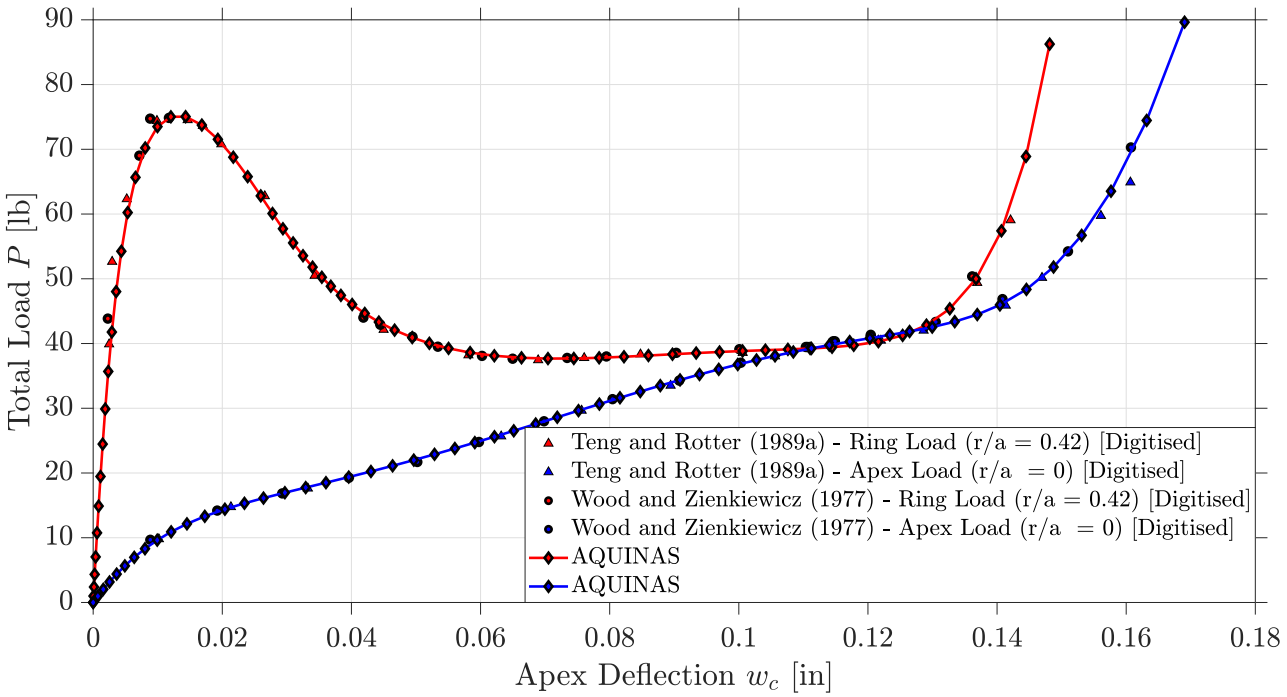


Figure A.65: GNA04 - Load-deflection curves of ring loaded spherical caps

A.5.5 Example GNA05: Snap-through of a shallow spherical cap

Computing the snap-through load of an axisymmetric shell in AQUINAS is equivalent to the evaluation of the limit point in the shell's response, identified as the point where the determinant of the tangent stiffness changes sign. In `input_Example_GNA05.m`, the snap-through loads for a range of shallow spherical caps are computed and compared against those obtained from the works of Budiansky (1959) and Dumir *et al.* (1984). The caps are parametrised with respect to a rise parameter λ (not to be confused with the slenderness parameter of a shell system λ), given as:

$$\lambda = 2[3(1-\nu^2)]^{1/4}\sqrt{h/t} \tag{A.12}$$

The radius and thickness of the spherical caps are constant for all models at $r = 100.0\,mm$ and $t = 1.0\,mm$ accordingly, with only the height h of the caps (projection on to the axial coordinate axis z) varying according for each λ of Eq. (A.12). The characteristic pressure p_0 applied on the spherical caps is set to:

$$p_0 = \frac{2Et^2}{r^2\sqrt{3(1-\nu^2)}} \tag{A.13}$$

The edge of the spherical caps considered are fully clamped. The geometry, loading and boundary conditions of the cap models are presented in Figure A.66, while the numerical comparison of the snap-through loads for each rise parameter λ is summarised in Table A.7. As expected, the AQUINAS results are very close its parent publication Teng & Rotter (1989a), with any minor discrepancies attributed to differences in the implementation or discretisation of the spherical caps.

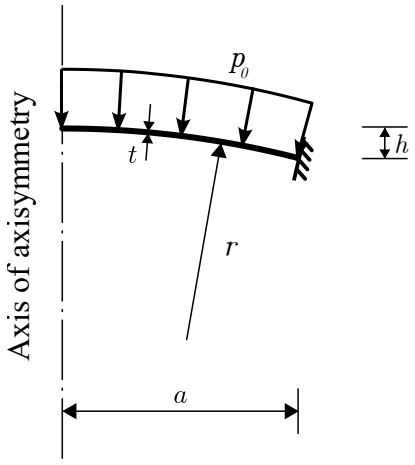


Figure A.66: GNA05 - System diagram.

A.5.6 Example GNA06: Nonlinear buckling analysis of a clamped shallow spherical cap under uniform external pressure

As discussed earlier, the critical circumferential mode that the axisymmetric shell wants to bifurcate into may change as the nonlinear analysis proceeds yielding a different result to the LBA prediction. The script `input_Example_GNA06.m` identifies the critical buckling pressures and associated modes n of shallow spherical shell models, similar to the ones analysed in these last GNA examples. The geometry of the caps is once again characterised with the aid of

Table A.7: GNA05 - Snap-through loads $\frac{p_{cr}}{p_0}$ of shallow clamped spherical caps for a range of rise parameters λ.

λ	Budiansky (1959)	Dumir *et al.* (1984)	Teng & Rotter (1989a)	AQUINAS
4	0.578	0.580	0.563	0.560
5	0.629	0.630	0.615	0.619
5.5	0.789	0.785	0.746	0.754
6	0.995	0.986	0.972	0.968
7	1.068	1.042	1.046	1.040
8	1.130	1.115	1.109	1.103

the rise parameter λ of Eq. (A.12), with the magnitude of the external pressure p_0 applied determined from Eq. (A.13). The radius and thickness of the spherical caps is $r = 100.0\,mm$ and $t = 1.0\,mm$, constant for all models, while their outer edge is fully clamped. This nonlinear axisymmetric shell problem is presented in Figure A.67, with the critical buckling pressure ratios p_{cr}/p_0 and associated modes n_{cr} showcased in Tables A.8 and A.9 accordingly. The FE results obtained from AQUINAS are not only compared with those of Teng & Rotter (1989b), but also with the computational solution of Huang (1964). A good agreement between the three nonlinear computations is showcased, with minor differences that may be attributed to the critical circumferential mode identification scheme applied (see discussion in Teng & Rotter (1989b)), as well as to the extensive inclusion of terms pertaining to the bifurcation of axisymmetric shells in the continuation publication of the previous article by the same authors (Teng & Rotter, 1989a).

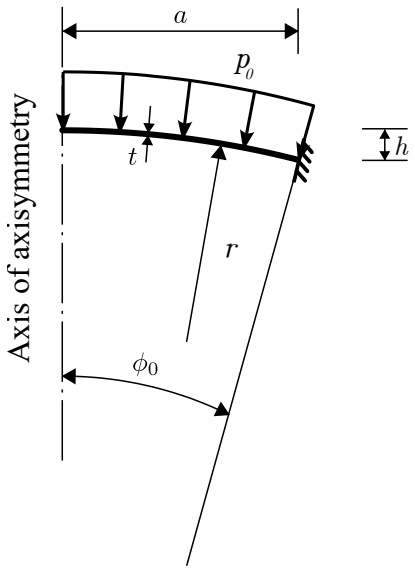


Figure A.67: GNA06 - System diagram.

A.6 GNIAs

Midsurface imperfections can be explicitly defined in AQUINAS at the level of generating an axisymmetric shell segment. The imperfect shape is approximated through an Akima interpolation (Akima, 1970) that fits a polynomial of up to cubic order on the series of points provided as input to the `AQUINAS_Segment_Object`. It is important to remember that these imperfection shapes are purely axisymmetric, since AQUINAS neglects any circumferential

Table A.8: GNA06 - Critical nonlinear buckling pressure ratios p_{cr}/p_0 for a range of rise parameters λ.

λ	$\frac{p_{cr}}{p_0}$ of Huang (1964)	$\frac{p_{cr}}{p_0}$ of Teng & Rotter (1989b)	AQUINAS $\frac{p_{cr}}{p_0}$
6	0.775	0.777	0.768
7	0.760	0.763	0.754
8	0.766	0.769	0.762
9	0.777	0.778	0.773
10	0.776	0.778	0.772
12	0.780	0.782	0.778
14	0.782	0.787	0.784
16	0.790	0.792	0.789

Table A.9: GNA06 - Critical circumferential buckling mode n_{cr} for a range of rise parameters λ.

λ	n_{cr} of Huang (1964)	n_{cr} of Teng & Rotter (1989b)	AQUINAS n_{cr}
6	2	2	2
7	3	3	3
8	4	4	4
9	4	4	5
10	5	5	5
12	7	7	7
14	9	9	9
16	11	11	10

displacements in tracing the pre-buckling response of any shell. The analysis submitted shares all of its formulation and processing aspects as those of the GNAs presented in the previous section.

A.6.1 Example GNIA01: GNIA of a thin unpressurised cylinder under uniform axial compression with a weld depression imperfection

The first GNIA example to be presented explores the effect of a weld depression imperfection on the strength of cylinders under meridional compression, an axisymmetric shell system also explored during the extensive generation of capacity curves demonstrating the numerical capabilities of AQUINAS in Section 3.8.1. The weld depression is positioned at the mid-height of the cylindrical shell models, where the shape of the imperfection itself is given in Eq. 3.96, repeated here for convenience as:

$$\delta = \delta_m e^{-\left(\frac{\pi|z-z_\delta|}{\Lambda}\right)} \left(\cos\left(\frac{\pi|z-z_\delta|}{\Lambda}\right) + \sin\left(\frac{\pi|z-z_\delta|}{\Lambda}\right)\right) \tag{A.14}$$

with δ_m being the mathematical amplitude of the weld imperfection, z_δ being the distance from the position of the weld along the meridian of the cylinder, k a parameter that takes the value $k = 1$ for a TYPE A weld or $k = 0$ for a TYPE B (Rotter & Teng, 1989) and Λ being the linear meridional bending half wavelength according to classical shell theory, as given earlier in this document (see Eq. 2.14).

Following the modelling guidelines of Rotter & Teng (1989), different boundary conditions are considered for the pre-buckling analysis of the axisymmetric FE models and the bifurcation checks. Boundary conditions that represent continuity at the ends of the cylindrical model are considered, with the radial displacement u being free and the rotation of the meridian β fixed. For the buckling configuration however, a BC2f - S3 boundary condition is considered at both ends, with an axial displacement w restraint applied at the position of the weld instead of the base of the cylinder (where it is applied for the pre-buckling state), to ensure that numerical issues that may arise from computation of geometric definitions through an interpolation scheme are avoided. The external load applied on top edge of the cylinders is related to the classical elastic critical stress of Eq. (2.15) so that $N = \sigma_{cl} t$.

The geometric definition of a cylinder with a TYPE A weld depression imperfection, as given by Eq. (A.14) at mid height is presented in Figure A.68 (where the boundary conditions, alternating between pre-buckling/buckling configurations of the shells, are omitted). The reader may also wish to run `input_Example_GNIA01.m` for a TYPE B weld, but should be warned that the included results for comparison are only relevant to a TYPE A imperfection shape. All of the cylindrical models are of constant unit thickness $t = 1.0\,mm$, with their radius set to $r = 1000.0\,mm$. The length of the cylindrical shell models is chosen such that $L/r = 3$.

In Figures A.69 - A.70, the nonlinear critical bifurcation loads and associated circumferential modes are plotted for a series of increasing amplitudes δ_0 for a weld depression imperfection at the mid-height of the cylindrical shell models. An almost perfect agreement is illustrated between the results presented in Rotter & Teng (1989) and Teng & Rotter (2004a), with the first one obtained through a computational analysis with the FELASH software (Rotter, 1989). On the other hand, the panel analysis results of Sadowski *et al.* (2018) display a considerable deviation from those of the three other FE solutions (AQUINAS included), making the case for the existence of the current software even stronger. The disagreement between AQUINAS and Rotter & Teng (1989) -Teng & Rotter (2004a) for the critical circumferential mode of a perfect cylinder is not considered alarming, as numerous competing harmonics n essentially coexist for the same critical level of load. The results of `input_Example_GNA01.m`, presented earlier, provide enough proof for the ability of AQUINAS to accurately predict the critical circumferential modes of cylinders under meridional compression.

The bifurcation modes for a selected few imperfection amplitudes δ_0 are also presented in Figure A.71, with the shapes normalised so that the peak modal displacement is equal to unity and scaled by a factor of 10. The reader may wish to compare those against the corresponding shapes presented in Rotter & Teng (1989) and confirm that the bifurcation modes obtained from AQUINAS are indeed valid. It should be noted that this example may take some time to run.

A.6.2 Example GNIA02: GNIA of a thin pressurised cylinder under uniform meridional compression with a weld depression imperfection

Continuing the topic of computing the strength of cylinders with weld depression imperfections, `inpute_Example_GNIA02.m` examines the development of thin cylindrical models' resistance under the combined effect of meridional compression and internal pressure. A few selected imperfection amplitudes δ_0 are considered for the imperfect geometry of the cylinders, but also different characterisation parameters $\bar{p}$ for the internal normal pressure, given as

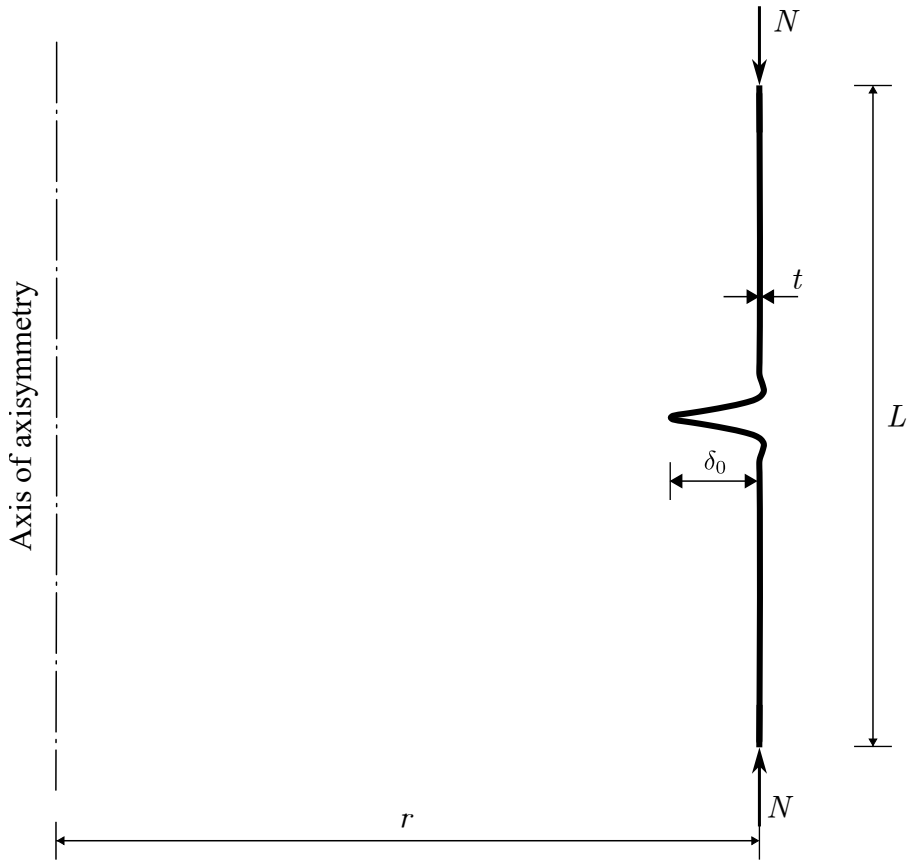


Figure A.68: GNIA01 - System diagram.

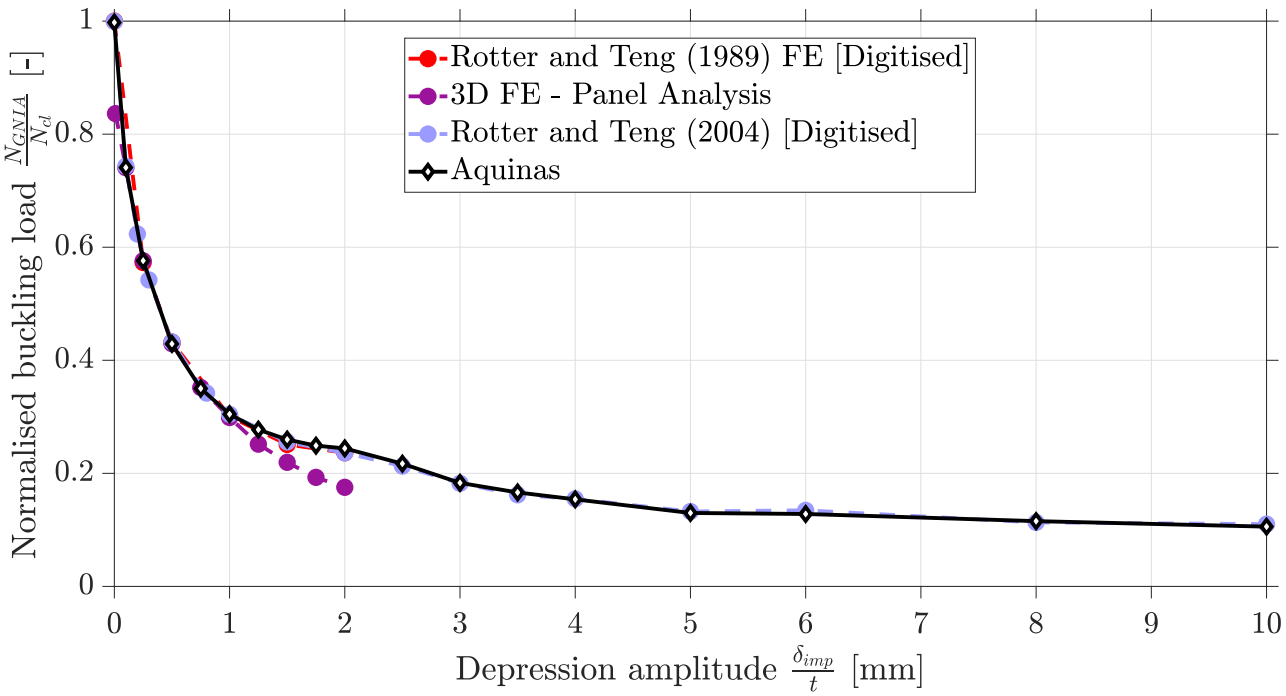


Figure A.69: GNIA01 - Critical dimensionless loads for increasing amplitudes of a TYPE A weld depression imperfection.

$$\bar{p} = \frac{pr}{\sigma_{cl} t} \tag{A.15}$$

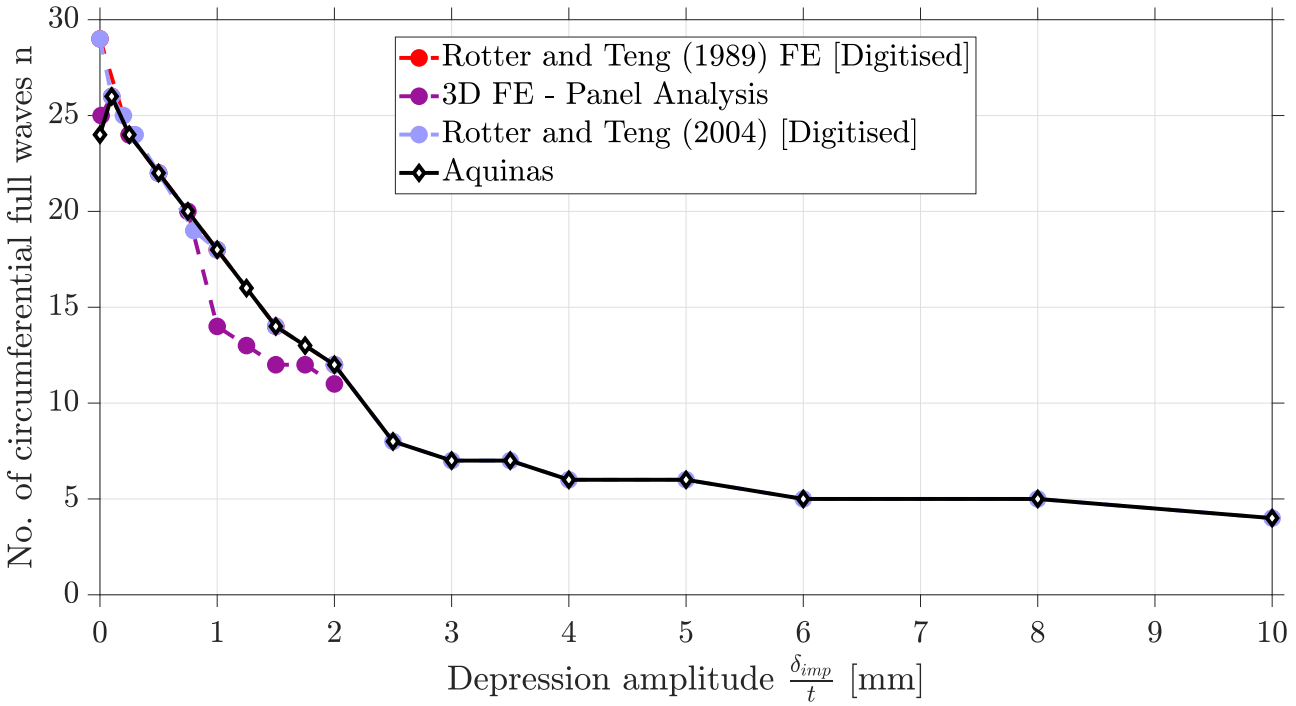


Figure A.70: GNIA01 - Critical circumferential bifurcation modes for increasing amplitudes of a TYPE A weld depression imperfection.

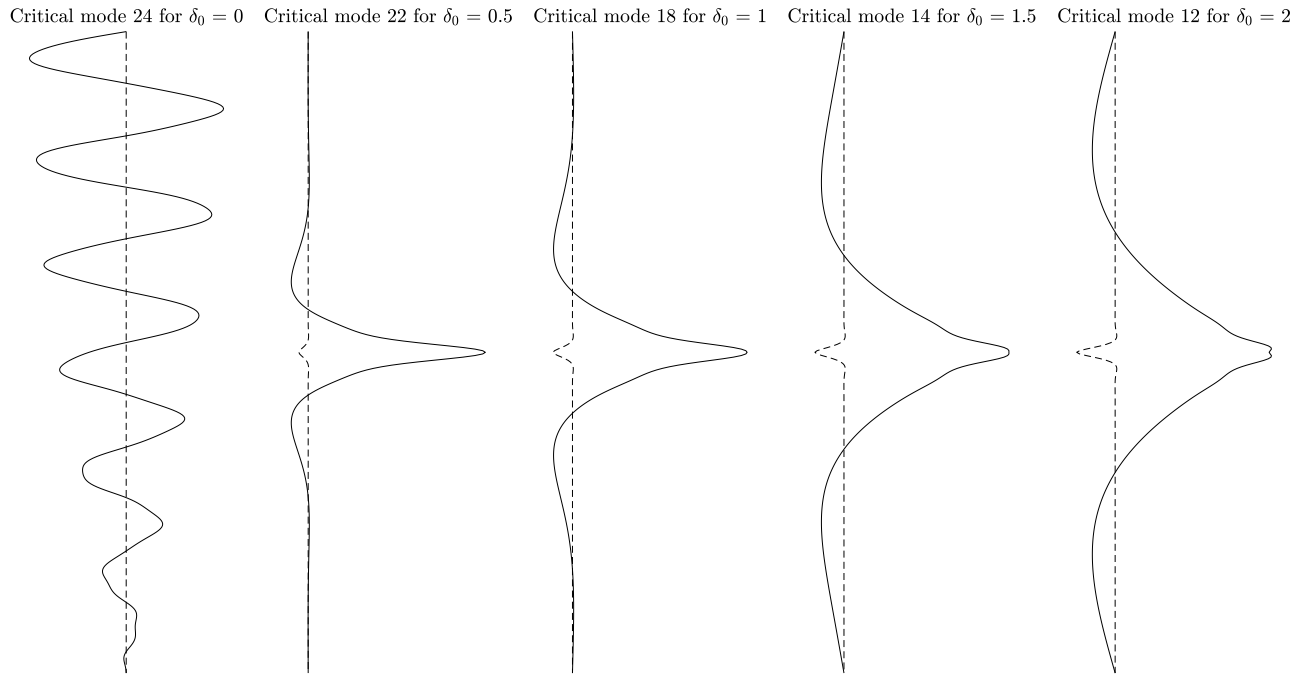


Figure A.71: GNIA01 - Bifurcation modes for selected imperfection amplitudes of a TYPE A weld depression.

with the classical elastic critical stress given in Eq. (2.15). The geometry and boundary conditions are similar to those of `input_Example_GNIA01.m` ($t = 1.0\,mm$, $r = 1000.0\,mm$ and $L/r = 3$), with the loading now including a varying internal pressure, illustrated in Figure A.72.

For comparison purposes, the results of Rotter and Teng (1989) Rotter & Teng (1989) have been digitised, as obtained with the use of the FELASH (Rotter, 1989) suite of software. The results of the two FE toolboxes (that share the same axisymmetric shell formulation) are plotted in

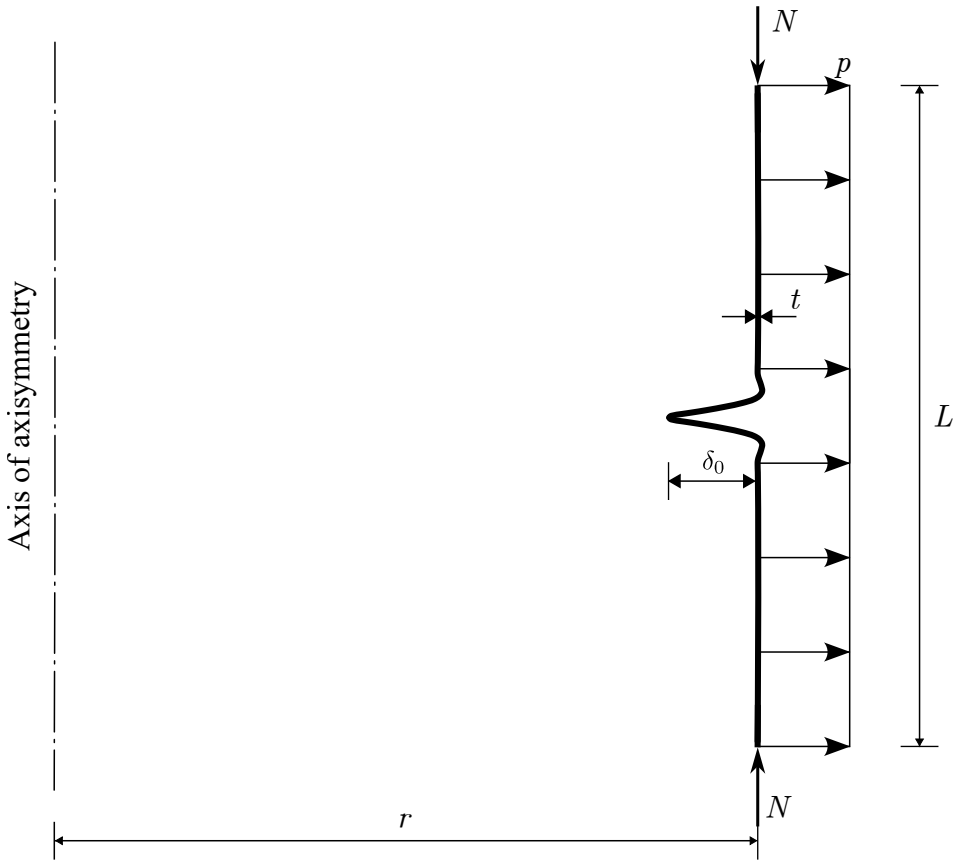


Figure A.72: GNIA02 - System diagram.

Figure A.73, illustrating the beneficial effects of internal pressure on the response of cylinders with varying weld depression imperfections under meridional compression. Discrepancies that are visible for the higher dimensionless pressure ratios $\bar{p}$ considered are attributed to potential differences in the definition of the geometric derivatives ($\frac{\partial\phi}{\partial s}$, $\frac{\partial^2\phi}{\partial s^2}$ etc.) associated with the imperfect geometry, for which an Akima interpolation scheme has been used here (Akima, 1970), but also on discretisation choices along the meridian of cylindrical shell models. While it is mentioned in Rotter & Teng (1989) that a 'very fine finite element mesh was used in the neighbourhood of the weld depression, with elements of length only $0.25\sqrt{rt}$', it is unclear what is the extent of the 'neighbourhood of the weld depression', and consequently what was the discretisation for the rest of the meridian. The reader is encouraged to run the input script with a lower meridional discretisation than the one used for the generation of Figure A.73 and notice that there is a better agreement for the higher end dimensionless pressure parameters $\bar{p}$.

The bifurcation modes for selected values of the dimensionless pressure parameter $\bar{p}$ of cylinders with a weld imperfection amplitude ratio of $\delta_0/t = 1.5$ are also presented in Figure A.74, where the reader may appreciate the similarity of the computed shapes and those of Figure 12 in Rotter & Teng (1989). Once again, the modes are normalised and scaled, and should not be treated as an actual deformed shape. The reader is cautioned that this example may take some time to run.

A.7 GMNAs

All the individual pieces of the FE formulation and computational schemes are coordinated in `AQUINAS_GMNA.m`, for the geometrically and materially nonlinear analysis of axisymmetric shells

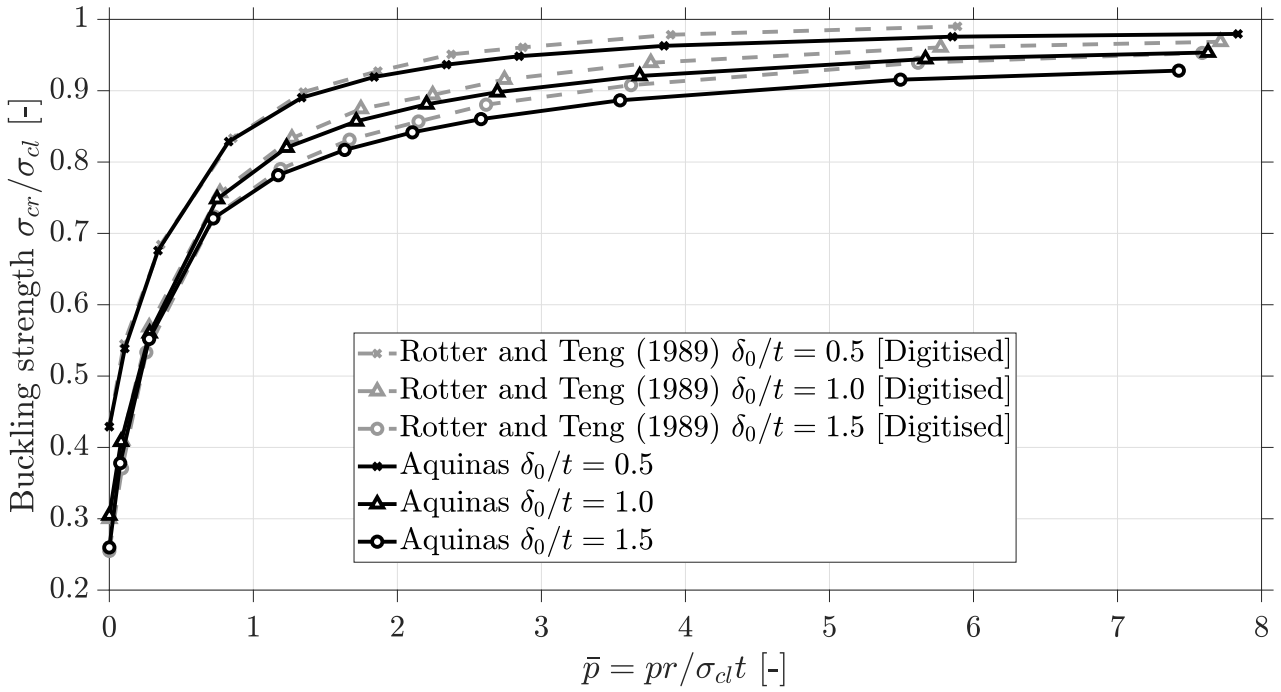


Figure A.73: GNIA02 - Critical dimensionless loads for increasing amplitudes of a TYPE A weld depression imperfection for cylinders under combined meridional compression and internal pressure.

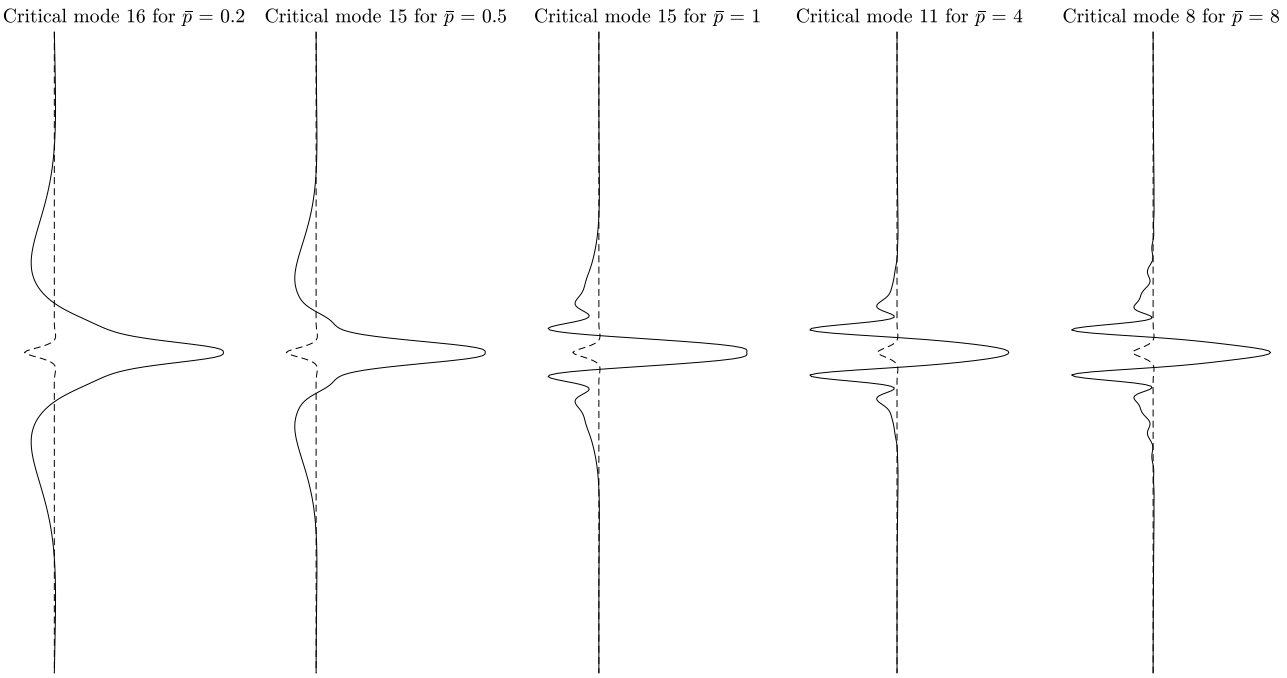


Figure A.74: GNIA02 - Bifurcation modes for selected dimensionless pressure ratios $\bar{p}$ of cylinders with a TYPE A weld imperfection shape, with an amplitude ratio of $\delta_0/t = 1.5$, under combined meridional compression and internal pressure.

with a uniform pre-buckling stress state, according to the European Standard EN 1993-1-6 (2025). As was the case with the geometrically nonlinear benchmark examples presented earlier, a series of competing circumferential modes n may be trialled, for each converged load increment applied, to check for bifurcation into an axisymmetric or non-axisymmetric mode.

In the following exploration of the two cylindrical GMNA problems, the very good behaviour of AQUINAS for solving advanced nonlinear problems will be showcased, while the reader can appreciate the almost effortless execution of GMNA type of problem by having a look through the relevant scripts. At the same time, the necessity for a computational tool that can accurately detect bifurcation into any circumferential mode, with just a single axisymmetric shell model, will be highlighted as the only sensible option for the generation of nominal 'capacity curves' for reference shell systems. These curves are of paramount importance for the application of EN 1993-1-6 (2025) for the design of shell problems, especially in the context of the LBA-MNA (Rotter, 2011) or Reference Resistance Design (Rotter, 2016a; Sadowski *et al.*, 2017a) methodologies.

A.7.1 Example GMNA01: Nominal capacity curve generation for cylinders of varying slenderness under uniform meridional compression

The fully nonlinear resistance of cylindrical shells of varying slenderness under meridional compression is examined in `input_Example_GMNA01.m` for the computation of a capacity curve for this reference system, aiming to reveal the underlying relationships of material and geometric nonlinearities as the cylindrical models become increasingly more slender. The cylinders considered in this GMNA example are characterised by a unit dimensionless length parameter $\Omega = 1$, as defined by Eq. (4.2). While the thickness of the shell wall is kept constant at a unit thickness of $t = 1.0\,mm$, the radius of the meridian's midsurface varies for the cylindrical models through a series of considered r/t ratios. The elastic-perfectly plastic material law is characterised by a yield stress $f_y = 250\,N/mm^2$, even though the relationships of normalised resistances presented through the construct of a capacity curve are unaffected by the yield stress of the material. The base of the cylinders are fully clamped with a BC1r-C1 boundary condition, while the top edge, where the compressive line load N is applied, is restrained through a BC2r-C3 condition. The cylindrical shell model is presented in Figure A.75.

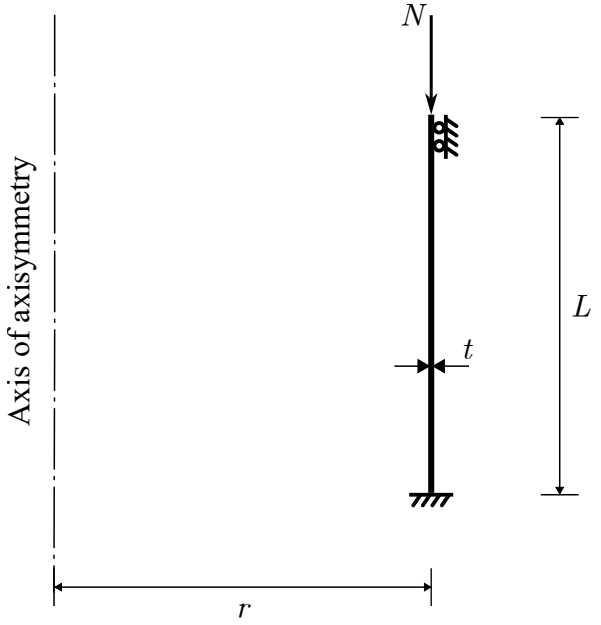


Figure A.75: GMNA01 - System diagram.

Three different sets of AQUINAS analyses are executed for each r/t ratio, in an attempt to isolate the nonlinear effects that dominate the resistance of the cylinders as they transition from thick, stocky models to very slender ones. A geometrically and materially nonlinear model

that is only allowed to fail through an axisymmetric failure mode is expected to accurately identify the strength of the cylinders for low intermediate slenderness models, but is also expected to be under-conservative for the thinner models, where elastic bifurcation into any one of the competing circumferential modes n is anticipated to be the determining factor of the shell's resistance. An attempt to also capture the completely elastic bifurcation into a non-axisymmetric mode n is made, for the higher end of the r/t ratio range, by submitting a GNA for each of the cylindrical model. Finally, an AQUINAS nonlinear solution with both types of nonlinearities included and bifurcation checks for all potentially competing harmonics n is included in `input_Example_GMNA01.m`, with the expectation to be capable of accurately converging to the appropriate resistance for cylindrical shells of low, intermediate or high slenderness. The very different failure modes that are critical for the slendernesses considered constitute a very demanding benchmark test not only for AQUINAS, but for any FE solver.

These three AQUINAS analyses required more than 24-hours on an 8 core AMD Ryzen 7 4800h CPU. It is apparent that if an analysis where only the meridian requires discretisation is of such computational expense, then the generation of the same capacity curve through the 'panel analysis' technique, as demonstrated by Sadowski *et al.* (2018), can be deemed as completely impractical in terms of time efficiency (without mentioning any other potential computational pitfalls discussed therein). In Figure A.76, the capacity curve for the cylindrical shell problem under consideration is presented, where the relationships between the normalised resistance R_{GMNA}/R_s of a system against either its dimensionless slenderness $\lambda = \sqrt{R_s/R_{cl}}$ (the 'traditional' form Fig. A.76 left), and against an alternatively normalised resistance R_{GMNA}/R_{cl} (the 'modified' form Fig. A.76 right as conceived by Rotter (2002)), are explored. A reader taking a closer look in the publications presenting the capacity curves construct in the context of axisymmetric shell analyses may notice that an LBA and MNA need to be executed for the computation of the corresponding resistances, namely R_{LBA} and R_{MNA}. Instead R_{cl} and R_s have been used in `input_Example_GMNA01.m` as the reference resistances in their place, computed through the classical elastic bifurcation load $P_{cl} = 2\pi r t \sigma_{cl}$ (relevant to the classical elastic critical stress σ_{cl} of eq. (2.15)) and a simple membrane theory prediction of the plastic load $P_s = 2\pi r f_y t$ that would lead to extensive membrane yielding, and therefore collapse. This simplification, and associated economy in computational time, is only possible in this case due to the extensive research and availability of background results on the topic of cylindrical shell buckling under meridional compression. In the absence of a sufficient scientific background for a shell problem, the analyst would have to actually compute the LBA and MNA resistances.

An axisymmetric GMNA ABAQUS (2022) model is also examined for each cylinder, not only to verify the result obtained from an AQUINAS 'axisymmetric failure only' analysis, but also to illustrate the consistent overestimation of the shells' strength by this well established, commercial software, as there is no way to detect bifurcation into a non-axisymmetric harmonic mode n. It may be appreciated how clean the generated capacity curve appears to be, with its form being exceptionally similar to the characteristic capacity curve presented in Sadowski *et al.* (2017a). The full GMNA AQUINAS result has an excellent agreement with the axisymmetric ABAQUS GMNA (and of course with its very own axisymmetric failure GMNA), and gradually starts to agree with the elastic GNA result, as the cylinders become thinner and thinner. The predicted bifurcation modes are also in excellent agreement between the AQUINAS GMNA and AQUINAS GNA (black and red numbers on modified capacity curve accordingly) solutions for the high-slenderness cylinders, indicating that there is little to no yielding occurring as the cylindrical models deform. It should be once again noted that this example can take some time until execution is completed.

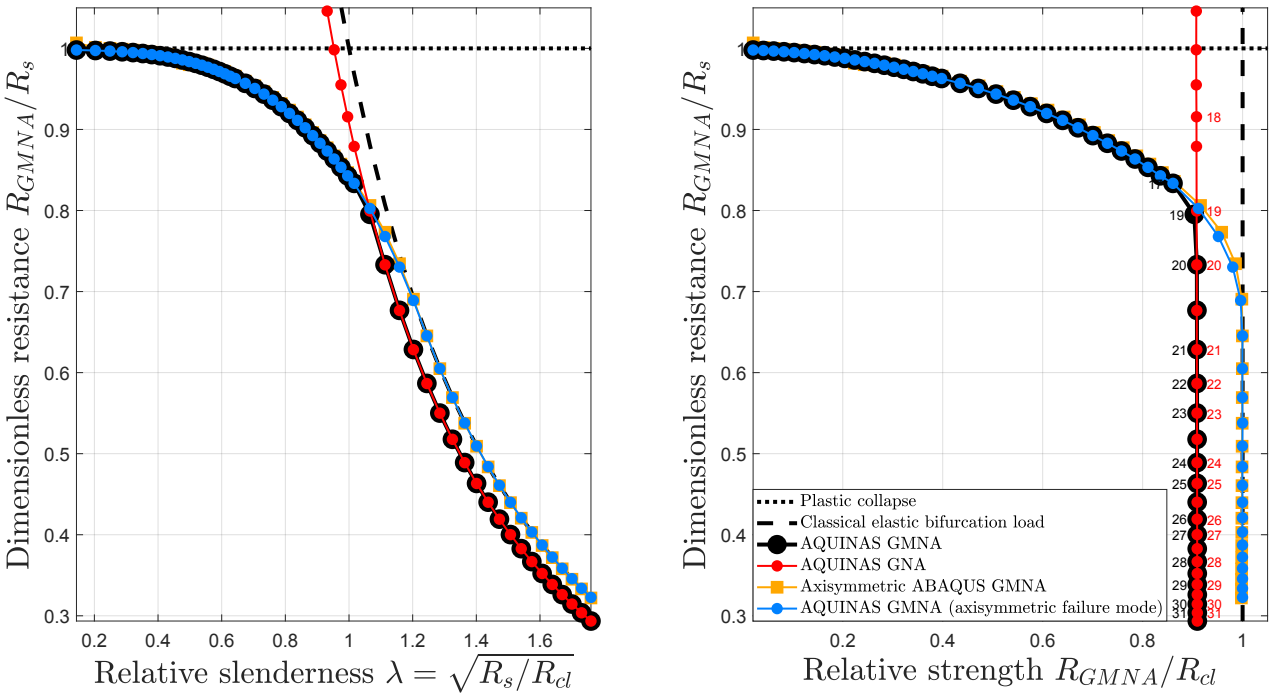


Figure A.76: GMNA01 - Traditional (left) and modified (right) capacity curves for cylinder under meridional compression for a dimensionless length $\Omega = 1$.

A.7.2 Example GMNA02: Elastic-plastic collapse load predictions for a pressurised cylinder under uniform meridional compression

The elastic-plastic collapse loads of pressurised and meridionally-compressed cylinders will be examined in this GMNA validation example, where the focus is still on axisymmetric shells of infinite meridional radius of curvature. Four different r/t ratios will be considered for the cylindrical models, ranging from rather thick and stocky ($r/t = 250$) to very thin and slender ($r/t = 2000$). The applied internal pressure p will also be varying with respect to the applied meridional load N, as a higher internal pressure may lead to uniform circumferential yielding faster and significantly undermine the strength of the cylinders under meridional compression. This behaviour is thoroughly investigated in Rotter (1990), where the finite difference BOSOR5 program (Bushnell, 1976), very popular for shell analyses in this past era of extensive shell research, is used for computing the solution of this demanding geometrically and materially nonlinear problem. This will allow AQUINAS to compare its full GMNA results with a very different, yet well established, approach to the solution of axisymmetric shell problems.

As discussed in Rotter (1990), the shell models studied are chosen to represent the bases of cylindrical on-ground silos and tanks. The length of the cylinders' meridian is chosen to be equal to five elastic bending half-wavelengths Λ as defined by Eq. (2.14), leading to a length of approximately $L \approx 12\lambda$ or a Batdorf parameter $Z = 142$. Their base is fully clamped (BC1r-C1), while a BC3r boundary condition is applied at their top edge to represent meridional continuity, as illustrated in Figure A.77. The wall is of unit thickness $t = 1.0\,mm$ for all r/t ratios, with the fabrication material having a yield stress of $f_y = 250\,MPa$ with no strain hardening considered. The magnitude of the internal pressure is related to the meridional compressive stress σ_x, as defined through the applied line edge load $N = \sigma_x t$, so that a series of $pr/\sigma_x t$ ratios are submitted for a nonlinear analysis for each r/t ratio examined.

The GMNA results of this exploration are presented in Figure A.78, with the digitised collapse

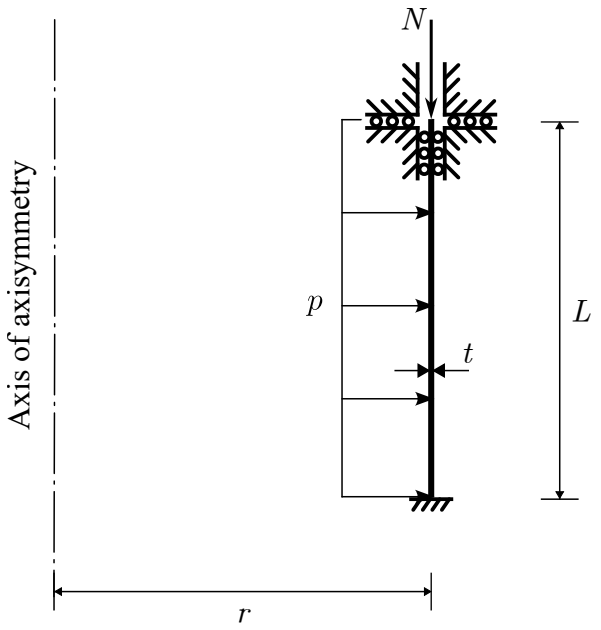


Figure A.77: GMNA02 - System diagram.

loads obtained in Rotter (1990) with the BOSOR5 suite included for comparison. A very good agreement is illustrated between the two very different computational approaches, where some minor discrepancies are to be expected due to the inevitably poor quality of a digitisation result.

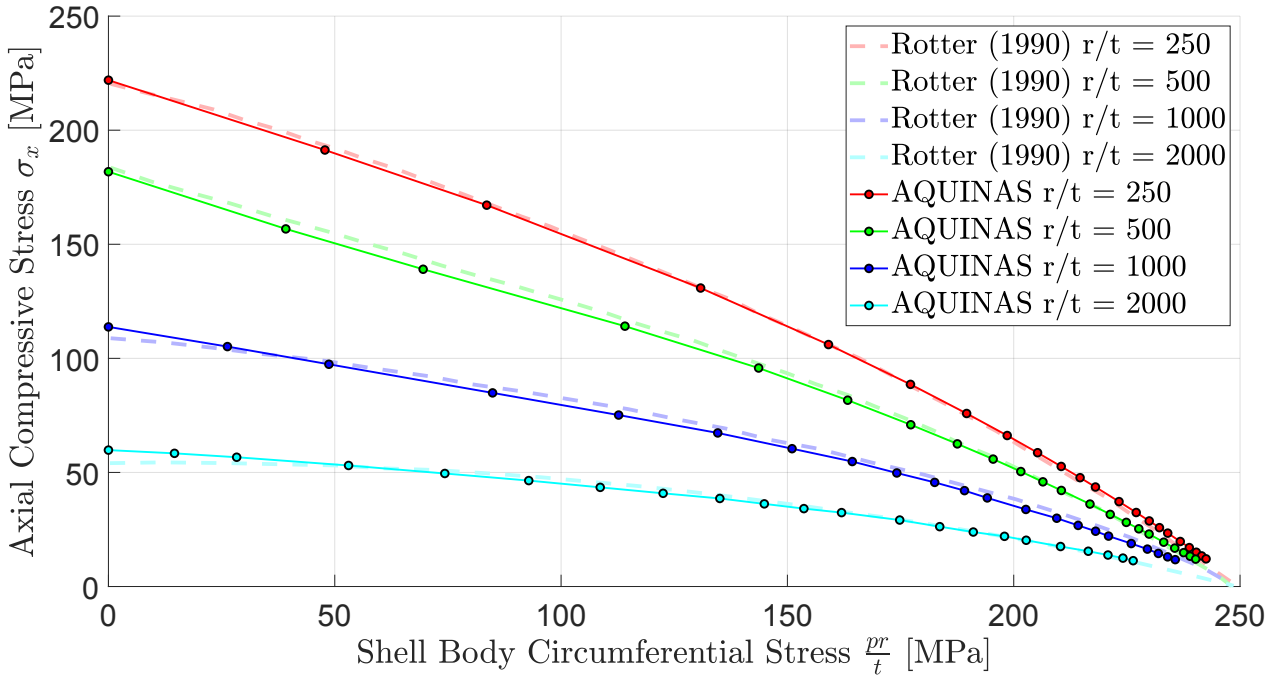


Figure A.78: GMNA02 - Collapse load predictions for pressurised cylinders under meridional compression for $r/t = 250, 500, 1000, 2000$ ratios.

A.8 GMNIAs

No Geometrically and Materially Nonlinear Analysis are included with the official AQUINAS Github repository and documentation at this time, although undertaking one is possible with only trivial changes to the GNIA and GMNA examples presented above. Whilst the capacity

curves of Sections 3.8.1-3.8.2 have been generated on the basis of a GMNIA, with additional GNIAs performed to identify the slenderness at which plasticity first affects the resistance of the models, model generation scripts have not been made available through the repository due to their role as an illustration of AQUINAS' computing capabilities rather than an insightful example for users to build on. Once such a model has been explored to the same standard of detail showcased for the previous validation examples, the corresponding section of the AQUINAS manual shall be updated accordingly.

A.9 Miscellaneous

A.9.1 Example MISC01: Parallel scaling analysis

The script `input_Example_MISC01.m` file implements a simple 'strong' scaling analysis of the parallel performance of the AQUINAS C++ version for the FE assembly on a generic LA problem, the geometry of which is of no interest in this case as it is not the quality of the FE solution that is examined. The system stiffness matrix and the distributed force vector assembler is currently parallelised, the operation involving a computationally expensive `for` loop with independent iterations, using threading with OpenMP. The results are presented in A.79, as generated with an 8-core AMD Ryzen 7 4800H CPU. The reader is cautioned that the data presented strongly depend on the number of processors, clock speed and background processes in an analyst's computer, and replication of the distributions presented might not be possible. The serial fraction of the AQUINAS runtime is evaluated through application of Amdahl's law (Amdahl, 1967), demonstrating the significance of the parallel OpenMP loop in speeding-up the solution process.

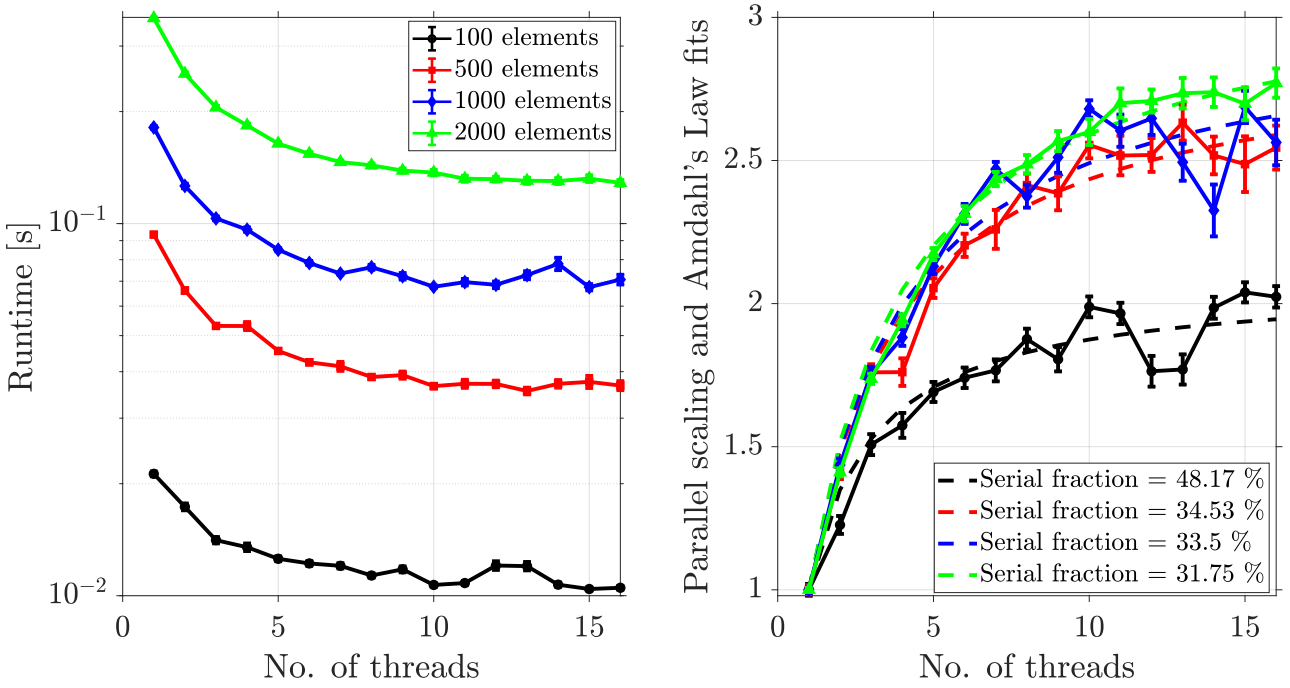


Figure A.79: MISC01 - Parallel scaling analysis of AQUINAS on a simple LA problem, where the source of concurrency is the matrix assembler.

Analysts wishing to use the C++ parallelisation capabilities are advised to perform this analysis first to establish an approximately optimal number of threads beyond which performance has reached a plateau and requesting additional parallel resources offers little further benefit.

Appendix B

Comparative assessment of the AQUINAS element performance in the context of different EN 1993-1-6 analyses

A study on the efficiency of the finite element formulation (Teng & Rotter, 1989a,b) coded into the AQUINAS software will be undertaken in the current section as a logical extension of the comprehensive computational examination of its solution accuracy presented earlier in Appendix A. For the characteristics of the thin axisymmetric shell element of the MATLAB FE toolbox to be appropriately assessed across different types of analysis procedures, a comparative reference point that is as fundamentally similar as possible in terms of computational features but is also simultaneously considered a well programmed and scientifically robust formulation is necessary. Once again, the best available such option for the computational evaluation of AQUINAS is provided through ABAQUS, leveraging its axisymmetric shell modelling capabilities to obtain indicative values of CPU times corresponding to the numerical solution of a model, albeit with a series of simplifications on the interpretation of these time estimates. To ensure reliability of the obtained execution time measurements, all analyses were performed on the same computer station, utilising an Intel Core i7-6700 3.40GHz CPU and 16.0 GB of RAM installed, available to the author during his studies at Imperial College London. Only single-threading was permitted for all numerical procedures, as this study is not an exploration of potential parallel scaling of large model simulations but rather a closer look to the computational resource cost for an analysis with AQUINAS.

The problem of a cylindrical shell under meridional compression will once again be revisited, providing a simple geometric basis for an axisymmetric shell problem without an elaborate meridional definition for easy modelling in both AQUINAS and ABAQUS. An $r/t = 1000$ ratio is considered for all models, with the length characterised through a dimensional group $\Omega = 0.5$, according to Eq. 3.95. The efficiency of AQUINAS in computing stiffness coefficients, assembling global stiffness matrices and residual force vectors, but also in solving the system's equilibrium equation or eigenvalue problem is assessed through an LA, an LBA and a path-tracing GNA. Each of these three analysis procedures target different parts of an element's stiffness matrix, with only the linear strain material stiffness part assembled during an LA, both material and geometric stiffnesses computed during an LBA while a GNA requires additional terms corresponding to nonlinear strains in the computation of the tangent stiffness matrix, as presented earlier in Section 3.5.

B.1 Element efficiency comparison against the ABAQUS SAX1 and SAX2 formulations

Whilst the open source nature of AQUINAS permits for precise measurements to be obtained for specific parts of the solution process to be independently timed through appropriately placed lines of code, such a strategy cannot be possibly adopted for the ABAQUS solver, provided in an executable binary format. Consequently, alternatives to compute these timings need to be devised for a meaningful comparison to be made. Some of the output files generated during submission and execution of a job in ABAQUS appear to provide insights on the time needed for parts of the solution process, rounded however to the first decimal point and thus limiting their usefulness. Hence, a workaround to produce these timing estimates was devised, accompanied however with some significant simplifying assumptions corresponding to the background processes performed during their execution. It was observed that even the most coarse of mesh resolutions would require a few seconds for even an LA to be executed, a counter-intuitive result considering that the GUI of the software is not invoked when an input file is submitted through a Python script running on a terminal window, while an equivalent AQUINAS analysis that doesn't utilise its pre-compiled MEX binaries is about 10 times faster. The author's experience with the software has led him to believe that there is significant computation overhead in every ABAQUS run due to the extensive input file pre-processor for error checks but also due to the necessary communication of the software with its license server, ensuring that a number of tokens is available before execution of an analysis can proceed. Therefore, all ABAQUS times, originally evaluated during execution of a master Python script as the time necessary to communicate the submission of an input file to ABAQUS and to eventually return control to this master script, are further processed and decreased by the time required for a single element model to be analysed. This assumption is made on the basis that the actual CPU time needed for the solution of such a simple modelling problem is negligible, thus allowing the conceptual isolation of finite element analysis time associated with each simulation through a lower bound estimate of this overhead time accompanying submission of any axisymmetric shell problem in ABAQUS. As this is a major simplification introduced in these comparisons, it should be emphasised that all following metrics and figures should be treated as rough estimates of timings for the different types of analyses considered and are by no means a definitive guide on the efficiency of these elements.

B.1.1 Performance comparison through controlling the meridional discretisation

A first approach on this computational efficiency comparison of AQUINAS and ABAQUS is made on the simplistic basis, for reasons outlined shortly, of models discretised through the same total number of elements. Results from AQUINAS include both runtime interpretation of MATLAB code for arithmetic operations relevant to stiffness coefficients evaluation but also the use of pre-compiled MEX libraries written in C++, allowing a better comparison with the executable binary format of ABAQUS. Both SAX1 and SAX2 elements are employed in the comparison of Figure B.1, showcasing the development of average times and associated standard deviations across the 10 out of 15 fastest runs for both 'compiler' options in AQUINAS and the two axisymmetric shell ABAQUS elements. The slowest 5 of these 15 trial runs were discarded to protect the ABAQUS timings from some unreasonably high time measurements, suggesting that either ABAQUS needs several attempts to acquire the necessary tokens from its license server or that its execution is hindered by some other background processes, a sensitivity that is now encountered through the use of AQUINAS. Scaling of the meridional mesh resolution

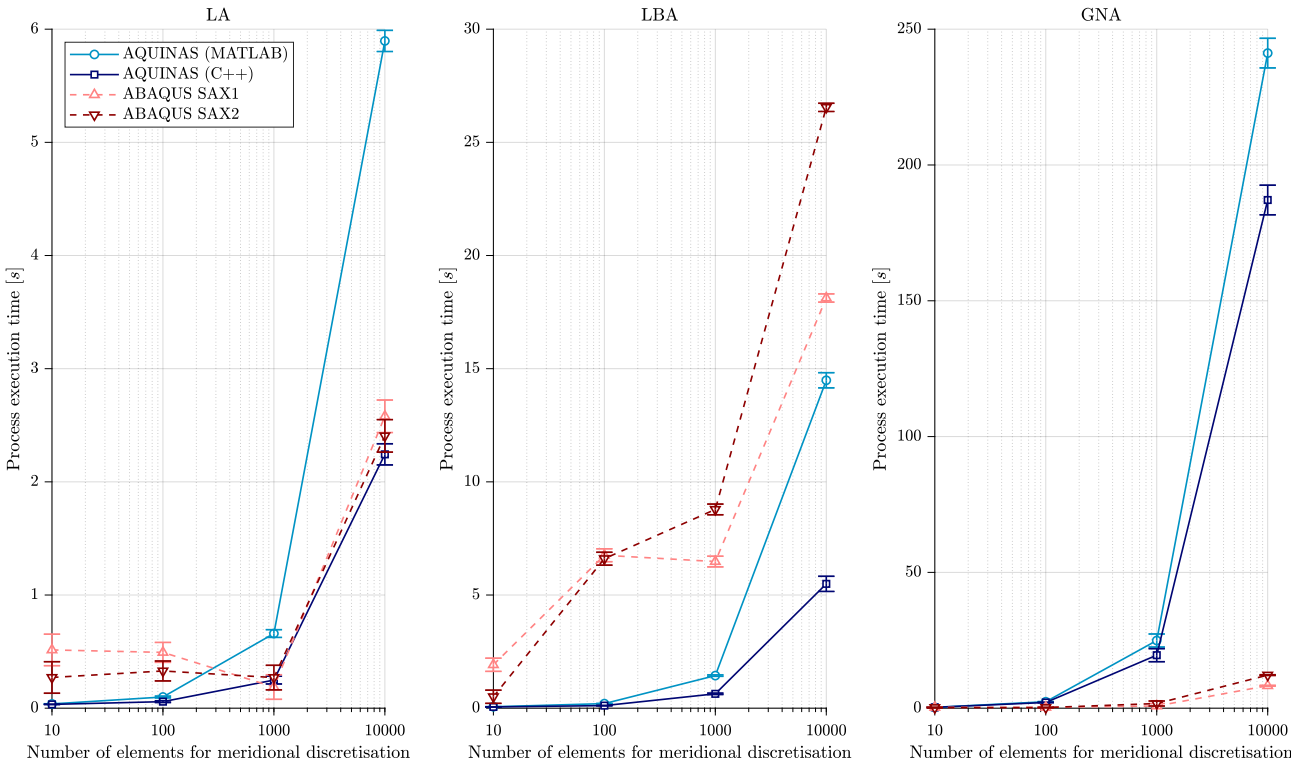


Figure B.1: Development of average execution times and associated standard deviations in a direct comparison of total solver times between ABAQUS and AQUINAS for meridional mesh resolutions corresponding to equal numbers of elements employed.

to further challenge stiffness assembly and solutions of equilibrium or eigenvalue systems for the two software portrays a competitive development of average execution times for AQUINAS, especially in the context of an LBA where both MATLAB and C++ measurements outperform the corresponding ABAQUS jobs.

The GNA reality appears to be somewhat less antagonistic for AQUINAS in Figure B.1, with ABAQUS total execution times after reduction of the assumed overhead discussed above being only a fraction compared to the MATLAB written FE toolbox. There are however some important points that need to be considered in the interpretation of these results. As a nonlinear incrementation of externally applied loads inevitably requires the use of an iterative scheme until convergence is achieved, the actual CPU time spent by the main computational processes of the analysis will be proportional to the number of iterations necessary to achieve this convergence. Even though a Newton-Raphson incrementation scheme is adopted in both AQUINAS and ABAQUS in order to avoid the extensive calculations necessary when an arc-length algorithm is employed, and the tolerances to achieve convergence are set to irrationally high numbers so as to achieve convergence in the very first attempt at an increment (since the quality and accuracy of the solution is not the subject of this investigation), it is nonetheless still the case that AQUINAS requires at least 2 iterations at an increment in order to check the relative error between the first and second attempt, as described in Section 3.7.3.3 and visually illustrated in Figure 3.19. Hence, its results correspond to twice the time spent in solving the equilibrium system and assembling residual forces (but fortunately not in assembling the stiffness matrix as a modified Newton-Raphson approach is adopted). Additionally, the `AQUINAS_GMNA` function includes extensive parts of code that correspond to checks and data processing written in MATLAB, adding another layer of computational inertia in the solution process. Finally, reorganising of the computed data into an output MATLAB struct for further processing by the user takes up a significant portion of total execution time, as will be demonstrated below.

Furthermore, it needs to be reminded that AQUINAS requires at least 3 Gauss-Legendre integration points along its meridian (Jumikis, 1987), leading to the computation of stiffness coefficients and residual force vectors at least 3x more when compared with the SAX1 element and 1.5x more when compared with SAX2 element in ABAQUS (with the additional consideration that for the same number of elements N, an SAX2 discretisation is associated with 2N+1 nodes instead of the N+1 nodes for SAX1 discretisations or use of the AQUINAS element (Teng & Rotter, 1989a)). A better way to compare the efficiency of the cubic thin axisymmetric shell element in AQUINAS would therefore be through controlling the total number of integration points along the meridian of the cylindrical shells, leading to the exploration of the following section.

B.1.2 Performance comparison through controlling the sum of integration points along the meridian

As there is no way to directly control the number of integration points used for the computation of stiffness matrices in both SAX1 and SAX2 elements, the workaround of increasing the discretisation in order to achieve the targetted number of integration points along the meridian will be adopted. A comparison of the equally integrated cylinders under meridional compression is presented in Figure B.2, where even though there are no unforeseen findings in any of the analyses executed it is clear that the performance of AQUINAS compares a bit better when the comparison is made on the basis of computations relevant to stiffness and residual force evaluations, including a better relative performance for the GNA solution. It should however be noted that this time there is a negative bias associated with total ABAQUS execution times, since for the SAX1 discretisation to have the same number of integration points involved in an AQUINAS analysis triple the amount of elements need to be generated and processed. This leads to a higher total DOF count and internal processing logistics that slow down overall execution time, with an analogous negative bias for SAX2 discretisations.

B.2 Performance characteristics of the AQUINAS element in the scope of different analysis procedures

A closer look into the particular timings corresponding to pre-processing, main FE processing and post-processing parts of the AQUINAS solution procedures can provide some insights on the distribution of CPU operations once an analysis is submitted. Pre-processing and post-processing parts are always written in MATLAB for all types of analyses, with charts representing the internal procedure average times and their variability considering 95% confidence intervals on the total of 15 repeats per analysis type, discretisation and compiler option, without needing to discard any runs in this examination as there is no comparison with ABAQUS and the results of AQUINAS are not that easily affected by background processes running on a computer. Pre-processing portions gradually take up less and less of the overall execution time for all three analyses when more elements N are involved in the solution process, and while same principle appears to apply for post-processing of the LBA runs in Figure B.4, the charts for the LAs of Figure B.3 and GNAs of Figure B.5 suggest that the post-processing part of the analysis scales in analogy to the number of elements employed for the meridional discretisation. As earlier stated, post-processing routines are only written in MATLAB as the main objective is the creation of a struct to provide organised output of displacement, strains and stresses to the analyst. Due to the need for this struct to include strains, stresses and stress resultants in the cases of an LA or a GNA, but not for an LBA, the post-processing required after a solution has been obtained is substantial and includes an additional layer for these structs, that of Gauss

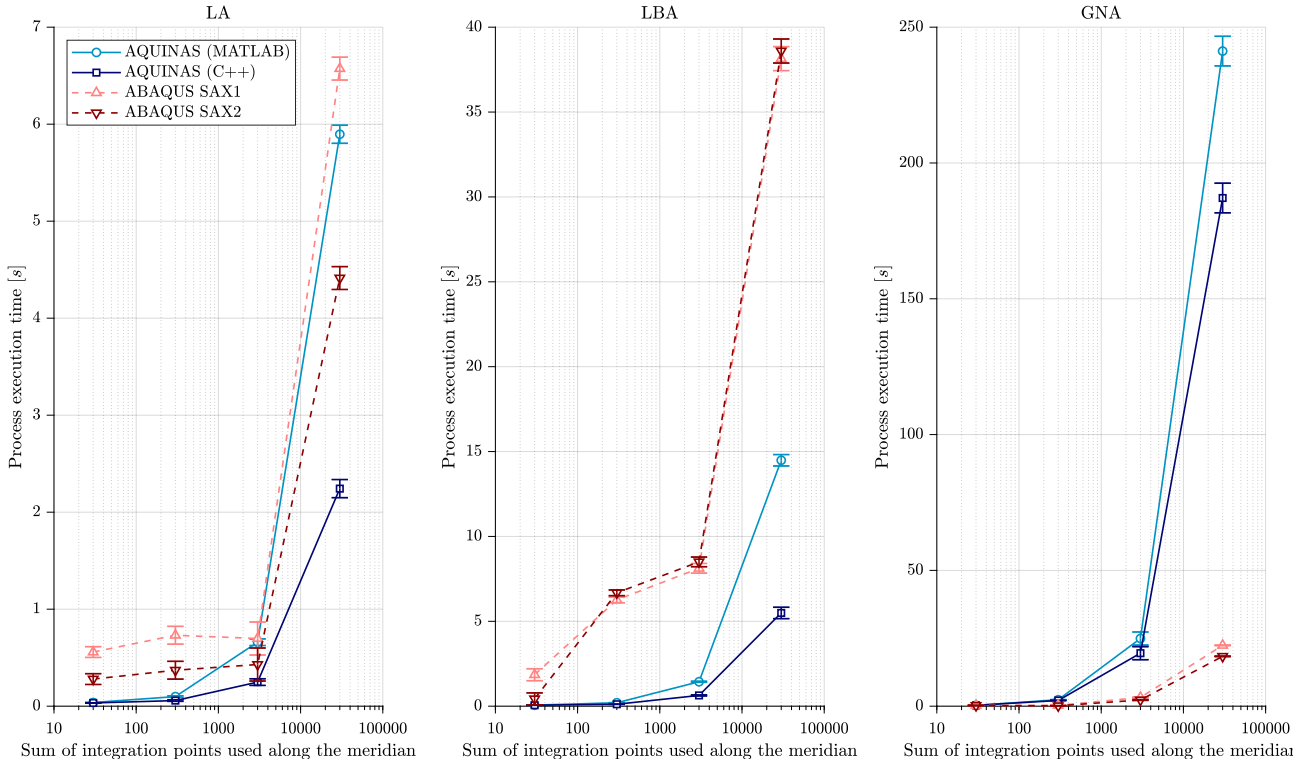


Figure B.2: Development of average execution times and associated standard deviations in a direct comparison of total solver times between ABAQUS and AQUINAS for meridional mesh resolutions corresponding to equal total sums of integration points used.

point defined values, justifying the higher post-processing averages for the charts of Figures B.3 and B.5.

Assembly of stiffness matrices expectedly requires more and more time as higher meridional mesh resolutions are considered, a behaviour that is common across all analysis types for both MATLAB and C++, whilst time spent in solving the equilibrium equation or eigenvalue problem is relatively only a minor portion of overall CPU time, mainly due to taking full advantage of sparsity patterns in the stiffness matrix and the efficiency of MATLAB built-in routines corresponding to these operations. A portion of the overall solution time is termed as 'unaccounted', corresponding to operations that do not formally fall under the 'pre-process', 'main-process' or 'post-process' categories, such as the I/O operations necessary to write the timings into text files for this investigation to be possible, while the 'Other main' category includes parts of the analysis scripts `AQUINAS_LA`, `AQUINAS_LBA` and `AQUINAS_GNA` that do not correspond to assembly operations or solutions of a system of equations. Especially in the case of the GNA runs these times are more significant due to the internal convergence checks and data processing between increments. Comparison of MATLAB and C++ compiler options for the same number of elements N also demonstrate that common MATLAB written parts of the analysis (such as pre-processing checks) take up a higher portion of the overall solution time due to the relative speed-up achieved when the C++ MEX binaries are employed, even with only single-threading permitted.

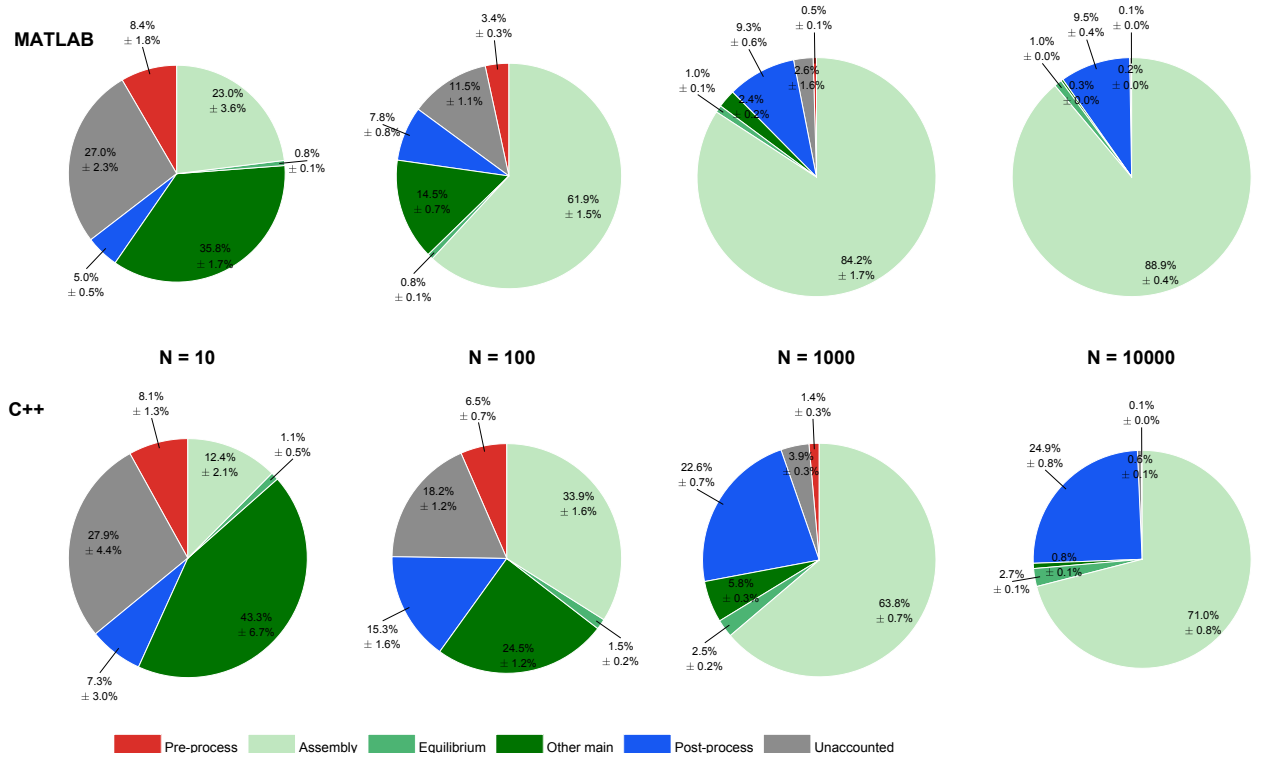


Figure B.3: Scaling of average computation times and associated 95% confidence intervals variability with progressively higher mesh resolutions for individual internal processes in AQUINAS associated with an LA, expressed as a percentage of total execution time.

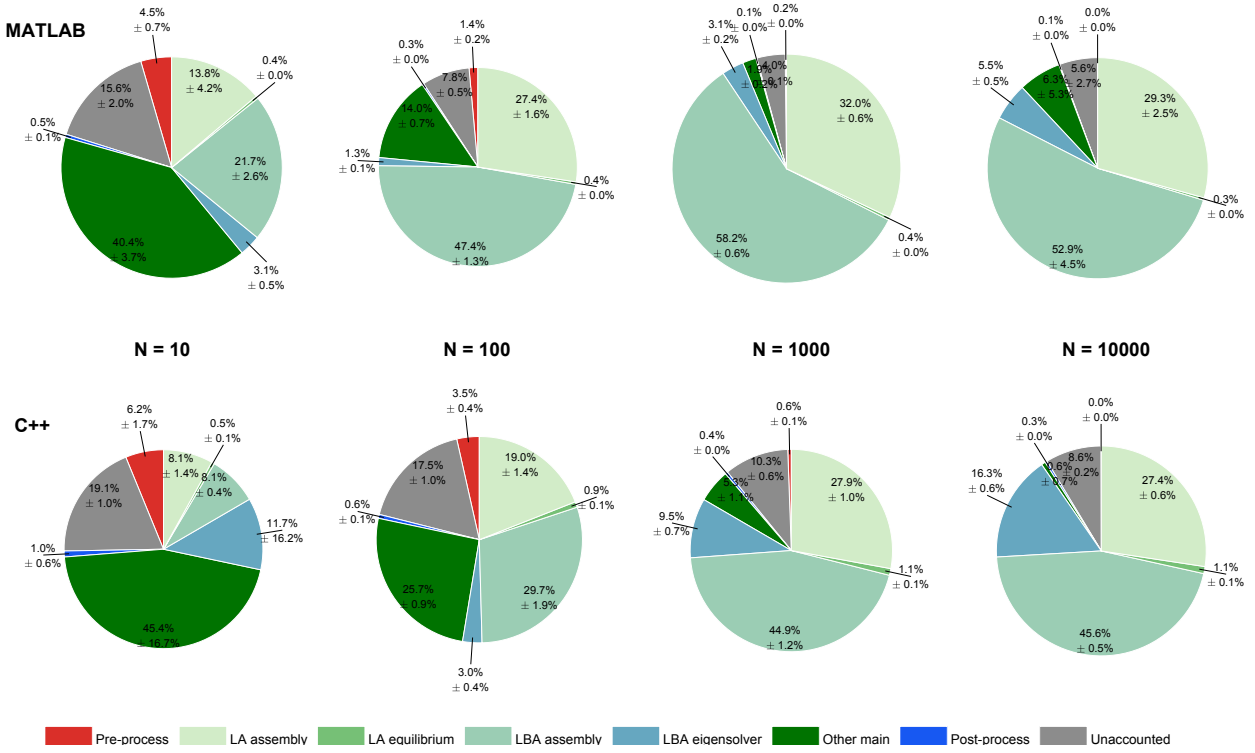


Figure B.4: Scaling of average computation times and associated 95% confidence intervals variability with progressively higher mesh resolutions for individual internal processes in AQUINAS associated with an LBA, expressed as a percentage of total execution time.

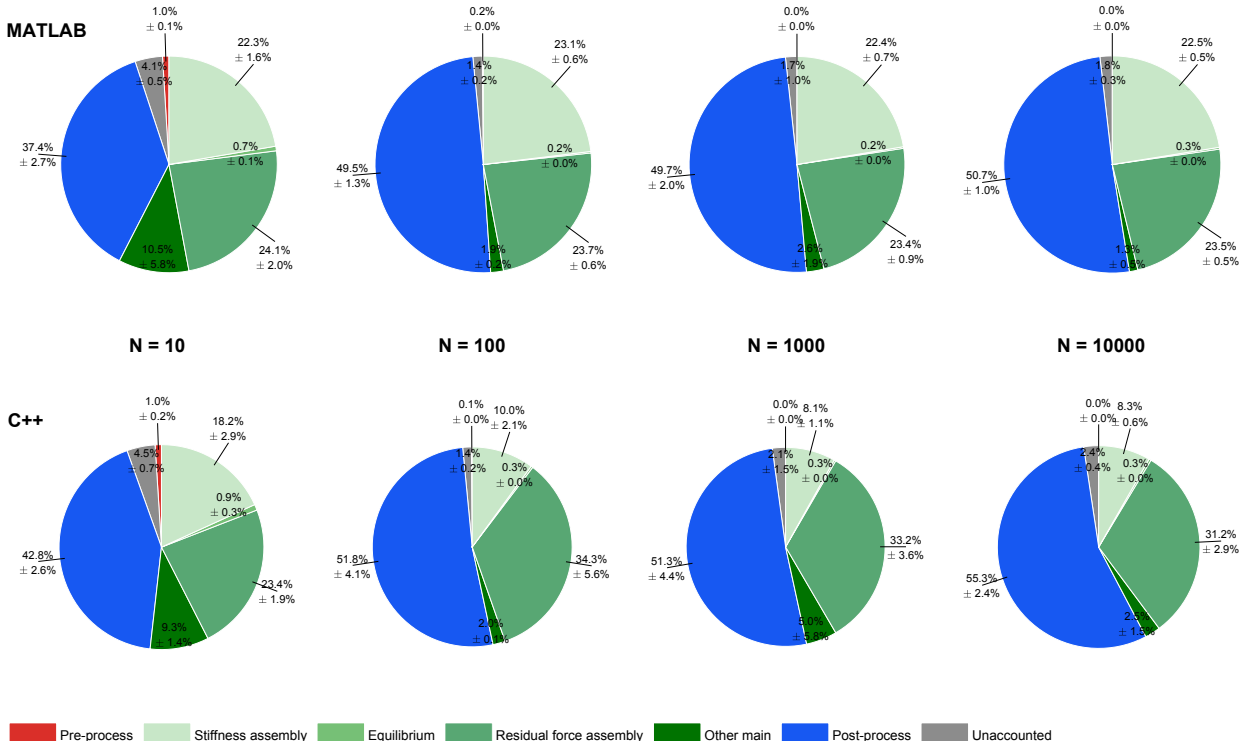


Figure B.5: Scaling of average computation times and associated 95% confidence intervals variability with progressively higher mesh resolutions for individual internal processes in AQUINAS associated with an GNA, expressed as a percentage of total execution time.

Appendix C

Closed-form relationships for the critical bifurcation buckling load of shear-flexible cylinder under uniform meridional compression or normal pressure

C.1 Uniform meridional compression

The full analytical closed-form relationship for the bifurcation of non-shallow shear-flexible cylinders under uniform meridional compression is:

$$N_{m-n,thick} = Et\frac{\sum_{i=0}^{5}\sum_{j=0}^{5} N_{m-n|n,i-j}m^{2i}n^{2j}}{\sum_{i=0}^{5}\sum_{j=0}^{5} N_{m-n|d,i-j}m^{2i}n^{2j}} \tag{C.1}$$

where the $N_{m-n|n,i-j}$ terms in the numerator are given as:

$$\begin{aligned}
N_{m-n|n,5-0} &= 2kr^{10}t^3\\
N_{m-n|n,4-1} &= 10kr^8t^3\\
N_{m-n|n,4-0} &= 2r^8t^2(12k^2r^2 + k^2t^2 + 2\nu + 2)\\
N_{m-n|n,3-2} &= 20kr^6t^3\\
N_{m-n|n,3-1} &= r^6t(8t + 8\nu t - 8kt^2 + 5k^2t^3 - 4k\nu t^2 - k^2\nu t^3 + 96k^2r^2t)\\
N_{m-n|n,3-0} &= r^6t(-24k\nu^2r^2 + 48k\nu r^2 + 4k\nu t^2 + 72kr^2 + 4kt^2)\\
N_{m-n|n,2-3} &= 20kr^4t^3\\
N_{m-n|n,2-2} &= 2r^4(2\nu t^2 - 10kt^3 + 2t^2 + 2k^2t^4 - 4k\nu t^3 - k^2\nu t^4 + 72k^2r^2t^2)\\
N_{m-n|n,2-1} &= 2r^4(-24k^2\nu r^2t^2 - 48k^2r^2t^2 - 12k\nu^2r^2t + 24k\nu r^2t + 4k\nu t^3 + 36kr^2t + 5kt^3)\\
N_{m-n|n,2-0} &= 2r^4(-144k^2\nu^2r^4 - 12k^2\nu^2r^2t^2 + 144k^2r^4 + 12k^2r^2t^2)\\
N_{m-n|n,1-4} &= 10kr^2t^3\\
N_{m-n|n,1-3} &= -kr^2t^2(16t + 4\nu t - 96kr^2 - kt^2 + k\nu t^2)\\
N_{m-n|n,1-2} &= kr^2t^2(8t + 4\nu t - 144kr^2 - 48k\nu r^2)\\
N_{m-n|n,1-1} &= kr^2t^2(60kr^2 + 36k\nu r^2)
\end{aligned}$$

$$N_{m-n|n,0-5} = 2kt^3$$
$$N_{m-n|n,0-4} = 24k^2r^2t^2 - 4kt^3$$
$$N_{m-n|n,0-3} = 2kt^3 - 48k^2r^2t^2$$
$$N_{m-n|n,0-2} = 24k^2r^2t^2$$

while the $N_{m-n|d,i-j}$ denominator terms:

$$N_{m-n|d,5-0} = -r^{10}t^2(4\nu + 4)$$
$$N_{m-n|d,4-1} = -r^8t^2(16\nu + 16)$$
$$N_{m-n|d,4-0} = -r^8t(4\nu + 4)(18kr^2 + kt^2 - 6k\nu r^2)$$
$$N_{m-n|d,3-2} = -r^6t^2(24\nu + 24)$$
$$N_{m-n|d,3-1} = -r^6(2\nu + 2)(5kt^3 - k\nu t^3 + 108kr^2t - 36k\nu r^2t)$$
$$N_{m-n|d,3-0} = -r^6(2\nu + 2)(144k^2r^4 - 144k^2\nu r^4 + 12k^2r^2t^2 - 12k^2\nu r^2t^2)$$
$$N_{m-n|d,2-3} = -r^4t^2(16\nu + 16)$$
$$N_{m-n|d,2-2} = -r^4(4\nu + 4)(2kt^3 - k\nu t^3 + 54kr^2t - 18k\nu r^2t)$$
$$N_{m-n|d,2-1} = -r^4(4\nu + 4)(3k^2\nu^2r^2t^2 - 144k^2\nu r^4 - 6k^2\nu r^2t^2 + 144k^2r^4 + 15k^2r^2t^2)$$
$$N_{m-n|d,1-4} = -r^2t^2(4\nu + 4)$$
$$N_{m-n|d,1-3} = -kr^4t(48\nu + 48) - r^2t(2\nu + 2)(12kr^2 + kt^2 - 12k\nu r^2 - k\nu t^2)$$
$$N_{m-n|d,1-2} = -kr^4(24\nu + 24)(12kr^2 + kt^2 - 12k\nu r^2 - k\nu t^2)$$

C.2 External pressure

In a similar format to that of Appendix C.1 for $N_{m-n,thick}$, the shear-flexible critical external normal pressure $p_{m-n,thick}$ for the bifurcation of non-shallow cylinders under centrally directed pressure, with finite-thickness effects considered, is provided as:

$$p_{m-n,thick} = \frac{Et}{r}\frac{\sum_{i=0}^{5}\sum_{j=0}^{5} p_{m-n|n,i-j}m^{2i}n^{2j}}{\sum_{i=0}^{5}\sum_{j=0}^{5} p_{m-n|d,i-j}m^{2i}n^{2j}} \tag{C.4}$$

with the terms involved in the numerator of the above relationship defined as:

$$p_{m-n|n,5-0} = 2kr^9t^3$$
$$p_{m-n|n,4-1} = 10kr^7t^3$$
$$p_{m-n|n,4-0} = 2r^7t^2(12k^2r^2 + k^2t^2 + 2\nu + 2)$$
$$p_{m-n|n,3-2} = 20kr^5t^3$$
$$p_{m-n|n,3-1} = r^5t(8t + 8\nu t - 8kt^2 + 5k^2t^3 - 4k\nu t^2 - k^2\nu t^3 + 96k^2r^2t)$$
$$p_{m-n|n,3-0} = r^5t(-24k\nu^2r^2 + 48k\nu r^2 + 4k\nu t^2 + 72kr^2 + 4kt^2)$$
$$p_{m-n|n,2-3} = 20kr^3t^3$$
$$p_{m-n|n,2-2} = 2r^3(2\nu t^2 - 10kt^3 + 2t^2 + 2k^2t^4 - 4k\nu t^3 - k^2\nu t^4 + 72k^2r^2t^2)$$
$$p_{m-n|n,2-1} = 2r^3(-24k^2\nu r^2t^2 - 48k^2r^2t^2 - 12k\nu^2r^2t + 24k\nu r^2t + 4k\nu t^3 + 36kr^2t + 5kt^3)$$
$$p_{m-n|n,2-0} = 2r^3(-144k^2\nu^2r^4 - 12k^2\nu^2r^2t^2 + 144k^2r^4 + 12k^2r^2t^2)$$
$$p_{m-n|n,1-4} = 10krt^3$$
$$p_{m-n|n,1-3} = -krt^2(16t + 4\nu t - 96kr^2 - kt^2 + k\nu t^2)$$
$$p_{m-n|n,1-2} = krt^2(8t + 4\nu t - 144kr^2 - 48k\nu r^2)$$
$$p_{m-n|n,1-1} = krt^2(60kr^2 + 36k\nu r^2)$$

$$
\begin{aligned}
p_{m-n|n,0-5} &= \frac{2kt^3}{r} \\
p_{m-n|n,0-4} &= -\frac{4kt^3 - 24k^2r^2t^2}{r} \\
p_{m-n|n,0-3} &= \frac{2kt^3 - 48k^2r^2t^2}{r} \\
p_{m-n|n,0-2} &= 24k^2rt^2
\end{aligned}
$$

and those in the denominator as:

$$
\begin{aligned}
p_{m-n|d,4-1} &= -r^8t^2(4\nu+4) \\
p_{m-n|d,4-0} &= r^8t^2(4\nu+4) \\
p_{m-n|d,3-2} &= -r^6t^2(16\nu+16) \\
p_{m-n|d,3-1} &= r^6t^2(16\nu+16) - 4r^6t(\nu+1)(18kr^2 + kt^2 - 6k\nu r^2) \\
p_{m-n|d,3-0} &= 4r^6t(\nu+1)(18kr^2 + kt^2 - 6k\nu r^2) \\
p_{m-n|d,2-3} &= -r^4t^2(24\nu+24) \\
p_{m-n|d,2-2} &= r^4t^2(24\nu+24) - 2r^4(\nu+1)(5kt^3 - k\nu t^3 + 108kr^2t - 36k\nu r^2t) \\
p_{m-n|d,2-1} &= 2r^4(\nu+1)(5kt^3 - k\nu t^3 + 108kr^2t - 36k\nu r^2t) - 2r^4(\nu+1)(144k^2r^4 \\
&\qquad -144k^2\nu r^4 + 12k^2r^2t^2 - 12k^2\nu r^2t^2) \\
p_{m-n|d,2-0} &= 2r^4(\nu+1)(144k^2r^4 - 144k^2\nu r^4 + 12k^2r^2t^2 - 12k^2\nu r^2t^2) \\
p_{m-n|d,1-4} &= -r^2t^2(16\nu+16) \\
p_{m-n|d,1-3} &= r^2t^2(16\nu+16) - 4r^2(\nu+1)(2kt^3 - k\nu t^3 + 54kr^2t - 18k\nu r^2t) \\
p_{m-n|d,1-2} &= 4r^2(\nu+1)(2kt^3 - k\nu t^3 + 54kr^2t - 18k\nu r^2t) - 4r^2(\nu+1)(3k^2\nu^2r^2t^2 \\
&\qquad -144k^2\nu r^4 - 6k^2\nu r^2t^2 + 144k^2r^4 + 15k^2r^2t^2) \\
p_{m-n|d,1-1} &= 4r^2(\nu+1)(3k^2\nu^2r^2t^2 - 144k^2\nu r^4 - 6k^2\nu r^2t^2 + 144k^2r^4 + 15k^2r^2t^2) \\
p_{m-n|d,0-5} &= -t^2(4\nu+4) \\
p_{m-n|d,0-4} &= t(4t(\nu+1) - 4kr^2(12\nu+12)) - t(2\nu+2)(12kr^2 + kt^2 - 12k\nu r^2 - k\nu t^2) \\
p_{m-n|d,0-3} &= (2t(\nu+1) - 2kr^2(12\nu+12))(12kr^2 + kt^2 - 12k\nu r^2 - k\nu t^2) \\
&\qquad +kr^2t(48\nu+48) \\
p_{m-n|d,0-2} &= kr^2(24\nu+24)(12kr^2 + kt^2 - 12k\nu r^2 - k\nu t^2)
\end{aligned}
$$

Appendix D

Strain-displacement $[B_l]$ and pseudo rotation $[G]$ matrices for shear-flexible axisymmetric shell element

The two necessary components for the computation of element stiffness matrices are provided here for completeness of the present document, as formulated according to the shear-flexible kinematic descriptions of Chapter 6. The linear strain-displacement matrix $[B_l]$ can subsequently be combined with the nonlinear component of Eq. 6.37 to produce the strain-displacement $[B]$ of Eq. 6.36 or be employed on its own to compute the material stiffness matrix in the context of a linear analysis (i.e. LA or LBA).

For both $[B_l]$ and $[G]$ arrays, presented shortly after, nodal DOF terms are assumed to be expressed in the local coordinate system of the element, a concept of this formulation that has been emphasised during the discussion of Chapter 6 as to facilitate a versatile interpolation framework that can accommodate further enhancements, corresponding to the discussion of Section 6.2.1 on the barriers introduced through a formulation built on global system DOFs. To maintain compactness of the arrays exhibited, only terms relating to an individual node are presented, with the notation relating to shape functions N (as well as their derivatives N' with respect to the isoparametric coordinate η) and geometric components that vary with respect to the meridional arc-length component s implying a reference to each node of the element (i.e. $N \equiv N_i$, $r \equiv r_i$, $\phi \equiv \phi_i$ etc.). This also permits extension of the element constructed to higher-order interpolation formulations through the introduction of additional nodes (see Fig. 2.9), facilitated by the necessary alterations of element topology and integration considerations.

D.1 Linear strain-displacement matrix $[B_l]$

The linear strain-displacement matrix $[B_l]$ is provided herein, defined in the more general context of a doubly-curved axisymmetric shell formulation, retaining terms relating to meridional curvature characteristics which can be readily dropped by setting $\partial\phi/\partial s = 0$ to obtain the straight meridian formulation employed in the computational examinations of Section 6.4. The terms in the following Eq. D.1 are derived on the basis of the linear kinematic expressions of Eqs. 6.16-6.18, with the rows of $[B_l]$ corresponding to the strains in that particular order.

$$
[B_l] = \begin{bmatrix}
\frac{N'}{L}\cos(n\theta) & 0 & N\frac{\partial\phi}{\partial s}\cos(n\theta) \\
\frac{N}{r}\cos\phi\cos(n\theta) & \frac{N}{r}n\cos(n\theta) & \frac{N}{r}\sin\phi\cos(n\theta) \\
-\frac{N}{r}n\sin(n\theta) & -\frac{N}{r}\cos\phi\sin(n\theta)+\frac{N'}{L}\sin(n\theta) & 0 \\
0 & 0 & 0 \\
0 & 0 & 0 \\
0 & 0 & 0 \\
-N\frac{\partial\phi}{\partial s}\cos(n\theta) & 0 & \frac{N'}{L}\cos(n\theta) \\
0 & -\frac{N}{r}\sin\phi\sin(n\theta) & -\frac{N}{r}n\sin(n\theta)
\end{bmatrix} \quad \cdots
$$

$$
\cdots \begin{bmatrix}
0 & 0 \\
0 & 0 \\
0 & 0 \\
\frac{N'}{L}\cos(n\theta) & 0 \\
\frac{N}{R}\cos\phi\cos(n\theta) & \frac{N}{R}n\cos(n\theta) \\
\frac{N'}{L}\sin(n\theta) & -\frac{N}{R}\cos\phi\sin(n\theta)+\frac{N}{R}n\sin(n\theta) \\
N\cos(n\theta) & 0 \\
0 & N\sin(n\theta)
\end{bmatrix} \tag{D.1}
$$

D.2 Pseudo rotation matrix $[G]$

Following presentation of the linear strain-displacement $[B_l]$ matrix in Eq. D.1 , the matrix $[G]$ relating local nodal DOFs to the pseudo rotations of the element according to Eq. 6.34. Whilst the pseudo rotations of Eqs. 6.22 are 12 in number, it is convenient to include the meridional β_ϕ and circumferential β_θ rotations of the element as the last rows of the $[G]$ array to aid in the computation of terms relating to nonlinear transverse shear strains as dictated by Eq. 6.21. These are not included here however to avoid their interpretation as pseudo rotations. The $[G]$ array formulation corresponding to s doubly-curved element is provided in Eq. D.2, where once again a singly-curved element may be obtained by setting $\partial\phi/\partial s = 0$.

$$
[G] = \begin{bmatrix}
-\frac{N}{L}\frac{\partial\phi}{\partial s}\cos(n\theta) & 0 & \frac{N'}{L}\cos(n\theta) \\
0 & \frac{N'}{L}\sin(n\theta) & 0 \\
\frac{N'}{L}\cos(n\theta) & 0 & N\frac{\partial\phi}{\partial s}\cos(n\theta) \\
0 & -\frac{N}{r}\sin\phi\sin(n\theta) & -\frac{N}{r}n\sin(n\theta) \\
-\frac{N}{r}\sin\phi\cos(n\theta) & -\frac{N}{r}n\cos(n\theta) & -\frac{N}{r}\cos\phi\cos(n\theta) \\
0 & \frac{N}{r}\cos\phi\sin(n\theta) & \frac{N}{r}n\sin(n\theta) \\
0 & 0 & 0 \\
0 & 0 & 0 \\
0 & 0 & 0 \\
0 & 0 & 0 \\
0 & 0 & 0 \\
0 & 0 & 0
\end{bmatrix} \quad \cdots
$$

$$
\cdots \begin{bmatrix}
0 & 0 \\
0 & 0 \\
0 & 0 \\
0 & 0 \\
0 & 0 \\
0 & 0 \\
-\frac{\partial\phi}{\partial s}\cos(n\theta) & 0 \\
0 & \frac{N'}{L}\sin(n\theta) \\
\frac{N'}{L}\cos(n\theta) & 0 \\
0 & -\frac{1}{r}\sin\phi\sin(n\theta) \\
\frac{N}{r}\cos\phi\cos(n\theta) & \frac{N}{r}n\cos(n\theta) \\
-\frac{N}{r}n\sin(n\theta) & -\frac{N}{r}\cos\phi\sin(n\theta)
\end{bmatrix} \tag{D.2}
$$

D.3 Stress resultants array $[N_0]$

Necessary for computation of destabilising effects introduced through the geometric stiffness matrix of Eq. 6.33b is the array $[N_0]$ comprising membrane, bending and shear stress resultants. Whilst the element programmed for the purposes of the computational investigations of Section 6.4 ignores the destabilising effects associated with bending behaviour of the axisymmetric shell, following the discussion provided by Jumikis (1987) on their importance for axisymmetric shell systems explored here, the corresponding terms are included in the following relation for $[N_0]$ to furnish a complete presentation of the element constructed in Chapter 6.

$$[N_0] = \begin{bmatrix} N_\phi & 0 & 0 & N_{\phi\theta} & 0 & 0 & M_\phi & 0 & 0 & M_{\phi\theta} & 0 & 0 \\ 0 & N_\phi & 0 & 0 & N_{\phi\theta} & 0 & 0 & M_\phi & 0 & 0 & M_{\phi\theta} & 0 \\ 0 & 0 & N_\phi & 0 & 0 & N_{\phi\theta} & 0 & 0 & M_\phi & 0 & 0 & M_{\phi\theta} \\ N_{\phi\theta} & 0 & 0 & N_\theta & 0 & 0 & M_{\phi\theta} & 0 & 0 & M_\theta & 0 & 0 \\ 0 & N_{\phi\theta} & 0 & 0 & N_\theta & 0 & 0 & M_{\phi\theta} & 0 & 0 & M_\theta & 0 \\ 0 & 0 & N_{\phi\theta} & 0 & 0 & N_\theta & 0 & 0 & M_{\phi\theta} & 0 & 0 & M_\theta \\ M_\phi & 0 & 0 & M_{\phi\theta} & 0 & 0 & 0 & 0 & 0 & 0 & 0 & 0 \\ 0 & M_\phi & 0 & 0 & M_{\phi\theta} & 0 & 0 & 0 & 0 & 0 & 0 & 0 \\ 0 & 0 & M_\phi & 0 & 0 & M_{\phi\theta} & 0 & 0 & 0 & 0 & 0 & 0 \\ M_{\phi\theta} & 0 & 0 & M_\theta & 0 & 0 & 0 & 0 & 0 & 0 & 0 & 0 \\ 0 & M_{\phi\theta} & 0 & 0 & M_\theta & 0 & 0 & 0 & 0 & 0 & 0 & 0 \\ 0 & 0 & M_{\phi\theta} & 0 & 0 & M_\theta & 0 & 0 & 0 & 0 & 0 & 0 \end{bmatrix} \tag{D.3}$$